CRANFIELD UNIVERSITY

CRANFIELD UNIVERSITY
LIBRARY

VOON HON WONG

AN EXPERIMENTAL AND NUMERICAL STUDY OF FLOW DISTRIBUTION CHAMBERS

1999.

SCHOOL OF MECHANICAL ENGINEERING

PhD THESIS

CRANFIELD UNIVERSITY

APPLIED MATHEMATICS AND

COMPUTING DEPARTMENT

SCHOOL OF MECHANICAL ENGINEERING

PhD THESIS

ACADEMIC YEAR: 1998-1999

VOON HON WONG

AN EXPERIMENTAL AND NUMERICAL STUDY OF FLOW DISTRIBUTION CHAMBERS

SUPERVISOR: Dr. C.P. THOMPSON

MAY 1999

Submitted in partial fulfilment of the requirements for the degree of Doctor of Philosophy

ACKNOWLEDGEMENTS

The author wishes to acknowledge the following people who have helped and contributed to the research: Chris Thompson, Pauline Avery, Stuart McGowan, Maurice Fayers, Bryan Bruce and all the lads in the workshop who built the test rig, John Knopp, Yolande Herbath who did a lot of the dirty work, Chris Riley, Sam Yang and Martin Yates who helped with the CFD, Tyrone White kindly donated his Cray time, Jacquie Barker allowed the use of her flume, Alan Reade, Clare Harper, and all the other people whom I have neglected to mention. Without their assistance, this PhD would have been so much more difficult. Many thanks to all of them.

CRANFIELD UNIVERSITY
LIBRARY

ABSTRACT

Flow distribution chambers are devices commonly used by the water industry to distribute flows in water and sewage treatment plants. These have simple designs, and are required to operate over a range of volumetric flowrates. Many chambers surveyed (Herbath and Wong, 1997b) were found to perform poorly. They suffered from flow mal-distribution, where the flow was not distributed according to design. The most common cause of flow mal-distribution was hypothesised to be due to the presence of a pipe bend below the chamber (Herbath and Wong, 1997a, 1997b). Therefore, an experimental and numerical study of the flow within a distribution chamber was conducted in this thesis to prove this hypothesis.

A novel large-scale model (1:13) of a typical distribution chamber was constructed. This allowed the collection of high quality and novel velocity and turbulence measurements near the free surface using hot film anemometry. The free surface location was measured using a vernier point gauge while the flow distribution between the outlets was metered by orifice plates. Records of the flow patterns were also kept.

The experimental results showed that flow mal-distribution did not occur as expected since the model distribution chamber was designed with a long length of straight inlet pipe, to eliminate the suspected cause of flow mal-distribution. Novel velocity and water surface data were also collected in the experiments, which contributed towards the small body of knowledge in this area of research into flow distribution.

CFD models of the physical model were created and solved using a commercial CFD code, CFX 4.1, developed by CFX International of AEA Technology. Steady state and transient two- and three-dimensional calculations of the symmetrical chamber were carried out in the course of the study. A novel adaptation of the existing code was made

in obtaining solutions to the numerical models. A new solution strategy was made and refined in this stage of the research using the two-dimensional representation of the distribution chamber, for reasons of reduced computational time. Differencing schemes, surface sharpening, mass residuals, mesh refinement and different turbulence models were investigated during model refinement. The accuracies of the calculated results were determined by comparison with experimental results. It was found that the 3D model, incorporating the RNG k-ε model, without surface sharpening, and using the Van Leer differencing scheme, gave good quantitative agreement with the experimental velocities, free surface location and flow distribution. The 2D results gave qualitatively good predictions. Quantitatively, the results were over-predicted which was due to dimensional effects. The volume of the 2D model was reduced from the 3D model, while the inlet velocity was made the same. This replicated the momentum effects near the free surface that were the governing causes of flow mal-distribution. Nevertheless, this approach was much more practical in terms of computational effort. More importantly, the correct trends for flow mal-distribution could be predicted accurately. Therefore, the next stage of the research used the 2D model developed and validated here.

This part of the research involved the novel adaptation of the existing symmetrical 2D results for investigating the asymmetric effects of pipe bends. Three different approaches for modelling the asymmetric effects of a pipe bend were investigated. The first, and the most simplistic, was to incline the incoming flow at an angle to the vertical. The second was to calculate the velocities and turbulence at the outlet of a simple 2D pipe bend, separate from the chamber. These calculated variables were then input into the chamber, to build up a picture of the asymmetric flow, iteratively. The third, and the most accurate method, was to couple the bend to the chamber. It was found that only the third method was capable of accurately representing the conditions within the chamber. Two different pipe bend lengths were examined using the third approach. The distances chosen were typical of the bend distances found in some treatment plants.

The results from both simulations produced large flow mal-distribution and asymmetric flows within the chamber. A value of 10% difference between the flows from the two outlets was taken to be the maximum limit for mal-distribution. However, values of 44.5% and 22.8% were obtained for the larger pipe distance and short pipe distance respectively.

Novel remediation strategies using numerical techniques were used to determine the most effective means of improving the flow distribution. The first, used a vertical flow splitter, placed directly above the chamber inlet. Although it altered the path of the jet, it was felt that it would be ineffective for all situations. Although the magnitude of the asymmetry was improved with the use of the splitter, the improvement was insufficient to warrant its recommendation. The other device tested was a horizontal plate located at a certain distance from the chamber inlet. For the longer bend case, a separation distance equivalent to two inlet hydraulic diameters was sufficient to deflect the jet, and reduced the magnitude of the flow asymmetry to around 2%. When the same plate location was used for the shorter bend case, the efficiency of the plate was reduced. Although there was an improvement in the distribution, the magnitude of the asymmetry was greater than 10%. The plate was subsequently lowered by half a hydraulic diameter. This gave a large improvement to the effectiveness of the plate, and the resulting asymmetry was reduced to 7.31 %.

The horizontal plate was considered more promising since its function was to deflect and reduce the peak velocities of the jet. With the reduction in velocities, the magnitudes of the nonlinear terms in the Navier-Stokes equations are reduced. The solution to the equations would be more likely to be symmetrical.

TABLE OF CONTENTS

ABSTRACT i

LIST OF FIGURES vii

NOMENCLATURE LIST xiii

1. INTRODUCTION 1

2. OBJECTIVES 4

3. LITERATURE REVIEW 6
- 3.1 Design of flow distribution chambers 6
  - 3.1.1 Estimation of the magnitude of the surface disturbance 7
  - 3.1.2 Effect of chamber geometry 12
  - 3.1.3 Estimation of the flow discharged from the outlet weirs 12
  - 3.1.4 Type and location of the inlet 15
  - 3.1.5 Outlet design 16
- 3.2 Hot wire anemometry 17
  - 3.2.1 Sensor frequency response 21
  - 3.2.2 Probe Calibration 23
    - 3.2.2.1 Steady state or static calibration methods 23
    - 3.2.2.2 Dynamic calibration techniques 26
  - 3.2.3 Heat transfer laws 26
  - 3.2.4 Yaw Calibration 30
- 3.3 Computational Fluid Dynamics 37
- 3.4 The Governing equations for fluid flow 39
- 3.5 Finite differencing schemes 40
  - 3.5.1 Discretisation of Diffusion terms 41
  - 3.5.2 Discretisation of the Advection terms 42
    - 3.5.2.1 Upwind Differencing 44
    - 3.5.2.2 Central Differencing 45
    - 3.5.2.3 Hybrid Differencing (HDS) 46
    - 3.5.2.4 Higher-order upwind differencing (HUW) 47
    - 3.5.2.5 MUSCL Schemes 47
- 3.6 Time stepping 49
- 3.7 Turbulence models 50
  - 3.7.1 k-ε turbulence model 50
  - 3.7.2 Renormalization Group (RNG) k-ε turbulence model 53
- 3.8 Multiphase model 55
  - 3.8.1 Homogeneous or Volume of fluid (VOF) model 55
- 3.9 Wall boundary conditions 57

	3.10	Summary of Literature Review	59
4.	THE EXPERIMENTAL TEST RIG		61
	4.1	Scaling Laws	65
	4.2	Instrumentation	68
		4.2.1 Flow measurement	68
		4.2.2 Turbulence measurements	68
		4.2.3 Measurement of water levels	69
		4.2.4 Temperature Measurements	69
		4.2.5 Data Acquisition System	70
	4.3	Sampling times, sampling frequencies and error estimates	70
		4.3.1 Experimental sampling frequencies	73
		4.3.2 Experimental Sampling times	74
	4.4	Measurement Accuracy	75
		4.4.1 Probe and vernier point gauge location	75
		4.4.2 Hot film measurements	76
		4.4.3 Free surface measurements	76
		4.4.4 Flow measurements and flow distribution	77
	4.5	Summary of Experiments	77
5.	EXPERIMENTAL TEST PROCEDURES		79
	5.1	Calibration of Instruments	79
		5.1.1 Hot Film Calibration	79
		5.1.2 Determination of probe effective angles and yaw factors	83
		5.1.3 Calibration of the vernier point gauge	83
	5.2	Test Procedures	84
	5.3	Test Matrix for Model A	85
	5.4	Conversion of raw voltages to velocities	86
	5.5	The determination of Reynolds normal and shear stresses	89
	5.6	Experimental Results	90
	5.7	Summary of Experimental Test Procedures	91
6.	NUMERICAL MODELLING		92
	6.1	The CFD Package	92
		6.1.1 The Pre-Processor	92
		6.1.2 The Solver	94
		6.1.3 Post-Processing	95
	6.2	Numerical models for symmetrical flows	95
		6.2.1 Two-dimensional, single phase, steady state flow	96
		6.2.2 Two-phase, two-dimensional steady-state model	97
		6.2.3 Two-phase, 2D transient models	100
		6.2.4 3D, transient two phase runs	106
		6.2.5 Solution strategy	107
		6.2.6 Turbulence levels	111

6.3 Numerical models for asymmetric flows 111
6.3.1 Uniform angled inflow 114
6.3.2 Decoupled pipe bend 114
6.3.3 Coupled pipe bend 115
6.4 Remedies to flow mal-distribution 117
6.4.1 Vertical flow splitter 117
6.4.2 Horizontal Plate 118

7. DISCUSSION OF RESULTS 120
7.1 Experimental results 120
7.1.1 Flowrate and distribution measurements 121
7.1.2 Water Level measurements 123
7.1.3 Velocity and turbulence measurements 127
7.1.4 Flow patterns 128
7.1.5 Quantification of the performance of a distribution chamber 130
7.1.6 Summary of Experimental Results 134
7.2 Validation of 2D steady-state CFD model 136
7.2.1 Single phase flow 137
7.2.2 2D steady-state, 2 phase flow model 139
7.2.3 Summary of the 2D Steady State CFD models 140
7.3 Validation of 2D and 3D transient models 141
7.3.1 Grid independence and turbulence models 141
7.3.2 Effects due to the surface sharpening algorithm 148
7.3.3 The Van Leer MUSCL differencing scheme 151
7.3.4 Reduced mass residuals 156
7.3.5 Increased volume in the flow domain 158
7.3.6 Dimensional Effects 160
7.3.7 Time Histories 165
7.3.8 Summary of numerical model validation 167
7.4 Asymmetric flow calculations 169
7.4.1 Approach 1: Angled inflow into chamber 169
7.4.2 Approach 2: Decoupled pipe bend 171
7.4.3 Approach 3: Coupled pipe bend 174
7.4.4 Summary of Pipe Bend Calculations 177
7.5 Solutions to flow mal-distribution 178
7.5.1 Vertical flow splitter 178
7.5.2 Horizontal Plate 180
7.5.3 Summary of results for mal-distribution reduction tests 184
7.6 Engineering Considerations 185
Figures for Chapter 7 189

8. CONCLUSIONS 338

9.	FUTURE WORK	346
10.	BIBLIOGRAPHY	348
APPENDIX A	CALIBRATION CERTIFICATES	A1
APPENDIX B	SETUP AND FORTRAN FILES	B1

LIST OF FIGURES

Chapter 3

Figure 3.1-1a Flow pattern for discharge of a jet into a shallow pool of water

Figure 3.1-1b Comparison between measured and predicted maximum water surface elevation

Figure 3.2-1 Schematic of the hot film probe used in the experiments

Figure 3.2-2 Simplified sketch of a typical constant current anemometer circuit

Figure 3.2-3 Simplified sketch of a typical constant temperature anemometer circuit

Figure 3.2-4 Sketch of hot wire probe showing yaw angle and velocity components

Figure 3.2-5 Definition of velocity components in cross wire coordinates

Figure 3.5-1 Illustration of notation used in description of control volume and nodes

Chapter 4

Figure 4-1 Schematic of the flow distribution model

Figure 4-2 Photograph of test rig.

Figure 4-3 Schematic showing inlet and outlet lines leading into test rig.

Chapter 5

Figure 5.1-1 View of perspex flume used in the calibration of the cross-wire probe

Figure 5.1-2 Photograph showing the probe connector and probe holder assembly with a protractor mounted on a vernier point gauge

Figure 5.4-1 Relationship between corrected voltages and square root of speed.

Chapter 6

Figure 6.2.3-1 17,850 cell geometry as used in 2D1, 2D2, 2D3, 2DRNG1 and 2DRNG2

Figure 6.3-1 Sketch showing pipe bend below distribution chamber.

Chapter 7

Figure 7.1-1 Measured flow distribution between outlets 1 and 2 at 2.95 l/s

Figure 7.1-2 Measured flow distribution between outlets 1 and 2 at 4.38 l/s

Figure 7.1-3 Measured flow distribution between outlets 1 and 2 at 5.51 l/s

Figure 7.1-4 View of free surface at 2.95 l/s

Figure 7.1-5 Photograph of boil on free surface at 4.38 l/s

Figure 7.1-6 Views of developing boil at 5.51 l/s

Figure 7.1-7 Example of raw voltage traces measured at the centreline of the jet, 0.631 m from chamber invert.

Figure 7.1-8 Photographs showing streaklines describing recirculation within chamber at 5.51 l/s.

Figure 7.1-9 View of air bubbles within collection box.

Figure 7.1-10 Photograph showing plunging curtain of water and subsequent air entrainment within collection box.

Figure 7.2-1 Calculated results for ST1, single phase steady state run using mass flow boundaries at outlets.

Figure 7.2-2 Calculated results for ST2. Run is similar to ST1 except pressure boundaries are used at outlets.

Figure 7.2-3 Calculated results for 2PH1. Steady state, two phase calculations.

Figure 7.3-1 Calculated results for 2D1. Transient two phase calculation, with flow at 2.95 l/s. Surface sharpening, hybrid differencing scheme and k-ε model used.

Figure 7.3-2 Calculated results for 2D2. Same as 2D1 except flow was increased to 4.38 l/s.

Figure 7.3-3	Calculated results for 2D3. Flow was increase to maximum of 5.51 l/s.
Figure 7.3-4	Calculated results for 2DIndy, the grid independence run with flow at 4.38 l/s.
Figure 7.3-5	Quantitative comparisons of 2D2 and 2DIndy.
Figure 7.3-6	Quantitative comparisons of experimental results and the 2D calculations (2D2, 2DIndy, 2DRNG1, 2DRNG2, 2DRNGV1, 2DRNGV2).
Figure 7.3-7	Calculated results for 2DRNG1. Flow in is 4.38 l/s. Van Leer differencing scheme, and RNG k-ε models used.
Figure 7.3-8	Calculated results for 2DRNG2. Similar to 2DRNG1 except for tighter mass source tolerance.
Figure 7.3-9	Quantitative comparisons of velocities, turbulence and water levels for Pipebnd3 and Pipebnd4. Coupled pipe bend calculations which direct comparisons of hybrid and Van Leer differencing schemes.
Figure 7.3-10	Calculated results of 2DRNGV1. Similar to 2DRNG1 except flow domain has been increased in volume.
Figure 7.3-11	Calculated results of 2DRNGV2. Similar to 2DRNGV1 except for tighter mass source tolerance.
Figure 7.3-12	Calculated results of 2DRNGC1. Similar to 2DRNGV1 except that weir crest level set to 0.631 m, as in experiments.
Figure 7.3-13	Calculated results of 2DRNGC2. Similar to 2DRNGC2, with tighter mass source tolerance.
Figure 7.3-14	Quantitative comparisons between experimental, 2DRNGC1 and 2DRNGC2 results, showing effects of mass source tolerance.
Figure 7.3-15	Calculated results for 3DRNG1. 3D, two phase, transient run with flow at 2.95 l/s.
Figure 7.3-16	Calculated results for 3DRNG2. Flow in is 4.38 l/s.
Figure 7.3-17	Calculated results for 3DRNG3. Flow in is maximum at 5.51 l/s.

Figure 7.3-18	Quantitative comparisons between experimental and 3DRNG1 results.
Figure 7.3-19	Quantitative comparisons between experimental and 3DRNG2 results.
Figure 7.3-20	Quantitative comparisons between experimental and 3DRNG3 results.
Figure 7.3-21	Time history plots for 3DRNG2.
Figure 7.4-1	Calculated results for Bend2. Pipe bend simulation, using results from 2DRNGC2, with inflow at 2° to vertical axis.
Figure 7.4-2	Calculated results for Bend5. Flow in is at 5° to vertical.
Figure 7.4-3	Calculated results for Bend10. Flow is at 10° to vertical.
Figure 7.4-4	Calculated results for Bend12. Flow is at 12.5° to vertical.
Figure 7.4-5	Calculated results for Bend15. Flow is at 15° to vertical.
Figure 7.4-6	Calculated results for Pipebnd1. Pipe bend simulation using a decoupled pipe bend. This is the first iteration in simulation.
Figure 7.4-7	Time history plots for Pipebnd1.
Figure 7.4-8	Calculated results for Pipebnd2. This is similar to Pipebnd1, except that the inlet boundary conditions were changed as this is the second iteration.
Figure 7.4-9	Time history plots for Pipebnd2.
Figure 7.4-10	Calculated results for Pipebnd3. Pipe bend is coupled to chamber. Hybrid differencing scheme is used. The pipe bend is 2.12 D_h from chamber.
Figure 7.4-11	Calculated results for Pipebnd4. This is similar to Pipbnd3 except that Van Leer differencing scheme is used.
Figure 7.4-12	Calculated results for Pipebnd5. The pipe bend distance is decreased to 1.25 D_h. Van Leer scheme is used.
Figure 7.4-13	Plot of asymmetry, a, for Bend2, Bend5, Bend10, Bend12 and Bend15.

Figure 7.5-1	Calculated results for Bndsplt1. A vertical flow splitter is added to chamber in order to correct flow mal-distribution.
Figure 7.5-2	Time history plots for Bndsplt1.
Figure 7.5-3	Calculated results for Plate1. A horizontal plate is placed above inlet of chamber with the longer pipe bend.
Figure 7.5-4	Calculated results for Plate2. Similar to Plate1 except that the shorter pipe bend is used.
Figure 7.5-5	Calculated results for Plate3. Similar to Plate2 except that the horizontal plate has been lowered by half a hydraulic diameter.
Figure 7.5-6	Time history plots for Plate3.
Figure 7.6-1	Quantitative comparison between pressure gradients for Pipebnd4, Bndsplt1 and Plate1.
Figure 7.6-2	Quantitative comparison between pressure gradients for Pipebnd5, Plate2 and Plate3.

NOMENCLATURE LIST

Symbol	Meaning	Units
a	Asymmetry. Difference between the flow out of each outlet	%
A	Cross-sectional area	m^2
B	Height from channel invert to weir crest	m
B	Body force term in momentum equations (Consists of buoyancy force only in this type of flow)	$kg/(ms)^2$
C_D	Coefficient of discharge	-
C_{cell}	Cell convection coefficient	-
c	Specific heat of fluid	J/Kg K
D	Diameter	m
D_{cell}	Cell diffusion coefficient	-
D_h	Hydraulic diameter	m
E	Wheatstone bridge voltage	V
E_0	Jet energy flux	-
Fr	Froude number	-
f_{min}	Minimum frequency	1/s
f_{max}	Maximum frequency	1/s
G	Production term due to body force in k-ε and RNG k-ε models	
g	Acceleration due to gravity	m/s^2
ΔH	Head loss	m
H	Total head	m
h_h	Piezometric or hydraulic head	m
h	Height of boil	m
h_{cl}	Height of boil at the centreline of the jet	m
h_v	Velocity head	m

h	Yaw factor for binormal component of velocity	-
h_w	Distance between neighbouring nodes of cells	m
I_s	Total current through hot wire sensor	A
$\overline{I_s}$	Averaged component of total current	A
i_s	Fluctuating component of total current	A
k	Turbulent kinetic energy	m^2/s^2.
k	Yaw factor for tangential components of velocity	-
L_w	Length of weir	m
l	Length of hot wire sensor	m
N	Number of samples	-
N_p	Number of phases	-
P, p	Pressure	N/m^2
P	Turbulent shear production term	
Pe_h	Cell Peclet number	-
Q	Volumetric flowrate	m^3/s.
Q	Magnitude of mean velocity vector	m/s
R	Half width (or radius) of distribution chamber	m
R_s	Total electrical resistance of hot wire sensor	Ω
$\overline{R_s}$	Mean resistance of hot wire sensor	Ω
R_0	Reference electrical resistance of hot wire sensor	Ω
R_f	Electrical resistance of fluid	Ω
Re	Reynolds number	-
r	Volume fraction	-
S	Volumetric source term	
T_s	Hot wire sensor temperature	K
T_f	Fluid temperature	K
t	Time	s

TV	Total variation of the domain	-
TV_h	Total variation of the cell	-
U	Velocity in vector notation	m/s
$\overline{U}$	Averaged velocity	m/s
U	Averaged inlet velocity	m/s
U_T	Velocity averaged over time	m/s
U_N	Ensemble average of velocity	m/s
u	Fluctuating component of velocity in vector notation	m/s
u_m	Centreline jet velocity	m/s
u_i	Inlet velocity	m/s
V	Volume	m^3
V_{app}	Velocity of approach	-
v	Flow velocity	m/s
W	Width of chamber upstream of outlet weir (Section 3.1.3)	m
y	Total head of flow	m

Greek notations

α	Temperature coefficient of resistivity	-
γ	Yaw angle	°
α_1, α_2	Cross wire angles for first and second sensors	°
ρ	Density	Kg/m^3
ε	Dissipation rate of turbulent kinetic energy	m^2/s^3
ϵ_f	Expansibility factor	-
ϵ	Relative error	-
T	Time constant	s
τ	Wall shear stress	N/m
Φ	Scalar quantity	-

ϕ	Transported quantity	-
ς	Bulk viscosity	Pa s
Γ_T	Eddy diffusivity	Pa s
ψ	Flux limiter	-
μ	Dynamic viscosity	Pa s
ν	Kinematic viscosity	m^2/s
μ_T	Eddy viscosity	Pa s
μ_{eff}	Effective viscosity	Pa s
σ_T	Turbulent Prandtl number	-
η	Kolmogorov micro scale	-

Subscripts

α	Phase number
E	East cell face
W	West cell face

1. INTRODUCTION

The distribution of flow is important in both water and waste water treatment plants. Raw water and sewage will undergo several treatment stages before being piped away to the consumer or discharged into rivers or the sea. Within each treatment stage, there are usually multiple tanks that treat the water or sewage in parallel. Flow distribution devices serve to divide the incoming flow to those tanks. To ensure effective treatment, the incoming flows into each tank must firstly be within the efficient range of the design, and secondly be within the designed percentage split.

One consequence of a poor flow split may result in the necessity to recycle the output from that treatment stage back to the inlet, effectively treating the flow again. Also, if chemicals are added as part of the treatment process, under-treatment may result if the flow is greater than the designed value. Conversely, the reverse will happen if the flow is less than the designed value. Hence the treatment process will become less efficient, with implications for the overall running costs of the entire treatment plant.

Flow distribution chambers are commonly used in sewage treatment plants to distribute flows. They are simple structures, consisting of a tank, rectangular or circular in plan. The top is open to atmosphere. It would have two or more outlets, with either side weirs or orifices as flow control devices. The flow exiting the chamber would be conveyed to the treatment tank downstream. The flow entering the chamber can enter either from the side or from the bottom of the chamber, via a pipe or a rectangular culvert. Despite their simplicity, the performance of distribution chambers and the flow behaviour within it are still not well understood. The usual assumption made by many designers is that the provision of a symmetrical layout for the chamber would result in symmetrical flow distribution, which is rarely true.

Previous physical model studies had examined the performance of distribution chambers (Reade et al, 1994, Reade and Wong, 1995). Despite the apparent symmetry of the

design, mal-distribution is found to occur for a range of flows.

Measurements of the flow distributions were made in those studies, but not velocities, nor turbulence. Hence, there is insufficient experimental data for these structures. There is no information available for distribution chambers in the open literature, despite their widespread use in the water industry. Thus, it is necessary to obtain the relevant velocity, turbulence and free surface information in this study. The experimental data presented in the following chapters is a first contribution of quality information towards flow distribution chambers. This also allowed the CFD models to be validated.

CFD modelling of the flow behaviour in these structures provides advantages in both cost and time, especially when different flow conditions and geometries need to be investigated. While many researchers have modelled free surfaces for a variety of applications in the past, none have applied this to distribution chambers. Thus, the novel use of CFD modelling techniques is applied to distribution chambers in this study. Additionally, the difficult region of flow near the discharge weirs of a chamber is modelled. The turbulent region downstream of the weirs, within the flow collection boxes, which contained a large amount of entrained air bubbles are also modelled successfully in this study.

The objectives for this study are given in Chapter 2.

A literature review of the relevant work on distribution chambers is made in Chapter 3. Experimental techniques involving hot film/wire anemometry and flow visualization are also touched upon. Finally, an introduction to CFD modelling is covered.

Chapter 4 is a description of the physical model which was constructed. Discussions of the scaling laws are also given. The accuracies of the experimental measurements are discussed.

The experimental procedures for the test rig are described in Chapter 5. The descriptions give an insight into the methods and procedures necessary to run the test rig, and the operation of the hot wire anemometer.

Chapter 6 details the CFD work carried out. Descriptions of the numerical validations, pipe bend simulations and calculations involving flow modifying structures are given. The solution strategy refined during the validation phase of the study is described.

A discussion of the results of the experiments and CFD modelling are given in Chapter 7. The various factors of importance, affecting the accuracy of the calculations are investigated and described. Qualitative and quantitative comparisons between the two are also shown and discussed. The asymmetric calculations and the remediation phases of the study are also discussed in detail here. Additionally, the practicality of the solutions investigated are also considered.

The conclusions arising from the results are given in Chapter 8. The recommendations for further work are presented in Chapter 9.

2. OBJECTIVES

This chapter serves as a guide through the various stages of the research work carried out and presented here in the thesis.

The first objective was to conduct a literature search of any related work on flow distribution chambers. Experimental techniques used by other researchers, to measure velocities and turbulence in fluid flow were also reviewed. CFD techniqués to accurately model free surface flows were also researched.

High quality and novel experimental data had to be collected from a simple distribution chamber, whose design was typical of those found in treatment plants. The chamber was also required to generate symmetrical flows, which would allow validation of the symmetrical CFD models of the chamber.

Numerical models of the distribution chamber had to be created. Due to the nature of the flow, which is ill-posed, it was necessary to begin with a simple 2D representation of the chamber, with single phase water and steady state calculations. This was followed by two-phase, steady state calculations for the 2D model. This progression of model complexity allowed the determination of the most appropriate outlet boundary conditions to be determined. Also, the time dependancy of the problem could also be determined. This finally led to transient two-phase calculations were made for both 2D and 3D models.

The accuracies of the 2D and 3D transient, two phase models were validated against the experimental data. This allowed the development of the solution techniques necessary for more accurate answers. It was hypothesised that the presence of a pipe bend below the chamber was the main cause of flow mal-distribution (Herbath and Wong, 1997a). Thus, the validation allowed the numerical models to be used for the next stage of the research - simulation of the effect of pipe bends and the remediation techniques.

The most accurate and cost-effective method for simulating pipe bends had to be determined. The degree of flow mal-distribution caused by the pipe bends had to be quantified.

Different remediation techniques for reducing or eliminating the flow mal-distribution identified, had to be found.

3. LITERATURE REVIEW

3.1 Design of flow distribution chambers

The distribution of the flow of sewage or raw water in sewage and water treatment works, respectively, is a very common function which plays a vital and important role in the efficient operation of the plant. There are various ways with which to distribute the flow, such as pipe manifolds, distribution channels, cut waters, and flow distribution chambers. Miller (1990) lists the important variables which govern the performance of pipe manifolds. An iterative procedure for the determination of the distribution flow is given. A rule of thumb method where the performance of the manifold can be estimated readily is also given. The design of flow distribution channels are also equally well understood. Chao and Trussell (1980) lists a similar iterative method which can be used to determine the distribution of flow between outlets of the channel.

There are numerous ways in which flows in water and sewage plants can be distributed among the numerous treatment stages. Sewage contains solids present in the flow. Plant designers try to maintain flow velocities above a critical value (usually greater than 0.1 m/s) in order to keep the solids in suspension. It is only desirable to allow the solids to come out of suspension in the relevant treatment tanks, where they can be removed. Thus, distribution channels, with their long lengths, would be in danger of being silted up over time if flow velocities within them are insufficient to keep the solids in suspension. Similarly, for pipe manifolds, the pipes can become silted/sludged up over time. Physically removing the sludge would be even more difficult in pipes than an open channel. Cut waters are simple flow devices usually placed in an open channel. Their function is to divide the channel into two or more sections. In this way, as the water flows past, the cut waters act like vanes and divert the flow into the various branches of the channel downstream. Thus, cut waters can suffer from the same disadvantages as distribution channel, ie. solids coming out of suspension. This is especially true when flow separation occurs immediately downstream of these vanes.

Flow distribution chambers, on the other hand, usually have relatively high flow velocities due to the jet that is formed within the chamber. Most of the solids would remain in suspension, due to the relatively intense mixing resulting from the recirculation zones that would be formed within the chamber. Another advantage a distribution chamber would have in comparison with a channel is its relatively compact dimensions. While it would be necessary to excavate a much deeper hole during construction, its dimensions allow the chamber to be fitted in amongst the treatment tanks much more easily, than a long channel. Since very little is known about the correct design of chambers in terms of good flow distribution, plant designers assume that a symmetrical layout would suffice to ensure equal flow distribution. Distribution channels and pipe manifolds, on the other hand, require tedious iterative calculations in order to obtain the correct spacing between the outlets or side branches along the channel or manifold. Hence, chambers are relatively easier to design than the other devices, thus their attraction.

There is still very little knowledge about distribution chambers. Simple design rules were produced by Herbath and Wong (1997a) which were based on the site measurements and surveys made by Herbath and Wong (1997b) for Dwr Cymru. These design steps are reviewed in the following subsections.

3.1.1 Estimation of the magnitude of the surface disturbance

One of the features of a distribution chamber is the appearance of surface disturbance or surface "boil". This is caused by the formation of a jet due to the flow leaving the inlet into the chamber. Herbath and Wong (1997a) estimated the magnitude of this boil by determining the centreline jet velocity at the water surface. The Goertler equation for an axisymmetric jet (Rajaratnam, 1976) was used. When $6.5 < B/D < 30$,

$$u_m = 6.5\ u_i \times \frac{D}{B} \qquad (3.1\text{-}1a)$$

where D is the diameter of the chamber, and B is the height of the weir crest measured from the invert

when B/D < 6.5, then,

$$u_m = u_i \qquad (3.1\text{-}1b)$$

where u_m = centreline jet velocity,

u_i = inlet velocity

The vertical component of the centreline jet velocity was then converted into velocity head, giving an estimate of the deflection of the free surface,

$$h = \frac{u_m^2}{2g} \qquad (3.1\text{-}2)$$

where h = height of the boil.

In his state of the art review of turbulence models, Rodi (1993) compared the experimental data from Murota and Muraoka, (1967) with the k-ε model predictions by McGuirk and Rodi (1977), for a non-buoyant submerged jet discharging in shallow water. In their model the free surface was treated as a "rigid lid". The model was found to give good prediction for the flow. The maximum water surface elevation was also compared and shown in Figure 3.1-1b. The predicted flow patterns are shown in Figure 3.1-1a.

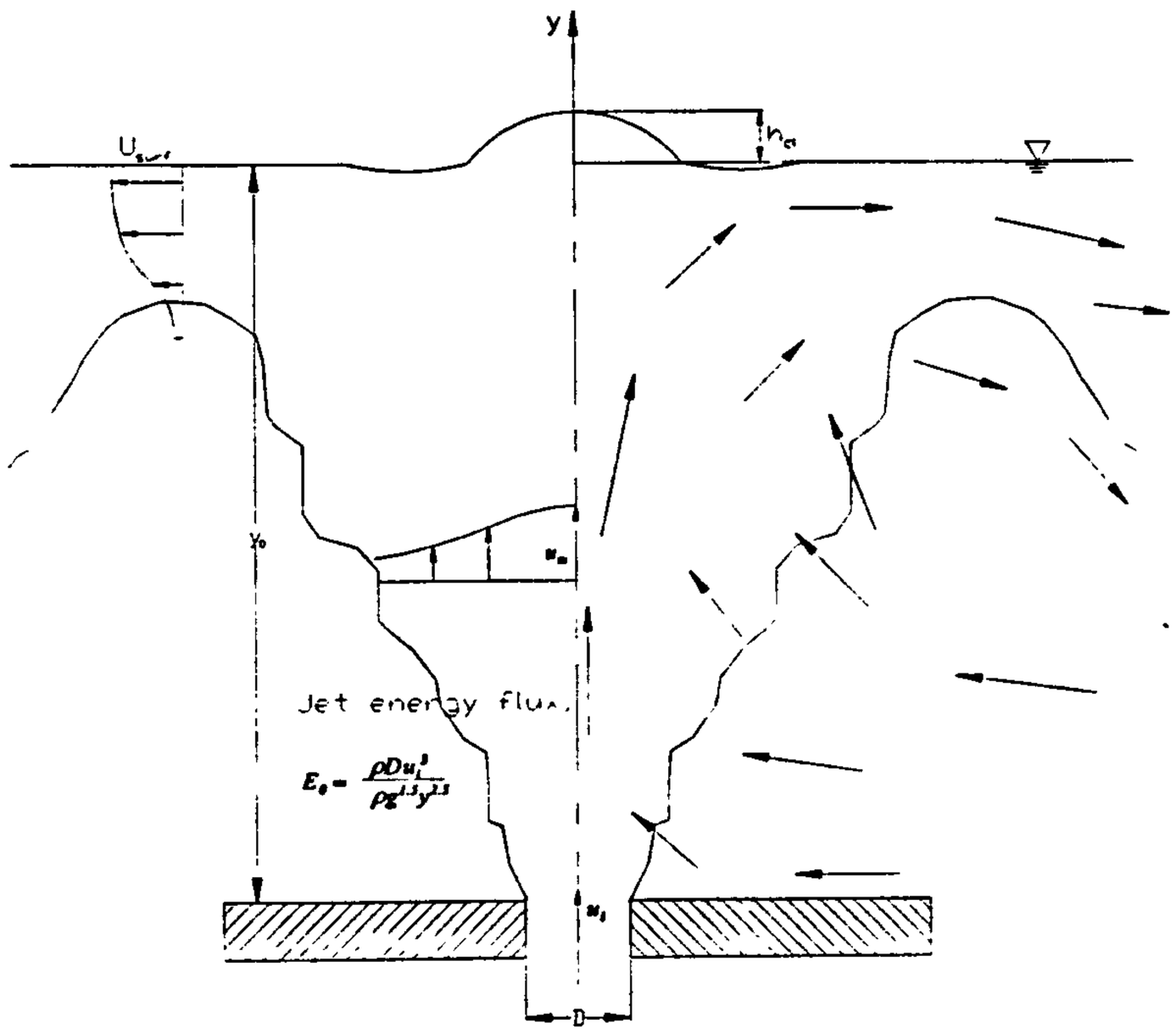
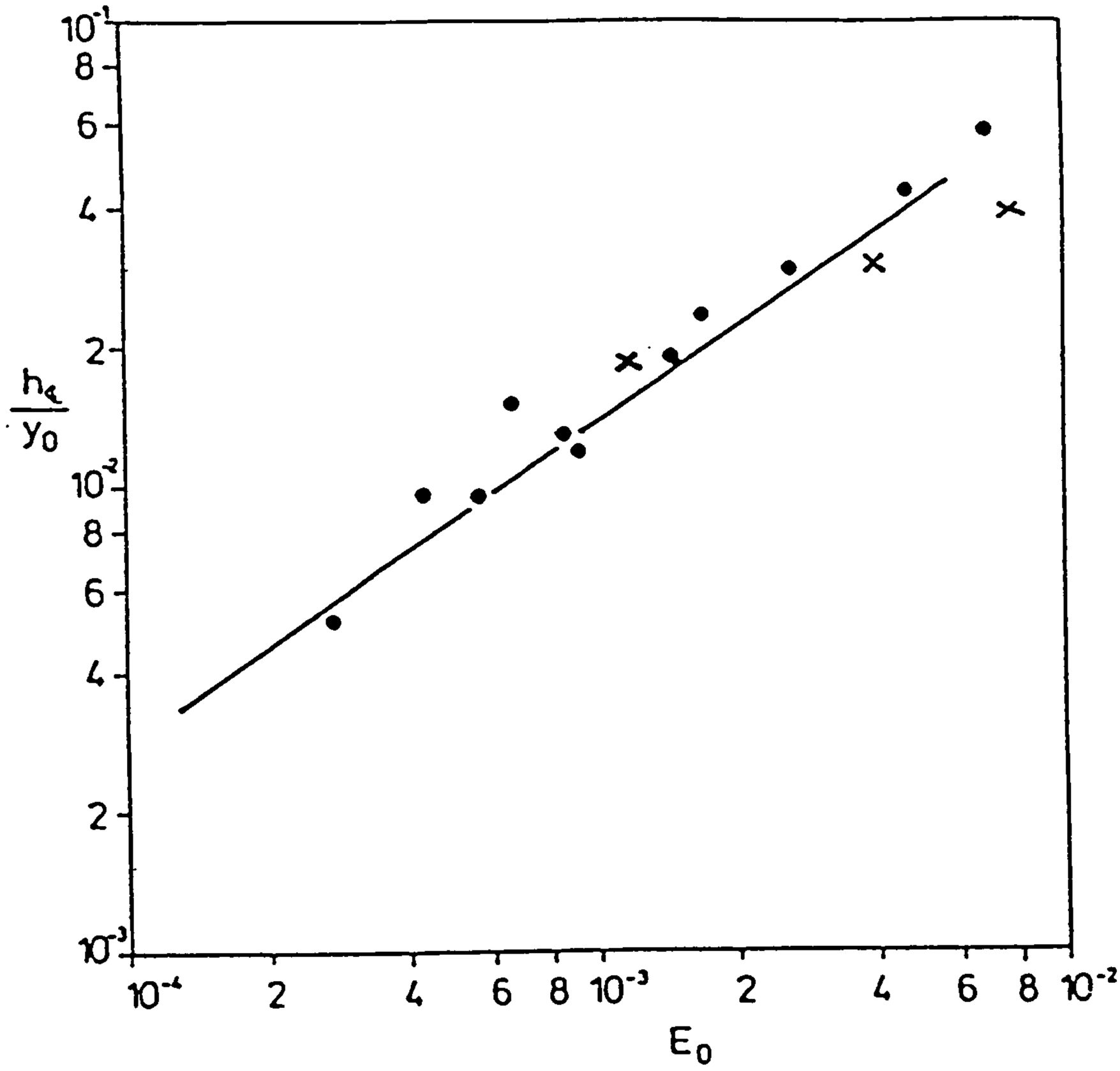


Figure 3.1-1a Flow pattern of the discharge of a jet into a shallow pool of water showing the surface boil and recirculating flow patterns (after McGuirk and Rodi, 1977)

The experimental data from this study is superimposed on the graph in Figure 3.1-1b. These show that the present study's results are comparable to the model using the k-ε turbulence model with a rigid lid. It should be noted that the experimental data of Murota and Muraoka (1967) are strictly for a jet discharging into a large, shallow pool of water, as opposed to a distribution chamber. The flow within a chamber are bounded by walls, and the turbulence would not be isotropic. Hence, the use of the k-ε model would not give an accurate prediction of the flow behaviour. Nevertheless, the results shown in Figure 3.1-1b do suggest that as a first approximation, the rigid lid assumption

using the k-ε model can give an indication of the magnitude of the boil.



× Expt. data from present study.

• Expt. data of Murota and Muraoka

- Predictions with rigid lid assumption by McGuirk & Rodi

where

$$E_0 = \frac{\rho D u_i^2}{\rho g^{1.5} y_0^{2.5}}$$

u_i = inlet velocity
D = inlet diameter
ρ = fluid density
y_0 = water level
g = acceleration due to gravity
h_{cl} = height of boil at the centreline

Figure 3.1-1b Comparisons between experimental data of Murota and Muraoka (1967), and present study, and the predictions by McGuirk and Rodi (1977), for a non-buoyant plane vertical jet in shallow water

3.1.2 Effect of chamber geometry

Due to the unsteady nature of the "boil" formation (i.e. the magnitude, and location varies over time), a "boil" of sufficient magnitude can affect the distribution of the flow between the multiple outlets of the chamber.

The displacement of the boil from the centreline of the tank can be partly due to the presence of a pipe bend upstream of the inlet into the chamber. This can have an adverse effect on the flow distribution. The effects of the pipe bend, as well as the size of the chamber, was accounted for in the recommendations given by Herbath and Wong (1997a). The half width, or radius of the chamber, the ratio of the distance of the bend to the inlet, and the diameter of the inlet, are taken into account. Recommended ranges of these values are given in order to avoid poor flow distribution. The details of these are given and discussed in Section 7.1.5.

While the guide presents the plant designer with the variables of importance, and useful rules of thumb for the design of distribution chambers, there is no quantification for the effects of any asymmetry within the system on the distribution of flow. Also, the values given in the geometry ratios of importance were based on experiments on distribution chambers. These are by no means universally applicable to all distribution chambers.

3.1.3 Estimation of the flow discharged from the outlet weirs

Herbath and Wong (1997a) recommends a method based on a weir discharge equation, as given in ISO-1438/1-1980(E), for the determination of the discharge of flow from each outlet of the distribution chamber. This method is applicable only for chambers with freely discharging side weirs. The calculation method is based on that given by Rehbock (Webber, 1971).

This method involves the measurement of the head over the weir crest. The value is substituted into the equation given below:

$$Q = \frac{2}{3}\sqrt{2g}\,L_w\left(0.602 + 0.083\frac{(y - B)}{B}\right)[(y - B) + 0.012]^{3/2} \qquad (3.1\text{-}3)$$

where Q is the volumetric flowrate

L_w is the weir length

y is the total head of the flow

B is the height of the channel invert to the weir crest

y-B is the head of water over weir crest

The limits of application of this equation are:

$0.3\text{ m} < y < 0.75\text{ m}$, $L_w > 0.3\text{ m}$, $B > 0.1\text{ m}$, and $y < B$, which were empirically derived.

The SIA equation (ISO-1438/1-1980(E)) gives an alternative way to determine the head of water over the weir for a given discharge. The equation is,

$$Q = \frac{2}{3}C_D L_w (y - B)^{3/2}\sqrt{2g} \qquad (3.1\text{-}4)$$

C_D is given by the following relationship,

$$C_D = \left[0.578 + 0.037\left(\frac{L_w}{W}\right)^2 + \frac{0.003615 - 0.003\left(\frac{L_w}{W}\right)^2}{(y - B) + 0.0016}\right]$$

$$\times \left[1 + 0.5\left(\frac{L_w}{W}\right)^4 \cdot \left(\frac{y - B}{y}\right)^2\right]$$

where W is the width of the chamber upstream of the weir.

This equation, is applicable for structures whose dimensions which fall within the following ranges,

$0.025W/(L_w) < (y\text{-}B) < 0.8$ m, $L_w/W > 0.3$, $(y\text{-}B)/B \leq 0.1$, and $B > 0.3$ m, which were also empirically derived.

The use of equation 3.1-3 will give a crude estimate of the discharge from each weir. This method of estimation requires the physical measurement of the head over each discharge weir which may not be practical on some plants as the chambers may be covered or the weirs may be inaccessible.

Both equations were developed for a steady, fully developed flow discharging over a modular (or freely discharging weir). These conditions may not be met for the flow in a distribution chamber due to the limited size of the chamber to allow fully developed flow. Note that in open channel flows, the recommended minimum length in the channel for fully developed flow is 40 hydraulic diameters upstream of the weir (Hinze, 1975). This figure was based on Nikuradse's experiments (1932).

Hence, the use of these methods would not be strictly applicable for distribution chambers, since the flow upstream of each discharge weir would not be fully developed. Nevertheless, these equations provided a means of estimating the head levels over the weir crests.

3.1.4 Type and location of the inlet

Most flow distribution chambers would have one inlet piping in flow into the chamber to be re-distributed to the next treatment stage.

There are usually two locations for the inlet. The first is in the centre of the chamber, entering it vertically from the floor. The other would have the flow enter horizontally from an opening in one of the walls of the chamber. The choice of entry for the flow may be dictated by construction costs. Excavating a deep hole to accommodate a pipe entering the chamber vertically would be less attractive than a side inlet. Hence, it is not unusual to see both types of designs in the treatment plants.

The problem with a side inlet is that the jet is directed towards the opposite wall of the chamber. This would result in a very turbulent flow within the chamber. It would also make any modifications to improve flow distribution more difficult.

The subject of this investigation is the more common chamber of the two - one where the inlet is located at the floor, and coinciding with the centreline of the chamber.

A chamber with a side entry would have a significantly different flow patterns within it. Also, the probability of flow mal-distribution would also be much greater since the flow within the chamber would be inherently asymmetric. The methods described above in estimating discharge over the weirs would similarly suffer from the same drawbacks described previously, ie. developing flows upstream of the weir crests. One would also expect the degree of accuracy of the adapted prediction methods to be even more

inaccurate for such cases. Side entry chambers would warrant further work since it is anticipated that the flows within the chamber would be even more complex than the type of chamber studied here.

3.1.5 Outlet design

As with the design of the inlet, there are usually several types of outlets used in chambers. The more common type is to have discharge weirs acting as flow control devices. However, submerged orifices may also be used. These are essentially openings, square or round, cut into the walls of the chamber. The flow will pass out into the culverts or pipes downstream of the orifices, and be passed directly into the treatment tanks downstream.

The flowrate through a submerged orifice is dependant on several factors, such as the discharge coefficient associated with the design of the orifice and the head difference across the orifice. In such situations, if the water levels downstream of the chambers are equal for all tanks, then the distribution is likely to be equal (Herbath and Wong, 1997b). The discharge through an orifice is given by :

$$Q_{orifice} = C_D A \sqrt{2g\Delta H}$$

where ΔH = head loss across the orifice (difference in head between the upstream and downstream side of the orifice).

The cross-sectional area, A, of the orifice opening, and gravity, g are fixed. The value for the discharge coefficient is dependent on the Froude number of the flow passing through the orifice. The empirical loss coefficient can be expressed as:

$$C_D = 0.611 \left(1 - 0.475 \left(\frac{v}{\sqrt{gy}} \right)^2 \right)$$

In order to have the same flowrate across each orifice, the velocities and the head difference across the orifice will have to be the same.

However, if there is flow mal-distribution, remedies for this would be more difficult and expensive since the flow conditions downstream in the treatment tanks affect the flow conditions within the chamber (ie. the flow within the chamber is drowned)

The more common of the two types of outlets is to use discharge weirs, which is the subject of the investigation.

3.2 Hot wire anemometry

The experimental measurements of the velocities and turbulent kinetic energies were obtained using hot wire anemometry. An introduction to these devices and their construction is given below. The calibration techniques, and the analysis of the hot wire data are also reviewed.

Researchers have been using the hot wire or hot film anemometry for turbulent flow measurements for many years. It is a mature and well developed technique. Experiments using hot wires were carried out as early as 1902 by Shakespear (Lomas, 1986). King (1915) published an important paper that described the design and the theory of convection of heat from cylinders immersed in a stream of liquid that is the basis of hot wire anemometry. A brief review of the history of hot wire anemometry is given by Comte-Bellot (1976).

Hot wire and hot film anemometers are devices used to measure the turbulent flow properties such as the mean and fluctuating velocity components, temperature, kinetic energies. The sensors are thin metallic elements heated by an electric current and cooled by the incident flow. From the resistance and/or temperature attained by the sensor, deduction of information of the flow is then possible. Nowadays, with electronic

amplification and shaping networks added to the anemometers, this instrument has become a sophisticated, high-frequency response research instrument whose popularity has grown. Lomas (1986) mentions that a frequency response of 400 kHz from hot wires is attainable from commercial equipment. Only the Laser Doppler, but non-intrusive anemometer can compete against this although it is up to ten times the cost. Additionally, the hot wire anemometer has excellent sensitivity at low velocity, good spatial resolution, and an output signal in the form of a voltage difference for convenient data analysis.

Figure 3.2-1 is a schematic of a hot film probe as used in the experiments. Figure 3.2-3 shows a simplified Wheatstone bridge circuit of a constant temperature anemometer unit, to which the hot wire sensor forms just one arm of the bridge. With a feedback amplifier, a constant resistance may be maintained in the sensor despite any changes in cooling velocity of the surrounding fluid medium. Measuring the voltage output of the bridge circuit will give information on the flow velocities.

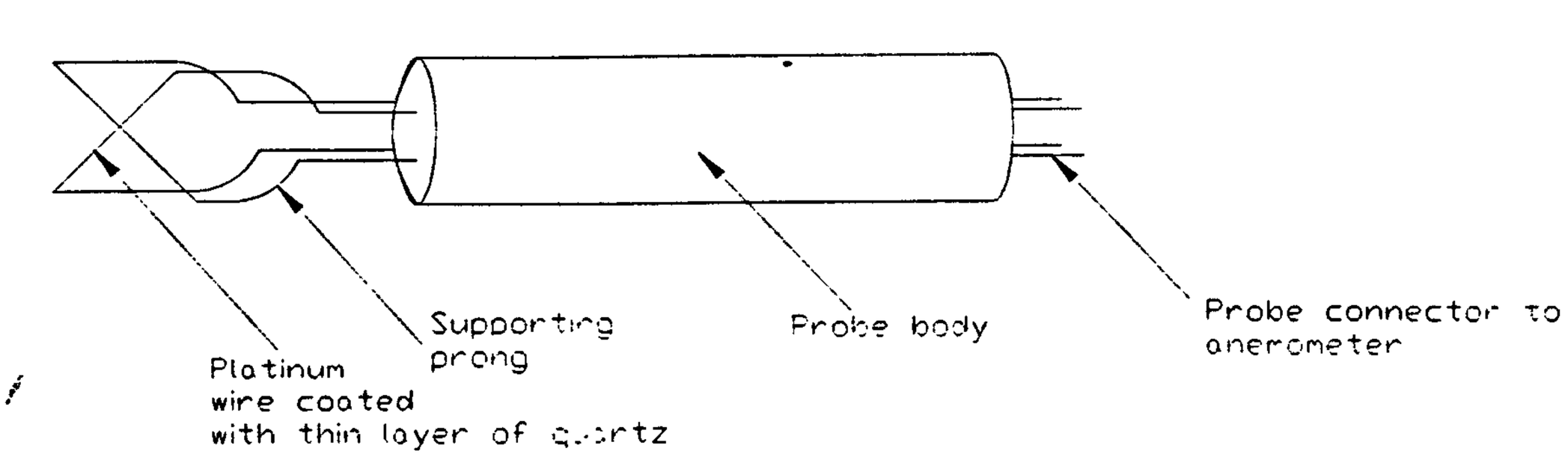


Figure 3.2-1 Schematic of the hot film probe used in the experiments

Hot wire sensors are usually constructed from platinum or tungsten wire with a thickness of approximately 5 μm (Ref. Dantec), which are designed for use in air. For use in conducting fluids such as water, the sensor has to be insulated from the surrounding medium. In this case, a thin film of quartz is deposited on the cylindrical wire, which results in an increased thickness ranging from 25 μm to 150 μm or more. In addition

to the benefits of insulation of the wire sensor from the electrical conductivity of the water, say, the film deposited on the sensor also serves to protect the delicate wire from damage or breakage from any dust particles or impurities being carried in the flow of water past the sensor. However, a thick protective film of quartz would also serve to reduce the frequency response of the probe. Hence, the selection of an appropriate probe for flow measurements in water is a compromise between sensor longevity and frequency response of the probes.

There is a distinction between hot wire and hot film sensors available commercially. Hot wires are for use in air, while films are usually used for measurements in conducting liquids. However, the term "hot wire anemometry" has become a generic term describing the use of both heated wires and films for velocity and temperature measurements. It does not solely imply the use of uncoated hot wires in measurements in water. In keeping with this widely used convention, the term "hot wire anemometry" is used throughout this thesis to describe the hot film measurements in water.

There are two types of hot wire anemometers in use. They are the constant current (CCA) and constant temperature (CTA) anemometers. The constant current anemometer was the first type of hot-wire system to be used, and there is a great deal of literature available on the design and construction of these instruments (Kovaszny, 1948, 1965, Betchov, 1948a, 1948b, 1949, Hinze, 1975, Grant and Kronauer, 1962). A simple CCA circuit is shown in Figure 3.2-2.

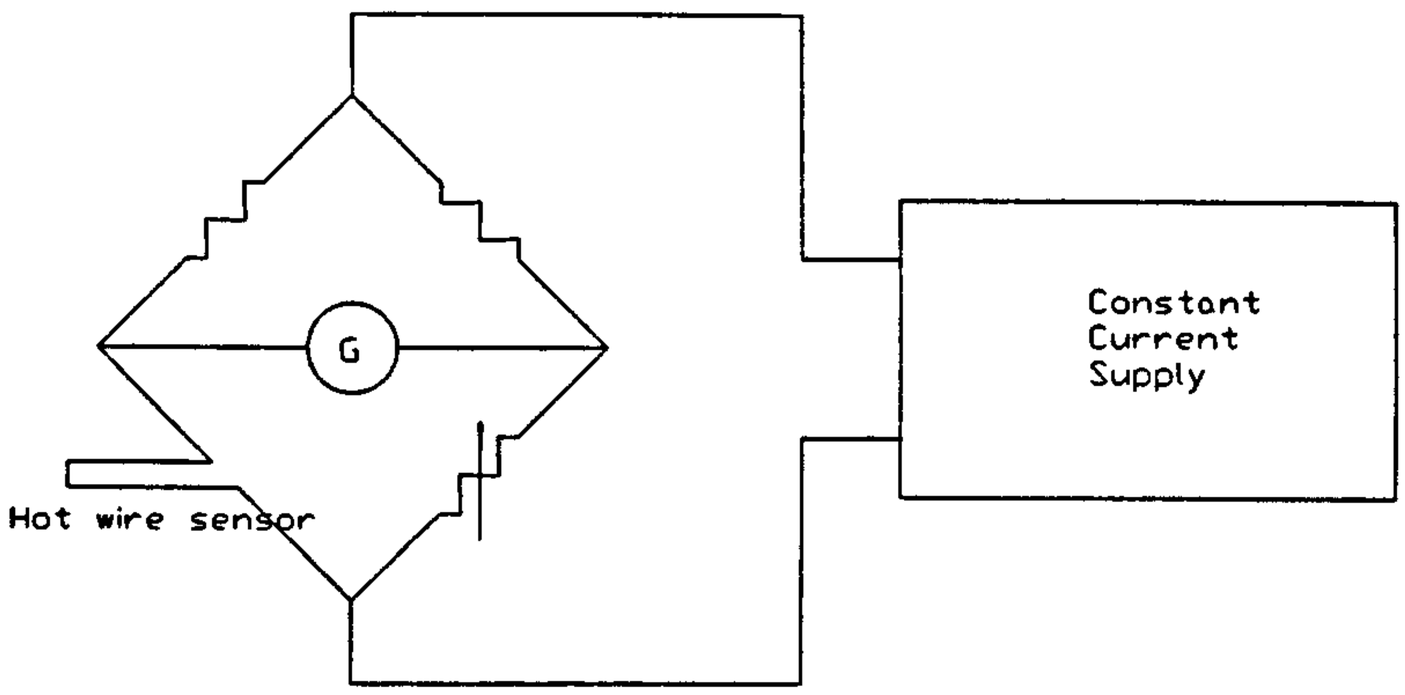


Figure 3.2-2 Simplified sketch of a typical constant current anemometer circuit

Lomas (1986) summarises the typical way in which the CCA is operated. A constant bridge current is maintained by either with a constant power supply, or using a battery placed in series with a large resistor. The probe is first placed in a flow of known velocity. The probe heating current is adjusted for a suitable unbalanced voltage. Initially, to calibrate the anemometer, the probe is placed in the fluid to be tested. The fluid velocity is varied over the range of interest while recording the calibration data. Then without changing the bridge current, the probe is placed into the flow which is to be measured. Perry (1982) also derived the relationship between the bridge voltage and the fluctuating component of velocity for the CCA.

The constant temperature anemometer (CTA) has proven superior, and has largely replaced the CCA. This system, in contrast to the CCA, compensates for the thermal inertia of the hot wire filament by continuous automatic adjustment. The temperature of the wire is maintained approximately constant automatically by a feedback circuit. When the feedback amplifier sees an imbalance in the Wheatstone bridge, it adds current to the bridge to restore balance. A typical CTA circuit is shown in Figure 3.2-3.

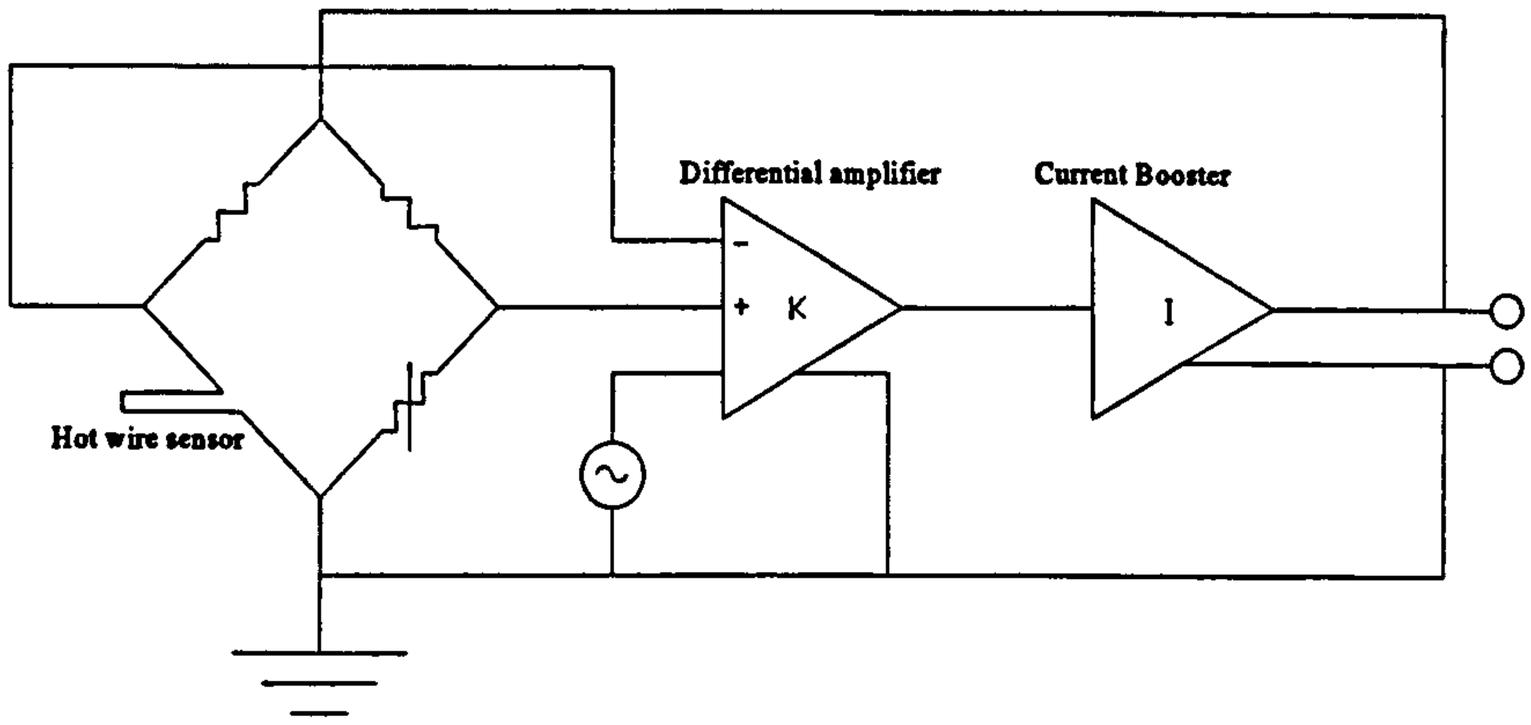


Figure 3.2-3 Simplified sketch of a typical constant temperature anemometer circuit

A differential amplifier is designed so that the voltage difference between the two terminal inputs will be amplified, where as a voltage common to both terminals will not. Therefore, a change in the overall bridge voltage will not be sensed by the amplifier, but it will respond when the bridge resistance is off-balance. In order to ensure an adequate heating current to maintain a constant temperature at high velocity applications, the current from the differential amplifier is increased by a unity gain amplifier acting as a current booster.

3.2.1 Sensor frequency response

When a hot wire sensor experiences a sudden change in flow velocity, a finite time is required for the sensor temperature to reach its new value. This is caused by a number of effects, the most important being the heat storage by the sensor.

The reciprocal of the time constant for a typical hot wire sensor shows it will be the order of a few hundred hertz - which is too low for turbulence measurements in air flows. However, if a constant temperature anemometer (CTA) is used, the frequency

response would be much higher. As before, Hinze (1975) derived the following time constant equation for a CTA,

$$\tau_{CTA} = \frac{\rho c A l(\overline{R}_s - R_f)}{\alpha R_0 \bar{I}_s^2 [2g R_s(\overline{R}_s - R_f) + R_f^2]} \qquad (3.2\text{-}1)$$

where R_s = total electrical resistance of the sensor

$= \overline{R}_s + r_s$ *(sum of the mean and fluctuating resistances)*

$I_s = \bar{I}_s + i_s$

ρ = density

c = specific heat

A = area

l = length

$\overline{R}_s$ = mean electrical resistance of sensor

R_f = electrical resistance of the fluid

$\bar{I}$ = mean current

α = temperature coefficient of resistivity

R_0 = reference electrical resistance

A common and more practical method to test and measure the frequency response of the entire anemometer system is to use the square wave test. A square wave with a small amplitude is added to the sensor in a steady flow to allow the square wave signal to be superimposed on the mean signal. When the square wave current is introduced, the sensor current will go high and then drop to its original value as the feedback amplifier reduces the heating current to balance the bridge. A sudden decrease in velocity will have the same effect.

The time constant for the system can be calculated by measuring the time required for the output voltage to drop from its peak amplitude to an amplitude that is 63.2% less than the peak value. In the experiments, the time constant for the hot film probe is 0.002s, after adjustments were made to the anemometer.

3.2.2 Probe Calibration

Prior to the use of the hot wire anemometer system in a flow field of interest, the system has to be calibrated. The calibration procedure is an essential and vital part of the measurement of the turbulent quantities of interest in the flow field.

The design and construction of the hot film or hot wire probes is such that there is no "universal" calibration law available. There are numerous factors unique to the construction of an individual probe which govern the heat transfer for that probe such as the wire diameters, and the lengths of the sensors. Hence it is not unusual to have variations in seemingly identical probes.

There are a number of calibration methods derived by different researchers. These methods may be grouped into two categories. They are the steady state, or static calibration method, while the other, is the dynamic method.

3.2.2.1 Steady state or static calibration methods

In the steady state methods, the probe is held stationary while the fluid passes over it. Alternatively, the probe is traversed at constant speed through the quiescent fluid. In either case, the anemometer output voltage is recorded at discrete velocities, or the velocity is slowly varied with time while the output voltages recorded continuously.

For measurements in air, a steady, uniform flow is set up, and directed at the hot wire sensor. The sensor may be placed within a wind tunnel, or it may be mounted on a

calibration rig such that a jet is directed towards the sensors (ref. DANTEC). By measuring the air pressures (total and static pressure) with a pitot tube, the voltages measured across the Wheatstone bridge in the hot wire anemometer may be correlated to velocities measured by the pitot tube. Thus, in the calibration of the a hot wire sensor, an accurate and independent means of measuring the free stream velocities will be required to correlate the velocity to voltage readings.

Pitot tubes convert the pressure differences to velocity by the following relationship,

$$V = \sqrt{2gh} \tag{3.2-2}$$

where h is the difference in the total and static head.

If measurements are to be made in water, there is a lower limit with which a pitot tube will not be sensitive enough to measure the velocity accurately. This lower limit is normally greater than or equal to 2 m/s.

The velocity-voltage relationship for a hot wire sensor is non-linear, while its percentage sensitivity to increasing flow velocity remains relatively constant. These two characteristics make the hot wire anemometer a useful tool for a wide range of flow velocities. However, due to the limitations of the pitot tube, in order to calibrate the hot wire sensor in water where the typical velocities are several orders of magnitude less than in air, other methods have to be used. One method is that of a towed wire within a towing tank. (Deardorff and Willis, 1967, Fabula, 1968, Dring and Gebhart, 1969, Persen and Saetran, 1983). The hot wire sensor is towed along the tank at a constant velocity by an electric motor.

Another method is to use the jet emanating from a container full of water (ref. DANTEC, Rubatto, 1970). The jet is aimed at the sensor. This method uses Torricelli's formula, Equation (3.2-2). If the orifice is small in comparison to the head

of water above the orifice, then the velocity of the jet is uniform across the *vena contracta* (Massey, 1983). As with the calibration using a pitot tube, there is a lower limit to the velocity at which the probe can be calibrated. For example, for a flow velocity of 0.5 m/s, the head of water would have to be 0.013 m. This is a small value for which the experimental error would be considerable. Pichon (1970) gives a practical lower limit of 1 m/s. Another difficulty associated with this method is the difficulty in measuring the height of the water column.

An open circular container filled with water has also been used by Delleur, Toebes and Tin (1966), and James and Acosta (1970). This a common method where the tank is rotated at a constant rotational velocity. The probe is then immersed and measurements taken. Ideally the immersion time should be less than one rotation as the probe body will induce rotation in the container too.

Other calibration methods include the use of particle (or hydrogen bubble) tracking techniques, phase measurements in the wake of a sinusoidally heated wire (Walker and Westernburg, 1956), the measurement of shedding frequency of cylinders, and the use of whirling arms (King, 1914, Tsobuchi and Sato, 1956).

If a cross-wire probe is used, then the sensitivity to both velocity and yaw angles will have to be determined during calibration. This is usually done by conducting a yaw calibration as described by Bradshaw (1971). The method using the rotating tank is limited by the fact that a full yaw calibration is not be possible. Yaw calibrations using a tank with an orifice at the side would have a lower limit to the calibration velocity. Thus, the towed probe method or the use of a flow channel facility (similar to a wind tunnel) would be the most suitable methods for a full velocity and yaw calibration to be carried out.

The above methods avoid the specification of the exact characteristics of the wire (length, diameter, resistivity etc). They also allow for some of the deficiencies of the

setups (e.g. deviations from the "cosine law" (see section 3.2.4) due to the finite length of the wire, etc. Hinze, 1975). All the above methods should be done in flows with low levels of turbulence. This can be obtained in potential core of jets, external flow of boundary layer etc. Highly turbulent flows have to be avoided because of the nonlinear errors affecting the measurements.

3.2.2.2 Dynamic calibration techniques

In this method of calibration, the probe is oscillated at a known frequency. Schubauer and Klebanoff (1946) first devised this method. Perry and Morrison (1971b) developed this further. Their device moves the hot wire at an accurately known small sinusoidal motion from 0 to 10 Hz in a steady stream. Since the output voltage is a nonlinear function of velocity, the probe must be oscillated over a velocity range small enough to allow Wheatstone bridge variations to be considered a linear function of velocity. Thus, Perry and Morrison (1971b) limited probe velocity to less than 10% of the free stream velocity.

This method of calibration would require custom made mechanisms to be developed. There are a number of designs shown by Mulhearn and Finnegan (1978), and Gunkel et al (1971). Hence, the main advantage of the dynamic calibration techniques over the static method is that it allows the slope of the calibration curve (usually taking the form of $E^2 = A + BU^n$), to be found.

3.2.3 Heat transfer laws

The main purpose of the hot wire calibration exercise is to determine the voltage - velocity relationship for the probe. There are a variety of different probe designs, ranging from the common cylindrical wires strung between two prongs, to wedge shaped or conical shaped film probes. In the experiments described in the following sections, an X-probe or a cross-wire probe was used in the measurements of velocities, i.e. this

particular probe design is capable of simultaneous measurements of two components of velocity. Consequently, the following review of the probe voltage - velocity relationship shall concentrate on X-probes.

A number of researchers have calibrated their hot wire or film probes by assuming forced convection cooling of a heated cylinder according to King's law (1914).

$$\frac{I^2 R_s}{T_s - T_f} = A_0 + B_0 \sqrt{Re} \qquad (3.2\text{-}3)$$

where A_0 and B_0 are constants,

R_s = sensor resistance

T_s = sensor temperature

T_f = fluid temperature

For hot wire anemometers, the relationship is written as,

$$E_b^2 = A + BU^n \qquad (3.2\text{-}4)$$

where E_b = output voltage taken across the Wheatstone bridge

The relationship between the fluid velocity and the output voltage of the hot wire anemometer is non-linear, and would require two calibration constants for each sensor. To calibrate an X-probe using King's law, the calibration constants are estimated for each sensor by measuring the output voltage from each sensor for several velocities with the probe orientated at a single angle with respect to the flow. By linearizing the outputs, one component of velocity is proportional to the sum of the output voltage, while the other is the difference between the outputs. The sum and difference can then be correlated to obtain the mean of the shear stresses (Bradshaw, 1971). There are several problems inherent in this calibration process. Firstly, the effective velocity has to be corrected to account for the finite aspect ratio of the sensor and the effective cooling caused by the velocity component parallel to the sensor. Secondly, the

calibration scheme does not expose the X-probe to the components of velocity which will be measured. The calibration is based on results derived from measurements made with the probe axis at a single angle with respect to the calibration flow. Hence, if the probe is calibrated so that its axis is along the calibration velocity vector, then any velocity component that is not parallel to the probe axis can only be estimated from the cosine law. Thirdly, the calculation of the individual components of velocity from the voltages is dependent on the assumption that the sensors are at right angles to one another. Bradshaw (1971) estimates that the ratio of the sensitivity of the fluctuating V component of velocity to the sensitivity of the fluctuating U component of velocity for a single sensor changes by 10% when the angle of the sensor to the flow is changed from 45° to 48°. Consequently, small deviations from this angular assumption can have a significant effect on the measured results.

Bruun et al (1988) compared four different calibration relationships based on the above power law relationships and determined their accuracies. The first was the basic power law relationship, based on the early work of King (1914). A value of n=0.5 was used by King, while Collis and Williams (1959) suggested a value of 0.45.

The second is the extended power law relationship,

$$E^2 = A + BV^n + CV \qquad (3.2\text{-}5)$$

This relationship was studied by Siddall and Davies (1969, 1972). The third, which uses polynomial fits, take several forms. The first,

$$V = A + BE + CE^2 + \ldots\ldots \qquad (3.2\text{-}6)$$

was suggested by George et al. (1981). Polynomial fits of up to the fourth order were examined. They also looked at variations to the above relationships, viz.

$$V = A + B(E^2) + C(E^2)^2 + \ldots. \qquad (3.2\text{-}7)$$

as suggested by Swaminathan et al (1984) and,

$$V = A + BE^{1/n} + CE^{2/n} + DE^{3/n} + ... \qquad (3.2\text{-}8)$$

which was applied by Thompson and Whitelaw (1983). The final method they looked at were spline fits.

By using the various methods on the data, which ranged from a velocity of 1 to 90 m/s, Thompson and Whitelaw (1983) found that the spline fit method gave the best accuracy at the cost of greatest computational time. The simple power law method gave a good data fit with a low standard deviation. As for the extended power law relationship, it was worse than the simple power law relationship. The polynomial fits performed the worst.

While the power law relationship and its variants have been widely used, there is some contention to the value of the exponent. Numerous values have been suggested based on empirical data and most values are around 0.45 and 0.5. Additionally, many of these relationships have been based on calibrations carried out in air, at relatively high velocities. Consequently, the applicability and universality of some of the suggested values for the exponent to water flows is questionable. Conversely, using a polynomial fit to the data points would preclude any assumptions to the value of the exponent. A least squares polynomial fit would be performed. However, as Bruun et al (1988) have found, the form of the polynomial equation would have an effect on the accuracy of the fit.

Richardson and McQuivey (1968) have found that the value of the exponent n, in the power law relationship for a hot film sensor varies from 0.3 for a velocity range of 6.10 m/s to 18.29 m/s. The value increases to 0.41 for a velocity range of 18.29 m/s to 45.72 m/s. However, in water, the value of n for the same probe was 0.31 for velocity range of 0.06 m/s to 0.18 m/s. For a range of 0.18 m/s to 0.46 m/s, this increased to 0.35. Finally, for a range of 0.46 m/s to 0.91 m/s, the value of n went up 0.45. Thus,

it can be seen that there is a wide variation in the value of n for a different fluids and velocity ranges.

Polynomial least squares regression is an alternative to the power law relationship, however, there is a limit to the order of the polynomial. An oscillation in the fitted curve can be produced at higher polynomial orders. This can occur as low as the third or fourth order, and is dependent on the velocity range. While spline fits have been found to give good accuracy, researchers have found that there is a trade-off in the computational time and storage space required for the determination of the relationship between voltage and velocity.

3.2.4 Yaw Calibration

The use of cross-wire probes allows not only the speed of the flow to be measured, but also its direction. The yaw angle, α, is defined to be the angle between the velocity vector and the normal to the sensor, both of which lie in the plane of the supporting prongs. This is shown in Figure 3.2.4

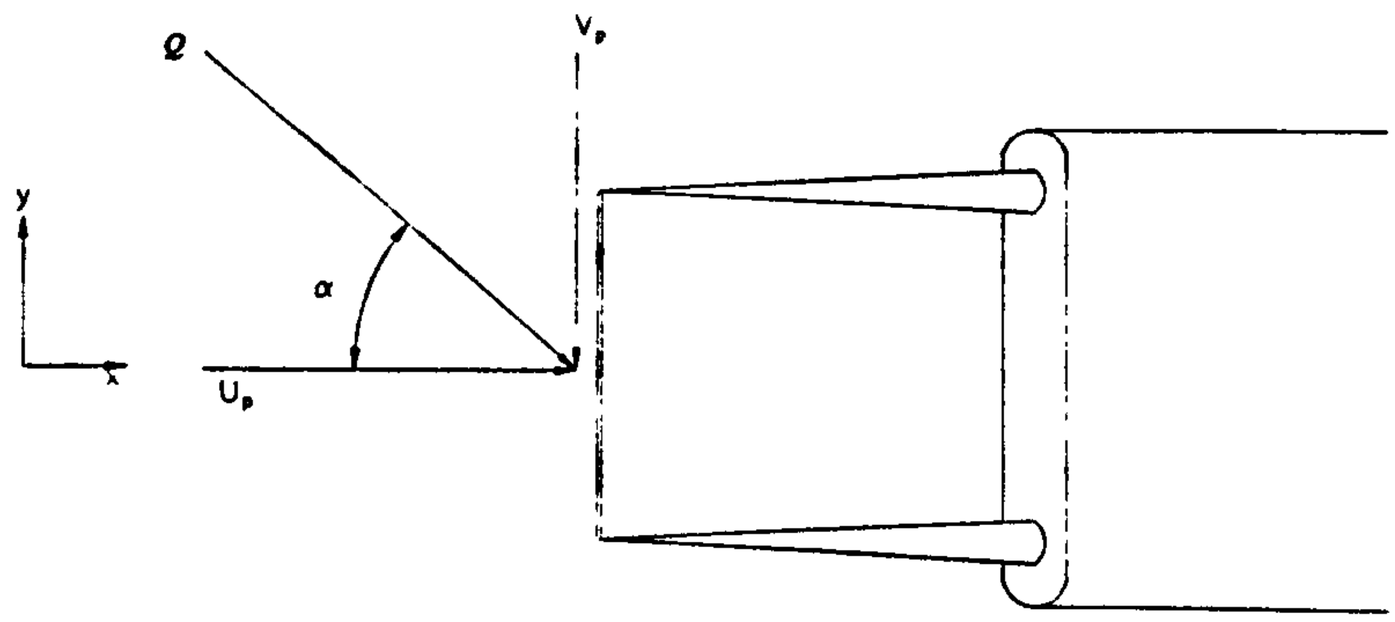


Figure 3.2-4 Sketch of hot wire probe showing yaw angle and velocity components

The effective velocity, U_{eff}, measured by the sensor is equal to the transverse component of velocity, i.e.,

$$U_{eff} = U_x$$

$$\text{but } U_p = Q \cos \alpha$$

$$\rightarrow U_{eff} = Q \cos \alpha$$

where Q = magnitude of the mean velocity vector

The above expression is the cosine law. Champagne, Sleicher and Wehrmann (1967) showed that very good results can be obtained by using the cosine law if the sensor aspect ratio is greater than 600 (aspect ratio = length of sensor/diameter of sensor). However, since few probe designs have such large aspect ratios, the law is then regarded as an approximation.

Hinze (1975) proposed a modification to the Cosine law to overcome the inaccuracy. The new relationship is,

$$U_{eff}^2 = U_x^2 + k^2 U_y^2 \qquad (3.2\text{-}9)$$

where k is the yaw factor, included to account for the additional cooling by the tangential component of velocity. The equation can be rewritten as,

$$U_{eff}^2 = U^2(\cos^2\theta + k^2 \sin^2\theta) \qquad (3.2\text{-}10)$$

The value of k was found to be 0.20 ± 0.01 by Webster (1962) for most conventional hot wire probes.

Thus, the use of inclined wire probes (e.g. in multi-axes probes) also require a yaw calibration of the sensor in order to determine yaw sensitivity of the probe. Various methods have been devised by numerous researchers, and are summarised below.

The first method is to simply measure the geometric angle between the cross-wire sensors (Kreplin and Eckelmann, 1979). Another method is to set up a constant velocity across the probe which is yawed at different angles. From there, an average single effective angle is determined. (Bradshaw, 1971). In the third method, a similar calibration procedure is set up as in the first method, except that a constant k^2 factor to allow for the longitudinal cooling of the wire (Hinze, 1975). Alternatively, a fourth way is to introduce a variable k^2 factor instead of the constant value. This method was used by Andreopoulous and Rodi (1984). In the fifth method, the longitudinal cooling effect on the wire can be accounted for using some formulae (Friehe and Schwarz, 1968, Bruun and Tropea, 1985) instead of the factor k^2. The sixth method is to develop a full velocity - yaw calibration method. There are two variations in the way in which the data is used. Willmarth and Bogar (1977), Johnson and Eckelmann (1984) and Lueptow (1988) all have described analysis methods for the look-up table method. Browne et al. (1989) on the other hand have used a different approach for relating measured voltages to velocity components..

The look-up table calibration method requires the sensor to be yawed at different angles in addition to the range of velocities in which it will be exposed to. As a result, this technique would require more time to carry out. The advantage with this method is that assumptions concerning sensor cooling are not made and does not suffer from the possible inaccuracies inherent in either the geometric angle or effective angle approaches. Willmarth and Bogar (1977) were the first to suggest this method for a cross-wire probe. Essentially, there is a unique pair of output voltages from both sensors which correspond to the magnitude and direction of the fluid velocity, relative to the probe axis. They created a calibration grid of 400 discrete points corresponding to the combination of 20 discrete output voltages from each sensor. The velocity can then be resolved into its components, so that for each of the 400 discrete points. the corresponding U and V velocities were allocated. They also stored the derivatives of the U and V velocities with respect to the output voltages at each point. In this way, for any given value of measured pair of voltages, the values of U and V at the nearest

discrete point and the derivatives can be used to interpolate values of U and V corresponding to the measured voltages.

Johnson and Eckelmann (1984) also described a similar method. The difference between their method and Willmarth and Bogar's was in the interpolation scheme. A two-variable Taylor series expansion up to the second-order was used. The interpolation required the estimation of the second order derivatives of voltage with respect to velocity and yaw angle. A total of 14 quantities had to be stored at each discrete point.

Lueptow, Breuer and Haritonidis (1988) also developed a variation to the look-up table method. Their method of interpolation for the velocities were based on the creation of a separate grid of points relating the voltage pairs to velocities and yaw angles. Instead of determining the derivatives as in the previous methods, polynomial regression or cubic spline technique was used to determine the voltage and velocity relationships.

The main advantage associated with the look-up calibration table technique is that it requires no assumptions about the physical laws governing the cooling of the sensor or the geometry of the X-probe.

An alternative to the look-up table calibration method is the method devised by Browne, Antonia and Chua (1989). The calibration technique is identical to that for the look-up table method, i.e. the probe is yawed at various angles and exposed to the fluid flow at the different velocities which are expected to be encountered during the experiments. In this way, for each yaw angle and flow velocity, a unique pair of voltages are obtained for the X-probe.

By plotting the calibration velocities against sensor output voltages for a series of constant yaw angles, a family of curves were obtained. They used a third order polynomial fit for each family of data points. The experimental voltages obtained can be then transformed by determining the corresponding values of yaw angles and

velocities for each discrete pair of sensor voltages.

This method has some similarities to the look up table method. The relationships for a family of curves for velocity, voltage and yaw angles has to be determined. Instead of linear interpolation between the values in the tables, the velocity and flow angles were found from the solution of two simultaneous non-linear equations.

In the experiments, the yaw calibration method of Wubben (1991) was used, due to its relative simplicity, accuracy and ease of calculation. This method is based upon that described by Bradshaw (1971).

In the calibration of a cross wire probe, the axis of the probe connector is orientated so that it is to parallel the mean velocity component of the flow. The sensors are then yawed to obtain the sensitivity of the tangential velocity components. The effective velocities for both sensors are written as:

$$U_{eff_1}^2 = (U_p \sin\alpha_1 + V_p \cos\alpha_1)^2 + h_1 W_p^2 + k_1^2 (U_p \cos\alpha_1 - V_p \sin\alpha_1)^2 \quad (3.2\text{-}11a)$$

$$U_{eff_2}^2 = (U_p \sin\alpha_2 - V_p \cos\alpha_2)^2 + h_2 W_p^2 + k_2^2 (U_p \cos\alpha_2 + V_p \sin\alpha_2)^2 \quad (3.2\text{-}11b)$$

α_1 and α_2 are the wire angles and are manufactured generally to 45°

k and h are the yaw factors for the t and binormal components of velocities.

Subscripts 1 and 2 refer to the first and second sensors.

U_p, V_p, and W_p are the velocity components in the probe coordinate system.

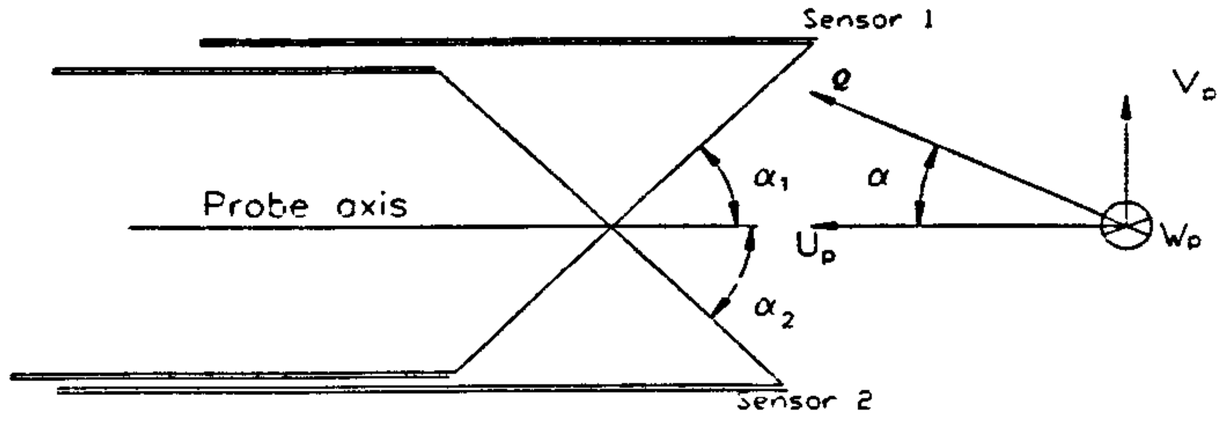


Figure 3.2-5a Definition of velocity components in cross wire coordinate system

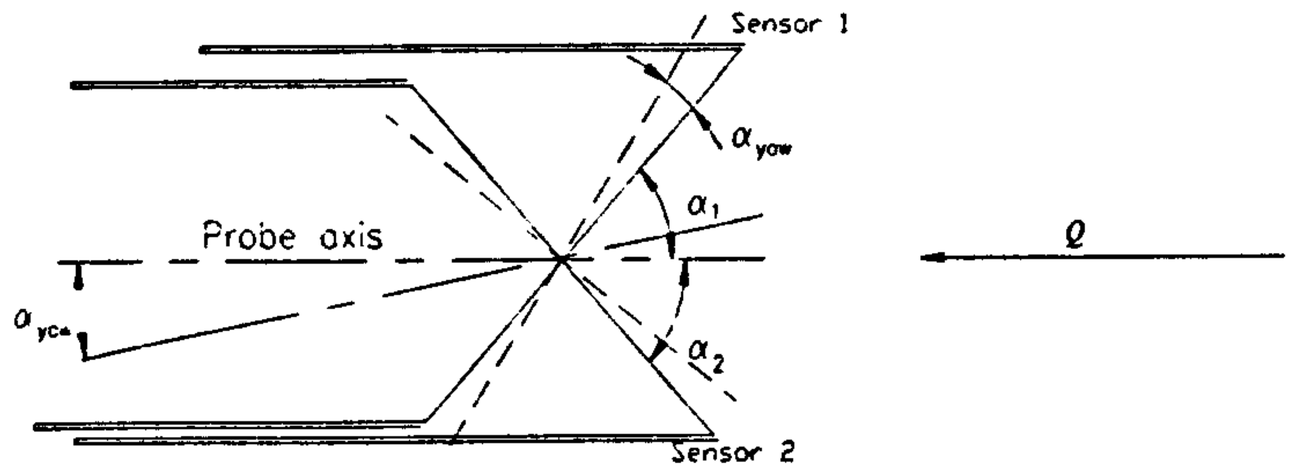


Figure 3.2-5b Yaw calibration of cross wire probe - the probe is yawed by angle α_{yaw}, whilst the same flow angle is maintained.

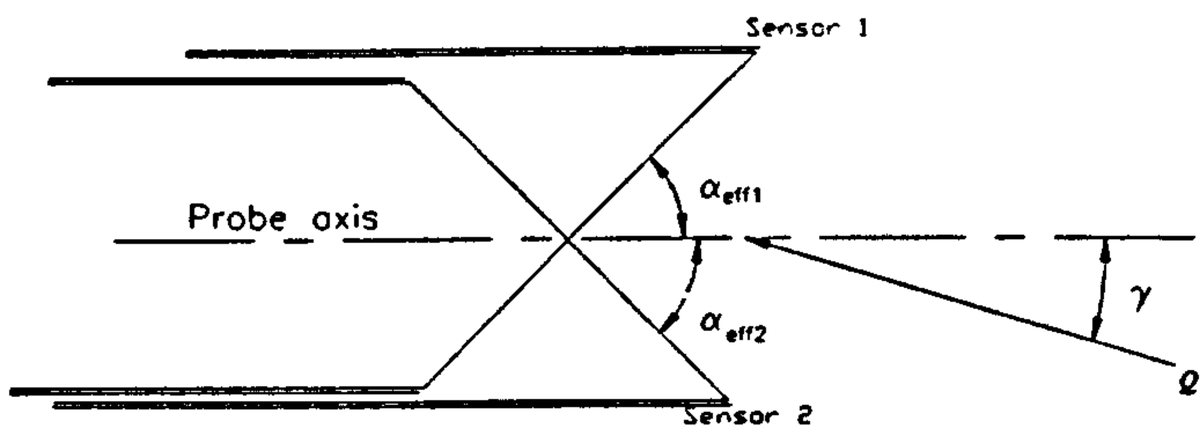


Figure 3.2-5c The yawing of the probe (above) is equivalent to the change in flow direction, γ, if the probe position is unchanged.

The binormal component of velocity, W_p, can be neglected since its cooling effect on the sensors are insignificant. The square of the velocity magnitude, Q^2 ($=U_p^2 + V_p^2$) is introduced to the above equations, giving:

$$U_{eff_1}^2 = Q^2[\sin^2(\alpha_1 + \alpha_{yaw}) + k_1^2\cos^2(\alpha_1 + \alpha_{yaw})] \quad (3.2\text{-}12a)$$

$$U_{eff_1}^2 = Q^2[\sin^2(\alpha_2 + \alpha_{yaw}) + k_2^2\cos^2(\alpha_2 + \alpha_{yaw})] \quad (3.2\text{-}12b)$$

In practice, the values of α_1 and α_2 cannot be determined with sufficient accuracy. Hence the effective angle procedure was developed by Bradshaw.

In this method, the voltage pair, E_{11} and E_{12} are obtained for the probe at zero yaw angle. At the next yaw angle, α_{yaw}, the voltage pair, E_{21} and E_{22} are determined. This is carried out for a number of different yaw angles. The magnitudes of the velocities, Q_{21} and Q_{22} can also be determined. These can be interpreted as the velocities which, if the probe was used in the un-yawed position, would produce the same voltage outputs, E_{21} and E_{22} as obtained from the yawed wire. This relationship is obtained from King's Law (see equation 3.2-4). Hence,

$$Q_1^2[\sin^2(\alpha_1 + \alpha_{yaw}) + k_1^2\cos^2(\alpha_1 + \alpha_{yaw})] = Q^2{}_{21}[\sin^2\alpha_1 + k_1^2\cos^2\alpha_1] \quad (3.2\text{-}13a)$$

$$Q_1^2[\sin^2(\alpha_2 - \alpha_{yaw}) + k_2^2\cos^2(\alpha_2 - \alpha_{yaw})] = Q^2{}_{22}[\sin^2\alpha_2 + k_2^2\cos^2\alpha_2] \quad (3.2\text{-}13b)$$

Choosing values of k_1, and k_2 gives the values of the effective angles, α_1 and α_2. By repeating this procedure for a number of different yaw angles, the resulting variance in

the effective angles can be minimized by considering k_1 and k_2 as active iteration parameters. Thus the optimum values of k and effective angles are obtained.

In order to convert the measured voltage pairs E_1 and E_2 obtained in the course of the experiments, into both the magnitude of velocity and the direction, γ, the following equations are used:

$$Q^2[\sin^2(\alpha_1 + \gamma) + k_1^2\cos^2(\alpha_1 + \gamma)] = Q_1^2[\sin^2\alpha_1 + k_1^2\cos^2\alpha_1] \quad (3.2\text{-}14a)$$

$$Q^2[\sin^2(\alpha_2 - \gamma) + k_2^2\cos^2(\alpha_2 - \gamma)] = Q_2^2[\sin^2\alpha_2 + k_2^2\cos^2\alpha_2] \quad (3.2\text{-}14b)$$

3.3 Computational Fluid Dynamics

Computational Fluid Dynamics or CFD is the analysis of systems involving fluid flow, heat transfer and associated phenomena by means of computer-based simulations. The technique is very powerful and spans a wide range of industrial and non-industrial application areas.

CFD codes are structured around the numerical algorithms that can tackle fluid flow problems. There are three distinct sets of numerical solution techniques: finite difference, finite element and spectral methods, all of which perform the following steps:

1. Approximation of the unknown flow variables by means of simple functions.
2. Discretisation by substitution of the approximations into the governing flow equations and subsequent mathematical manipulations.
3. Solution of the algebraic equations.

The main differences between the three separate methods are associated with the way in which the flow variables are approximated and with the discretisation processes. The finite difference method describes the unknowns of the flow problems by means of point samples at the node points of a grid of co-ordinate lines. Truncated Taylor series expansions are often used to generate finite difference approximations of the derivatives of the unknowns in terms of point samples at each grid point and its immediate neighbours. Those derivatives appearing in the governing equations are replaced by finite differences yielding an algebraic equation for the aspects of the finite difference method.

Finite element methods use simple piecewise functions (e.g. linear or quadratic) valid on elements to describe the local variations of unknown flow variables. The governing equation is precisely satisfied by the exact solution for the unknown variables. If the piecewise approximating functions for the variables are substituted into the equation it will not hold exactly and a residual is defined to measure the errors. The residuals (and hence the errors) are minimised by multiplying them by a set of weighting functions and integrating. A set of algebraic equations for the unknown coefficients of the approximating functions are obtained as a result.

Spectral methods approximate the unknowns by means of truncated Fourier series or series of Chebyshev polynomials. Unlike the finite difference or finite element approaches the approximations are not local but valid throughout the entire computational domain. Again the unknowns in the governing equation are replaced by the truncated series. The constraint that leads to the algebraic equations for the coefficients of the Fourier or Chebyshev series is provided by a weighted residuals concept similar to the finite element method or by making the approximate function coincide with the exact solution at a number of grid points.

The finite volume method was originally developed as a special finite difference formulation. This method is central to the commercial CFD code used in the course of

this project, CFX 4.1. The numerical algorithm consists of the following steps:

1. Formal integration of the governing equations of fluid flow over all the control volumes of the solution domain.

2. Discretisation involves the substitution of a variety of finite difference type approximations for the terms in the integrated equation representing flow processes such as convection, diffusion and sources. This converts the integral equations into a system of algebraic equations.

3. Solution of the algebraic equations by an iterative method.

The first step, the control volume integration, distinguishes the finite volume method from other CFD techniques. The resulting statements express the exact conservation of relevant properties for each finite size cell. This clear relationship between the numerical algorithm and the underlying physical conservation principle forms one of the main attractions of the finite volume method.

3.4 The Governing equations for fluid flow

The governing equations for a single phase flow is described by the Navier Stokes equations, given below:

Continuity equation,

$$\frac{\partial \rho}{\partial t} + \nabla\cdot(\rho \boldsymbol{U}) = 0 \qquad (3.4\text{-}1)$$

Momentum equation,

$$\frac{\partial \rho \boldsymbol{U}}{\partial t} + \nabla\cdot[\rho \boldsymbol{U}\times\boldsymbol{U} - \mu(\nabla \boldsymbol{U} + (\nabla \boldsymbol{U})^T)] = \boldsymbol{B} + \nabla p \qquad (3.4\text{-}2)$$

where $\nabla \boldsymbol{U}^T$ is the transpose of the vector $\nabla \boldsymbol{U}$)

Temperature/concentration equation,

$$\frac{\partial \rho \Phi}{\partial t} + \nabla\cdot(\rho \boldsymbol{U} \Phi) = \nabla\cdot(\Gamma \nabla \Phi - \rho \boldsymbol{u} \phi) + \boldsymbol{S} \qquad (3.4\text{-}3)$$

$\boldsymbol{U}$ and $\boldsymbol{u}$ are the mean and fluctuating parts of the velocity vector

Φ is a scalar quantity which may represent temperature or species concentration

S is a volumetric source term

p is the pressure

Γ is the diffusion coefficient.

3.5 Finite differencing schemes

The basis of the code is a conservative finite-difference, or finite-volume method with all the variables defined at the centre of the control volumes which fill the physical domain being considered. Each equation is integrated over each control volume to obtain a discrete equation which connects the variable at the centre of the control volume with its neighbours. The numerical accuracy of the modelled equations is dependent on the discretisation method chosen for the advection or convection terms. There are a variety of discretisation methods available in CFX4. These range from the robust yet relatively inaccurate hybrid and upwind schemes to the more accurate but less robust higher order schemes. The default scheme used in the solver is the hybrid differencing scheme.

All the equations to be solved, apart from the continuity equation, have the same general form:

$$\frac{\partial \rho \phi}{\partial t} + \nabla \cdot (\rho \boldsymbol{U} \phi) - \nabla \cdot (\Gamma \nabla \phi) = S \qquad (3.5\text{-}1)$$

where the second term on the LHS is the advection or convection term

the third term on the LHS is the diffusion term and

Γ is the relevant effective diffusivity for the variable ϕ.

Integrating over the control volume gives:

$$\int \frac{\partial \rho \phi}{\partial t} dV + \int \rho \phi \boldsymbol{U} \cdot \boldsymbol{n} \, dA - \int \Gamma \nabla \phi \cdot \boldsymbol{n} \, dA = \int S \, dV \qquad (3.5\text{-}2)$$

$$\textit{time variation} + \textit{convection} + \textit{diffusion} = \textit{source}$$

All terms in all the equations are discretised in space using the second-order centred differencing apart from the advection terms. The convection coefficients are obtained using the Rhie-Chow interpolation formula (Computational Fluid Dynamic Services, 1995).

The treatment of the advection terms determines the accuracy of the solutions of the model equations in the solver. There is a balance between the robustness of the differencing schemes and the robustness in terms of convergence of the solution. Generally, the more accurate the scheme, the more difficult it is to obtain convergence.

3.5.1 Discretisation of Diffusion terms

The diffusion term in equation (3.5-2) is discretised using centred differencing. Thus the term can be written as,

$$\int \Gamma \nabla \phi \cdot \boldsymbol{n} \, dA = \frac{\Gamma A_w}{h_w} (\phi_p - \phi_w) \equiv D_w (\phi_p - \phi_w) \qquad (3.5\text{-}3)$$

This centred differencing scheme may be illustrated in Figure 3.5-1 below.

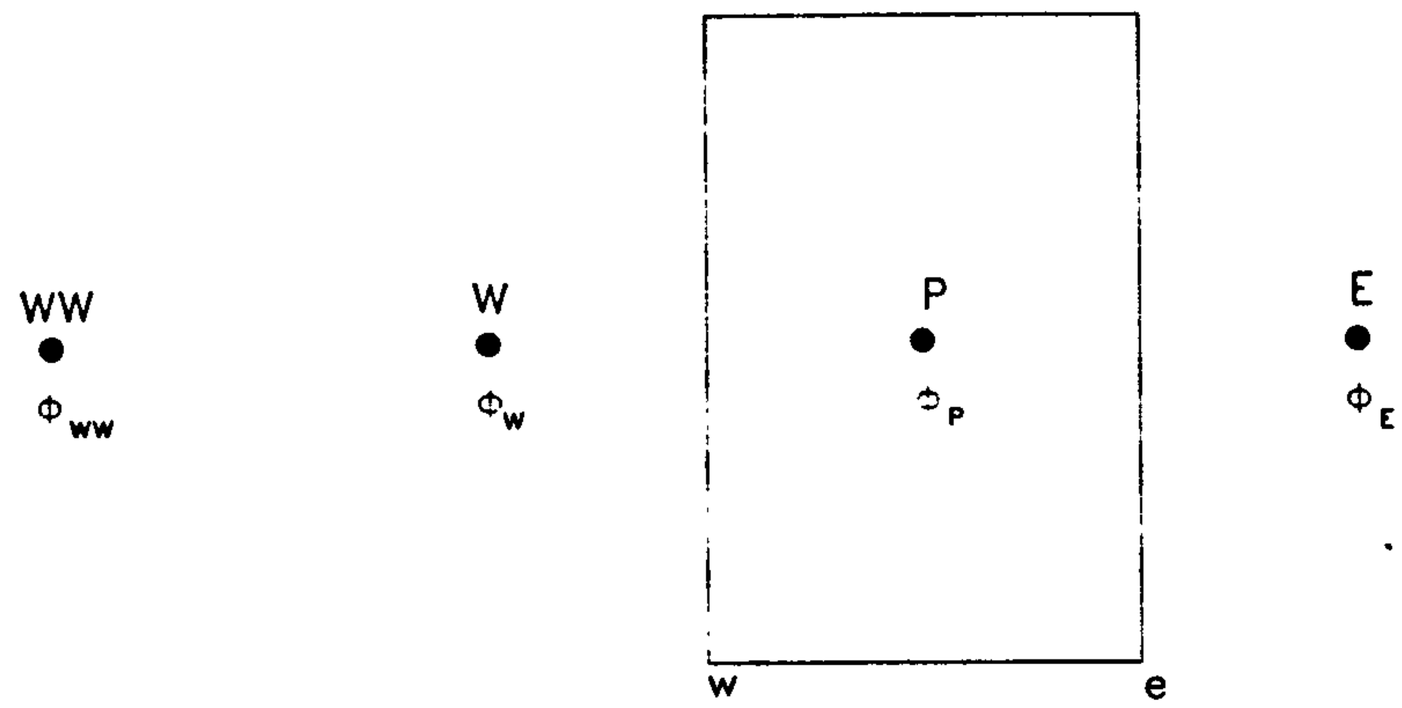


Figure 3.5-1 Illustration of notation used in description of control volume and nodes

The term A_w in Equation (3.5-3) is the area of the west face (w), h_w is the distance between the west node (W) and the central node (P), while D_w is the west diffusion coefficient.

3.5.2 Discretisation of the Advection terms

The advection terms in the equations are discretised using the hybrid differencing scheme by default. There are, however, a number of other different schemes available in the code. In order for the numerical solution to be physically realistic, the chosen discretisation scheme must have the following properties:

1. Conservativeness
2. Boundedness
3. Transportiveness

When the advection-diffusion equation is integrated over a finite number of control volumes, it yields a set of discretised conservative equations involving fluxes of the

transported quantity ϕ through the control volume faces. To ensure conservation of ϕ for the whole solution domain the flux of ϕ leaving a control volume across a certain face must be qual to the flux of ϕ entering the adjacent control volume through the same face. To achieve this the flux through the common face must be represented in a consistent manner, regardless of which cell one considers.

The discretised equations at each nodal point in the flow domain represent a set of algebraic equations which needs to be solved using iterative techniques. These methods begin by using an initial approximation of the variable ϕ and perform successive updates until a converged solution is obtained. Scarborough (1958) has shown that a sufficient condition for a converged iterative method can be expressed in terms of the values of the coefficients of the discretised equations:

$$\frac{\sum |A_{nb}|}{|A'_p|} \leq 1 \quad at\ all\ nodes$$

where A'_p is the net coefficient of the central node P (A_p - S_p)
and S_p is the source term.
The summation in the numerator is taken over all the neighbouring nodes (nb)

If the differencing scheme produces coefficients that satisfy the above criterion the resulting matrix of coefficients is diagonally dominant. To achieve diagonal dominance we need large values of the net coefficient (A_p - S_p) so the linearisation of source terms should ensure that S_p is always negative.

The boundedness criterion states that in the absence of sources, the internal nodal values of the property ϕ should be bounded by its boundary values. Another requirement for boundedness is that all coefficients of the discretised equations should have the same sign (usually positive). Physically, this means that an increase in the variable ϕ at one node should result in an increase in ϕ at the neighbouring nodes. If the discretisation scheme does not satisfy the boundedness requirements it is possible that the solution did not

converge or, if it does, then it contains spurious oscillations.

The transportiveness property of a fluid flow can be expressed by the cell Peclet number, which is a measure of the relative strengths of convection and diffusion. It is important that the relationship between the magnitude of the Peclet number and the directionality of influencing, or transportiveness, is borne out in the discretisation scheme.

The differencing schemes used, described below, will have different accuracies of solution. These are described below.

3.5.2.1 Upwind Differencing

Figure 3.5-1 is a representation of a cell in which the transport equations are to be solved. The advected value of the variable ϕ at the west face of the control volume is taken to be ϕ_w, so that at the west face,

$$\int \rho\phi \boldsymbol{U}\cdot\boldsymbol{n}\, dA = \rho U_w A_w \phi_w = C_w \phi_w$$

The corrected value of ϕ_w is assumed to vary in a stepwise fashion, with ϕ_w taking the upstream value. C_w is the convection coefficient at the west face. This gives a matrix coefficient for the west point of:

$$A_w = MAX(C_w,0) + D_w$$

This scheme is based on the backward differencing formula (Computational Fluid Dynamics Services, 1995) so it is first order accurate. A major drawback of this scheme is that it produces erroneous results when the flow is not aligned with the grid lines. The scheme causes the distributions of the transported properties to become smeared in such problems (note that smearing is also produced when the flow is aligned to the grid, but it is not as noticeable). The resulting error is known as numerical diffusion. Grid

refinement can overcome this problem, but at much greater computational costs. Therefore this scheme is not suitable for accurate flow calculations.

3.5.2.2 Central Differencing

This is a second-order accurate scheme (Computational Fluid Dynamics Services, 1995) which uses consistent expressions to evaluate convective and diffusive fluxes at the control volume faces. The internal coefficients of the discretised scalar transport equation are for the west face:

$$A_w = D_w + \frac{C_w}{2}$$

Correspondingly the east face:

$$A_e = D_e - \frac{C_e}{2}$$

Central face:

$$A_p = A_w + A_e + (C_e - C_w)$$

It may be seen from the equation for the convective contribution to the east face is negative. If convection dominates it is possible for A_e to be negative. Given that D_w and $D_e > 0$ (i.e. the flow is unidirectional), for A_e to be positive, D_e and C_e must satisfy the following condition:

$$\frac{C_e}{D_e} = Pe_h^{\,e} < 2$$

If $Pe_h^{\,e}$ (East cell Peclet number) is greater than 2 the east coefficient will be negative. This violates one of the requirements for boundedness and may lead to physically unrealisable solutions.

This differencing scheme introduces influencing at node P from the directions of all its neighbours to calculate the convective and diffusive flux. It does not recognise the direction of the flow or the strength of convection relative to diffusion (Versteeg and Malalalsekera, 1995).

3.5.2.3 Hybrid Differencing (HDS)

The hybrid differencing scheme of Spalding (1972) is based on a combination of central and upwind differencing schemes. The mesh Peclet number, Pe_h is defined as the ratio of the convection coefficient to the diffusion coefficient, C/D. Central differencing is used if the mesh Peclet number is less than 2. If the mesh Peclet number is greater than 2, then upwind differencing is used, but ignoring diffusion. The west matrix coefficient in this case is,

$$A_w = MAX\left(\frac{1}{2}C_w, D_w\right) + \frac{1}{2}C_w$$

This scheme is also first-order accurate, but is slightly better than the upwind differencing because second-order central differencing will be used across streams and in regions of low flow.

This scheme exploits the favourable properties of the upwind and central differencing schemes. It switches to upwind differencing when central differencing produces oscillations at high Peclet numbers. The scheme is fully conservative and since the coefficients are always positive it is unconditionally bounded. It satisfies the transportiveness requirement by using an upwind formulation for large values of Peclet number. This scheme is highly stable when compared with the other higher order schemes. It is formally second-order accurate, although if the mesh is too coarse, then the accuracy is reduced (it becomes effectively a first order accurate upwind differencing scheme).

3.5.2.4 Higher-order upwind differencing (HUW)

This is an upwind scheme (Thompson, Wilkes, 1982) made second-order accurate by extrapolating to the face from the two upwind points. Thus ϕ_w is given by,

$$\phi_w = \frac{3}{2}\phi_w - \frac{1}{2}\phi_{ww}$$

This scheme is less compact than the previous schemes because of the presence of the ϕ_{ww} term. To retain the matrix structure in the code, this scheme is written as,

$$\phi_w = \phi_w + \frac{1}{2}(\phi_w - \phi_{ww})$$

and the second term is included in the source terms as a deferred correction. At the east face,

$$\phi_e = \frac{3}{2}\phi_p - \frac{1}{2}\phi_w$$

which can all be kept in the matrix structure so that,

$$A_w = MAX(C_w, 0) + \frac{1}{2}MAX(C_E, 0) + D_w$$

3.5.2.5 MUSCL Schemes

MUSCL or TVD schemes are modifications to the higher-order upwind scheme with flux limiters to ensure boundedness of the solution. These have been developed to avoid the "undershoots" and "overshoots" of the QUICK scheme. TVD schemes are specially formulated to achieve oscillation free solutions.

For simplicity, consider a model equation,

$$\frac{\partial u}{\partial t} + \frac{\partial f(u)}{\partial x} = 0 \qquad (3.5\text{-}4)$$

$|\partial u/\partial x|$ integrated over the entire domain on the x axis does not increase with time. The integrated quantity is called the total variation, that is,

$$TV = \int \left|\frac{\partial u}{\partial x}\right| dx \qquad (3.5\text{-}5)$$

Hence for a physically proper solution, TV does not increase with time. In terms of a numerical solution, $\partial u/\partial x$ can be discretised by $(u_{i+1} - u_i)/\Delta x$, then,

$$TV_h(u) = \sum_i \left|u_{i+1} - u_i\right| \qquad (3.5\text{-}6)$$

Equation (3.5-6) defines the total variation in x of a discrete numerical solution. If $TV(u^{n+1})$ and $TV(u^n)$ represent (3.5-6) evaluated at time level n+1 and n, respectively, and if,

$$TV(u^{n+1}) \leq TV(u^n) \qquad (3.5\text{-}7)$$

the numerical algorithm is to be Total Variation Diminishing (TVD).

The second order upwind scheme described previously is not a TVD scheme. In order to enjoy the advantages of the second order higher upwind scheme, the scheme is modified to obey the TVD condition by using flux limiters to force the difference equations to obey the TVD condition of equation (3.5-7).

There are three different schemes available in the solver, they are: (1) the Min-Mod (MSLM-M), (2) Van Leer (MSLV-L) and (3) the Superbee (MSLS-B) schemes (Computational Fluid Dynamics Services, 1995). These differ only through their flux

limiter. The MUSCL scheme used in the numerical models of the distribution chamber, was the Van Leer scheme (Van Leer, 1982).

In MUSCL schemes, ϕ_w is given by,

$$\phi_w = \left(1 + \frac{1}{2}\psi\right)\phi_w - \frac{1}{2}\psi\phi_{ww}$$

where ψ is the flux limiter which is given in terms of the ratio r;

$$r = \frac{\phi_p - \phi_w}{\phi_w - \phi_{ww}}$$

For the Van Leer scheme, the flux limiters is as follows:

Van Leer,

$$\psi = \frac{r + |r|}{1 + |r|}$$

For this scheme the split of the terms into the matrix and deferred correction terms is carried out in the same way as for the higher order upwind scheme.

3.6 Time stepping

In the transient calculations of the flow field, an implicit backward difference time stepping procedure has been used by the software to discretise the rate of change of a variable with respect to time, i.e. if the term is written as,

$$\frac{\partial\phi}{\partial t} = F(\phi)$$

then the discretised form is,

$$\frac{\phi^n - \phi^{n-1}}{\Delta t} = F(\phi^n)$$

The term on the LHS is absorbed into the sources and sinks for each equation and the resulting equations at the nth time step will look like the discrete steady state equations. These are then solved using the standard steady state techniques.

3.7 Turbulence models

The turbulence models used in the course of the study, the standard k-ε and RNG k-ε models are described in this section.

3.7.1 k-ε turbulence model

The first turbulence model used in the calculations was the k-ε model (Launder and Spalding, 1974). In this model, the molecular viscosity term, μ, is replaced by the effective viscosity, which is the sum of the molecular viscosity and the turbulent or eddy viscosity,

$$\mu_{eff} = \mu + \mu_T$$

The eddy viscosity is written as,

$$\mu_T = C_\mu \rho \frac{k^2}{\varepsilon}$$

where C_μ is a constant, k is the turbulence kinetic energy (an approximation of the kinetic energy in the turbulent eddies), and ε is the turbulent dissipation rate.

The turbulent kinetic energy, k,

$$k = \frac{1}{2}(u'^2 + v'^2 + w'^2)$$

satisfies,

$$\frac{\partial \rho k}{\partial t} + \nabla\cdot(\rho U k) - \nabla\cdot\left[\left(\mu + \frac{\mu_T}{\sigma_k}\right)\nabla k\right] = P + G - \rho\varepsilon$$

The dissipation rate of turbulent kinetic energy, ε, is approximated by,

$$\frac{\partial \rho \varepsilon}{\partial t} + \nabla\cdot(\rho U \varepsilon) - \nabla\cdot\left[\left(\mu + \frac{\mu_T}{\sigma_\varepsilon}\right)\nabla \varepsilon\right] = C_1 \frac{\varepsilon}{k}\left(P + C_3 \max(G,0)\right) - C_2 \rho \frac{\varepsilon^2}{k}$$

where C_1 and C_2 are constants.

The strain tensor is,

$$E_{ij} = \frac{1}{2}\left(\frac{\partial U_i}{\partial x_j} + \frac{\partial U_j}{\partial x_i}\right)$$

P is the shear production term, and is defined by,

$$P = 2\mu_t E_{ij} E_{ij}$$

and G is the production term due to buoyancy,

$$G = -\frac{\mu_{eff}}{\rho\sigma_\rho} g\cdot\nabla\rho$$

This model focuses on the mechanisms that affect the turbulent kinetic energy. The

model contains five constants which were arrived at by comprehensive data fitting for a wide range of turbulent flows.

The model is one of the most widely used and validated turbulence model. It has achieved notable successes in calculating a wide variety of thin shear layer and recirculating flows without the need for case-by case adjustment of the model constants. This model has been found to perform well in confined flows where the Reynolds shear stresses are most important. However, the model was found to show only moderate agreement in unconfined flows. The model is reported not to perform well in weak shear layers (far wakes and mixing layers) and the spreading rate of axisymmetric jets in stagnant surroundings is severely over predicted. In large parts of these flows the rate of production of turbulent kinetic energy is much less than the rate of dissipation and the difficulties can only be overcome by making ad hoc adjustments to model constants. (Versteeg and Malalalsekera, 1995).

The model has problems in swirling flows and flows with large, rapid, extra strains (e.g. highly curved boundary layers) since it does not contain a description of the subtle effects of streamline curvature on turbulence. Secondary flows in long non-circular ducts, which are driven by anisotropic normal Reynolds stresses, can also not be predicted owing to the deficiencies of the treatment of normal stresses within the k-ε model (Speziale, 1987). The model has been found to over estimate the turbulence levels in situations where the flow is perpendicular to a wall (Mohammadi and Pirroneau, 1994). In simulations of flows around cylinders, high levels of turbulence were predicted before the cylinder even in the subcritical range of $Re < 2 \times 10^5$ where the boundary layer remains laminar before the separation points (Achenbach, 1986).

In summary, the deficiencies of the k-ε model include:

1. inability to account for rotational strain or shear
2. inaccurate prediction of normal Reynolds stress anisotropies,
3. inability to account for the amplification or the relaxation of the components of

the Reynolds stress tensor.

3.7.2 Renormalization Group (RNG) k-ε turbulence model

Renormalization group (RNG) methods (Yakhot and Orszag, 1986, Martinelli and Yakhot, 1989) are a general framework for "model building" in which the complex dynamics of physical problems are described in terms of "coarse grained" equations of motion governing the large-scale, long-time behaviour of the physical system.

The use of the RNG theory allows the small scales of the flow (small eddies) to be described. These should be statistically independent of the external initial conditions and dynamical forces that create them through various kinds of instability phenomena. This method gives a theory of the Kolmogorov equilibrium range of turbulence, comprising the inertial range of small-scale eddies whose energy spectrum follows the Kolmogorov law, $E(k) \propto k^{-5/3}$. This approach allows the inertial range eddies to be accounted for in a quantitative way, which allows the coarse-graining of the equations of motion for the other turbulence variables.

The RNG model is an alternative to the k-ε model for high Reynolds number flows. The model which is derived from a renormalization group analysis of the Navier-Stokes equations, differs from the standard k-ε model only through a modification to the equation for ε, and through the use of a different set of model constants.

The transport equations for k and ε are given respectively now given as:

$$\frac{\partial \rho k}{\partial t} + \nabla\cdot(\rho U k) - \nabla\cdot\left[\left(\mu + \frac{\mu_T}{\sigma_k}\right)\nabla k\right] = P + G - \rho\varepsilon$$

$$\frac{\partial \rho \varepsilon}{\partial t} + \nabla \cdot (\rho U \varepsilon) - \nabla \cdot \left[\left(\mu + \frac{\mu_T}{\sigma_\varepsilon} \right) \nabla \varepsilon \right] =$$

$$(C_1 - C_{1RNG}) \frac{\varepsilon}{k} [P + C_3 \max(G,0)] - C_2 \rho \frac{\varepsilon^2}{k}$$

where $C_{1\,RNG}$ is given by,

$$C_{1RNG} = \frac{\eta \left(1 - \frac{\eta}{\eta_0} \right)}{(1 + \beta \eta^3)}$$

β and η_0 are constants

and,

$$\eta = (2 E_{ij} E_{ij})^{1/2} \frac{k}{\varepsilon}$$

P and G are as defined in the previous section on the k-ε model.

The RNG k-ε model goes some way in overcoming some of the deficiencies found in the standard k-ε model (Mohammadi and Pirroneau, 1994). This is especially so for the regions of anisotropic turbulence, eg. swirling flows. Orszag et al (1992) have also compared the experimental results from a backward facing step with the RNG model predictions, which showed good agreement. Versteeg and Malalalsekera (1995) have noted that some researchers have made favourable reports for the RNG model, which warranted its inclusion in a number of general CFD codes. However, they have also

mentioned that the model would need to undergo more testing and validation prior to giving any definitive recommendations for its use.

3.8 Multiphase model

The model which describes the interaction between the two phases, for example, air and water, considered in this study is described below. Since the flow within the distribution chamber is largely stratified, with no significant mass transfer between the two phases, the Homogeneous or VOF model was used in the calculations.

3.8.1 Homogeneous or Volume of fluid (VOF) model

In the VOF model, for a given transport process, it assumes that the velocities for the process are the same for all phases at any (x, y, z, t).

The resulting equation for continuity is written as,

$$\frac{\partial}{\partial t}(r_\alpha \rho_\alpha) + \nabla\cdot(r_\alpha \rho_\alpha \boldsymbol{U}) = 0$$

the single momentum conservation equation is,

$$\frac{\partial \rho \boldsymbol{U}}{\partial t} + \nabla\cdot[\rho \boldsymbol{U}\times\boldsymbol{U} - \mu(\nabla \boldsymbol{U} + (\nabla \boldsymbol{U}^T))] = \boldsymbol{B} + \nabla p$$

Since the flow under consideration is isothermal, the temperature equation is zero. Also,

$$\rho = \sum_{phases} r_\alpha \rho_\alpha$$

where $\nabla \boldsymbol{U}^T$ is the transpose of the vector $\nabla \boldsymbol{U}$,

r_α is the volume fraction of the phase α

B is the body force, and p is the pressure

ρ_α is the fluid density

μ is the total viscosity of the fluid

The total viscosity of either fluids is a weighted average of the laminar (or molecular) viscosity and turbulent viscosity, which is written as,

$$\mu_{effective} = \sum_{phases} r_\alpha \mu_\alpha + C_\mu \frac{k^2}{\varepsilon} \left(\sum_{phases} r_\alpha \rho_\alpha \right) \quad .$$

where k is the turbulence kinetic energy,

ε is the dissipation of the turbulence energy

C_μ is a constant with a value of 0.09

The homogeneous model is considered a good approximation when the flow is under the influence of gravity, and where the phases are stratified, for example, free surface flow. The volume fractions of the individual phases are equal to zero or unity everywhere except at the phase boundaries. The use of a single velocity field for each phase is valid.

A surface sharpening algorithm is incorporated in the CFX solver. In the flow domain, the volume fractions of the two phases are normally specified such that their values change sharply across the interface between the two fluids. It is possible that the interface can become smeared in time due to numerical diffusion in the volume fraction equations, in the course of the solution to the problem. To overcome this, the surface sharpening algorithm is used to overcome this problem.

The algorithm carries out a modification to the volume fractions of the two fluids at the end of each time step. The interface is defined to be the surface where the volume fractions of the two fluids, r_1 and r_2 are both equal to 0.5. Firstly, the code identifies control volumes on the interface by determining whether r_1 - 0.5 for the cell is different

in sign from any of the surrounding cells. The code then identifies fluid on the "wrong" side of the interface and moves it onto the "correct" side of the interface ensuring that volume is conserved (note that the momentum is not conserved). If however, the interface is vertical, there may be problems. Also, the turbulent eddies are not considered for in the VOF model. The presence of an interface would cause the eddies, being transported up towards the free surface, to be deformed. This would then lead to a reduction in turbulent kinetic energy, k, since the velocity gradients at the interface are reduced.

3.9 Wall boundary conditions

The velocity at the walls of the domain are specified to be zero (i.e. no-slip). Many of the variables vary rapidly near the walls. Their behaviour is specified with wall functions instead of using very fine grids in those regions. In the solver, for a fully developed turbulent flow over a stationary wall, at a distance y = d from the wall, the wall shear stress, τ, is related to the turbulence kinetic energy by,

$$\tau^2 = C_\mu \rho^2 k^2$$

A new quantity, τ_k is defined,

$$\tau_k = \rho C_\mu^{1/2} k$$

This is then used to define scaled variables,

$$y^+ = \frac{(\rho \tau_k)^{1/2}}{\mu}(d - y)$$

and

$$u^+ = \frac{(\rho \tau_k)^{1/2}}{\mu} u$$

The scaled velocity component parallel to the wall and in the x direction is,

$$u^+ = y^+, \quad for \quad y^+ < y_0^+$$

or

$$u^+ = \frac{1}{k} \ln(E y^+), \quad for \quad y^+ > y_0^+$$

y_0^+ is the cross-over point between the viscous sublayer and the logarithmic region. This is given by,

$$y_0^+ = \frac{1}{k} \ln(E y_0^+)$$

The turbulent kinetic energy, k, is solved in the control volume immediately adjacent to the wall. From this, the wall shear stress is found. The turbulent dissipation is obtained from k by the relationship,

$$\varepsilon = \frac{C_\mu^{3/4} k^{3/2}}{k(d - y)}$$

Experience and comparison with a wide variety of experimental data shows that this approach is accurate (Versteeg and Malalasekera, 1995).

3.10 Summary of Literature Review

In the review, it was found that there was little work done specifically on flow distribution chambers. There is only a small body of knowledge available, in the design of chambers. An simple method for the estimation of the magnitude of the surface

disturbance was put forward by Herbath and Wong (1997a), which was based on estimates of the centreline velocity of the jet formed within the chamber. Alternatively, Rodi's method (1993) can also be used. Although the magnitude of the surface disturbance within a chamber may be estimated to varying degrees of accuracy, the assumption that the presence of a boil in a chamber can be equated to flow mal-distribution will have to be proven.

Herbath and Wong (1997a) also produced an empirical method for estimating the effect of chamber geometry on the onset of flow mal-distribution. However, the variation in the magnitude of mal-distribution with chamber geometry was not quantified. Consideration was also given to the type of flow control devices used at the outlets of the chamber. For discharge weirs, the likelihood of mal-distribution was higher than that of submerged orifices.

A practical means of measuring flow mal-distribution in treatment plants are given by Herbath and Wong (1997a). This method involved the measurement of the height of the water surface immediately above the weir crest. This height may then be related to the total flow into the chamber (if the individual chamber flows are not metered). Consequently, the percentage mal-distribution may then be obtained. This method for estimating water levels was based on an empirical method developed for fully developed flows in long, open channels. Consequently, the accuracy of this method is questionable for distribution chambers.

Since hot-wire anemometry was to be used in the experiments, a review of the different calibration techniques was made. Numerous techniques had been put forward by many researchers in the past. However, the technique used in this work (discussed in Chapter 5), was an adaptation of the various techniques described here.

Since the outputs from hot wire or hot film anemometers are in voltages, the relationship between the raw outputs from the probes and velocities had to be determined. Many

researchers have put forward numerous relationships, with varying degrees of accuracies and complexities. The most appropriate method for use in the data analysis was identified here. This method was based on Bradshaw (1971), and is relatively simple and accurate.

A commercial CFD code, CFX 4.1, was used in the research. Consequently, the technology associated with CFD was reviewed. The various differencing schemes, used in the course of the investigation, and the two turbulence models used in the calculations were examined. The mechanics of the VOF multiphase model, and the treatment of the flow at the wall were also reviewed.

4. THE EXPERIMENTAL TEST RIG

A 1:13 scale model of a typical flow distribution chamber as found in a sewage treatment plant was designed and constructed. This design was based on an actual distribution chamber constructed at the Davyhulme sewage treatment plant (Reade and Wong, 1995). The design was such that two separate distribution chamber models can be combined into one. Model A was had two symmetrical outlets. Model B had four outlets of unequal dimensions. Experiments were carried out on both models although only the results from Model A were used to validate the CFD model. Consequently the model descriptions given in this chapter shall concentrate on Model A. Figure 4-1 is a schematic showing the layout and dimensions of the two models. Figures 4-2 is a photograph of Model A.

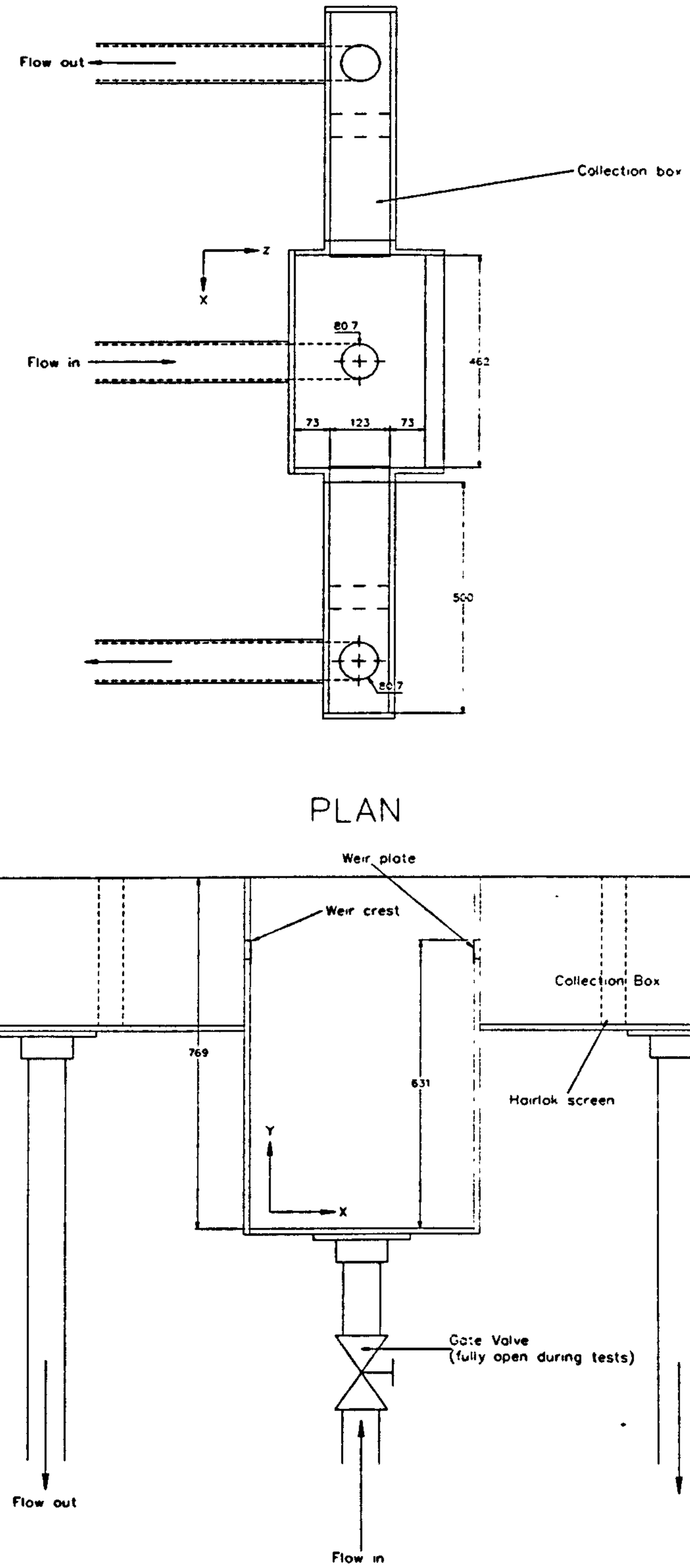


Figure 4-1 Schematic of Model A. Dimensions are model scale.

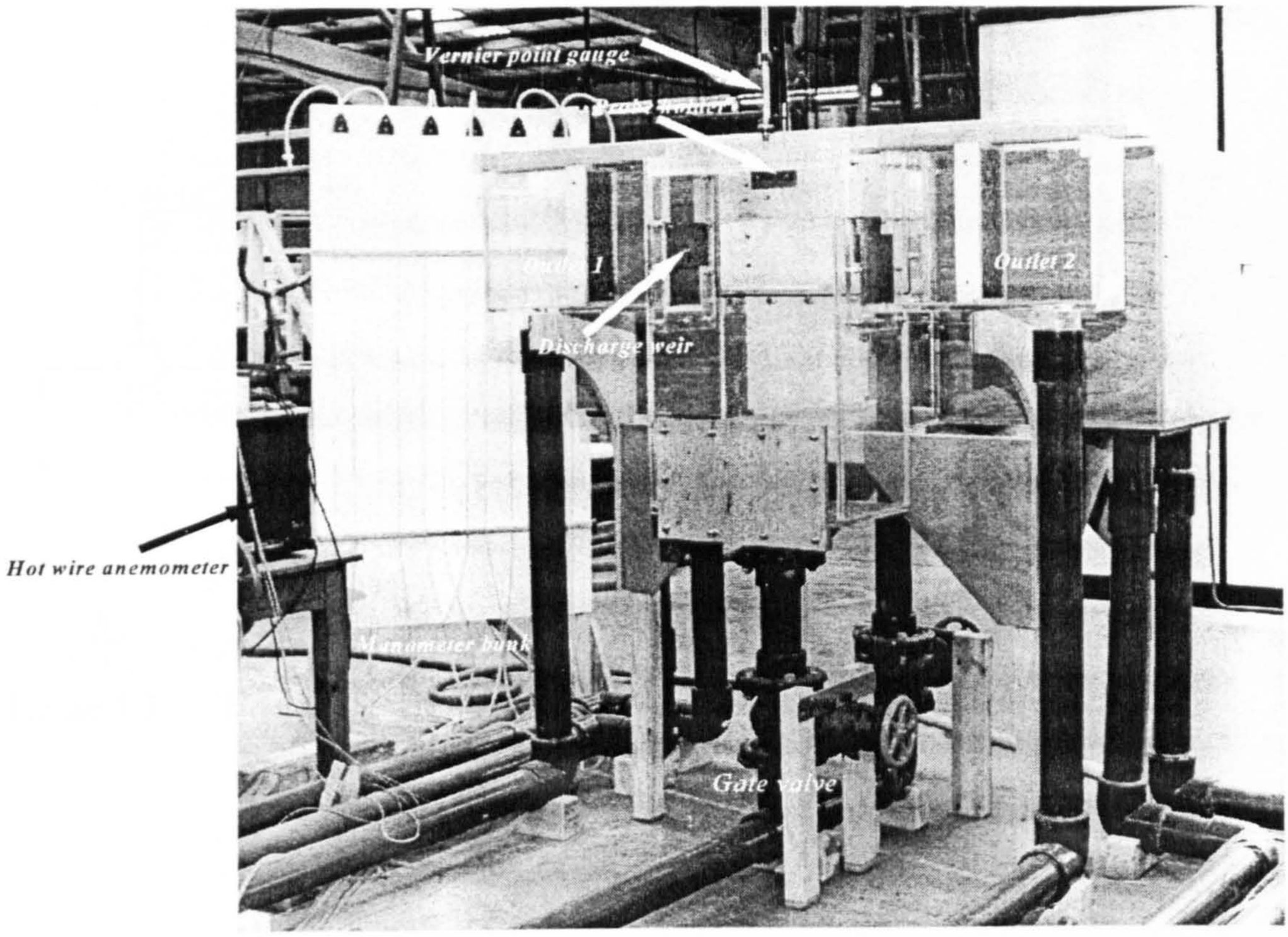


Figure 4-2 Photograph showing the test rig and Model A in the foreground. Salient features of the test rig as described in the text are arrowed

A pump drew water from the laboratory sump during the experiments. The flowrate into the model was controlled by a gate valve downstream of the discharge end of the pump. A by-pass loop with another gate valve linked the discharge line to the suction line. This by-pass loop allowed finer adjustments to the flow into the model. Figure 4-3 is a schematic showing the layout of the test facility.

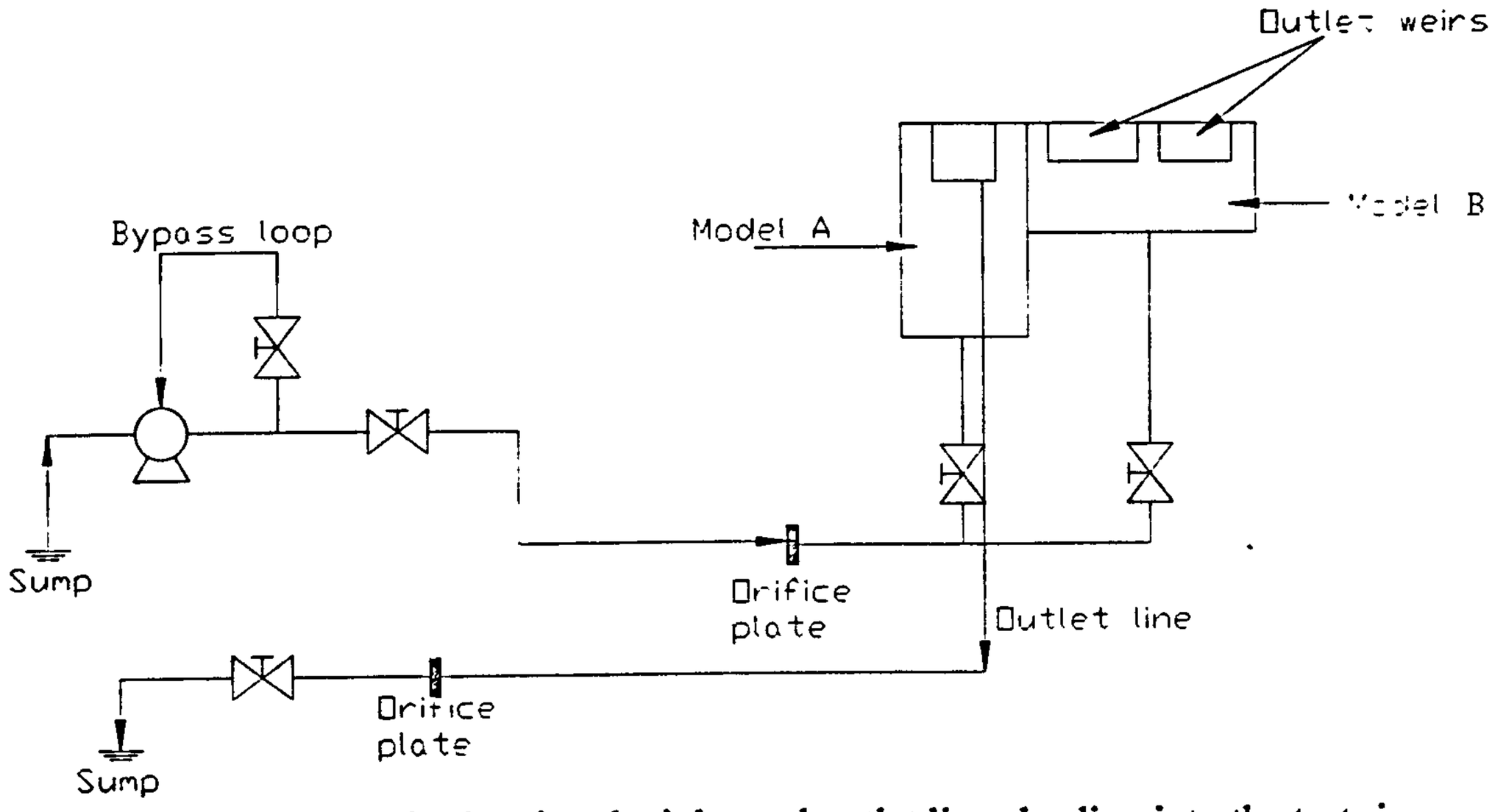


Figure 4-3 **Schematic showing the inlet and outlet lines leading into the test rig**

The inlet into model A was via a tee-junction, while for model B, a 90° pipe elbow was used. The pipework was constructed from uPVC, and had a nominal bore of 3" (outer diameter of 88.9 mm, and inner diameter of 80.7 mm).

The flow of water leaving the distribution chambers was via freely discharging weirs. Collection boxes were constructed downstream of each discharge weir, which channelled the flow into discharge lines. 3" uPVC pipes were used. These discharge lines led back to the laboratory sump. Gate valves were installed on the discharge lines. Pipe reducers were also found downstream of the gate valves. These 3" to 2" pipe reducers, in addition to the gate valves helped to back up the flow leaving the model. "Hairlok" screens were also installed within the collection boxes so as to reduce the amount of air bubbles entering the discharge lines. The purpose of these were to ensure the discharge lines were full of water, submerging the orifice plates on the discharge lines. Thus, the

plates would be operating in the correct operating flow regime, namely single phase water.

Model A was 0.769 m high, 0.462 m wide and 0.269 m deep. It had two discharge weirs, 0.123 m wide, and the weir crest levels were 0.631 m from the floor of the chamber. The weirs were adjustable, and were set to the correct heights with a theodolite during construction. The estimated accuracy of this level was ± 0.001 m. The walls of the model was constructed from transparent Perspex so as to facilitate flow visualization.

Model B had a larger surface area than model A at 0.462 m width and 0.708 m depth. The height of the chamber was much shallower at 0.281 m. There were 4 discharge weirs and the crest levels were set at 0.159 m above the chamber floor. The width of the weirs ranged from 0.165 m to 0.259 m. The chamber was originally designed to split the discharge flows proportionally, hence two weirs had equal width weirs of 0.212 m, while the other two were 0.165 m and 0.259 m. The width of each weir was determined by the ratio of the required discharge over that weir and the total flow into the chamber. The discharge lines were similar in layout to that of Model A.

4.1 Scaling Laws

Model dimensions and flows were based on Froude scaling, so that the prototype and model Froude numbers are equal, ensuring inertial forces were representative of the prototype. The Froude number is given by,

$$Fr = \frac{U}{\sqrt{lg}} \qquad (4.1\text{-}1)$$

where U is the inlet fluid velocity measured within the structure

l is the characteristic length

g is the acceleration due to gravity

The Froude number can be interpreted as a ratio of the convective to gravitational force. For large Froude numbers, inertial forces predominate and gravity has little influence on the motion of the particle. Conversely, for low Froude numbers, gravity force is the major contributory factor to the fluid motion. For free surface flows, the characteristic length, l, is taken to be the water depth for this gives a measure of the gravitational forces acting on the fluid.

In a reduced scale model, it is impossible to have both Reynolds number and Froude number the same as in the prototype if the same fluid is used. In practice, it is highly desirable to use water. Thus one of the similarity conditions must be relaxed. In the flow geometry considered, the key mechanisms governing the top of the upwards flowing jet are buoyancy controlled. It is also the behaviour of the flow at the top which is critical for flow asymmetry. It is therefore preferable to maintain the Froude number in the model, since this quantity defines the relative importance of buoyancy to convection.

The Reynolds number is given by,

$$Re = \frac{\rho U l}{\mu} \qquad (4.1\text{-}2)$$

where ρ is the fluid density

and μ is the fluid dynamic viscosity.

The scale selected for the model was sufficiently large to ensure that any effects due to viscous forces can be assumed to be negligible due to the high Reynolds numbers in the model.

Thus, for a Froude scale model,

$$Fr = \frac{U_m}{\sqrt{l_m g}} = \frac{U_p}{\sqrt{l_p g}} \qquad (4.1\text{-}3)$$

where the subscripts m and p refer to the model and prototype respectively.

The relationship between model and prototype velocity may be derived as,

$$\frac{U_m}{U_p} = \left(\frac{l_m}{l_p}\right)^{1/2} \qquad (4.1\text{-}4)$$

For flowrate, Q is proportional to Ul^2, the relationship is,

$$\frac{Q_m}{Q_p} = \left(\frac{l_m}{l_p}\right)^{5/2} \qquad (4.1\text{-}5)$$

The relationship for Reynolds number, when the same fluid is present in both the model and prototype is,

$$Re = \frac{Ul}{\mu}$$

therefore,

$$\frac{Re_m}{Re_p} = \left(\frac{l_m}{l_p}\right)^{3/2} \qquad (4.1\text{-}6)$$

The relationship between lengths, diameters etc. is a direct relationship between the model and prototype dimensions.

4.2 Instrumentation

4.2.1 Flow measurement

The flow into and out of the models were metered by orifice plates designed, constructed and installed in accordance to BS1042 (British Standards Institution, 1989) and ISO 5167/1 (ISO 1980). All plates had a conical orifice, where a 45° chamfer was present. A 60 mm diameter orifice plate was installed on the inlet line, while the 6 individual discharge lines had a 40 mm diameter orifice plate each. Water manometers were connected to the upstream and downstream pressure tappings found at each orifice plate location. By measuring the head loss across the orifice plate, the volumetric flowrate through the orifice plate can be determined by the following relationship (International Standard 5167, 1980):

$$Q = \frac{1}{\rho} C E \epsilon_f \frac{\pi}{4} d^2 \sqrt{2 g \Delta H} \qquad (4.2\text{-}1)$$

where C is the coefficient of discharge, 0.734

ϵ_f is the expansibility factor = 1.0 for incompressible fluids

ρ is the density of the fluid,

d is the diameter of the orifice,

ΔH is the measured headloss across the orifice plate.

and V_{appr} is the velocity of approach, given by,

$$V_{appr} = \frac{D^2}{\sqrt{D^4 - d^4}} \qquad (4.2\text{-}2)$$

D is the diameter of the pipe

4.2.2 Turbulence measurements

The water velocities within the model were measured by the use of hot wire

anemometry. A hot film probe (cross-wire, or X-probe configuration), was used to measure the two components of velocity within the models. The probe, a 6525/F65W model, was manufactured by Prosser Scientific Instruments. Figure 3.2-1 in Chapter 3 is a simplified view of the probe. The layout of the probe allowed the measurement of the two spatial components of velocity. A 65 micron layer of platinum film was deposited onto the two active sensors, thus allowing the use of the probe in conducting liquids, such as water. The resistances of sensors 1 and 2 were 8.70 Ω and 8.88 Ω, measured at 19°C, respectively. The temperature coefficient of the probe was 0.0025 %/°C. The probe was connected to a probe holder, which in turn was connected to a two channel, constant temperature anemometer, Model 6100. The system response time was adjusted prior to the experiments to be 0.002 s, or a frequency of 500 Hz.

4.2.3 Measurement of water levels

A vernier point gauge was used to determine the water levels during the experiments. The gauge was mounted onto a wooden beam, which was placed on top of the models. With the use of graduated scales on both the walls of the models and on the beam, the point gauge could be traversed by moving the wooden beam. A plastic clamp was also manufactured. This was designed to position the hot film probe holder relative to the vernier point gauge. The point gauge was zeroed to the weir crest levels prior to the experiments.

4.2.4 Temperature Measurements

Temperature of the flow within the distribution chamber was recorded in the course of each test. This was done by using a Digitron Instrumentation Ltd. thermocouple model 1408-K.

4.2.5 Data Acquisition System

The voltage outputs from both channels of the anemometer were captured by a 16 channel National Instruments Corp. analog-digital conversion card model number AT-MIO16E, connected to a Pentium PC. The PC ran the National Instruments Labview data acquisition program which allowed the data acquisition rates, sampling times, and calibration constants to be altered. Data was captured at a rate of 300 Hz for a total time of 120 seconds during the tests, and was saved to the hard disk of the PC.

4.3 Sampling times, sampling frequencies and error estimates

Nychas (1987) presented a method for linking sampling times and error analysis of the data. This is given below.

The instantaneous value of a turbulent quantity, U(t), can be represented by the use of Reynolds decomposition, which is the sum of the average value and the instantaneous value,

$$U(t) = \overline{U} + u(t) \qquad (4.3\text{-}1)$$

where the average value is represented by the overbar.

If the averaging time is very long in the experiments, the time averages of the turbulent quantities converge to a mean value. In practice, it is impossible to integrate over an infinitely long time. Thus, in the design and planning of an experiment it is important to estimate the error associated to a finite integration time. The data storage capacity, limitations on the maximum time available for an experiment, electronic and sensor drift are problems which are directly related to the time length of the acquired signal. For the instantaneous velocity component, U(t), the average corresponding to the averaging time, T, can be written as,

$$U_T = \frac{1}{T}\int_0^T U(t)\,dt \qquad (4.3\text{-}2a)$$

and

$$\lim_{T\to\infty} U_T = \overline{U} \qquad (4.3\text{-}2b)$$

The velocity autocorrelation coefficient, $\rho(\tau)$ is defined by,

$$u_{rms}^2\,\rho(\tau) = \overline{u(t)\,u(t+\tau)} = \overline{[U(t) - \overline{U}]\,[U(t+\tau) - \overline{U}]} \equiv b_u(\tau) \qquad (4.3\text{-}3)$$

where,

$$u_{rms}^2 = \overline{[u(t)]^2} = \overline{[U(t) - \overline{U}]^2} = \sigma_u^2 = var(U)$$

An integral time scale, T_u, can be defined from the autocorrelation coefficient,

$$T_u = \int_0^\infty \rho_u(\tau)\,d\tau \qquad (4.3\text{-}4)$$

Monin and Yaglom (1971) showed that for integrating time $T >> T_u$,

$$var(U_T) = \overline{(U_T - \overline{U})^2} \approx 2\overline{u^2}\,\frac{T_u}{T} \qquad (4.3\text{-}5)$$

The relative error in the estimator U_T of $\overline{U}$ is,

$$\epsilon = \sqrt{\frac{2T_u}{T}} \left| \frac{u_{rms}}{\overline{U}} \right| \qquad (4.3\text{-}6)$$

For the ensemble average, U_N, of N samples of U_i, the expression is,

$$U_N = \frac{1}{N} \sum_{i=1}^{N} U_i \qquad (4.3\text{-}7a)$$

The true average, $\overline{U}$, is expressed as,

$$\lim_{N \to \infty} U_N = \overline{U} \qquad (4.3\text{-}7b)$$

Then the relative error for N samples is,

$$\epsilon = \frac{1}{\sqrt{N}} \left| \frac{\sigma_U}{\overline{U}} \right| \qquad (4.3\text{-}8)$$

where,

$$\sigma_u^2 = var(U_N) = \langle (U_N - \overline{U})^2 \rangle$$

(the brackets $\langle \rangle$ denote ensemble average)

It may be seen from equations (4.3-6) and (4.3-8) that both estimators, U_T and U_N, converge to the true average when $T \to \infty$ and $N \to \infty$ respectively. The number of independent samples in the ensemble average is,

$$N = \frac{T}{2T_u} \qquad (4.3\text{-}9)$$

Thus, the total sampling time equal to two integral scales is statistically independent, and therefore adequate.

The error estimates of (4.3-6) and (4.3-8) relate the sampling time, T, to an acceptable error, ϵ, and other parameters such as autocorrelation coefficient. These are, however, not known prior to data acquisition.

Bradshaw (1971) suggested a method for estimating the required sampling time for an experiment. For spectrum analysis, the required filtered bandwidth is Δf, and an acceptable normalized standard deviation is σ, then the record length, T, is estimated from,

$$T = \frac{1}{\sigma^2 \Delta f} \approx \frac{1}{\sigma^2 f_{min}} \qquad (4.3\text{-}10)$$

where f_{min} is the lowest frequency for which accurate results are required.

Therefore, the total number of digitized data points, N, is

$$N = (sampling\ rate) \times (sampling\ duration) = \left(\frac{2}{\sigma^2}\right) \frac{f_{max}}{f_{min}} \qquad (4.3\text{-}11)$$

where f_{max} is the highest frequency encountered in the signal of the quantity to be measured.

The quantity f_{max}/f_{min} increases with Reynolds number and is proportional to the ratio of the mean flow width to the Kolmogorov microscale, η. The Kolmogorov microscale is the smallest turbulent fluctuation that can withstand the damping effect of viscosity.

4.3.1 Experimental sampling frequencies

In order to determine the value of f_{max} over the range of test flowrates, the cross-wire probe to be used in the experiments was connected to the anemometer system. The bridge outputs were then connected to a FFT analyser. The flowrates of interest and the flow conditions representative of the tests to be carried out were set up in the test rig.

In this way, the maximum frequencies occurring in the flow was captured and measured by the FFT analyser. The maximum frequency was found to be just under 100 Hz. The use of the FFT analyser also allowed the determination of any background noise which can corrupt the actual signals from the cross-wire probe. It was found that there was very little noise, and were at a frequency of a few hertz.

In order to avoid the aliasing of the hot film probe signals, the Nyquist criterion states that the sampling rate for the acquired data has to be a minimum of 2 x f_{max}, i.e. approximately 200 Hz.

Since the data acquisition equipment used was PC based, there was no bottleneck in sampling frequency imposed by both the custom written data acquisition software and storage requirements of the PC. Hence, a sampling frequency of 3 x f_{max}, or 300 Hz (300 samples per second per channel) was chosen for the all the tests.

4.3.2 Experimental Sampling times

The determination of the minimum sampling time for a given accuracy can be found using equation (4.3-11). In this case, f_{max} = 100 Hz, f_{min} = 200 Hz, and the required standard deviation for the data is say, 1%, then the number of samples, N is 10,000. But the sampling rate is 300 samples/second, therefore the sampling duration must be 33.3 seconds.

The sampling time in the experiments was chosen to be 2 minutes. Therefore, the total number of samples was 36 000 per test. This gave the equivalent of a normalized standard deviation for the data of 0.5%.

The total number of data points, sampling times and frequencies were in excess of the minimum requirements for the required standard deviation of the data points. Nevertheless, the collection of additional data points lends more confidence to the time

average of the velocity measurements, as indicated in equation (4.3-2a) and (4.3-2b).

4.4 Measurement Accuracy

The uncertainty of any experimental measurement can be estimated if the uncertainties from various sources are combined. Uncertainty is defined in ISO-5167(International Standard, 1980) as the range of values within which the true value of the measurement is estimated to lie at 95% probability.

Experimental errors may be classified as either random or systematic. The former affects the reproducibility (precision) of measurement and the latter affects its true accuracy.

The contribution of random uncertainty in experimental measurements to the total uncertainty of the mean value is twice the standard deviation of the variable (if the number of measurements is large) for 95% probability.

Experimental measurements are subject to both systematic and random errors. As repetition of the measurement does not eliminate systematic errors, the actual value can only be determined by an independent measurement known to be more accurate.

The accuracy of the measurements made in the course of the experiments are discussed below.

4.4.1 Probe and vernier point gauge location

The cross wire probe was clamped onto the stem of a vernier point gauge. The location of the probe assembly was kept constant in relation to the vernier gauge for the duration of the tests. The assembly was only able to be traversed in the vertical (y) direction by

the movement of the point gauge stem. The accuracy of the vernier point gauge was ± 1 mm.

In the horizontal direction, the probe assembly was traversed by moving the wooden support beam onto which the vernier point gauge was mounted. The markings on the walls of the model (using lined paper) provided the necessary reference marks across which the beam may be moved. The accuracy of the x and z positions for the probe was ± 2 mm.

4.4.2 Hot film measurements

The maximum error of the anemometer was quoted as $\pm 0.1\%$ by the manufacturer. The maximum errors from the measurements and conversions of the raw voltages to give U, V and k are found to be $\pm 1\%$, $\pm 8\%$ and $\pm 9\%$ respectively. These values include the measurement errors of the anemometer. The values were determined from 95% confidence levels of the raw voltage data. The maximum and minimum variance of the voltages were then converted into velocities and turbulence. The difference between the mean and variance gave the percentage uncertainties quoted above.

4.4.3 Free surface measurements

The location of the free surface was measured using a vernier point gauge whose accuracy is ± 1 mm. However, the shape and location of the free surface varied in time. As a result, the values measured in the experiment were also subject to random error. The maximum error at the lowest flowrate of 2.95 l/s was ± 2 mm, ± 3 mm at 4.38 l/s and ± 5 mm at 5.51 l/s. Therefore the total uncertainty for the location of the free surface was ± 3 mm at 2.95 l/s, $\pm$ 4 mm at 4.38 l/s and $\pm$ 6 mm at 5.51 l/s.

4.4.4 Flow measurements and flow distribution

The volumetric flow into and out of the model were metered by orifice plates. The systematic errors in the calculation of the flow were due to:

1. estimation of the coefficient of discharge, C
2. the value of the orifice diameter and pipe internal diameter, and
3. the measurement of water columns in the water manometer.

The value of g, the acceleration due to gravity, will vary with location; however, the variations were small enough to be negligible (see equation (4.2-1)).

The value of the discharge coefficient was given in BS1042 as 0.734 with an uncertainty value (X_1) of $\pm$ 2%. The estimated tolerance in the manufacture of both the orifice plates and pipes were both $\pm$1 mm. Expressed in percentage, these were approximately $\pm$ 2.5% and $\pm$ 1.5% (X_2 and X_3) respectively. The estimated experimental error in measuring the heights of the water columns (X_4) were estimated to be $\pm$5 mm, or a maximum of $\pm$5%. Hence the total uncertainty, X, was calculated from,

$$X = \pm \sqrt{X_1^2 + X_2^2 + X_3^2 + X_4^2}$$

The total uncertainty, X, was calculated to be $\pm$6.12%.

Since percentage distribution between the two outlets were determined from the flow measurements out of the test rig, the uncertainty associated with the flow distribution values were the same for flow measurement uncertainty, i.e., $\pm$ 6.12%.

4.5 Summary of Experiments

A 1:13 scale model of an existing distribution chamber was constructed in accordance to Froude scaling laws. The scale was chosen to be as large as practicable in order to

ensure sufficiently large Reynolds number in the model. In this way the viscous forces may be considered to be negligible.

The volumetric flow into and out of the model was metered by orifice plates which had accuracies of $\pm$ 6.12 %. The measurement of turbulence and velocities near the free surface was made by hot film anemometry. The response time of this system was adjusted to be 0.002 s. A vernier point gauge was used for the water level measurements. The accuracy of this instrument is $\pm$ 1 mm.

The sampling frequency chosen in the tests was 300 samples/second, for a duration of 2 minutes. This gave the equivalent of a normalized standard deviation for the data of 0.5 %. The estimated errors in the conversion of the raw voltages measured by the anemometer to U, V, and k are $\pm$1%, $\pm$8%, and $\pm$9% respectively.

5. EXPERIMENTAL TEST PROCEDURES

Prior to the start of the experiments on the physical model, the instruments used in the experiments had to be calibrated. Section 5.1 describes the calibration procedures. Following the calibration, tests were conducted. The procedures are described next, followed by the test plan. Since hot wire anemometry was used, the raw voltages recorded had to be converted into meaningful velocities and turbulent kinetic energies. The procedures by which these were achieved are given below.

5.1 Calibration of Instruments

The calibration of the instruments used in the course of the experiments, such as the hot film probe, and the vernier point gauge are described below. Other instruments such as the hot film anemometer, miniature propeller meter, and the thermocouple were calibrated by the manufacturers/suppliers. The calibration certificates, where relevant, are included in Appendix A.

5.1.1 Hot Film Calibration

Prior to the use of the cross wire probe in the physical model, it had to be calibrated in order to determine the voltage-velocity-yaw angle relationship, valid for the range of velocities encountered during the tests.

The calibration method chosen in this study was a variation of the usual method of calibrating in a wind tunnel. In this case, a water flume was used. This is a novel technique and made use of the existing facilities available.

The cross-section of the flume was rectangular in shape. It was 10 m in length, 0.3 m in width and 0.4 m in height, constructed from transparent perspex. An adjustable control weir at the downstream end of the flume was installed. This allowed the water

levels, and hence, the flow velocities within the flume to be controlled. As in the distribution chamber model, the flume was supplied with water from the laboratory sump by means of a pump. A 77 mm diameter orifice plate, manufactured and installed in accordance to BS1042 (British Standards Institute,1989) and ISO 5167 (International Standards, 1980), was used in the inlet pipework to meter the flow into the flume. A rectangular header tank was installed upstream of the inlet into the flume. Since the width of the header tank was greater than that of the flume width, tapered wooden blocks or nosings were installed within the tank. These allowed a smoother and fully developed flow transition from the header tank into the rectangular flume. A metal screen was placed upstream of the inlet. This filtered out any large particles of dirt and other contaminants which would otherwise damage or destroy the hot film probe. It also served to create a more uniform velocity distribution throughout the width and depth of the flume. Figure 5.1-1 is a photograph of the flume.

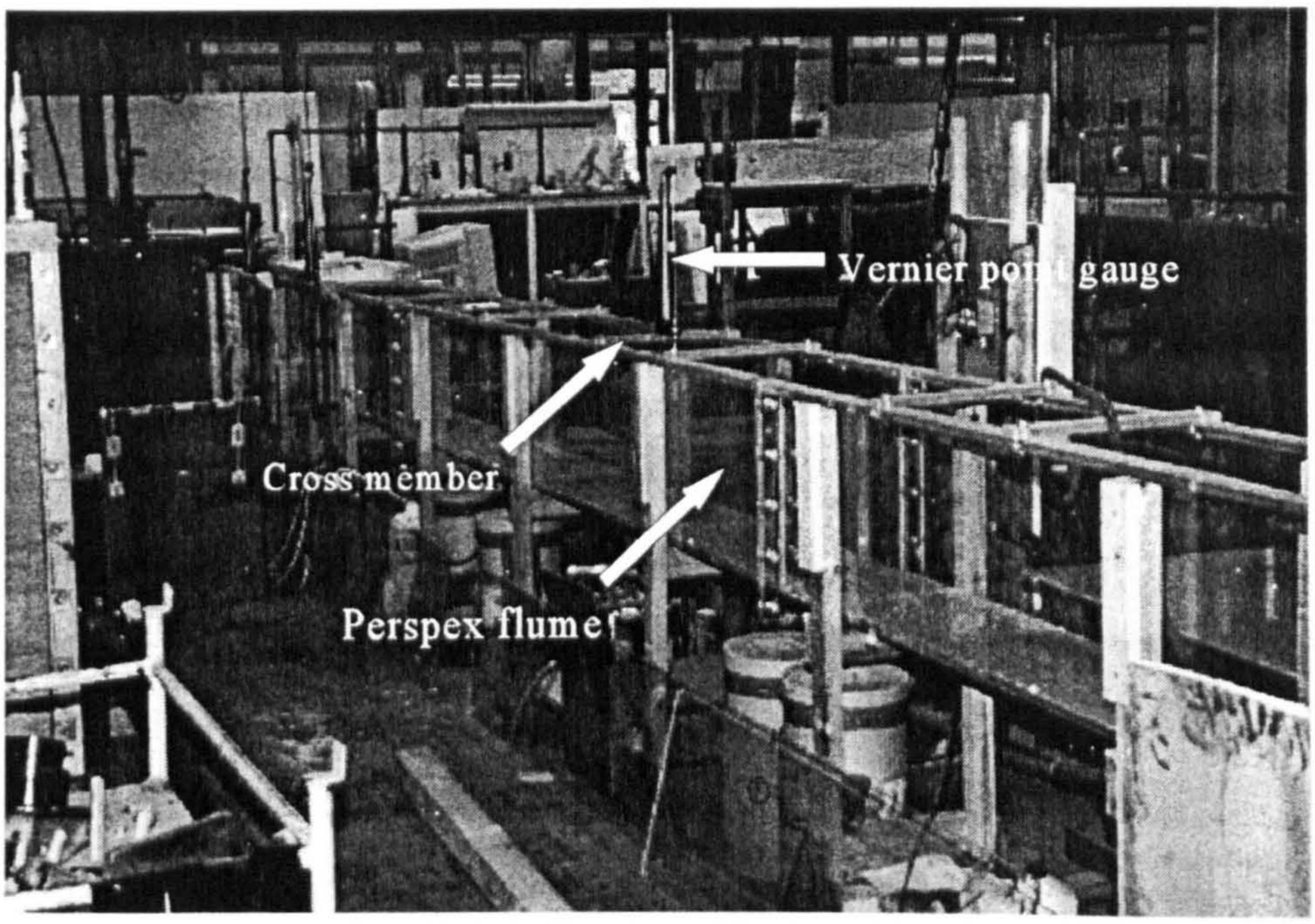


Figure 5.1-1 View of perspex flume used in the calibration of the cross-wire probe

A vernier point gauge was mounted on a cross-member, 8 m downstream from the inlet. A plastic clamp was used to mount the hot film probe holder onto the stem of the point gauge. A protractor was also screwed onto the clamp so that in conjunction with a pointer on the stem of the probe holder, the probe could be yawed through the range of angles required in the calibration procedure (Figure 5.1-2). A Nixons Instrumentation miniature propeller meter was mounted on a retort stand 10 cm downstream of the probe/point gauge assembly.

During the calibration phase, the probe was mounted in a central position in the flume, away from the boundary layer effects of the walls or the floor. The angles at which the probe were yawed through, ranged from -40° to +40°, in 5° intervals, for each test flowrate. The propeller meter downstream of the probe was traversed accordingly so as to measure the velocities immediately behind the probe. (A copy of the calibration certificate for the propeller meter is given in Appendix A). A range of up to six different velocities were set up within the flume, these ranged approximately from 0.08 m/s to 0.6 m/s. Additionally, the voltage outputs from the probe at 0 m/s was also measured. This involved immersing the probe into a beaker full of still water at the conclusion of the calibration tests in the flume. The water temperature for the whole range of tests was also recorded using the same thermocouple described previously. Table 5-1 summarizes the cross wire probe yaw calibration tests.

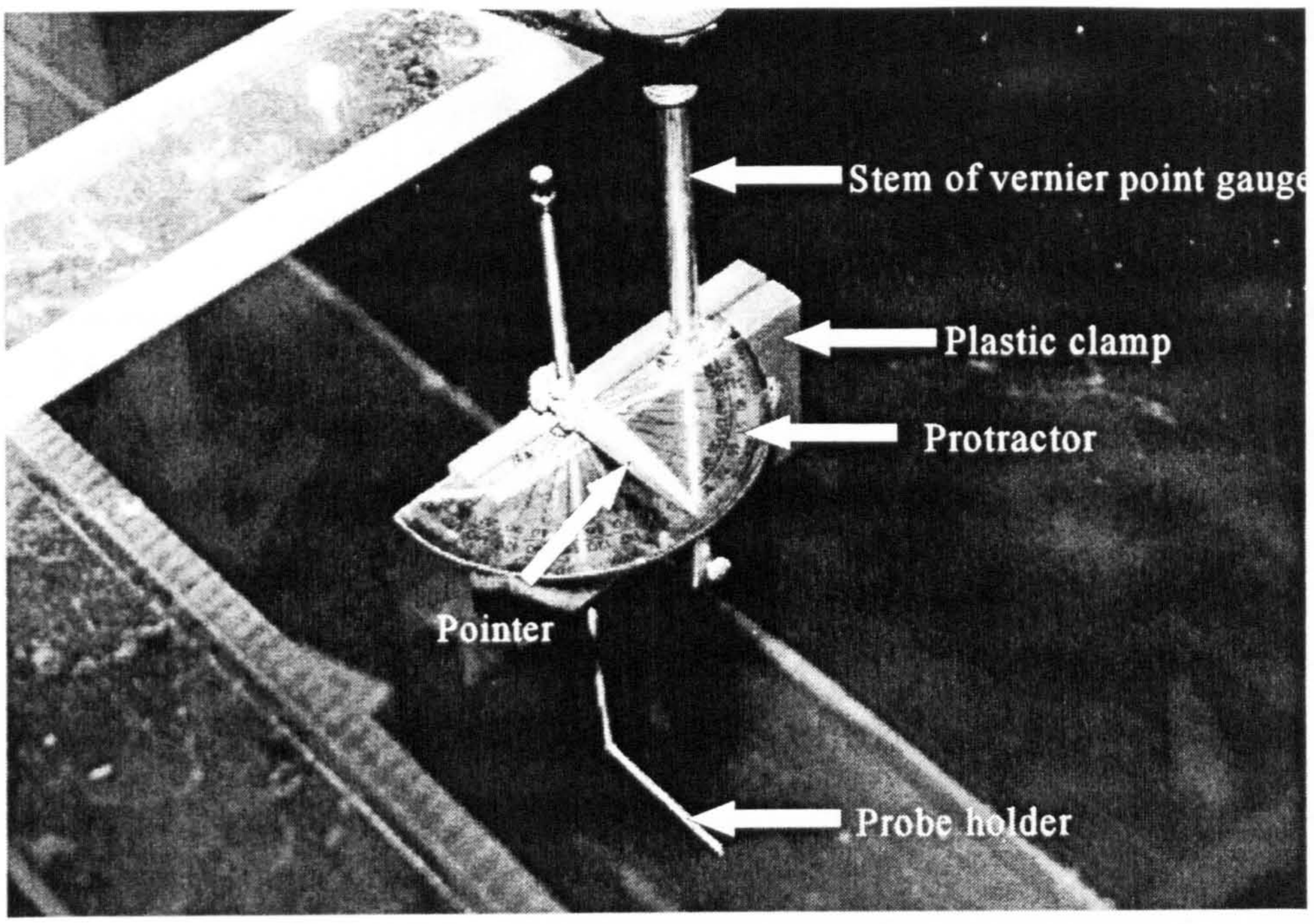


Figure 5.1-2 Photograph showing the probe connector and probe holder assembly with a protractor mounted on a vernier point gauge

As in the experiments on the distribution chamber, the output voltages from the anemometer were collected and recorded by the data acquisition system. The flowrate readings, water temperature, and propeller meter readings were also recorded in the course of the tests.

This calibration procedure was conducted when the probe was new, repeated again after the probe had undergone approximately ten hours of use, so as to check for drift in the calibration.

Flow velocity (Propeller meter) (m/s)	Yaw angles	Channel A (Volts)	Channel B (Volts)	Water temperature (°C)
0.08 to 0.6 in steps of approx. 0.1 m/s	-40° to +40°, in steps of 5° for each velocity	✔	✔	✔
		Acquired at 50 Hz for 60 seconds		

Table 5-1 Summary of yaw calibration test matrix

5.1.2 Determination of probe effective angles and yaw factors

The procedures described above for the yaw calibration tests gave the relationships between the simultaneous two sensor outputs for given velocity. From these results, the probe effective angles, α_1 and α_2, and the yaw calibration factors k_1 and k_2. The equations used to determine these were (3.2-13a) and (3.2-13b), as described in Chapter 3. The choice of the appropriate values of k_1 and k_2 would give minimal variance for the values of α_1 and α_2. The two equations can be solved by an iterative method with the values of k_1 and k_2 as the active iterative parameters.

5.1.3 Calibration of the vernier point gauge

The vernier point gauge used in the experiments with the distribution chamber models had to be calibrated so as to allow the probe to be located in the vertical direction accurately. This was done by zeroing the probe to the level of the outlet weir crests. Thus, all levels measured in the experiments were in relation to the weir crest levels.

Note that the crest levels could also be checked against the invert level of the chamber of Model B.

The outlet weir crests were set by means of a theodolite. The crest levels were at 0.631 m measured from the floor or invert of the chamber. The accuracy of this value was $\pm$0.001 m.

5.2 Test Procedures

The layout of the test rig is shown in Figure 4-3. On priming the laboratory pump, the flow drawn from the laboratory sump was controlled by both inlet and by-pass valves, so as to set the correct flow. The flow into the model was metered by an orifice plate located 1.5 m (18 pipe diameters) from the upstream pipe bend, and 0.8 m (10 pipe diameters) from the downstream bend leading into Model A.

Once set up, the flow of water was allowed to circulate for approximately 5 to 10 minutes. This was sufficient to allow any transient effects associated with the introduction of flow into the chamber to disappear. In the meantime, the gate valves on the outlet lines from the model were adjusted so that the water levels in the collection boxes remained constant. The manometer lines were also checked and bled of any air bubbles during this setting up period. Periodic checks were made on the flowrates into and out of the model to ensure that the flow into the model was correct, and that the flow out did not vary over time.

Once the flow into and out of the model had been set up correctly, the hot wire anemometer and computer were switched on. The hot wire probe (which had already been connected to the probe connector and the joints sealed with RTV sealant at least 12 hours prior to the test) was connected to the anemometer using the BNC connection leads. The entire measurement system (consisting of the hot wire probe and holder and

the vernier point gauge) was traversed to the correct measurement position according to the test plan.

There were two "on" switches for both measurement channels on the hot wire anemometer. These were switched on prior to the start of the data acquisition program. The sampling rate for the tests were set at 300 samples per second for 120 seconds. This gave a total of 36,000 test points per channel. A countdown timer was written into the data acquisition program which stopped the data collection automatically. Monitoring of this timer also allowed the manual shut-off of the two hot wire channels. The useful life of the hot wire probes could be increased by switching off power to them when not in use. The flow into and out of the model and the water temperature were measured and recorded while the data was being collected from the hot film probe. At the completion of the data collection phase, the vernier gauge was traversed down to determine the water level at that measurement point. Since the water levels fluctuated in the course of the measurements, an average value was taken for the levels at each of the 15 different locations on the free surface (see Table 5-2).

The measurement procedure described above was then repeated for the various measurement points as listed in the test procedures.

5.3 Test Matrix for Model A

The test matrix for the model, is shown in Table 5-2.

In the tests, three different flowrates were tested. The ratio between the highest and lowest flow was approximately 3. This is representative of a typical distribution chamber where it is designed to handle flows of up to 3 times the dry weather flow.

Flow in (l/s)	Flow out		Water temperature	Measurement location			Water levels
	Outlet 1	Outlet 2		x (m)	y (m)	z (m)	
2.95	✔	✔	✔	0.077, 0.154, 0.231, 0.308, 0.385	0.628, 0.633, 0.643, 0.653 (0.663 for 5.51 l/s)	0.1037, 0.1337, 0.1637	✔
4.38	✔	✔	✔				✔
5.51	✔	✔	✔				✔

Table 5-2 Summary of Model A test matrix. (The horizontal (U) and vertical (V) components of velocity were measured in the tests.

Markings were made on each of the four sides of the model using graph paper. In this way, the probe may be traversed in any of the three axes. A total of 15 measurements were made (5 x 3) for each of the y positions. Therefore a total of up to 60 measurements were obtained for each flowrate (75 in the case of the highest flow).

The three test flowrates, when scaled up to prototype scale (1:13) were 1800 l/s, 2760 l/s, and 3360 l/s. These flows were typical of the flows through a treatment plant.

5.4 Conversion of raw voltages to velocities

The measured voltages from the two channels of the hot wire anemometer were recorded onto the computer hard disk. The cosine law was used to convert the voltages, E_1 and E_2, to velocity. The magnitude and directions of the two velocity vectors are found from equations (3.2-14a and 3.2-14b), first given in chapter 3, reproduced below,

$$Q^2[\sin^2(\alpha_1 + \gamma) + k_1^2\cos^2(\alpha_1 + \gamma)] = Q_1^2[\sin^2(\alpha_1) + k_1^2\cos^2(\alpha_1)] \quad (3.2\text{-}14a)$$

$$Q^2[\sin^2(\alpha_2 - \gamma) + k_2^2\cos^2(\alpha_2 - \gamma)] = Q_2^2[\sin^2(\alpha_2) + k_2^2\cos^2(\alpha_2)] \quad (3.2\text{-}14b)$$

where k_1 and k_2 are yaw constants

α_1 and α_2 are the effective yaw calibration angles which are characteristic for the that particular probe

γ is the yaw angle with which the probe rotated about its axis

Q_1 and Q_2 are the speeds corresponding the voltages which are determined from the calibration exercise

Subscripts 1 and 2 refer to the first and second channel on the anemometer.

The values of k_1^2 and k_2^2 were found from the calibration of the probes to be 0.065 and 0.06 respectively. The effective angles for both sensors, α_1, was 44.58° and α_2 was 30.85°.

In addition to equations (3.2-14a and b), the remaining unknowns are the values of Q_1 and Q_2. These can be determined using the relationships found in the calibration tests,

The above equations are also shown graphically in Figure 5.4-1 below.

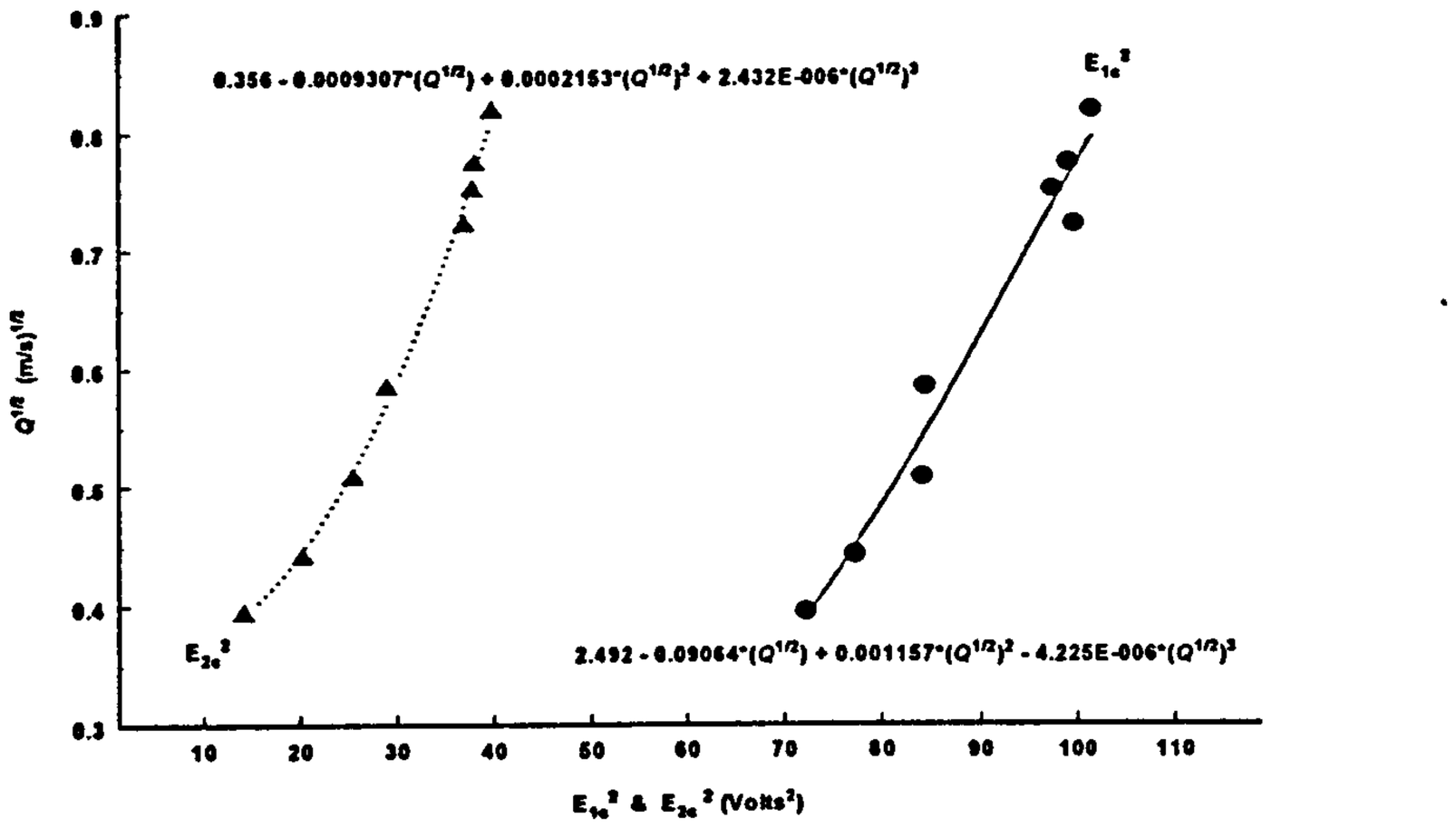


Figure 5.4-1 Calibration plot showing the relationship between the square of the temperature corrected voltages and the square root of the measured speeds. (The circles represent sensor 1, the triangles represent sensor 2).

The relationship between the voltages and the speeds are as shown since a better polynomial fit between the two variables may be achieved, with the square root of speed as the dependent variable. Note that the above relationship is a variation of that given by Swaminathan et al (1984) - see Chapter 3.2.3.

The subscript c indicated that the voltage readings had been corrected for temperature and zero velocity voltage. The equation (after Wubben, 1991) used to determine corrected voltage is given below:

$$E_C^2 = \frac{E^2}{\left(1 - \frac{T_a - T_c}{T_w - T_c}\right)} \qquad (5.4\text{-}3)$$

where E is the raw voltage reading

T_a is the test temperature in degrees Celsius

T_c is the ambient fluid temperature at which the cold resistance of the probe was measured at (19°C)

T_w is the wire temperature

There is a relationship linking the denominator term, $T_w - T_c$, to the overheat ratio,

$$T_w - T_c = \frac{a}{b} \qquad (5.4\text{-}4)$$

where a is the overheat ratio (0.08 in the tests)

b is the temperature coefficient of the sensor (0.0025 %/°C for the probe used).

5.5 The determination of Reynolds normal and shear stresses

Considering the flow approaching one of the sensors on the probe, and since the anemometer output voltages have both a mean and fluctuating part, which may be expressed as:

$$E = \overline{E} + e \qquad (5.5\text{-}1)$$

and the corresponding velocity as,

$$Q^2 = (\overline{U} + u)^2 + v^2 + w^2 \qquad (5.5\text{-}2)$$

The normal stresses can be determined from (Lomas, 1986),

$$\overline{u}^2 = \left(\frac{\overline{U}}{2\overline{E}}\right)^2 \overline{(e_1 + e_2)^2} \qquad (5.5\text{-}3)$$

$$\overline{v}^2 = \left(\frac{\overline{U}}{2\overline{E}}\right)^2 \overline{(e_1 - e_2)^2} \qquad (5.5\text{-}4)$$

The shear stress can be found from the relationship,

$$\overline{uv} = \left(\frac{\overline{U}}{2\overline{E}}\right)^2 (\overline{e_1^2} - \overline{e_2^2}) \qquad (5.5\text{-}5)$$

Thus, the turbulence kinetic energy k for 2-dimensional flow, was determined from,

$$k = \frac{1}{2}(u^2 + v^2) \qquad (5.5\text{-}6)$$

5.6 Experimental Results

Using the relationships given in the preceding sections, the values of the water velocities and the turbulent kinetic energies near the free surface were obtained. Water levels and the percentage flow distribution were also measured. The results from the three sets of tests carried out are shown in Chapter 7, as part of the discussion and comparison between the CFD results. This avoids the duplication of the relevant graphs.

5.7 Summary of Experimental Test Procedures

In the experiments, one of the most crucial measurements made were those of water velocities near the free surface. Correspondingly, additional effort was devoted to ensuring the calibration and set up of the hot wire anemometer and the hot film probe used were correct and of sufficient accuracy.

The hot film probe used was calibrated in a 10 m long water flume. This is a novel technique, combining existing yaw calibration methods of Wubben (1991) and Bradshaw (1971), with a long length of flume. This structure allowed well developed flow past the probe, and the water velocities were easily controlled.

The relationships between temperature corrected voltages and the speeds as "seen" by each of the cross-wire probe is determined from the calibrations. Since this relationship is unique to that particular probe alone, the calibration procedure had to be carried out for all probes that were used in the course of the experiments. The calibration curve for the probe is also affected when the sensors "age". Therefore the calibration procedure was repeated again after 10 hours of use, to check the validity of the calibration curves.

Besides the hot film probe, the vernier point gauge also had to be calibrated using the weir crests on Model A. The weir crests were, in turn, adjusted using a theodolite with an accuracy of $\pm$ 0.001m.

The procedures necessary to run the tests are also listed in this chapter. The various precautions taken to ensure steady flow into the chamber, and the steps taken to reduce the amount of air expelled by the pump into the model, are also given. The test matrix for Model A is listed.

The techniques used to convert measured voltages into velocities are listed. The determination of the normal and shear stresses from the measured results are also given.

6. NUMERICAL MODELLING

6.1 The CFD Package

Numerical models of the distribution chamber being investigated in the experimental programme described in Chapters 4 and 5, were carried out using a commercial CFD package, CFX 4.1. This was developed by Computational Fluid Dynamics Services of AEA Technology. This package consists of three main constituents, the pre-processor, the solver and the post-processor. A brief introduction of the solver is given below.

6.1.1 The Pre-Processor

To model the distribution chamber, it was necessary to create a flow domain encompassing the region of interest. Blocks were created from the grid points defining the distribution chamber. The inlet, two outlets, and weir plates were then created. These structures were two-dimensional (no variation in the z-direction), and were designated as patches in the geometry. Different types of patches can be specified in this code. Here, the pipe inlet was made to be an inlet patch (which accept flow velocities, volume fraction and turbulence as boundary conditions). The two outlets were specified as pressure patches (pressure patches required the specification of pressure as boundary conditions). The weir plates were specified as thin surfaces (these surfaces do not require boundary conditions. They are similar to wall patches, except that flow can exist on either side of the patch). The regions within the blocks were then discretised into cells. A higher concentration of cells was clustered around the regions of interest-near the free surface.

Besides the creation of the geometry file, a command file had to be written. This file contained the relevant keywords and commands that would be used by the solver. These commands and keywords may be grouped under the following headings:

1. `CFXF3D`

2. Model topology
3. Model data
4. Solver data
5. Grid
6. Boundary conditions
7. Output options

The first command, CFXF3D, allowed the user to set the memory allocation for the run. The type of flow and the problem must be specified, eg. a two-dimensional, two-phase transient, isothermal, incompressible, Newtonian flow was specified for the distribution chamber. The user Fortran files that would be used by the solver must be listed here.

The second command allowed the creation, renaming or modification to any of the patches, or blocks in the geometry file read in by the solver.

The third command contained all the relevant commands controlling the solver and other information needed, eg. the ambient temperatures and viscosities of the fluids, the body forces present, the type of differencing schemes used, and the initial guesses used by the solver.

The fourth command contained the keywords and commands related to the model. Commands for the transient calculations, the turbulent models, the controls for improved convergence etc. were specified in this section. Information regarding the fluid, such as density and viscosity were also specified here.

The user can create a grid from any new blocks created in the command file, under the fifth heading. The keywords to read in an existing geometry file and the grid were specified here.

The model boundary conditions for the inlets and outlets must be specified here. The type of information to be entered depended on the type of inlet or outlet patch in the geometry.

Finally, the output options for the files created at the end of the calculations were specified here. The information given in the output files or any additional text files was given. The type and format of the dump file, which contained all the information for each cell in the domain, were specified.

A degree of flexibility is built into the code. Fortran files may be included besides the command file. These files allow more complex control of all aspects of the solver, which would not be possible in the command files. In the calculations, frequent use of an initial guess of the volume fraction was made.

An example of a command file used in the calculation of a simulated, shortened pipe bend with a horizontal plate (Plate3 in Table 6-4), is given in Appendix B. The accompanying Fortran file, giving the initial guess for the free surface location, is also shown.

6.1.2 The Solver

Steady state or transient runs could be performed by the solver. Round-off errors could also be reduced by the double precision option available. The solver had default solution and differencing scheme (Hybrid Differencing Scheme) which ensured the robustness of the code. However, it was necessary to select other options and differencing scheme for greater accuracy, and improved rate of convergence. The details of which are given in section 6.2.5.

6.1.3 Post-Processing

On the completion of a run, an output file and a dump file were generated. The contents of the output file varied according to the options selected by the user in the command file, but would usually contain a record of the convergence and time step history of the calculations. Either the final absolute values of variables such as velocities, pressures, densities etc. at each cell in each block, or the residual values at each of those cells would be created in the output file. The dump file contained sufficient information for the user to conduct a restart based on the previous results. The post-processor also read in the dump file to create vector, contour or line plots of the results.

6.2 Numerical models for symmetrical flows

Many different numerical models of the distribution chamber were created in the identification of the most appropriate CFD model. These included, two- and three-dimensional models, single phase and two-phase flows in the domain, and runs using different turbulence models. These are described below. The solution strategy identified during the development was explored and refined, to minimise the required CPU time for the calculations. This strategy is described in section 6.2.5.

In all the numerical models, clean water was used as the fluid medium, as in the experiments. It was not envisaged that the presence of solids present in the fluid. as in sewage treatment plants, would affect the flow distribution. In addition, the treatment plants contain several treatment and filtration stages. At the head of the works, most of the large solids would be screened and removed. By the time the flow reaches the distribution chambers, most of the solids remaining would be in suspension. Although CFX4 had the capability to model the presence of solid particles in the flow, this was not used, since the use of a single phase water to represent the fluid in the chamber would be a valid assumption.

6.2.1 Two-dimensional, single phase, steady state flow

Simulations were initially carried out using a two-dimensional, single phase flow model. This simple model allowed the assessment of the boundary conditions, different types of inlet and outlet patches, and the solution strategy. The inlet was at the bottom of the model, with two outlets at the upper edges of the domain. The inlet was specified as an inlet patch. The velocities, k and ε, were required to be entered as the boundary conditions. The cross-sectional area of the two-dimensional slit was made the same as the cross-sectional area of the inlet pipe found in the test rig. Hence, the average velocity through the inlet was kept the same as in the experiments.

Two different patch types were used for the outlets. They were: pressure patches, where the pressures at both outlets were specified as atmospheric (ST1); and mass flow boundaries, where the mass flows out of both patches were specified, and assumed to be equal (ST2). This is a reasonable assumption to make since the experimental results showed that the flow distribution between the two outlets to be equal for the flow conditions being simulated. However, the selection of mass flow boundary conditions would be invalid for asymmetric flows within the chamber. This is due to the lack of any experimental data available to fix the flows out of the two outlets. The top of the domain or lid, was specified as a frictionless, no shear boundary, for the two steady state runs.

An initial test flow of 4.69 l/s into the domain was setup. The limiting mass source residuals by which the solution was deemed to be converged, was set as 1×10^{-6} kg/s. This small value was selected based on the non-dimensional value of the value of the mass residual divided by the total mass inflow. This was sufficiently small to ensure an accurate solution.

The details of the two runs, ST1 and ST2, conducted for the single phase model are given in Table 6-1.

6.2.2 Two-phase, two-dimensional steady-state model

An extension of the single phase model described above is the two phase, air and water, model. The Volume of Fluid (VOF) multiphase model (Hirt and Nichols, 1981) was used in the calculations, with the surface sharpening algorithm set. An inlet patch was specified at the inlet as before, with pressure patches for the outlets. This run is labelled as 2PH1 in Table 6-1.

One of the goals of the numerical analysis was to determine the amount of flow mal-distribution for a given set of flow conditions. The main governing factor for mal-distribution is the buoyancy effects at the free surface. Consequently, modelling the two phases, reproduced the forces acting at and near the free surface with a much greater degree of accuracy than with a single phase model. In this way, the formation of the "boil" on the water surface, and the head of water over the weir crests, may be simulated. Therefore, any flow asymmetry developed, can be reproduced much more accurately.

The flow patterns for this type of flow, was essentially stratified. The interface between the air and water was clearly defined. The VOF model assumed that there was no mass transfer between the two phases, which was a reasonable assumption.

Since the flow out of the domain consisted of two-phases, assumptions of the initial water levels were made. Assumption of equal distribution was not necessary when pressure patches were used. Instead, atmospheric pressure was set at the patches. Note that the pressures specified in the setup file were modified pressures, the hydrostatic component was subtracted from the total pressure values. With different phases being present at the outlet, the pressures varied according to the density of the mixture (which in turn was a function of the volume fraction).

Table 6-1 lists the numerous runs that were carried out with the assumption that the solution to the flow is at steady state. As will be discussed in Chapter 7, physically realistic solutions were not able to be obtained, since non-unique solutions were possible for this particular problem.

CFD run number	Flowrate (l/s)	Turbulence model	Mass residuals (kg/s)	No. of phases	Comments
ST1	4.69	k-ε	1×10^{-6}	1	Initial run - outlets are mass flow boundaries, lid is shear free boundary
ST2	4.69	k-ε	1×10^{-6}	1	Initial run - outlets are pressure patches, lid is shear free boundary
2PH1	4.69	k-ε	1×10^{-6}	2	Steady state 2 phase flows - no physically realistic results found

Table 6-1 List of two dimensional-steady state single phase and two phase runs

6.2.3 Two-phase, 2D transient models

In this set of calculations, the geometry of the distribution chamber was modified from the one created for the single and two phase steady state runs. To facilitate the specification of boundary conditions at the outlets, collection boxes were added to the main body of the distribution chamber. The outlets were now located on the bottom of the two boxes. In that way, a layer of water would always be present over the outlets, and therefore the flow out of the outlets consisted of single phase water. This arrangement was representative of the physical model as illustrated in Figures 4-1 and 4-2. The addition of collection boxes on either side of the chamber allowed the specification of the boundary conditions to be better posed. At the inlet, single phase water entered the chamber at one of three flowrates (see Table 6-2). A fully turbulent flow profile for the inlet pipe would be present for the range of flows and Reynolds numbers considered. This profile was approximated by a uniform velocity profile across the inlet. The value of the velocity was obtained by dividing flowrate by the inlet cross-sectional area. The turbulent quantities at the inlet, turbulent kinetic energy, k, and turbulent energy dissipation, ε, were also required. These values were calculated from equations (7.3.8-1) and (7.3.8-2) (see Chapter 7, section 7.3.8). The outlets in the collection boxes were made to be pressure patches. Atmospheric pressure was specified in both outlets. In this way, any flow asymmetry and hence, flow mal-distribution would not be artificially constrained. In addition to the two collection boxes, weirs were also created within the geometry. These were simulated by thin surfaces. The lid of the geometry was specified as symmetry plane, close to open air as in the experiments.

Figure 6.2.3-1 shows the outline of the geometry created initially. This was discretised into 17,850 cells. The width of the domain was 0.462 m, and height was 0.769 m. Although the geometry was approximately two-dimensional, the depth of the domain was made to be 0.055356 m, to maintain the correct cross-sectional area for the inlet (which spans the third dimension, z). Since the key features of the flow is dominated by the jet, the behaviour of the jet at the free surface and the vertical momentum must be modelled.

Consequently, the experimental inlet velocities were taken to be the inlet boundary condition. The width of each collection box was 0.531 m.

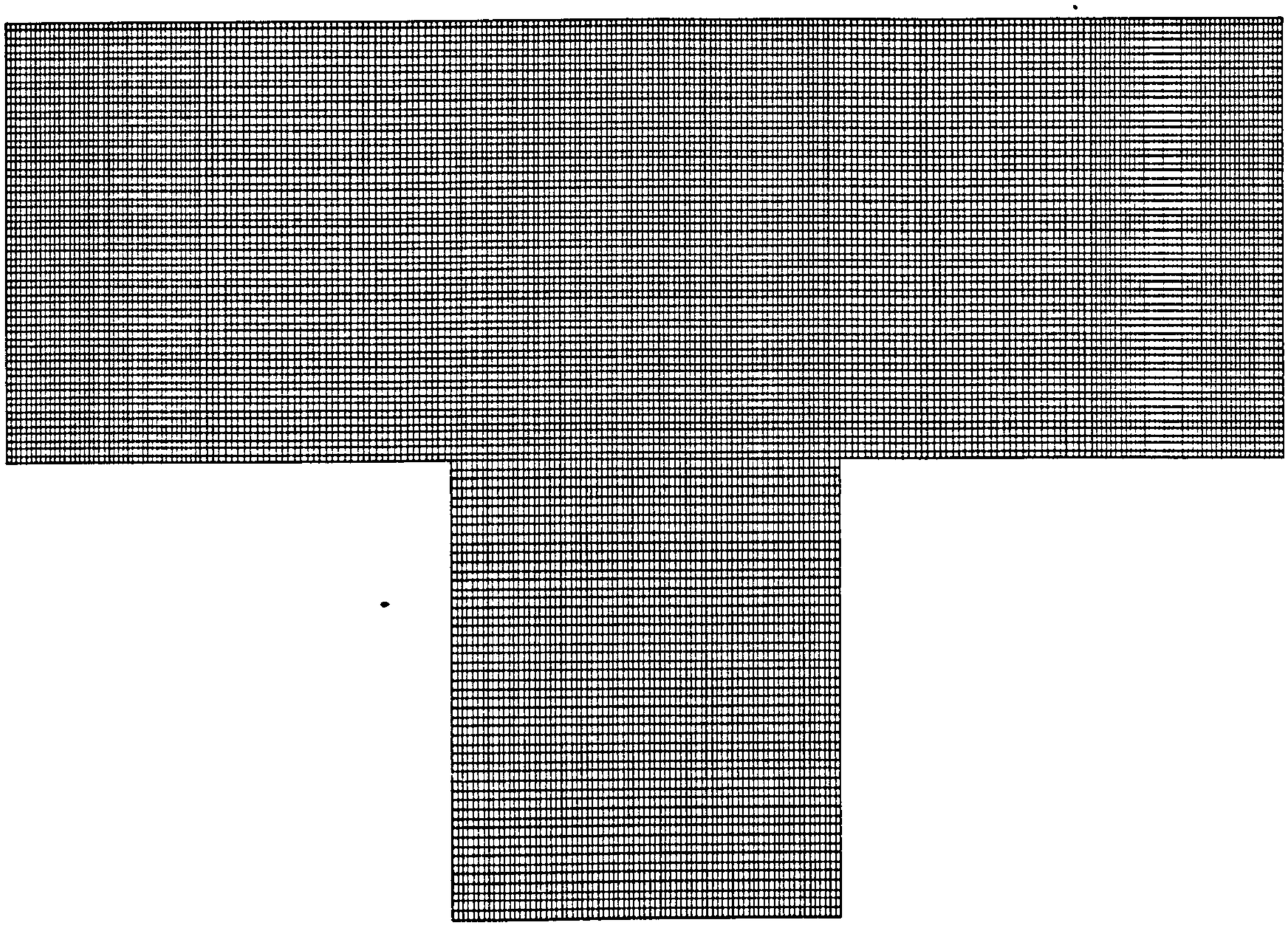


Figure 6.2.3-1 Two-dimensional geometry created for the two-phase transient model calculations. The two collection boxes had been include. Number of cells are 17,850.

Tables 6-2 lists the transient 2D runs that were conducted. Runs number 2D1 to 3, and 2DRNG1 & 2 used the 17,850 cell geometry (Figure 6.2.3-1). The standard k-ε model, VOF multiphase model with surface sharpening were used in the calculations. The mass residuals were set to 1 x 10^{-5} kg/s. This value was found to allow a threefold reduction in the errors, from the second iteration to the final iteration. The default differencing scheme, the hybrid scheme (HDS), was used. The flowrates for these runs were 2.95 l/s, 4.38 l/s and 5.51 l/s respectively. The mid-flow of 4.38 l/s was selected as the base case for comparisons with the different models and solution strategies used.

The next set of runs, 2DRNG1 and 2DRNG2 substituted the k-ε model with the RNG k-ε model. Additionally, the surface sharpening algorithm was turned off, while the second-order accurate Van Leer differencing scheme was used for the volume fractions and density equations. As before, the base case flowrate of 4.38 l/s was input. 2DRNG1 used a less stringent mass tolerance value of 1 x 10^{-5} kg/s, while 2DRNG2 used a value of 1 x 10^{-7} kg/s. The use of a more stringent convergence criteria allowed the further reduction of the errors. Here, it allowed a decrease of five orders of magnitude in the continuity error. Consequently, more accurate answers may be obtained.

A grid independence test was necessary to justify the numerical results obtained from the previous runs. This test used the same model as before, but with an increased number of grid cells, from 17,850 to 27,300. The region of importance was near the free surface. The velocity gradients there were expected to be the largest too. Thus, selective refinement of the grid was made to the solution domain. The region near the free surface had the size of the cells reduced in half, effectively doubling the number of cells there. The regions occupied by the collection boxes were unchanged, since this region was unimportant, while the region close to the inlet also had the number of cells increased to account for the development of the jet properly. In this way, a reasonable trade-off between CPU time, RAM requirements and solution accuracy were achieved. This run was named 2DIndy. The conditions for this run were the same as in run 2D2,

i.e. the k-ε model, VOF with surface sharpening, hybrid differencing scheme, and mass residuals of 1 x 10^{-5} kg/s, were used.

As part of the optimisation process for the problem representation, the height of the domain was increased from 0.769 m to 1 m. This was due to the results from 2DRNG1 and 2DRNG2. This increase was achieved by the addition of 5 more blocks above the existing geometry. The goal for this increase in the height of the domain was to obtain accurate calculations for the behaviour of the water phase. 2DRNG1 and 2DRNG2 showed that there was air-water coupling at the free surface. The air flow was unrealistic and affected the water phase. Consequently, the lid for the domain was raised to eliminate the unrealistic air flow patterns and thus, its effect on the water surface. Since the exact behaviour of the air was unimportant, the top layer blocks (containing air) were divided into coarse cells, giving a new total number of cells - 19,025. The resolution of the top layer was kept coarse to keep the computational effort to a minimum. Also, the accuracy of the solution within those new cells would not affect the solution within the chamber. Runs 2DRNGV1 and 2 (see Table 6-2) used this new geometry. As before, the RNG k-ε model was used in conjunction with the Van Leer scheme without the surface sharpening algorithm. The difference between the two runs was that the mass residuals were reduced in 2DRNGV2 (1 x 10^{-7} kg/s).

The weir levels set in the geometry files for all the above runs were set at 0.643 m. This was higher than the experimental level of 0.631 m. Hence the subsequent runs had the crest levels amended accordingly. The number of cells in the new geometry was 18,085. The results from the runs, 2D1, 2D2, 2D3, 2DRNGV1, 2DRNGV2 cannot be compared directly with the experimental results. Nevertheless, they were included in the discussion since these runs were part of the development process for the CFD model. Although the above runs could be corrected, but using the existing data was more efficient. Useful information was also obtained from the comparison of these CFD results with one another.

Runs 2DRNGC1 and C2 used the new geometry and were essentially repeats of 2DRNGV1 and V2. These runs allowed direct comparison between the CFD and the experimental data.

Transient CFD run number	Flowrate (l/s)	Turbulence model	Mass residuals (kg/s)	Surface sharpening	Van Leer scheme	Other comments
2D1	2.95	k-ε	1×10^{-5}	Yes	No	17,850 cell geometry
2D2	4.38	k-ε	1×10^{-5}	Yes	No	"
2D3	5.51	k-ε	1×10^{-5}	Yes	No	"
2DIndy	4.38	k-ε	1×10^{-5}	Yes	No	27,300 cell geometry - grid independence check
2DRNG1	4.38	RNG k-ε	1×10^{-5}	No	Yes	17,850 cell geometry
2DRNG2	4.38	RNG k-ε	1×10^{-7}	No	Yes	"
2DRNGV1	4.38	RNG k-ε	1×10^{-5}	No	Yes	Volume of domain expanded - 19,025 cells
2DRNGV2	4.38	RNG k-ε	1×10^{-7}	No	Yes	"
2DRNGC1	4.38	RNG k-ε	1×10^{-5}	No	Yes	Weir levels corrected - new geometry used (18,085 cells)
2DRNGC2	4.38	RNG k-ε	1×10^{-7}	No	Yes	"
3DRNG1	2.95	RNG k-ε	1×10^{-7}	No	Yes	3D Geometry (38,232 cells)
3DRNG2	4.38	RNG k-ε	1×10^{-7}	No	Yes	"
3DRNG3	5.51	RNG k-ε	1×10^{-7}	No	Yes	"

Table 6-2 List of transient CFD validation runs (Details of Van Leer differencing scheme and surface sharpening apply to final results - see text for details)

6.2.4 3D, transient two phase runs

For greater realism to the simulations, 3D models were created. This geometry had a total of 38,232 cells (details of the 3D mesh are given in Appendix C). The dimensions of the domain are similar to the 2D model, except the depth (z direction) is 0.269 m. The pipe inlet into the chamber was rectangular in cross-section. The area was made to be the same as that of the circular pipe in the experiments. The choice of such a shape was determined by the need to keep the amount of distortion to the mesh, to a minimum. A distorted mesh can be detrimental to the accuracy of the solution, and may also lead to convergence difficulties. The formation and behaviour of a turbulent jet are governed by two phenomena, self-similarity and Reynolds number similarity. The extent of the jet is independent of the fluid density or jet momentum at large Reynolds number (Bradshaw, 1971, Rajaratnam, 1976). Thus, all jets grow at the same rate. Far from the orifice, the properties of the jet are independent of the orifice shape and size, and are only dependant on momentum flux. In this model, the free surface is approximately 8 pipe diameters away from the inlet. The jet was fully developed and turbulent in that region. Any difference between square and round jets would be minimal.

The dimensions of the grid cells near the regions of importance - free surface and near the inlet, were made to be same order of magnitude as the 2D cases.

Three 3D runs were conducted. They were 3DRNG1, 2, and 3. The respective flowrates for these were 2.95 l/s, 4.38 l/s, and 5.51 l/s. All three runs used the RNG k-ε model with the Van Leer differencing scheme. The surface sharpening algorithm was not used, while the mass residuals were set to 1×10^{-7} kg/s.

The computation time required for the 3D models were considerably greater than the 2D models. For every run conducted, the simulation time was equivalent to 3 residence times. In the case of the 3D models, because of the increase in the volume of the

domain over that of the 2D geometry (approximately five times), three residence times for the 3D models were some five times longer. Added to that, the number of grid cells was nearly doubled. Also, an additional equation (the momentum equation in the z direction) had to be solved. Thus, the computational times for the 3D models were at least ten times longer than the 2D models (which approximately took some 30 hours of CPU time on a Cray C90 supercomputer, for a flowrate of 4.38 l/s, and a residence time of 12 seconds). Consequently, 2D models are much more preferable to the 3D models as a practical design tool.

6.2.5 Solution strategy

From the above runs conducted in the course of identifying and developing the most appropriate CFD models, a refined solution strategy was developed. This strategy is new, and was worked out specifically for this particular type of problem. The flow into the chamber was steady and did not vary. However, the formation of the jet within the chamber, and its interaction with stagnant water surrounding it as it developed, and also with the free surface, meant that the flow was time-dependant. Hence, transient calculations had to be performed as the steady state calculations of 2PH1 showed that non-unique solutions existed. The dominant solution for the steady state case was physically unrealistic. Thus, this strategy had to be determined and used otherwise realistic CFD results would not have been possible.

This strategy was optimised for efficiency in the CPU effort and solution accuracy. The details are given below:

1. When the calculation started from time zero, the default hybrid differencing scheme (HDS) was used. This allowed the flow field to be developed within the domain for a minimum of CPU effort. The mass residuals were set to 1×10^{-5} kg/s during this flow development phase to facilitate convergence. While the use of the HDS introduced numerical diffusion, especially near the free surface, the

use of surface sharpening helped to reduce this. Nevertheless, there were regions that displayed unrealistic and non-physical results. Also, small time steps (approximately 0.0001 s) were necessary during the initial flow startup phase. This was because of the very large and quick changes in the flow at startup. An initial guess of the water levels was set to the weir crest level. This helped save a lot of computational effort if the domain was to be completely empty of water. Meanwhile, the appropriate turbulence model was specified in the command file at this stage.

The rate of convergence was found to be improved if the set of linearised equations, for the pressure variable for both phases, was solved using the algebraic multi-grid (AMG) solver (Computational Fluid Dynamics Services, 1995). In some cases, under-relaxation factors for the velocity, turbulence, volume fraction and pressure were necessary. The values of the under-relaxation were reduced by no more than half the default values when convergence was particularly difficult. The exact values would be dependant on the behaviour of the residuals of each variable during the iterations. It was crucial not to reduce the under-relaxation values too much since they will have a direct effect of the maximum time step that could be used effectively, the number of iterations to reach convergence and thus, the duration of the calculations. (As an illustration, the required CPU time for a run beginning from a constant initial guess, using the solution strategy set out above, to approximately 0.5 to 1.0 s, will require 20,000 to 40,000 seconds of CPU time on a Cray C90. This value would be approximately 4 times more on a Unix workstation with a single MIPS R10000 processor). The jet would have reached the level of the weir crests in that time (for the 2D model). The development of the flow, especially around the weirs was rapid. Thus, very small initial time steps was necessary to model these processes accurately. The number of time steps required was large, with the resulting overhead on CPU time.

2. The solution was allowed to advance to more than one residence time (defined as the volume of the chamber divided by the volumetric flowrate). This ensured that any transient effects of introducing flow into the domain had disappeared. The major flow features such as the jet, recirculating regions, the plunging curtains of water, the boil on the free surface, were developed within the chamber during this time (see Chapter 7 for a description of the flow features). The simulation time could have been increased further, however, the CPU effort would have been prohibitively expensive. The experimental results also showed that three residence times would be sufficient to allow the flow within the chamber to develop.

Six monitoring points were set up within the water phase in the distribution chamber. Two were in the centreline of the domain, and four on either side of the chamber, below the free surface but above the weir crests. The locations of these points were chosen for their sensitivity to any perturbations in the flow. The monitoring of the behaviour of U, V and k over time helped to determine whether the calculations needed to proceed further. It also gave indications of any problems with convergence, or any errors introduced during the restarts. For example, if the results showed that the velocities had a periodic variation in time, then the calculation would be allowed to continue until at least one cycle was displayed.

3. If the time history plots showed the solution had either reached a quasi-steady state, or had displayed at least one cycle, the mass residuals were then reduced to 1 x 10^{-7} kg/s. The Van Leer differencing scheme was used for the volume fraction and density equations, while the surface sharpening algorithm would be switched off. The purpose of changing the conditions was to refine the solution to obtain better accuracy. The computational time required for this stage of the simulation was generally much greater than the previous stages. The number of iterations per time step was larger, and the sizes of the time steps were smaller,

up to ten times less than before, to obtain convergence. As before, the monitoring points helped to determine whether the solution had sufficiently been advanced in time to be stopped.

The method described above is highly accurate. It allowed accurate solutions to be obtained from the simulations. The method also required a large amount of user interaction since the behaviour of the velocities and turbulence at the different monitoring points had to be determined before the strategy for the next set of runs could be determined.

4. Adaptive time stepping was used in all the runs. This allowed the time steps to increase in user defined step intervals as the solution progressed. A very small time step had to be specified (approximately 0.0001 s) initially when the solution was started from time zero. The steps were then allowed to increase by a factor of no more than 1.25 after 3 or 4 successive converged time steps. If any time step failed to converge, then the step size would be reduced by the same factor. The solution was allowed to advance to either the limiting time, or the maximum number of time steps allowed.

When restarts were performed from a dump file, it was necessary to have the first time step smaller than the final value reached at the end of the previous calculation. This was believed to be due to an inconsistency in the solver that caused some instability in the solution when performing restarts. These instabilities were shown up in the time history plots as peaks in the values of both velocities and turbulence. However, these quickly settled down within a few time steps.

6.2.6 Turbulence levels

The values of turbulent kinetic energy and turbulent energy dissipation had to be specified at the inlet. All the calculations performed, used the inlet values of k and ε given below.

$$k_{inl} = C_{p1} u_{inl}^{2}$$

$$\varepsilon_{inl} = \frac{k_{inl}^{1.5}}{C_{p2} D_{inl}}$$

where,

$C_{p1} = 0.002$

$C_{p2} = 0.3$

6.3 Numerical models for asymmetric flows

Following the validation of the symmetric CFD models against the experimental data, asymmetric flow calculations were set up. The most likely cause of flow asymmetry and mal-distribution due to the presence of a pipe bend below the inlet into the chamber, was investigated. Different simulations of a pipe bend were made. Table 6-3 is a list of the runs that were carried out in the course of the investigation. Three different strategies were adopted for the simulation of the presence of a pipe bend. The first assumed a uniform angled inflow into the chamber. This used the existing geometry. The second strategy considered a simple 2D pipe bend separate, or decoupled from the existing chamber geometry. The third strategy coupled the two separate geometries to give a simple 2D representation of a typical chamber with a pipe bend close to the inlet.

The first two different modelling methods were attempts to find an accurate method for modelling the presence of a pipe bend with the least amount of computational effort. The addition of a pipe bend below the chamber would result in a change in the geometry. Consequently, the number of grid cells would also change. Therefore, the results from 2DRNGV2 cannot be used as an initial guess for the flow. This in turn, meant that additional computational time had to be spent allowing the flow to develop from a constant initial guess.

The results from the first method resulted in an asymmetric flow within the chamber. However, the inlet boundary conditions were physically unrealistic. The second method showed that the jet formed within the chamber exhibited time dependant behaviour. The monitoring points revealed that there was a cyclical pattern for the velocities and turbulence. Thus, the inlet boundary conditions for the chamber (when modelled separately from the bend) were not constant. There was interaction between the jet and the flow within the bend. The interaction rate was not known, therefore, decoupling the bend and the chamber was not accurate. Thus, the third method, was necessary.

Asymmetric run number	Cause of asymmetry	Flowrate in (l/s)	Asymmetry		Comments
			Outlet 1 (%)	Outlet 2 (%)	
Bend2	2° inflow	4.38	48.81	51.19	RNG k-ε turbulence model, Van Leer finite differencing scheme, mass residuals of 1 x 10^{-7} kg/s, and no surface sharpening. Run restarted from symmetric case dump file, using 18085 cell geometry
Bend5	5° inflow	"	47.44	52.56	"
Bend10	10° inflow	"	45.17	54.83	"
Bend12	12.5° inflow	"	48.56	51.44	"
Bend15	15° inflow	"	48.78	51.22	"
Pipebnd1	Simulated Pipe bend	"	44.02	55.98	Solution parameters as above. 18085 cell geometry used. Pipe bend decoupled from chamber. Inlet boundary conditions taken from steady-state 2D pipe bend run.
Pipebnd2	"	"	33.48	66.52	Inlet boundary conditions altered. Average values of pressures obtained from Pipebnd1 and steady-state 2D pipe bend run. Averaged values input as new pressure boundary conditions for pipe bend run. Outcome of this input as new boundary conditions for Pipebnd2.
Pipebnd3	"	"	70.59	29.41	A 2D pipe bend is coupled to 18085 cell geometry. Bend is 2.12 D_h from chamber. Solution parameters as in angled flow runs except that Hybrid differencing scheme is used
Pipebnd4	"	"	72.24	27.76	Similar run as pipebnd3 except that Van Leer scheme used. Results from pipebnd3 and 4 compared to investigate effect of Van Leer scheme.
Pipebnd5	"	"	38.59	61.41	Shorter pipe bend added to 18085 cell geometry. Bend is 1.25 D_h from chamber. Solution parameters as in pipebnd4.

Table 6-3 List of asymmetric flow simulation runs conducted.

6.3.1 Uniform angled inflow

A simple approach was used initially to generate asymmetric flows within the chamber. A uniform flow into was assumed. The flow was inclined at various angles, ranging from 2° to 15° , measured from the vertical axis. Five sets of calculations were made, Bend2, Bend5, Bend10, Bend12 and Bend15. These runs were restarted from the symmetric results of 2DRNGC2 and the boundary conditions were altered accordingly to reflect the additional horizontal velocity component. The solution was allowed to march forward in time for 3 to 4 residence times (1 residence time was 3.68 s for the flow of 4.38 l/s into the 2D domain). This was sufficient to allow any transient effects due to the change in boundary conditions to disappear. As mentioned above in the solution strategy section, the time histories of the velocities and turbulence at the six monitoring points determined the length of the calculations. The same solution parameters were adopted here as in the symmetric flow calculations.

6.3.2 Decoupled pipe bend

Two geometries were used. The first was a 2D pipe lying horizontally. It had a 90° bend at the end. The outlet of the bend was 2.12 hydraulic diameters from the centreline of the pipe. The second geometry was the 18,000 cell geometry used in 2DRNGC2.

A single phase flow was set up in the separate pipe geometry. An inlet patch was used at the inlet, and a uniform velocity and turbulence distribution setup. At the outlet, a pressure boundary was specified since the flow at the outlet was not expected to be fully developed. The pressure values at that boundary were initially taken from the results of 2DRNGC2. The solution to the pipe bend was a steady state calculation. The calculated values of the velocities and turbulence at the outlet of this two-dimensional pipe bend were then used as the boundary conditions for the chamber, in Pipebnd1.

Pipebnd1 was allowed to advance in time for approximately 3.8 residence or retention times. The solution strategy adopted was similar to that detailed previously and summarized in Table 6-3. At the end of the simulation, the pressure values at the inlet were compared with the initial input values. The average between these two sets of results was taken and input again into the 2D pipe bend case.

With new pressure values at the outlet, the pipe bend calculations were restarted again. The second set of results from the pipe bend run were then input into Pipebnd2.

At the termination of Pipebnd2, after 2 residence times, the pressure values at the inlet were compared with the pipe bend values. The results showed significant differences (see Chapter 7). This meant that this approach was a poor method for simulating the effects of a pipe bend.

6.3.3 Coupled pipe bend

In order to overcome the inaccuracies obtained from Pipebnd1 and 2, Pipebnd3 was setup. This was a new geometry created from coupling of the distribution chamber with the 2D pipe bend. The bend was 2.12 pipe hydraulic diameters from the inlet into the chamber, measured from the centreline of the horizontal pipe section. Figure 6.3-1 illustrates this arrangement.

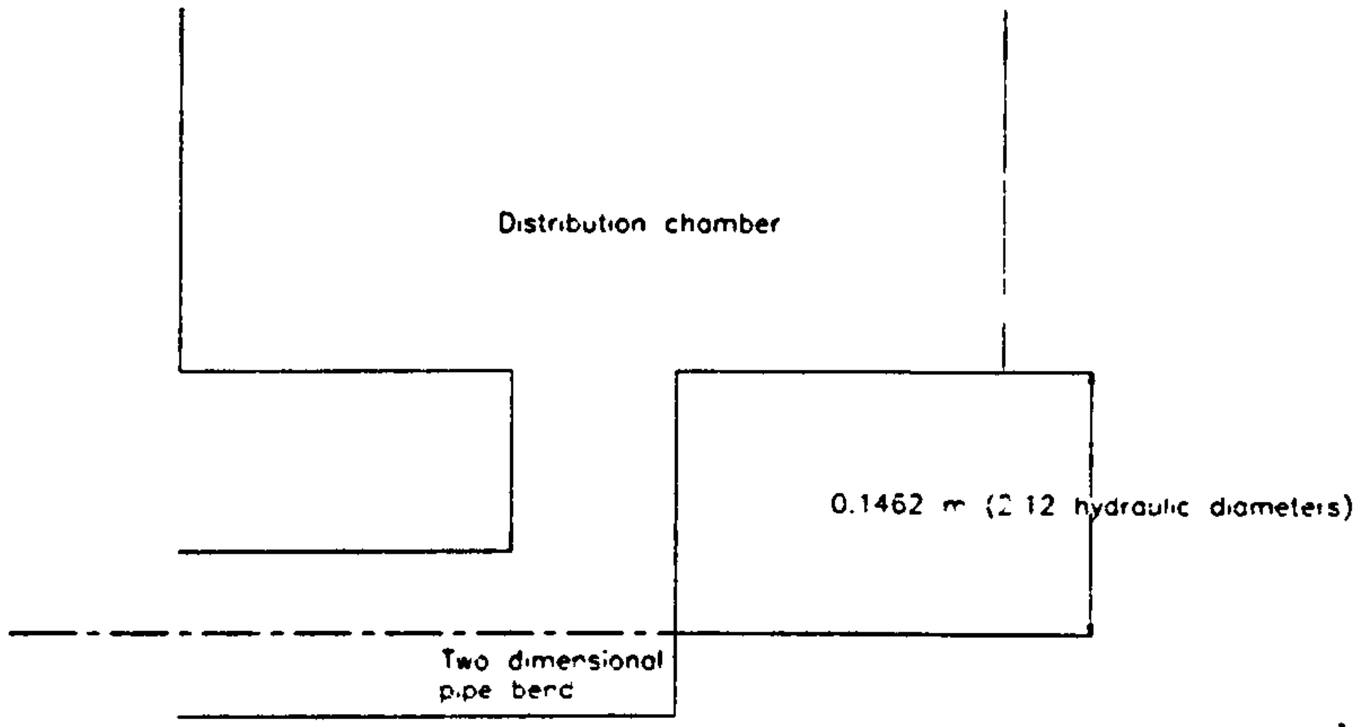


Figure 6.3-1 Sketch showing pipe bend below distribution chamber (the two collection boxes are not shown for simplicity).

In this run, the inlet patch was moved from the chamber inlet to the inlet into the horizontal pipe, found on the left hand side.

Two runs, Pipebnd3 and Pipebnd4, were carried out using this geometry. The solution strategy was similar to that detailed in Section 6.2.5, with the following exception. In Pipebnd3, the hybrid differencing scheme was used throughout the solution, up to 2 residence times. In Pipebnd4, the Van Leer differencing scheme was used instead. This run was restarted from the same dump file as Pipebnd3, and allowed to continue to the same end time. In that way, a direct comparison between the two sets of results was possible. These two runs allowed the determination of the effects of a pipe bend and a comparison between the effects of both the Van Leer and Hybrid scheme.

To determine the effects of the pipe bend geometry on flow distribution, Pipebnd5 was set up. A shortened pipe bend, 1.25 pipe hydraulic diameters from the chamber inlet,

was created in the geometry. The boundary conditions and the solution strategy were the same as Pipebnd4.

6.4 Remedies to flow mal-distribution

To improve upon the flow distribution between the two outlets, additional flow structures were added to the flow domain. Two different designs were tested. These were a vertical flow splitter, and a horizontal plate.

6.4.1 Vertical flow splitter

The flow splitter was simulated using a "thin surface" patch. The splitter was located centrally at the inlet. Initial trials were carried out to test the effectiveness of different flow splitter heights using the uniform angled inflow geometries. The flow splitter was placed midway above the inlet. Two heights were tested, 0.069 m (1 D_h) 0.1035 m (1.5 D_h) for two cases - 10° and 15°. These four runs were test cases and were not listed in the summary tables since the boundary conditions were incorrect. However, the results suggested that the shorter splitter was more effective. Hence, this shortened splitter was used in the subsequent runs using the coupled pipe bend with the chamber.

Table 6-4 lists the calculations carried out using the vertical splitter placed above the pipe bend. Bndsplt1 used the dump file from Pipebnd4. The shorter splitter was added to the geometry. Bndsplt2 and Bndsplt3 were continuation of Bndsplt1. Bndsplt1 was run to 6.2s. Bndsplt2 was run to 7.936 s, and Bndsplt3 was stopped at 11.01 s. Results from the three runs illustrated the periodic nature of the solution. The solution strategy used was based on that described in section 6.2.5.

6.4.2 Horizontal Plate

There were three sets of runs using the horizontal plate. Initially the plate was placed two hydraulic diameters from the inlet, for Plate1 and Plate2. The width of the plate was made the same as the inlet opening, 0.0924 m. The distance of the pipe bend from the chamber was 2.12 hydraulic diameters from the chamber invert for Plate1. The geometry and restart file used for Plate1 came from Pipebnd4.

In Plate2, a shortened pipe bend was created. The bend was 1.25 hydraulic diameter from the chamber. The horizontal plate was placed in the same position as Plate1.

Examination of the results of Plate2 revealed that further optimization of the plate location was necessary. Hence Plate3 was run. The geometry of this was similar to Plate2, with the exception that the plate was placed closer to the inlet, 1.5 hydraulic diameters away (0.102 m).

Asymmetric run number	Remedy for asymmetry	Flowrate in (l/s)	Asymmetry		Comments
			Outlet 1 (%)	Outlet 2 (%)	
Bndsplt1	Vertical splitter	4.38	47.41	52.59	Vertical flow splitter, 1 D_h high, added at centre of and above inlet. Simulation to 6.2 s. Solution parameters - Van Leer differencing scheme, no surface sharpening, RNG k-ε model, and 1 x 10^{-6} kg/s mass residuals. Geometry used is modification of Pipebnd1 to 4 runs.
Bndsplt2	"	"	33.83	66.17	Continuation of above run to 8 s.
Bndsplt3	"	"	37.13	62.87	Continuation of Bndsplt2 to 11 s.
Plate1	Horizontal plate	"	48.82	51.18	Horizontal plate, with same width as inlet (0.0924m) placed 2 D_h from inlet. Similar geometry as Bndsplt runs except vertical splitter replaced with horizontal plate.
Plate2	"	"	40.37	59.63	Geometry used is modification of Pipebnd5. A shorter pipe bend (1.25 D_h) used. Plate placed in same position as Plate1.
Plate3	"	"	46.35	53.65	Similar to Plate2, except the horizontal plate is placed closer to inlet, 1 D_h from the inlet.

Table 6-4 List of runs investigating possible remedies for flow mal-distribution

7. DISCUSSION OF RESULTS

In this chapter, a discussion of the results obtained from both experimental and numerical work is carried out. The experimental work is examined in section 7.1. Section 7.2 covers the steady state numerical models of the distribution chamber. Section 7.3 looks at the results from the two-phase transient models. The numerous factors affecting the accuracy of the model are examined in turn, and the results of each compared against the experimental data. The steps by which the solution strategy is obtained, given previously in chapter 6, are also outlined.

On obtaining a suitable solution strategy for solving flows within the distribution chamber, the discussion of asymmetric flows is carried out in section 7.4. Here the asymmetric effects due to a pipe bend are investigated. A suitable way of replicating the effects due to a pipe bend are examined. This is in order to reduce the amount of CPU time required for the calculations. The most accurate method is found and the effects due to the bend at two different distances below the chamber floor, are discussed.

The results from the simulation of two pipe bend distances are used to investigate the remediation of flow mal-distribution. This is discussed in section 7.5. Two different methods are used. The first uses a vertical splitter plate, and the second, a horizontal flow deflector. The impact of both types of remedial methods on the overall design and operation of a typical sewage treatment plant are also considered in section 7.6.

A summary of the findings and conclusion is given at the end of each main section of discussion.

7.1 Experimental results

Due to the lack of experimental data available for flow distribution chambers in the open literature, it was necessary to collect quantitative information on velocities, turbulence,

free surface locations and flow distribution for a typical distribution chamber, to validate the CFD models. The experimental results are novel and are useful contributions to the understanding of distribution chambers.

The experimental results from the Model A are discussed in the following subsections. These were also used to validate the CFD models. Due to the constraints of time, CFD models of Model B were not created. Therefore, the experimental results from this model are not reported here.

7.1.1 Flowrate and distribution measurements

The flow out of each of the two outlets in Model A was metered by orifice plates. The head losses across the orifice plates were then converted to volumetric flows using equation 4.2-1.

The flow out of each outlet was expressed in terms of percentage distribution between the two outlets. The volumetric flow out of each outlet was non-dimensionalised by the total flow out. The results of the three sets of tests are shown in Figures 7.1-1. 7.1-2, 7.1-3. The percentage uncertainty associated with the flow distribution measurements was $\pm$ 6.12% (see Section 4.4.4). The results showed that there was slightly more flow leaving outlet 1 than 2 for the 2.95 and 4.38 l/s tests, but these differences were within the uncertainty range. Similarly for the highest flowrate, the differences between the two outlets were within the range of uncertainty, and can therefore be considered equal. An additional consideration for flow distribution was the head of water over the weirs. If there was a difference of 1%, between the outlets, the difference in flow was 0.0438 l/s at an inflow of 4.38 l/s. Since the flowrates were obtained by converting the measured head losses across the orifice plates to volumetric flow, the actual head corresponding to that flow difference was 0.13 mm (from equation 4.2-1). This value would be impossible to measure with any accuracy in practice.

The test rig was designed and constructed to be symmetrical about its longitudinal axis. The purpose of these tests was to obtain data from symmetrical flows within the chamber. In practice, isolating all the factors that caused flow asymmetry or unsteadiness was not possible. For example, the tee-junction below the chamber could have been a contributor to any asymmetry present. However, this was minimized to some extent by its distance from the chamber, which was 10 pipe diameters away. The orientation of the tee also helped to reduce the occurrence of asymmetry. If the jet was deflected by the asymmetric geometric layout of the pipework below the chamber, it would be directed at the two walls between the weirs, rather than at the outlet weirs directly.

During the experiments, flowrate measurements were made for every change in hot film measuring points for velocities and turbulence. There were between 45-60 separate measurements of flow out of the system in one set of tests. Averaging these measurements showed that the flows out of the two outlets were relatively equal, as discussed above.

In the experiments, the location of the surface boil was observed to vary periodically in time. This is discussed in further detail in section 7.1.4. The boil was a consequence of the jet formed in the chamber. Any unsteadiness in the jet would cause this periodic behaviour. Additionally, any deviation of the jet from the centreline of the chamber can cause flow mal-distribution between the outlets. Thus, the variations measured in flow were partly due to this phenomenon of an unsteady jet.

When averaged over time, the flow distribution between the two outlets was within $\pm$ 5 % for all test cases. This value was within the uncertainty value of $\pm$ 6.12 %. Hence, for practical purposes, the flow distribution can be considered to be equal, since there can only be a unique solution to produce equal flow distribution.

For the purposes of comparison with the CFD results, the flows out of the chamber for the three sets of tests were considered to be equal, and the flow within the chamber was symmetrical.

7.1.2 Water Level measurements

The water levels at the various points in the chamber were measured using a vernier point gauge. The measured values are tabulated in Tables 7-1a, b and c.

Measurement location in z direction (m)	Measurement location in x direction (m)						
	0	0.077	0.154	0.231	0.308	0.385	0.462
0.1037	0.6545	0.6597	0.6608	0.665	0.6609	0.6597	0.6543
0.1337	0.6544	0.6594	0.6605	0.666	0.6607	0.6596	0.6542
0.1637	0.6545	0.6597	0.6606	0.6651	0.6608	0.6597	0.6543

Table 7-1a Measured water levels within chamber at 2.95 l/s

Measurement location in z direction (m)	Measurement location in x direction (m)						
	0	0.077	0.154	0.231	0.308	0.385	0.462
0.1037	0.6615	0.6648	0.6686	0.678	0.6685	0.6649	0.6613
0.1337	0.6603	0.664	0.669	0.6796	0.669	0.664	0.6603
0.1637	0.6613	0.6649	0.6685	0.6778	0.6686	0.6648	0.6615

Table 7.1b Measured water levels within chamber at 4.38 l/s

Measurement location in z direction (m)	Measurement location in x direction (m)						
	0	0.077	0.154	0.231	0.308	0.385	0.462
0.1037	0.6681	0.673	0.6805	0.688	0.6808	0.6731	0.668
0.1337	0.6663	0.67	0.678	0.691	0.678	0.67	0.6663
0.1637	0.668	0.6731	0.6808	0.6879	0.6805	.0.673	0.6681

Table 7.1c Measured water levels within chamber at 5.51 l/s

The water surface levels fluctuated over time. The estimated periods for the variation in the surface levels were 6 to 8 seconds for the two low flows, and decreased to 3 to 4 seconds for 5.51 l/s. (Note that the variation in the surface levels were related to the periodicity in the boil location. The boil location is further discussed in section 7.1.4). The estimated uncertainty associated with the vernier measurements were ± 0.2 cm at 2.95 l/s, ± 0.3 cm at 4.38 l/s, and ±1.0 cm at 5.51 l/s. These observations were further indications of the unsteadiness of the jet formed within the chamber.

There was a steep gradient in the water levels in the region near the centre of the chamber. This was especially pronounced in the tests at the largest flowrate, which was indicative of the formation of a boil within the chamber. The axial velocities at and near the centreline of the jet were sufficiently large to deflect the free surface.

Figure 7.1-4, 5 and 6 are photographs showing the shape of the free surface as observed during the experiments. Figure 7.1-6a shows the development of the boil over time. It is clear from these photos that the surface was relatively placid at the two lower flowrates. However, at the maximum flow, the magnitude of the boil was large. The unsteady behaviour of the boil and free surface was very evident in this test.

(Herbath and Wong, 1997a), suggested the use of the Rehbock method (equation 3.2-1) for estimating the water levels above the weirs for a given discharge over the weirs. However, this formula was strictly applicable for full sized weirs found in treatment plants as opposed to laboratory scale models. The minimum dimensions for which the Rehbock formula can be used, were given in Chapter 4.

An alternative method to the Rehbock method was the SIA method (ISO 1438, 1980). This method was more suitable for estimating the water levels above smaller weirs, such as those found on the physical model. The geometric ranges of suitability are:

$h/p \leq 1.0$, $b/B > 0.3$, $0.025B/b < h < 0.8$ m and $p > 0.3$ m

where p is the height of the weir crest above the floor of the chamber,

B is the width of the channel or chamber,

b is the width of the weir, and

h is the height of water above the weir crest.

Table 7-2 below gives a comparison between the SIA, CFD and measured values of the head of water over the weirs:

Flowrate (l/s)	Measured head of water over weirs (m)	Calculated values from :	
		SIA prediction (m)	CFD prediction (3D model)
2.95	0.023	0.0348	0.0234
4.38	0.029	0.0462	0.0293
5.51	0.035	0.0544	0.0353

Table 7-2 Comparison of predicted and measured water levels

The most accurate CFD model was used for the comparison in Table 7-2, which was the 3-dimensional model, employing the RNG k-ε model, and the VOF model without

surface sharpening (3DRNG1, 2, 3). A second-order accurate differencing scheme, the Van Leer scheme, was also used (more details of the CFD models are given in Section 7.2). Thus, it may be seen that the CFD predictions were very close to the measured values, unlike the SIA method.

It should be noted that both the SIA and Rehbock prediction method were strictly recommended for weirs in a channel. The underlying assumption for both methods was that the approach flow in the chamber was fully developed. There had to be an upstream distance equivalent to 4 to 5 times the head over the weir (y-B) to ensure fully developed flow. In the physical model the minimum distance was 0.175 m. In practice, it was extremely unlikely that there was sufficient distance within a chamber to ensure that fully developed flow upstream of the weirs. Thus, there will be a degree of uncertainty and inaccuracy associated with either of these algebraic equations.

If the above prediction method was to be used to determine the discharge from each weir based upon the experimentally measured values of head over each weir, then the flowrates would be under predicted. Table 7-3 below gives the comparison between the SIA predicted total discharge from the chamber (i.e. discharge from both weirs), and the actual discharge.

Actual flowrate (l/s)	Measured head over weir (m)	SIA predicted flow discharge (l/s)	Percentage difference (%)
2.95	0.023	1.68	-43.05
4.38	0.029	2.3	-47.49
5.51	0.035	2.98	-45.92

Table 7-3 Comparison between actual and predicted discharges based on experimentally measured head values

Thus, the incorrectly predicted head levels led to a significant over-prediction in discharge values for the chamber. Consequently, the simple algebraic method can only be used to give an initial guess for the discharge over each weir. More accurate values can only be found from CFD calculations. Also, a prominent boil was formed above the inlet for each test conducted. The location of this boil was found to vary periodically which suggested a time-dependant flow within the chamber, which cannot be predicted by the algebraic methods.

7.1.3 Velocity and turbulence measurements

The flow velocities and turbulence within the model were measured by a hot film probe. A sampling rate of approximately 3 times the maximum frequency of the fluctuations was set up (300 Hz).

Figure 7.1-7 shows the voltage traces from both channels of the probe for a test at the maximum flowrate, 5.51 l/s. The probe was placed within the channel coinciding with the centreline of the jet.

The degree of turbulence in the flow can be represented by the measurement of the turbulence intensity, i.e.

$$Turbulence\ intensity = \frac{\sqrt{\overline{u^2}}}{\overline{U}}$$

Relatively low levels of turbulence were measured in the experiments. As an illustration, the values of the vertical velocities (V) measured at the jet centreline were compared for the three test flowrates. These are shown in Table 7-4.

Flowrate (l/s)	Turbulence intensity	
	Average (%)	Standard deviation (%)
2.95	17.0	1.36
4.38	17.7	0.6
5.51	18.0	1.0

Table 7-4 Turbulence intensities for the three test cases

The above results showed that the intensity of turbulence was around 17% to 18% of the mean flow velocity for the three sets of tests. The measurement point, coincided with the centreline of the chamber just below the free surface. The velocity gradients there were large, and correspondingly, the amount of turbulence there would be larger than elsewhere in the chamber. This suggested low levels of turbulent kinetic energy and turbulent energy dissipation for most of the flow in the water phase. Thus, the measured values showed relatively small values of fluctuating components of velocities and energy, near the free surface.

Averaged values of the measured instantaneous velocities were used to compare against the CFD results, since the calculated velocities were the mean velocities.

7.1.4 Flow patterns

As the piped flow entered the chamber, a jet was formed, which spread out through the entire submerged depth of the water phase. The regions of high shear on the boundaries of the jet entrained the surrounding liquid into the core. This resulted in large recirculating regions on either side of the core. These recirculating zones are shown in the two photographs of the test at 5.51 l/s. Figure 7.1-8 shows the streak lines, formed from the air bubbles within the chamber, following the motion of the flow.

At the free surface, the jet was deflected horizontally away from the centre of the chamber towards the periphery of the structure. Thus, a horizontal shear layer was formed below the free surface. The impingement of the jet on the free surface caused a disturbance or boil on the surface. At the lowest test flowrate of 2.95 l/s, the boil was small. This is shown in Figure 7.1-4. The magnitude of the boil increased with increasing flowrates. Figure 7.1-5 shows the resulting free surface for a flow of 4.38 l/s into the chamber. Figures 7.1-6a, b and c show the sequence of the boil formation at the highest flowrate of 5.51 l/s. The shape of the boil can be seen to be circular.

The shape of the free surface changed over time. The boil formed on the surface was observed to be unsteady and oscillated about the centreline of the jet. The cycle time was estimated to be 6 to 8 seconds for the two low flowrates, while at the highest flow, the time was reduced to 3 to 4 seconds. This was the result of an unsteady jet. Its behaviour was time dependant, and its mean location coincided with the centreline of the chamber. This conclusion was reached from the results of the flow distribution measurements (Section 7.1.1), since the time averaged distribution between the two outlets were approximately equal.

The flow accelerated as it went over the discharge weirs. A thin layer of water was formed above the weir crests. The thickness of this layer increased with the increase in flow over the weirs. The model was set up to give a free (or modular) discharge over the weirs, This meant that the water levels downstream of the weirs, in the collection boxes, were lower than the level upstream of the weirs. In this way, the flow downstream did not affect the flow upstream. As a result, plunging curtains or sheets of water was formed immediately downstream of the weirs. They plunged down into the collection box entraining large amounts of air as a result. This is seen in Figures 7.1-9, 10, and 11. The photographs show the air bubbles formed.

In the model, fibre or hairlok screens were built into the collection boxes. These were 0.3 m downstream of the weirs. They had two purposes, one was to trap any air

bubbles formed, and secondly, smooth the flow into the discharge pipes (i.e. the velocity distribution downstream of the screens would be relatively uniform). This would ensure that the flow entering the return lines containing the orifice plates would be free of any pockets of air, which will adversely affect the flow measurement accuracy. There was a head loss across the screens, such that the water levels upstream and downstream of it were different. This is clearly seen in Figure 7.1-9 and 10 . Also, because of this flow restriction, regions of recirculating flow were set up upstream of the screens. The two hairlok screens were important for accurate flow measurement. They were, however, unimportant in terms of CFD modelling, since the behaviour of the flow here, had no effect on the flow within the distribution chamber.

The regions of high shear were expected to occur when there were large changes in the flow direction, i.e. where the velocity gradients, $\partial U/\partial x$, $\partial U/\partial y$ etc. were large. These included the region below the free surface and the recirculating zones on either side of the jet. These regions of high shear will also produce large amounts of turbulence.

Due to the limitations of the apparatus used, it was not possible to extend the hot film probe down to the recirculating flow region. It was only possible to measure the turbulence immediately below the free surface. The measured values of turbulent kinetic energies are shown in Figures 7.3-6, 7.3-14, 7.3-18, 7.3-19, and 7.3-20. As expected, the trend from these graphs shows that the turbulence is at a maximum at the centreline of the chamber, decreasing in magnitude, away from the centre.

7.1.5 Quantification of the performance of a distribution chamber

Herbath and Wong (1997a) presented a simple method to determine the magnitude of a surface boil based on the decay of the jet centreline velocity. The likelihood of flow mal-distribution may also be determined from the estimations given. This method incorporated the simple algebraic relationship derived by Goertler (Rajaratnam, 1976) for the jet centreline velocity. The steps given are reproduced below.

Step I.

$u_m = u_i$ when $B/D \leq 6.5$

$u_m = 6.5u_iD/B$ when $6.5 < B/D < 30$

where B is the distance between the weir crest level to the chamber invert

D is the pipe diameter

u_m is the jet centreline velocity (vertical component)

u_i is the inlet velocity

The value of the centreline velocity can be converted to a velocity head by,

$$h_v = \frac{u_m^2}{2g}$$

The following conclusions may be drawn from the estimates of the value of h_v,

If $h_v < 0.02$m, then the surface disturbance is negligible and flow distribution not adversely affected.

If 0.02 m $< h_v < 0.05$ m, then the disturbance is significant and may affect flow distribution.

If $h_v > 0.05$ m, then the disturbance is substantial and it may affect the distribution.

Step II

The asymmetry caused by the surface disturbance was also estimated. The ratio of L/D (where L is the distance of the bend, measured from the centreline, to the chamber invert) had to be determined. The following recommendations are given, based on empirical data:

Flow asymmetry is negligible for $L/D > 5$.

There is some asymmetry for $3 < L/D < 5$.

Very severe asymmetry when $L/D < 3$.

Step III

The dimensions of the chamber will need to be taken into account since this may interact with the jet if the extents of the jet core is large. The ratio h/R is determined. R is the half width, or radius of the chamber, and h is the head of water over the weir. As before, based on empirical data, the following recommendations are given:

When $h/R < 0.005$, surface disturbance is unlikely to influence flow distribution unless asymmetry is severe ($L/D > 3$).

When $0.05 < h/R < 0.1$, surface disturbance is unlikely to influence distribution if there is no flow asymmetry ($L/D > 5$)

When $h/R > 0.1$, then the boil can cause mal-distribution.

Applying the above calculation steps to both the physical model and the CFD models (3D and 2D), one may estimate the validity of the above empirical method. The values are tabulated below in Table 7-5

Variables	Experiments		CFD Results					
			3DRNG2 (symmetrical flow)		Pipebnd4 (asymmetric flow)		Pipebnd5 (asymmetric flow)	
	Measured	Predicted	CFD	Pred.+	CFD	Pred.+	CFD	Pred.+
B/D	8.829		8.829		9.1449		9.1449	
u_m	0.175*	0.631	0.35*	0.631	NA	0.019	NA	0.019
h_v	0.049	0.020	0.063	0.020		0.019		0.019
L/D	> 5		> 5		2.12		2.12	
h/R	0.119		0.119		0.383		0.383	
Flow distribution	good	good	good	good	poor	poor	poor	poor

* (measured at 0.0286 m below surface)

+ predicted results for CFD calculations are the results based on design guide procedures.

Table 7-5 Comparison of actual and predicted results using Best Practice Guide procedures (Herbath and Wong, 1997a)

Following the above design procedures, good flow distribution was expected for the physical model and the 3D CFD model (this assumed an infinitely long length of pipe leading into the chamber). These were proved to be correct. Similarly, for the two asymmetric flow cases, Pipebnd4 and Pipebnd5 (see Table 6-3), the predictions of poor flow distribution were subsequently proven to be correct (see the following sections for discussions of the CFD results). However, this did not in any way prove the validity and universality of the application for the design procedures. Taking the example of 3DRNG2, the predicted value of h_v was 0.02 m, whereas the CFD value (which was in close agreement with the experimental values), was 0.063 m, some three times greater. Clearly, the empirical prediction method had fortuitously predicted good flow distribution even though the predicted results were inaccurate. While the inclusion of the L/D ratio in the consideration of flow distribution was correct, the full effects of the pipe bend was not fully understood and accounted for in the design procedures. For

example, the orientation of the pipe bend in relation to the chamber layout, was not included. The orientation of the bend with respect to the location of the weirs can affect the location of the surface boil, i.e. the way in which the jet is deflected within the chamber.

The ranges of values of h/R given in Step III were arrived at from experimental observations. However, the range of applicability to different design scenarios has yet to be fully validated and tested. The agreement with the experimental and CFD results carried out here can be considered fortuitous. Two extremes in the values of h/R were considered. One where the value of h/R was infinity (symmetrical chamber case), and the other where the h/R was between 0.5 and 1, which guaranteed poor flow distribution.

In the above design method, the presence of a boil on the free surface was assumed to be the underlying cause of flow mal-distribution. While it was recognized that the formation of a jet within the chamber produced the boil, it was unclear whether the boil, or the jet, or both were the main cause of mal-distribution.

Despite the success in predicting the occurrence of flow mal-distribution using the empirical method, there are still many gaps in its ability to quantify flow mal-distribution, the location and exact magnitude of the boil, and the main cause of flow mal-distribution. Therefore, a more accurate and rigorous method is required.

7.1.6 Summary of Experimental Results

The test rig was designed to minimise flow mal-distribution, which was hypothesised to be caused by a pipe bend below the chamber floor. Observations made during the experiments showed that the jet formed, oscillated around the geometric centreline of the distribution chamber. However, the averaged values showed that the distributions of

flow between the two outlets were equal. This showed that the jet formed was unsteady, yet its mean location coincided with the geometric centreline of the chamber.

A periodicity was also observed for the surface boil formed during the experiments. This was further indication of the unsteadiness of the central jet. An empirical method was also available to estimate the water levels over the weir crests and hence the volumetric flows out of each outlet. However, the accuracy of this method was very poor compared to the CFD predictions.

The measurement of turbulence by the hot film probe showed that the turbulence intensity of the flow was relatively small near the free surface. Measurements of the turbulence kinetic energy, k, also showed that the value of k was a maximum at the centreline of the chamber as expected.

The flow patterns formed within the chamber showed that a central jet, oscillated around the geometric centreline of the chamber. Two recirculating regions were also setup. Since the flow over the weirs were modular, the flow downstream of the weirs had no effect on the flow upstream. These observations were useful and may be compared qualitatively with the CFD models, as part of the validation process.

A simple, empirical method of estimating the performance of a chamber was produced by Herbath and Wong (1997a). Compared against experimental data, and the various CFD models, it was found that this method was accurate. However, the applicability and accuracy of this method for a wider range of designs has yet to be tested. Therefore no conclusive judgement can be made regarding the method.

Despite the work done by previously, there are still gaps in the knowledge of distribution chambers. The empirical methods are of limited value. More accurate ways of predicting chamber performance still needs to be found. It is also not possible to

prove the hypothesis of the asymmetric effects of a pipe bend using the empirical design methods given.

7.2 Validation of 2D steady-state CFD model

There were two possible methods of approaching this study of distribution chambers. The first would be to conduct a pure experimental study of the chamber. Parametric studies would be required to quantify flow mal-distribution due to a pipe bend. The second approach would be to use CFD as a tool for identifying and solving the problem. While CFD techniques have been developed and used for many years, the application of this technique to flow distribution chambers is unique and novel. There are advantages in using CFD. First, the application and development of an accurate and validated CFD model of the chamber would be a useful tool in the overall design and planning of a sewage treatment plant. It will have the potential to perform detailed analysis of the flow behaviour. Secondly, CFD is far more versatile and cost-effective in terms of time, budget and materials requirements, compared with an experimental study. Thus, the CFD option was pursued in this study since it provided a far greater potential and had a much greater capability in providing accurate solutions. To use CFD to investigate the effects of asymmetry, it was vital to validate the solutions from these models with the experimental results.

A two-dimensional representation of the physical model of the distribution chamber was initially created as the CPU overheads were smaller than a full 3D model. A 2D solution to the 3D flow within the chamber would be a over-simplification. However, the number of CPU hours required for such a solution would be reduced considerably. This allowed much quicker turnaround times between test runs of different turbulence models, differencing schemes and grid dependence tests etc. In this way, the most accurate and cost-effective solution strategies were identified and used for the subsequent 3D calculations. The 3D results are discussed in section 7.3. This section concentrates

on the validation process for the 2D model and the identification of the variables conducive to an accurate model.

The results from the steady state runs using single and two phase flows are discussed initially. The list of runs carried out is shown in Table 6-1.

7.2.1 Single phase flow

A simple 2D model of the chamber was created. A flow of 4.69 l/s was input into the domain. The results of runs ST1 and ST2 are shown in Figures 7.2-1a..d, and Figures 7.2-2a..d, respectively. Two different outlet patches were used in the runs. ST1 used mass flow boundaries, where the flow out of the two outlets were assumed to be equally distributed. ST2 used pressure boundaries for the outlets. The pressures at the outlets were set to atmospheric pressure. The use of pressure patches was physically more realistic since the boundary conditions at the outlets mimic the actual conditions in the physical model. Pressure values were required at the outlet, but not velocity nor mass flow information. Thus, any asymmetries in the chamber would be allowed to develop.

Comparison between ST1 and ST2 showed that firstly, the flow patterns developed within the chamber were very similar. Both runs showed a symmetrical jet being formed, with equal flow distribution between the two outlets. Recirculating flows were formed due to the entrainment of the surrounding fluid by the jet. The deflection of the jet by the lid caused the flow to turn horizontally outwards towards the outlets. The results showed that there were several flow layers with different velocities at the outlets. Right at the top, near the lid, the velocities were largest. This decreased the further away from the lid. However, this did not agree with the experimental observations and physical intuition since the opposite effect was expected. The calculations in ST1 and ST2 were for a single phase fluid (water), and the flow was non-buoyant. Therefore, this resulted in the trends seen. The pressure plots showed the highest pressure occurred where the jet impinged on the lid of the chamber. Both results showed similar pressure

values. However, there were some differences between the two results. Note that the pressures shown in both diagrams were the total pressure minus the hydrostatic pressure. This meant that the actual pressures were not necessary to be input into the outlet boundary conditions, only the relative pressure differences were important here. The pressures in the outlets in ST2 were set to zero. As a result, the calculated pressure field below the inlet had to be less than zero. This accounted for the differences in pressure values between ST1 and ST2. However, the differences between the minimum and maximum pressures for both calculations were similar, i.e. around 340 to 350 Pa. Thus, it may be concluded that the pressure contours for both cases were similar since both showed similar patterns and the same differential pressures. The outlets of ST2 showed constant pressures, whereas ST1 had varying bands of increasing pressure. This difference was due to the outlet boundary conditions imposed on the solution. It was assumed that the pressures at the outlets for ST2 may be considered uniform throughout the height of the outlet. Thus, the contours did not vary there. On the other hand, for ST1, only the mass flowrate out of the outlets had to be specified as the boundary conditions. Thus, the calculated pressure field near the outlets had to vary to accommodate the flow velocity forced out, to satisfy the conservation of momentum. The varying pressure contours of ST1 were believed to be physically more realistic (for a fully symmetrical case) since the boundary conditions imposed were physically more realistic.

The k and ε contour plots for both runs were very similar, both in terms of calculated values and patterns. Large values of k and ε were found in the regions where large velocity gradients were present, i.e. at the jet boundaries, and at the outlets.

ST1 and ST2 showed the formation of the central jet and two recirculating regions beside it. This agreed qualitatively with the experimental results. However, no free surface information was available due to the use of a single phase flow in the calculations. Both types of outlet boundaries were valid for symmetrical flow within the chamber. These may be used in the following study of a 2-phase steady state flow

calculation. Despite the success of the single phase steady state calculations, there was some inaccuracy, such as the velocity distribution at the outlets. This was largely due to the simplifying assumption that the system may be represented by a single phase. These inaccuracies are addressed below in the 2-phase calculations.

7.2.2 2D steady-state, 2 phase flow model

Since the results of ST1 and ST2 gave reasonable qualitative agreement with the experimental observations, the same approach was extended to a two-phase, steady state flow calculation.

ST1 and ST2 showed that a unique, symmetrical solution was possible. 2PH1 (the two phase flow calculations), also assumed the same. The outlet boundary conditions were imposed using inlet boundaries with equal flow and uniform flow velocities out of the chamber. This was strictly incorrect since the velocity distribution was not uniform. Also, if there was any flow asymmetry present in the chamber, then the outlet boundary conditions would be incorrect. Nevertheless, as a first approximation, this simple assumption sufficed. The water levels were also assumed in this calculation. The levels over the weir crests were determined using the SIA (ISO1438, 1980) method given previously.

Figure 7.2-3 shows the results for 2PH1. The most prominent feature shown in the velocity vector plot was the lack of a jet. Instead, a relatively uniform velocity distribution was formed throughout the width of the chamber, which was not physically possible.

Besides 2PH1, other calculations were made, although they are not listed. These had different outlet boundary conditions, e.g. varying pressures according to the volume fractions of the phases present. However, all these steady state calculations had the same result, i.e. the disappearance of the jet and uniform velocity distribution across the

width of the chamber. In the calculations where volume fractions were not set as a boundary condition at the outlets, the domain was filled with water and all the air expelled.

The two phase steady state runs carried out showed that there existed non-unique solutions to the flow. Converged solutions were obtained where the continuity for the water phase was satisfied. However, the flow of air into the system was not specified. Therefore, any amount of air present in the domáin, at the end of the calculations, can be a valid solution. We see that for the boundary conditions imposed, the most likely solution is that seen in 2PH1. This is by no means a valid physical solution. Thus, the boundary conditions imposed here are considered to be ill-posed, and the neglect of the time-dependant term in the Navier-Stokes equations is also incorrect, judging by the experimental observations.

7.2.3 Summary of the 2D Steady State CFD models

From these runs, non-unique solutions were possible since the governing equations for the flow were non-linear. One would expect more than one mathematical solution to the system. However, the dominant solution in this case, was physically unrealistic. The boundary conditions for this problem specified a certain amount of water entering the system. This was balanced by the same amount leaving the domain. However, any amount of air within the domain can be considered a valid solution (since the volumetric flowrate of air was not required to be specified). Hence a converged solution is possible with no air present.

The boundary conditions for this particular problem were not well-posed. Additionally, experimental observations revealed an unsteady jet present in the flow. Consequently, an entirely different approach had to be adopted involving transient calculations.

7.3 Validation of 2D and 3D transient models

Transient calculations were carried out to determine the flow behaviour and the shape of the free surface within the distribution chamber. The geometry of the domain was altered from the steady state runs. The collection boxes present in the physical model were added to the chamber. The outlets were now situated on the floor, or invert, of the collection boxes instead of being above the weir crests. This facilitated the specification of the outlet boundary conditions since the flow at the outlets were single phase water. Pressure boundaries were used for the outlets for the same reasons given in Section 7.2.1, i.e. it would be physically representative of the actual conditions.

In the course of the transient runs, a number of variables were identified as being important to the performance of the models. They are:

1. turbulence models
2. surface sharpening algorithm
3. higher order differencing scheme
4. mass residuals
5. volume of domain
6. dimensional effects

Each of the six factors are discussed below.

7.3.1 Grid independence and turbulence models

Validation runs were made initially with the standard k-ε turbulence model in the 2D numerical models. The three test flowrates of 2.95 l/s, 4.38 l/s and 5.51 l/s were tested (Run numbers 2D1, 2D2, and 2D3). Additionally, a grid independence test was conducted (2DIndy). The results of these are shown in Figures 7.3-1, 2, 3, and 4

respectively. A list of the test runs are shown in Table 6.2. This table is reproduced below for easy reference.

Transient CFD run number	Flowrate (l/s)	Turbulence model	Mass residuals (kg/s)	Surface sharpening	Van Leer scheme	Other comments
2D1	2.95	k-ε	1×10^{-5}	Yes	No	17850 cell geometry
2D2	4.38	k-ε	1×10^{-5}	Yes	No	"
2D3	5.51	k-ε	1×10^{-5}	Yes	No	"
2DIndy	4.38	k-ε	1×10^{-5}	Yes	No	27300 cell geometry - grid independence check
2DRNG1	4.38	RNG k-ε	1×10^{-5}	No	Yes	17850 cell geometry
2DRNG2	4.38	RNG k-ε	1×10^{-7}	No	Yes	"
2DRNGV1	4.38	RNG k-ε	1×10^{-5}	No	Yes	Volume of domain expanded - 19025 cells
2DRNGV2	4.38	RNG k-ε	1×10^{-7}	No	Yes	"
2DRNGC1	4.38.	RNG k-ε	1×10^{-5}	No	Yes	Weir levels corrected - new geometry used (18085 cells)
2DRNGC2	4.38	RNG k-ε	1×10^{-7}	No	Yes	"
3DRNG1	2.95	RNG k-ε	1×10^{-7}	No	Yes	3D Geometry (38232 cells)
3DRNG2	4.38	RNG k-ε	1×10^{-7}	No	Yes	"
3DRNG3	5.51	RNG k-ε	1×10^{-7}	No	Yes	"

Table 6-2 List of transient CFD validation runs (Details of Van Leer differencing scheme and surface sharpening apply to final results - see text for details)

The velocity vector plots of Figures 7.3-1a, 2a, 3a and 4a showed physically realistic results. The jet and two recirculating regions were formed. Where the jet impinged on the free surface, a deflection was seen. The flow accelerated as it travelled over the weirs, and plunged down into the collection boxes. These agree, qualitatively, with the experimental observations.

Prior to the investigation into the effects of turbulence models on the results, a grid independence test was carried out. The purpose of this test was to check that the grid chosen was sufficiently well resolved. 4.38 l/s was chosen as the base case for comparison with subsequent runs. The run, coded 2DIndy, also used the k-ε model. Both this run and 2D2 were exactly the same except for the grid. 2DIndy had 27,300 cells compared with 17,850 cells used previously. The results of 2DIndy are shown in Figures 7.3-4a and b. Comparison with Figures 7.3-2 did not reveal any qualitative difference between the two runs.

The dips in the free surface, found in the collection boxes, for 2D2 and 2DIndy, were physically unrealistic. However, examining the shape of the dips revealed that both were different. There were more cells within the collection boxes for the 2DIndy run. Thus, the grid in the collection boxes was not sufficiently well resolved to achieve grid independence. However, this was unimportant provided mass conservation was achieved in the solution. Also, the region of interest in this study was the free surface in the chamber, and since the solution of the flow in the collection boxes did not affect the solution within the chamber, the cell resolution within the boxes were unimportant. Nevertheless, the non-physical dips in the collection boxes could be improved further. The cause of this non-physical behaviour was due to the surface sharpening algorithm. This will be discussed in the next section.

Quantitative comparisons were also made between the two runs (2D2 and 2DIndy). As mentioned in Chapter 6, the weir levels for both calculations were created at a different level from that of the experiments. Direct comparison with the experimental data would

therefore be misleading. Hence Figure 7.3-5 only gives the comparison between the 2 CFD results.

The graph of the free surface location shows a small difference in the prediction accuracy of the two models (Figure 7.3-5e). The mesh size chosen for 2D2 near the surface may be considered sufficiently small to achieve grid independence since the differences in water levels were around 1%. The differences between the CFD results in the values of U, V and k were insignificant. Therefore, the grid density chosen was sufficiently fine to resolve the flow within the chamber.

Direct comparison between 2D1, 2D2, 2D3, 2DIndy and the experimental data would be misleading. Nevertheless, useful information may be gleaned from such a comparison. Figures 7.3-6a..m are plots comparing the calculated velocities, turbulent kinetic energy and water levels with the experimental data. It was clear from the figures that the calculated values of all variables over-predicted the measured results by a significant amount. One obvious cause of this was due to the different weir levels. Examination of Figure 7.3-6m showed that the over-prediction of the water levels ranged from 7% to 9%, well in excess of the 1.9% higher weir crest levels. When considering the flow over a weir in isolation, i.e., ignoring any other effects within the chamber affecting the head over the weir, one may use equation (3.1-4). Here the head of water over the weir, (y-B), is raised to the power of 1.5. Taking the experimental value of y = 0.66 m, and flowrate out of each outlet is 2.19 l/s (equal distribution), the experimental value of the weir crest is B = 0.631 m. We substitute into equation (3.1-4), and write,

$$2.19 \text{ l/s} = A \cdot (0.66 - 0.631)^{1.5}$$

$$\therefore A = 443.45$$

where A is the lumped value of all the other components in the equation.

Since a different value of B was used in the CFD calculations, which was 0.643 m, the approximate value of y_{CFD}, is,

$$2.19 = 443.45\ (y_{CFD} - 0.643)^{1.5}$$

$$\therefore y_{CFD} = 0.67\ m$$

Thus, the above simple sum showed that the head of water over the weir crest should have increased to 0.67 m (+1.52%) when the weir crest level was raised from 0.631 m to 0.643 m (+1.90%). However the CFD calculated value of 0.68 m was equivalent to an increase of 3.03%, double the expected value.

The velocity and turbulence results showed that the over-predictions were even larger in magnitude. While there was no simple algebraic relationship to estimate the velocities and turbulence at those four measurement planes, one would not expect the differences to be over 100%. Therefore, there were other factors which resulted in the large over-predictions in the measured variables other than that of the incorrect weir levels. (Note that the CFD results showed a flattened peak. This was due to the lack of an additional measurement point in the centre of the chamber.)

The calculated and measured trends shown by the velocity and water level results were in agreement. However, calculated trends for k were opposite that of the measured results. The graphs of k showed a trough, or a minimum value of k at the centre of the jet, while the experimental values showed a peak. Clearly, the results of 2D2 could be improved upon.

One possibility for the source of errors was the choice of turbulence model. The standard k-ε model was used in 2D2. This was substituted by the RNG k-ε model in 2DRNG1. The choice of this model was made because it was reported to overcome some of the deficiencies of the standard k-ε model, i.e. it was superior in swirling flows and can account for anisotropic turbulence. The RNG k-ε model was also thought to give better predictions of k, unlike the standard k-ε model.

Examination of the results of 2DRNG1 showed that there was no change in any of the prediction trends, especially for turbulent kinetic energy. While there was reduction in the values of k predicted by the RNG model compared to the k-ε model, nevertheless, the differences between the experimental and the values of 2DRNG1 were still large. The use of this new turbulence model only made a small difference in the calculated values. It was obvious that there other factors affecting the solution accuracy.

It was also interesting to note the trends shown by the calculated V velocities and k near the walls of the domain. The results also exhibited secondary peaks in those regions. The velocity at the surface of the walls had to be zero. Away from the walls, in the turbulent boundary layer, the velocity varied in a logarithmic manner. However, the peaks were very pronounced in the calculations while a smoother transition was expected. Therefore, the calculated variables near the walls was erroneous. There were two ways of reducing this error. The first would be to increase the cell density near the walls. The second was to use the low Reynolds number k-ε turbulence model (Launder and Sharma, 1974). This model was a modification of the standard k-ε model. At low Reynolds numbers, the eddy viscosity was damped when the local Reynolds number was low. Therefore, at the walls, the value of ε is zero.

However, neither of the two solutions were implemented in the subsequent models, since boundary layer effects were localised and confined to a small region near the walls. The solution accuracy was not affected by the boundary layer. It was therefore not worthwhile fully resolving the boundary layer region for the additional cost in CPU time. The wall region was not in the region of interest in this study.

The total simulation in the transient calculations performed here and in the subsequent runs, was equivalent to three domain residence times (one residence time is equal to the volume of the flow domain divided by the volumetric flowrate). This value was observed experimentally, to be sufficient to allow the development of the jet and the other main characteristics of the flow. Any transient effects due to flow startup would

have been eliminated here too. In the 2D models, one residence time was equivalent to 3.7 s (for a flow of 4.38 l/s). In the 3D models, it was 11 s for the same flowrate. There is a dilemma for the 2D models. The inlet spans the domain in the z direction. Thus, either the correct mass flowrate, or the inlet velocities can be specified, but not both. The key features of the flow are controlled by the vertical momentum and its behaviour at the upper surface. Thus, the experimental velocity was specified at the inlet in order to preserve the momentum. At the base case of 4.38 l/s, the averaged inlet velocity was 0.87 m/s.

Thus, the results presented in this section showed that the grid used was sufficiently well resolved in the region of interest. The regions downstream of the weirs did not affect the flow conditions within the chamber. The choice of turbulence models had a small effect on the calculated solution. However, the velocities, turbulent kinetic energy and water levels were still over-predicted despite the different turbulence model. Also the calculated trends for k were incorrect whether the standard k-ε or RNG models were used.

7.3.2 Effects due to the surface sharpening algorithm

Figures 7.3-7a..c show the results of 2DRNG1 calculations. The RNG k-ε turbulence model was used as mentioned in the previous section. Also, the surface sharpening algorithm was turned off for this run. Comparing these results with 2D2 (Figures 7.3-2a and b), showed that the flow patterns within the chamber were similar. The interface between air and water was well-defined for both results. On the other hand, the volume fraction contours within the collection boxes were more diffuse in 2DRNG1 than 2D2. The dip in the free surfaces in the collection boxes of 2D2, were eliminated. The dip, which was not physically correct, was caused by to the surface sharpening algorithm. The algorithm moved all the air present in the water back into the air phase and vice versa. Hence, the local regions where the curtains of water plunged into the collection boxes had a much larger proportion of air than water, due to the air entrainment (as

observed in the experiments). However, the segregation of the phases by the algorithm resulted in the incorrect result. The volume fraction contours of Figure 7.3-7b indicated that air entrainment was present within the boxes caused by the plunging curtains of water flowing over the weirs. The exact pattern of the entrainment was not clear, nor was the formation of air bubbles seen, unlike the experiments. In order to model the air bubbles accurately within the water phase, smaller cells were required in order to model the phenomena in the boxes. Since the modelling of the air entrainment and air bubbles were not within the scope of this study, and had no effect on the flow distribution, the cell resolution within the collection boxes was not increased. It would also be computationally expensive if this were to be done. Additionally, the use of the VOF model when air bubbles were present in the water phase was not be appropriate. The model assumes that the velocities of air and water were equal at the interface. Hence, the air bubbles would be forced to travel at the same local water velocity. Yet in reality, the bubbles would rise towards the free surface due to buoyancy effects. A more appropriate model would be the multi-fluid model (Computational Fluid Dynamics Services, 1995).

The purpose of the surface sharpening was to reduce numerical diffusion present in the solution. Numerical diffusion behaves like an additional viscosity on the flow, and will subsequently cause errors in the calculated variables. Since numerical diffusion is a characteristic of the upwind differencing scheme used in the calculation of 2D2, a higher order differencing scheme was used in 2DRNG1. Further discussions of this scheme and numerical diffusion are given in Section 7.3.3.

Besides the differences in the volume fraction contours in the collection boxes, the flow patterns and the speeds of the air phase had changed. The speeds within the recirculating regions had increased in 2DRNG1. Comparison between the velocity vector plots of Figures 7.3-2 and 7.3-7 showed that numerical diffusion was present near the free surface. The result of this was reflected in the magnitudes of the velocities of air above the interface, which were smaller in 2D2 (suppressed by the additional

viscosity). The directions of the velocities, in some areas, did not follow that of the water velocities directly below the interface. In contrast, the flow patterns of 2DRNG1 were different, and appeared to be, intuitively, more realistic. However, the magnitudes of the velocities were too large. This was clearly due to numerical errors. The reduction of these errors will be touched on in the following sections.

The plot of the V velocities (Figure 7.3-6e, f, g and h) showed that the peak levels of V were higher in 2DRNG1. On the other hand, away from the centre of the chamber, near the two outlets, the 2DRNG1 values of V were lower. This suggested that the behaviour of the jet and the recirculating regions were different between 2D2 and 2DRNG1. These differences were more likely to be due to the different turbulence model used and the improved accuracy of the solution, using the Van Leer differencing scheme, rather than an effect of surface sharpening. Figure 7.3-6m showed the differences between the water levels for the various runs. 2DRNG1 predicted higher water levels than 2D2 (under 2% higher than 2D2). The difference may be attributable to both the different turbulence model used and the sharpening algorithm. The shape of surface predicted by the two runs were very similar.

Another issue associated with the surface sharpening algorithm was that of global mass conservation. In 2D2, using the algorithm, global mass conservation was achieved. However, with 2DRNG1, conservation was not achieved when the algorithm was turned off. (The mass residuals for this run was set to 1×10^{-5} kg/s). This effect was the result of the penetration of the water phase by air, in the collection boxes. The non-conservation of mass was a numerical error, and if allowed to continue over time, the magnitude of the error would increase. The coarseness of the cells in the collection boxes, and the size of the mass residuals were believed to play a contributory roles to the problem with continuity. Since it was not desirable to have additional computational effort for an area of the geometry that did not affect the free surface and flow distribution results, stricter convergence criteria was imposed. The tighter mass tolerances had a twofold effect. Firstly, it would improve the mass conservation with

a more accurate solution. Secondly, the additional iterations per time step ensured a more accurate solution for the rest of the domain. Hence 2DRNG2 was run with smaller mass residuals. This followed the same solution strategy and used the same solution parameters of 2DRNG1. The only difference between the two were the mass residuals. 2DRNG2 used a value of 1×10^{-7} kg/s. A four to five-fold reduction in mass source residuals was achieved. The results of 2DRNG2 are discussed in section 7.3.4.

The surface sharpening algorithm had a minimal effect on the shape of the free surface within the chamber. One reason for this was the use of the second order accurate Van Leer scheme in the runs without the algorithm. The effects with and without this scheme is further discussed in the following section. However, when air entrainment was present, the algorithm gave erroneous and non-physical shapes to the free surface. There was little or no quantitative improvement in the prediction accuracy of the variables of interest, with and without the use of the algorithm.

7.3.3 The Van Leer MUSCL differencing scheme

Run numbers 2DRNG1 (Figures 7.3-7a..c) and 2DRNG2 (Figures 7.3-8a..c) used the Van Leer finite differencing scheme for the convective terms within the transport equation for volume fraction. For consistency between the mass balance for the individual phases, and the mass balance for the total flow, which is determined by the density in the convection coefficients (Computational Fluid Dynamics Services, 1995), the same scheme was used for density too.

The use of the Van Leer scheme resulted in a reduction of numerical diffusion. The differences in the speeds of the water and air phases were much more distinct with the use of this second order accurate scheme (i.e. the surface was less "smeared"). In 2D2, there were regions of air that did not follow the flow direction of water near the surface, which was caused by smearing or numerical diffusion. This was cured by the Van Leer scheme. While it may be possible to reduce the numerical diffusion by using a more

refined mesh near the free surface, the CPU overhead would be large. Comparing the results of 2DIndy and 2D2, one can see similarities in the air phase. If a more accurate solution was required using the default hybrid differencing scheme, much smaller cells would be required compared to the grid used in 2DIndy. Thus, a MUSCL scheme was much more cost-effective.

The quantitative comparison of the predicted results shown in Figures 7.3-6a..l, revealed that there were only small differences between the runs with (2D2) and without (2DRNG1) the Van Leer scheme. This suggested that the improvements made to the solution accuracy in 2DRNG2 only had a small effect on the calculated variables in the water phase. Besides the Van Leer scheme in 2DRNG1, there were other differences between 2DRNG2 and 2D2, such as surface sharpening and the turbulence model. Hence, a more direct comparison was necessary, to isolate the effects of the scheme on the solution. To that end, another pair of runs were chosen to illustrate the effects.

A direct comparison of the results with and without this differencing scheme was carried out in run Pipebnd3 and Pipebnd4. Table 6-3 gives a summary of the details of the calculation. The velocity vector plots of both runs are shown in Figures 7.4-10a and 7.4-11a. Quantitative comparisons are shown in Figures 7.3-9a..e.

Both Pipebnd3 and Pipebnd4 were advanced to approximately 8 s (over 2 residence times). The default differencing scheme, the hybrid differencing scheme (HDS), was used in Pipebnd3, while the Van Leer scheme was used for Pipebnd4. The air velocities in Pipebnd3 were different from Pipebnd4. The magnitudes of air velocities in Pipebnd3 were smaller than Pipebnd4. Small regions of high velocity air were seen recirculating above the free surface. The air-water interface can also be seen to be better defined in the Van Leer case, since it was much thinner. Thus, it was clear that numerical diffusion present when HDS was used, was eliminated with the more accurate Van Leer scheme.

Examining the quantitative differences between Pipebnd3 and Pipebnd4 was also useful (Figure 7.3-9). The accuracy of the solution was more critical for these runs, since any improvements in the calculations of all the variables affected the flow distribution, which was unequal. Both runs were started and ended at the same time. The magnitudes of flow asymmetry between the two outlets were different. The magnitude of the flow mal-distribution was 1.65% more in Pipebnd4 than Pipebnd3. The horizontal velocities (U) for Pipebnd4 showed a kink near the right hand side of the chamber. The magnitude of the kink increased the closer to the free surface. In contrast, Pipebnd3 showed that the U velocity curves to be much smoother. There was no abrupt increase the magnitude of U. As for the vertical velocity, V, the shapes of the curves in Figures 7.3-9a and b were very similar. There was only a small difference between the calculated magnitudes. However, approaching the free surface, the Pipebnd4 results showed deviation at the right side of the geometry. Similar to U, the changes in values of V were much more abrupt than Pipebnd3. Physically, the kinks in U and V for Pipebnd4 represented a region of flow on the right side of the chamber which moved downwards. Part of the flow was also deflected upwards when it approached the chamber wall, at a distance approximately 0.07 m away from the right wall. This sudden change in direction was due to flow accelerating over the weir. The differences in the turbulent kinetic energy were even more marked between the two sets of runs. As before, on the right side of the chamber, very large values of k were calculated compared with Pipebnd3, whose results were much smoother with small deviations. There appeared to be much less smearing or numerical diffusion in Pipebnd4. Another consequence of the different predictions of flow mal-distribution between the two runs, the free surface location was different between the two. The water levels or free surface location were different for both calculations. The surface was calculated to be lower for Pipebnd4 than Pipebnd3 (Figure 7.3-9e), although the shapes of both surfaces were very similar. Consequently, Pipebnd4 predicted less flow out of the right hand side than the left weir. The two pairs of results, Pipebnd3 with Pipebnd4, and 2D2 with 2DRNG2, showed that the flow distribution was unaffected by numerical diffusion if it was equal. However, there was a small difference when it was unequal. This was a result of the differences

in calculated velocities within the water phase. The magnitude of the differences was small due to the density of the water. In context, the differences in the air phase was much greater.

Numerical diffusion is a problem found in upwind differencing schemes. This was illustrated by Bendiksen(1992) and reproduced here. The advective terms for a variable, ϕ_j, explicitly integrated in time, is written as:

$$\frac{\phi^{n+1}_j - \phi^n_j}{\Delta t^n} = -\frac{U^n_{kj}(\phi^n_j - \phi^n_{j-1})}{\Delta x} + \textit{truncation error} \qquad (7.3.3\text{-}1)$$

Equation 7.3.3-1 can be shown by Taylor series expansion of the function ϕ in x and t to be equivalent to,

$$\frac{\partial \phi}{\partial t} = -U_k \frac{\partial \phi}{\partial x} + \frac{u_k \Delta x}{2}(1 - \xi)\frac{\partial^2 \phi}{\partial x^2} + O(\Delta x^3) \qquad (7.3.3\text{-}2)$$

where $\xi \equiv u_k \Delta t/\Delta x$

This integration scheme thus leads to an additional diffusion term, not present in the original equation. The numerical diffusion coefficient is,

$$D \equiv \frac{u_k \Delta x}{2}(1 - \xi) \qquad (7.3.3\text{-}3)$$

The differences in water velocities within the region of interest were very small, even at the interface. It was the air phase that is affected most by the improvement in accuracy of the differencing scheme since the dynamic viscosity of air was 100 times smaller than water. Any changes to the velocity field due to the use of a second order accurate Taylor series representing the partial differential equations in the governing equations, will show up most clearly in the air phase.

In 2DRNG1 and 2, there were two small regions of recirculating air. These were found in the collection boxes above the plunging curtains of water. The speeds in those regions were large, much larger than the velocity of water at the free surface. Compared with 2D2, the velocities did not appear physically realistic. However, the differencing scheme used for 2D2 (the Hybrid Differencing Scheme), had an additional viscosity term associated with it. Therefore, recirculating flow would tend to be damped out, unlike 2DRNG1 and 2DRNG2, whose Van Leer scheme did not contain that additional viscosity term. Since the velocities of air and water at the interface had to be equal, according to the VOF model, the increase in air velocities above it should not occur, as momentum would not be conserved. Therefore, these results suggested two possible causes for these large velocities. The first could be due to the size of the flow domain. The vertical extents of the domain only extended to 0.769 m. Although a shear free boundary was placed at the top of the domain, the reduced volume available for the air phase artificially increased the flow velocities. The second possibility could be due to the difference scheme. Since the density of air was a thousand times than water, any small errors present would affect the less dense air phase more than water. The following sections will describe the steps taken to identify this source of error.

Thus, in summary, the results of the two comparison, 2D2 with 2DRNG1, and Pipebnd3 with Pipebnd4, showed the importance of the second-order accurate Van Leer differencing scheme. Numerical diffusion was reduced and the accuracy of the solution was improved. Although the symmetry of the solution was not affected when the flow into the chamber was fully symmetrical, it was critical to the calculated flow distribution when asymmetry was present. Despite the improvements in accuracy with the Van Leer scheme, the areas above the free surface exhibited physically unrealistic results. However, these had a small effect on the solution of the variables in the region of interest. What is more important, the calculated variables of 2DRNG1 still showed similar magnitudes with that of 2D2, and still over-predicted the measured values of velocity and turbulence.

7.3.4 Reduced mass residuals

Mass source residuals are values of the continuity error. It is the sum of the absolute values of the nett mass fluxes into or out of every cell in the domain, and has the units of kg/s. The values of mass residuals give an indication of the absolute errors in continuity. However, the ratio of the reduction in the magnitude of the mass residuals (between the second and final iteration), would be more indicative of the error reduction. Thus, for the calculations performed here, although the residual values of 1×10^{-5} kg/s and 1×10^{-7} kg/s are quoted - these represent a three-fold and five-fold reduction in the residual values respectively.

Runs 2DRNG1 and 2, 2DRNGV1 and 2, 2DRNGC1 and 2 can be compared together to examine the effectiveness of the reduced mass residuals in improving the solution accuracy. Direct comparisons between these runs allowed the effects of mass residuals to be investigated in isolation. All the runs with suffix 1 had mass residuals of 1×10^{-5} kg/s. The ones with suffix 2 had residuals of 1×10^{-7} kg/s. Table 6-2 summarizes the differences between these calculations.

Comparison between Figures 7.3-7a and 8a (2DRNG1 and 2 respectively) showed that the peak velocities for the recirculating regions of air were decreased from 18.8 m/s to 10.1 m/s. As for 2DRNGV1 and V2 (Figures 7.3-10a and 11a), which had a larger domain volume than 2DRNG1 and 2, the peak velocities were reduced further from 6.2 m/s to 2.5 m/s when the residuals were decreased. Section 7.3.5 gives a discussion of the effects of an increased volume of the domain. Additionally, near the top of the domain, there were two larger recirculation regions. In 2DRNGV1, the velocities there were more than 1m/s, while in 2DRNGV2, those velocities were reduced to reasonable values (less than 0.4 m/s). Clearly, the reduced mass residuals had an effect on the calculated air velocities developed above the free surface.

The weir crest levels for the 2DRNG and 2DRNGV series of runs were set too high compared with the actual test rig. This was corrected in 2DRNGC1 and 2 (Figures 7.3-12 and 13). The geometry used for these runs had the increased volume domain of 2DRNGV runs. Again, the reduction in residuals for those results also helped to reduce the peak velocities from 7.2 m/s to 5.7 m/s.

Figures 7.3-6 and 7.3-14 show the quantitative comparisons of the velocities, turbulence and volume fractions against the measured data for runs with the higher weir crest levels, and runs with the corrected weir crest levels respectively. The reduction in mass residuals had a small effect on the calculated variables, which were measured in the water phase. There were small differences between the results which were attributable to the reduced mass tolerances, but may be considered insignificant. This was due to values of the momentum errors which were reduced by a small amount for the water phase. With the density of water greater than air, most of the improvements would be readily apparent in air rather than water.

More importantly, despite the use of different turbulence models, smaller mass residuals, the correction to the weir levels (2DRNGC1 and C2) etc., the calculated results were still greater than the measured values. The increased accuracies of the solutions had not reduced the magnitude of the over-predictions by the different runs.

Thus, the use of tighter mass tolerances gave more accurate solutions for the air phase. The errors present in the calculations, due partly to momentum errors and numerical diffusion, were reduced with smaller mass residuals. The calculated variables in the water phase were also changed. However, those changes were small. Also, despite the overall improvement in the solution, the calculated variables were still over-predicted.

While the use of reduced mass residuals had a clear benefit in terms of reducing the errors found in the air phase, above the interface, the quantities in the water phase were only affected by a small amount. The calculated variables (in the water phase) were still

over-predicted. The errors in the air phase were due to two possible sources of error. The first was momentum errors being present. With air a thousand times less dense than water, it would be affected by the momentum errors more than water. Another possibility was that of dimensional errors, i.e. the actual system was three-dimensional, but was represented by a 2D geometry. This latter possibility could also account for the large over-predictions of the calculated variables too.

7.3.5 Increased volume in the flow domain

The air phase in the runs described previously exhibited numerical errors. The recirculating regions of air had large velocities which were physically incorrect. While the reduction of mass residuals had helped to reduce these errors, the effects of an increase in the volume of the domain on the errors were also examined.

There were several recirculating regions above the free surface. Those regions were close to the top of the domain and appeared to be constrained by it. Consequently, the lid was raised from 0.769 m to 1 m in height in runs 2DRNGV1, 2DRNGV2, 2DRNGC1 and 2DRNGC2. This increased the volume of the chamber by 30 %. Figures 7.3-10, 11, 12 and 13 show the results for the above four runs.

The peak velocities in the two small recirculating regions above the plunging curtains of water, were reduced from 8 m/s (2DRNG1) to 5 m/s (2DRNGV1). For the cases where mass residuals were reduced (from 1 x 10^{-5} kg/s to 1 x 10^{-7} kg/s), the velocities were reduced from 7 m/s (2DRNG2) to 2 m/s (2DRNGV1). For the geometry with the corrected weir crest levels, the peak velocities were 6 m/s (2DRNGC1) and 5 m/s (2DRNGC2).

The results showed that the increase in volume available for the air phase did help to reduce the errors present. Nevertheless, the magnitudes of the reduced air velocities were still too large to be realistic. The tops of the domains were symmetry planes.

There were no shear forces present which would cause air recirculation. This was representative the physical model since that was open to atmosphere. However, the side walls of the collection boxes were wall boundaries, where shear was present. Because of the constraint in the movement of air by the walls, recirculating regions of air was set up. The volume of the region above the free surface determined the magnitude of the air velocities. If the volume was too small, this may result in air-water interactions, which can have a detrimental effect on the calculated variables in the water phase. Therefore, an increase in the domain volume was made.

From the investigations carried out, it was safe to eliminate turbulence models and surface sharpening, as possible causes of the excessively large air velocities. The reduction in mass residuals and the increase in volume available for the air phase helped to reduce the magnitudes marginally. Use of the Van Leer differencing scheme actually increased the air speeds, but this was due to the reduction in numerical diffusion. This in turn removed that additional viscosity term, which resulted in the increase in air velocities. The main cause or causes of these errors was speculated to be due to two other factors. The first was the volume available in the domain. While 2DRNGV1, 2 and 2DRNGC1 and 2 had their volumes increased by 30%, nevertheless, the geometry was still some 2.7 times less than the physical model. Thus, in the next section, the dimensional effects would be examined. The second possible cause of the errors was due to momentum errors. The runs where the mass residuals were decreased by two orders of magnitude showed improved solutions. The use of smaller residuals resulted in more accurate solutions throughout the domain, including the air phase. Thus, the momentum errors present in the less dense air phase were reduced.

Quantitative comparisons of the results with experimental data, in Figures 7.3-6 and 7.3-14, showed that the calculated variables were largely unaffected by the changes in geometry and mass residual reduction. This indicated that the flow field in the water phase was insensitive to the changes investigated here and previously. This meant that at any incorrect air-water interactions, was negligible. Therefore the underlying cause

or causes for the large over-predictions in the measured variables may be due to dimensional effects. A three-dimensional geometry would need to be created to properly model the flow field developed within the chamber.

7.3.6 Dimensional Effects

3D models of the distribution chamber were created, and incorporated the increased height of the domain as in 2DRNGC1 and 2DRNGC2. The solution strategy used in the calculations were the same as that developed for the 2D models. Three test flowrates were considered, the runs were labelled as 3DRNG1, 3DRNG2 and 3DRNG3, whose flowrates were 2.95 l/s, 4.38 l/s, and 5.51 l/s respectively. The results of these runs are shown in Figures 7.3-15, 7.3-16 and 7.3-17. Quantitative comparisons between the 3D results and the experimental data are also shown in Figures 7.3-18, 7.3-19 and 7.3-20.

The calculated flow fields for the three test flowrates showed that the main flow features developed within the chamber were similar to those seen in the 2D results and the experiments. The central jet entraining the surrounding fluid was seen. Two recirculating regions were formed on either side of the jet. A boil was also present at the free surface. However, the gradients of the air-water interface either side of the boil were less steep than the 2D results. Comparison of the free surface shapes with the photographs (Figures 7.1-4, 7.1-5, 7.1-6) showed that qualitatively, there was good agreement. Even at the maximum flow of 5.51 l/s, the 3DRNG3 results showed a much more prominent, rounded boil coinciding with the centreline of the chamber. It was pleasing to see that the recirculating regions of air with very high velocities, seen in the 2D calculations, now had velocities that were almost stagnant. As the solution strategy was the same as in the 2D calculations, the conclusion was that the errors in air velocities were due to the dimensional effects. In the 3D runs, the inlet velocities were the same as the 2D runs. However, the volume of the domain had increased. Thus, we see that the air velocities were much more realistic.

Figures 7.3-18a..n are the quantitative comparisons for the low flowrate case of 2.95 l/s. In the experiments, a select number of repetitions were made for the various measurement points. Therefore, there were some figures where there were more than one experimental point displayed.

In the plots comparing the measured and calculated U velocities, it was seen that the calculated U velocities were much closer in value than the previous 2D results. The calculated values close to the centre of the chamber (where x = 0.154 m, 0.231 m, and 0.308 m) were close to the measured velocities. The largest deviation was approximately 25% at the measurement planes of y = 0.628 m and z = 0.1637 m. At the two extremities, at y = 0.077 m and 0.385 m, the deviation of the U velocities were much larger than the other measurement points. Moving closer to the walls of the chamber, one can see the effects of the boundary layer which resulted in two small peaks in the U velocity graphs (Figures 7.3-18a and 18c). In contrast, for the other plots of U velocities at higher y values, the differences between the measured and calculated results at the extremities of the chamber were much smaller. These deviations at the two extreme measuring points were due to the boundary layers. As discussed previously in section 7.3.1, the boundary layers in the calculations could be better treated with a more refined grid near the walls. However, as can be seen in the comparisons at higher y measurement planes, the closer to the free surface, the better the predictions for U. This was because at the higher measurement levels (above 0.628 m), the levels were above the weir crests, which had no wall effects present. Despite the effects of the boundary layer at the lower measurement points, the predicted values of U, even near the walls, were very good. Therefore the results reinforced the conclusion that the boundary layers close to the walls of the chamber only had a small effect on the 3D models. It only had a very small and localised effect on the accuracy of the predictions. Those graphs also showed an increase in magnitude of the velocities at the chamber extremities. These were the result of the flow accelerating over the weir as it left the chamber.

The graphs showing the V velocities revealed that the 3D CFD model still over-predicted the peak velocity occurring in the centre of the chamber, at measurement planes, y = 0.628 m, 0.633 m , 0.6358 m. At 0.653 m however, the calculated results began to under-predict the measured values. In the other measurement points away from the centre of the jet, the agreement was better. The trends suggested that as the measuring points approached the free surface, the predictions of the centreline jet velocity became better. However, there was insufficient experimental data at or near the interface to show this behaviour, nor to draw any firm conclusions regarding the accuracy of the numerical model near the free surface.

The turbulent energy plots showed different trends from those calculated in the 2D results. The new trend was in better agreement with the measured results than before. A small peak in k was calculated at the centre of the jet. However, the results were still up to ten times larger than measured.

At the next two flowrates of 4.38 l/s and 5.51 l/s, similar trends were seen in the calculated results as in 2.95 l/s. The U velocities were well predicted. The only exceptions to this were seen in Figures 7.3-19a, b, c and 7.3-20a, b, and c. This was the result of the boundary layer affecting the values of the calculated velocities at the chamber extremities. However, at levels above the weirs (0.631 m), the boundary layers were no longer present. Therefore, the accuracy of the calculated results became better.

The V velocities showed good agreement in the regions away from the centre of the jet. However, the velocities at the centre were still over-predicted as in the lower flowrate case. Similarly with the values of k, the calculated trends for all the flowrates were similar to the measured values. However, the values of k were still over-predicted by a large margin. These trends were the same as in 3DRNG1.

One possible cause for the discrepancies between the calculated and measured results of k was the lack of a correct model for surface effects in the turbulence model. Since the presence of the surface will have a dissipative effect on the turbulence, therefore, the values of k would be reduced at the free surface. The turbulent eddies being transported up towards the surface would become distorted, as in situations near walls. However the turbulence model did not contain any wall effect terms. The presence of the free surface was not accounted for. Consequently, we do not see the reduction of k at the measurement points.

It should be commented that the velocity gradients at the centreline of a symmetrical jet were zero. Consequently, the production of turbulence at the centreline was zero. Vigorous eddy mixing will transport turbulent fluid from nearby regions of high turbulence production towards and across the centreline. In the physical model, the W component of velocity was very small, but non-zero. Thus, there would be an additional third component compared to the total energy measured. In the 2D calculations, the third component was unaccounted for, which explained the dip in the k graphs. However, in the 3D calculations, this was present, which resulted in the different trends for k. The shape of the 3D calculated k graphs showed a small peak at the centreline of the chamber, in some cases, it was nonexistent, i.e. the curve was flat in the central region. It would appear that the transport of turbulence from the surrounding regions to the centre of the jet was insufficiently accounted for to reproduce the shape of the curve.

The results for the predicted water levels (Figures 7.3-18, 19 and 20) showed that the predicted values were in very close agreement with that of the measured values. Using the volume fraction value of 0.5 as the interface location was natural. This was also defined in the CFX-F3D (Computational Fluid Dynamics Services, 1995) user's manual. However, there was a discrete thickness for the calculated interface, unlike that of an actual interface. Physically, there would be a step change in volume fractions when going across the water phase to the air phase in a distribution chamber. However, in the

CFD calculations, the discrete interfacial thickness was due to some numerical "smearing" of the surface. This was expected to be worsened without the surface sharpening algorithm. However, it was compensated by the Van Leer differencing scheme. Nevertheless, the three calculated results showed that the differences between the calculated and measured values were in the order of only 1 to 2%, which can be considered very good.

The flow distribution was calculated to be equal, which agreed with the experimental results.

In the experiments periodic fluctuations in the free surface location were observed for all three tests. However, from the time history plots (of which 3DRNG2 is shown in Figures 7.3-21a..f), the calculated velocities were relatively constant over time (Certainly for the latter part of the calculations. The initial time steps displayed "blips" in the velocities, which were caused by numerical perturbations). The results indicated that the jet was symmetrical and did not vary with time. The values of the calculated variables taken at the end of the transient calculations may be considered equal to the time averaged experimental values. This may be explained by the fact that a simplifying assumption was made of the experimental test rig. Although the main features of the distribution chamber were reproduced in the geometry, the tee-junction below the actual test chamber, was not included. This structure could be the main cause of the periodic behaviour seen in the experiments. Its influence was relatively small since the averaged values of velocities and water levels were in very good agreement with the CFD values. It will be shown in section 7.4.3, the proximity of the pipe bend below the chamber, will deflect the jet away from the centreline of the chamber. Thus, if the influence of the tee-junction was any larger, we would not see such good agreement between the CFD and experimental data. There would also be a significant asymmetric flow set up within the chamber.

Thus, the 3D models were much more accurate than the 2D models. The U velocities were well predicted, although the regions close to the walls were affected to a small extent by the boundary layers. This problem may be solved by using a finer grid near the walls, or the use of the low Reynolds number k-ε model. The V velocities were well predicted in the regions away from the centreline of the jet. The values at the centreline itself were still over-predicted, but not to the same extent as the 2D models. The values of k were also over-predicted throughout the width of the chamber. However, the calculated trend for k was much closer to the measured results than before. The main reasons for the inaccurate predictions of the values of the turbulence and the centreline jet velocities were probably due to the lack of a wall effect term in the turbulence model, which did not dissipate k sufficiently. The cause of the over-predictions for the 2D velocities was due to the dimensional effects of the 2D models. Although the total volume of the domain was reduced, the inlet velocities were the same as in the experiments. Therefore, this resulted in large over-predictions of velocities and water levels everywhere. The flow distribution and water levels were well predicted in the 3D models. This gave the approach and solution parameters used in the calculations a large degree of confidence.

7.3.7 Time Histories

To ensure the quality of the transient 2D and 3D solutions, an additional criterion by which the solution can be considered to be converged or sufficiently developed, was set for the calculations. This criterion was the monitored time histories of the calculated variables, U, V and k.

Since the solutions for flows in distribution chambers of the type investigated, were time-dependent, it was necessary to advance the solution to greater than one theoretical domain residence time. The residence time is defined as the volume of the domain divided by the volumetric flowrate. For the 2D model base case (4.38 l/s), the residence time was 3.68 s. For the 3D geometry, the residence times were 26.58s, 17.90s, and

14.23s for 2.95 l/s, 4.38 l/s, and 5.51 l/s respectively. All solutions were in excess of these times. Allowing the solution to be advanced beyond one to two residence times was sufficient to ensure any transient effects due to flow start up would have disappeared.

The number of residence times allowed the determination of the minimum number of time steps required to overcome the initial flow startup effects. However, the maximum number of number of time steps, or the total time required for each solution had to be determined from the examination of the time history plots. This was an accurate method to ensure the quality of the solution. Three variables, U, V and k were monitored over time, at several critical point in the geometry.

Six points were chosen in the calculations. These were close to the free surface, in the region of interest. Two of the points were on the axis of symmetry for the domain, i.e in the geometric centreline of the inlet jet. The x and y coordinates were (0.231m, 0.633 m) and (0.231m, 0.643m). (For the 2D calculations, the z coordinate for all points coincided with the centre of the single cell in the z axis, 0.0277m. For the 3D calculations, the z coordinate was coincident with the centre of the z axis, 0.1345 m). Both these points were below the free surface. The other four monitoring points were also in the water phase. All were at the extremities of the chamber, two above the left outlet, and two above the right outlet. The x and y coordinates for these were (0, 0.633), (0, 0.653), (0.462, 0.633), and (0.462, 0.653). Examples of these are shown in Figures 7.3-21a..f. These are the results for 3DRNG2 which were for a symmetrical solution. The graphs showed that the solutions reached a quasi-steady state over time.

Some solutions were periodic in nature, especially for a number of the Pipebnd series of calculations. There was a clear cycle in the flow behaviour, such as that shown in Figure 7.4-7a..f. These were the time history plots of Pipebnd1. Many other solutions were subject to a relatively large perturbation at the start of the solution. This was physical in origin due to the transient nature of the flow conditions when the flow first

entered a chamber full of stagnant water. Minor perturbations were also seen in the graphs. Their occurrence coincided with the restart of a calculation using the previous results (dump files). These perturbations were numerical in origin, and were observed to occur although no changes were made to the command or Fortran files. It was also necessary to use a smaller time step at a restart, than the final value arrived at in the previous dump file.

The graphs of Figure 7.4-7 (Pipebnd1) showed a cyclical nature to the variations in velocities. In this particular run, the velocities at the inlet were not uniform, and the flow within the chamber was asymmetric. For V velocity, there was a cycle time of approximately 10 s. There were also mini-cycles of just under 1 s within the main cycle. The U velocity also exhibited very similar behaviour. However, the magnitudes of the velocity fluctuation for U was much less than that of V. If the path of each water particle was traced from the inlet to the weirs, then the distance travelled was approximately 0.631 m in the vertical direction and 0.231 m (distance from the centreline to the weir) in the horizontal, for a total of 0.862 m. The averaged velocity of each particle was 0.87 m/s. Thus, this gives a residence time of 0.99s. It is believed that movement of the water from the inlet to the outlet weirs caused this mini-cycle. The larger cycle of 10s is believed to be caused by the movement of the unsteady jet oscillating about its mean position.

7.3.8 Summary of numerical model validation

Fully symmetrical, two-dimensional and three-dimensional CFD models were set up. Transient calculations were performed for each of the models, and the simulation times for each were at least equivalent to three residence times.

In the 2D models, the same velocities as in the experiments, were specified. This ensured that the vertical momentum, which was important in the reproduction of the free surface behaviour and correct flow distribution, was maintained. Consequently, it was

found that large over-predictions of the measured variables occurred as a result. On the other hand, in the 3D models, where the volume of the domain and the inlet flow velocities were the same as the experiments, the agreement between the measured and calculated velocities were very good. However, the prediction for turbulent kinetic energy was still over-predicted, even though the trend shown by k was similar to the experimental trends. The reason for this was believed to be due to the lack of any wall terms in the RNG k-ε model. This turbulence model did not account for the dissipative effects of a free surface.

A grid independence test was conducted for the 2D model. This showed that the size of the cells used in the basic 2D models were sufficiently small to resolve the flow. In the 3D models, the cell sizes were made to be the same order of magnitude as the 2D models.

The surface sharpening algorithm present in the VOF model helped to reduce diffusion at the free surface within the distribution chamber. However, non-physical results were obtained in regions where air entrainment occurred, such as in the two collection boxes. Consequently, this algorithm was not used. Instead, a second-order accurate, Van Leer finite differencing scheme was used to reduce errors due to numerical diffusion at the free surface.

Initially, the k-ε turbulence model was used in the 2D models. However, due to the known limitations of this model, the RNG k-ε model was used instead. Direct comparisons between the standard k-ε and RNG k-ε models showed that both gave very similar results. Nevertheless, the RNG model was used for all the other models since it was thought that the production of turbulent kinetic energy would be better predicted.

7.4 Asymmetric flow calculations

In this section, the effects of a pipe bend found below the chamber were investigated. The presence of a bend below the chamber was the postulated to be the most likely cause of flow asymmetry and mal-distribution in a chamber. Thus, the techniques derived from the validation phase of this investigation, were adapted to prove this hypothesis. The novel results showing mal-distribution and flow asymmetry helped to allow a better understanding of the flow processes within the chamber. In that way, ways and means to reduce or eliminate flow mal-distribution can be investigated to improve chamber performance.

This investigation used three different approaches to model the presence of the pipe bend. The first, assumed uniform flow conditions into the domain, albeit at an angle to the horizontal axis. These runs are numbered as Bend2, Bend5, Bend10, Bend12 and Bend15. Table 6-3 gave details of these runs. The second approach decoupled both bend and chamber. The calculated results from a simple 2D bend were used as inlet boundary conditions for the chamber. The third approach coupled both bend and chamber. The numbering system for these runs are also given in Table 6-3.

7.4.1 Approach 1: Angled inflow into chamber

In these tests, the flow into the domain was angled at five different angles, 2°, 5°, 10°, 12.5° and 15°. The flow angles were created by the specification of both U and V velocity vectors in the inlet patch to give the desired values. The resulting flow was inclined towards the right outlet of the flow domain. The values of the k and ε at the inlet were also varied linearly. The purpose of these tests were to simulate the asymmetric effects expected of the flow passing through a pipe bend close to the chamber inlet. Predicting the flow behaviour from a pipe bend beforehand was not possible without simulating the pipe bend. Thus, the physical accuracy of the assumptions made here regarding the inlet boundary conditions were incorrect.

Nevertheless, this simplified approach allowed a quick and easy way of determining how flow asymmetry affected flow distribution. Approach 2 or 3 would be used to accurately simulate the presence of the pipe bend.

Figures 7.4-1..5 show are results for Bend2, Bend5, Bend10 and Bend15 respectively. The velocity vectors and volume fractions within the geometry are shown. Bend2, Bend5 and Bend10 showed that the resultant jet within the chamber was directed towards the right hand side of the chamber. As expected, the angle of the jet increased in accordance with the increase in inflow angle. At angles of 12.5° and 15°, the upper part of the jet was drawn towards the right chamber wall. A Coanda effect was observed to occur. The recirculating regions on either side of the jet produced low pressure regions. A low pressure region was formed on the right side of the jet. This was due to the higher velocities there. It was because of the unequal pressure forces acting on the jet that deflected it towards the right side of the chamber wall.

The degree of maldistribution was quantified by a percentage of asymmetry, a. This is defined as,

$$a = \frac{|Q_l - Q_r|}{\sum Q} \times 100\,\%$$

where Q is the flowrate

and the subscripts l and r refer to left and right hand side outlets respectively.

Figure 7.4-13 is a graph of the calculated values of a for the five tests. From 2° to 10°, a increased linearly with inflow angle. Beyond 10°, the magnitude of asymmetry decreased significantly, down to just over 2%. The value of a remained relatively constant for both 12.5° and 15°. The reason for this was the occurrence of the Coanda effect for Bend12 and Bend15. With the deflection of the upper part of the jet, the flow

direction of the jet near the surface was almost vertical. Thus, the distribution of flow between the two outlets was better than the previous cases.

While the occurrence of the Coanda effect within the chamber had a dramatic effect on the flow distribution, this was believed to be an extreme phenomenon due to the dimensional effects of the 2D model. It had not been observed before in experiments carried out.

The simple assumptions made in these runs, i.e. a uniform distribution of velocities across the inlet may not be realistic. One would not expect the flow entering the chamber to be fully developed due to the proximity of the bend to the chamber.

The runs conducted here were relatively easy to setup and run. The dump files from the 2D symmetric cases could be used (the file containing the results from 2DRNGC2 was used), which saved a lot of CPU time. However, the drawback with this method was the physical realism of the boundary conditions, and therefore the realism of the results. In order to verify the validity of this approach, a pipe bend had to be included in the calculations. The following approaches discuss the runs incorporating the pipe bend.

7.4.2 Approach 2: Decoupled pipe bend

In these runs, a separate 2D pipe bend was created in addition to the 2D geometry as used in the 2DRNGC2 run. The inlet and outlet sizes of the bend were matched to that of the chamber inlet. The runs conducted were Pipebnd1 and Pipebnd2. Their details are summarised in Table 6-3.

A steady state single phase flow calculation was carried out for the initial run with the decoupled 2D pipe bend. At the inlet, averaged velocity and correlated turbulence levels were specified. At the outlet, a pressure patch was used, with the pressure set to the inlet pressures calculated in 2DRNGC2.

The approach used in these series of runs was to use the values of velocities and turbulence determined from the decoupled pipe bend as the inlet boundary conditions for the chamber. In this way, the transient calculations necessary to start the flow from time zero if the pipe was joined to the chamber, could be avoided. (The calculations had to be started from an initial guess since coupling the bend to the chamber would result in a new geometry with a different number of grid cells. Therefore the results from the steady state run could not be used).

Figures 7.4-6a and b show the results from Pipebnd1. Figure 7.4-7a..f are the time history plots of the six monitoring points. The time history plots showed that the velocities and turbulence exhibited a periodic behaviour. At the centreline of the chamber, the vertical jet velocity was seen to fluctuate about the centreline at a frequency of 1 cycle for every 10 seconds. This was in keeping with the experimental observations, where it was noticed that the surface boil varied in position. There were also secondary fluctuations within the main (larger) cycle. These had a time period of about 1 second. The cause of this was explained previously in Section 7.3.7. As for the behaviour of the velocities above the two outlet weirs, there were also rapid oscillations with frequencies of around 1 to 1.5 seconds. Thus, these results indicated a very distinct time-dependent flow behaviour. One can see this in the plots of the flow field (Figures 7.4-6a). Snapshots of the resulting flow fields were taken at half second intervals. The jet remained largely undeviated compared to the previous angled inflow runs. It was only near the free surface that the jet had the largest deviations. The plots of the pressure fields showed the pressure gradients across the jet, which resulted in the periodic changes in the jet direction.

The spatial variation in the jet direction also resulted in the variations in the surface boil location. Because of these variations, the flow distribution was found to change over time. It was calculated that the percentages of the flow out of the left outlet were, 43.90%, 42.35% and 44.02% at times 17.52 s, 18.02 s, and 18.52 s respectively. For the right outlet the percentages were, 56.10%, 57.65% and 55.98% at the same time

intervals. These results illustrated that the flow within the chamber was time-dependent. It was also possible that the inlet boundary conditions for the chamber may also vary with time.

Since the inlet boundary conditions for the chamber were obtained from a symmetrical calculation, it was necessary to check that the solution obtained was correct. An iterative procedure was adopted here. The calculated pressures at the chamber inlet, taken from Pipebnd1, were averaged with that of the original pressures of 2DRNGC2. These new values were then re-substituted into the 2D pipe bend to be re-calculated again. The new velocities and turbulence from the second decoupled pipe bend iteration, were then entered as the new chamber inlet boundary conditions for Pipebnd2.

Figures 7.4-8a..c show the results of Pipebnd2. In these runs, the change in boundary conditions caused the jet to be deflected more than Pipebnd1. Also, the cyclic nature of the solution of Pipebnd1 was no longer present. Snapshots of the flow field after a difference of 3.5 seconds revealed very different solutions. As in the angled inflow calculations, the Coanda effect was present. The jet was increasingly drawn towards the right chamber wall, until the upper half of the jet was attracted to it. As seen in Bend12 and Bend15, the chamber wall ensured that the jet was deflected vertically upwards. This resulted in very different flow distribution results from Pipebnd1. The pressure plots also supported this conclusion. The distribution of flow at the final solution was 70.59% for the right outlet and 29.41% for the left outlet. The value of a was 41.18%, which was very extreme.

A comparison of the calculated pressure values at the chamber inlet showed that Pipebnd1 was significantly different from Pipebnd2. It would appear that the jet developed within the chamber interacted with the surrounding flow field. As a result, the values of the calculated variables at the inlet also changed over time. Since it was impossible to determine the rate at which these interactions occurred, this approach was not sufficiently accurate to justify its use. This approach assumed that the boundary

conditions at the inlet would remain constant over time, which was not. Thus, from these results, it was concluded that the simple 2D pipe bend had to be coupled with the chamber, in order to simulate the development of the flow field correctly.

7.4.3 Approach 3: Coupled pipe bend

Since the results from the previous approaches were unsuccessful in simulating the effects of a pipe bend, coupling the pipe bend with the chamber was necessary.

In most treatment works, the flow from one treatment stage to the next would be piped via distribution chambers. The lengths of pipe involved would be sufficiently long enough to ensure fully developed flow by the time the flow approached the distribution chamber. Therefore, the inlet boundary conditions for the new geometry reflected this. A horizontal pipe section was present upstream of the 90°bend, and then there was a vertical pipe section connected to the chamber. The inlet patch for the geometry was located at the inlet into the horizontal pipe section. A uniform velocity, and turbulence distribution was input. The boundary conditions at the outlets (pressure patches) were unchanged from the symmetrical runs.

In the first set of runs (Pipebnd3 and Pipebnd4), the distance of the centreline of the bend to the chamber invert, was the equivalent of 2.12 hydraulic diameters (D_h) or 0.146 m. In Pipebnd5, this distance was reduced to 1.25 D_h, or 0.086 m. Based on the information collected from Herbath and Wong (1997b), chamber designs varied from plant to plant. It was also clear was that the bend distances were usually kept to a minimum as far as possible. There were however, limits to how short the distances could be. The distances were dictated by the diameter of the pipe itself, and the radius of the pipe bend. The chosen pipe diameters were sized to handle the total flow through the system and minimise total head losses as a result of it. (Note that the pipes, pipe bends and other pipe fittings are usually made to standard sizes. Therefore the choices would be limited to the nearest sizes available for the designed optimum sizes).

Nevertheless, the choice of bend distances of 2.12 D_h and 1.25 D_h were reasonable. These may also be considered as the extremes for pipe bend lengths. As an example, one sewage treatment plant in North Wales, Treborth STW (Herbath and Wong, 1997b), had a pipe diameter of 1 m, leading into the final settlement tanks distribution chamber. The bend to chamber distance was 1.8 m, which was equivalent to 1.8 D_h. The straight section of vertical pipe above the radiused bend was 1.09 m.

In many designs, a diffuser section above the pipe inlet was usually present. The purpose of this was to reduce the likelihood of flow separation as the flow entered the chamber. It allowed the gradual reduction in velocities as the flow entered the chamber. Anecdotal evidence from treatment plant operators (Herbath and Wong, 1997b), indicated that flow mal-distribution still occurred for designs incorporating these transitions or diffuser sections.

A diffuser section was not included in the CFD analysis. The advantages accrued from excluding this section outweighed the disadvantages. The simplification of the geometry allowed the use of simplified cell shapes and structure in the region where the pipe joined the chamber. The cells would retain their ideal rectangular or square shapes, which in turn, would allow easier convergence and more accurate solutions. If a diffuser was included, the cells would have to be distorted into trapeziums. To overcome the anticipated problems with the less than ideal cell shapes, a larger number of cells would have to be used. Besides the larger amount of memory required, a greater amount of CPU time would be required. Also the main purpose of these calculations was not to simulate any particular chamber design, but rather conduct a parametric design study of the effects of different bend to chamber distances on the flow distribution and the flow field.

As mentioned in section 7.3.3, Pipebnd3 and Pipebnd4 were essentially the same calculations, the only difference being the differencing scheme used. The Van Leer scheme was used in Pipebnd4. Since it was shown and discussed that the Van Leer

scheme gave more accurate solutions, the discussions in this section shall concentrate on Pipebnd4. Figures 7.4-10a..c show the results for Pipebnd3. Figure 7.4-11a..c are the results of Pipebnd4.

For both results, the portion of the jet found on the extreme right of the vertical pipe section had a vertical component of velocity more than 1 m/s. On the left had side of the jet, the magnitudes of the velocity got progressively less, until there was a region of backflow. The pressure plot showed that a small region of low pressure was formed as a result of the backflow. On the other hand, the bottom right of the chamber showed a much higher pressure. With this pressure imbalance across the jet, the jet started to be drawn to the left side due to the net pressure force acting from the right. We see that the high pressure region on the right half extended to about halfway up the chamber. This further encouraged the jet to be increasingly deviated to the left.

The direction of the jet near the water surface was the opposite of what was expected intuitively. If the positive x direction is taken to be the flow direction in the horizontal pipe section, then the resulting boil would be located in the positive x direction away from the centreline of the inlet. As the flow emerged from the pipe, it would still contain a proportion of horizontal momentum. Consequently, one would expect the jet direction to be angled away from the horizontal direction of flow in the pipe.

Pipebnd5 had the distance between the bend centreline and the chamber invert reduced to 1.25 D_h. Figures 7.4-12a..c show the calculated results. The velocity vector plot showed that the resulting jet had a much larger positive U component of velocity, as it emerged into the chamber. This was due to the short vertical distance available to influence the deflected flow fully. Consequently, the jet had already started to deviate to the right of the chamber. There was an area of very low pressure in the bottom right corner of the chamber. This caused the jet to be increasingly drawn towards the right wall. This was another example of the Coanda effect occurring. Further up, the jet direction was vertical because of the interaction with the wall. The surface boil was

formed very close to the right hand side weir. As in the angled inflow calculations, the presence of the Coanda effect helped to improve the flow distribution. The interaction with the wall caused the flow to be directed vertically upwards, with a zero U velocity component. By the time the flow had reached the free surface, there was no bias in the flow direction of the deflected horizontal shear layer. In the case of Pipebnd5, the distribution was 38.59% and 61.41% for the left and right outlets respectively, and a = 22.82%. In contrast, the distribution for Pipebnd4 was 72.24% and 27.76% for the left and right outlets respectively, with a = 44.48%, which was double that of Pipebnd5.

The results demonstrated the sensitivity of the jet direction to the length of the pipe bends since the distances were the only difference in both calculations. One factor which was present in these calculations was the effect of dimensionality on the results. Since the ratio of the inlet velocity to the volume of the domain was greater than the equivalent 3D model, the occurrence of this Coanda effect may not appear if a 3D calculation was performed. It may occur at higher inlet volumetric flows.

7.4.4 Summary of Pipe Bend Calculations

The 2D calculations carried out in this phase of research showed that a pipe bend had to be coupled to the distribution chamber in order to obtain an accurate representation of the flow. The flow was strongly time dependent, and there was interaction between the flow conditions within the chamber and the conditions at the inlet into the chamber. Thus, it was this interaction which precluded the use of the second approach tested here (decoupled pipe bend).

The results from these simulations were not intuitively apparent. The jet in the upper part of the chamber was influenced readily by the flow conditions around it. At one extreme, with the pipe bend, 2.12 D_h away from the chamber, the jet was deflected back on itself as a result of the pressure differences across it. On the other hand, with the bend distance reduced to 1.25 D_h, a Coanda effect was present. This resulted in the jet

being increasingly drawn towards the chamber wall, which caused the upper half of the jet to flow vertically upwards.

Both results showed the sensitivity of flow distribution to the flow patterns developed within the chamber. It was made clear here that the jet had a very large influence on the flow distribution. By understanding the forces acting on the jet, one can design different ways of reducing the degree of asymmetry in the chamber.

7.5 Solutions to flow mal-distribution

With the quantification of the most common cause of flow mal-distribution in a chamber, this section discusses the various methods used to lessen the impact of the pipe bend on the chamber performance. Simple structures were added to the chamber and their effectiveness were tested by the novel application of CFD techniques.

Two different structures were used. The first used a vertical flow splitter placed above the inlet into the chamber. The second used a horizontal plate located at a distance from the inlet.

7.5.1 Vertical flow splitter

Bendsplt1 was the simulation used to determine the effectiveness of a vertical flow splitter placed above the chamber inlet, coincident with the centreline of the chamber. Table 6-4 summarises the details of the run. Figures 7.5-1a..c show the results. Figures 7.5-2a..c are the time history plots of velocities and turbulent kinetic energy monitored at the six measurement points. These plots showed that the results fluctuated over time, and the calculations were allowed to proceed to 11 seconds (equivalent to 3 residence times). The flow distribution for this case was 37.13% and 62.87% for the left and right outlets respectively, and asymmetry $a = 25.74\%$, which was an improvement over the values of 72.24% and 27.76 % ($a = 44.48\%$) obtained from

Pipebnd4. However, a was still too large to be acceptable. The maximum allowable value of a would depend on the specifications laid down by the operator, but would usually be around $\pm 10\%$.

Figure 7.5-1a showed that the jet was affected by the presence of the splitter. It can be seen that the right half of the vertical pipe contained flow with large magnitudes of velocity, unlike the left half. The presence of the splitter kept the two halves of the jet separate for a distance equivalent to one hydraulic diameter. Thus, the pressure forces acting on the jet, seen in Pipebnd4, were no longer present. Instead the right half of the jet was now drawn increasingly to the left due to the low pressure region caused by the recirculating zone on the right half of the chamber. The lower velocities on the left half of the jet resulted in a relatively large pressure field on the left. Consequently, the net pressure force acted leftwards, pushing the jet to the left.

The purpose of the plate was to provide a vertical surface so as to change the horizontal component of velocity (U) in the emerging jet, to the vertical. In a sense, its function was similar to that of the walls of a pipe or channel, where they constrained the flow so that the resultant flow direction was largely in the streamwise direction. If the plate was made high enough, up to the invert level of the collection boxes, then the jet may become almost symmetrical. The lengthened plate could prevent the pressure differential from deflecting the jet. In practice, this would not be very practicable due to the magnitude of the splitter dimensions involved. At model scale, the invert level for the collection boxes was 0.393 m. Scaled up to full-scale, it was more than 5 m. Clearly, if it was made out of concrete, the wall would have to be made thick enough to support both the total weight of the wall, and also to prevent any flexing. On the other hand, if the wall was to be made out of some composite materials, such as glass-fibre, or possibly stainless steel, then the weight and thickness may be reduced to manageable values. However, the stiffnesses of the alternative materials would have to calculated to ensure the wall was sufficiently stiff to prevent flexing. The problems involved with wall flexing was firstly, that of unpredictable performance of the chamber. If under

certain extreme conditions, the pressure differential developed across the wall may be very large. The wall may begin to flex or bend, causing unpredictable chamber performance since the flow direction of the jet would be dependent on the behaviour of the wall. The second problem with wall movement would be the danger of fatigue. If flow induced vibrations or "flutter" were produced and the natural frequency of the structure was reached, then resonance would occur and the splitter can eventually fail over time.

The other problem associated with a vertical splitter was the exact location for it. Without any knowledge of the subsequent flow behaviour of the splitter, it was natural to place it coincident with the centreline of the chamber. However, during construction, there would most certainly be an amount of inaccuracy in locating the wall, especially with a finite wall thickness.

While the practical problems with the installation of a flow splitter would not be insurmountable, it would be the difficulty in the design of the splitter that precluded it from being recommended as the most promising flow control device. Firstly, with an increase or decrease in flowrates, and hence jet velocities, the resulting pressure field would be different. The performance of the chamber would only be optimized for one set of flow conditions. A compromise in chamber performance must be accepted. Secondly, to increase the effectiveness of the design, the height of the splitter may have to be increased, which may prove impractical. Thus, a more effective solution had to be found.

7.5.2 Horizontal Plate

A horizontal plate was added to the chamber, replacing the flow splitter. Three cases were investigated, Plate1, Plate2 and Plate3. Plate1 and Plate2 had the horizontal plate located 2 hydraulic diameters (or 0.138 m) above the inlet. Plate1 had the larger bend to chamber distance of 2.12 D_h. The geometry for Plate2 and Plate3 had the shorter

bend to chamber distance of 1.25 D_h. In Plate3, the plate was placed closer to the inlet, at a distance of 1.5 D_h. Figures 7.5-3, 4 and 5 show the results of Plate1, Plate2 and Plate3 respectively. Table 6-4 gives a summary of these calculations. Figure 7.5-6 show the time histories of the velocities and turbulent kinetic energy for Plate3.

There was a bifurcation to the flow as seen in the flow field of Plate1 (Figure 7.5-3a). The jet impinged upon the plate at an angle close to the perpendicular. It was deflected, forming two recirculating regions, below the level of the plate. The rest of the flow was deflected upwards, so that there were two thin regions of upflow, close to the walls. These two regions were not identical since more flow was flowing into the right half of the chamber. This was a consequence of the pipe bend, as was seen previously in Bndsplt1. In the centre of the chamber, two regions of recirculation were formed with very low flow velocities. The direction of flow was downwards at the centre of the chamber. The volume fraction plot showed that the water levels were lower in the centre, but higher where the two regions of upflow were. The plot also suggested that air was drawn down into the chamber due to the recirculating flows. The pressure plots revealed a region of low pressure at the bottom right corner of the chamber. This low pressure region was caused by the high recirculating velocities. Unlike the previous runs such as Bendsplt1, the formation of a pressure difference across the width of the chamber here did not adversely affect the flow distribution. The jet had been "broken up" by the plate. Thus, the net pressure force acting on the upflow region was in the downwards direction. The horizontal plate also helped to reduce the peak velocities in the jet. Prior to encountering the plate, the peak V velocity was 1.4 m/s. After being deflected (which caused a region of high pressure under the plate), the maximum velocity was reduced to around 1 m/s. The reduction in velocities led a reduction in the Reynolds numbers and thus, the magnitude of the nonlinear terms in the Navier-Stokes equations. This helped to ensure a more symmetric solution to the problem.

Thus, by both deflecting the jet and reducing the peak velocities, the plate had helped to reduce the flow asymmetry. For Plate1, the distribution was 49.80% and 50.20% for the left and right outlets respectively, with $a = 0.4\%$

The results of Plate2 are shown in Figures 7.5-4a..c. This calculation had the same flow conditions as Plate1 except for the length of the pipe bend. The plot of the flow field showed different patterns to Plate1. The jet emerging from the inlet had a much larger U component of velocity than before. As a result, the jet struck the plate at an angle, instead of being perpendicular as in Plate1. A portion of the jet also missed the plate altogether. The pressure plot showed a much smaller region of high pressure below the horizontal plate. The high pressure region was offset to the right, since the flow was directed to the right. Large magnitudes of velocity were seen on the right of the chamber. Consequently, there was more flow going to the right half of the chamber. The water levels were seen to be higher there too. The flow distribution for Plate2 was 40.37% and 59.63% for the left and right outlets respectively, and $a = 19.26\%$. This was a small improvement over Pipebnd5 (where $a = 22.82\%$). Nevertheless, the value of asymmetry was too large to be considered acceptable. Thus, the location of the plate could be optimized to give better flow distribution.

In Plate3, the horizontal plate was lowered by half a hydraulic diameter, to 1.5 D_h above the inlet. Figures 7.5-5a..c show the results of this calculation.

The flow field showed that a larger portion of the jet had been "caught" by the plate. As before, bifurcation of the flow occurred. This resulted in two regions of upflow at the extremities of the chamber. Recirculating regions were also seen in the two bottom corners of the chamber, either side of the plate. There was a prominent and large region of recirculation to the left and above the plate. The magnitudes of velocities were relatively large, which caused a large region of low pressure. This large recirculation was different from the patterns seen in Plate1 and Plate2. In the previous runs, the flow patterns were more symmetrical. It was possible that this feature was a result of the

initial flow startup, i.e. it was a transient effect, and the flow within the chamber was not fully developed. The time history plots of Figure 7.5-6a and b showed that the velocities coincident with the centreline of the chamber, were still reducing in magnitude. Hence it was possible that the solution had not been advanced in time sufficiently.

The plots of k and ε showed that the calculated values were larger in comparison to Plate2. The contour patterns were very similar, with the regions of high turbulent energy and dissipation occurring at the bend and the plate. An interesting development for this particular calculation was the additional difficulty with the convergence of the solution. It was found that if the usual solution strategy was adopted for this run (i.e. the mass residual were allowed to reduce to 1×10^{-7} kg/s), the residual values of ε had not reduced sufficiently for convergence (generally, it had only reduced by one order of magnitude). Consequently, the strategy was modified by making the reduction of the ε residuals as the criterion by the calculation could advance forward in time. The ε residual had to be reduced by three orders of magnitude in order to be considered to be converged. Generally, when this reduction was achieved, the mass residuals were found to have reduced by up to eight or nine orders of magnitude. This resulted in a significant increase in CPU time required due to the more accurate solution required. Additionally, the maximum time step for this run was no more than 0.005 s, in contrast to 0.08 s for Plate2. The cause for this increased difficulty was believed to be caused by the new plate location. The presence of the plate increased the magnitudes of turbulence in the flow. Correspondingly, the magnitudes of the net difference in the transport of dissipation into and out of each cell also increased. By summing these net differences for all the cells in the geometry, a very large value of ε residual will result. The reduction in the residuals, i.e. the increase in the accuracy of the solution, was more difficult.

The difficulties in convergance were believed to be due to the geometry of that model. The proximity of the plate to the inlet resulted in very large dissipation of energy around it. The velocity gradients were also correspondingly very large.

The calculated flow distribution between the two outlets were 46.35% for outlet 1 and 53.65% for outlet 2. This gave an asymmetry of 7.31%. This was a large improvement over Plate2. Although the solution was suspected to be still developing, examining Figures 7.5-6c to f showed that the values of velocities directly above the weirs were relatively constant, at the end of the calculations. Thus, it may be speculated that the values of flow distribution and asymmetry, will be largely unchanged if the solution was allowed to advance further in time. However, this particular case would have to be advanced further in time in any future work. This would confirm the findings here.

7.5.3 Summary of results for mal-distribution reduction tests

The two obvious ways of reducing flow mal-distribution was tested. They were the addition of a vertical flow splitter, and a horizontal plate, both above the inlet into the chamber.

The vertical splitter worked by dividing the jet in the streamwise direction. By removing the pressure forces acting on the jet, the likelihood of the jet being deflected could be reduced. However, in order for it to be fully effective, the height of the splitter had to be increased from the existing tested value. Its effective height would be dependent on the flow conditions within the chamber. There would be engineering considerations, such as cost, weight, materials and structural integrity, which would preclude its recommendation for use.

A more promising structure would be that of the horizontal plate. It deflects the jet emerging from the inlet and reduces its vertical momentum. However, its effective

location was found to be sensitive to the flow conditions too. In some cases, it may be too far above the inlet (Pipebnd2) to be effective. This meant that it had to be lowered.

By "fine-tuning" the plate locations, acceptable values of flow distribution may be achieved. However, there would still be other engineering considerations associated with these plates. These are discussed in the next section.

7.6 Engineering Considerations

Within the time limits of this study, two simple devices to reduce or eliminate flow mal-distribution have been tested. The vertical plate, although logical, does not appear to be as effective as a horizontal plate. In a three dimensional distribution chamber, with more than two outlets, one would expect the effectiveness of a splitter to be further reduced. The jet formed, would spread in three dimensions, while the flow splitter being a flat plate, would be effective in only two dimensions. It was expected that the effectiveness of such a splitter would also be affected by different flow conditions such as inlet flowrates. While the plate can be optimized for one set of conditions, any reduction or increase in flowrates can be expected to affect the flow distribution. As seen in Bndsplt1, either experimental tests or CFD calculations would need to be carried out to determine the dimensions and orientation of the plate. It is anticipated that there would be no standard sized splitter that would work for all eventualities.

Another possible variant of the single plate splitter is to use a cruciform arrangement. This would affect the flow in three dimensions. However, the cruciform splitter would have to be orientated with the direction of deflection of the jet to optimize its performance fully.

The head losses associated with a flow splitter, or any other devices would have to be taken into account when implementing them onto an existing chamber. In some treatment plants, there may sufficient head of water to drive the flow through the various

structures, pipes and treatment tanks within the plant. Consequently, the additional losses imposed by the splitter or any other devices would not be critical. However, if the pressure losses are large, or if the excess pumping head is marginal, then clearly, careful consideration would have to be given to the design.

A flat plate was tested, and was more effective than the splitter. However, the losses associated with this plate were much greater. Figures 7.6-1a..f compare the calculated pressure gradients due to the splitter and plate (the gradients were obtained by the difference in pressures at the inlet and at half hydraulic diameter intervals above it, and dividing by the hydraulic diameter). The pressure gradients were determined at six levels, starting at half a hydraulic diameter form the chamber invert, to 3 hydraulic diameters away, at half diameter intervals. Negative values of gradients indicated a drop in pressures away from the inlet. In Figure 7.6-1a and b, the vertical splitter showed relatively similar results to Pipebnd4. The effects of the splitter were localised to the region above the inlet, unlike the plate. The plate caused negative gradients throughout the width of the chamber. In Figure 7.6-1c and d, 1.5 and 2 D_h from the inlet, there was a large increase in pressure gradients for Plate1. This was caused by the impingement of the jet onto the plate, causing locally high regions of pressure. In contrast, the results for Bndsplt1 showed that the values of the pressure gradients had begun to recover, and showed small deviations from the results of Pipebnd4. In Figure 7.6-1d, the negative gradients on the extremities of Plate1 indicated recirculating regions, which had low pressures. By the time the flow reached 2.5 D_h from the inlet, Plate1 showed that the central region of the chamber had negative pressure gradients, which was caused by the two recirculating regions formed there. The large differences seen, had begun to diminish by the 3 D_h level in Plate1. The region on the right showed larger pressure gradients than the left. This was due to the slight bias in the flow towards the right side of the chamber, i.e. there was more flow on the right than the left. The results for Bndsplt1, at this level, showed that its effect became minimal.

Figures 7.6-2a to f compare the pressure gradients of Pipebnd5, Plate2 and Plate3 at the same levels as before. Plate2 and Plate3 results showed similarities. The only difference between the two was the occurrence of the increased pressure gradients due to the jet impinging onto the plate. Obviously, these increased pressures occurred earlier for Plate3 than Plate2 due to the lowered plate position. However, the magnitudes of the pressure gradients between the two runs were very similar. Thus, the location of the plate did not cause any increases in the magnitudes of the pressure gradients within the chamber. Instead, it would be the design, layout and dimensions of the additional hydraulic devices which would affect the pressure losses within the chamber.

The results from Plate2 and Plate3 showed that the location of the plate, if it was to be adopted, had to be optimized for the particular chamber design. Even so, its effects may only be localised. In an ideal chamber design, eliminating the central jet completely would minimize the chances of flow mal-distribution considerably. To achieve both requirements for the minimization of the velocities and disappearance of a jet, the simplest structure would be a full width perforated plate placed above the inlet. Its purpose would be to break up the jet as it passes through the plate. In this way, a situation where the flow velocities would be as uniformly distributed as possible, would result. One may speculate that the resulting flow field may appear to be very similar to that of Figure 7.2-3, i.e. the 2D 2-phase, steady state calculation, where the jet had disappeared.

The drawback with a perforated plate would be an even larger pressure drop across it. The magnitude of the losses would be dependant on the open area of the perforations, and the shape of the edges (i.e. whether the perforations are rounded or square edged).

In conclusions, there are other engineering considerations which must be taken into account besides the effectiveness of a particular design. The pressure losses associated with the additional structures may have an cost implication, if pumping head is not

sufficient on a treatment plant. Alternatively, compromises must be accepted to the effectiveness of the structures if other engineering considerations have to be met, such as the cost of implementing the structures.

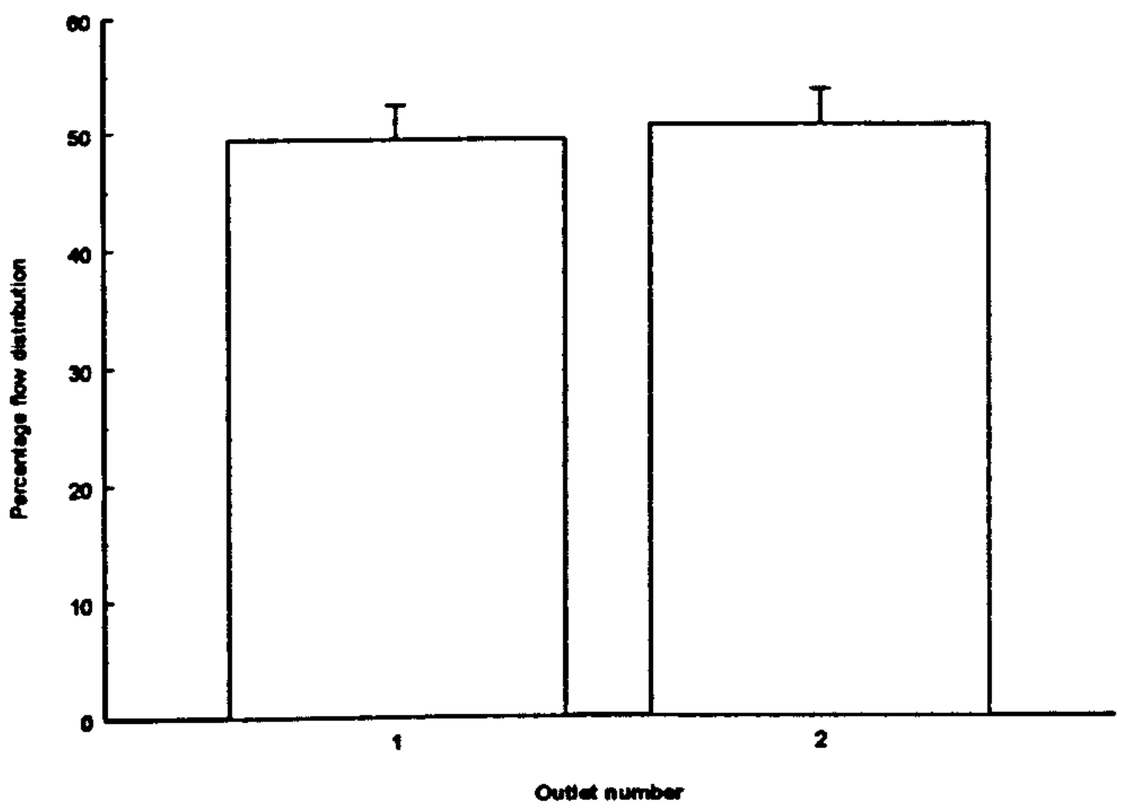


Figure 7.1-1 Measured flow distribution between outlets 1 and 2 (left and right outlets of Model A) at 2.95 l/s

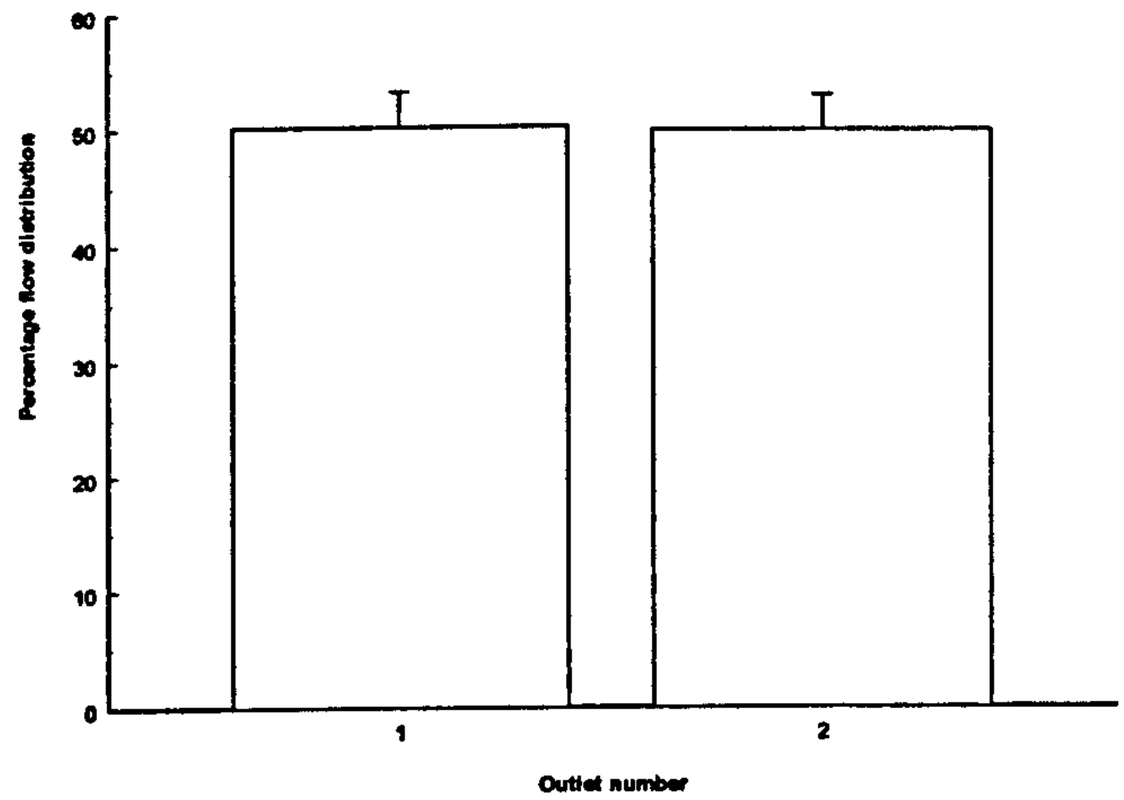


Figure 7.1-2 Measured flow distribution between outlets 1 and 2 at 4.38 l/s

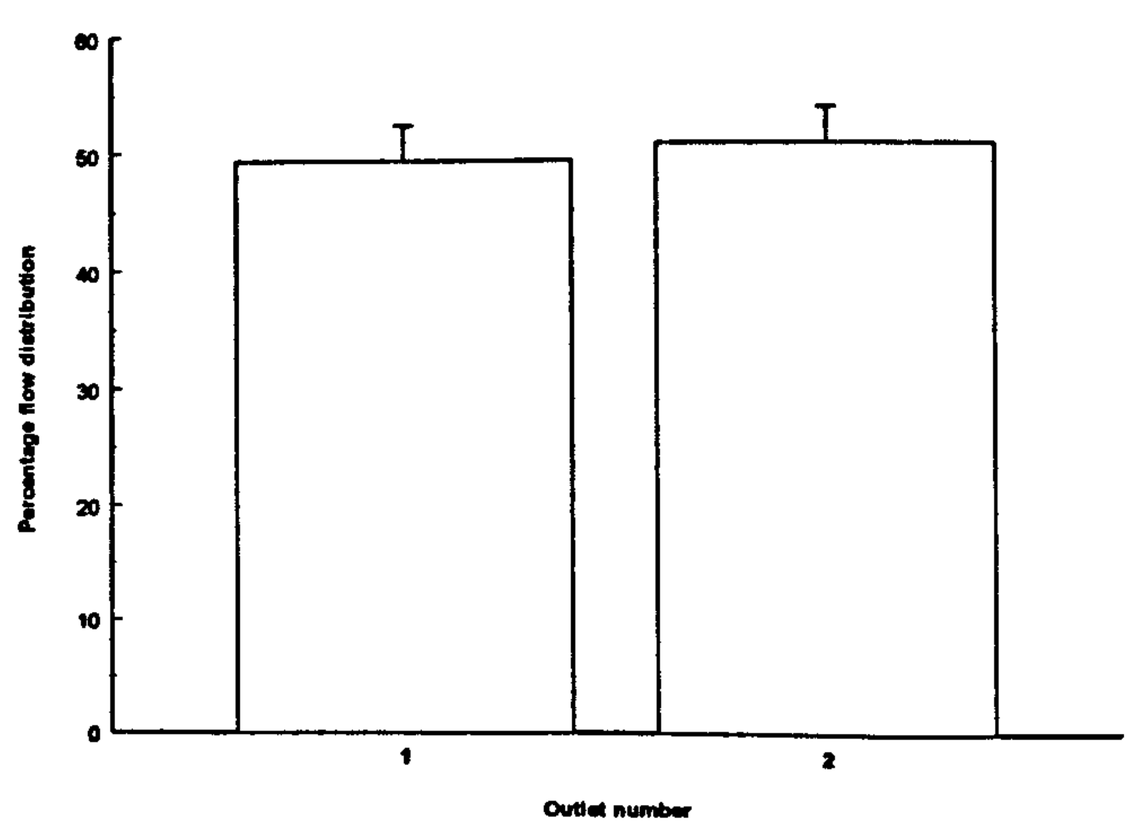


Figure 7.1-3 Measured flow distribution between outlets 1 and 2 at 5.51 l/s

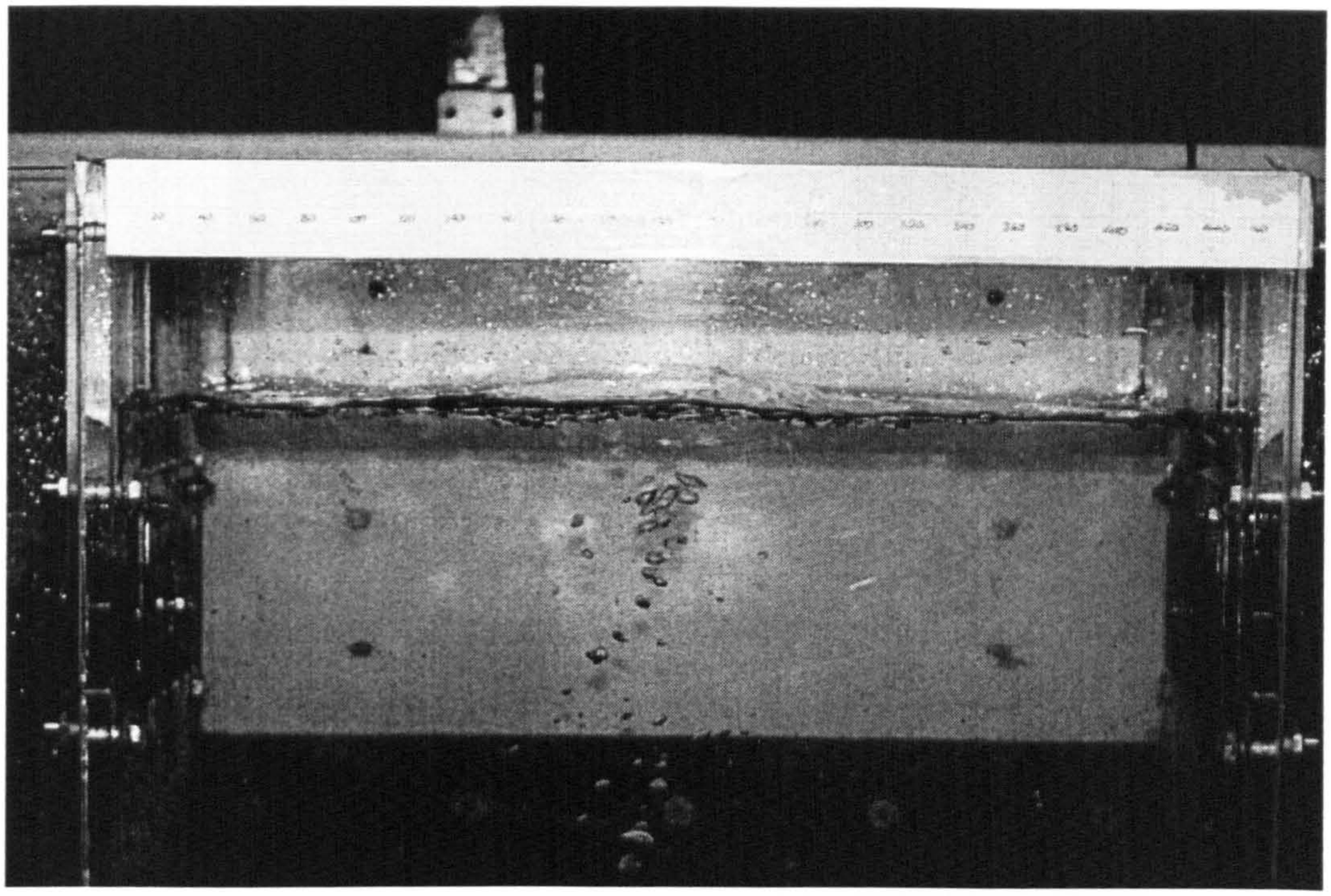


Figure 7.1-4 View of free surface at 2.95 l/s

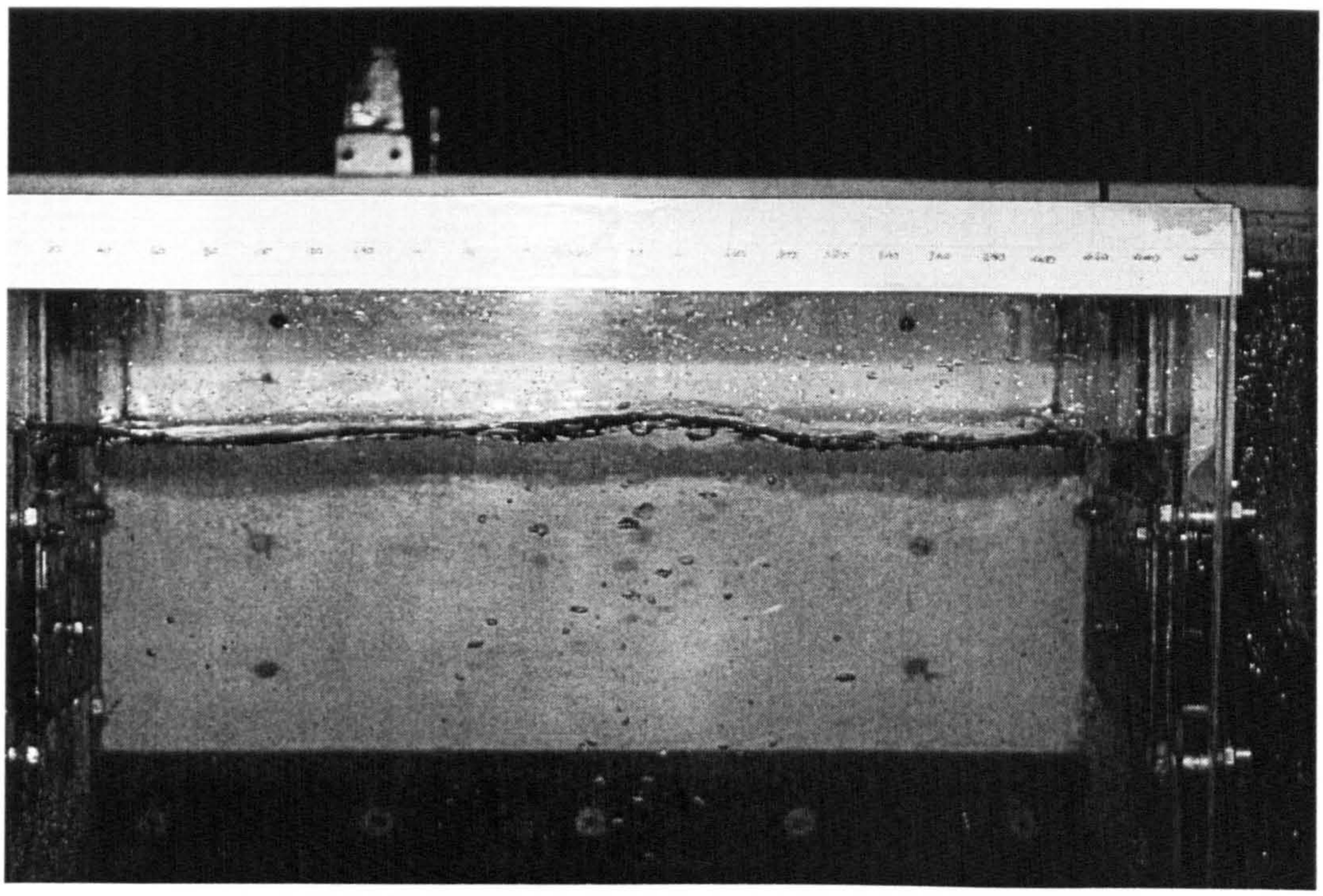


Figure 7.1-5 Photograph of boil on free surface at 4.38 l/s

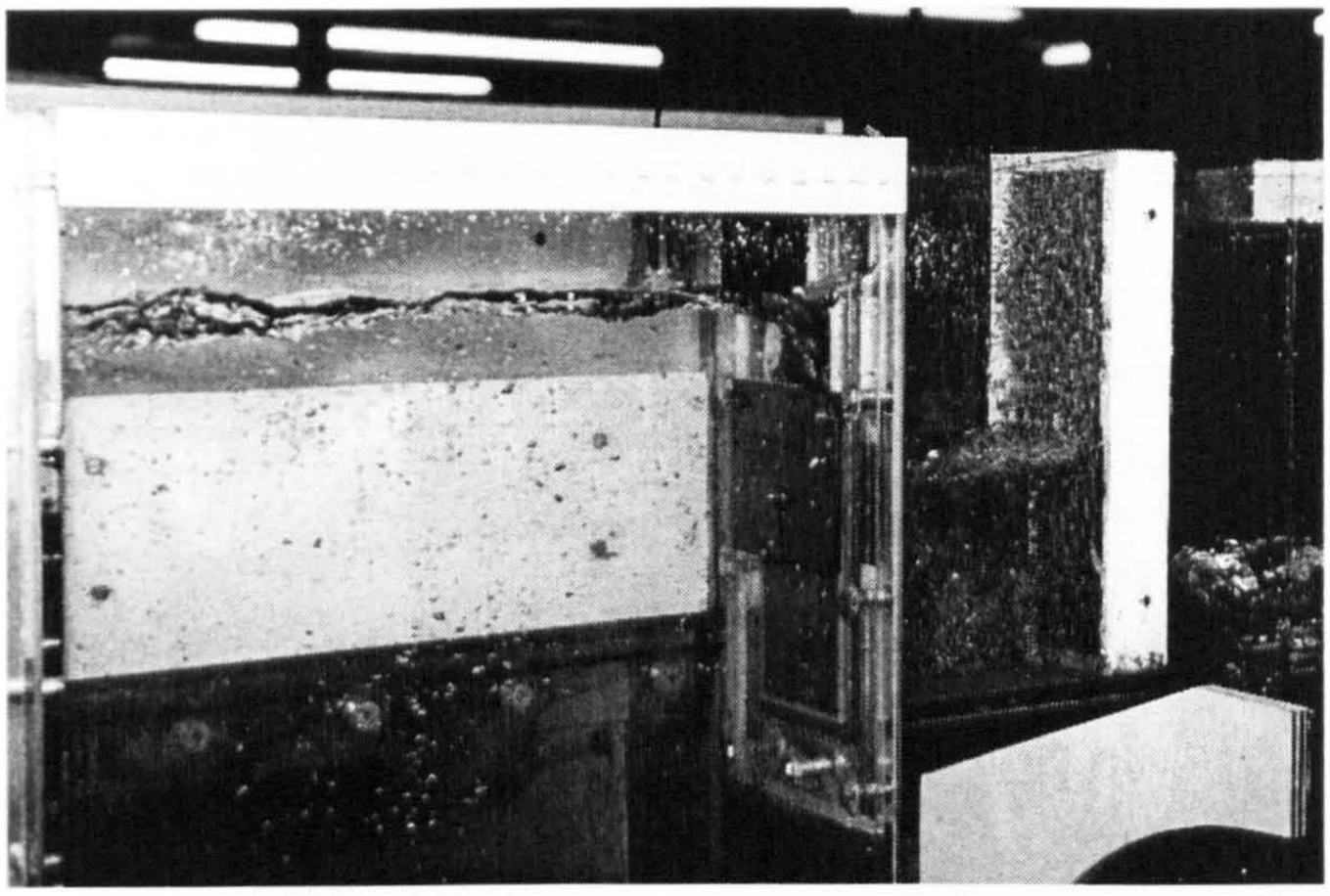


Figure 7.1-6a View of disturbance or boil developing at free surface at 5.51 l/s

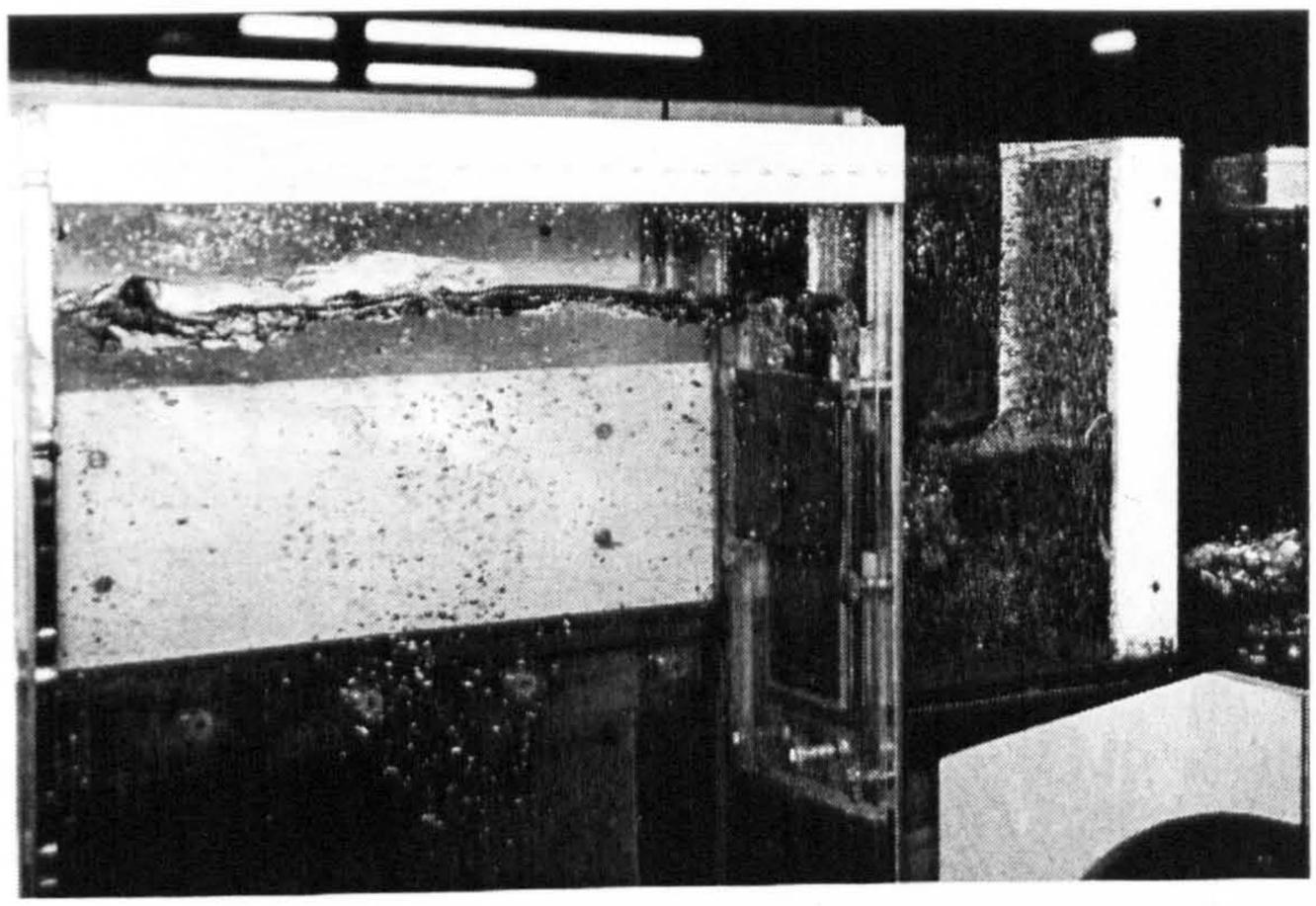


Figure 7.1-6b Magnitude of boil increasing

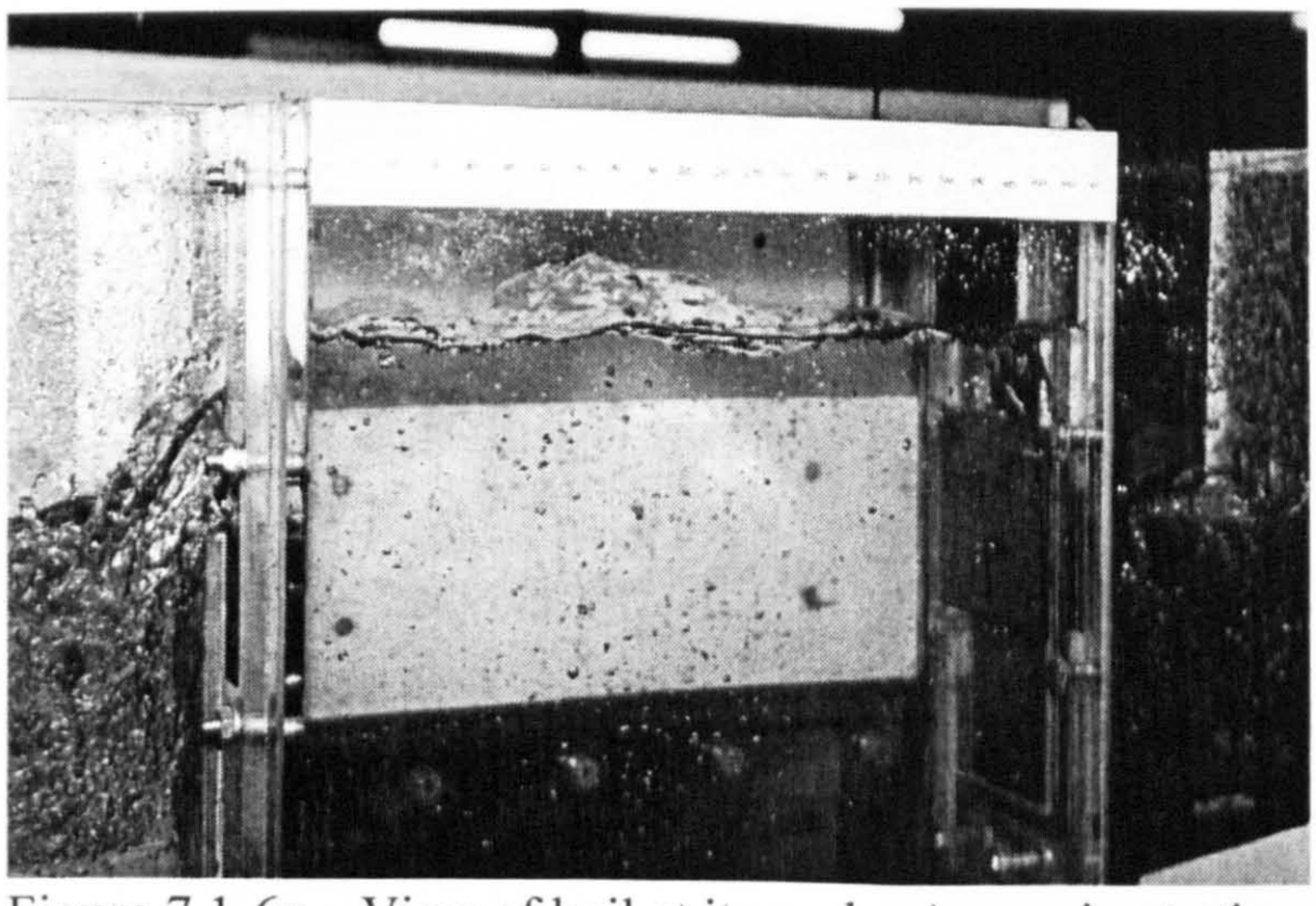


Figure 7.1-6c View of boil at its peak. Approximate time between first sequence (7.1.4-3a) to this sequence is 3 to 4 seconds.

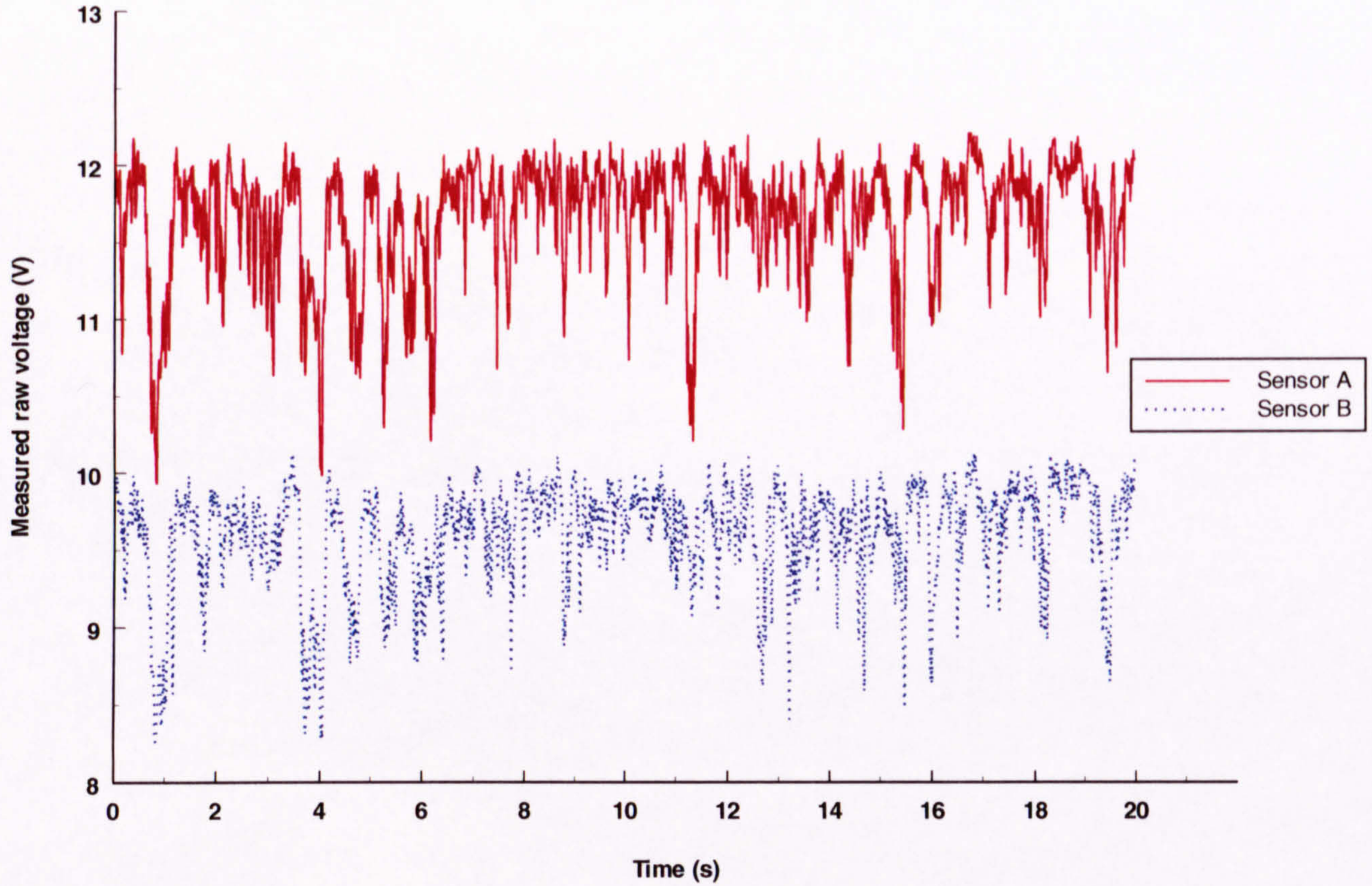


Figure 7.1-7 Raw voltage traces of hot film sensors A and B, measured at the centreline of the jet, 0.631 m from chamber invert. Flowrate = 5.51 l/s.

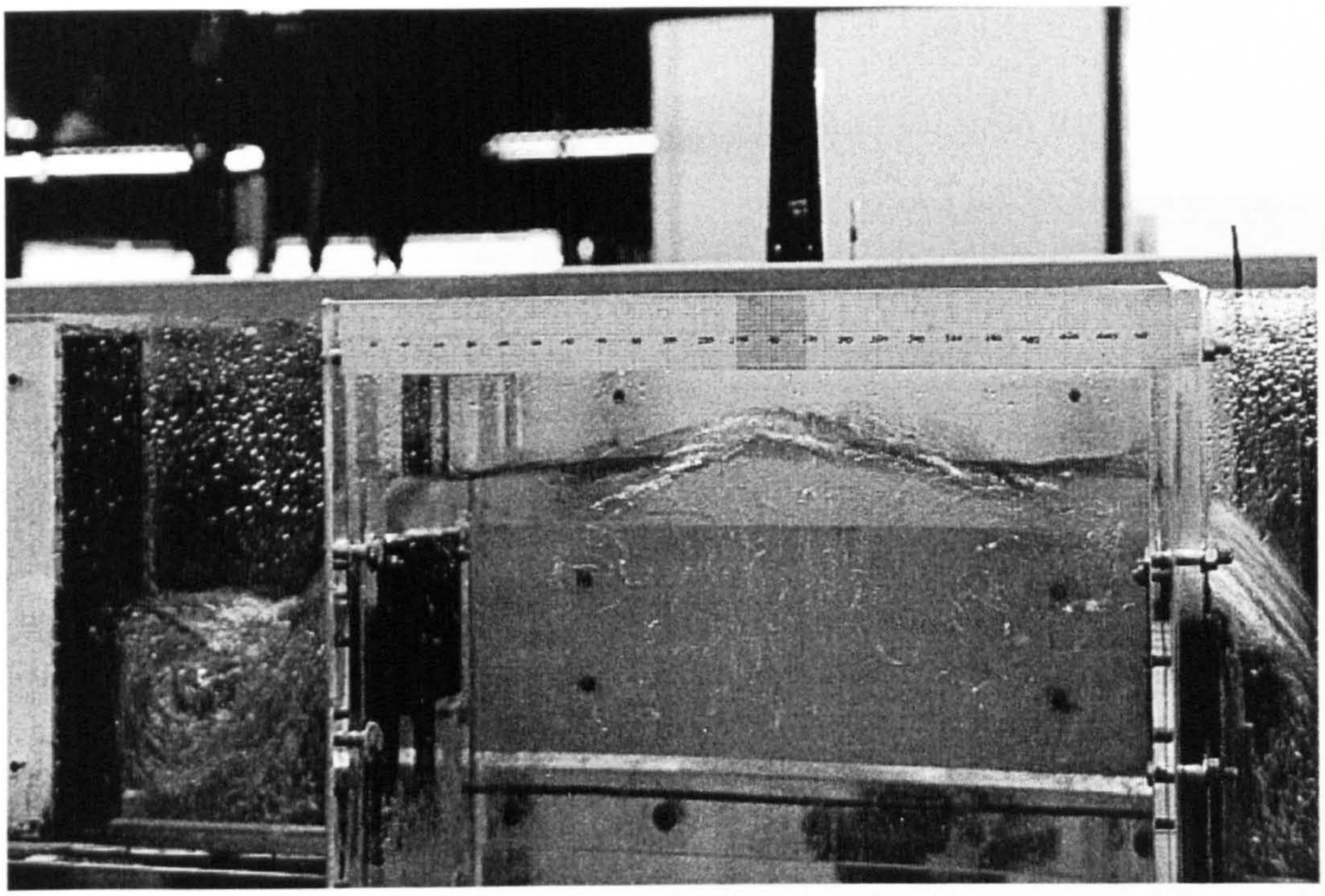


Figure 7.1-8a Photograph showing streaklines describing the recirculation within the chamber and the collection box at 5.51 l/s

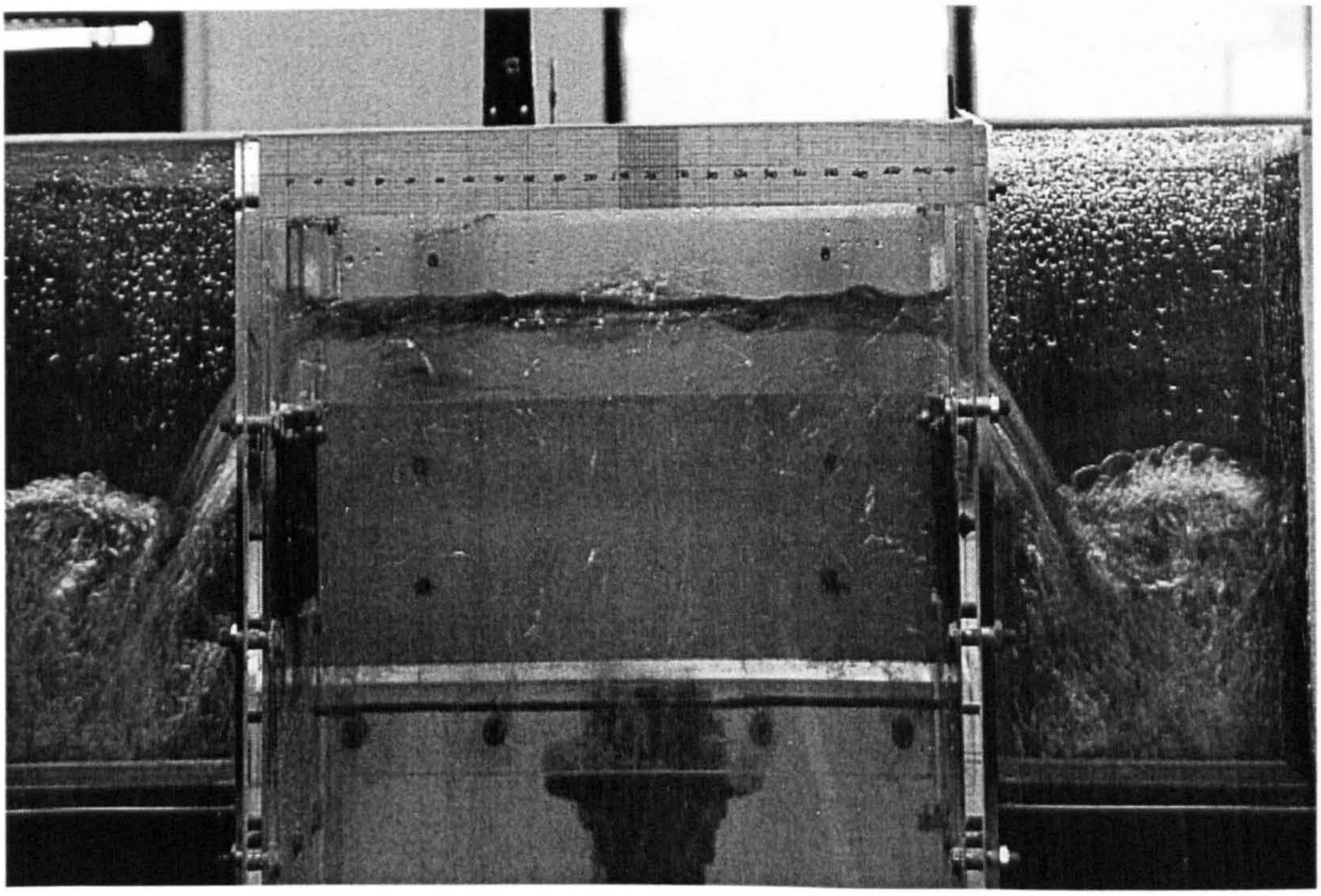


Figure 7.1-8b Another view of the recirculating flows within chamber and the two collection boxes at 5.51 l/s. Plunging curtains of water on either side of discharge weirs, and the resulting recirculation within the collection chambers are clearly seen.

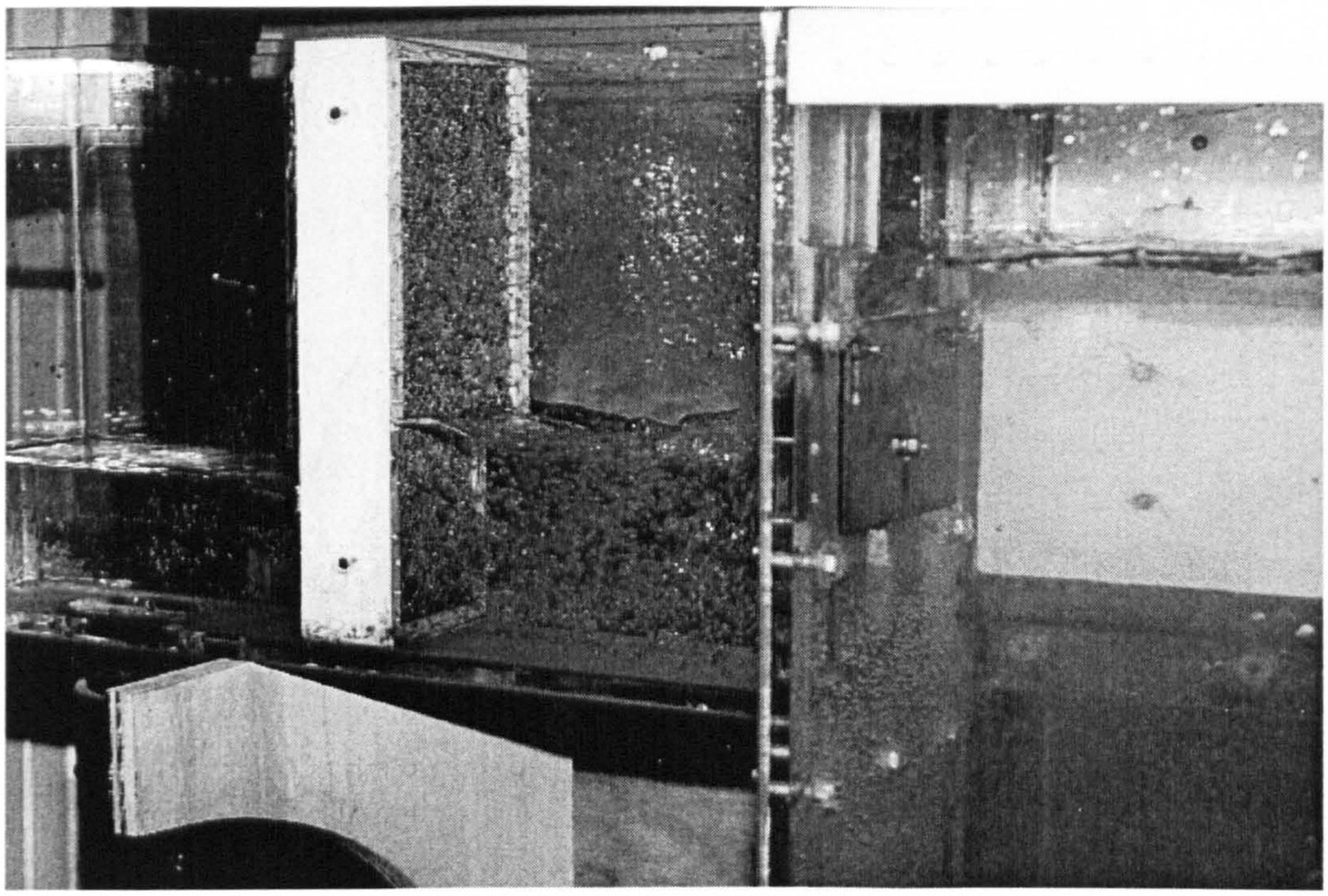


Figure 7.1-9 View of air bubbles formed within collection box due to entrainment of air by plunging curtain of water at 2.95 l/s. Note head loss across hairlok screen

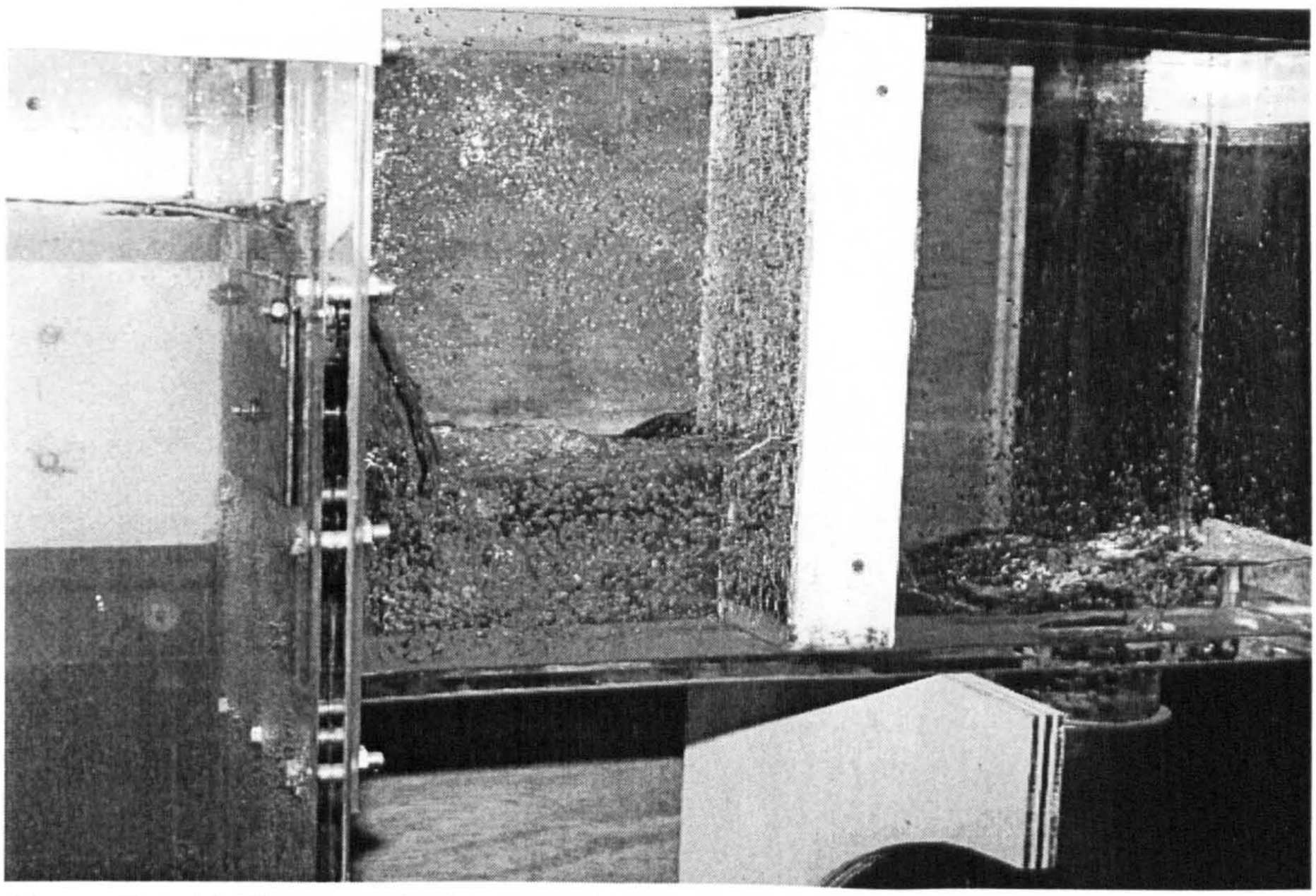


Figure 7.1-10 Photograph showing plunging curtain of water and air entrainment within collection box at 4.38 l/s

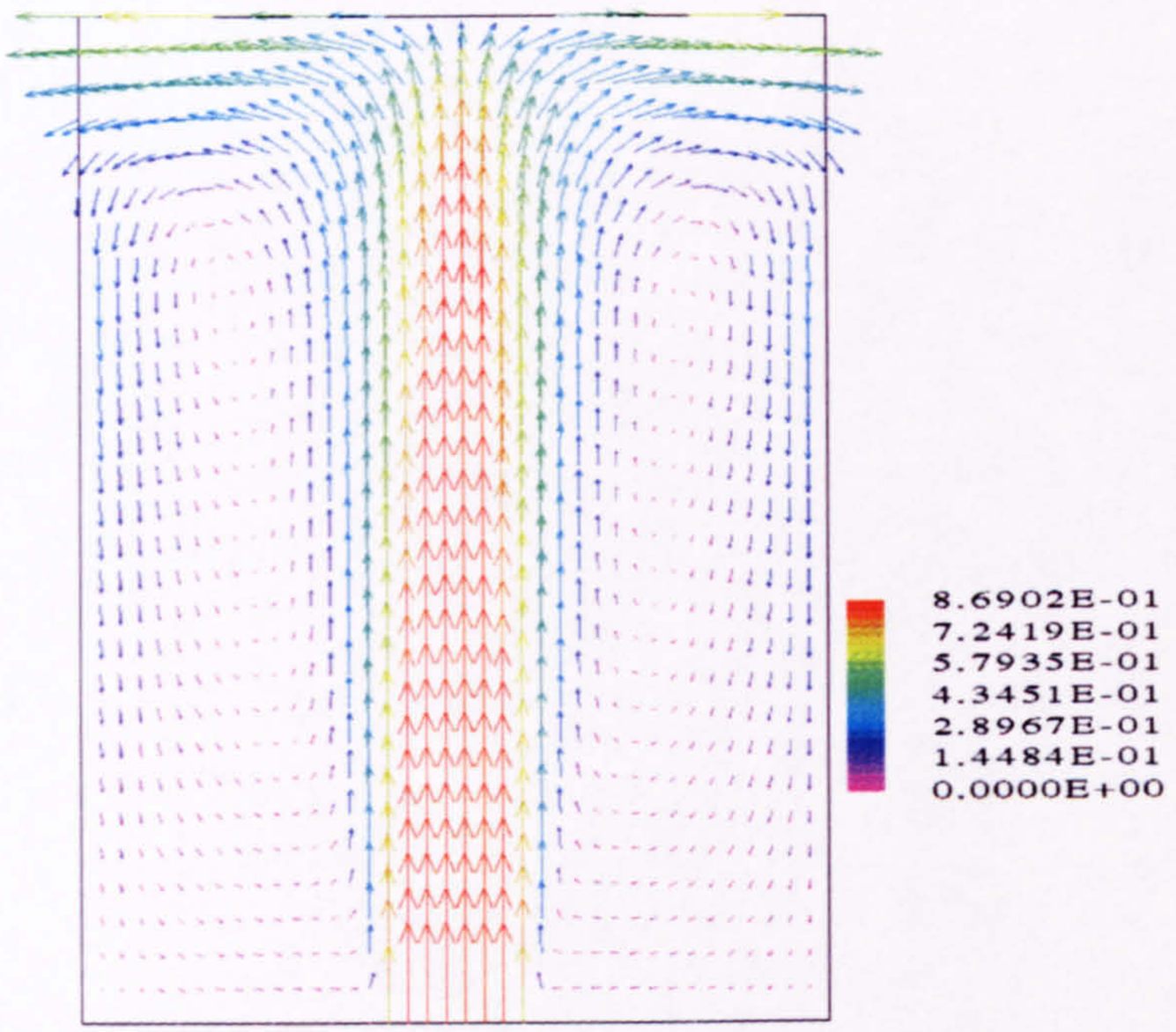


Figure 7.2-1a Velocity vector plot for ST1. Single phase flow of water at 4.38 l/s, steady state calculations performed. Mass flow boundaries used at outlets.

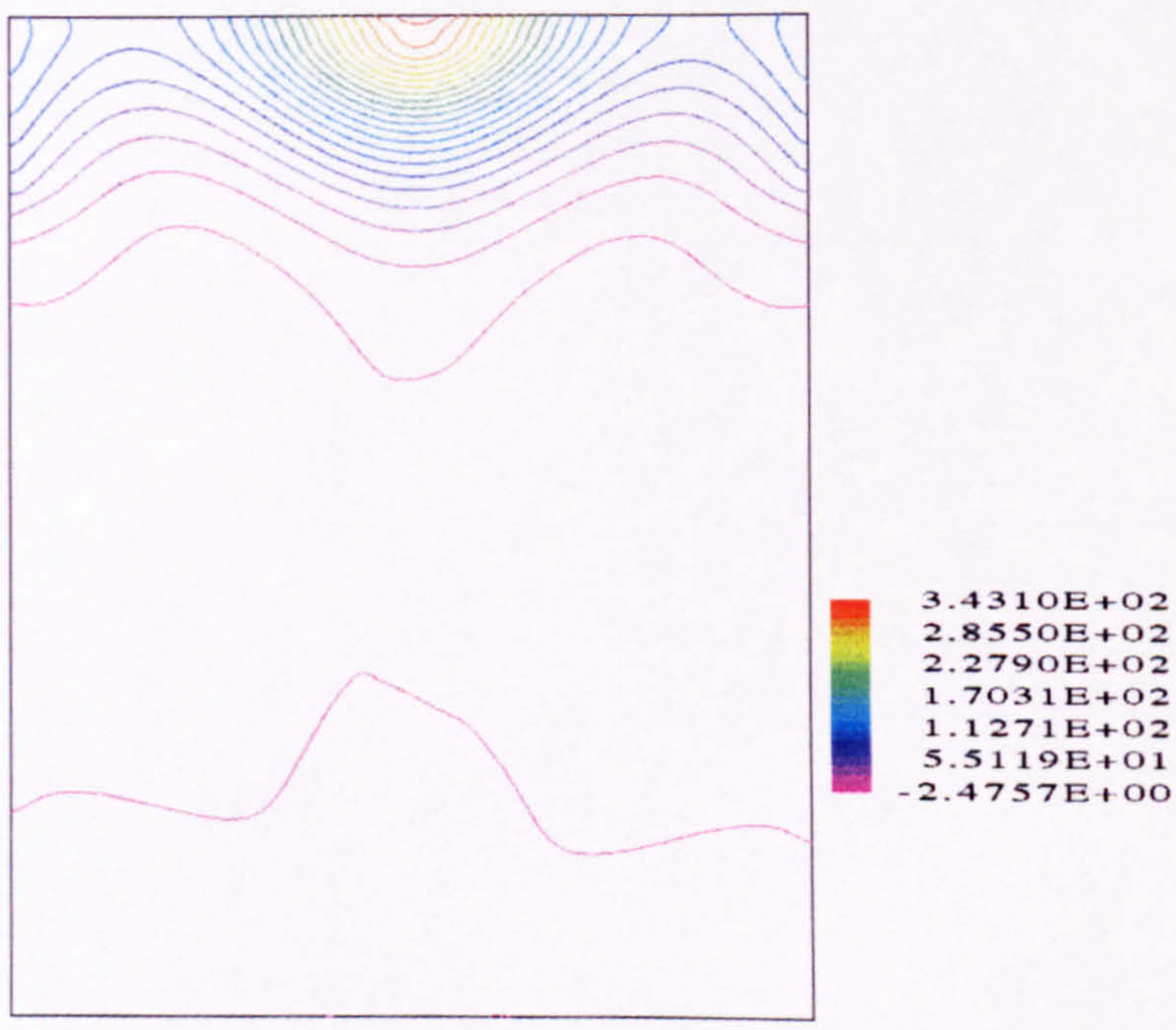


Figure 7.2-1b Pressure contour plot for ST1.

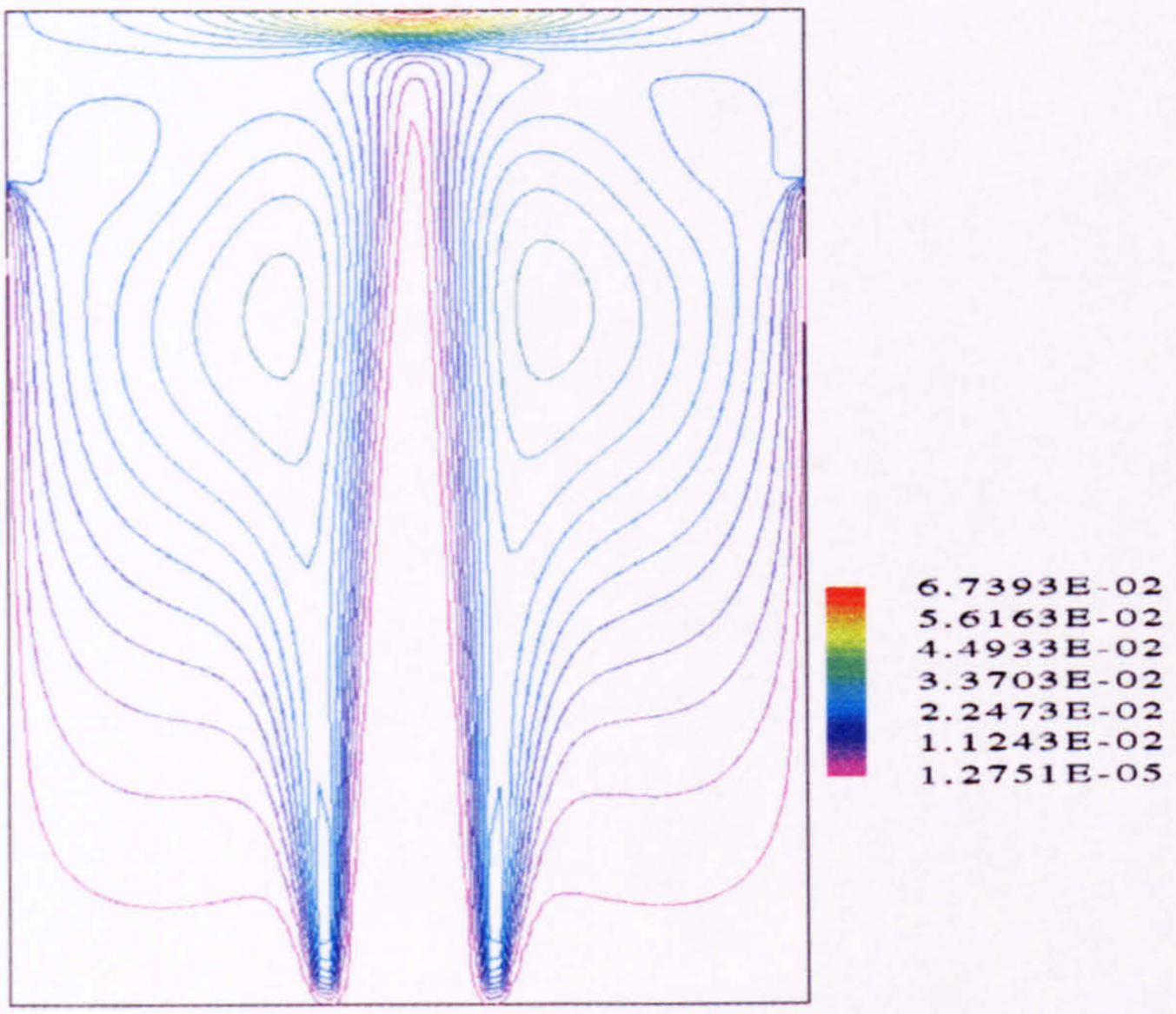


Figure 7.2-1c Contour plot of turbulent kinetic energy for ST1.

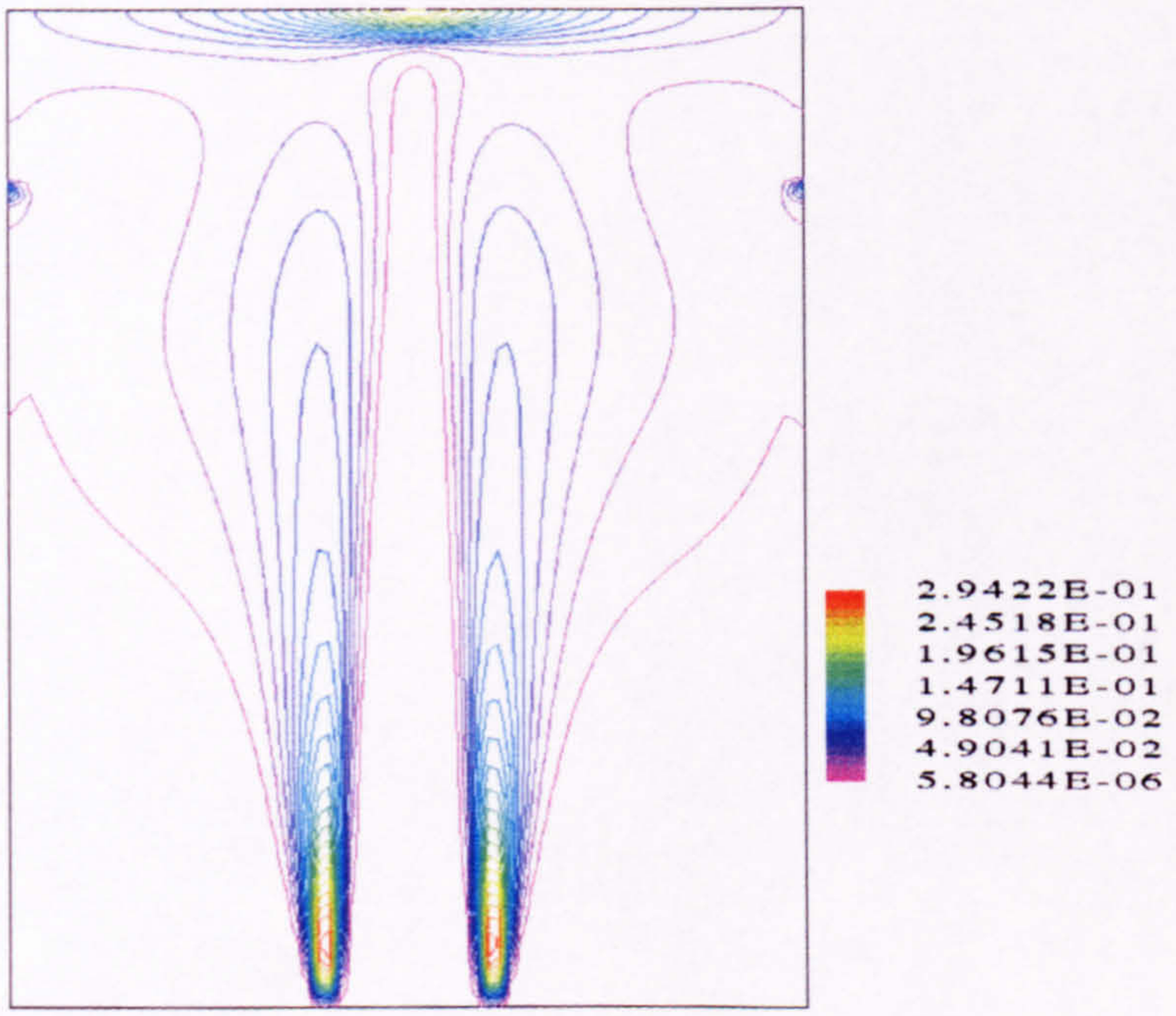


Figure 7.2-1d Contour plot of turbulent energy dissipation for ST1.

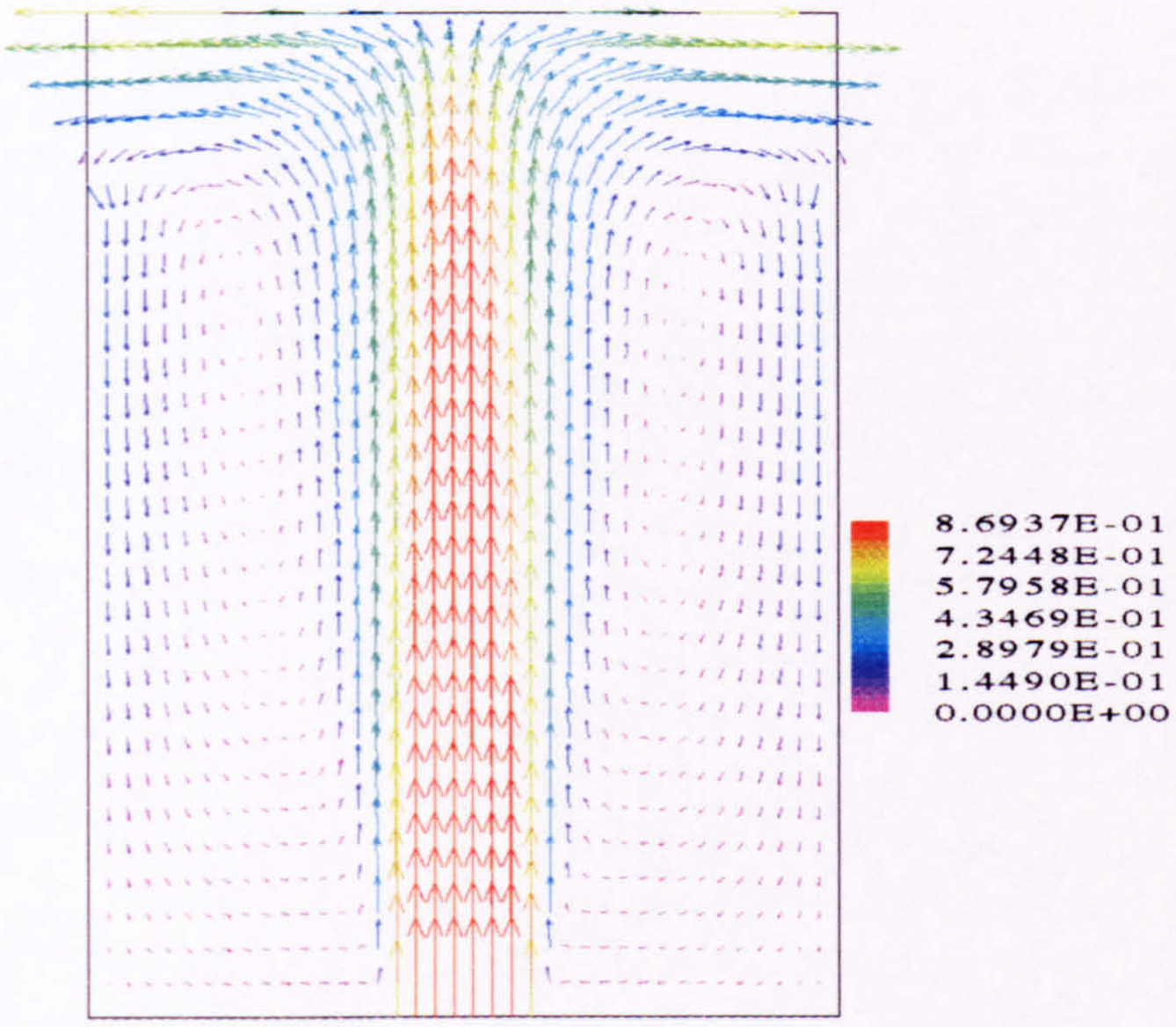


Figure 7.2-2a Velocity vector plot for ST2. Single phase water at 4.38 l/s flowing into domain. Steady state calculations performed. Pressure boundaries used at outlets.

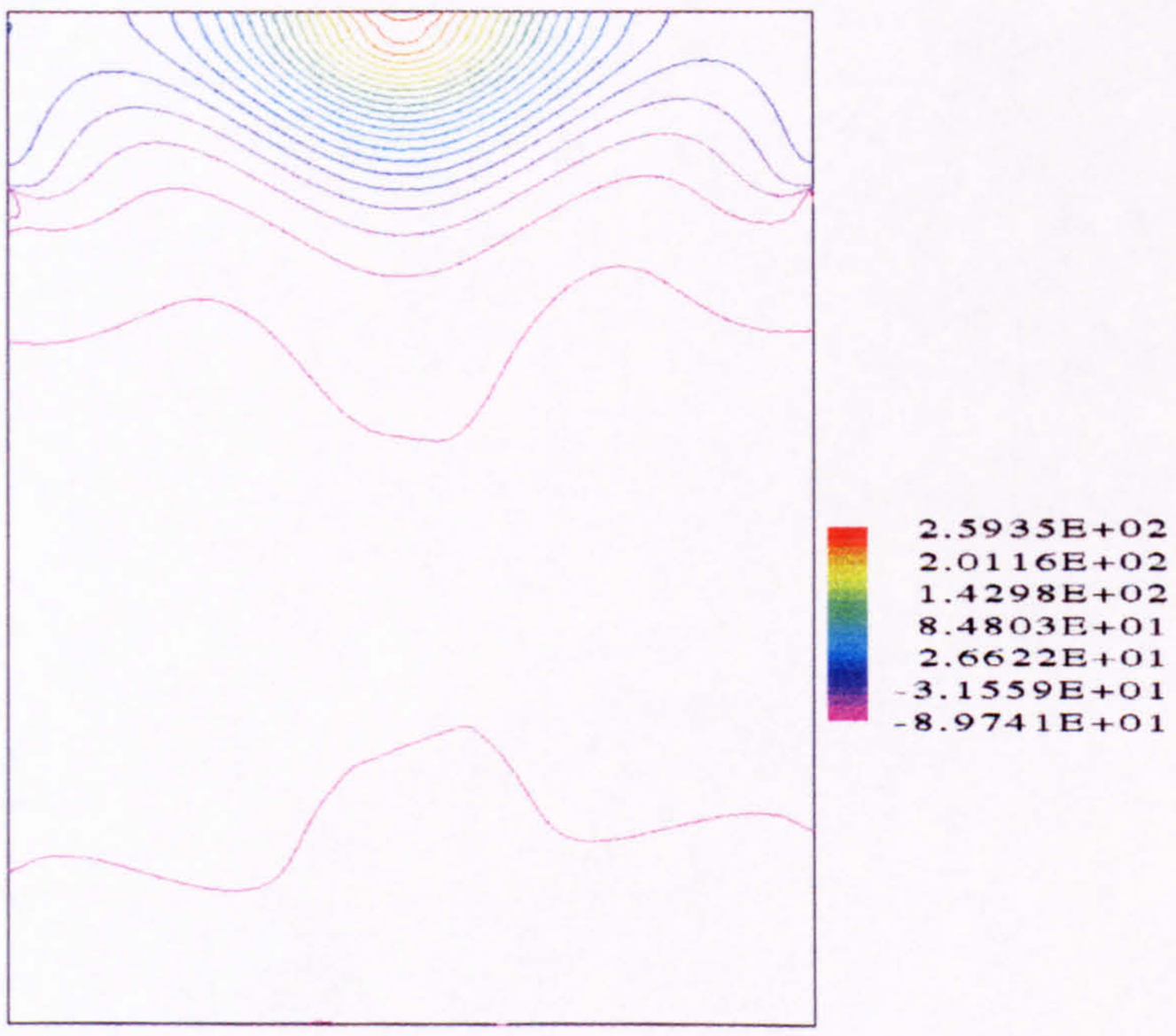


Figure 7.2-2b Pressure contour plot for ST2.

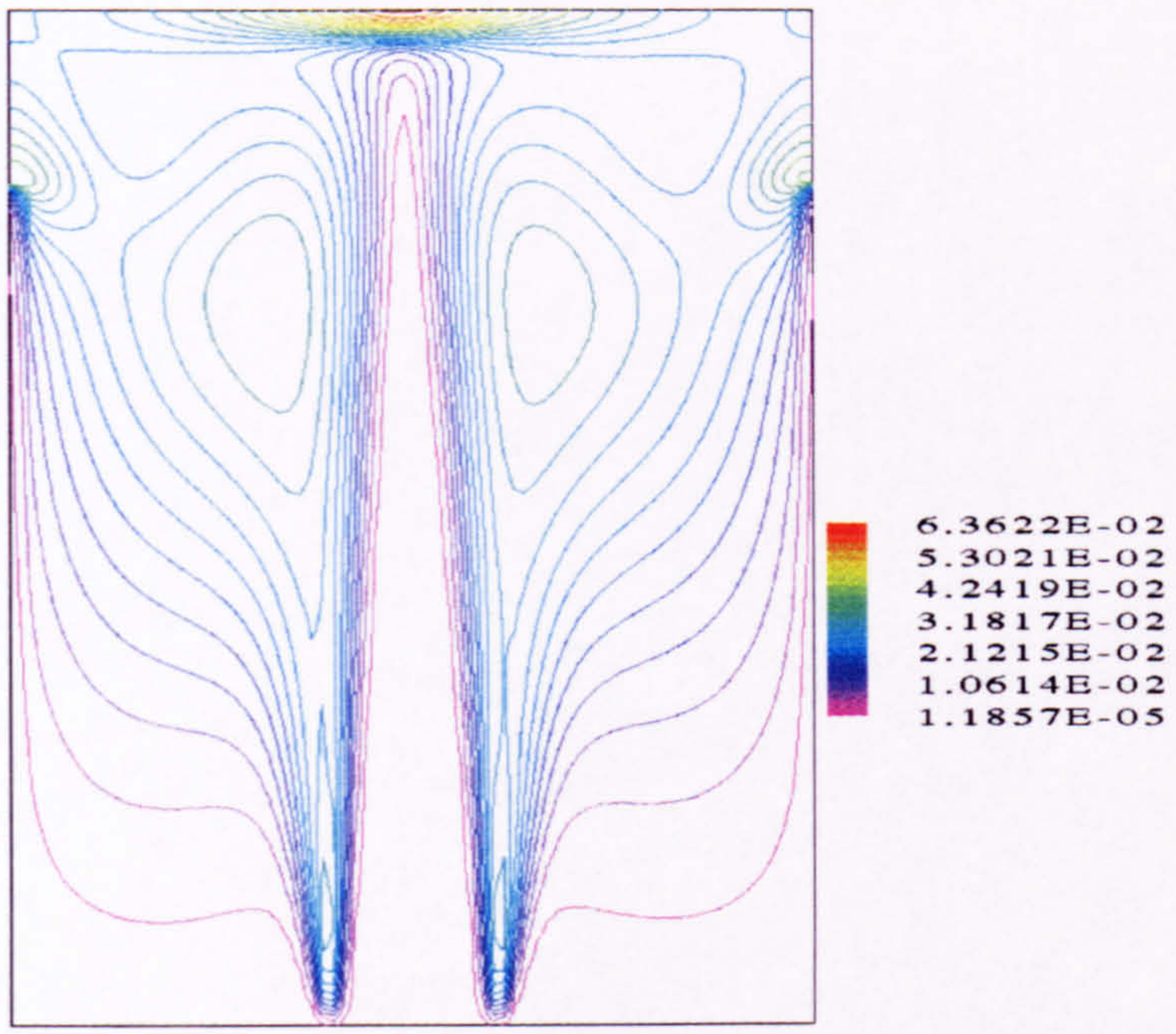


Figure 7.2-2c Contour plot of turbulent kinetic energy for ST2.

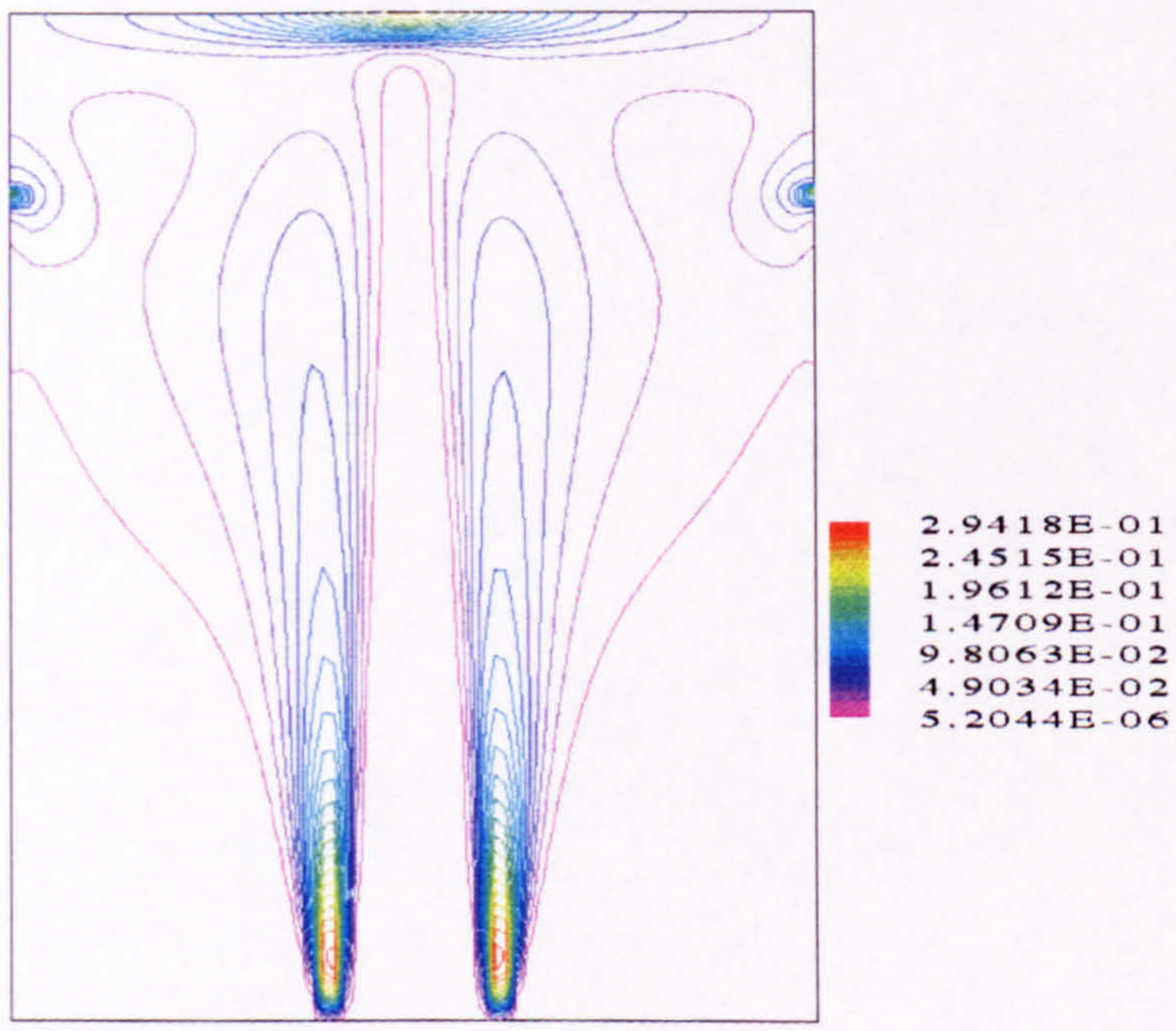


Figure 7.2-2d Contour plot of turbulent energy dissipation for ST2.

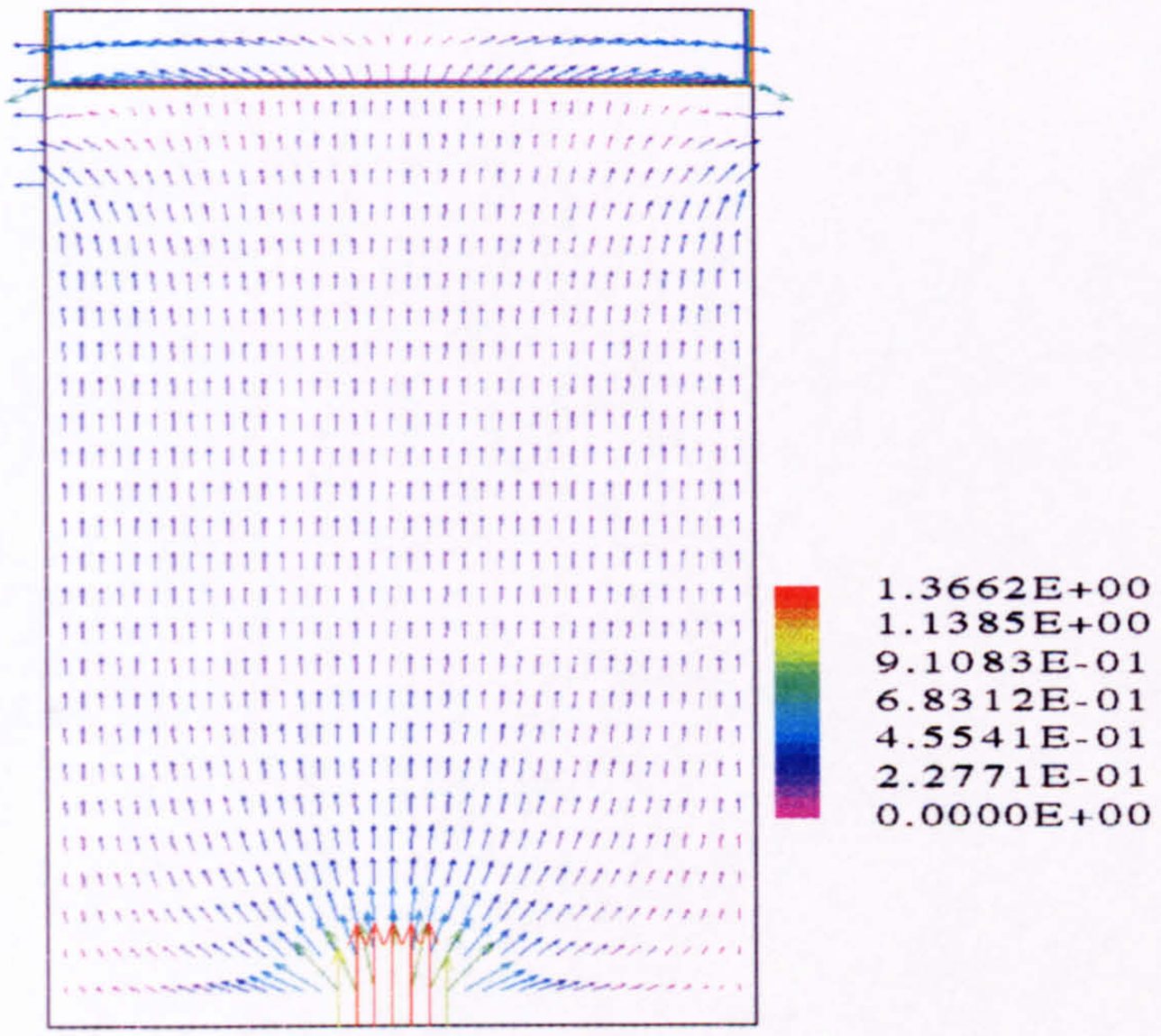


Figure 7.2-3a Velocity vector and volume fraction contour plot for 2PH1. Two phase, steady state calculation was performed. Velocities and volume fractions were specified at the two outlets.

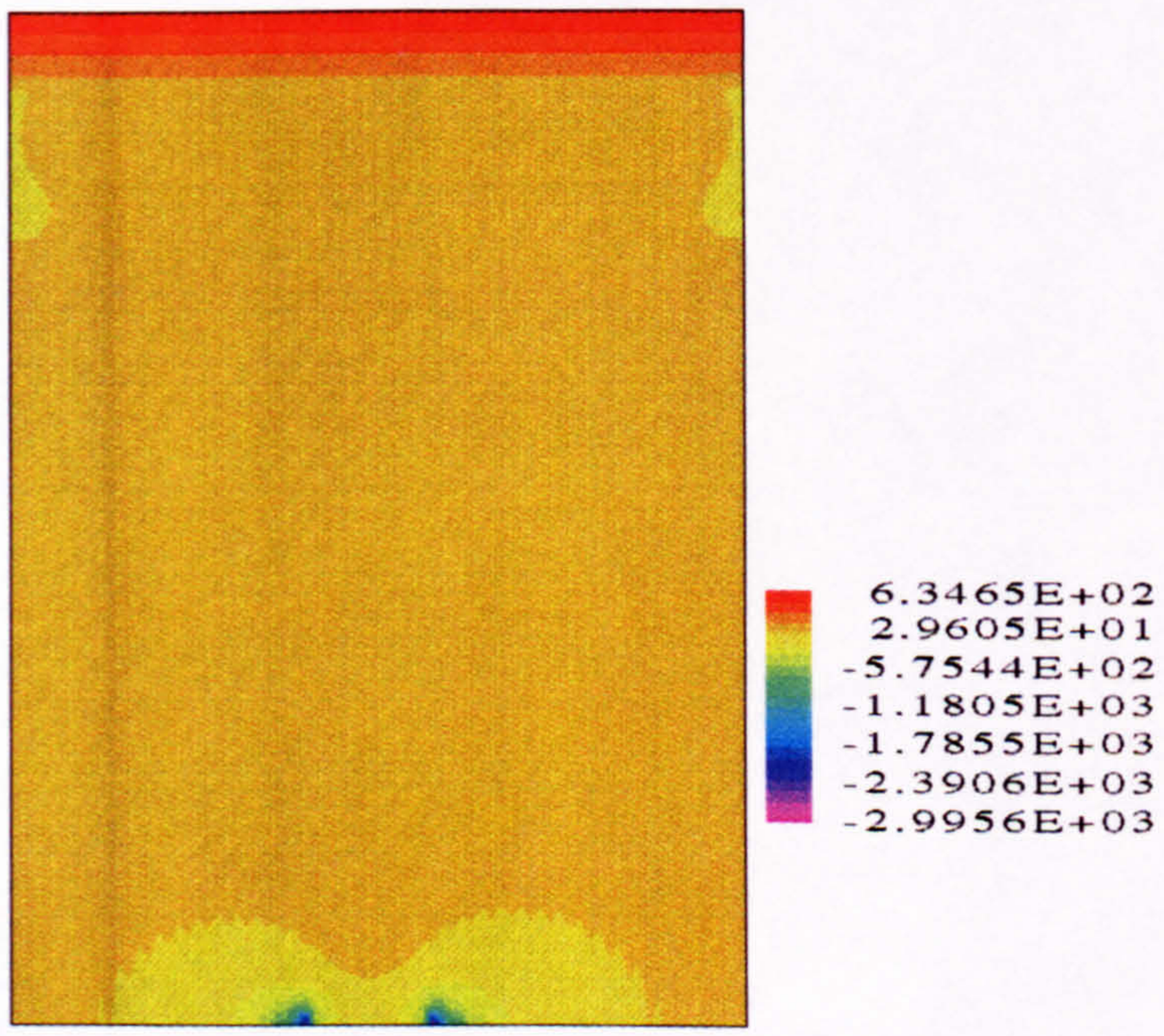


Figure 7.2-3b Pressure contour plot for 2PH1.

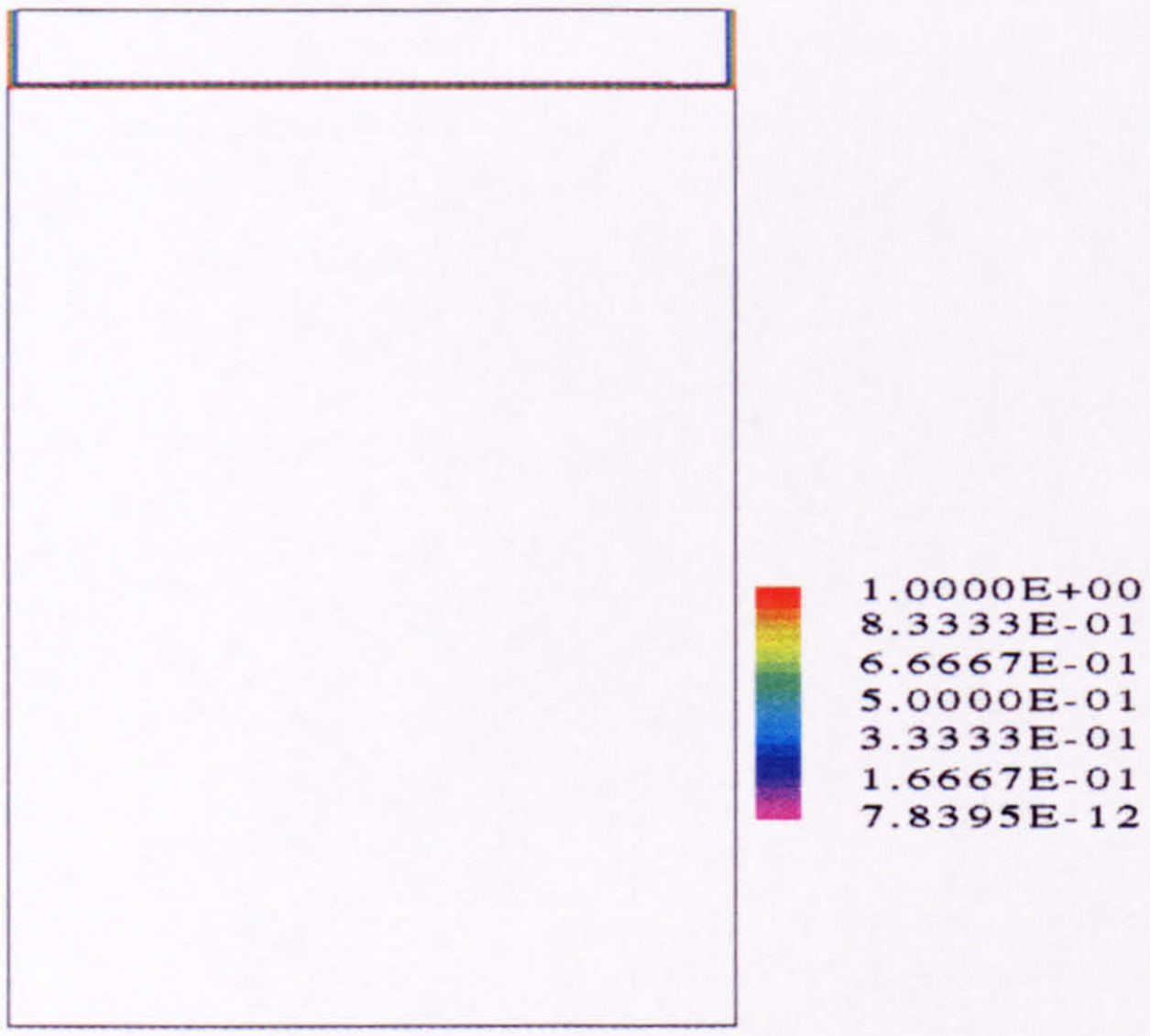


Figure 7.2-3c Volume fraction contour plot for 2PH1. Value of 1.0 represents water, 0.0 is air. Free surface has a value of 0.5.

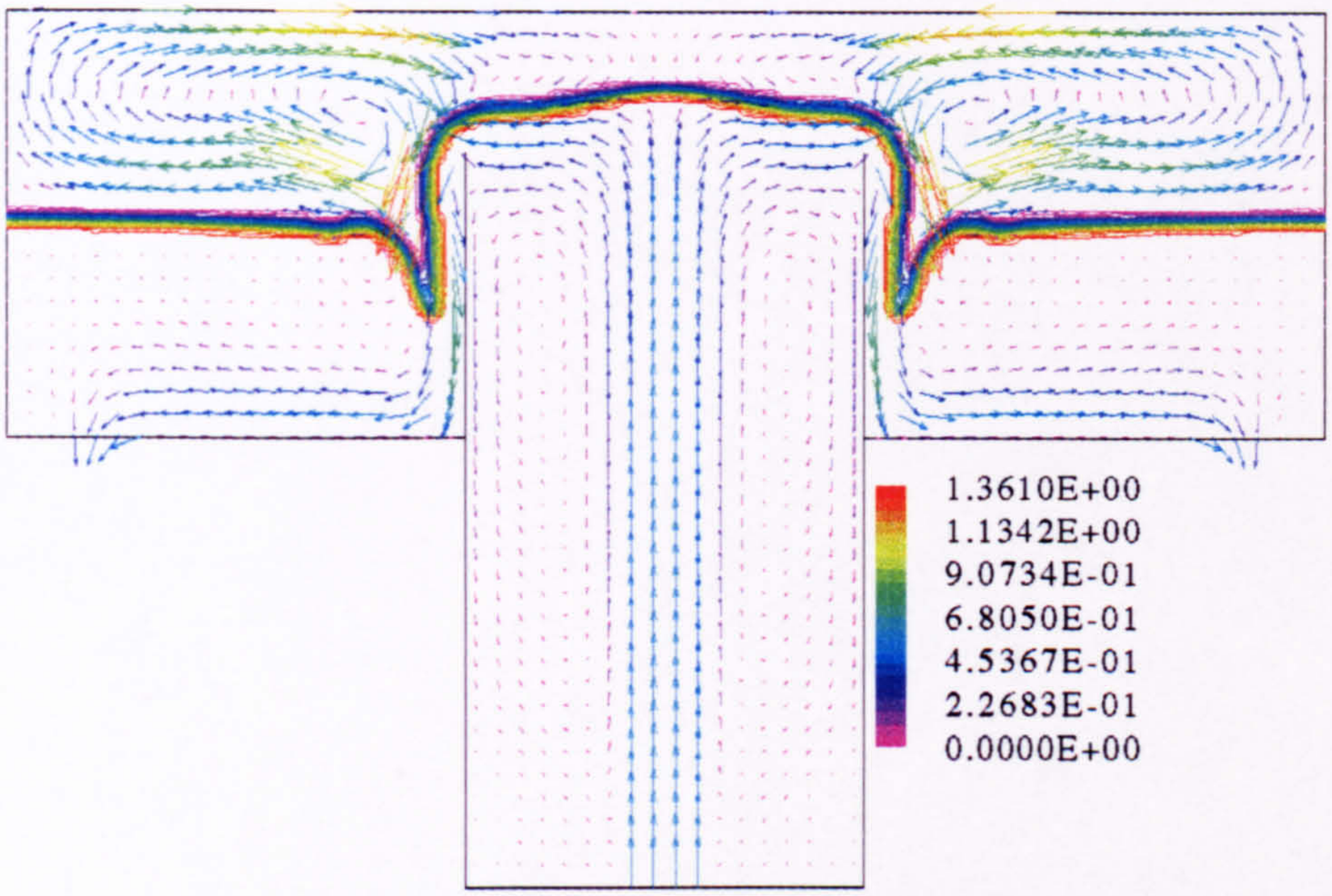


Figure 7.3-1a Velocity vector and volume fraction plot of 2D1. (Free surface represented by volume fraction contours). Flowrate = 2.95 l/s. Transient, 2D, 2-phase calculations performed. Hybrid differencing scheme, surface sharpening, and k-ε model used.

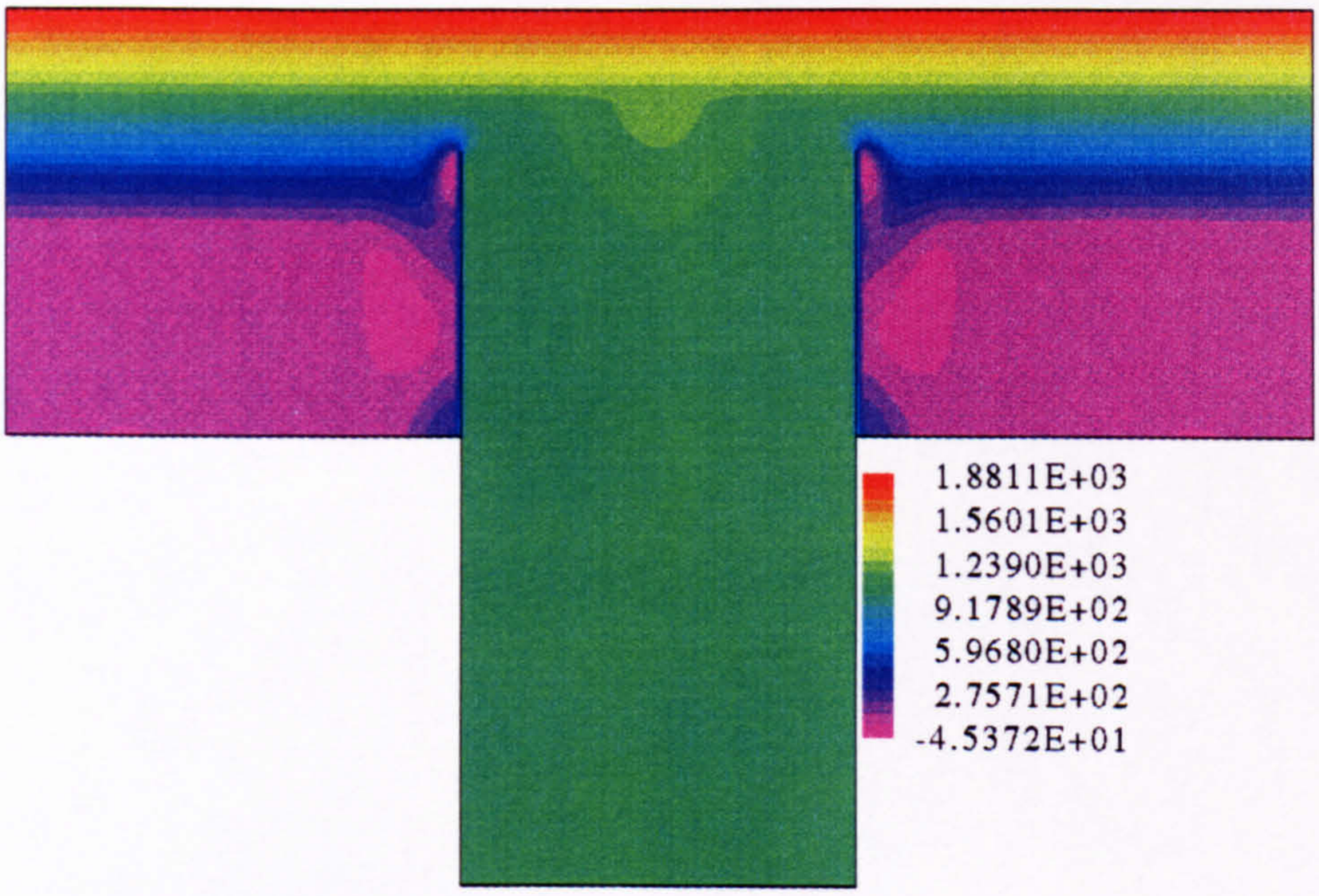


Figure 7.3-1b Pressure contour plot of 2D1

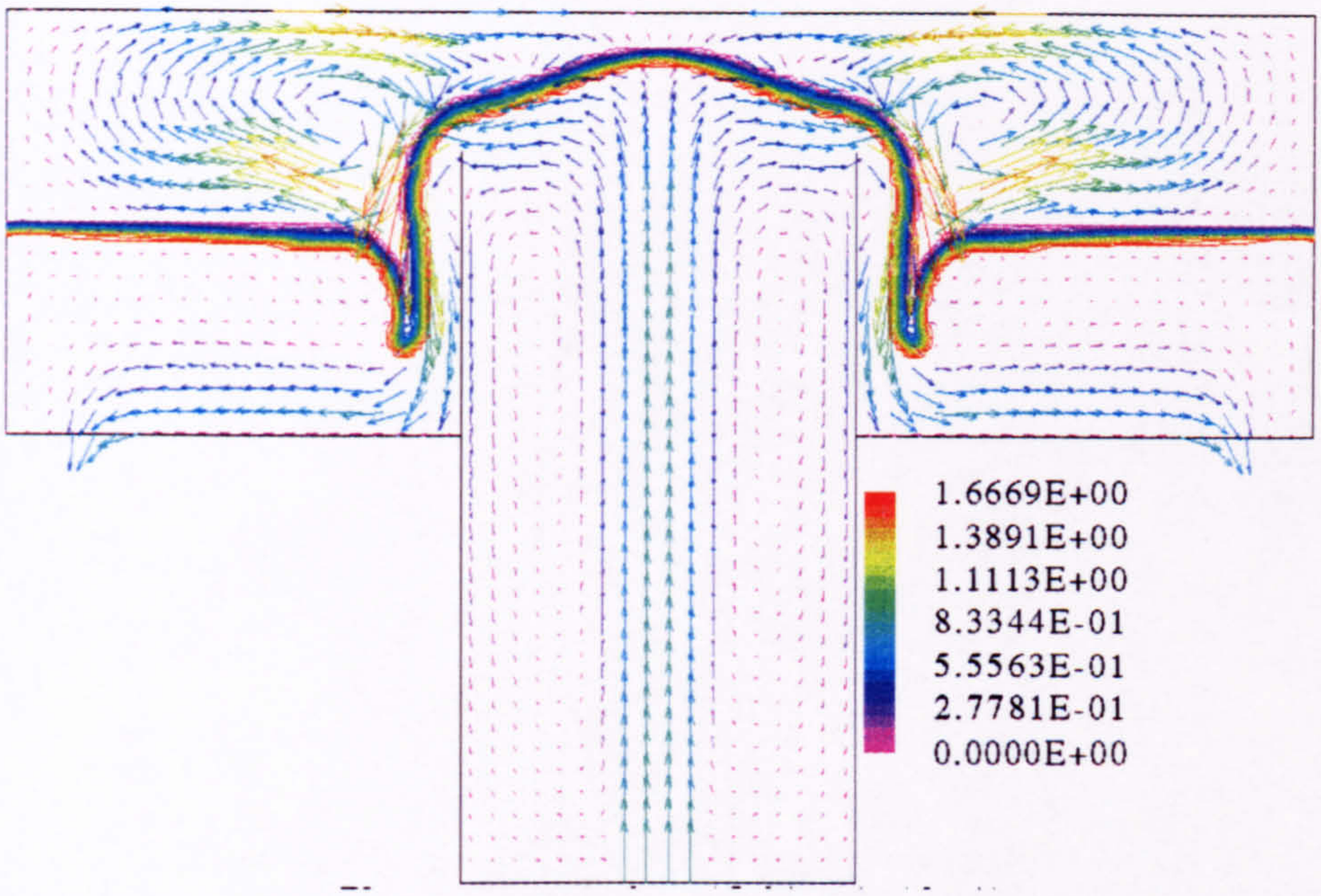


Figure 7.3-2a Velocity vector and volume fraction plot of 2D2. (Free surface represented by volume fractions). Flowrate = 4.38 l/s. 2D, 2-phase, transient calculations were performed. Hybrid differencing scheme, surface sharpening algorithm, and k-ε turbulence model used.

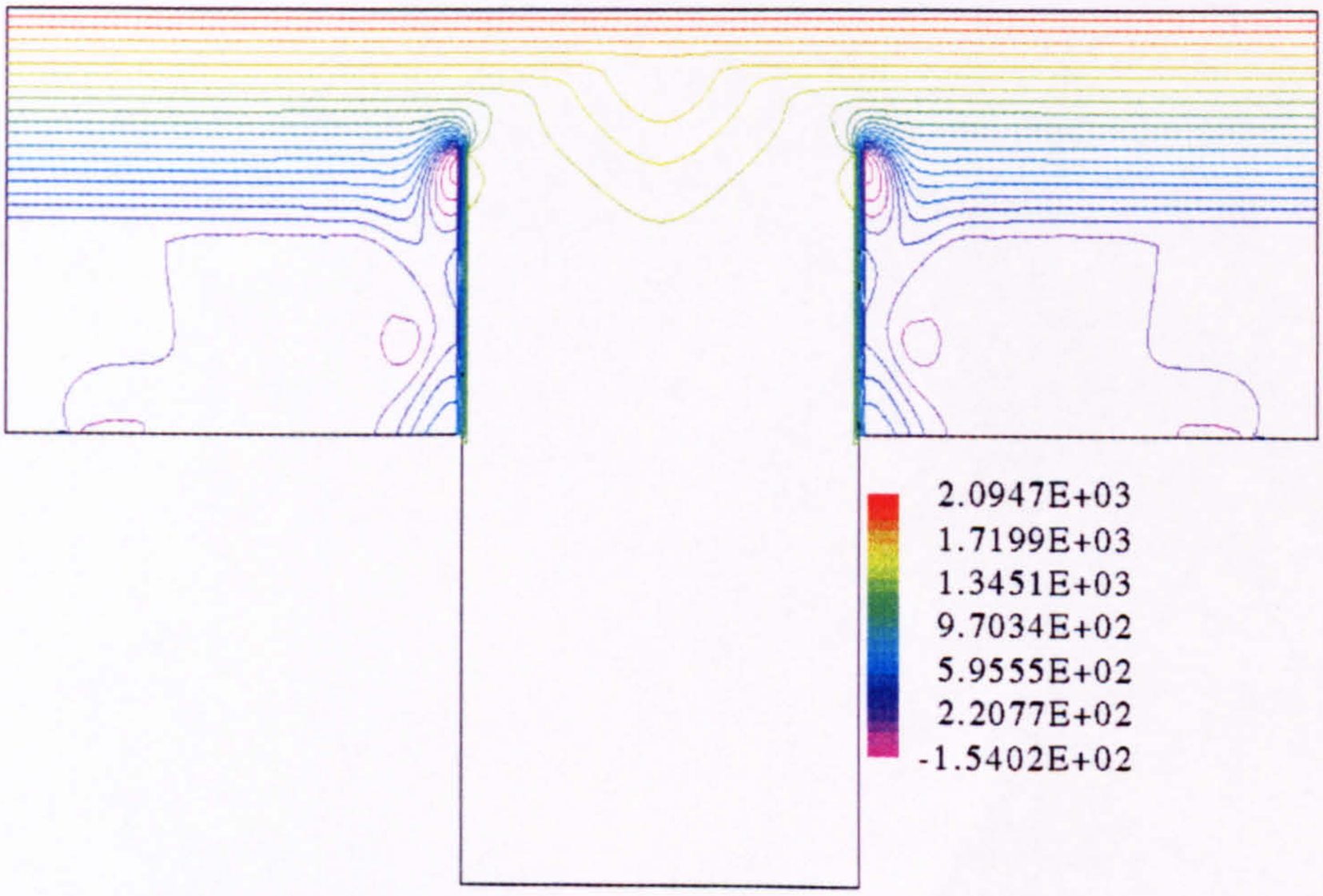


Figure 7.3-2b Pressure contour plot of 2D2.

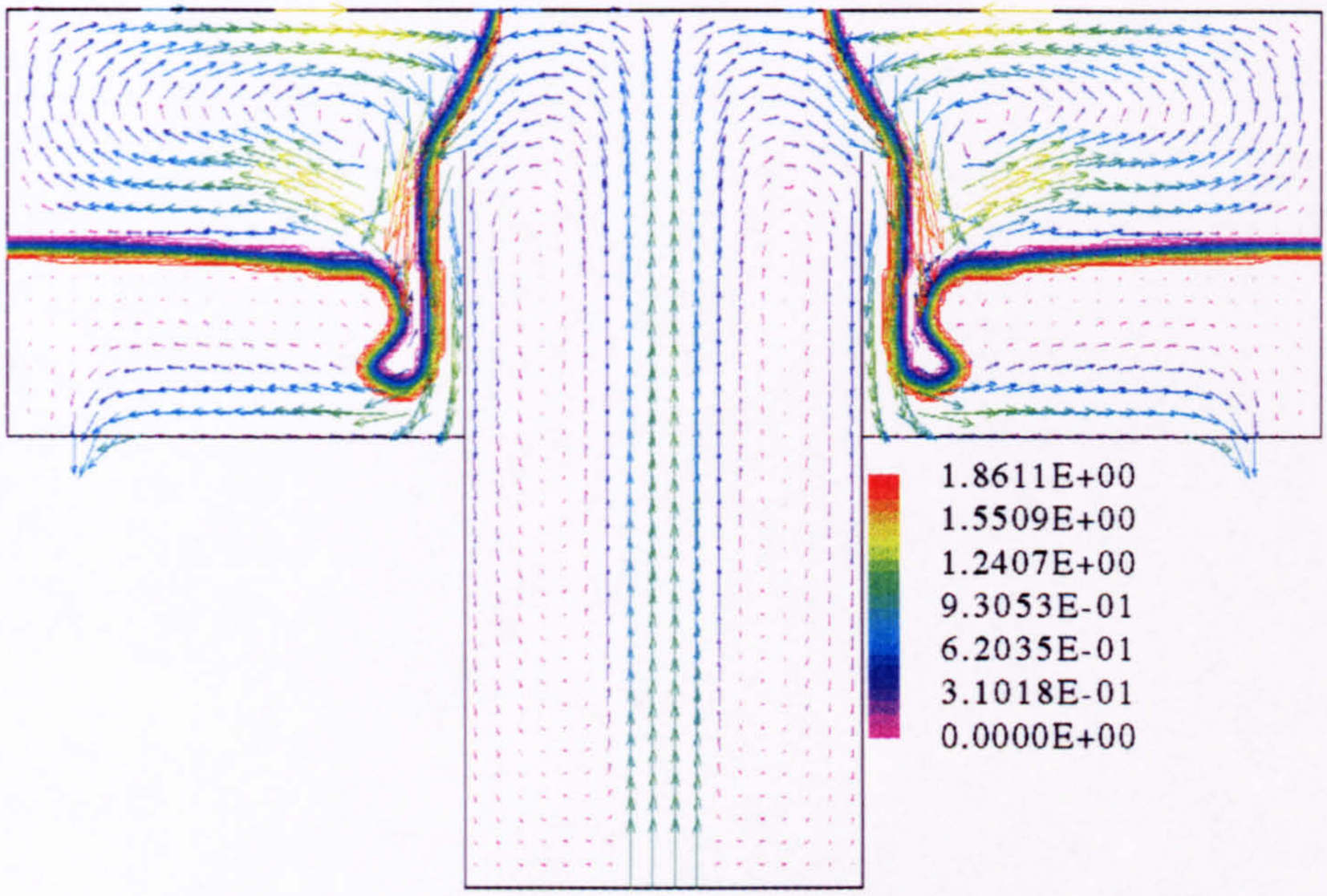


Figure 7.3-3a Velocity vector and contour plot of 2D3. (Free surface represented by volume fraction contours). Flowrate = 5.51 l/s. 2D, 2-phase, transient calculations performed. Hybrid differencing scheme, surface sharpening algorithm and k-ε turbulence model used.

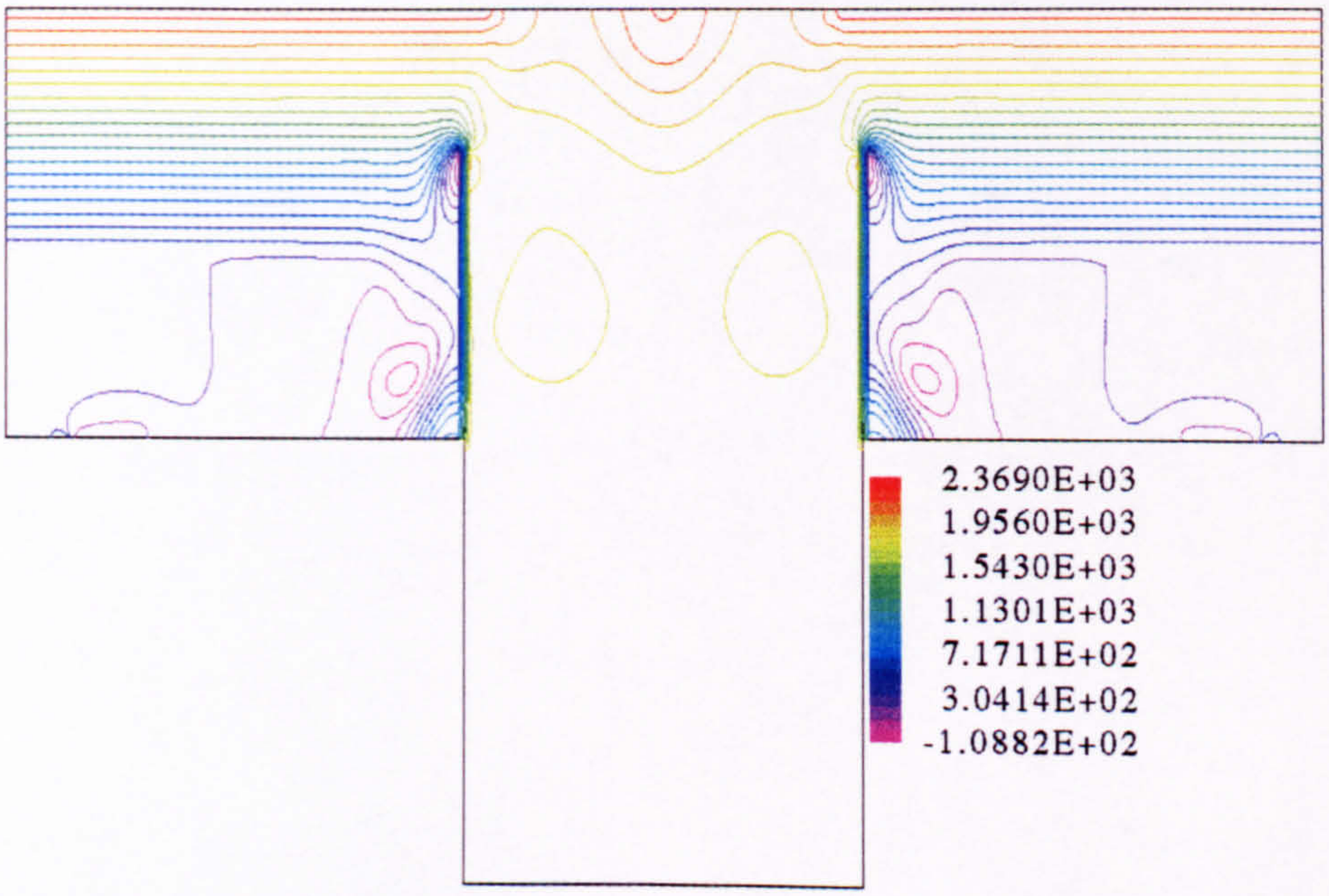


Figure 7.3-3b Pressure contour plot of 2D3.

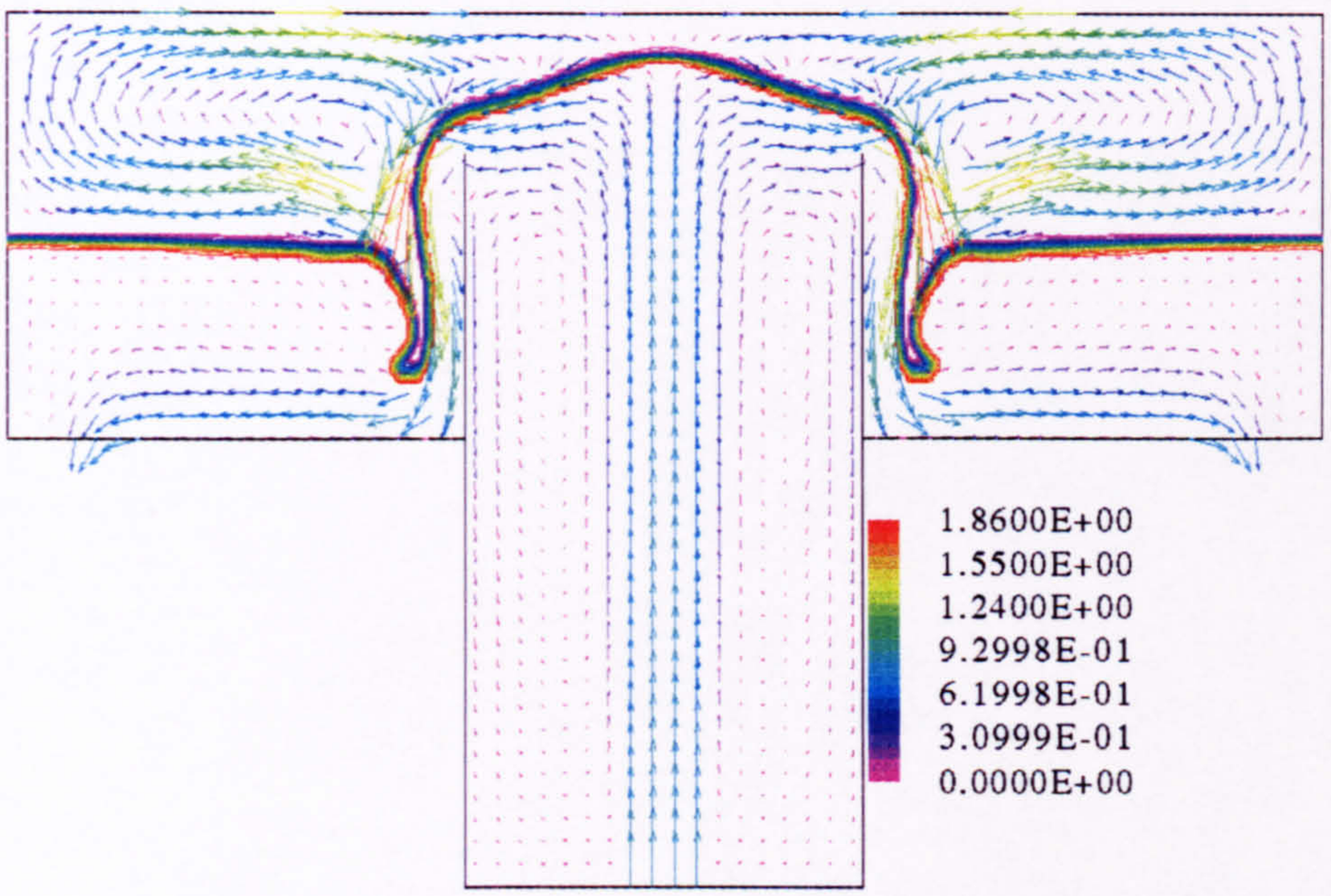


Figure 7.3-4a Velocity vector and volume fraction plot of 2DIndy (grid independence test). Free surface indicated by volume fraction contours. Flowrate = 4.38 l/s. 2D, 2-phase, transient calculations performed. Hybrid differencing scheme, surface sharpening algorithm and k-ε turbulence model used.

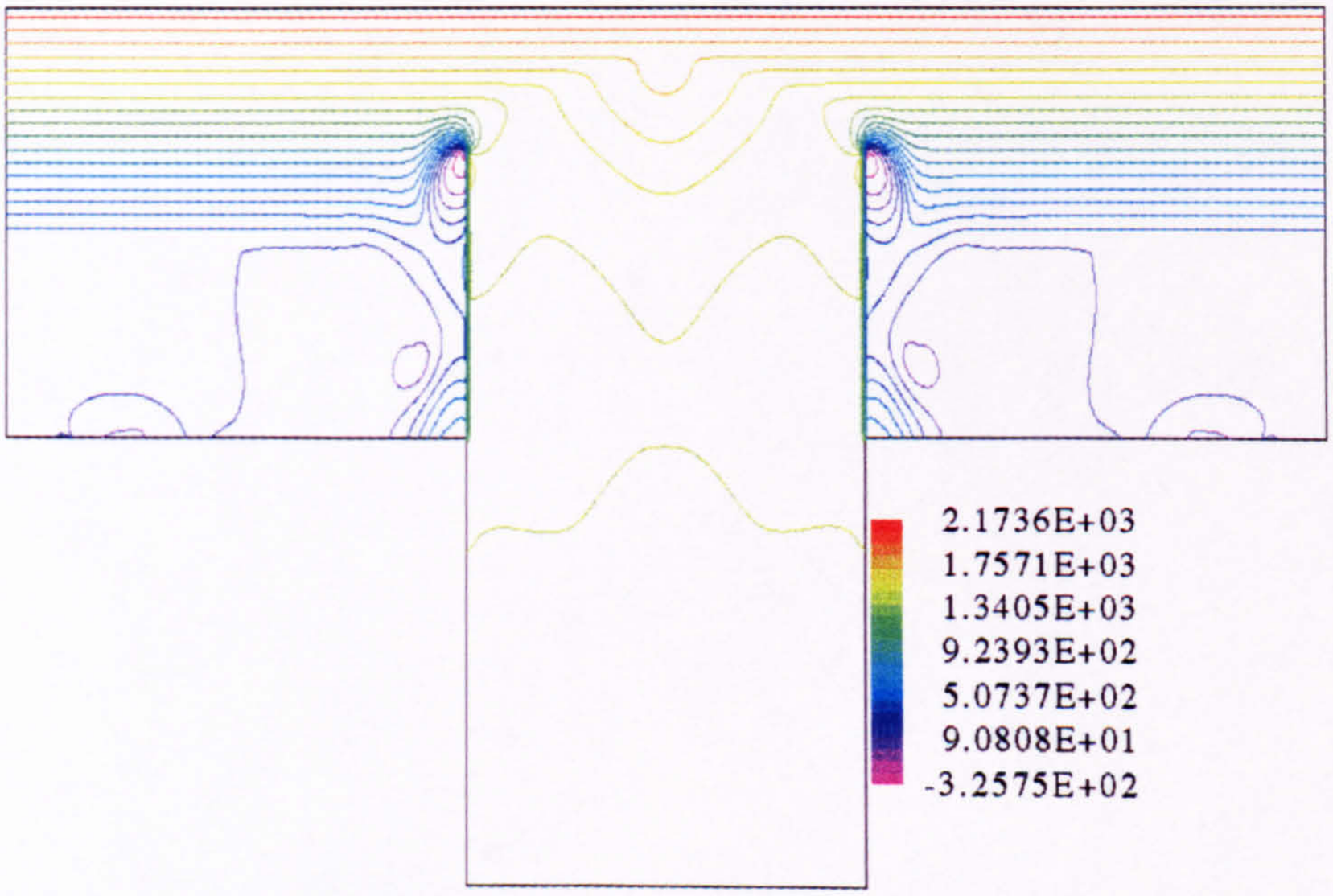


Figure 7.3-4b Pressure contour plot of 2DIndy

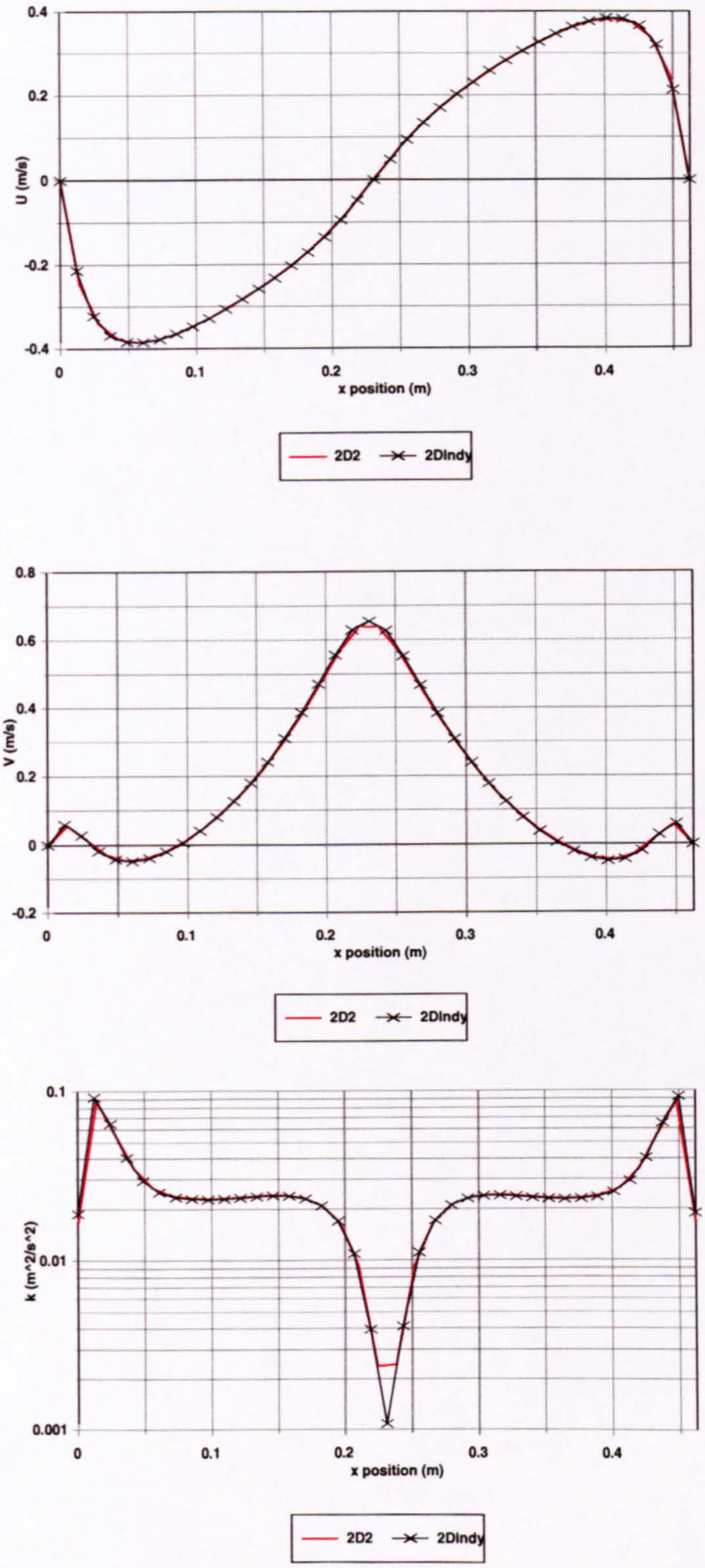


Figure 7.3-5a Comparisons of velocities and turbulent kinetic energy calculated using the 17,850 cell (2D2) and 27,300 cell (2DIndy) geometries, at y = 0.628 m. Flowrate = 4.38 l/s

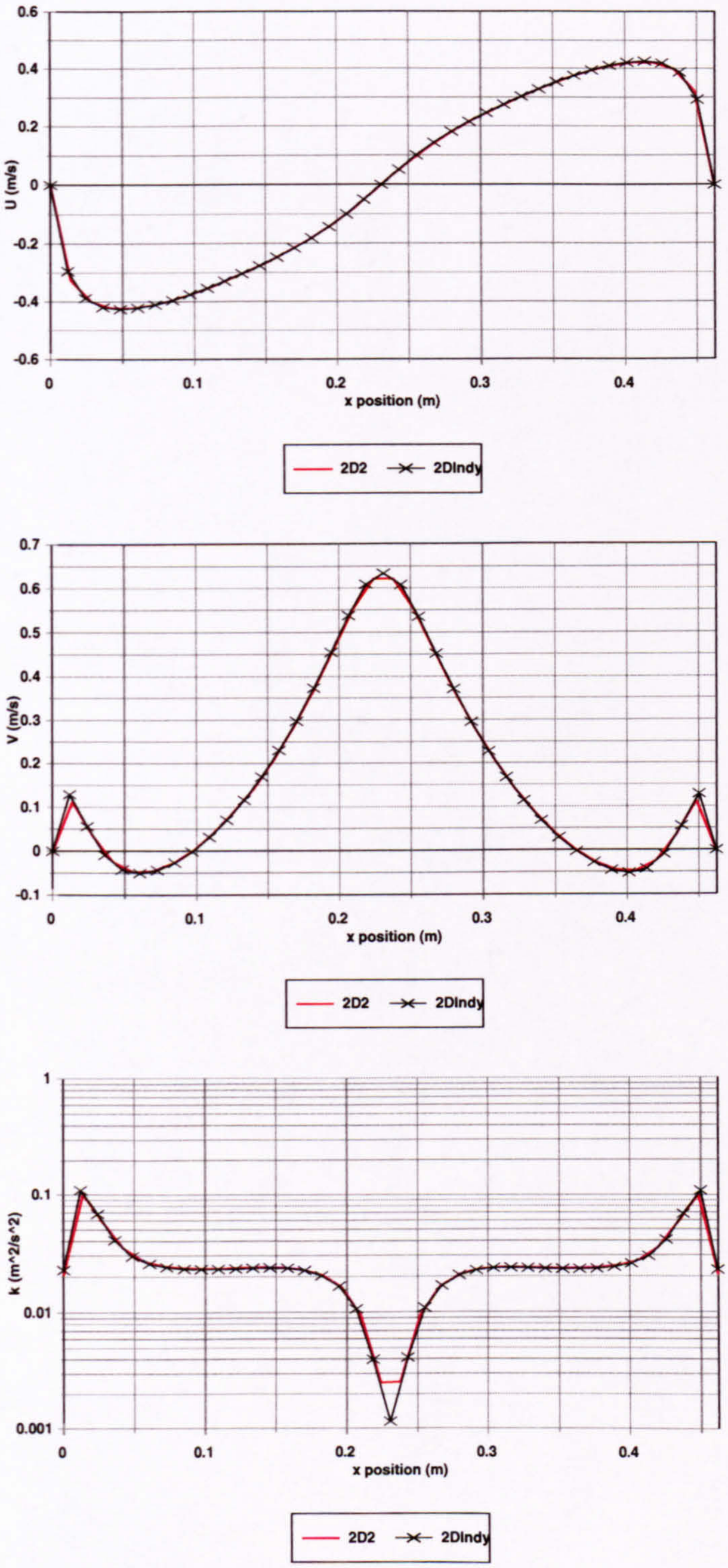


Figure 7.3-5b Comparisons of velocities and turbulent kinetic energy calculated using 17,850 cell and 27,300 cell geometries, at y = 0.633 m. Flowrate = 4.38 l/s

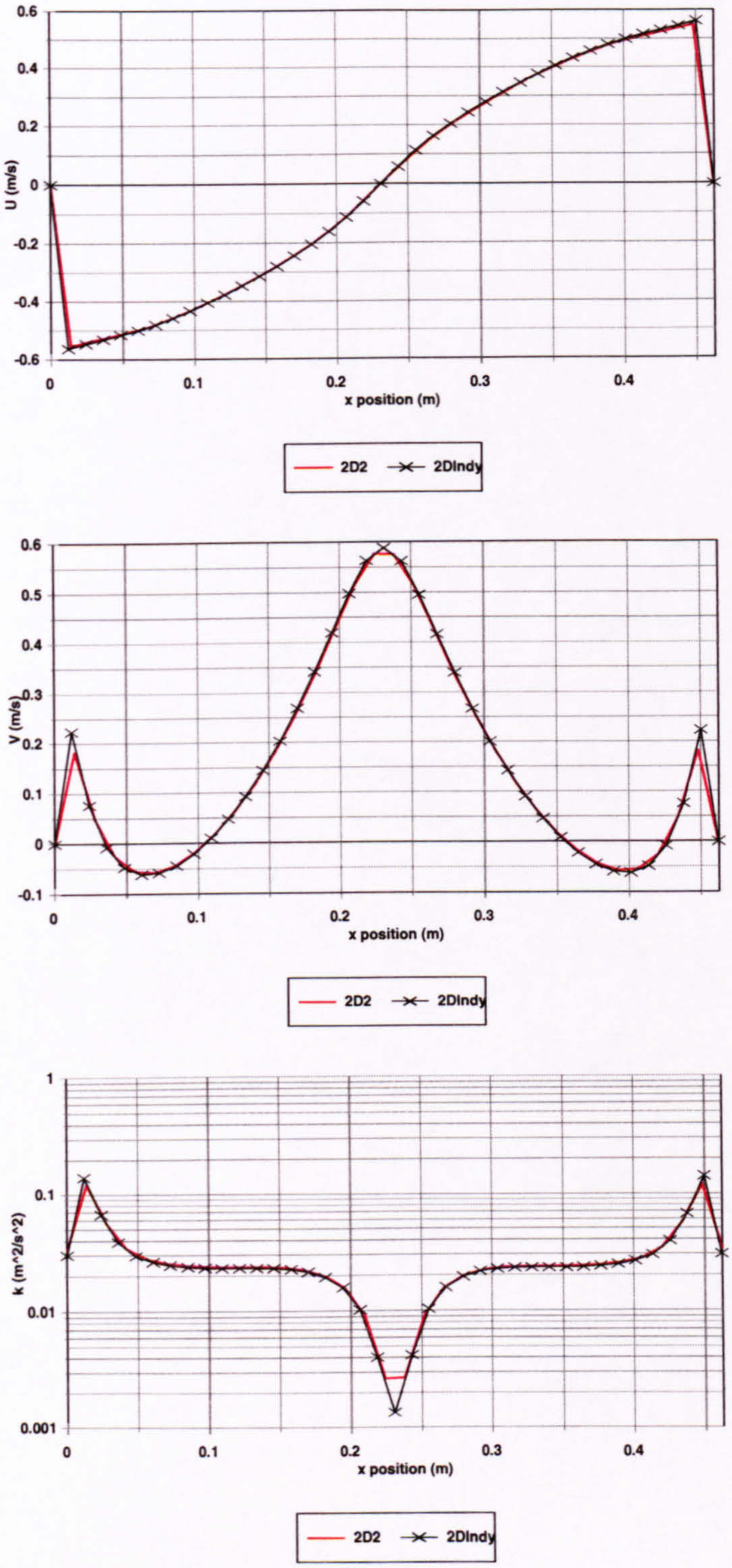


Figure 7.3-5c Comparisons of velocities and turbulent kinetic energy calculated using 17,850 cell and 27,300 cell geometries, at y = 0.643 m. Flowrate = 4.38 l/s

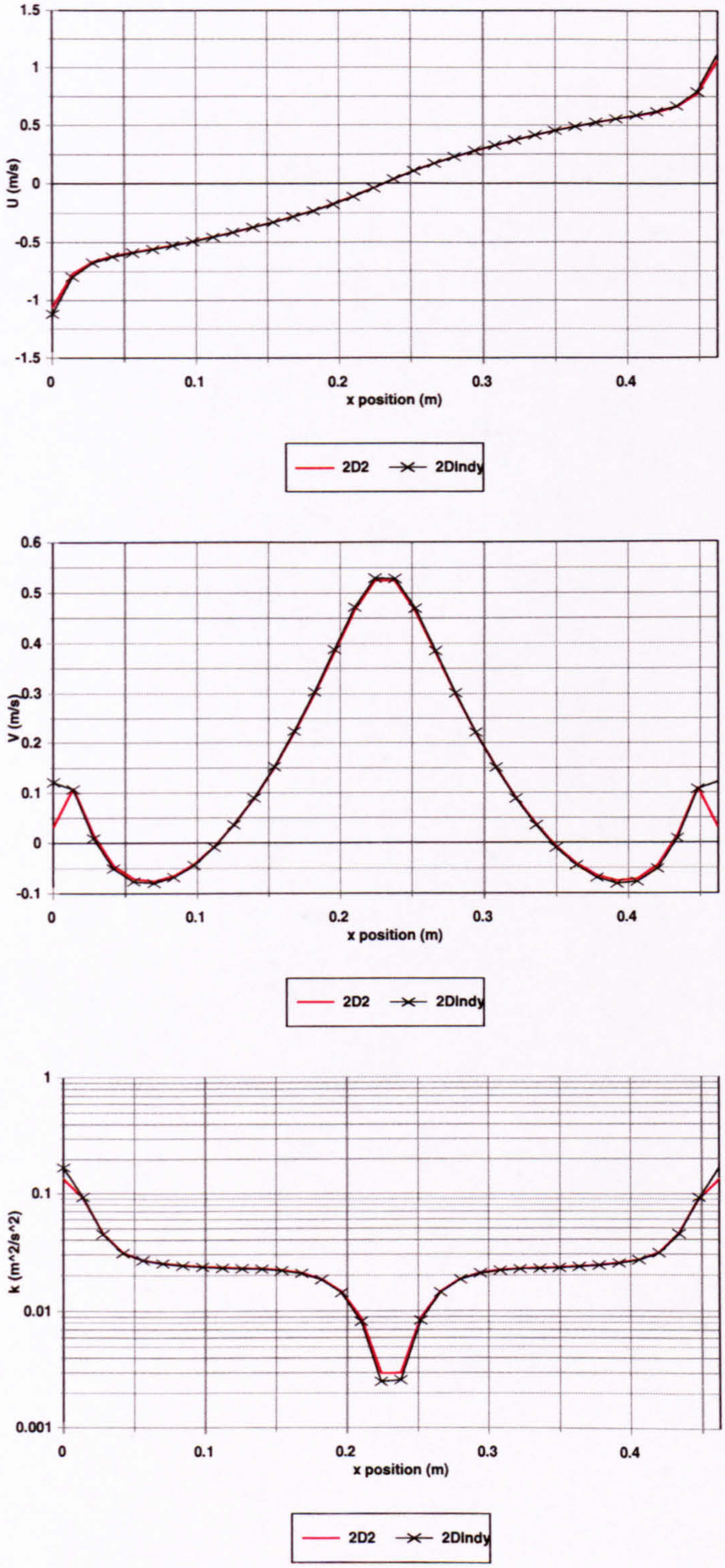


Figure 7.3-5d Comparisons of velocities and turbulent kinetic energy calculated using 17,850 cell and 27,300 cell geometries, at y = 0.653 m. Flowrate = 4.38 l/s

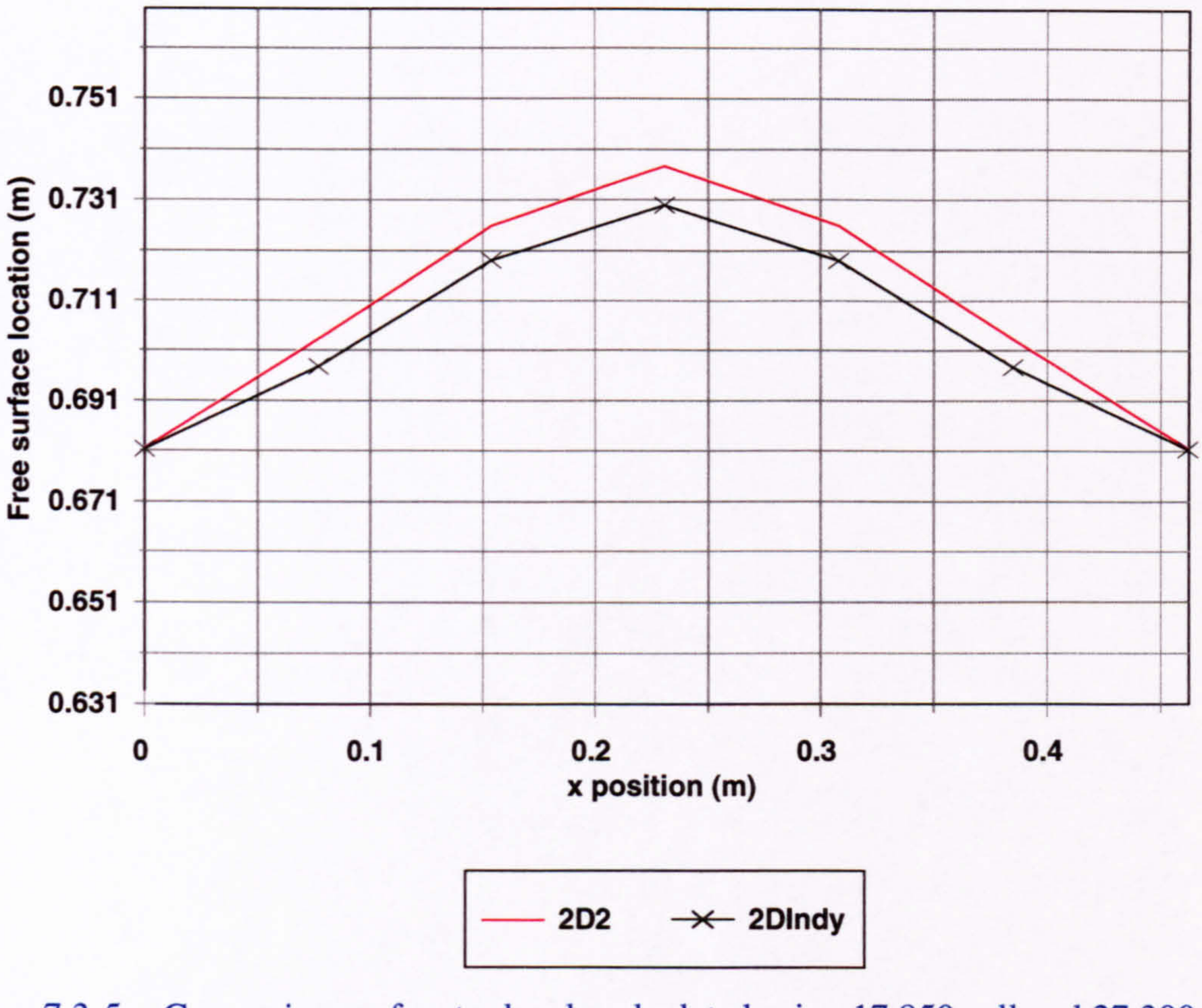


Figure 7.3-5e Comparisons of water levels calculated using 17,850 cell and 27,300 cell geometries. Flowrate = 4.38 l/s

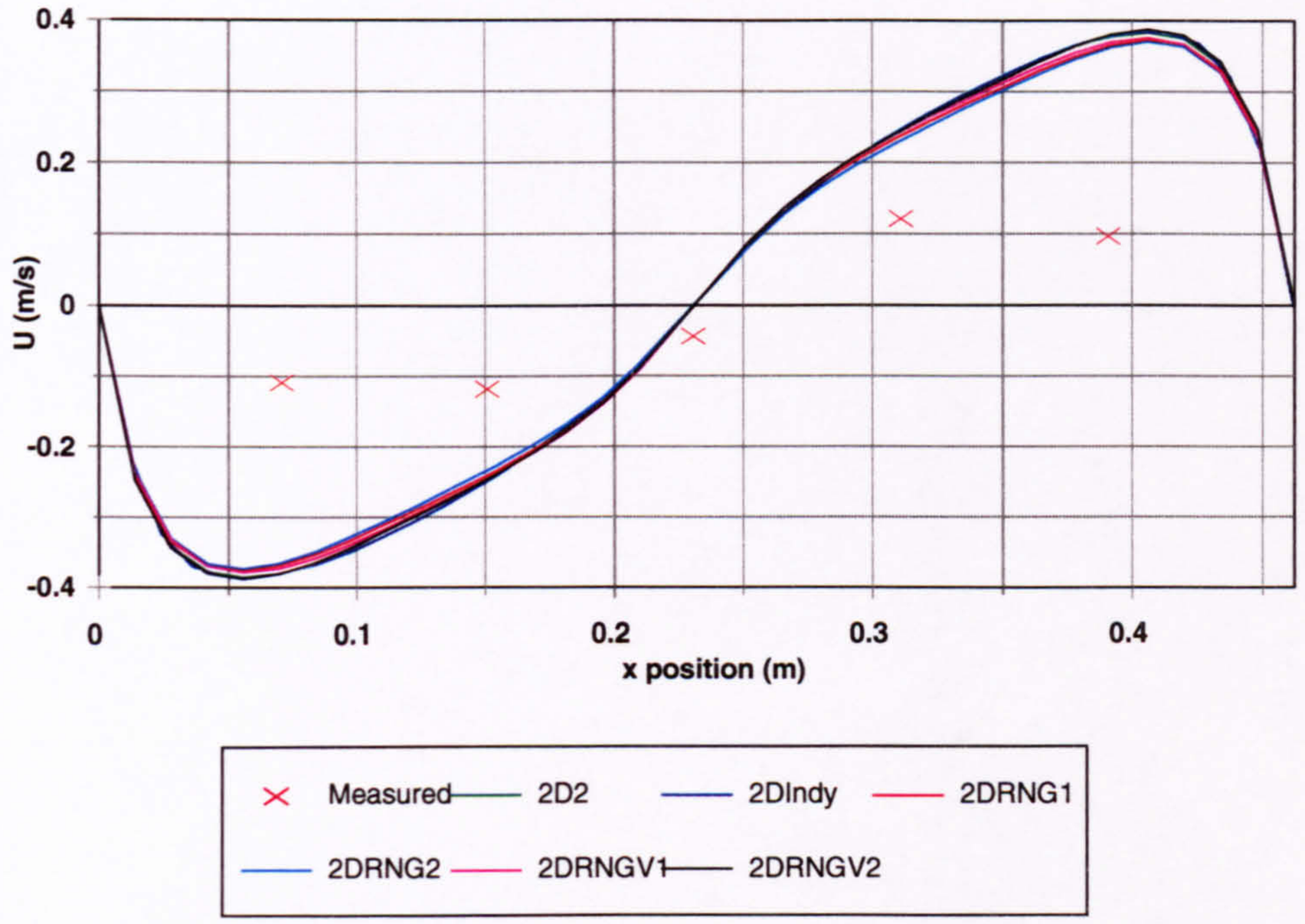


Figure 7.3-6a Comparison between calculated and experimental values of U velocity, at y = 0.628 m (from invert of chamber). Flowrate = 4.38 l/s

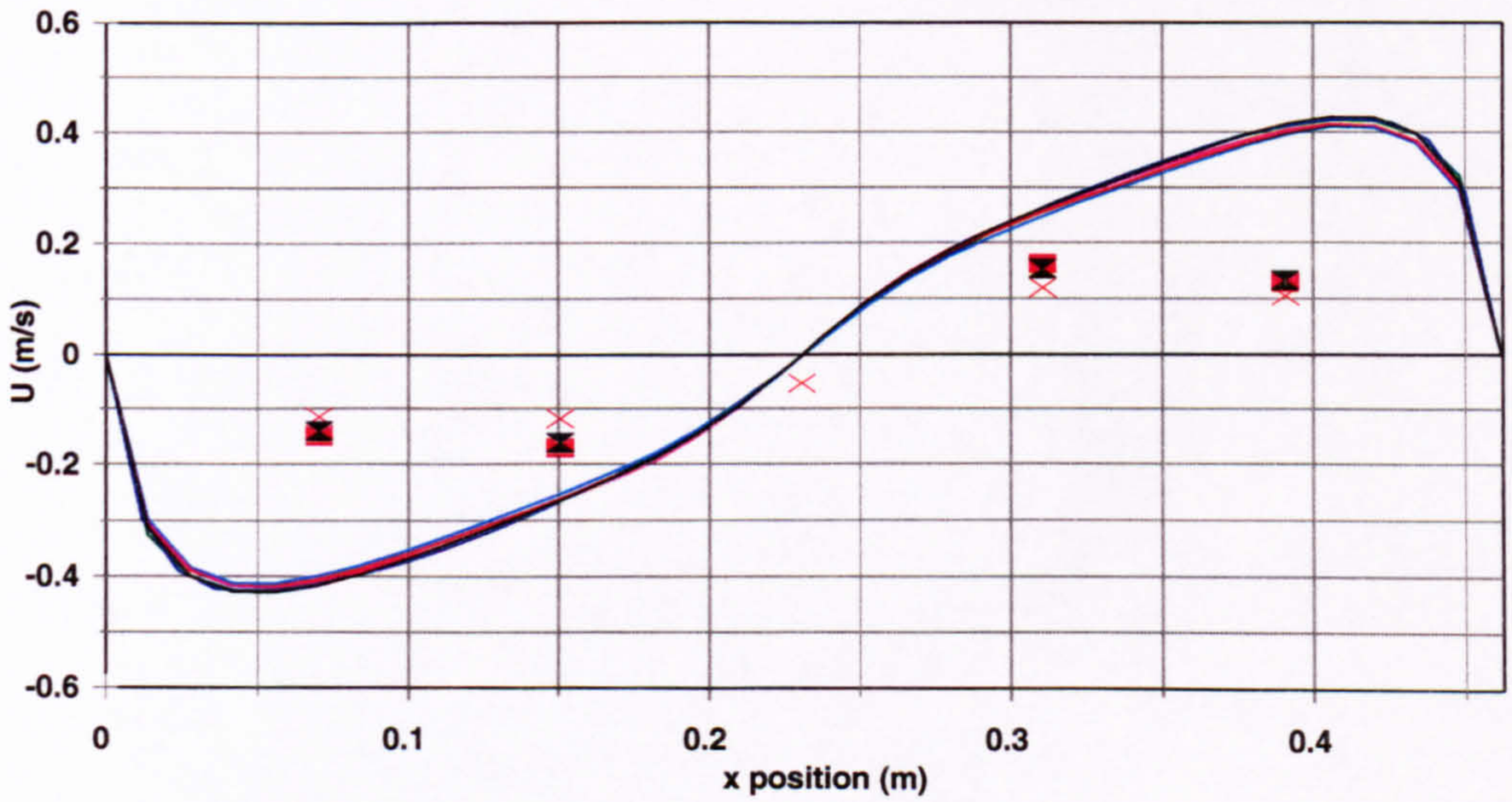


Figure 7.3-6b Comparison between calculated and experimental values of U velocity at y = 0.633 m (from invert of chamber). Flowrate = 4.38 l/s

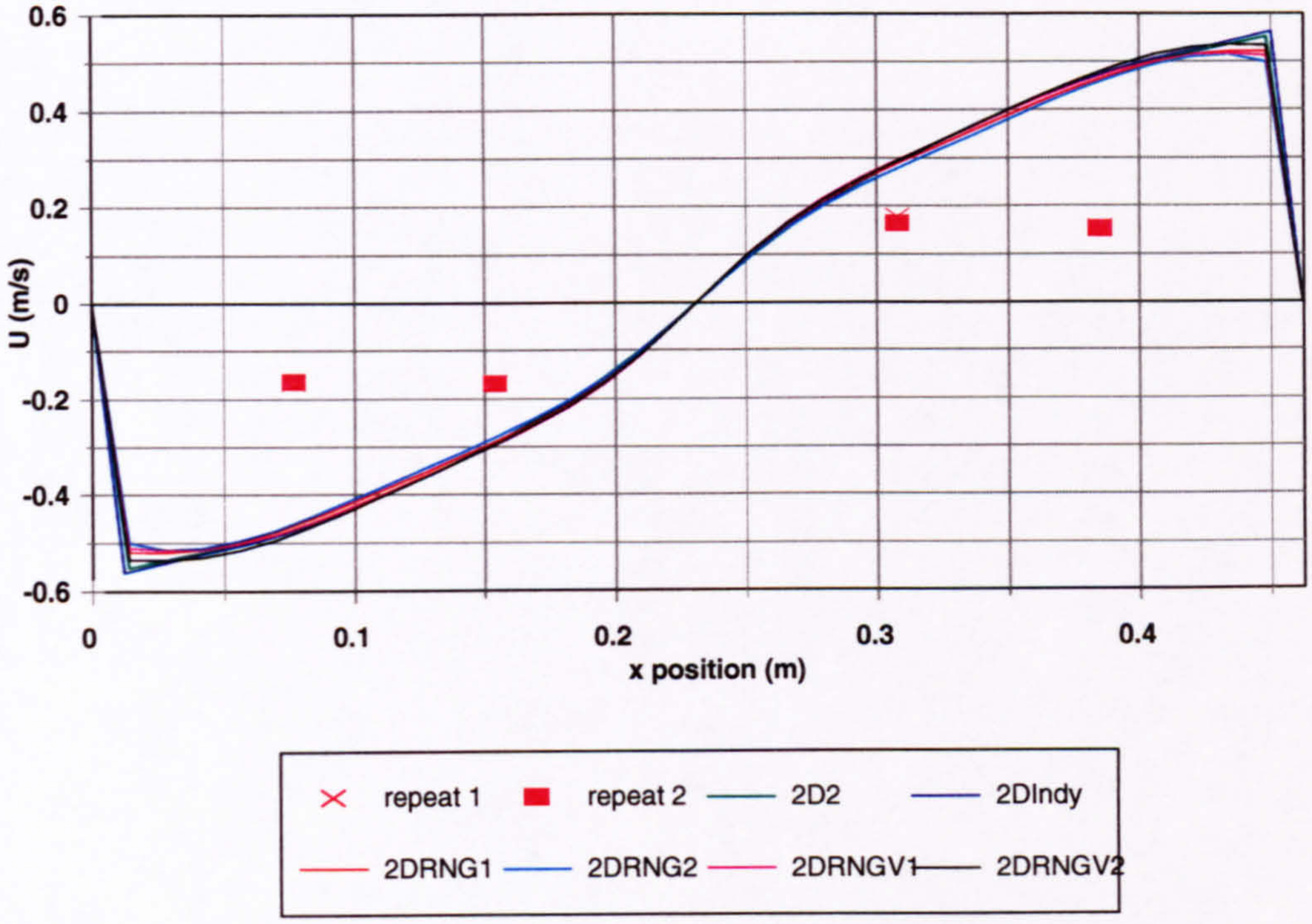


Figure 7.3-6c Comparison between calculated and experimental values of U velocity at y = 0.643 m (from invert of chamber). Flowrate = 4.38 l/s

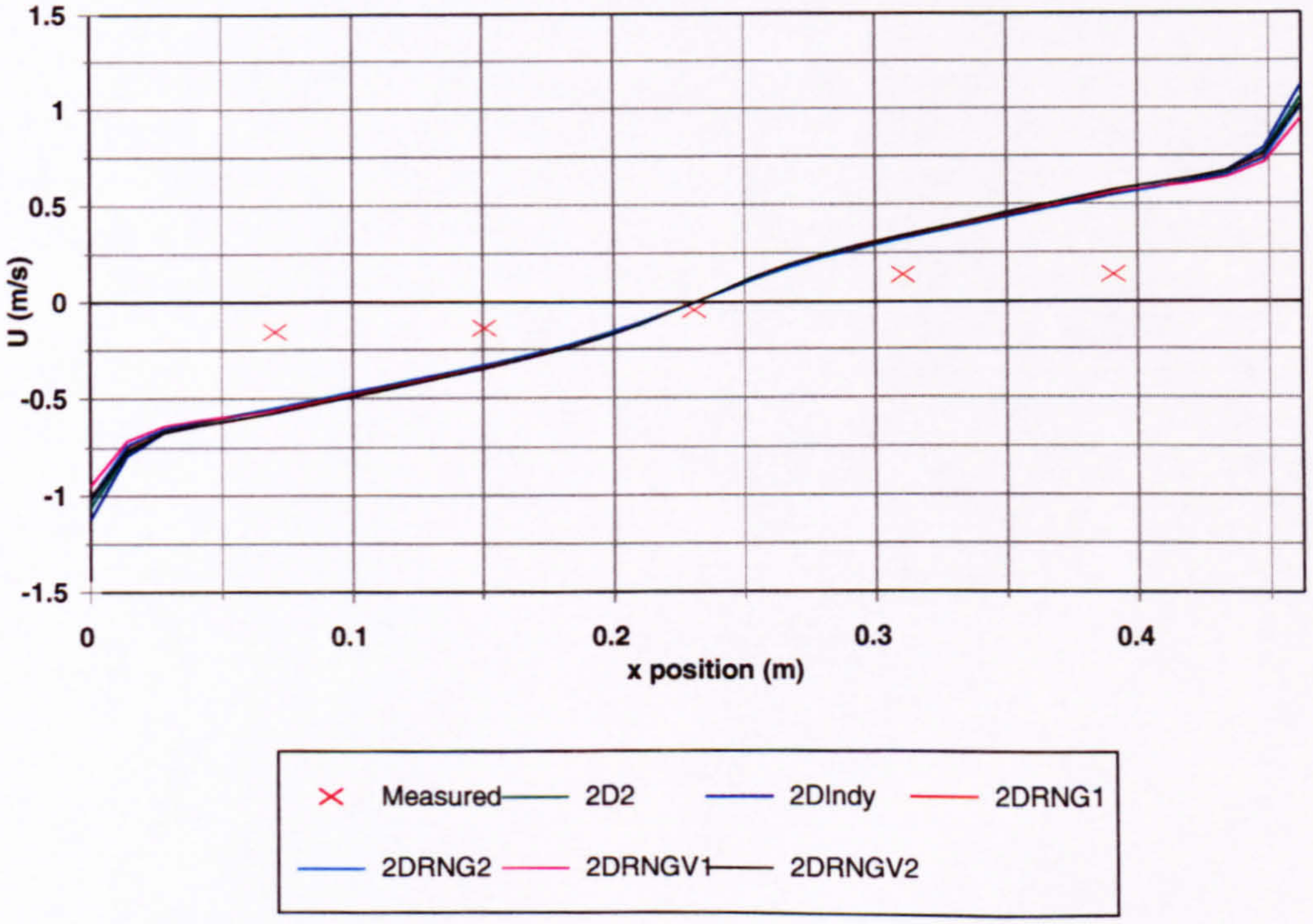


Figure 7.3-6d Comparison between calculated and experimental values of U velocity at y = 0.653 m (from invert of chamber). Flowrate = 4.38 l/s

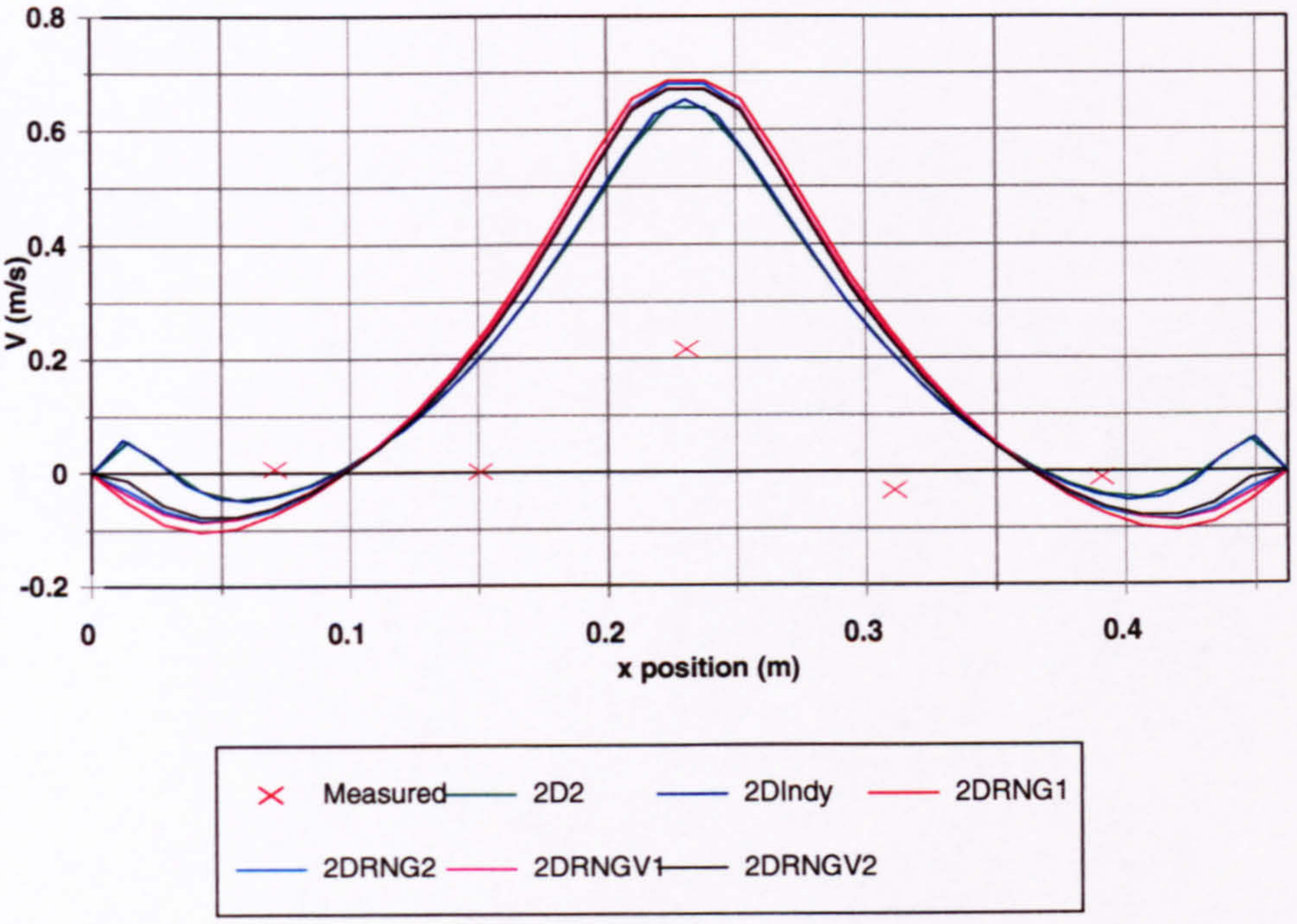


Figure 7.3-6e Comparison between calculated and experimental values of V velocity at y = 0.628 m (from invert of chamber). Flowrate = 4.38 l/s

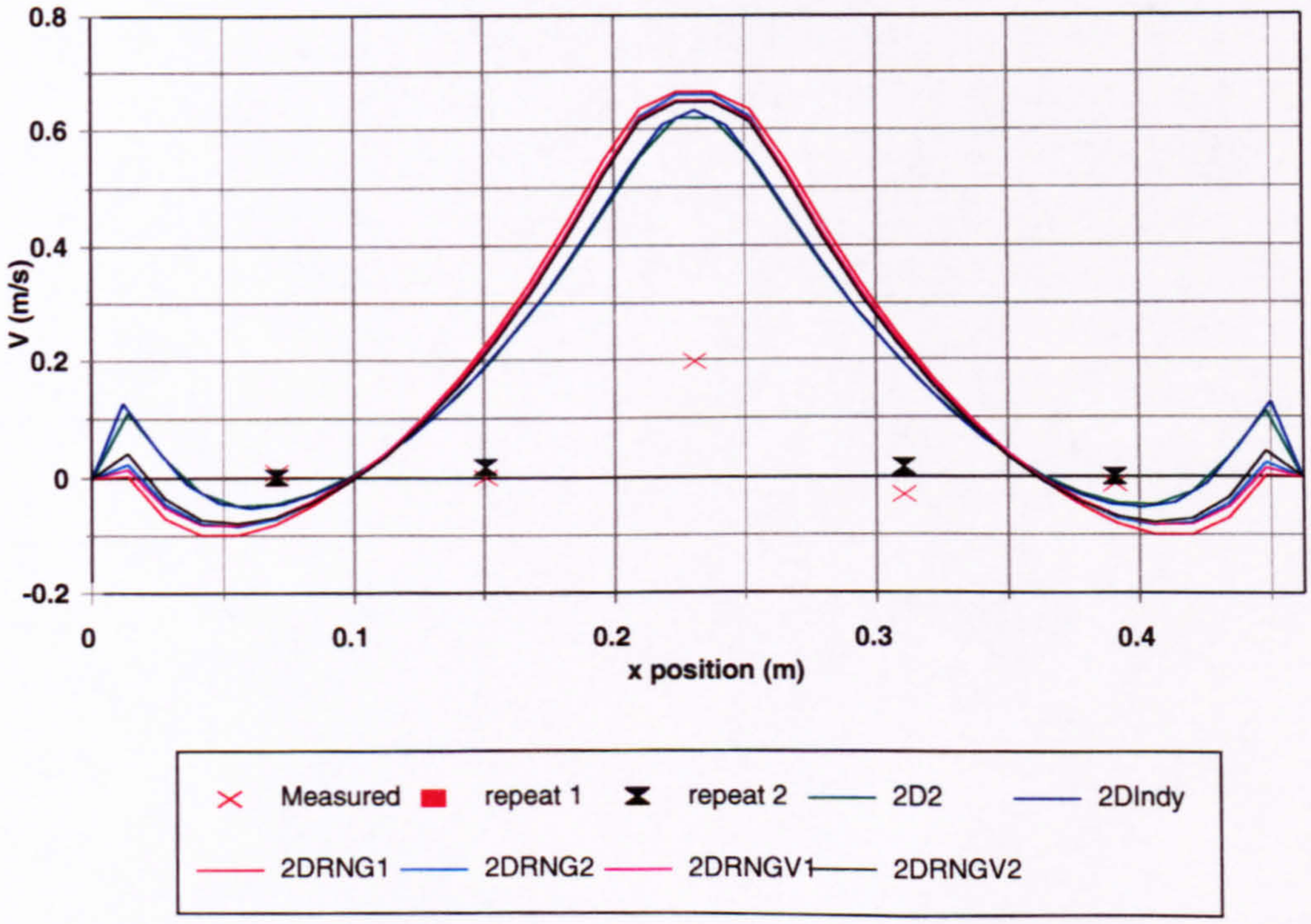


Figure 7.3-6f Comparison between calculated and experimental values of V velocity at y = 0.633 m (from invert of chamber). Flowrate = 4.38 l/s

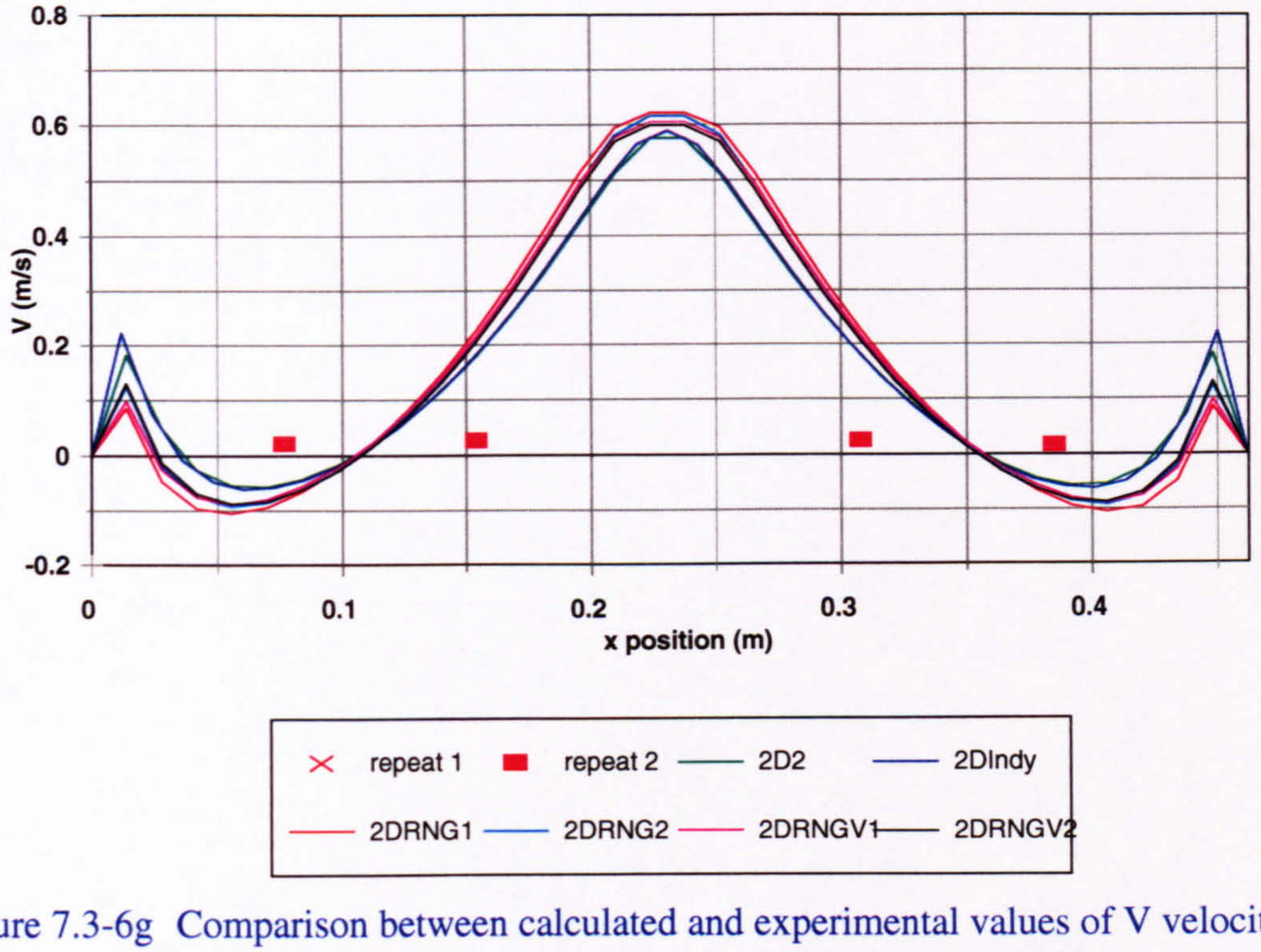


Figure 7.3-6g Comparison between calculated and experimental values of V velocity at y = 0.643 m (from invert of chamber). Flowrate = 4.38 l/s

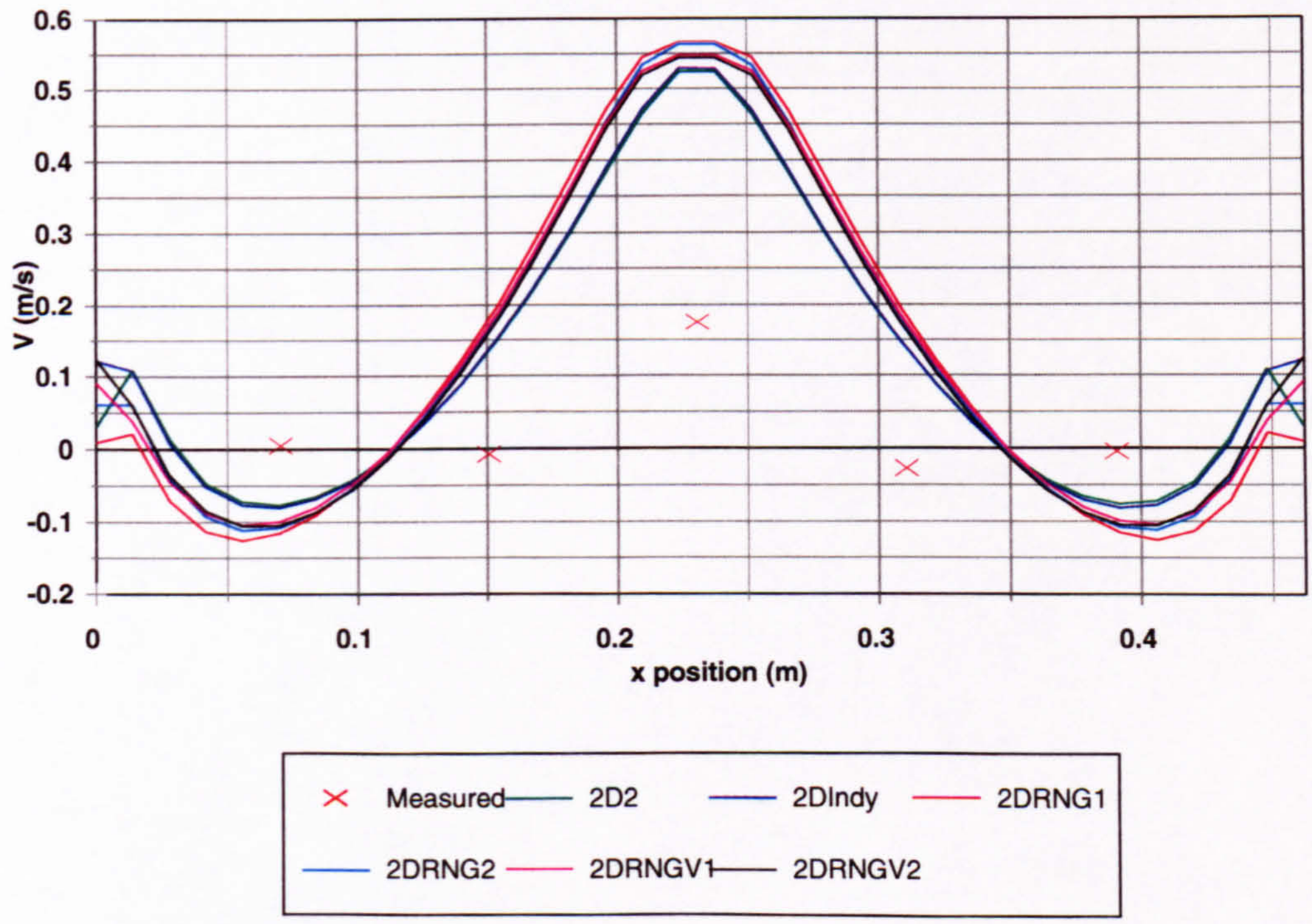


Figure 7.3-6h Comparison between calculated and experimental values of V velocity at y = 0.653 m (from invert of chamber). Flowrate = 4.38 l/s

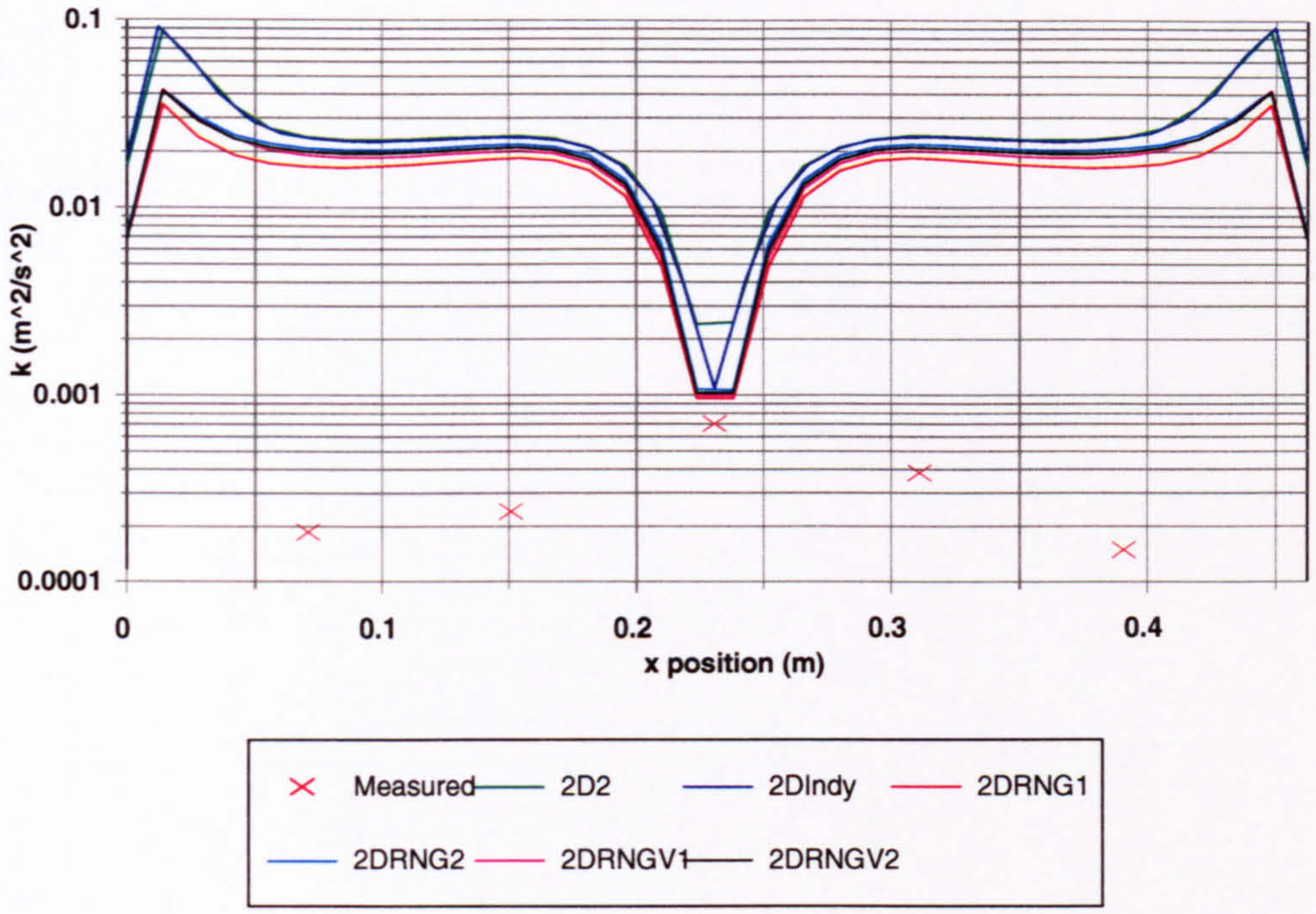


Figure 7.3-6i Comparison between calculated and measured values of turbulent kinetic energy at y = 0.628 m. Flowrate = 4.38 l/s

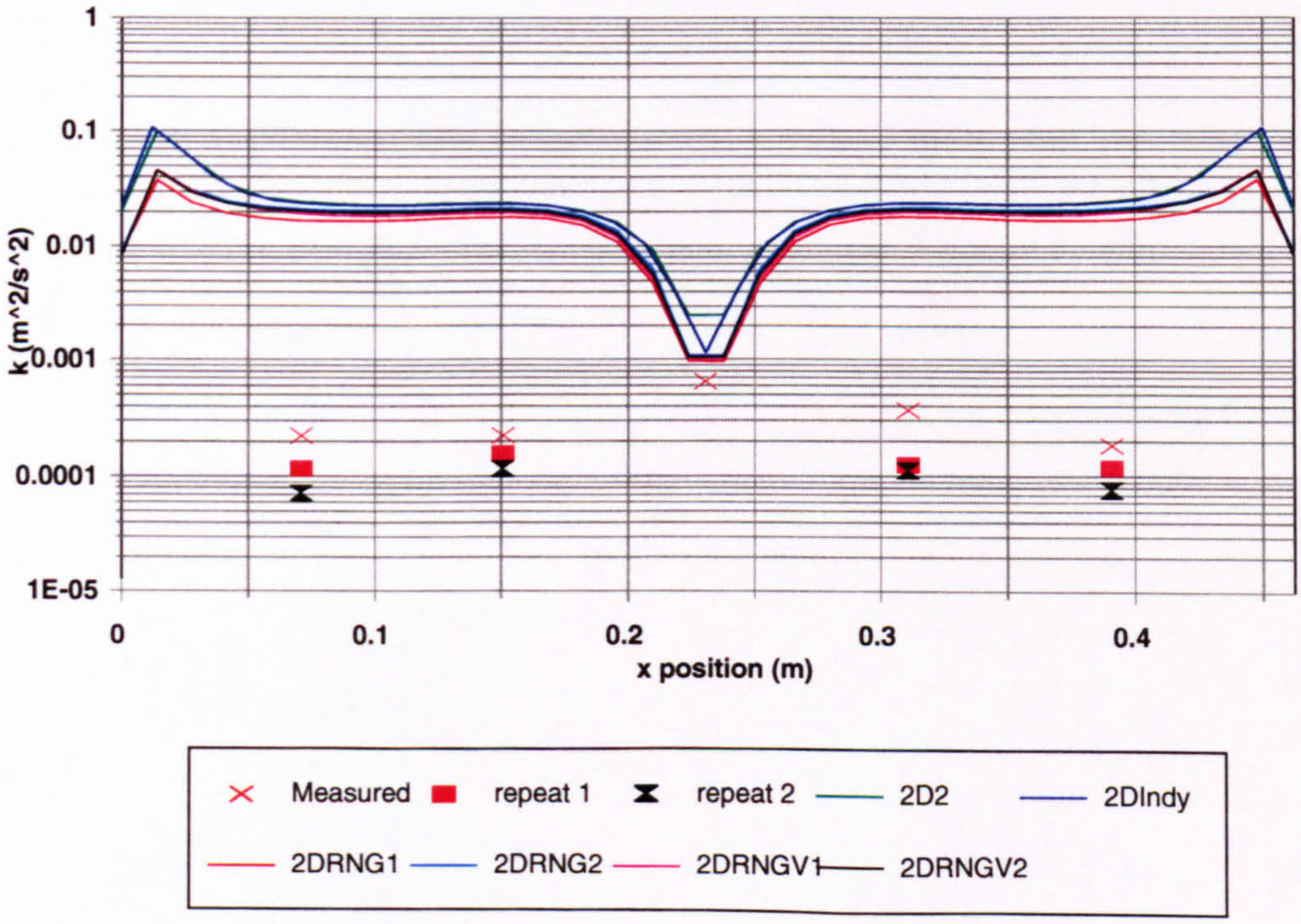


Figure 7.3-6j Comparison between calculated and measured values of turbulent kinetic energy at y = 0.633 m. Flowrate = 4.38 l/s

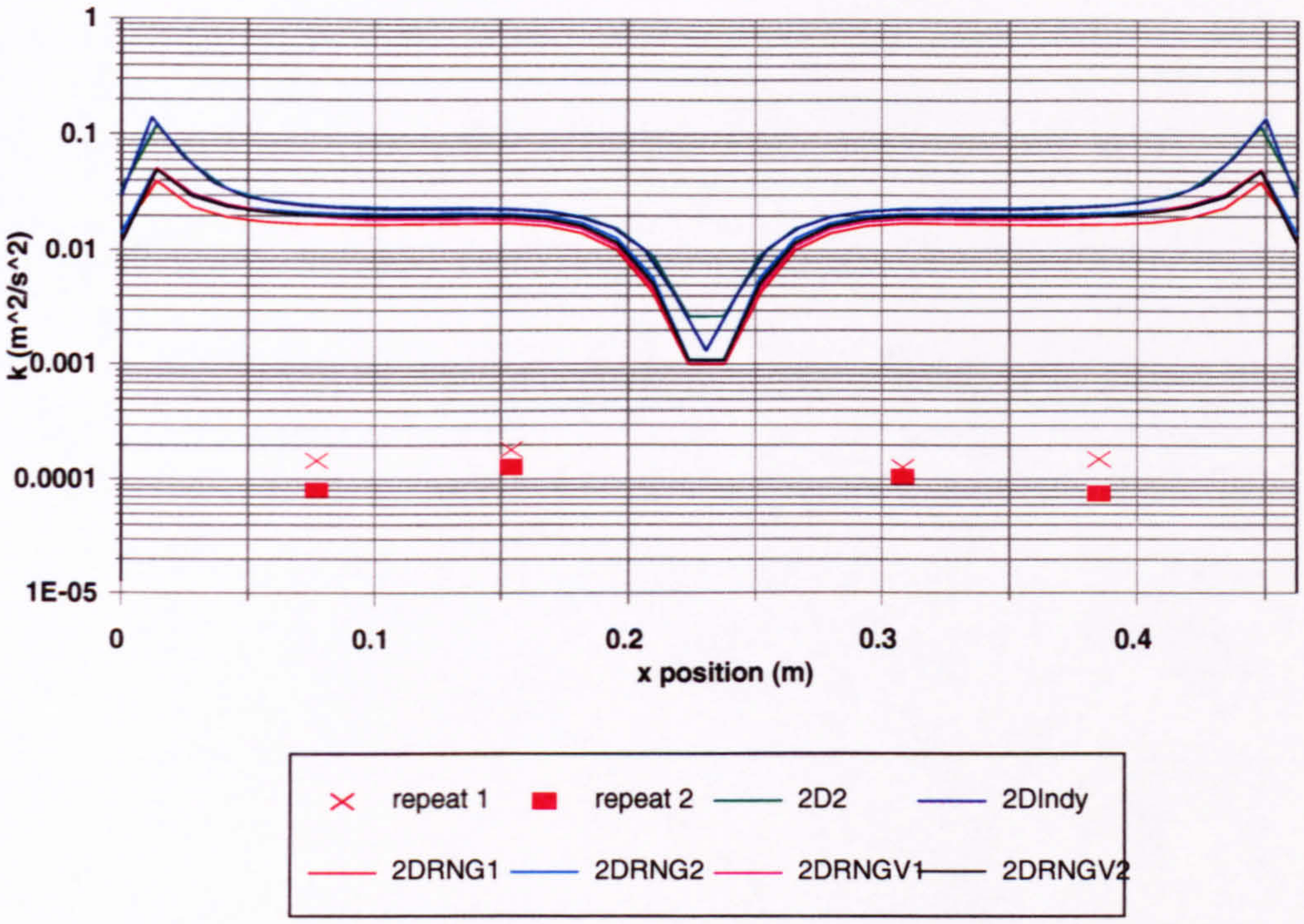


Figure 7.3-6k Comparison between calculated and experimental values of turbulent kinetic energy at y = 0.643 m. Flowrate = 4.38 l/s

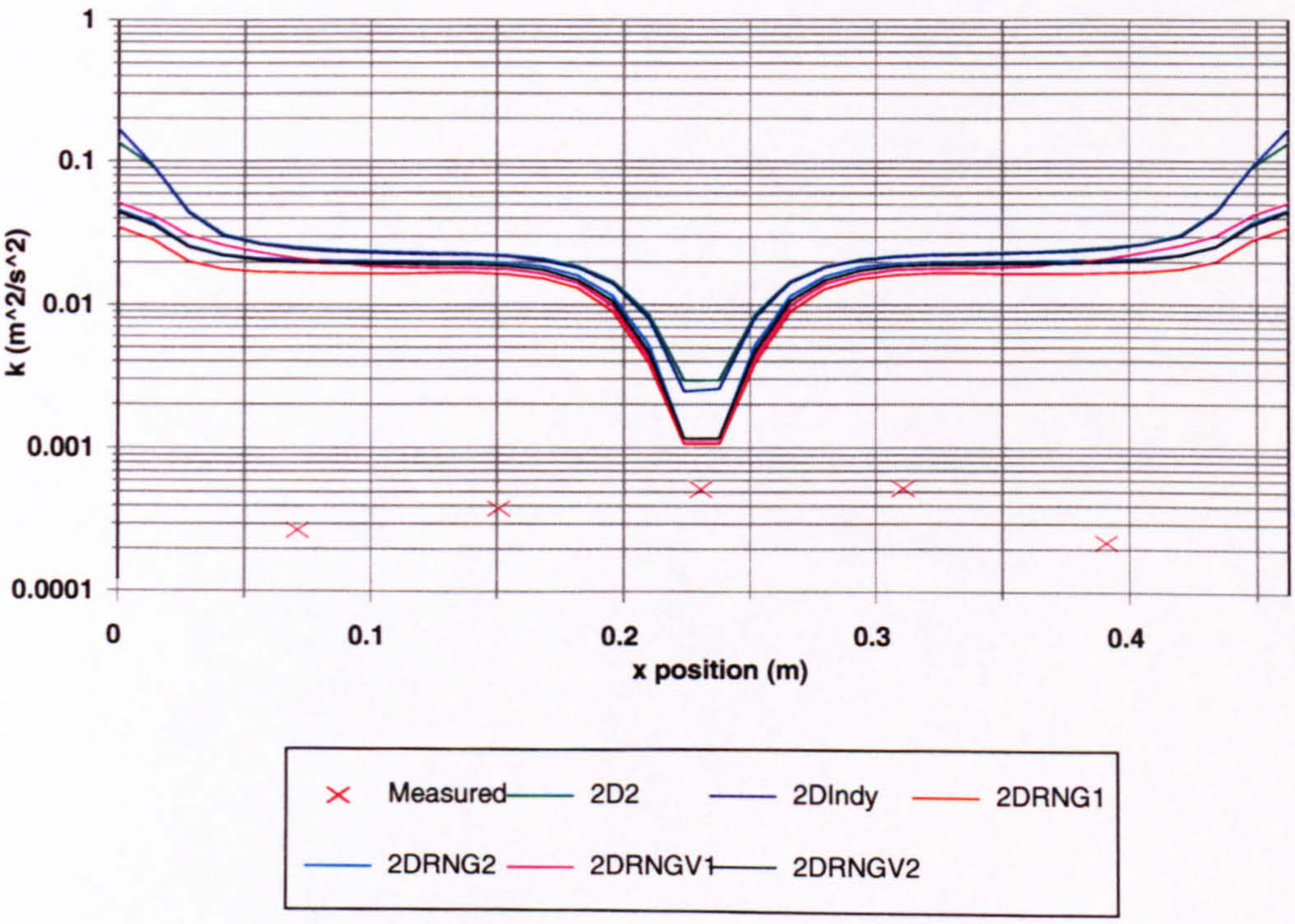


Figure 7.3-6l Comparison between calculated and experimental values of turbulent kinetic energy at y = 0.653 m. Flowrate = 4.38 l/s

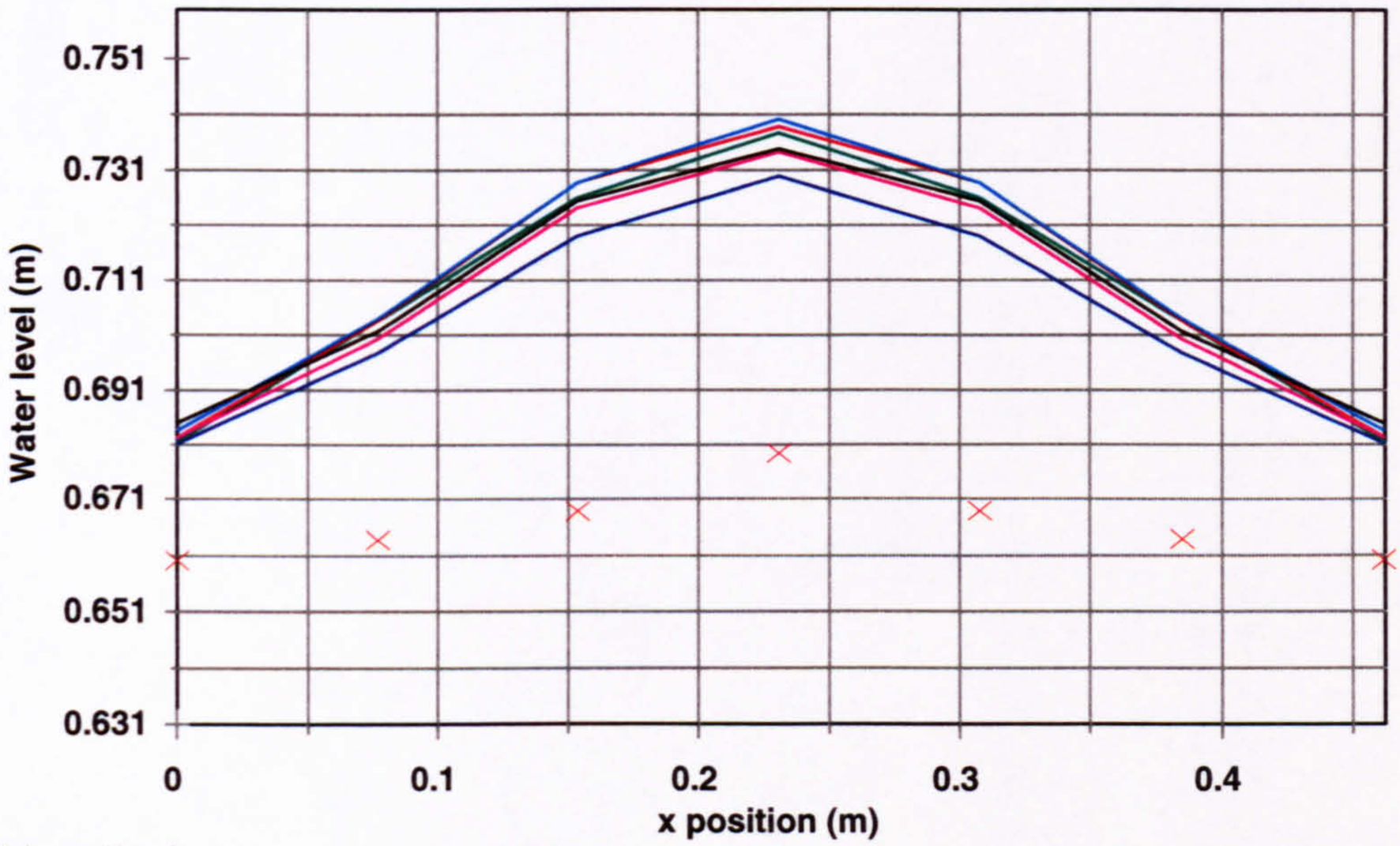


Figure 7.3-6m Comparison between calculated and measured values of water levels in chamber. Flowrate = 4.38 l/s

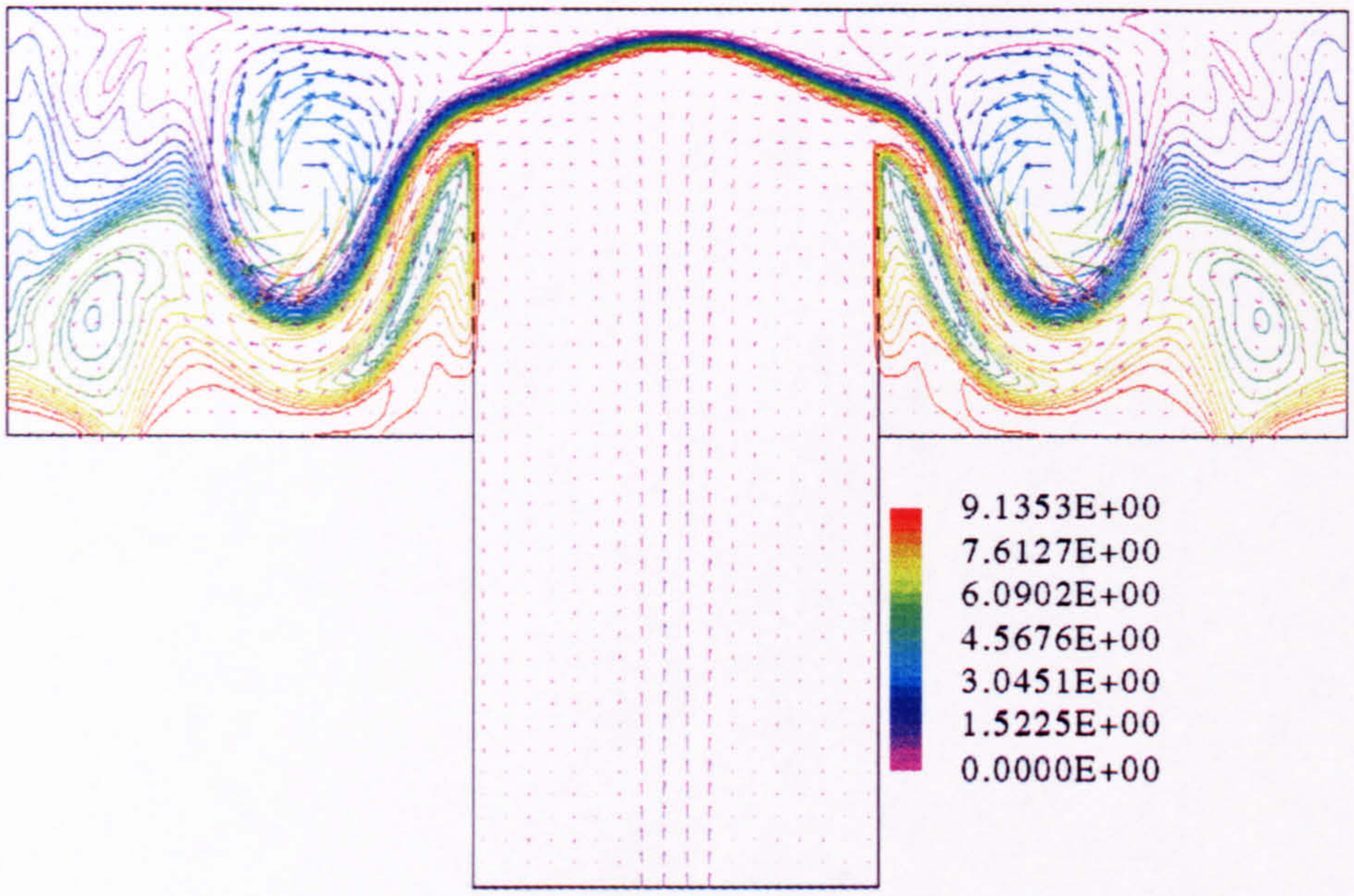


Figure 7.3-7a Flow field developed within chamber for 2DRNG1. (Free surface is represented by volume fraction contours). Flowrate = 4.38 l/s. Mass residuals = 1 x 10^{-5} kg/s (3 fold reduction in residuals). Van Leer differencing scheme and RNG k-ε model used. Surface sharpening algorithm not used.

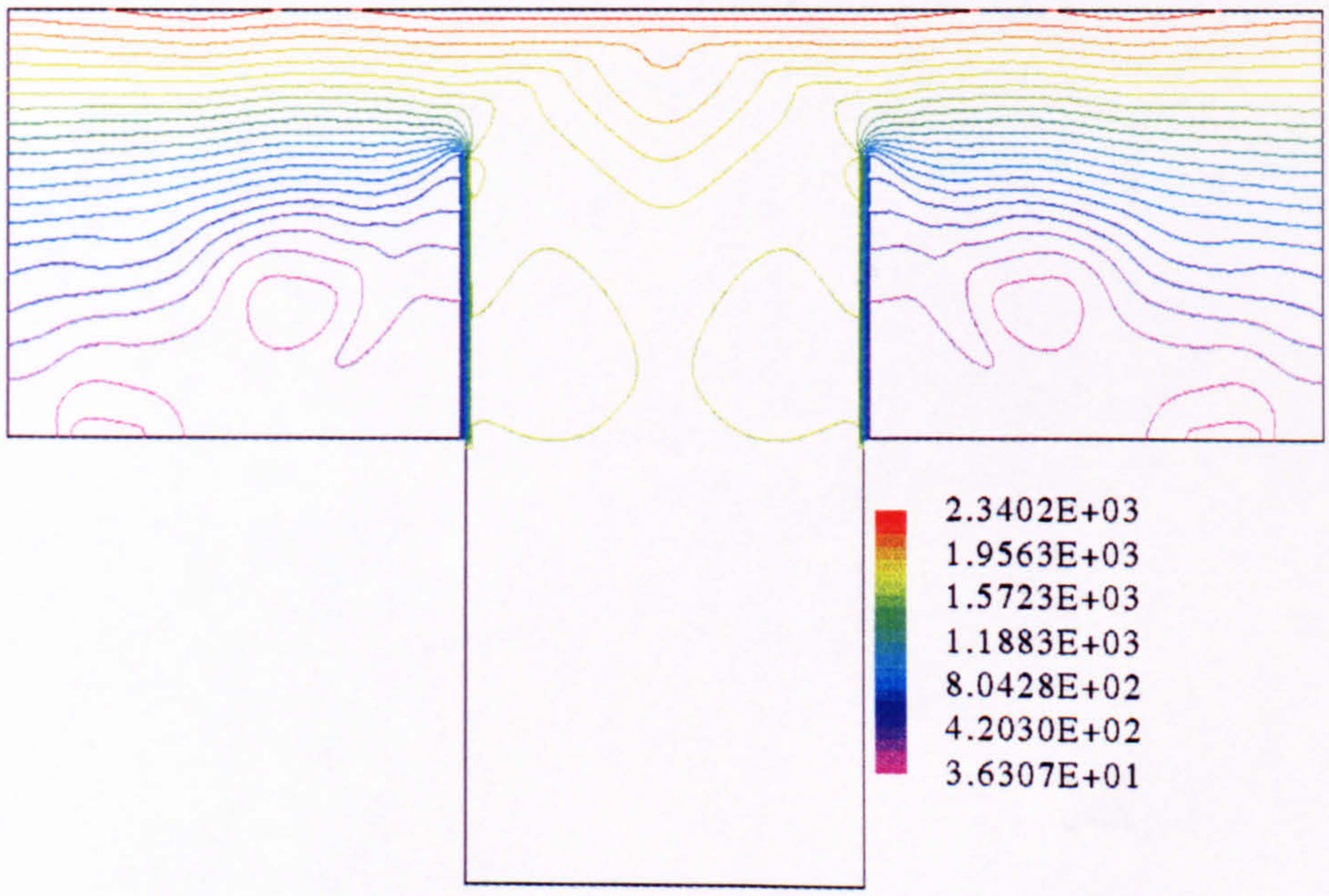


Figure 7.3-7b Pressure contour plot of 2DRNG1.

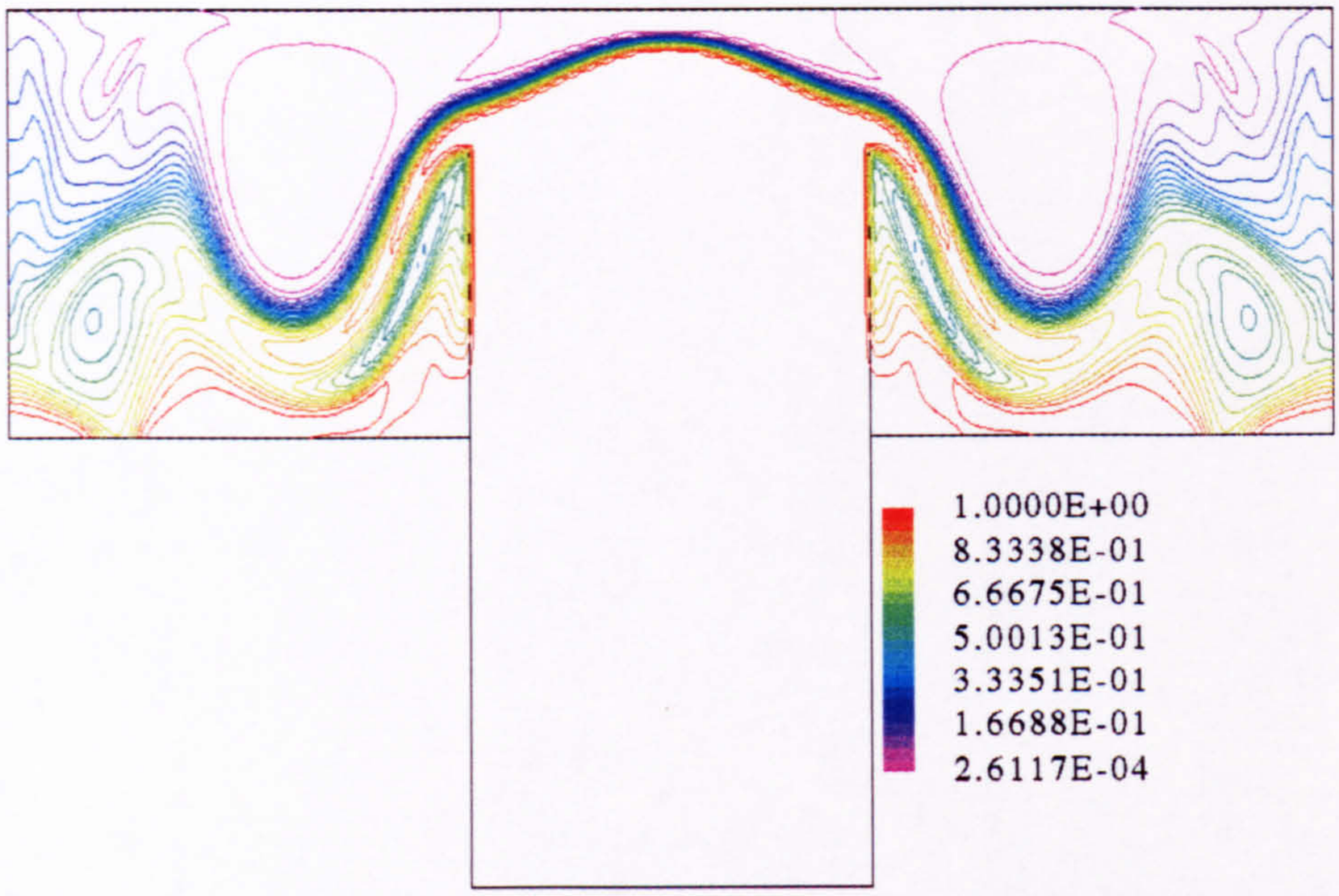


Figure 7.3-7c Volume fraction contours of water for 2DRNG1. Value of 1.0 represents water, 0.0 is air. Free surface has a value of 0.5.

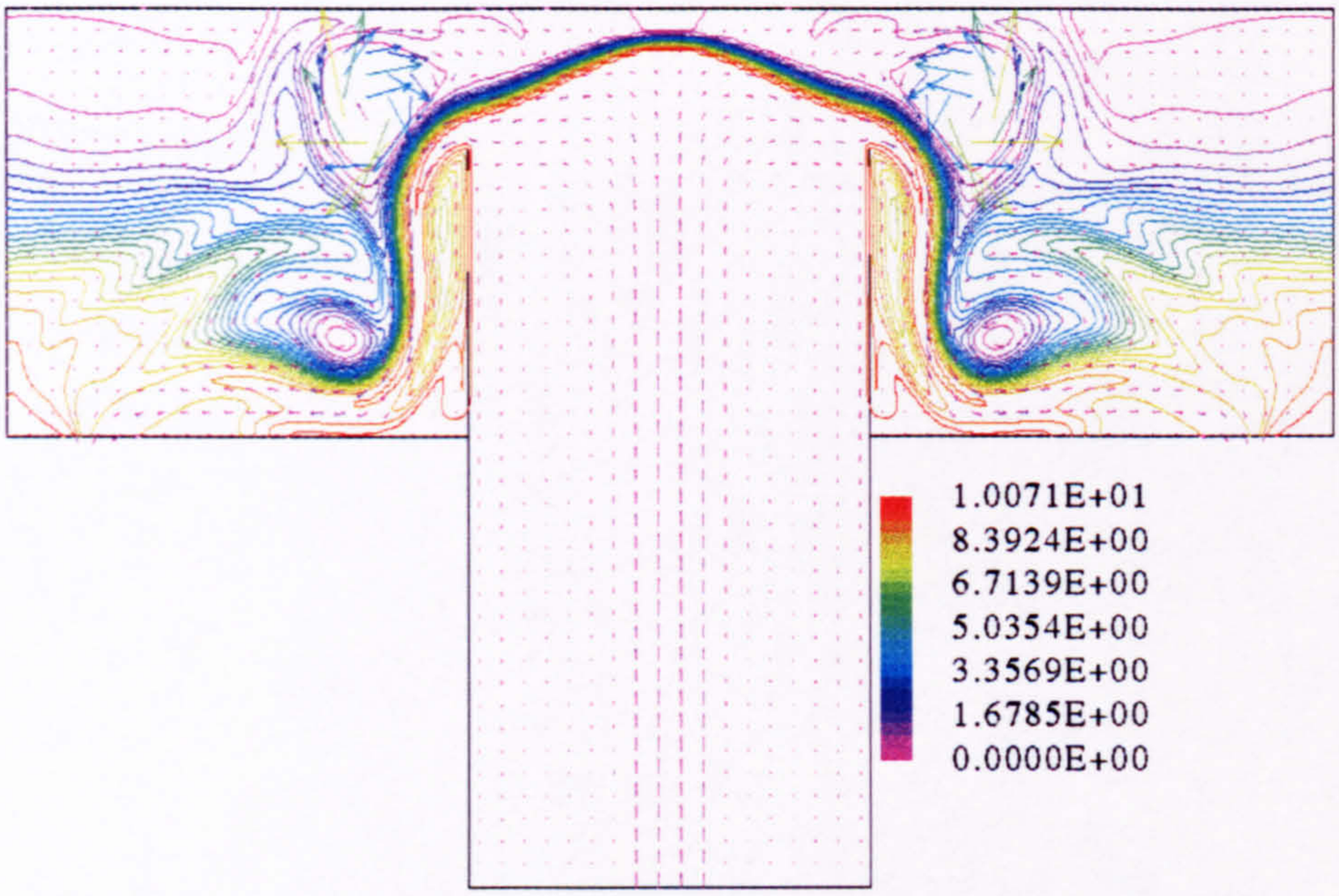


Figure 7.3-8a Flow field developed within chamber for 2DRNG2. (Flowrate is represented by volume fraction contours). Flowrate = 4.38 l/s. Mass residuals = 1 x 10^{-7} kg/s (5 fold reduction in mass residuals). Van Leer differencing and RNG k-ε turbulence model used. Surface sharpening algorithm not used.

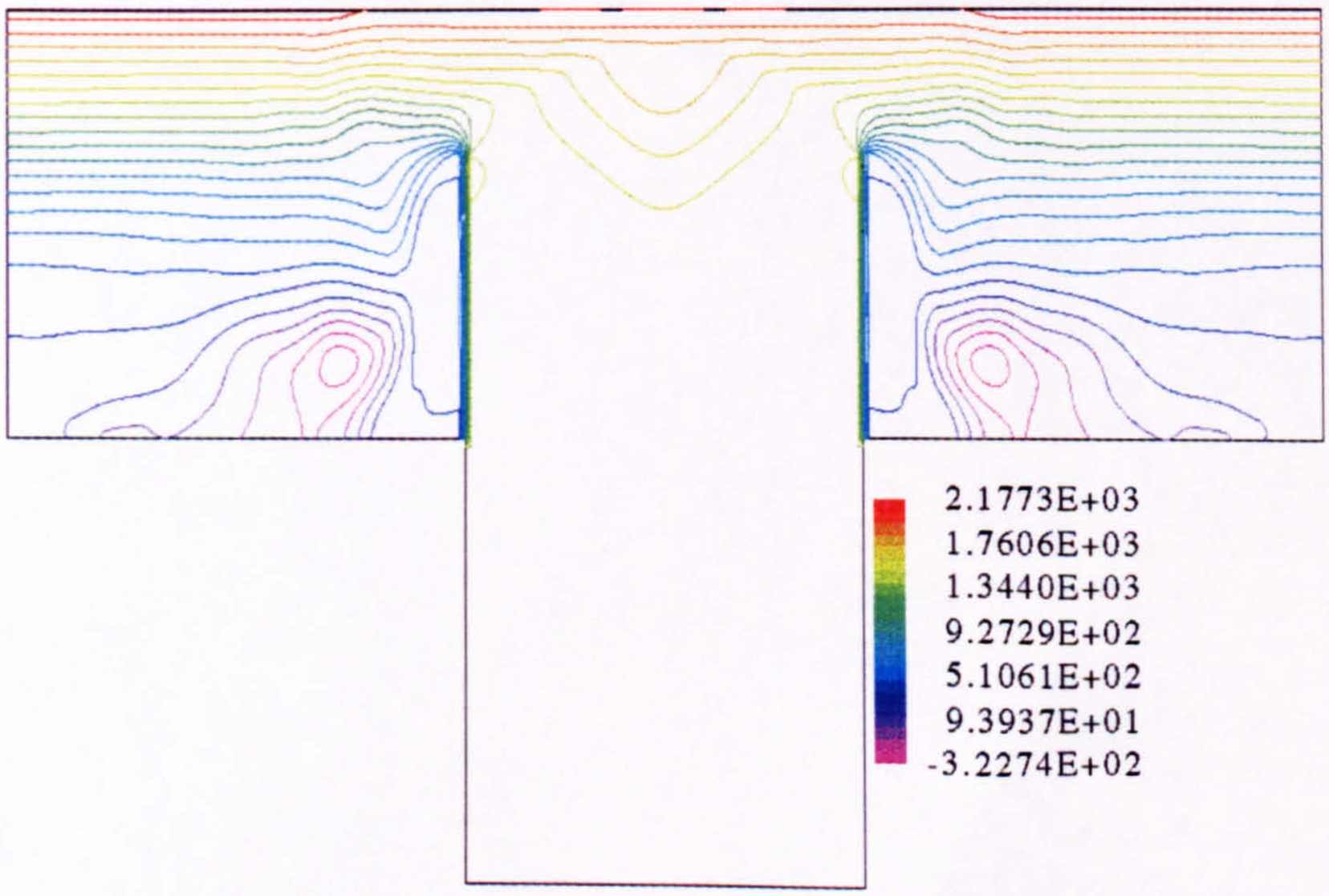


Figure 7.3-8b Pressure contour plot for 2DRNG2

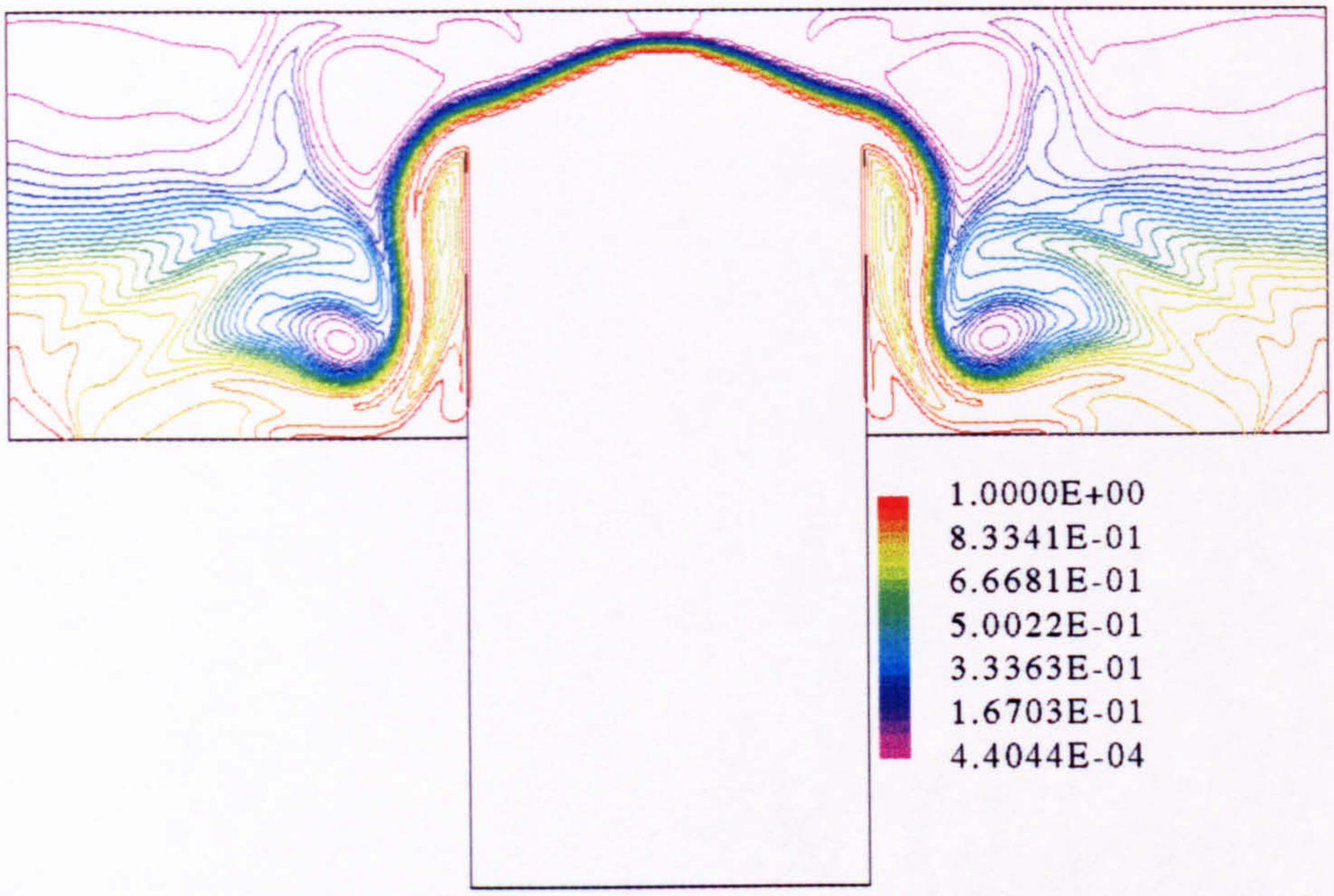


Figure 7.3-8c Volume fraction contours of water for 2DRNG2. Value of 1.0 represents water, air is 0.0. Free surface has a value of 0.5.

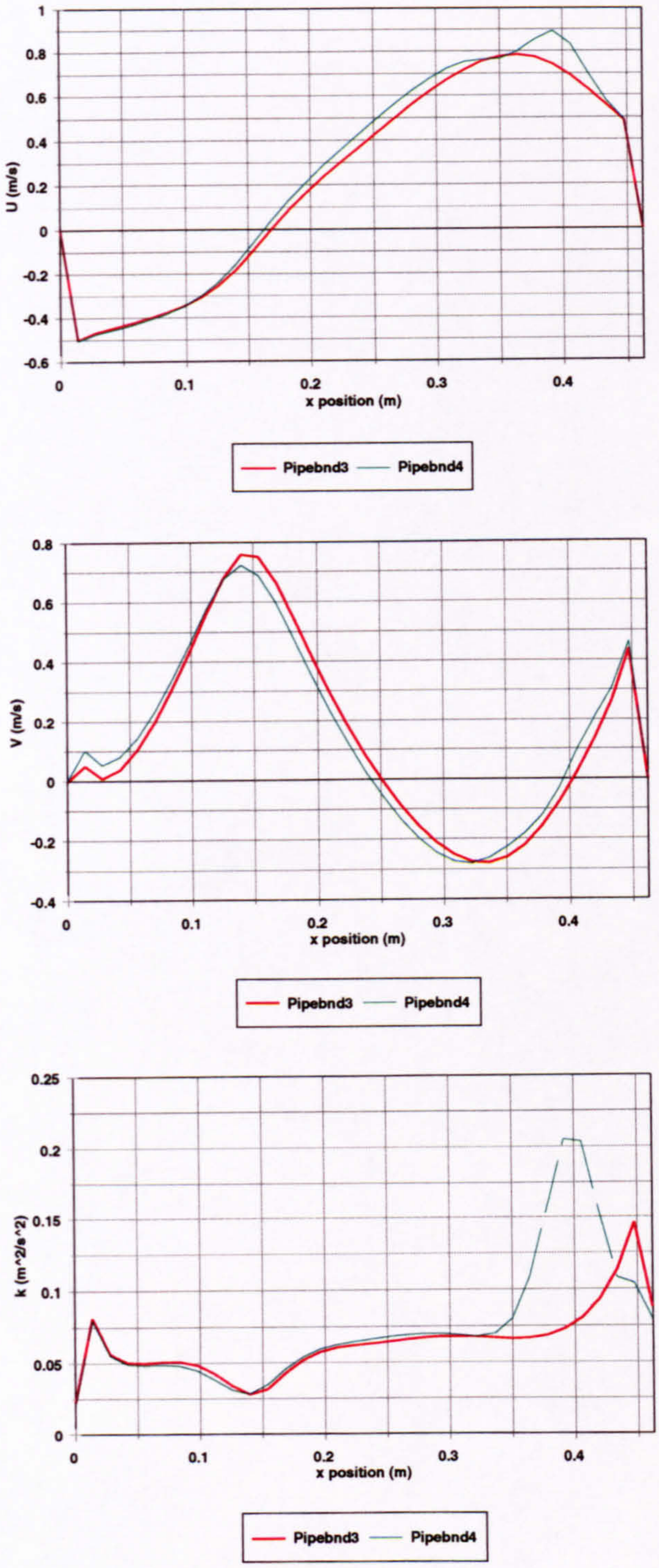


Figure 7.3-9a Comparisons of calculated velocities and turbulence for Pipebnd3 and Pipebnd4, at y = 0.628 m. A 2D pipe bend (2.12 hydraulic diameters from invert of chamber) is coupled to the chamber.

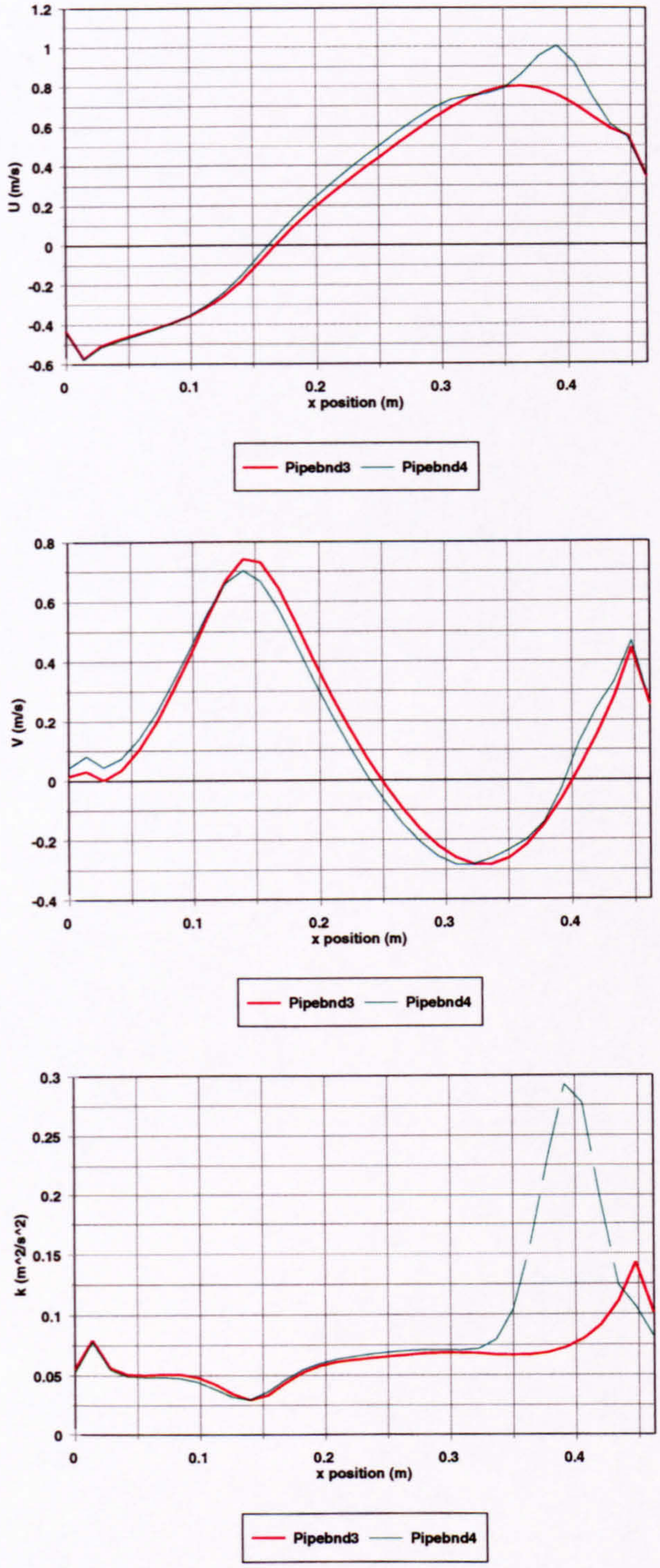


Figure 7.3-9b Comparisons of calculated velocities and turbulence at y = 0.631 m. A 2D pipe bend (2.12 hydraulic diameters from invert of chamber) is coupled to the chamber.

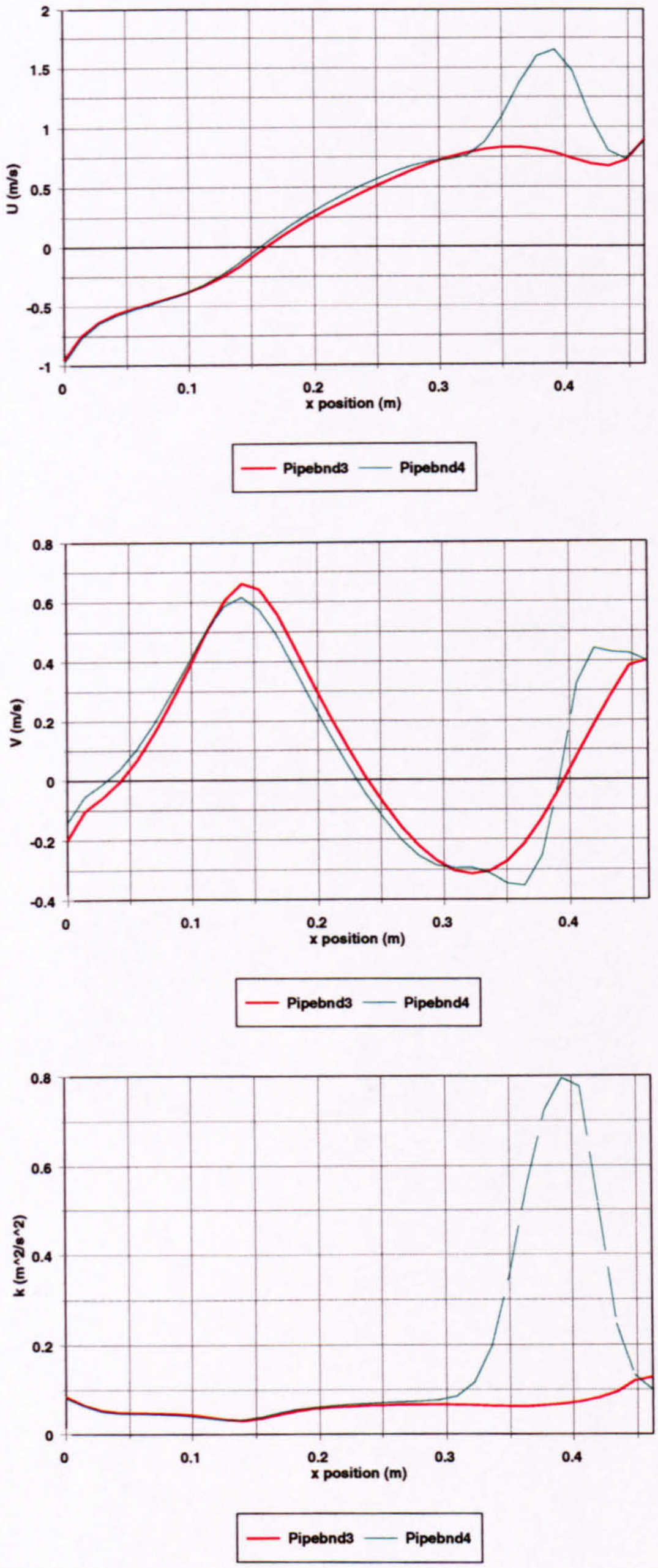


Figure 7.3-9c Comparisons of calculated velocities and turbulence at y = 0.643 m. A 2D pipe bend (2.12 hydraulic diameters from invert of chamber) is coupled to the chamber.

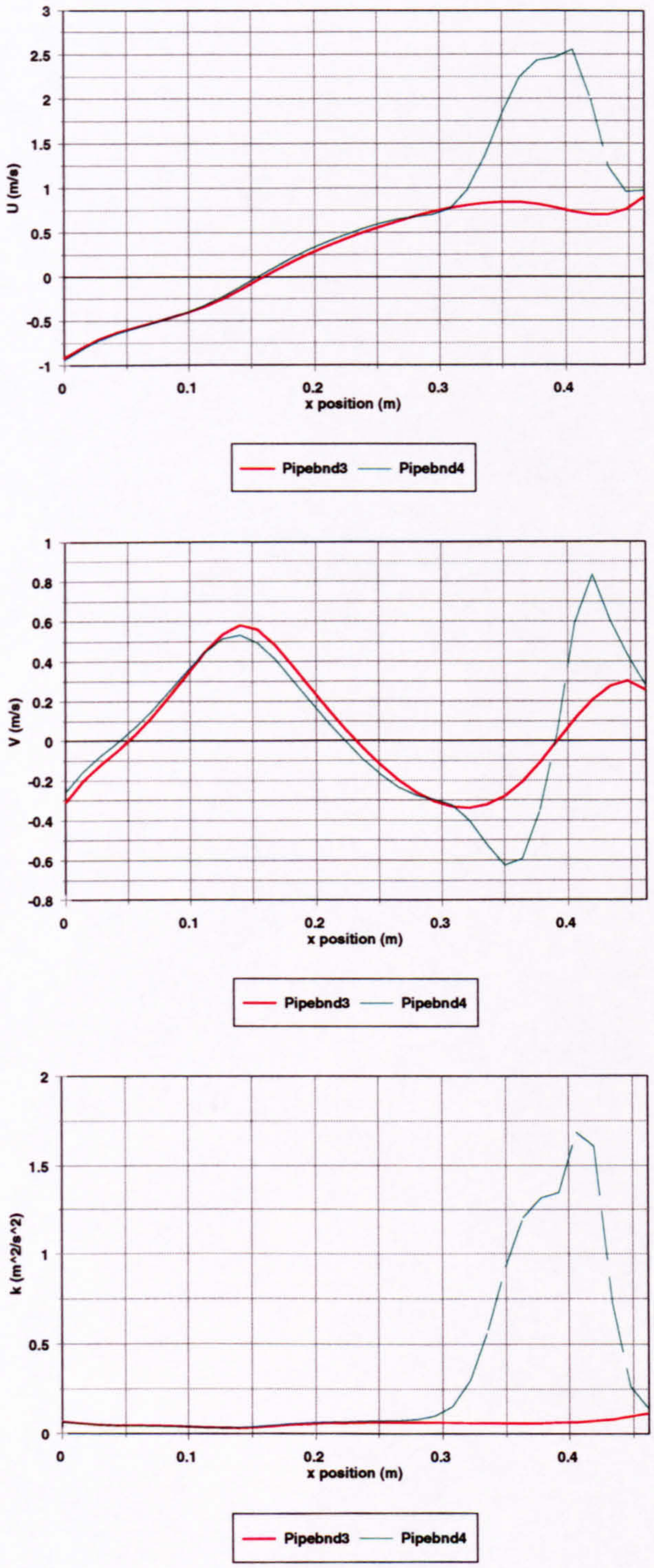


Figure 7.3-9d Comparisons of calculated velocities and turbulence at y = 0.653 m. A 2D pipe bend (2.12 hydraulic diameters from invert of chamber) is coupled to the chamber.

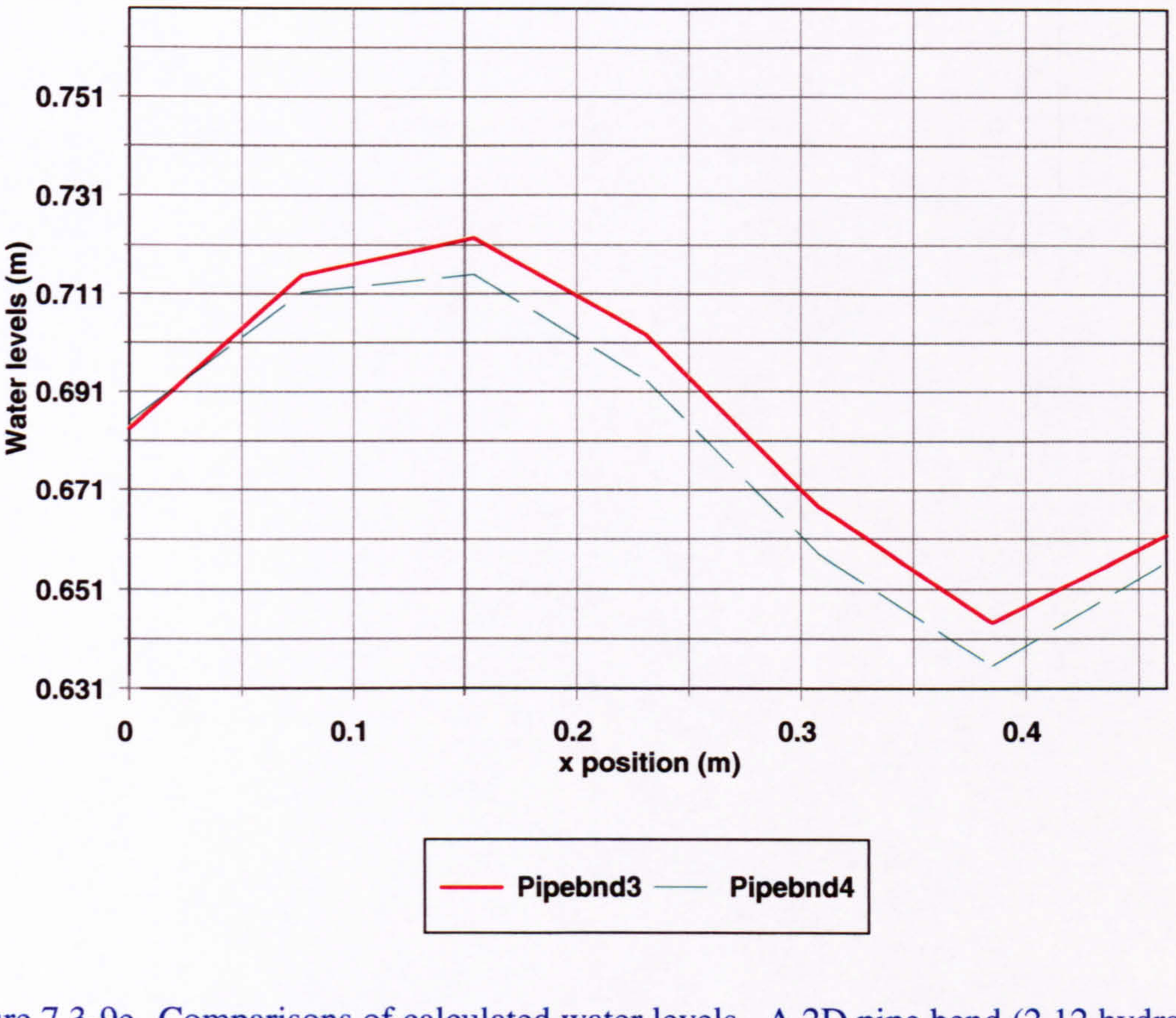


Figure 7.3-9e Comparisons of calculated water levels. A 2D pipe bend (2.12 hydraulic diameters from invert of chamber) is coupled to the chamber.

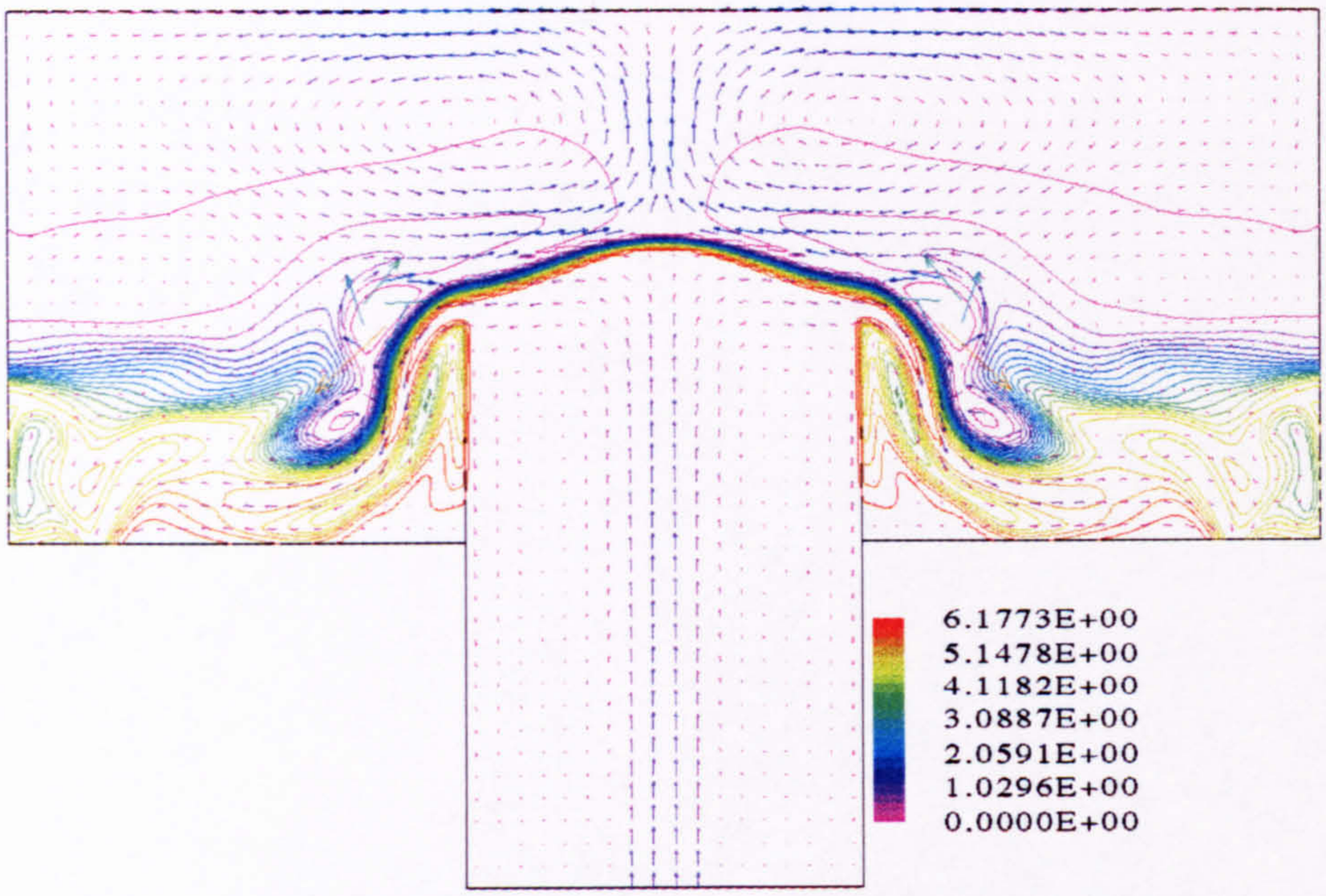


Figure 7.3-10a Velocity vector and volume fraction plot of 2DRNGV1. 2D, 2-phase transient calculations performed. Volume of domain for air phase increased. Flowrate = 4.38 l/s. Mass residuals = 1 x 10^{-5} kg/s (3 fold reduction in mass residuals). Van Leer differencing and RNG k-ε turbulence model used. Surface sharpening not used.

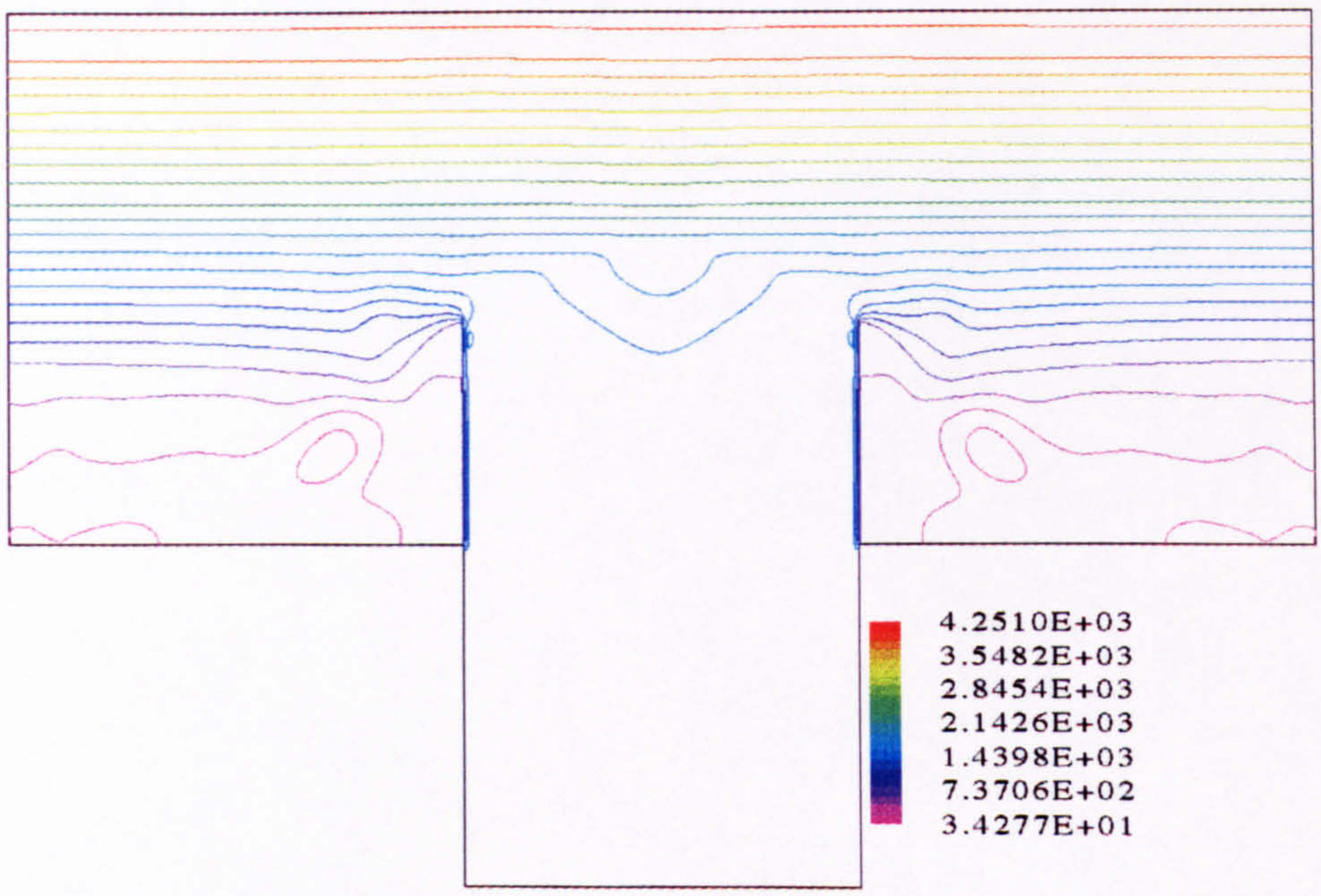


Figure 7.3-10b Pressure contours of 2DRNGV1

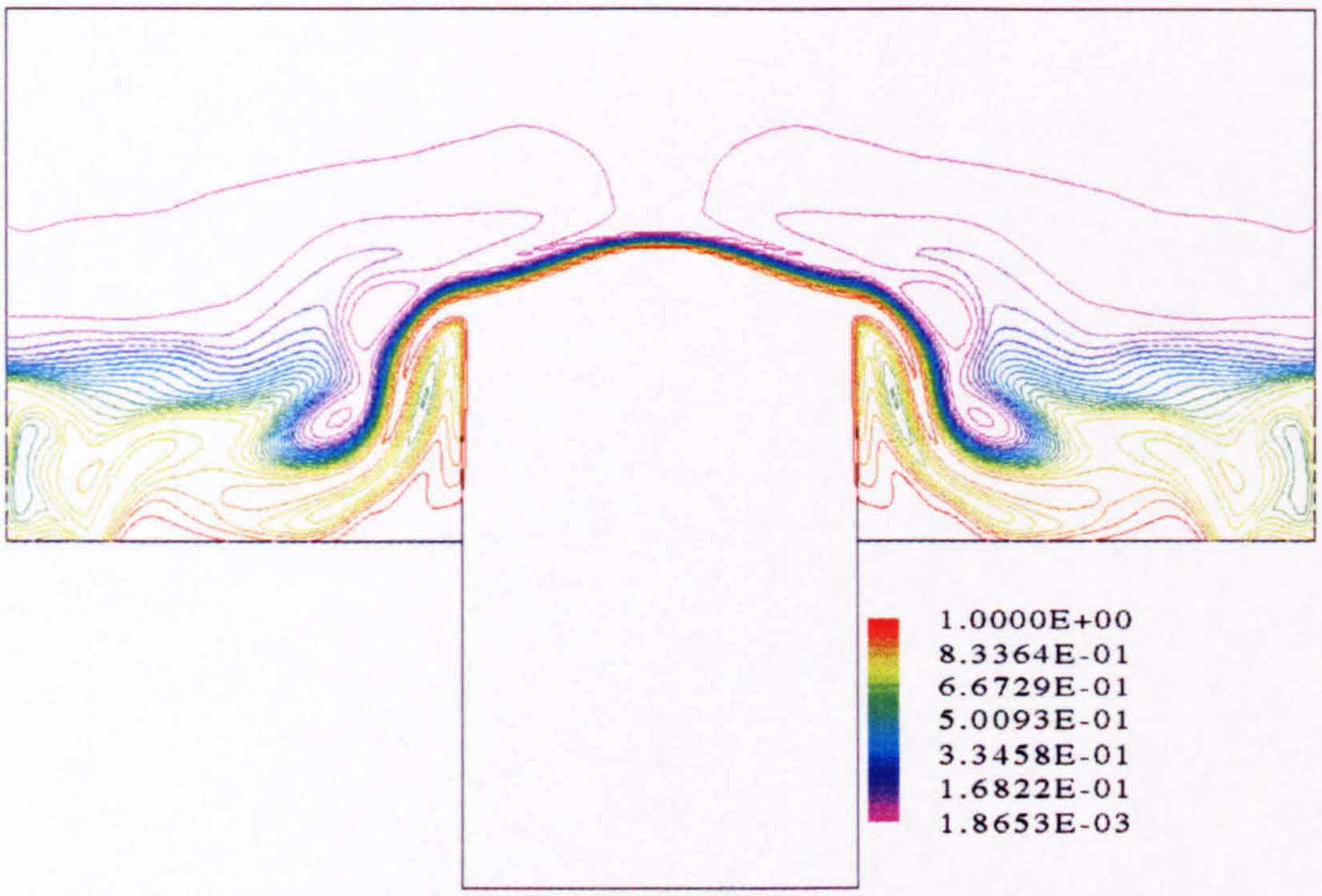


Figure 7.3-10c Volume fraction contours of water for 2DRNGV1. Value of 1.0 represents water, 0.0 is air. Free surface has a value of 0.5.

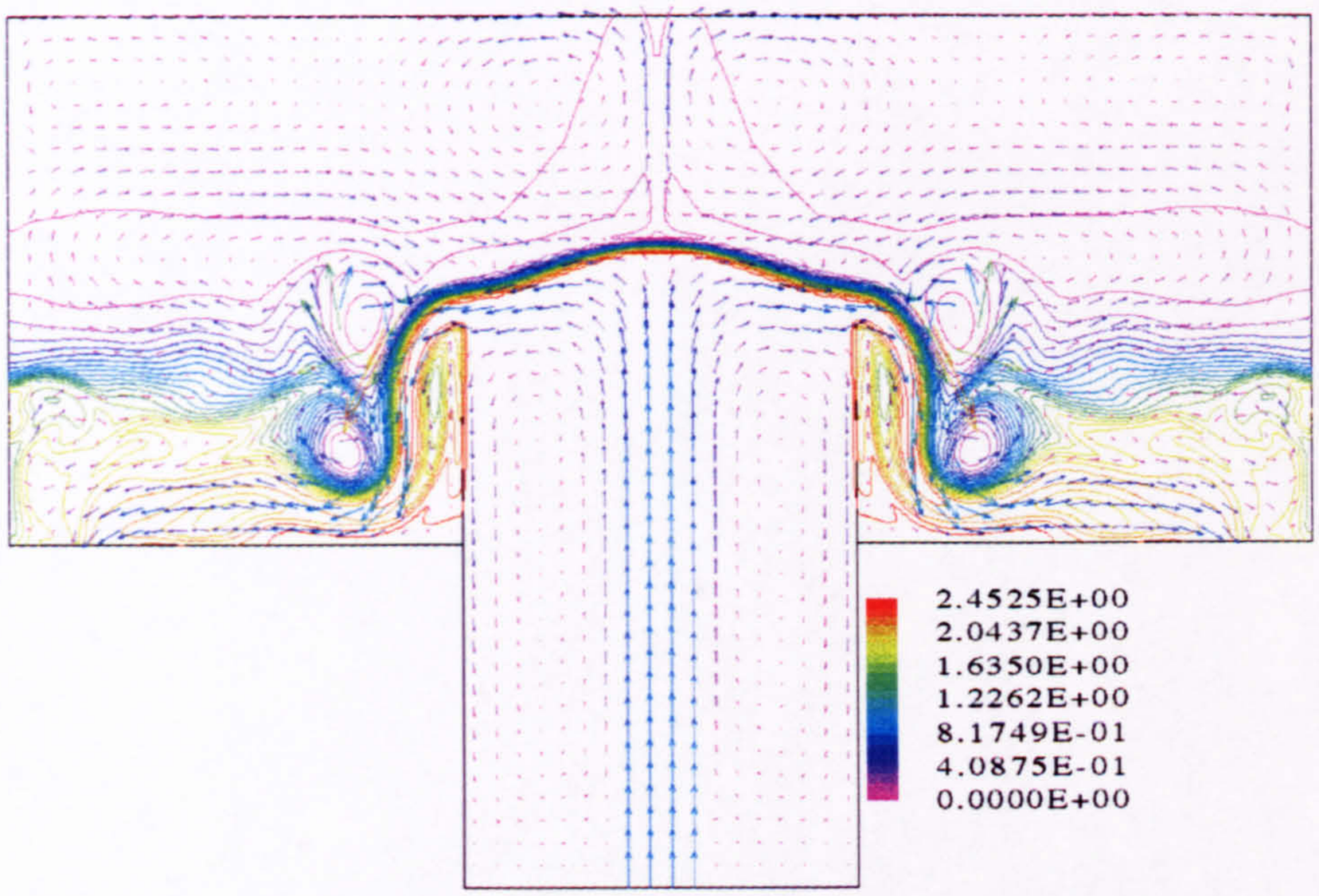


Figure 7.3-11a Velocity vector and volume fraction plot of 2DRNGV2. Flowrate = 4.38 l/s. Mass residual = 1 x 10^{-7} kg/s (5 fold reduction in mass residuals). Transient, 2-phase, 2D calculations carried out. Van Leer differencing scheme, and RNG k-ε turbulence model used. Surface sharpening algorithm not used.

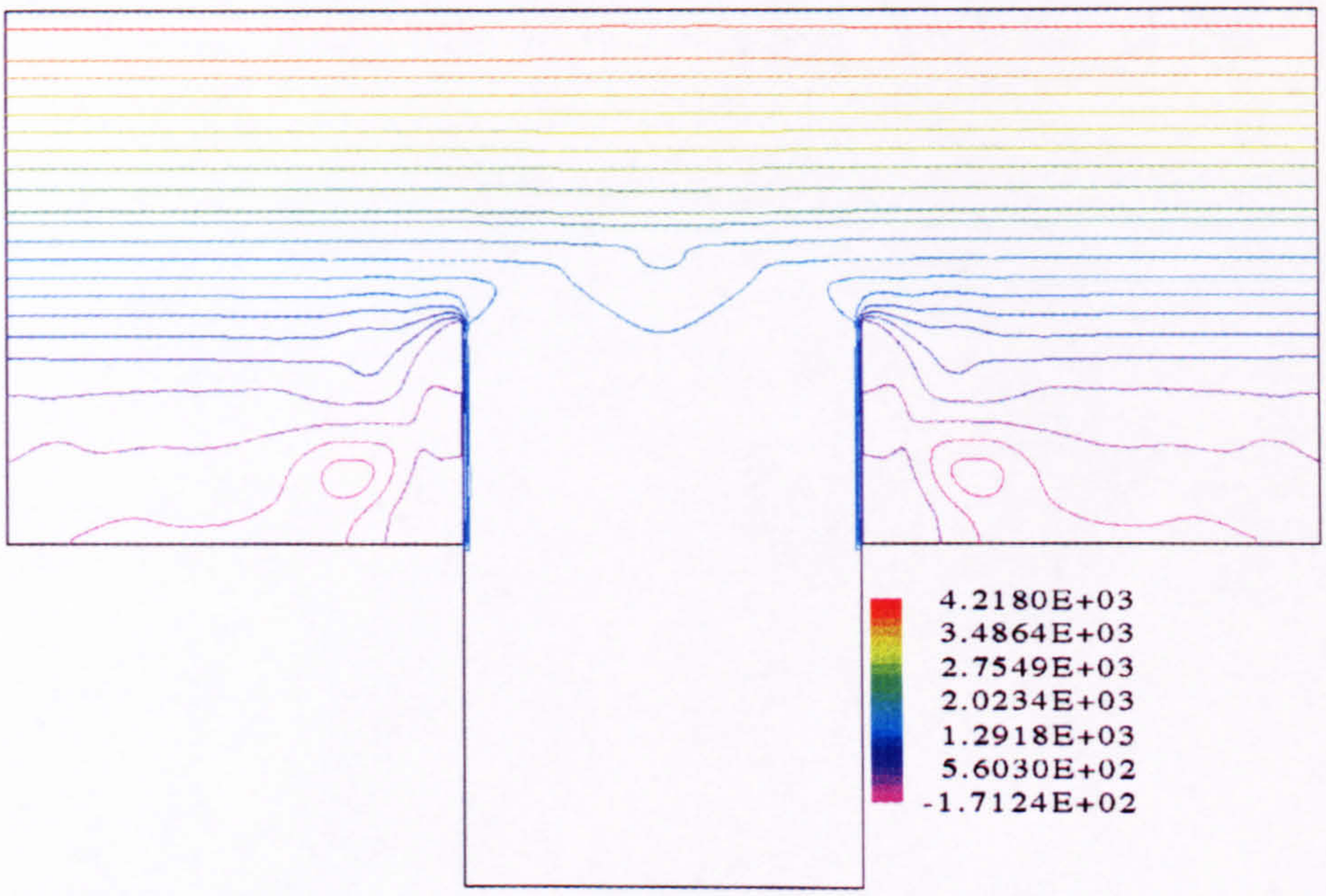


Figure 7.3-11b Pressure contour plot of 2DRNGV2

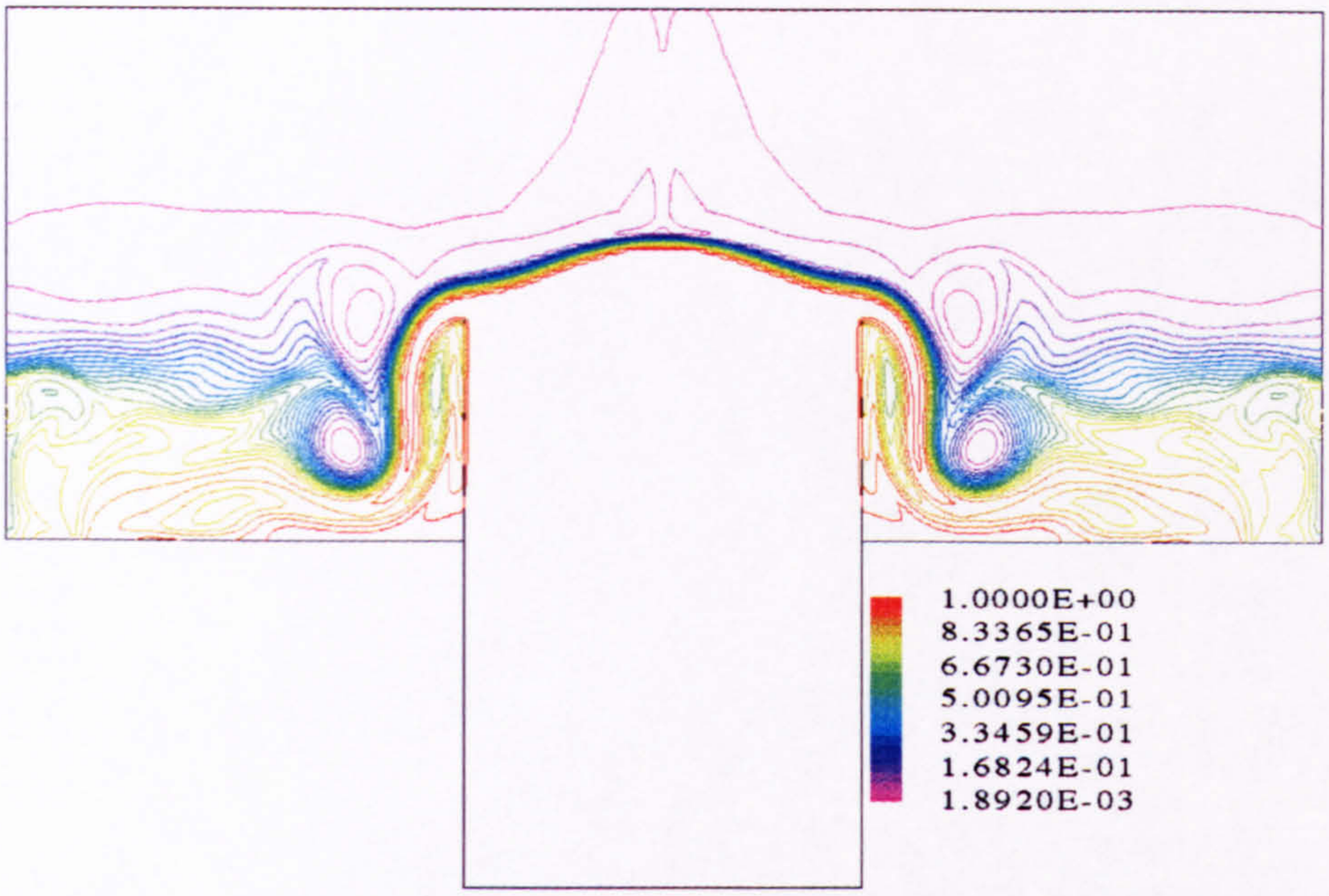


Figure 7.3-11c Volume fraction contours of water for 2DRNGV2. Value of 1.0 represents water, and 0.0 is air. Free surface has a value of 0.5.

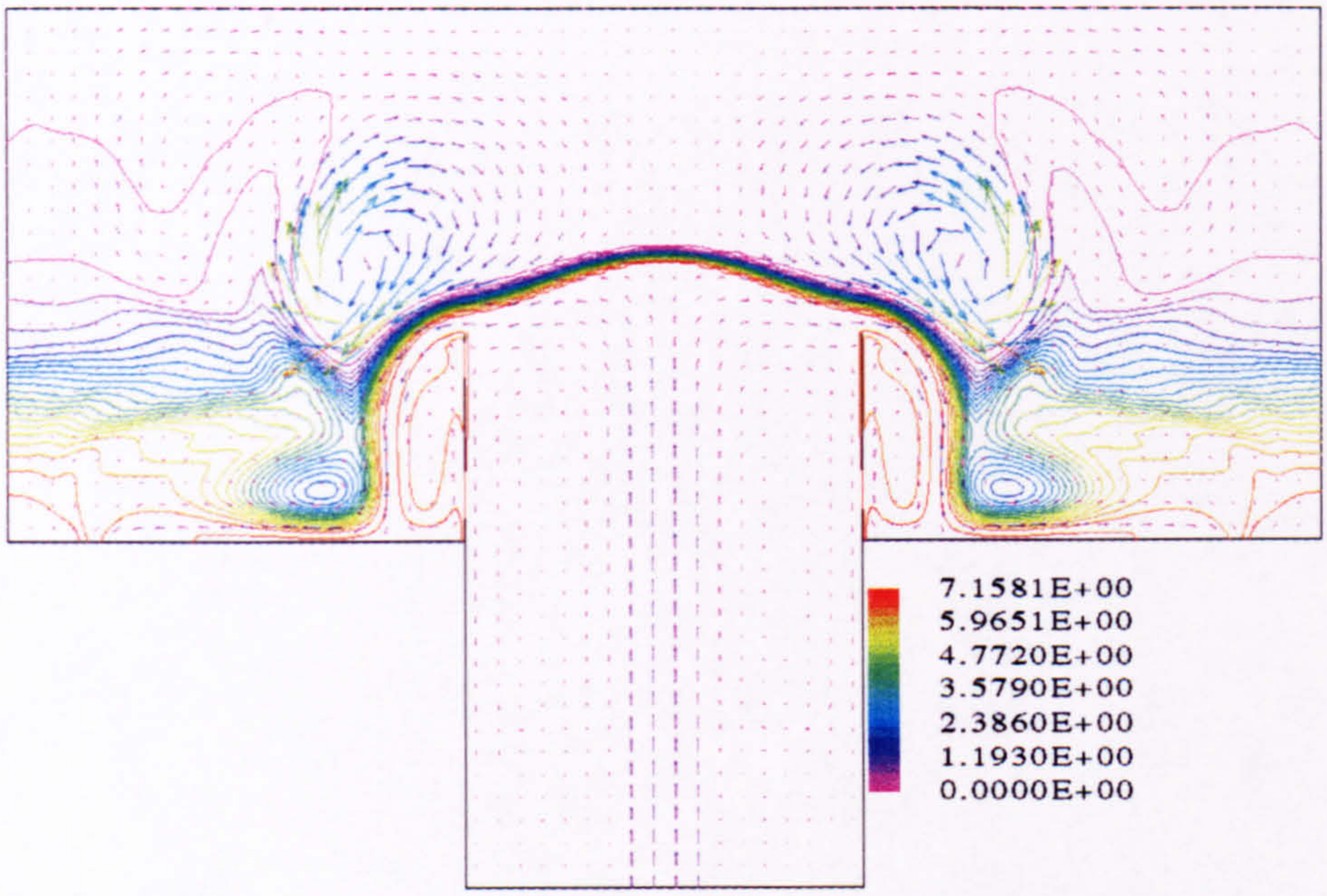


Figure 7.3-12a Velocity vector and volume fraction plot for 2DRNGC1. Weir crest levels were lowered to 0.631 m. Flowrate = 4.38 l/s. Mass residuals = 1 x 10^{-5} kg/s. 2D, 2-phase, transient calculations performed. Van Leer differencing scheme, RNG k-ε turbulence model used. Surface sharpening algorithm not used.

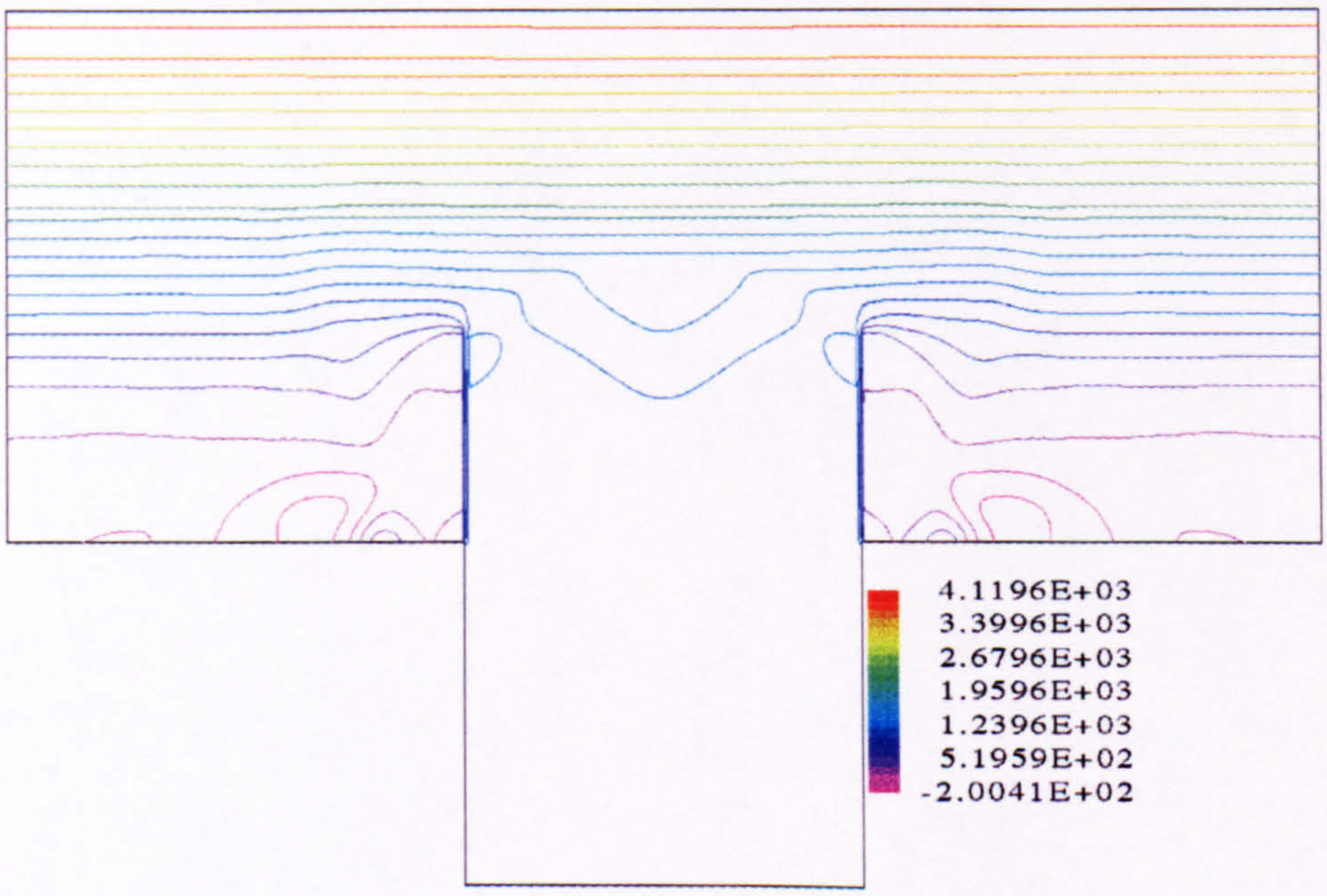


Figure 7.3-12b Pressure contours for 2DRNGC1

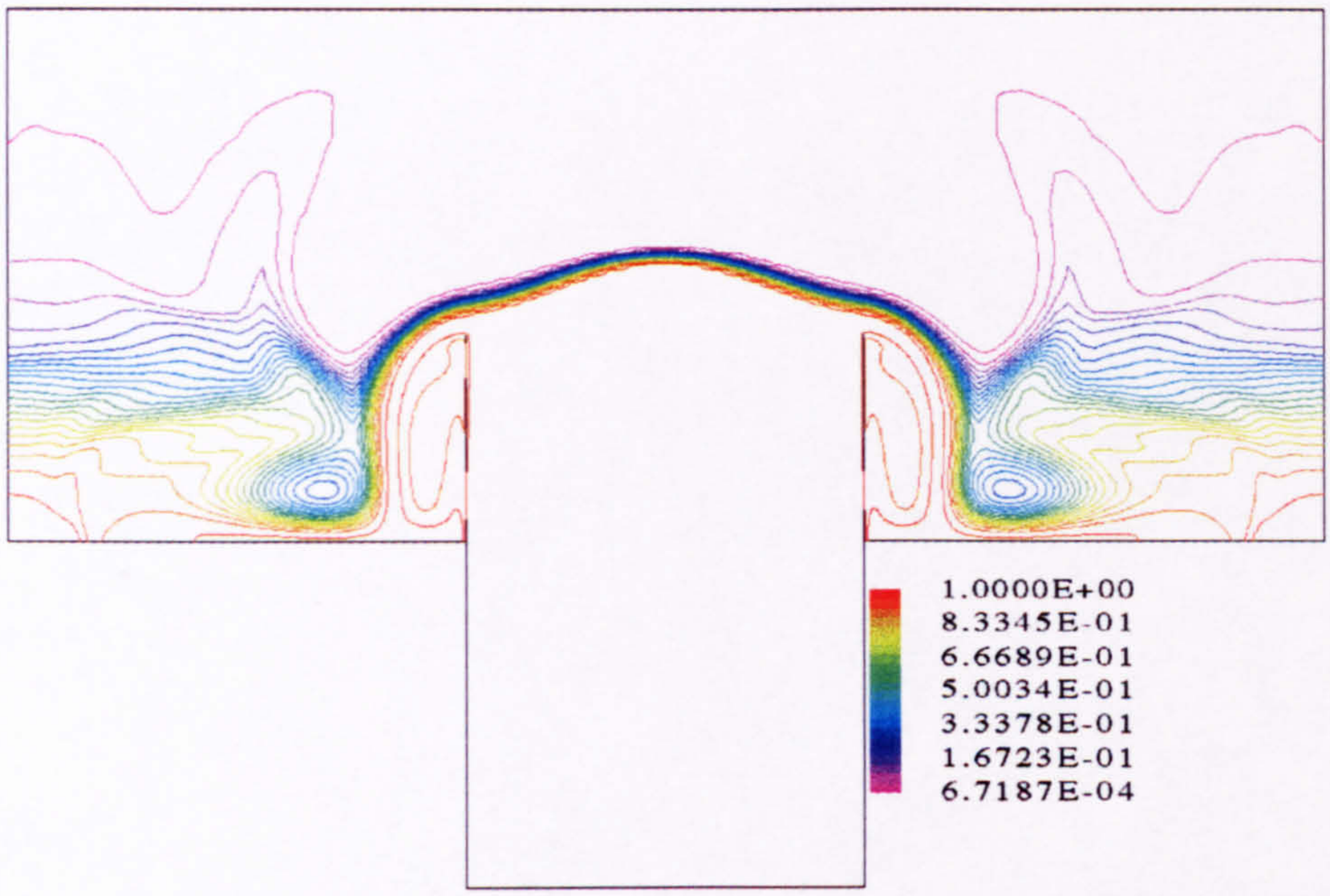


Figure 7.3-12c Volume fraction contours of water for 2DRNGC1. Value of 1.0 represents water, and 0.0 is air. Free surface has a value of 0.5.

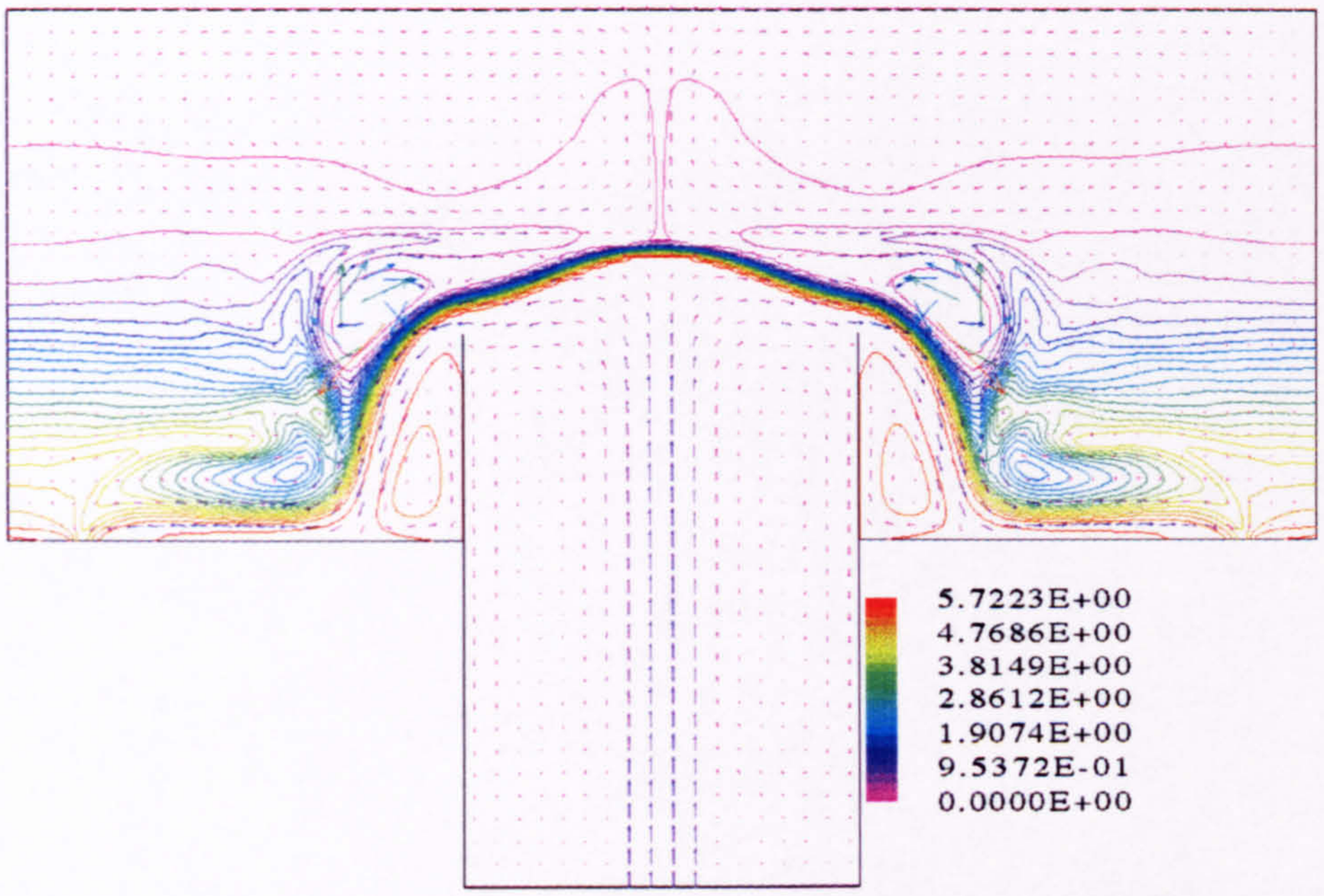


Figure 7.3-13a Velocity vector and volume fraction contour plot for 2DRNGC2. Weir crest levels set to 0.631 m. Flowrate = 4.38 l/s. Mass residuals = 1 x 10^{-7} kg/s (5 fold reduction in mass residuals). 2D, 2-phase transient calculations performed. Van Leer differencing scheme, and RNG k-ε turbulence model used. Surface sharpening algorithm not used.

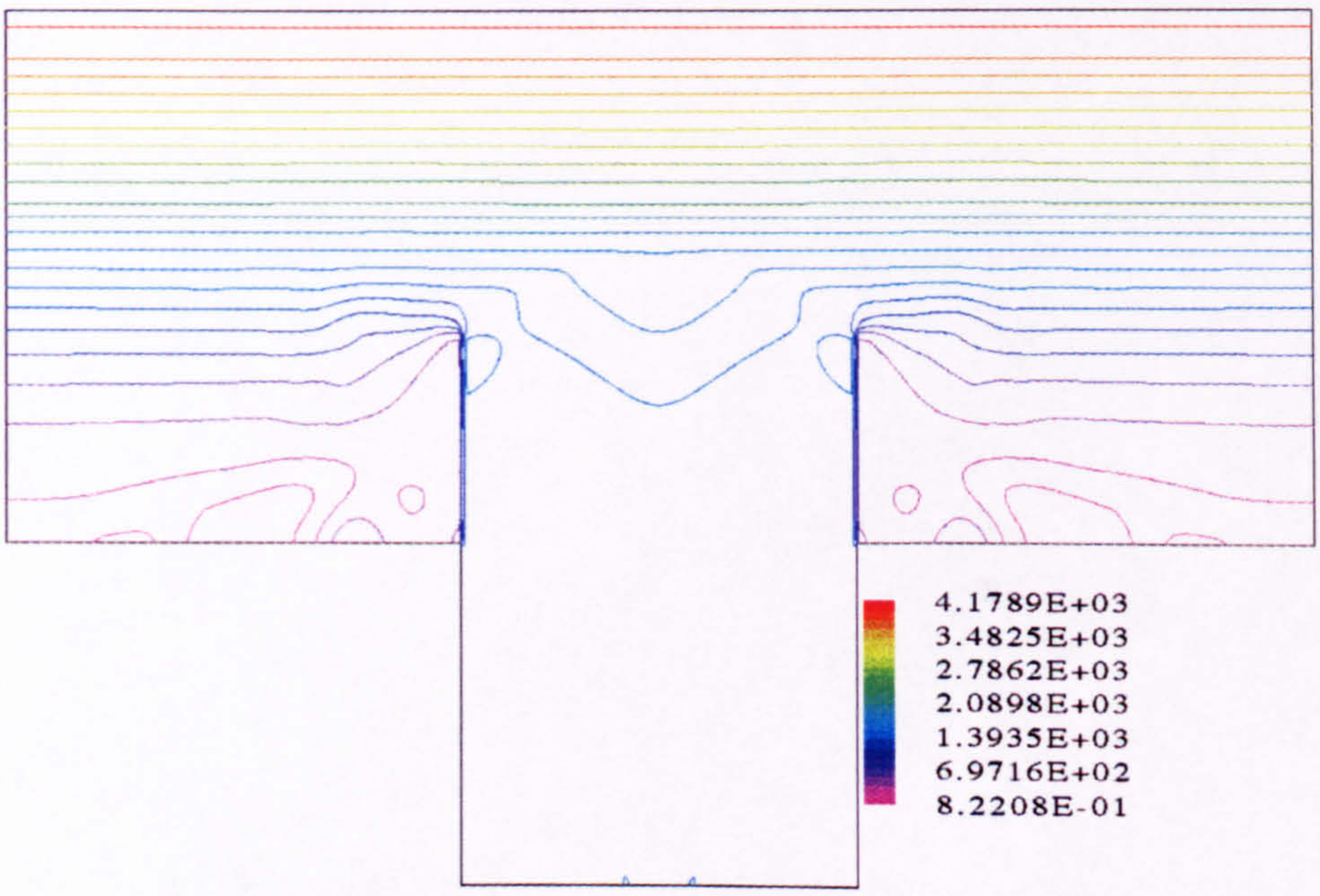


Figure 7.3-13b Pressure contour plot for 2DRNGC2

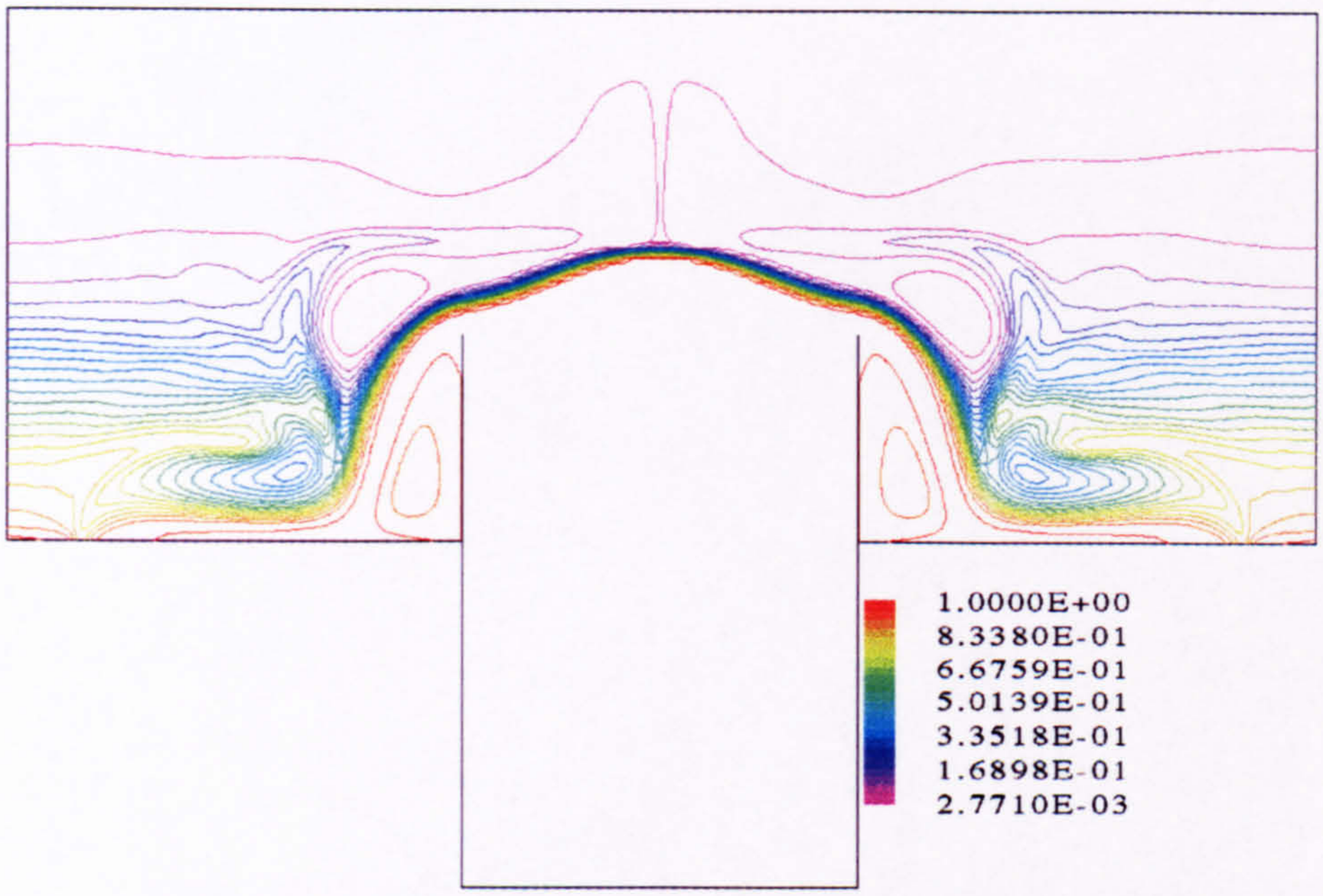


Figure 7.3-13c Volume fraction contours of water for 2DRNGC2. Value of 1.0 is water, and air is 0.0. Free surface has a value of 0.5.

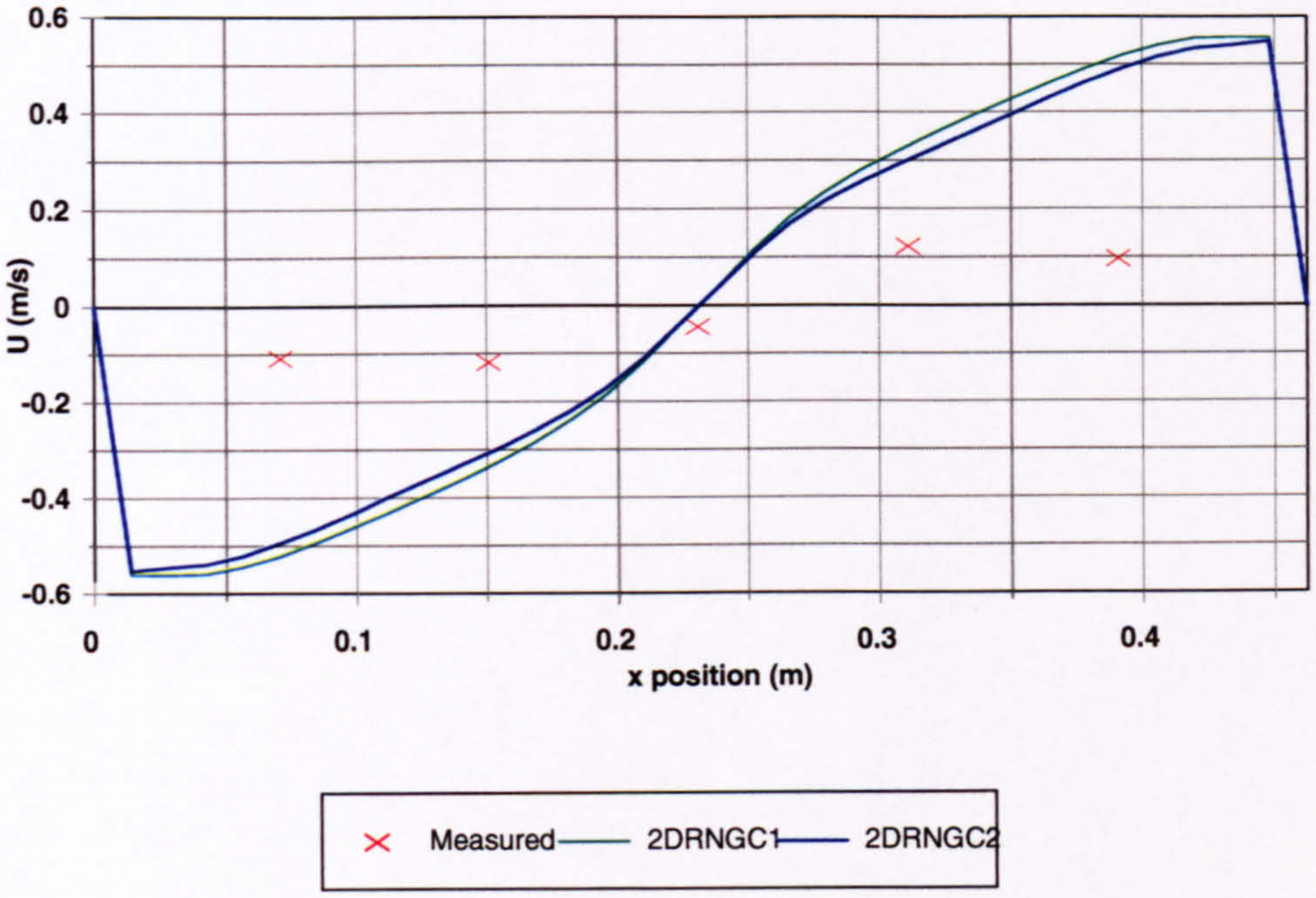


Figure 7.3-14a Comparison between experimental and calculated U velocities at y = 0.628 m. Flowrate = 4.38 l/s. (2DRNGC1 and 2DRNGC2 have weir levels set to the same as in the experiments).

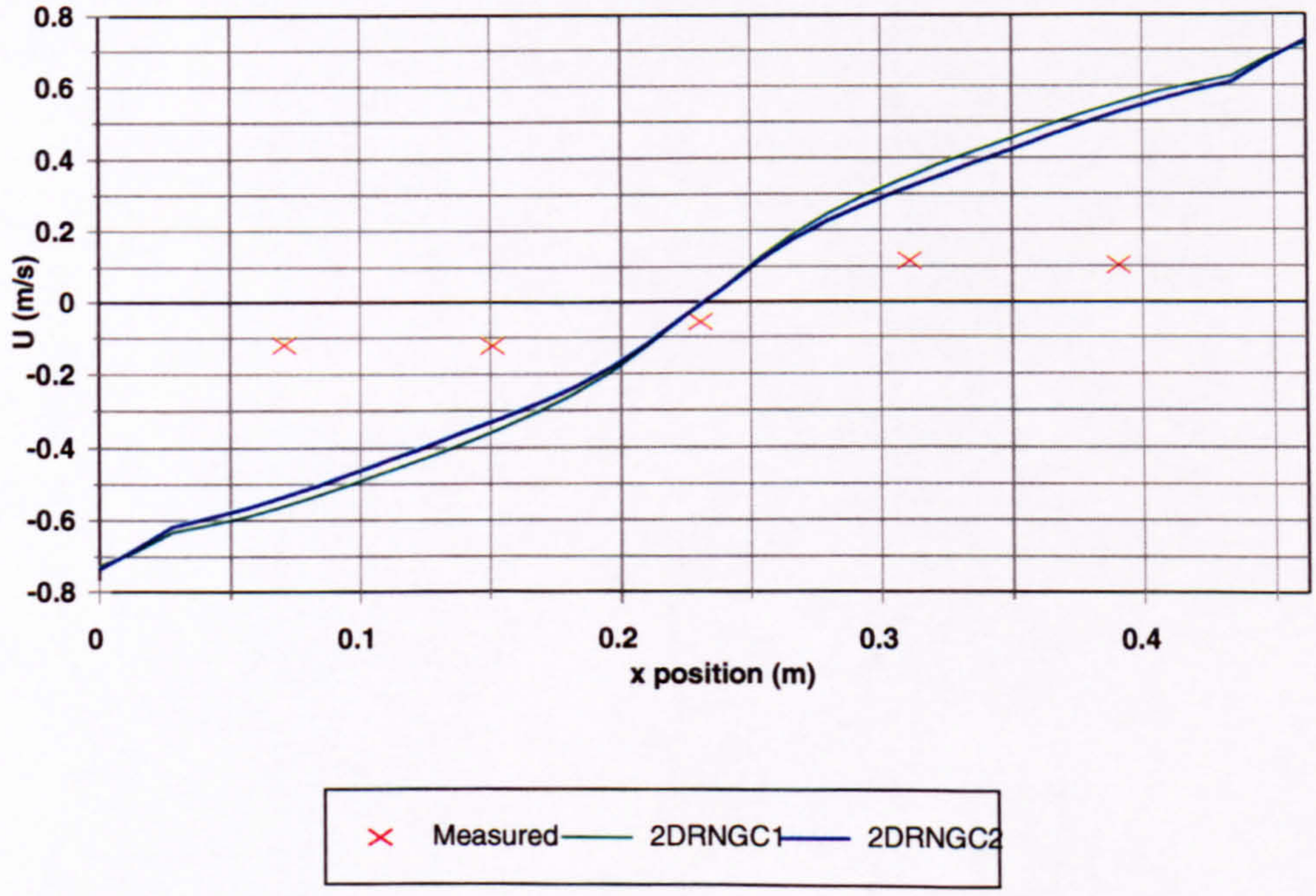


Figure 7.3-14b Comparison between experimental and calculated U velocities at y = 0.633 m. Flowrate = 4.38 l/s.

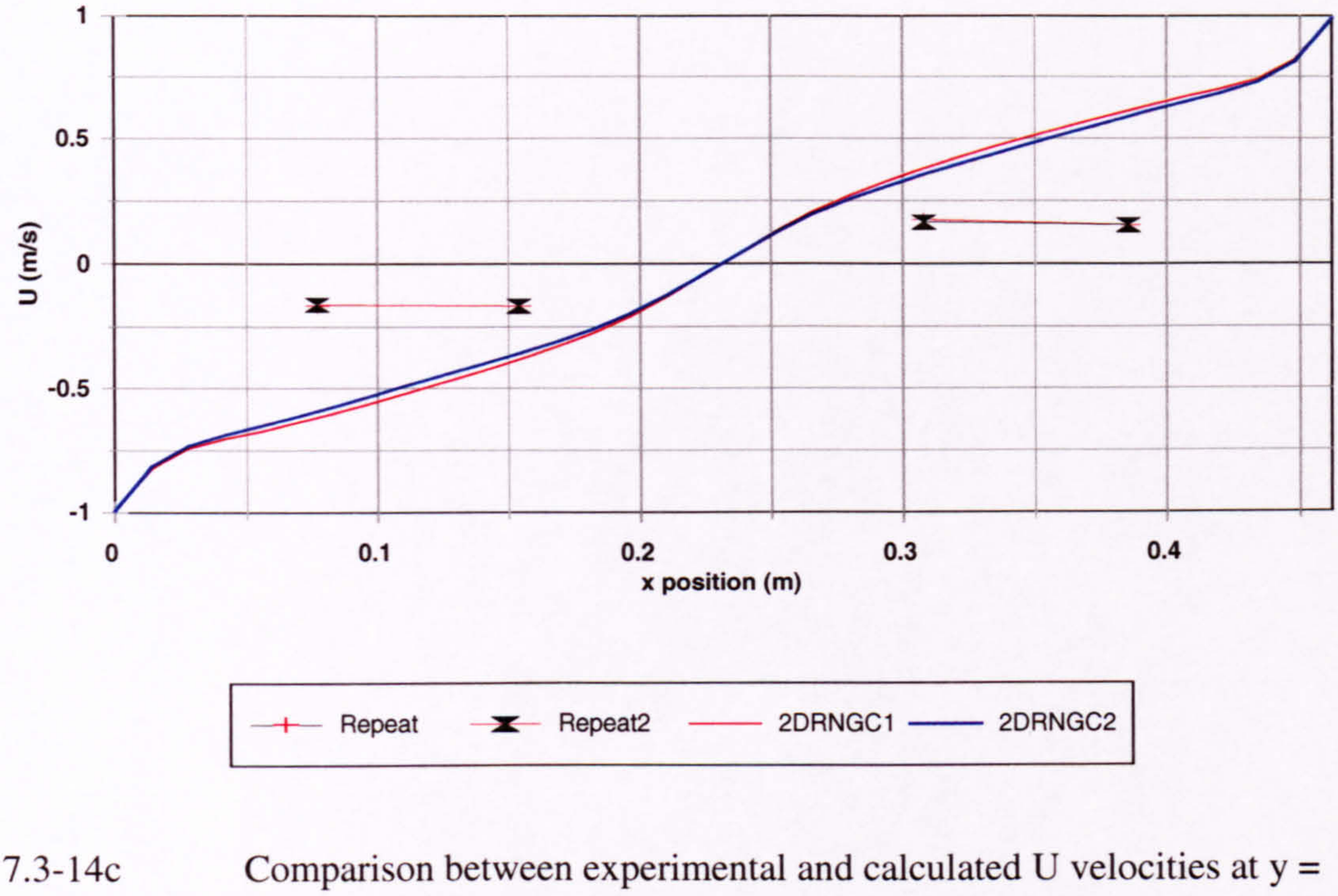


Figure 7.3-14c Comparison between experimental and calculated U velocities at y = 0.643 m. Flowrate = 4.38 l/s

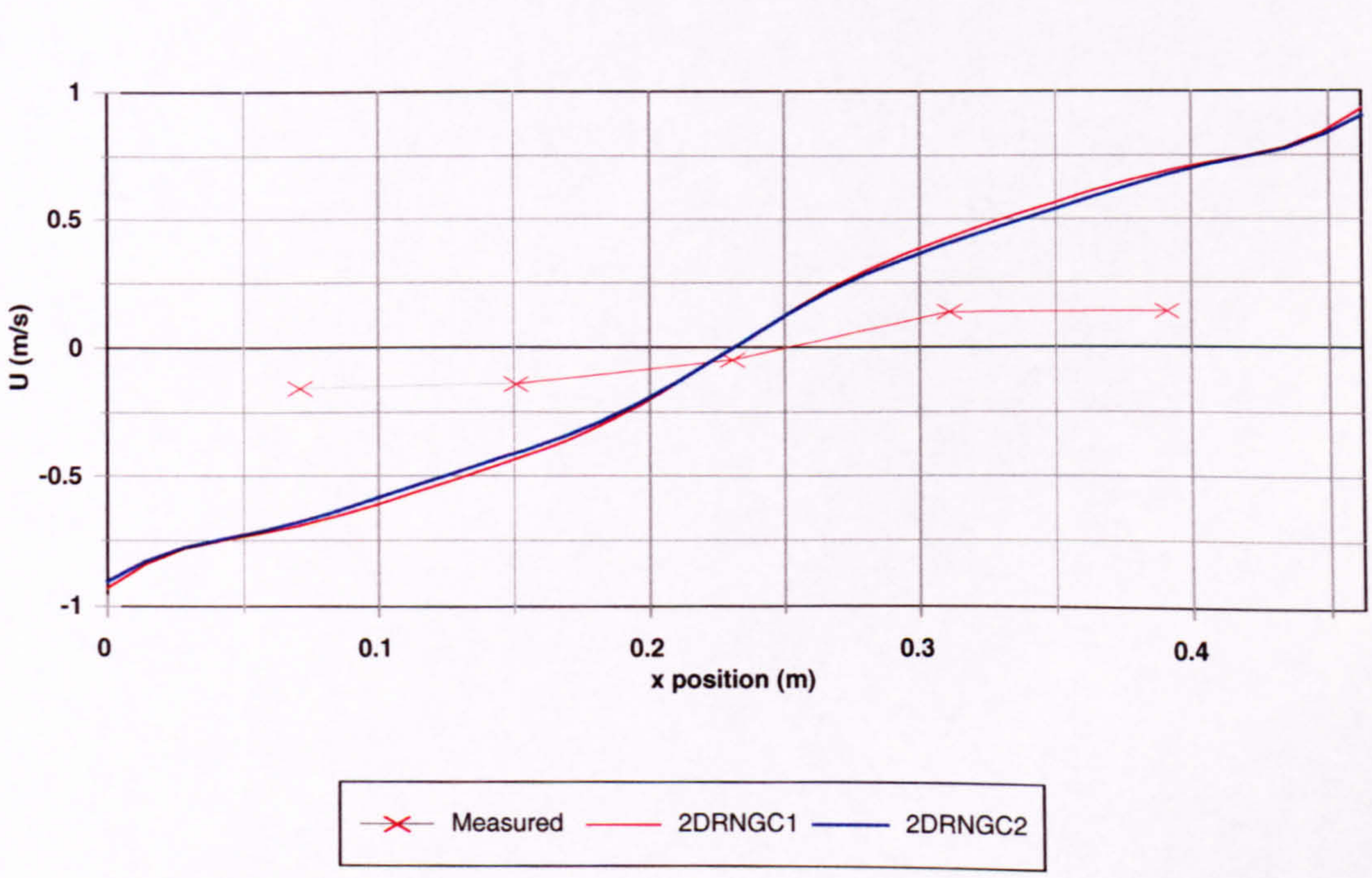


Figure 7.3-14d Comparison between experimental and calculated U velocities at y = 0.653 m. Flowrate = 4.38 l/s

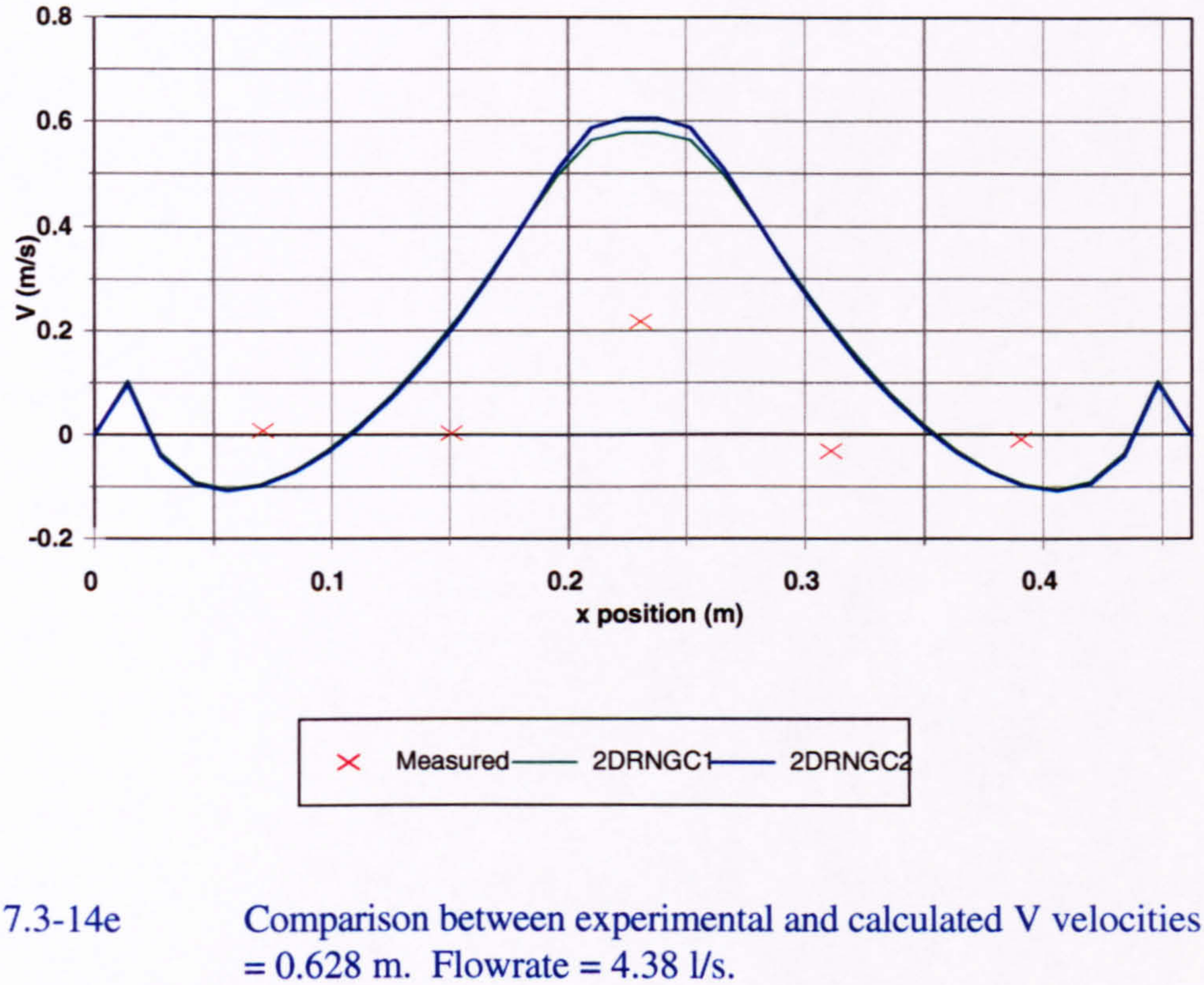


Figure 7.3-14e Comparison between experimental and calculated V velocities at y = 0.628 m. Flowrate = 4.38 l/s.

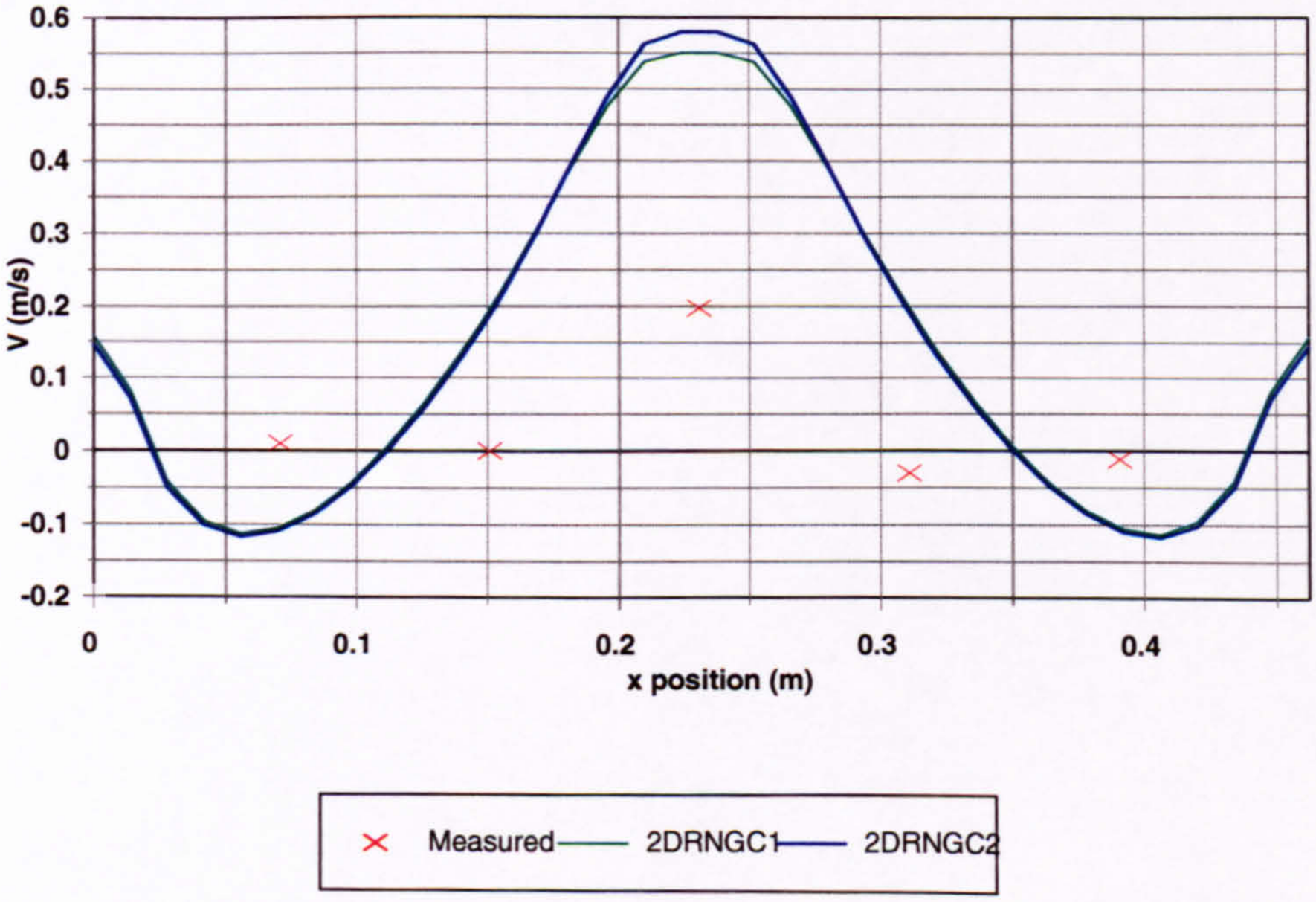


Figure 7.3-14f Comparison between experimental and calculated V velocities at y = 0.633 m. Flowrate = 4.38 l/s.

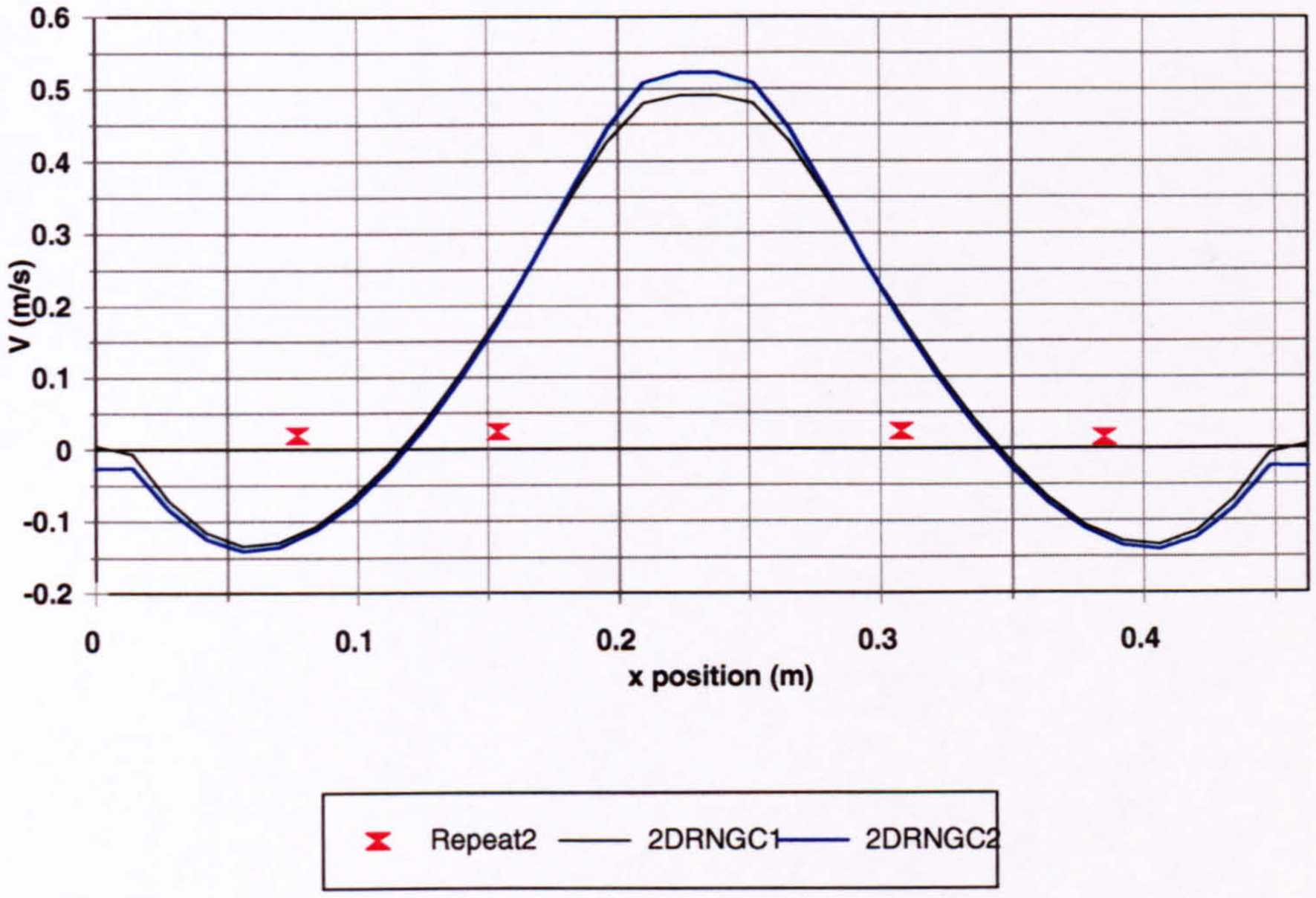


Figure 7.3-14g Comparison between experimental and calculated V velocities at y = 0.643 m. Flowrate = 4.38 l/s.

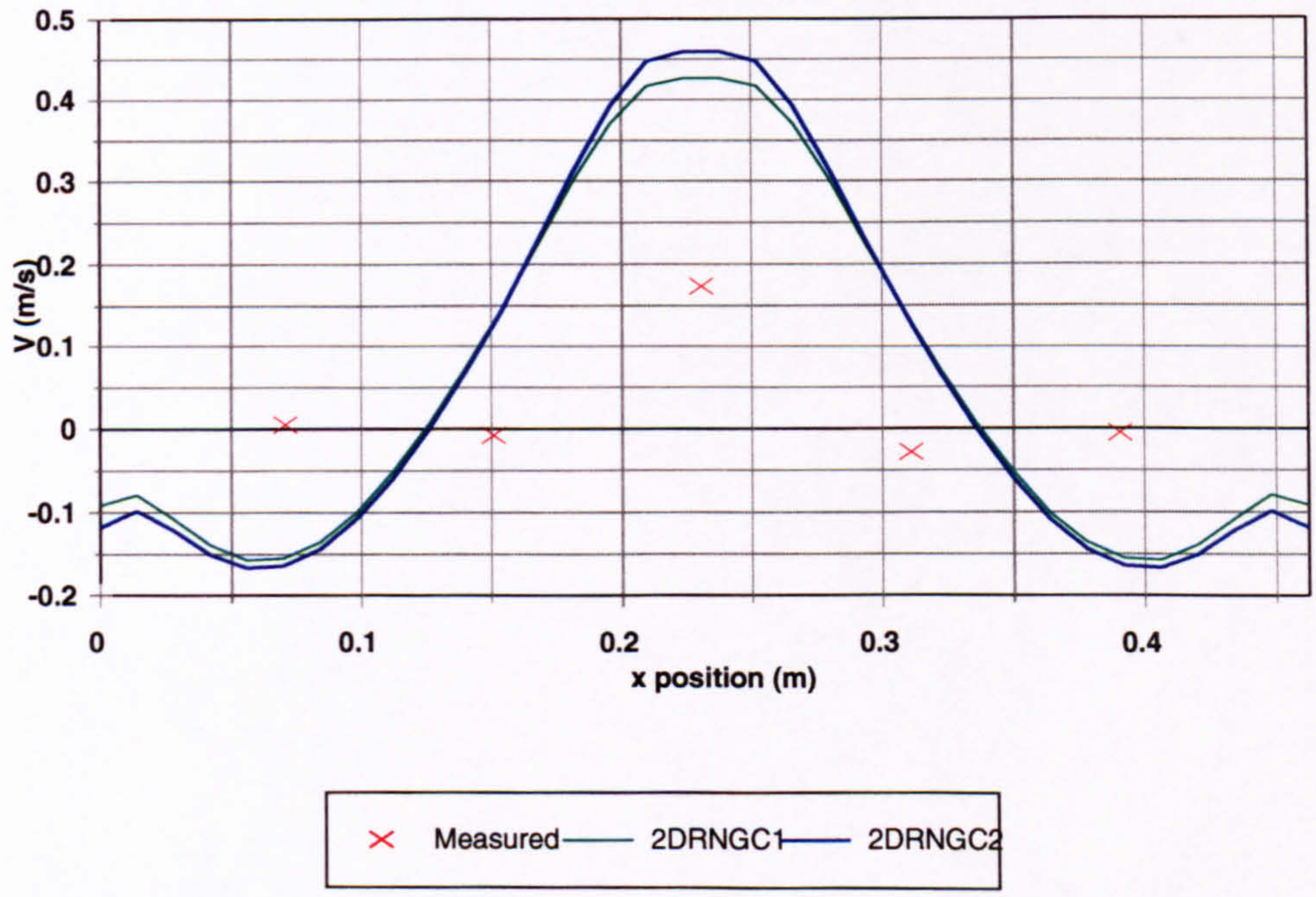


Figure 7.3-14h Comparison between experimental and calculated V velocities at y = 0.653 m. Flowrate = 4.38 l/s.

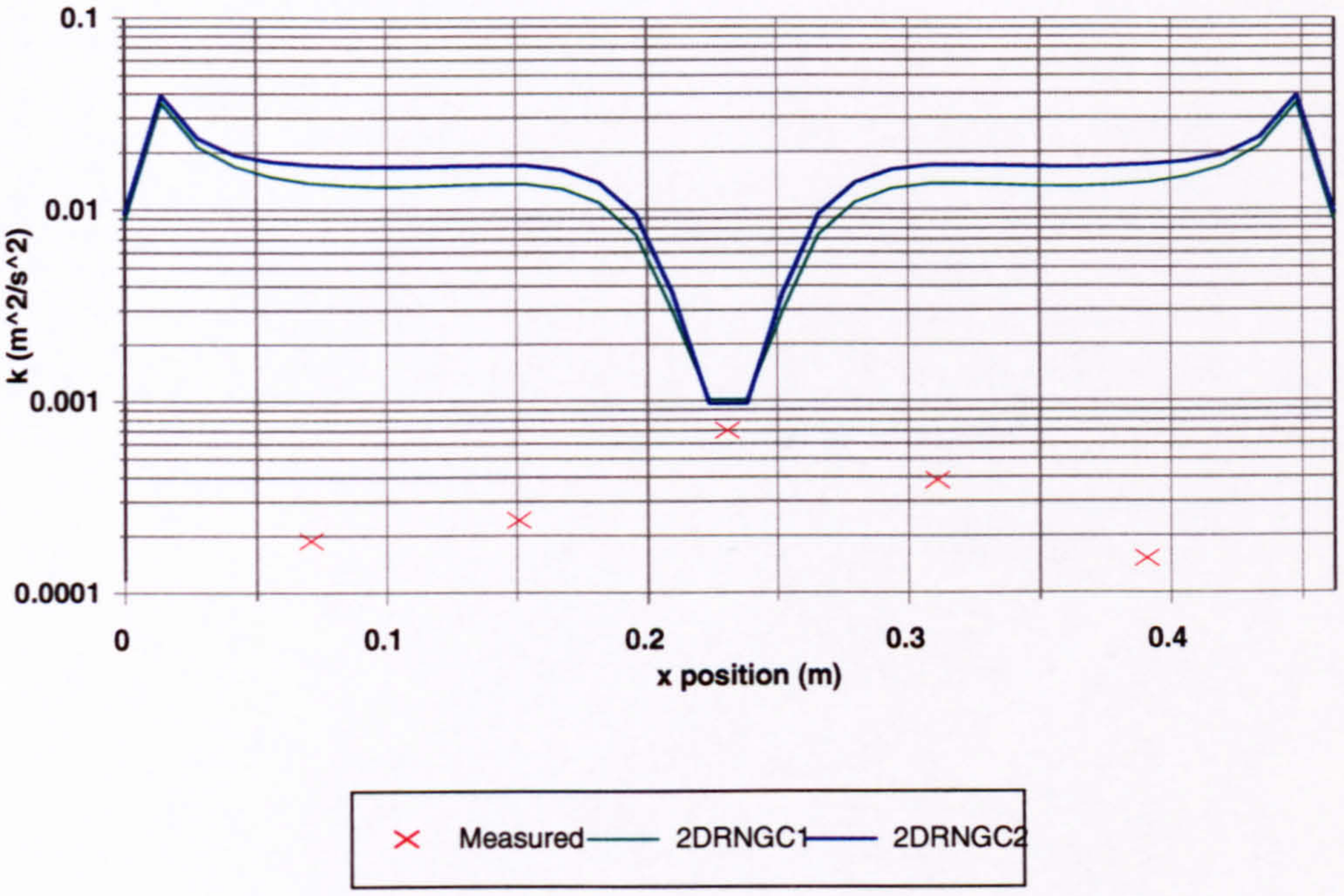


Figure 7.3-14i Comparison between experimental and calculated turbulent kinetic energy at y = 0.628 m. Flowrate = 4.38 l/s.

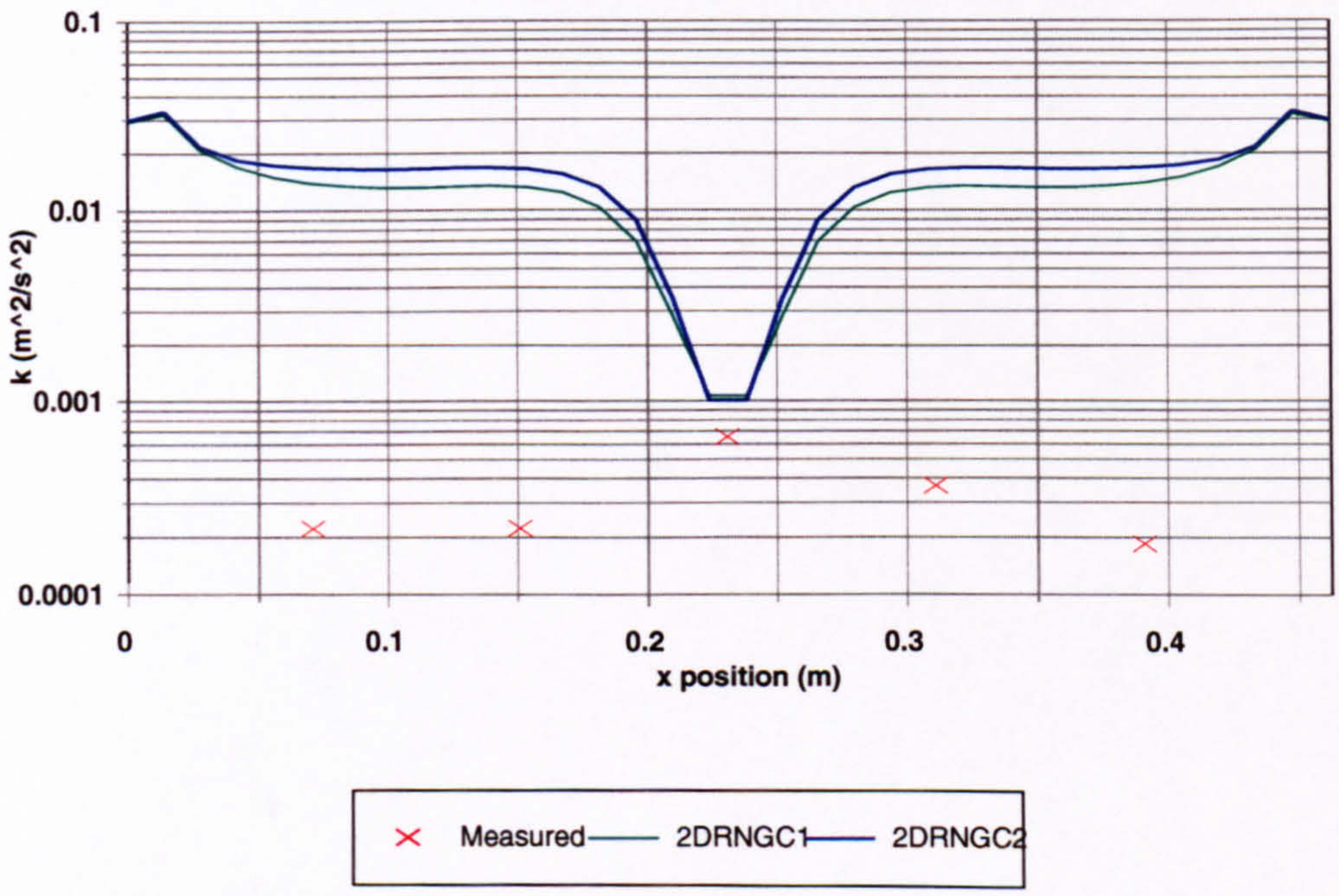


Figure 7.3-14j Comparison between experimental and calculated turbulent kinetic energy at y = 0.633 m. Flowrate = 4.38 l/s.

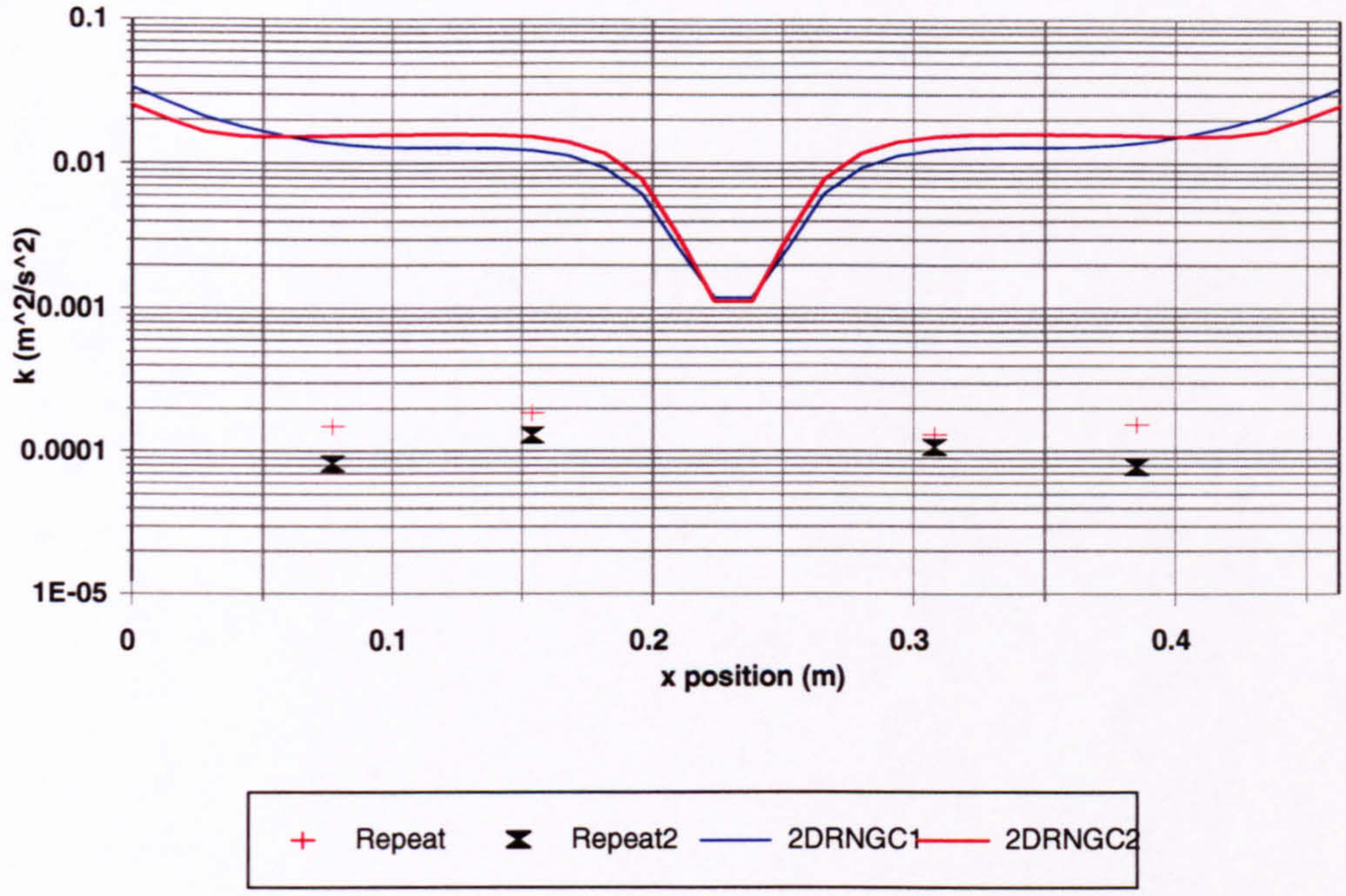


Figure 7.3-14k Comparison between experimental and calculated turbulent kinetic energy at y = 0.643 m. Flowrate = 4.38 l/s.

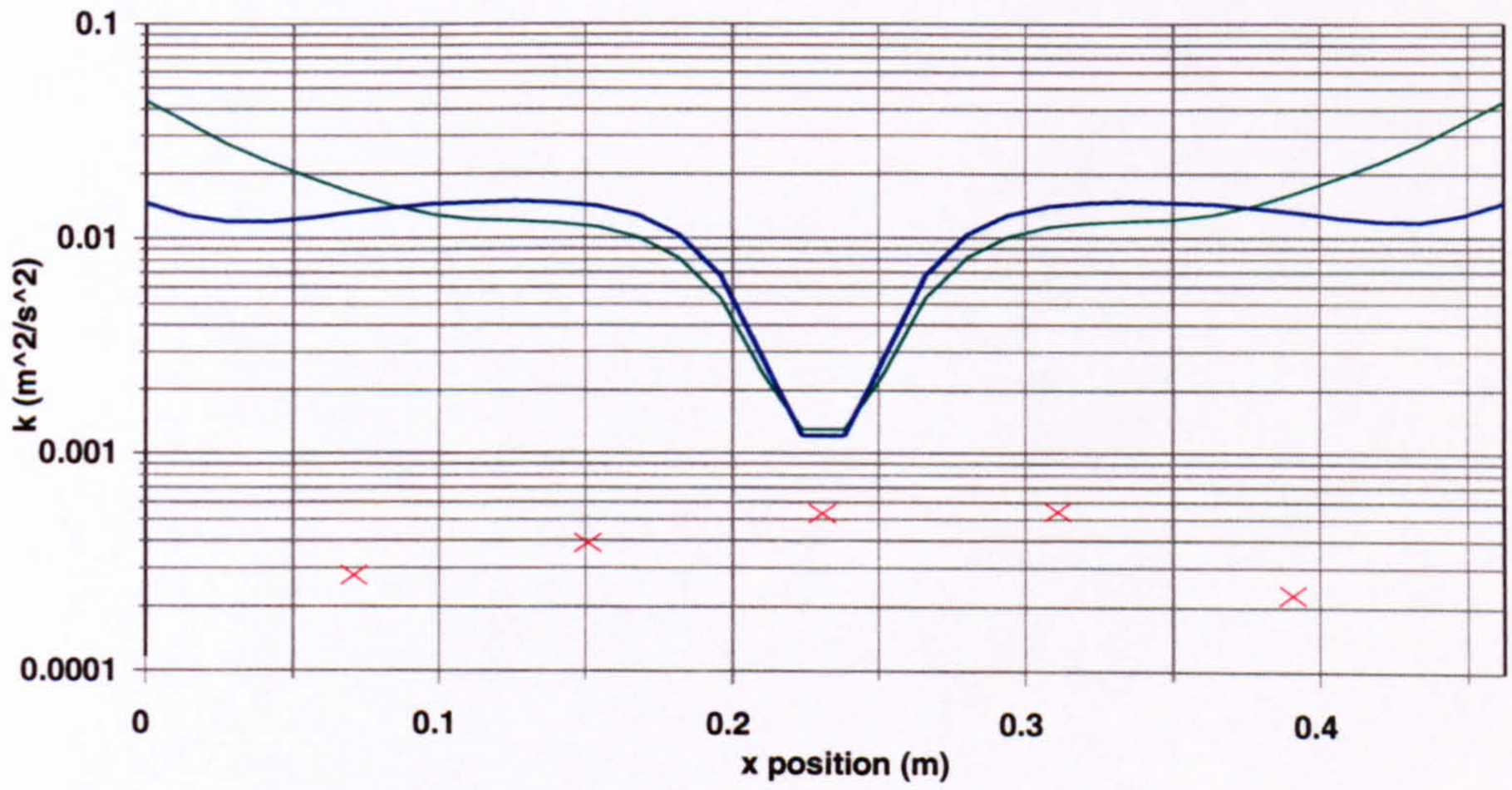


Figure 7.3-14l Comparison between experimental and calculated turbulent kinetic energy at y = 0.653 m. Flowrate = 4.38 l/s.

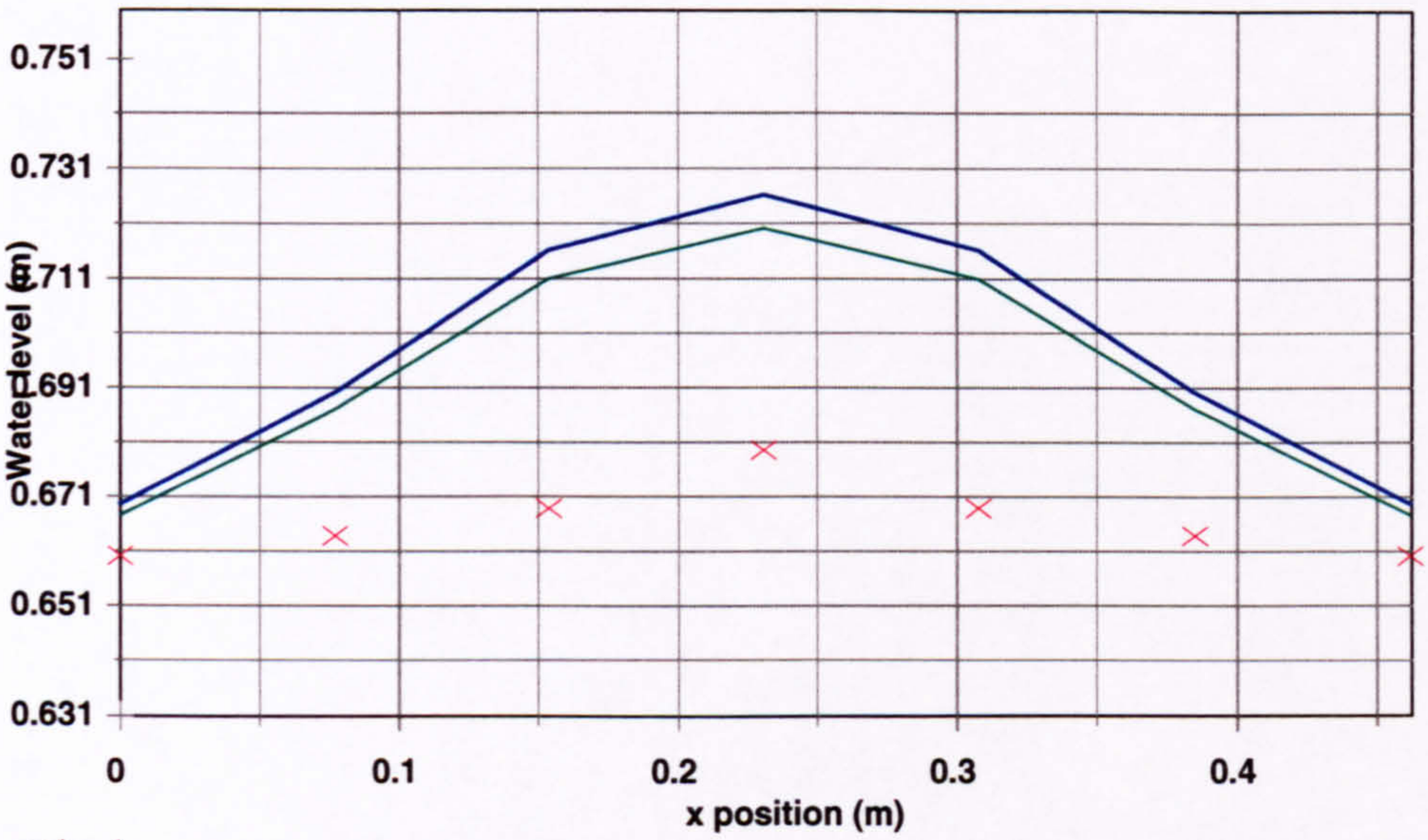


Figure 7.3-14m Comparison between experimental and calculated water levels. Flowrate = 4.38 l/s.

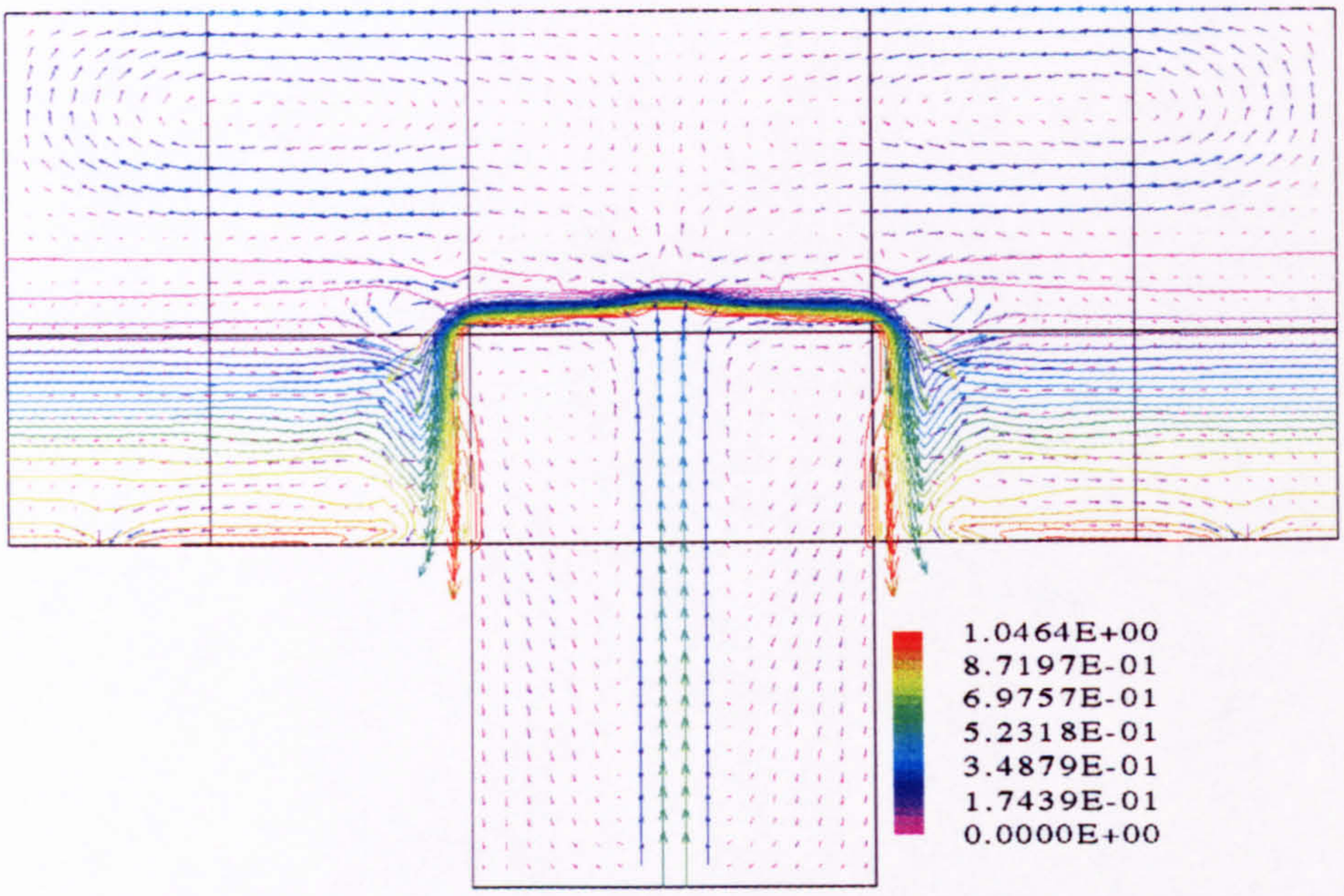


Figure 7.3-15a Velocity vector and volume fraction plot of 3DRNG1. 3D, 2-phase, transient calculations performed. Flowrate = 2.95 l/s. Mass residuals = 1 x 10^{-7} kg/s (5 fold reduction in mass residuals). Van Leer differencing scheme and RNG k-ε turbulence model used. Surface sharpening not used.

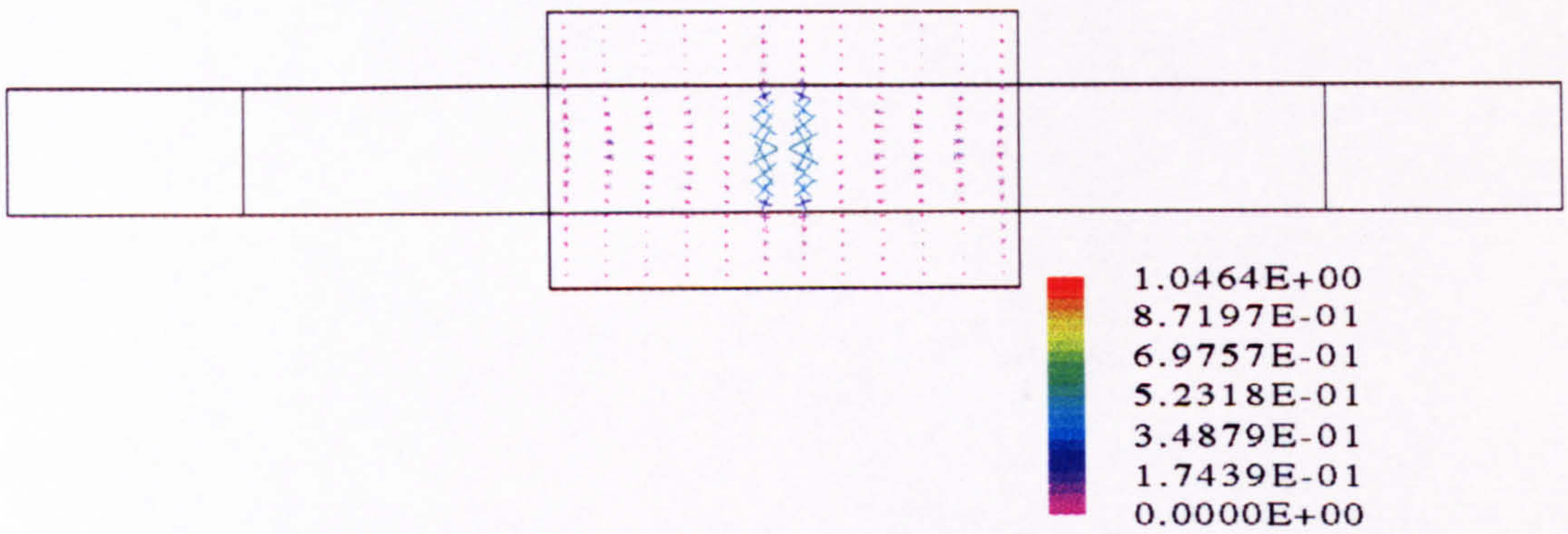


Figure 7.3-15b Velocity vector plot of 3DRNG1. Plan view of velocity vectors measured at y = 0.2 m (from invert of chamber)

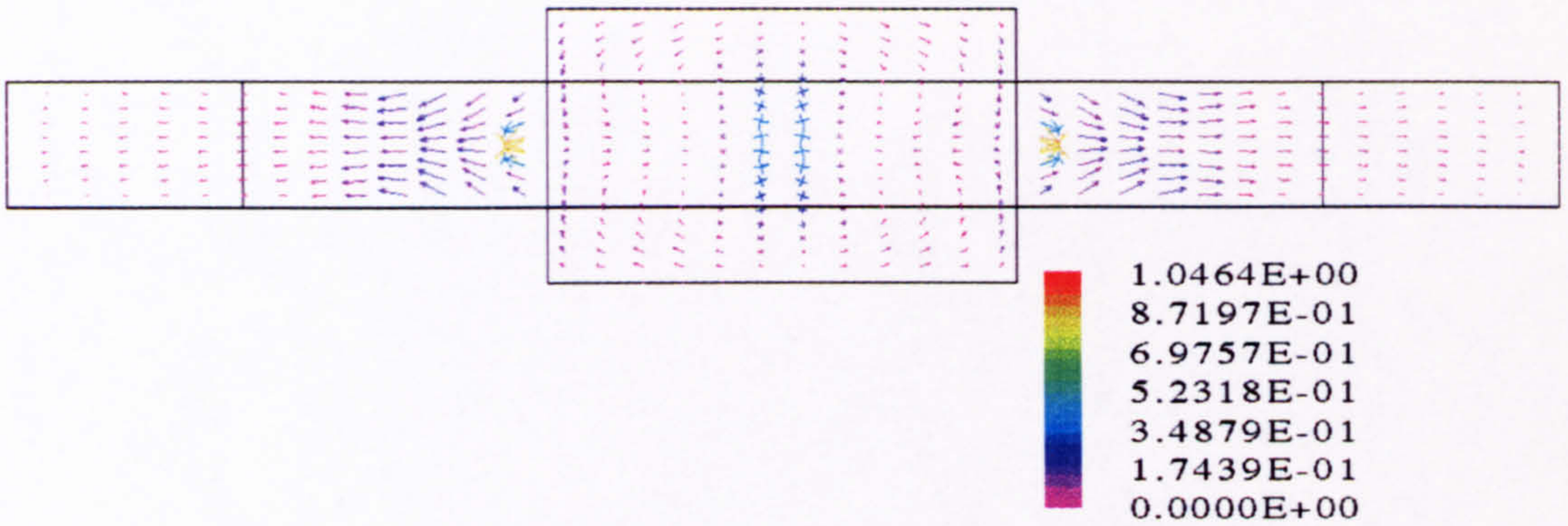


Figure 7.3-15c Velocity vector plot of 3DRNG1. Plan view of velocity vectors measured at y = 0.5 m (from invert of chamber).

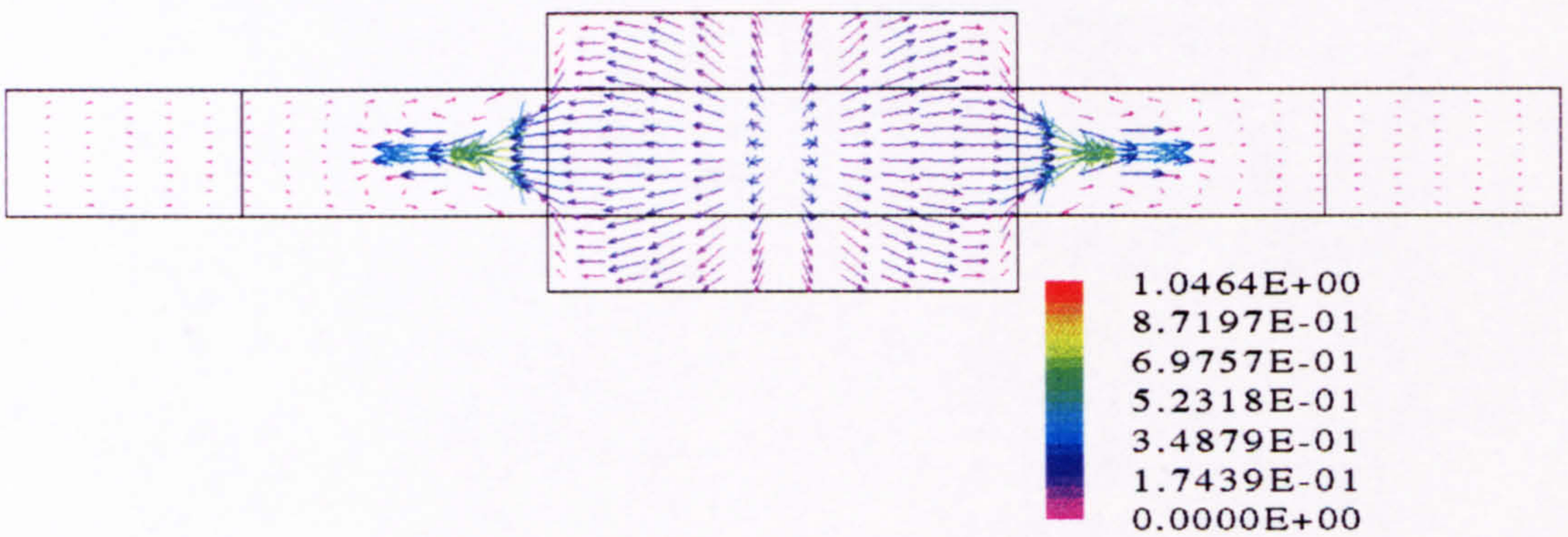


Figure 7.3-15d Velocity vector plot of 3DRNG1. Plan view of velocity vectors measured at y = 0.631 m (from invert of chamber).

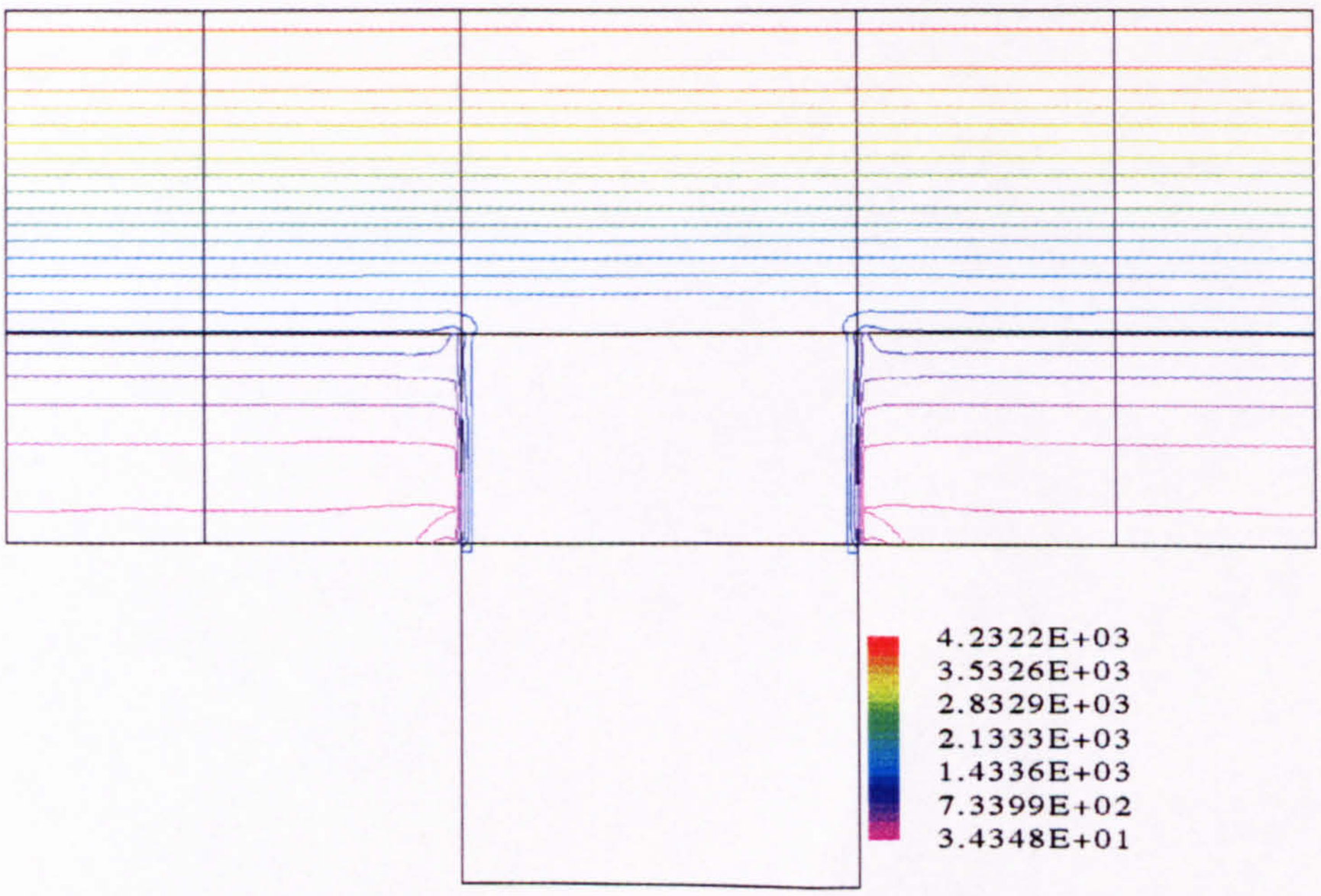


Figure 7.3-15e Pressure contour plot of 3DRNG1.

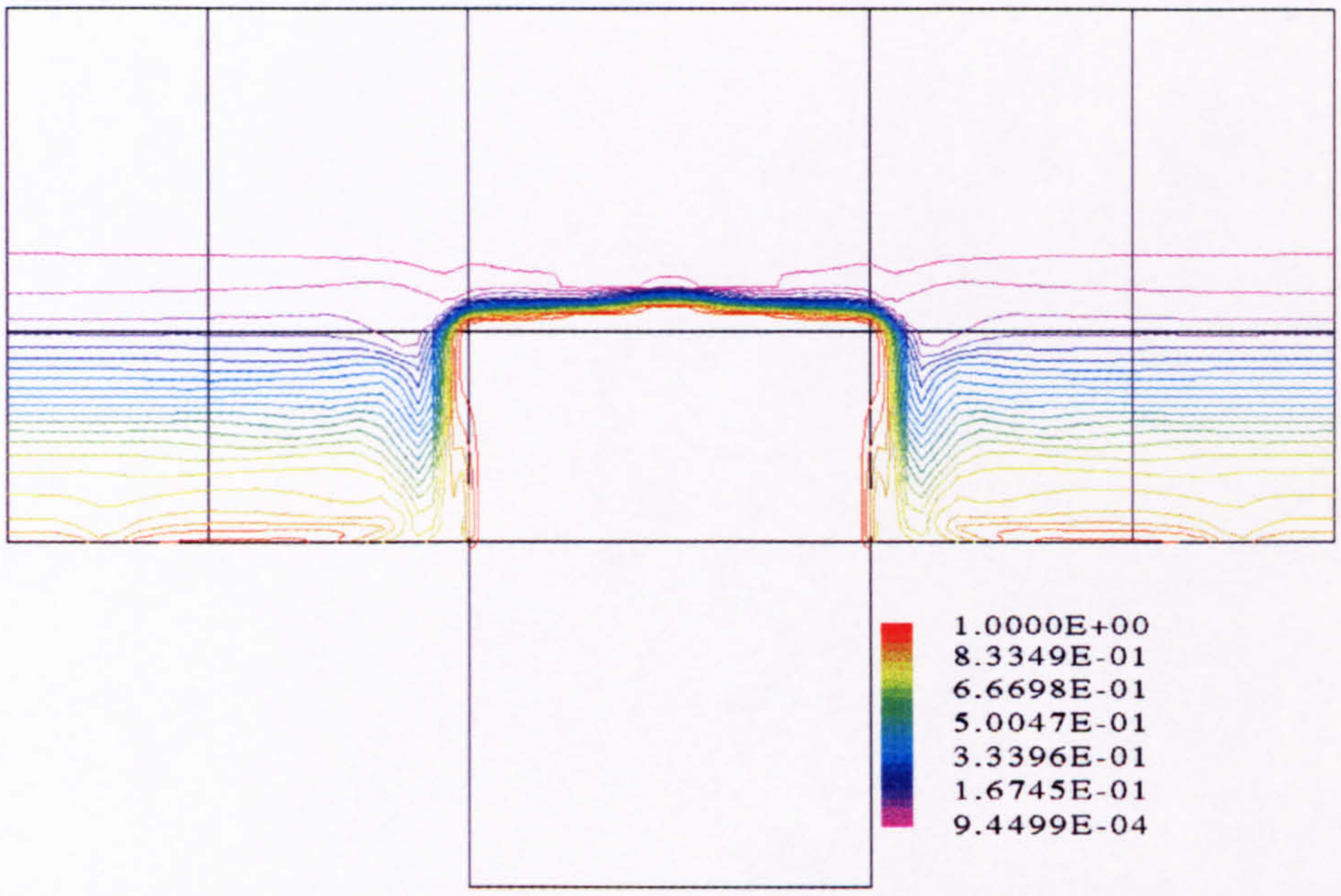


Figure 7.3-15f Volume fraction contour plot of water for 3DRNG1. Value of 1.0 represents water, and 0.0 is air. Free surface has a value of 0.5.

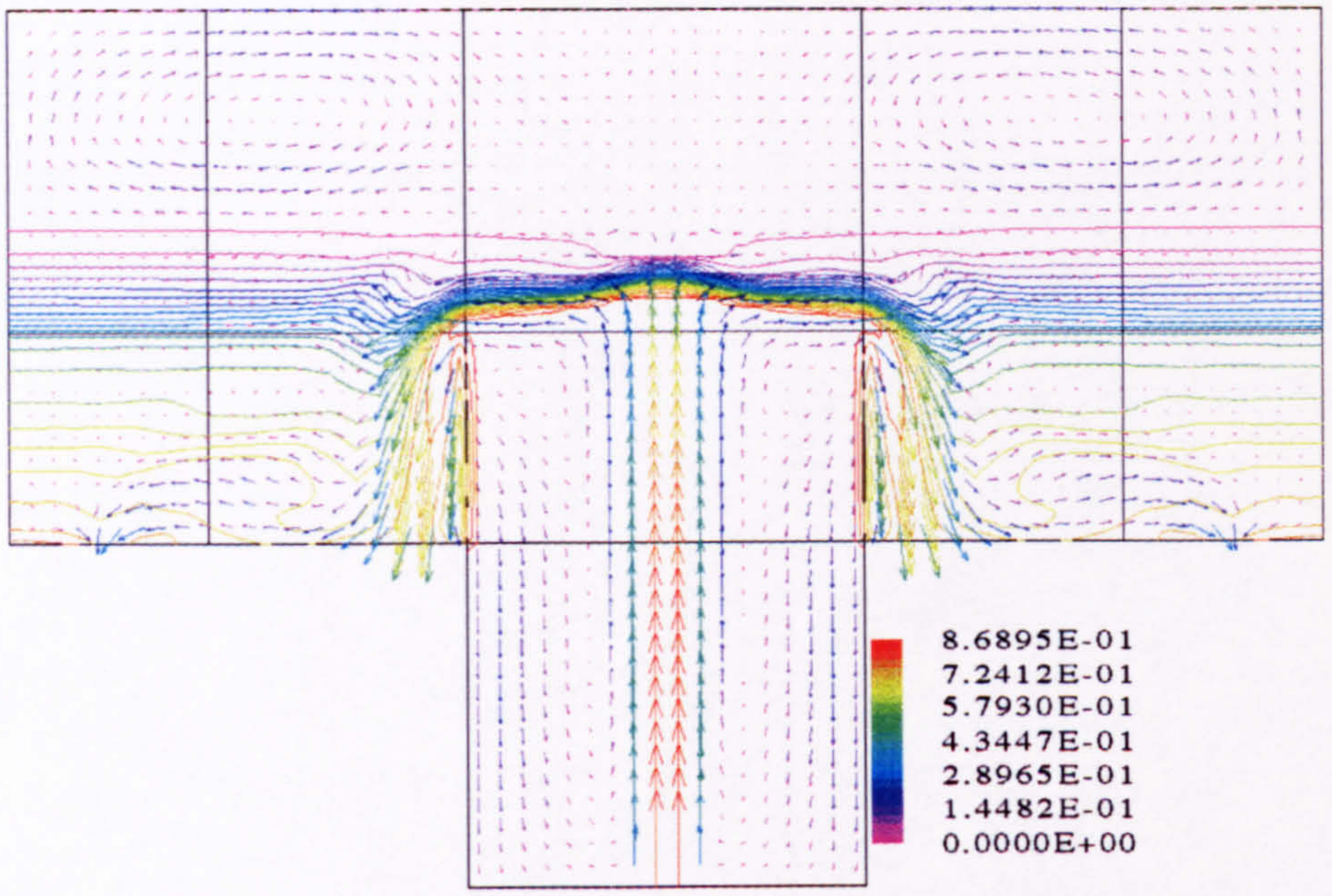


Figure 7.3-16a Velocity vector and volume fraction contour plot for 3DRNG2. 3D, 2-phase, transient calculations performed. Flowrate = 4.38 l/s. Mass residual = 1 x 10^{-7} kg/s (5 fold reduction in mass residuals). Van Leer differencing scheme and RNG k-ε turbulence model used. Surface sharpening not used.

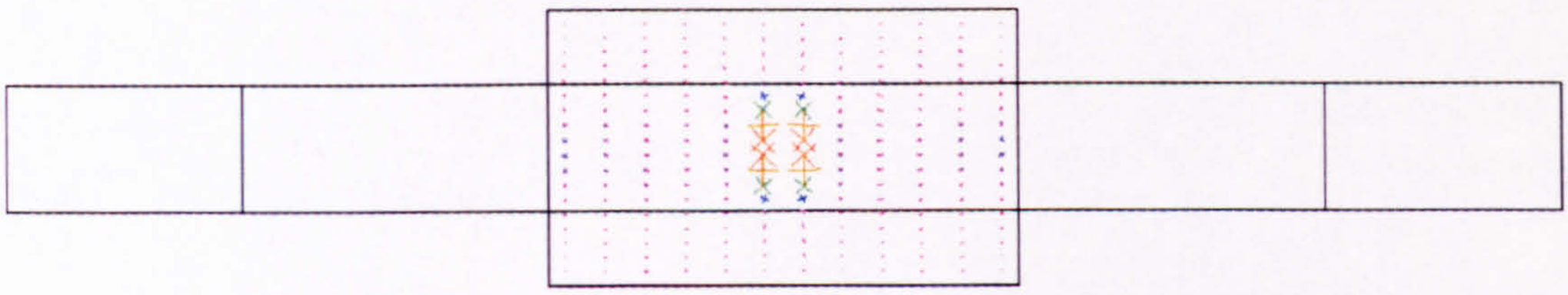


Figure 7.3-16b Velocity vector plot for 3DRNG2. Plan view of velocity vectors at y = 0.1 m (from invert of chamber).

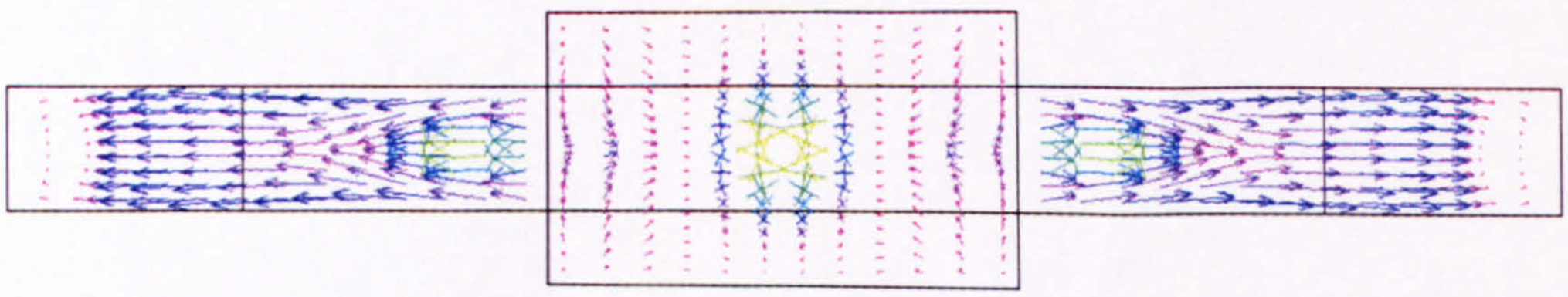


Figure 7.3-16c Velocity vector plot for 3DRNG2. Plan view of velocity vectors at y = 0.45 m (from chamber invert).

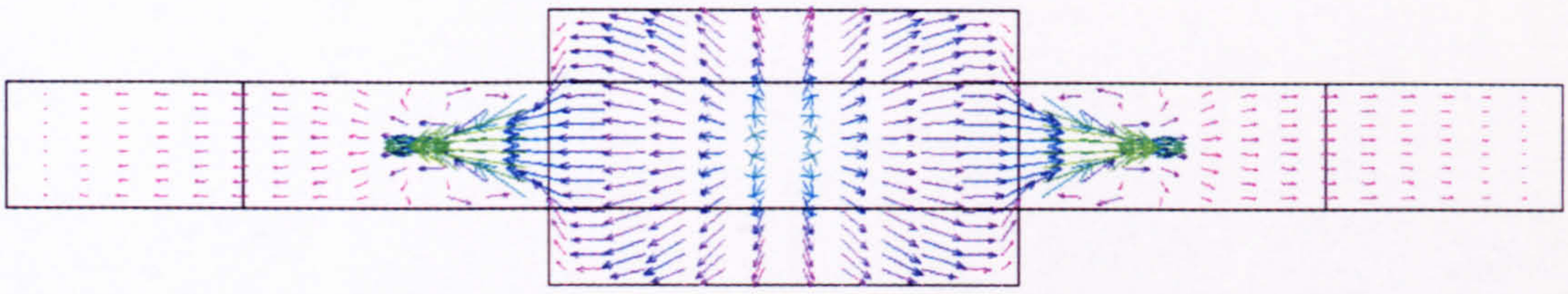


Figure 7.3-16d Velocity vector plot for 3DRNG2. Plan view of velocity vectors at y = 0.631 m (from chamber invert).

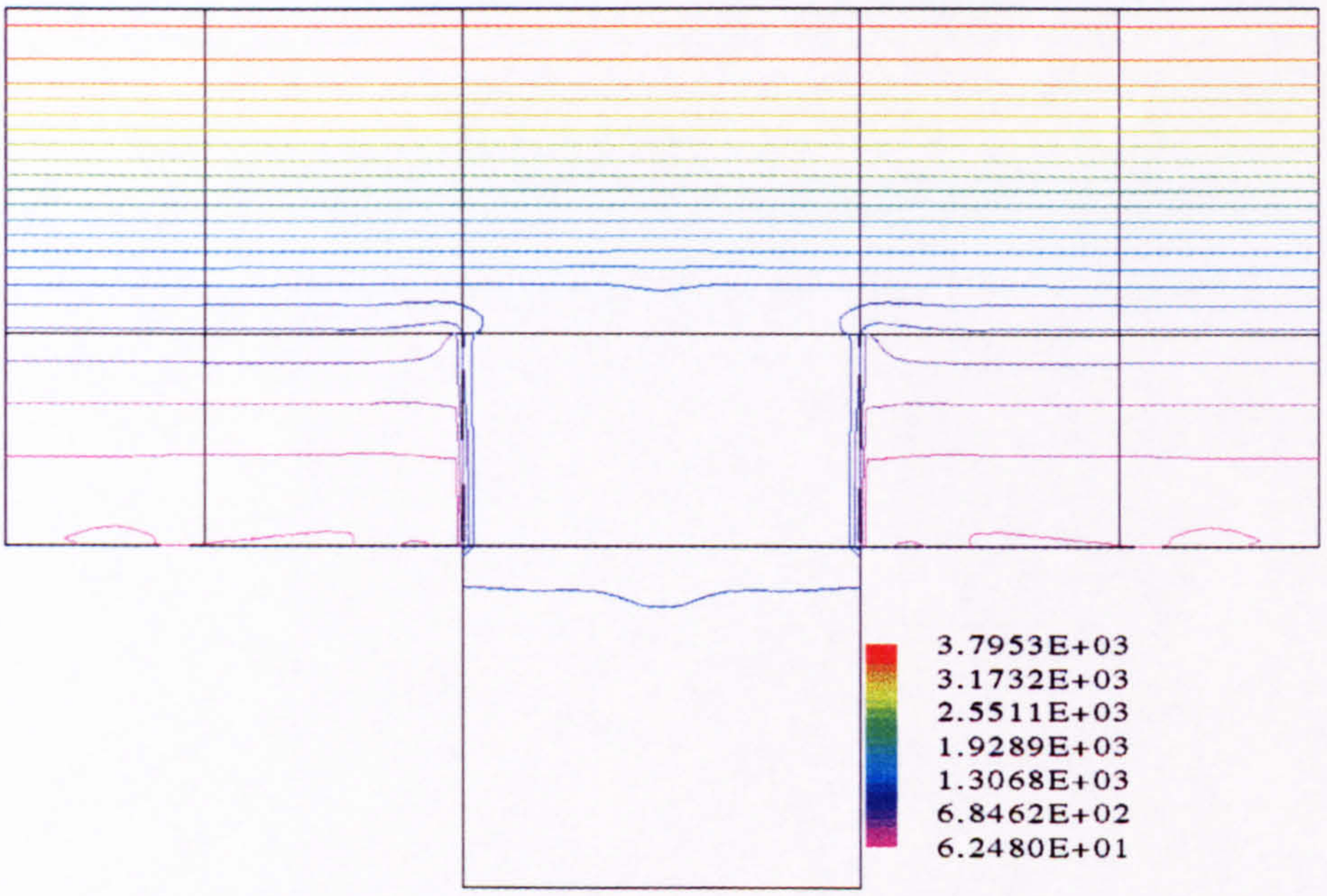


Figure 7.3-16e Pressure contour plot for 3DRNG2.

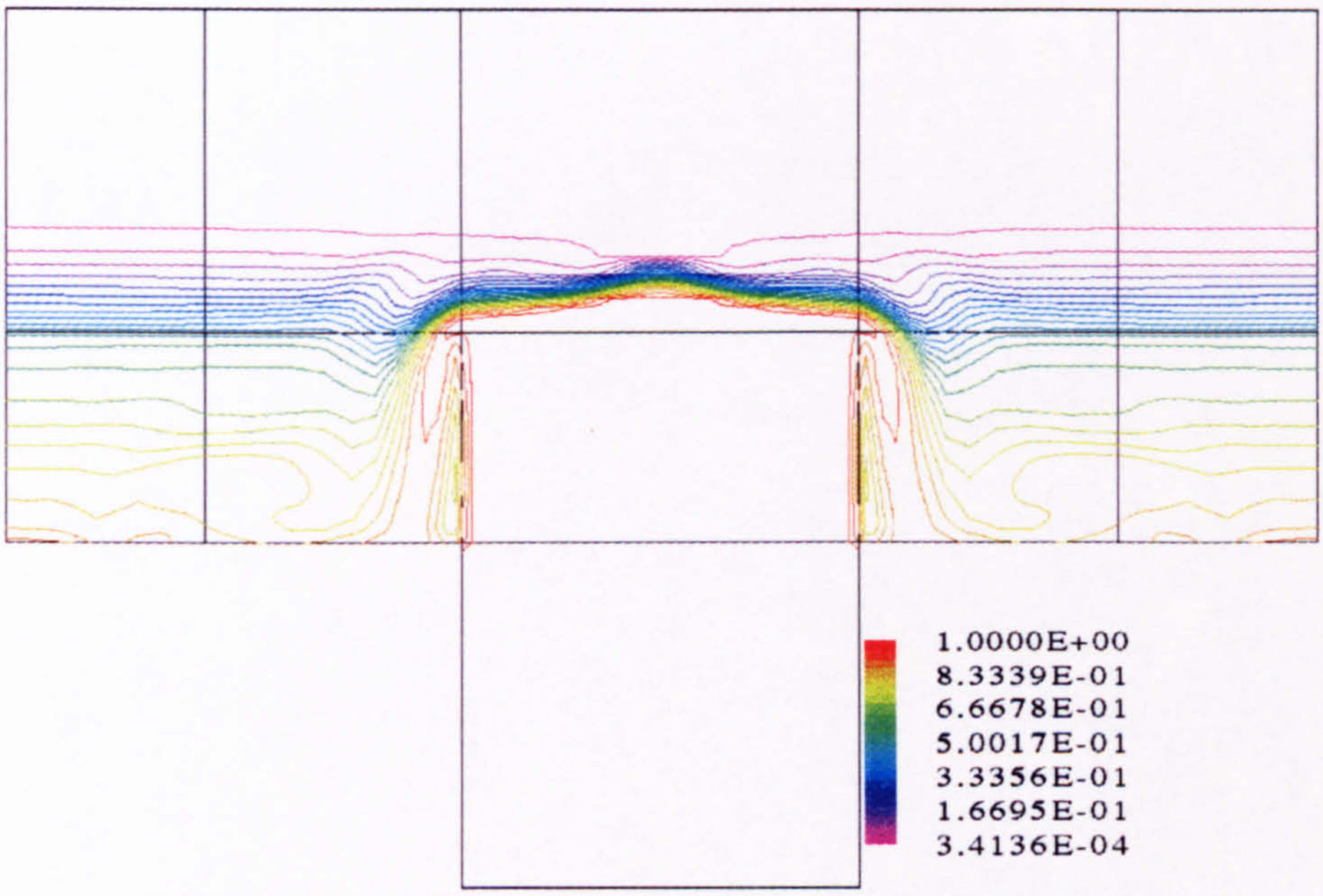


Figure 7.3-16f Volume fraction contour plot of water for 3DRNG2. Value of 1.0 is water, and 0.0 is air. Free surface has a value of 0.5.

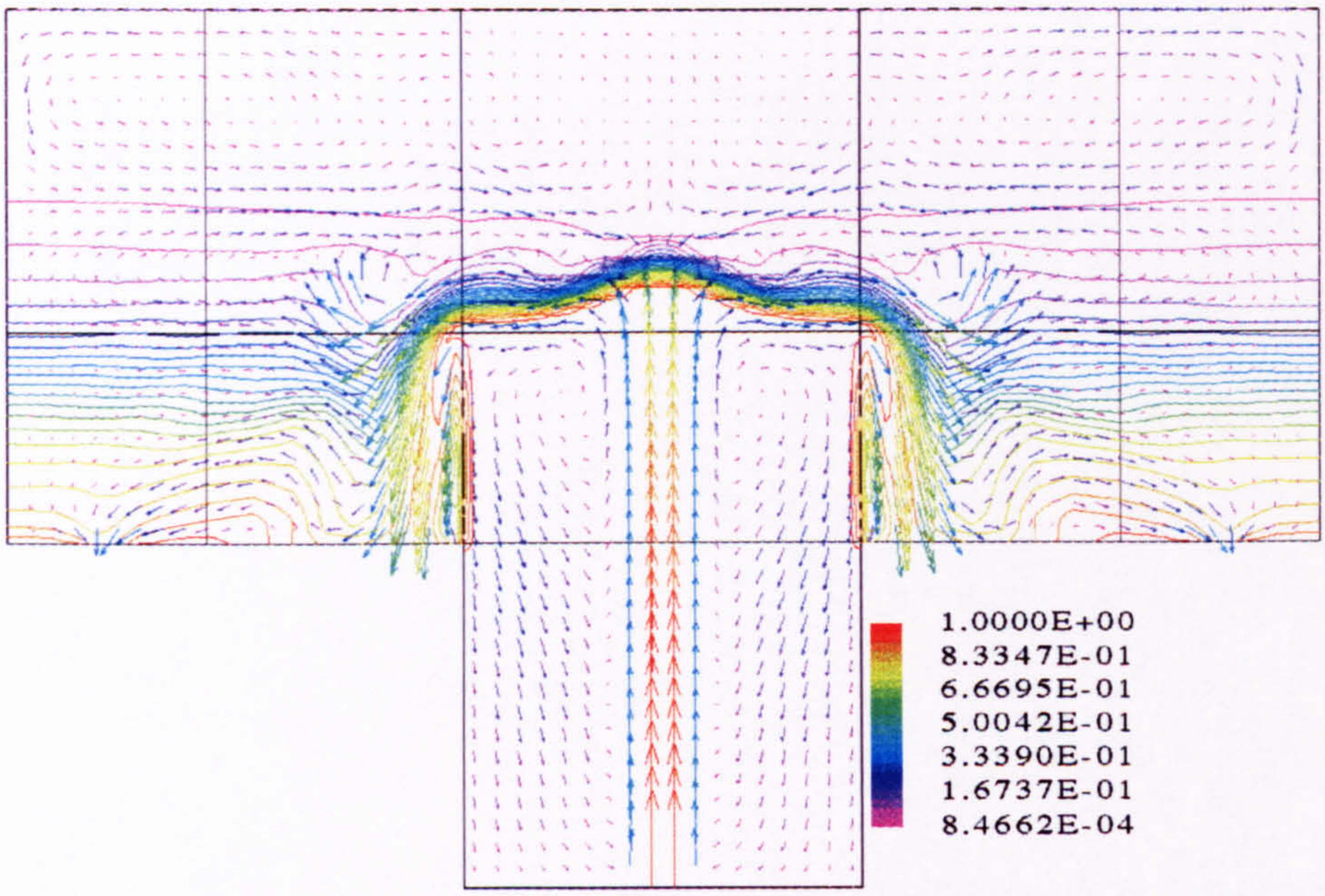


Figure 7.3-17a Velocity vector and volume fraction contour plot for 3DRNG3. 3D, 2-phase, transient calculations performed. Flowrate = 5.51 l/s. Mass residual = 1 x 10^{-7} kg/s (5 fold reduction in mass residuals). Van Leer differencing scheme, RNG k-ε turbulence model used. Surface sharpening not used.

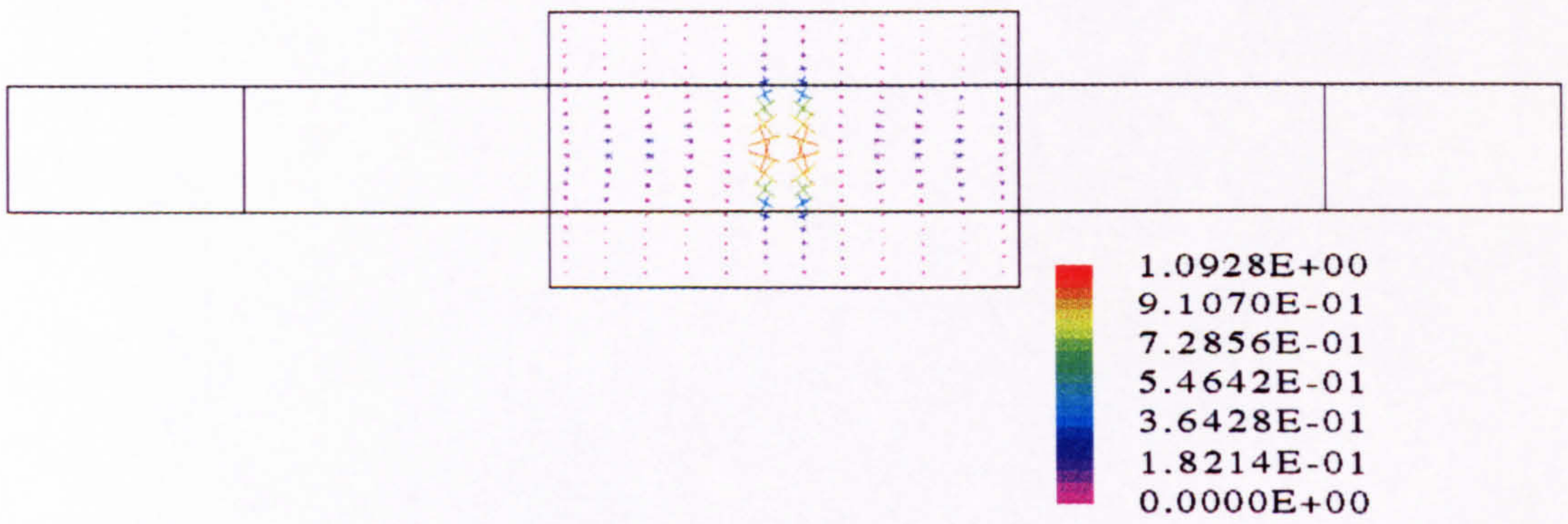


Figure 7.3-17b Velocity vector plot for 3DRNG3. Plan view of velocity vectors at y = 0.2 m (from invert of chamber).

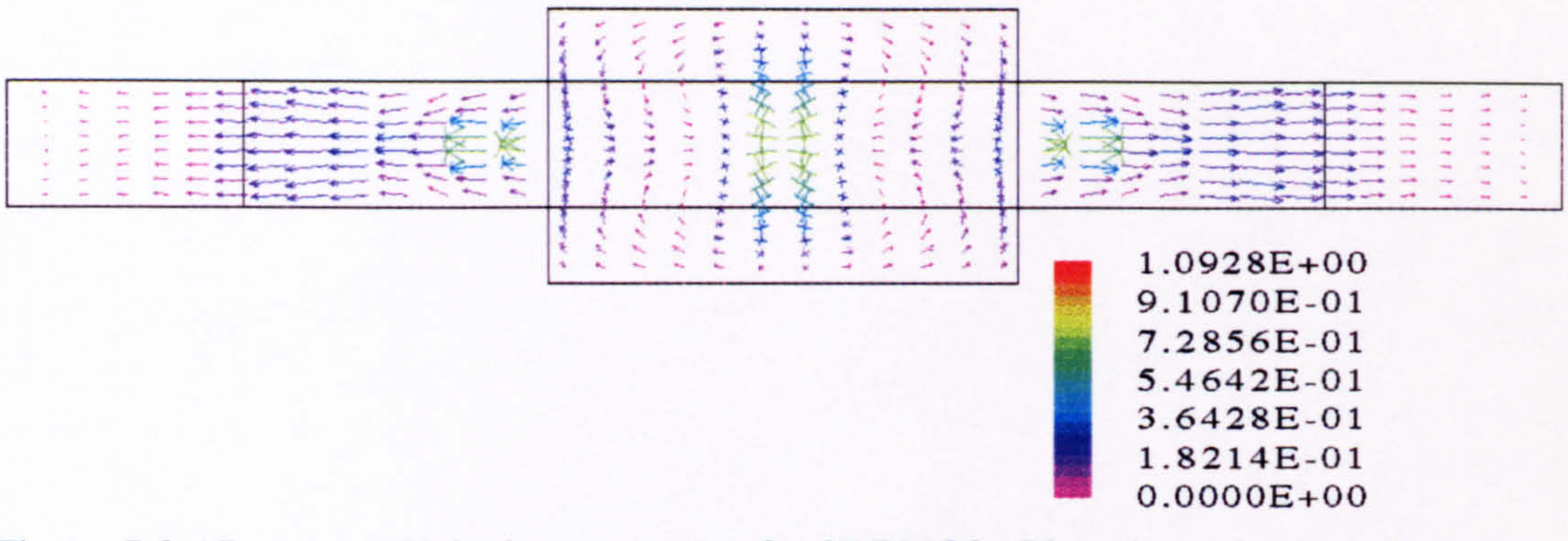


Figure 7.3-17c Velocity vector plot for 3DRNG3. Plan view of velocity vectors at y = 0.5 m (from chamber invert).

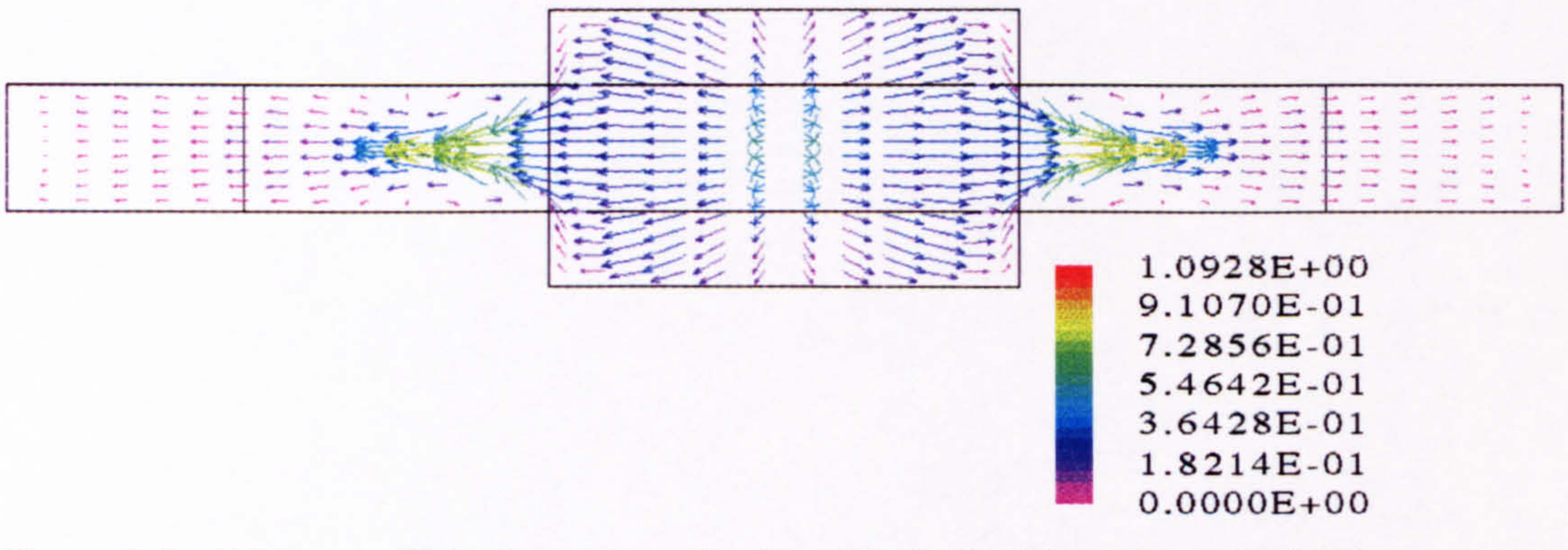


Figure 7.3-17d Velocity vector plot for 3DRNG3. Plan view of velocity vectors at y = 0.631 m (from chamber invert).

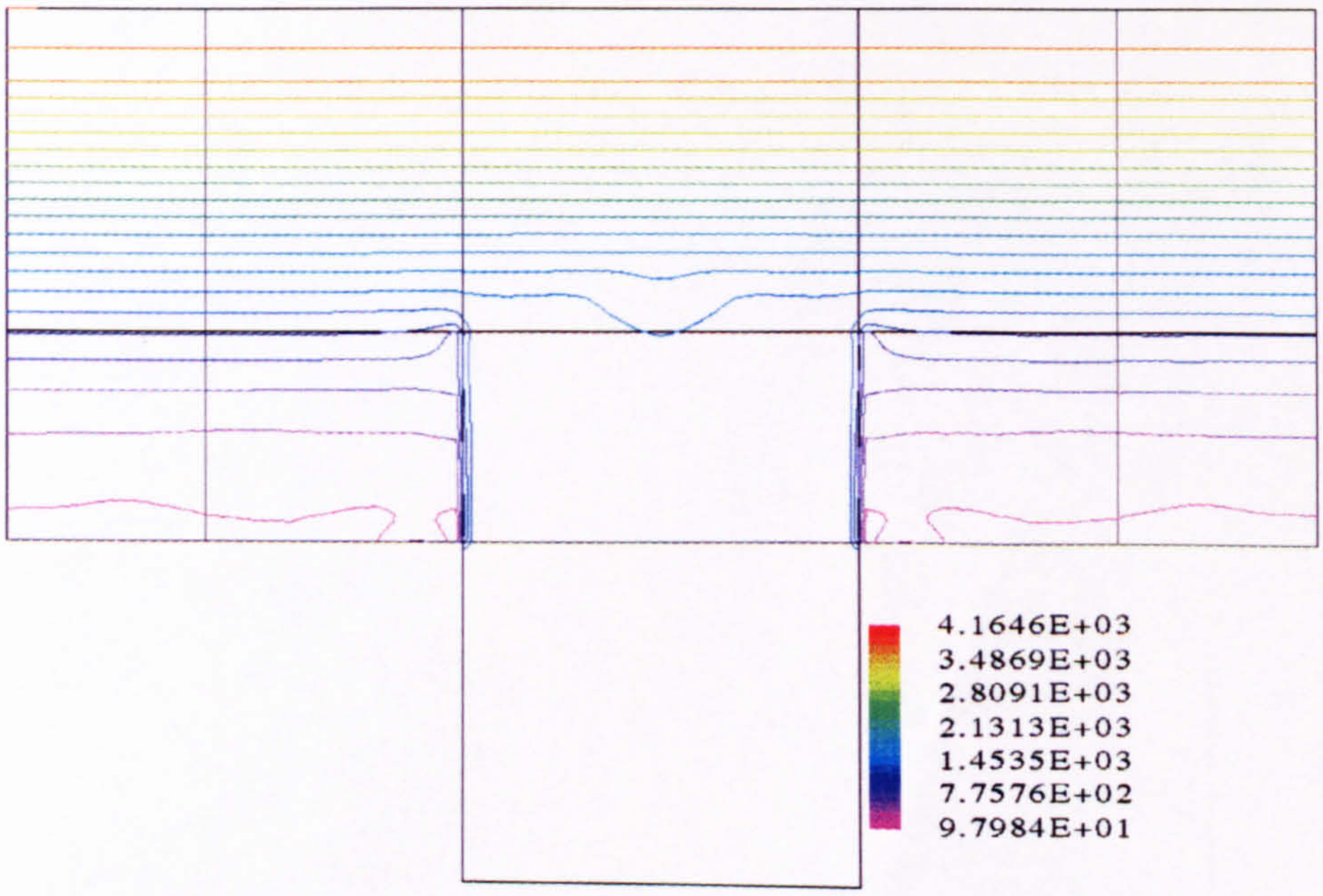


Figure 7.3-17e Pressure contour plot for 3DRNG3

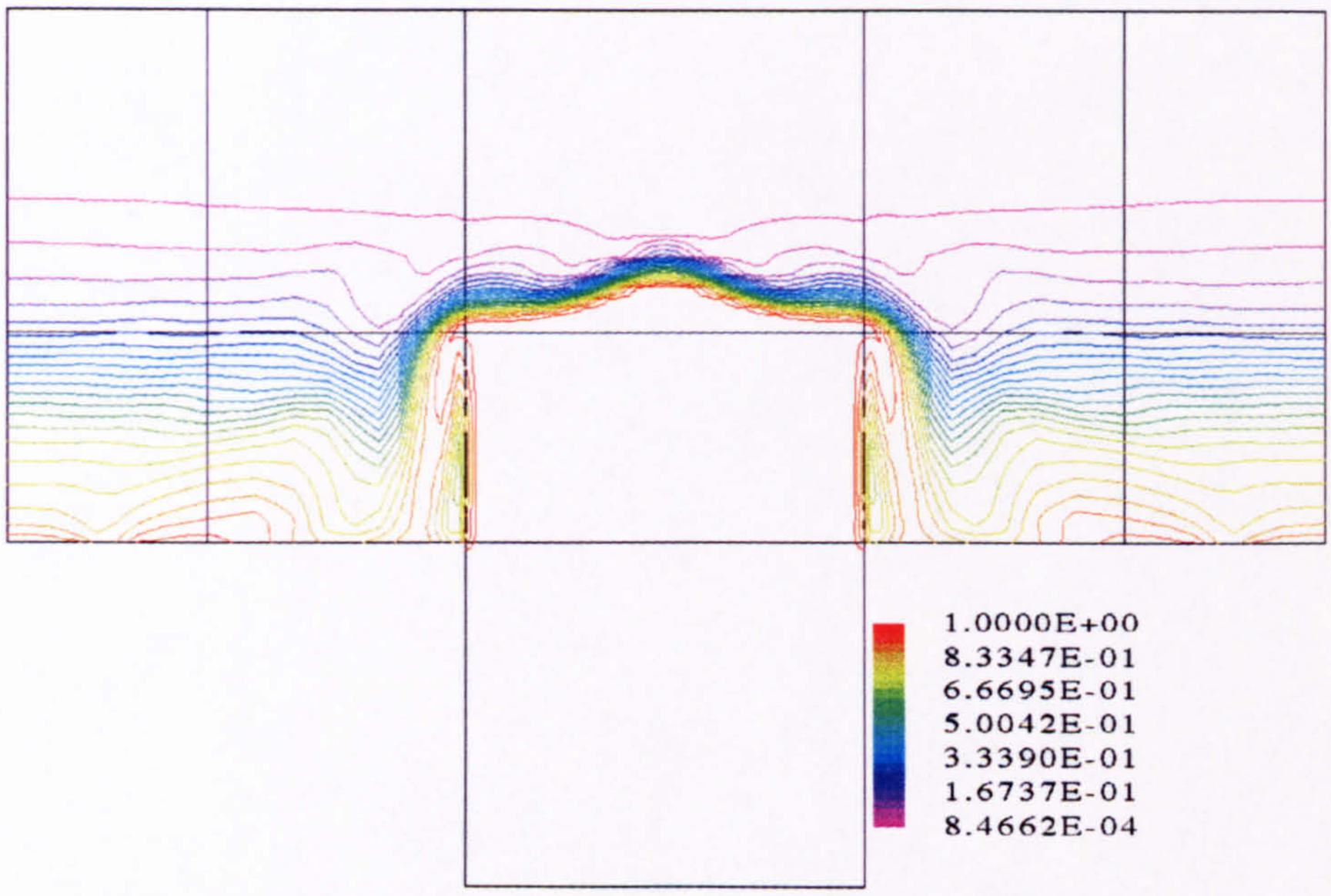


Figure 7.3-17f Volume fraction contour plot of water for 3DRNG3. Value of 1.0 represents water, 0.0 is air. Free surface has a value of 0.5.

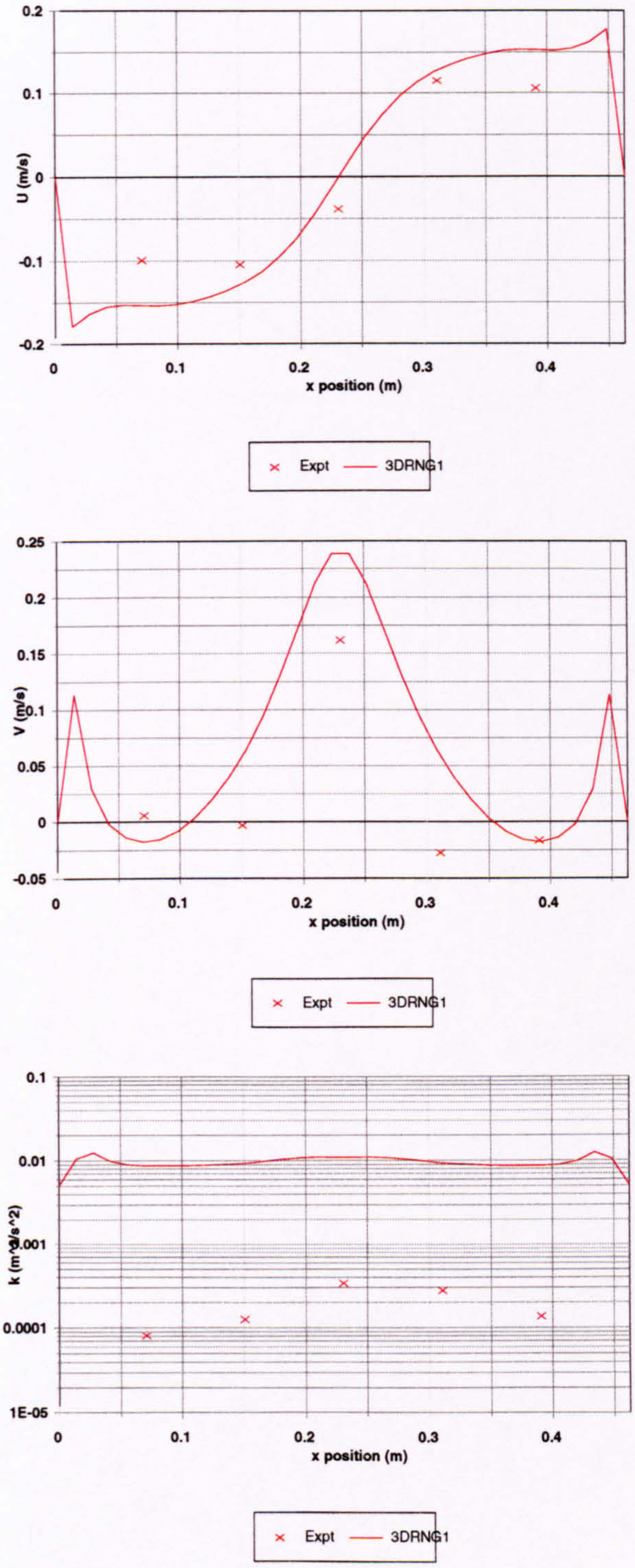


Figure 7.3-18a Comparison of measured and calculated velocities and turbulent kinetic energy, at y = 0.628 m, z = 0.1037 m. Flowrate = 2.95 l/s.

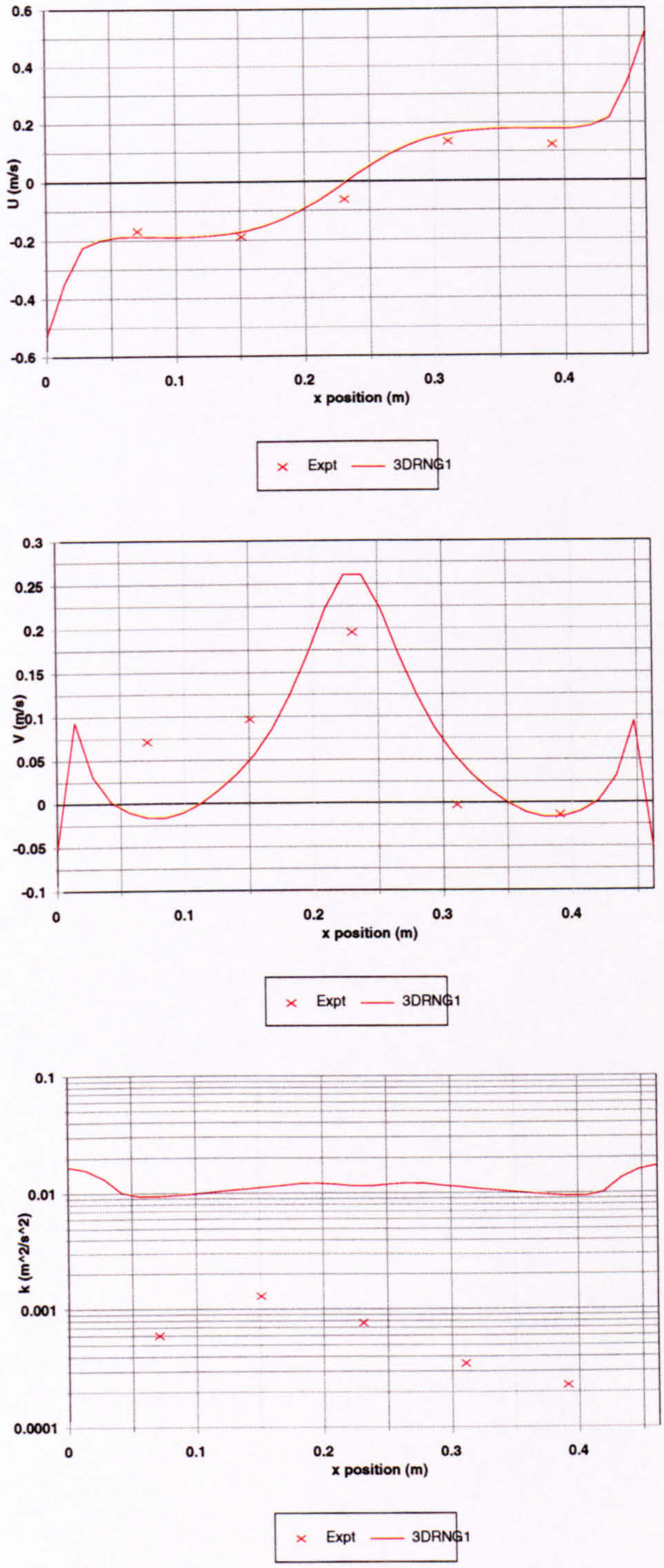


Figure 7.3-18b Comparison of measured and calculated velocities and turbulent kinetic energy, at y = 0.6358 m, z = 0.1337 m. Flowrate = 2.95 l/s.

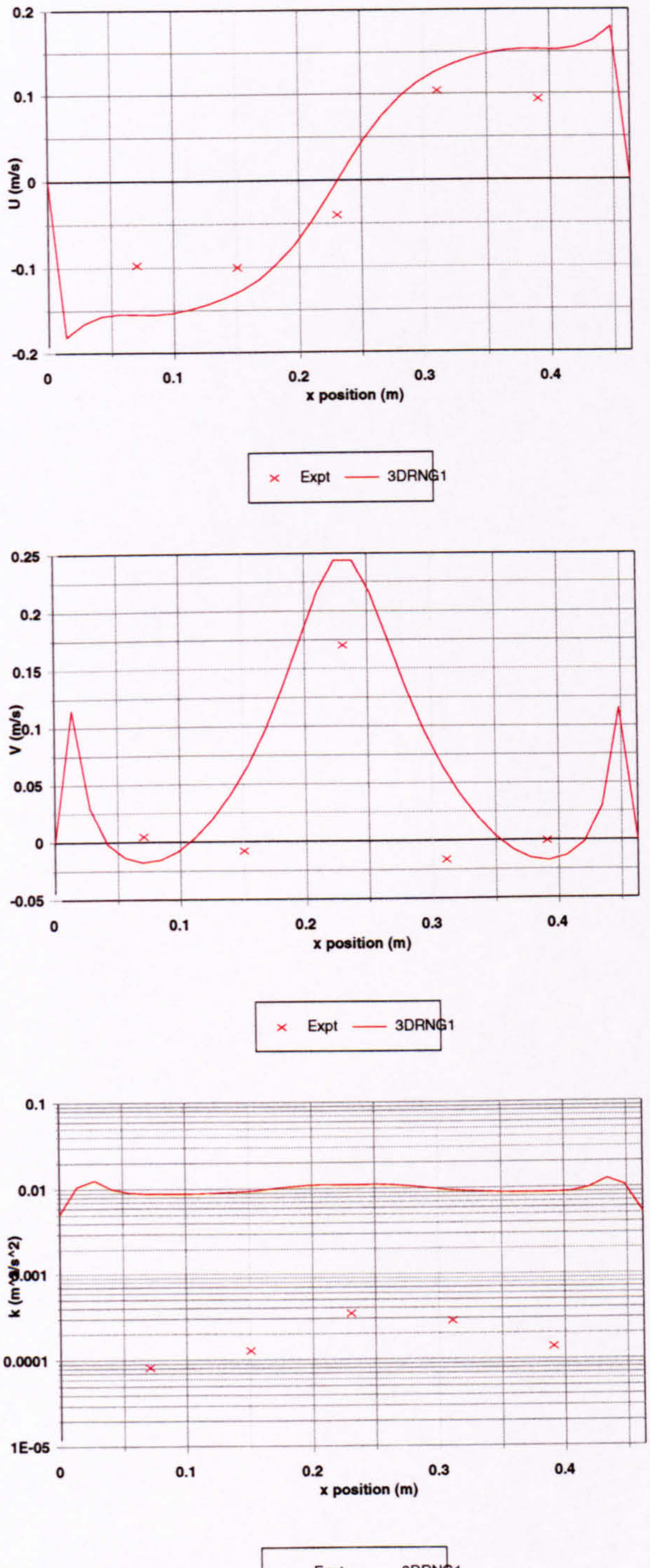


Figure 7.3-18c Comparison of measured and calculated velocities and turbulent kinetic energy, at y = 0.628 m, z = 0.1637 m. Flowrate = 2.95 l/s.

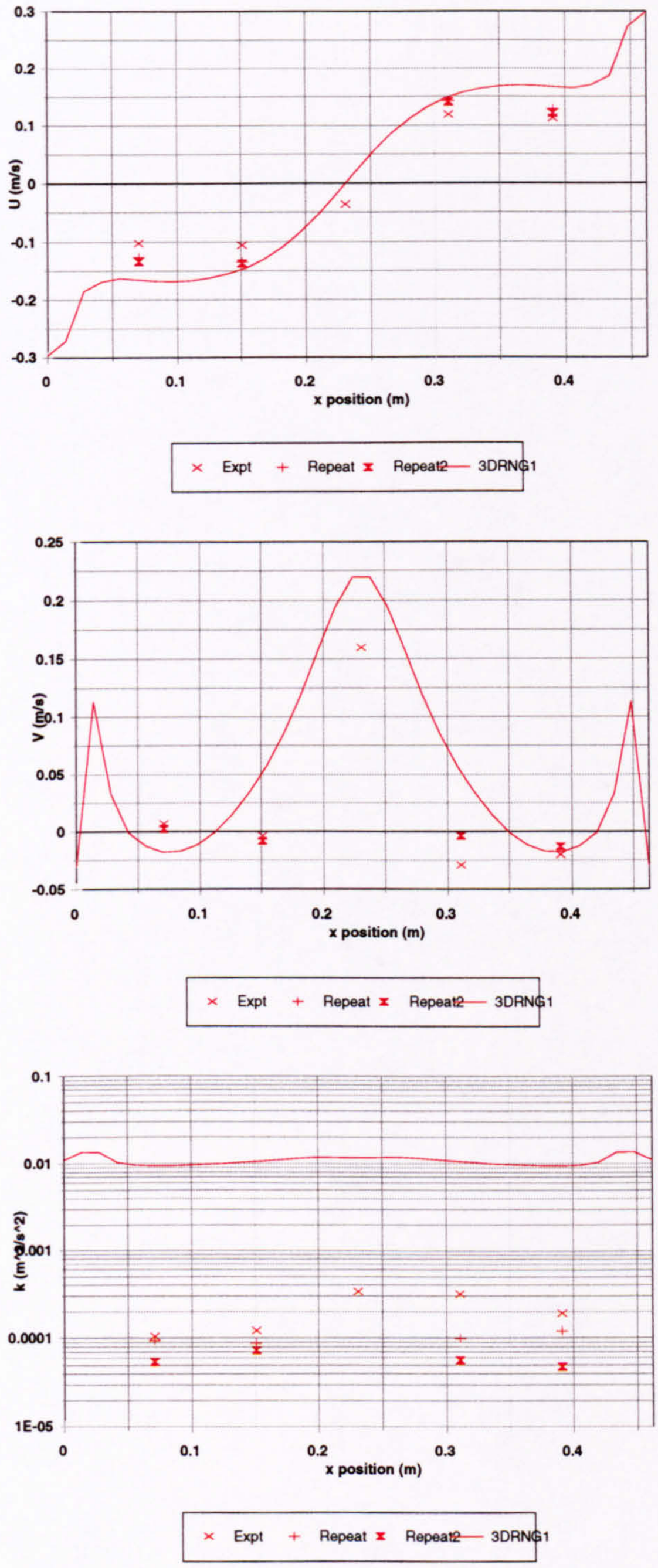


Figure 7.3-18d Comparison between measured and calculated velocities and turbulent kinetic energy, at y = 0.633 m, z = 0.1037 m. Flowrate = 2.95 l/s.

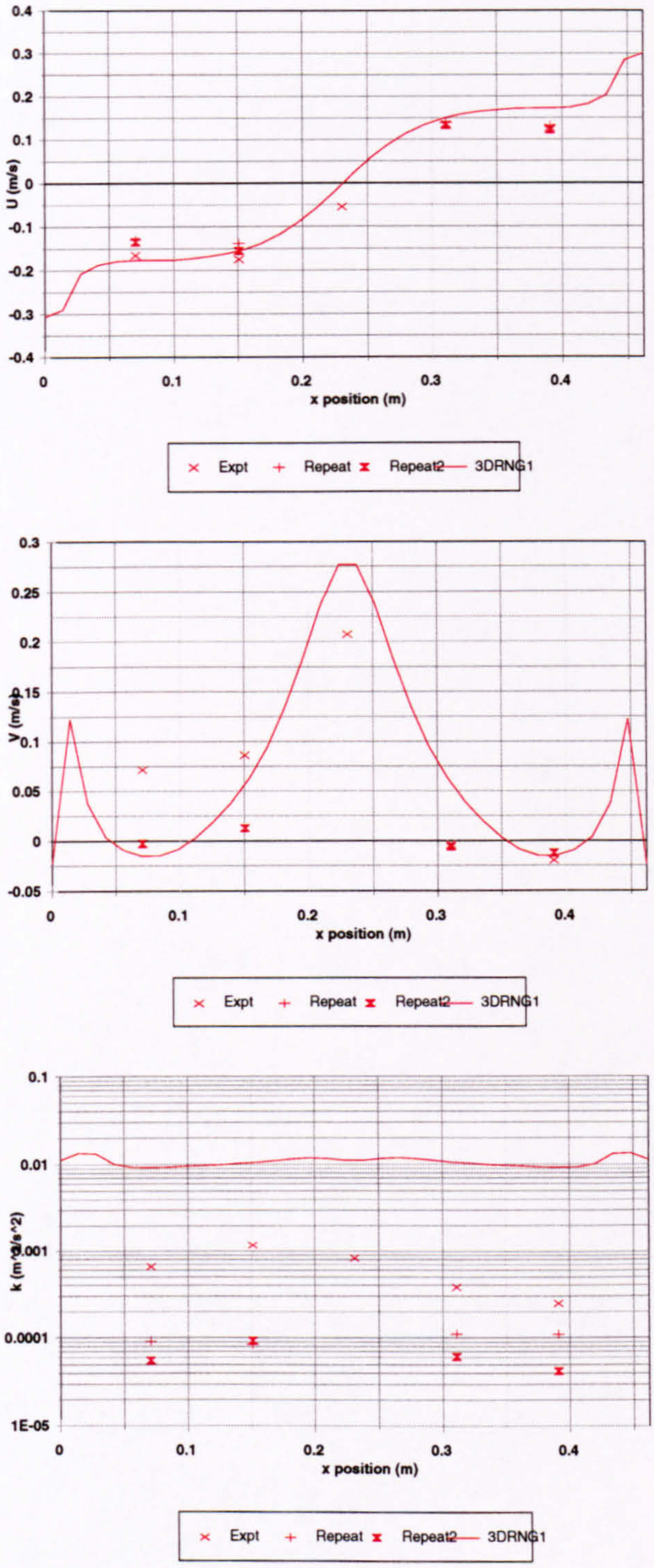


Figure 7.3-18e Comparison between measured and calculated velocities and turbulent kinetic energy, at y = 0.633 m, z = 0.1337 m. Flowrate = 2.95 l/s.

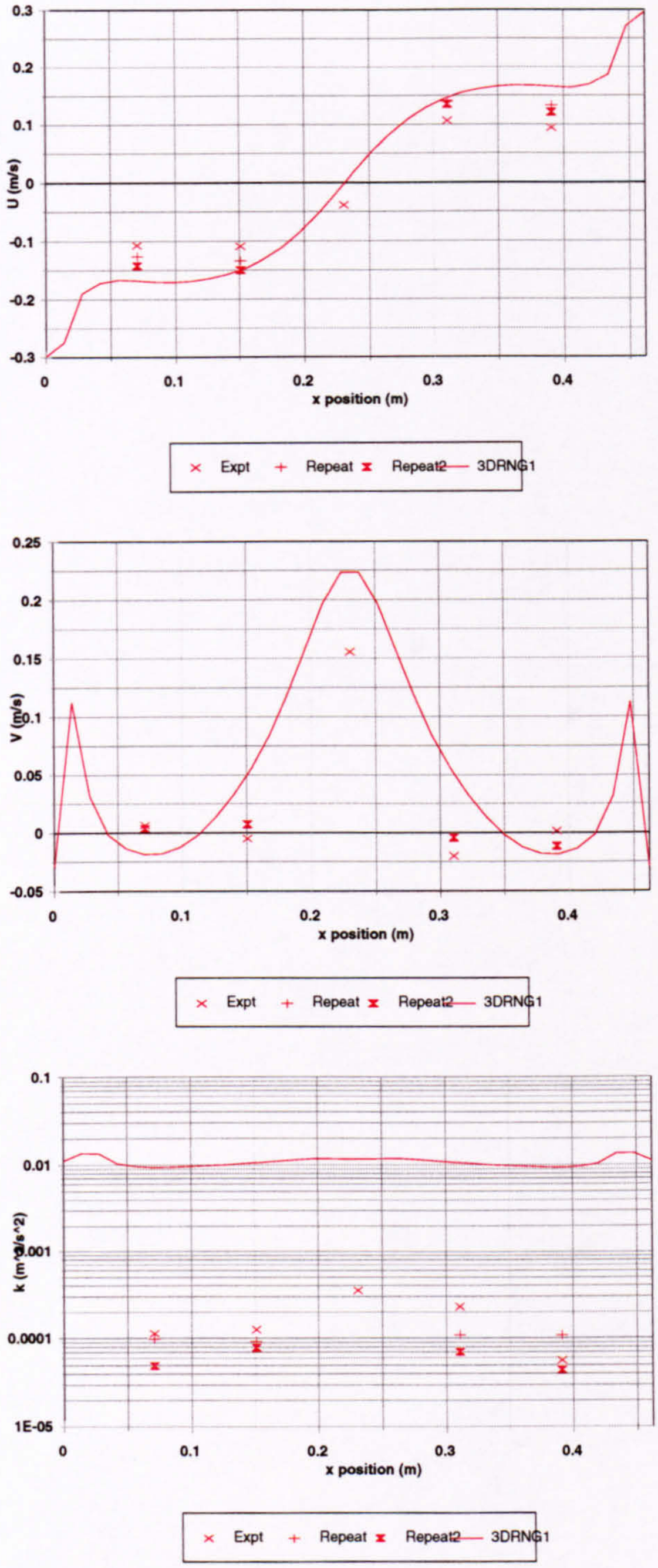


Figure 7.3-18f Comparison between measured and calculated velocities and turbulent kinetic energy, at y = 0.633 m, z = 0.1637 m. Flowrate = 2.95 l/s.

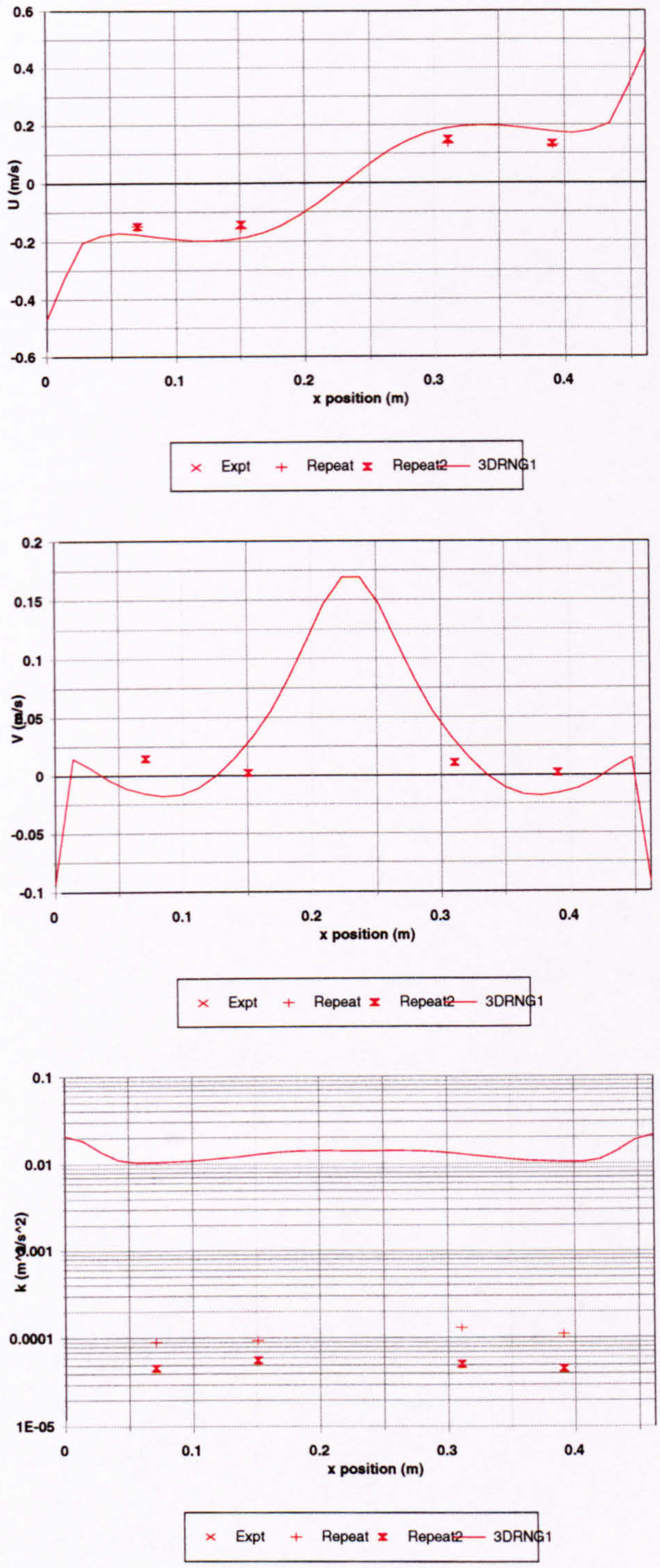


Figure 7.3-18g Comparison between measured and calculated velocities and turbulent kinetic energy, at y = 0.643 m, z = 0.1037 m. Flowrate = 2.95 l/s.

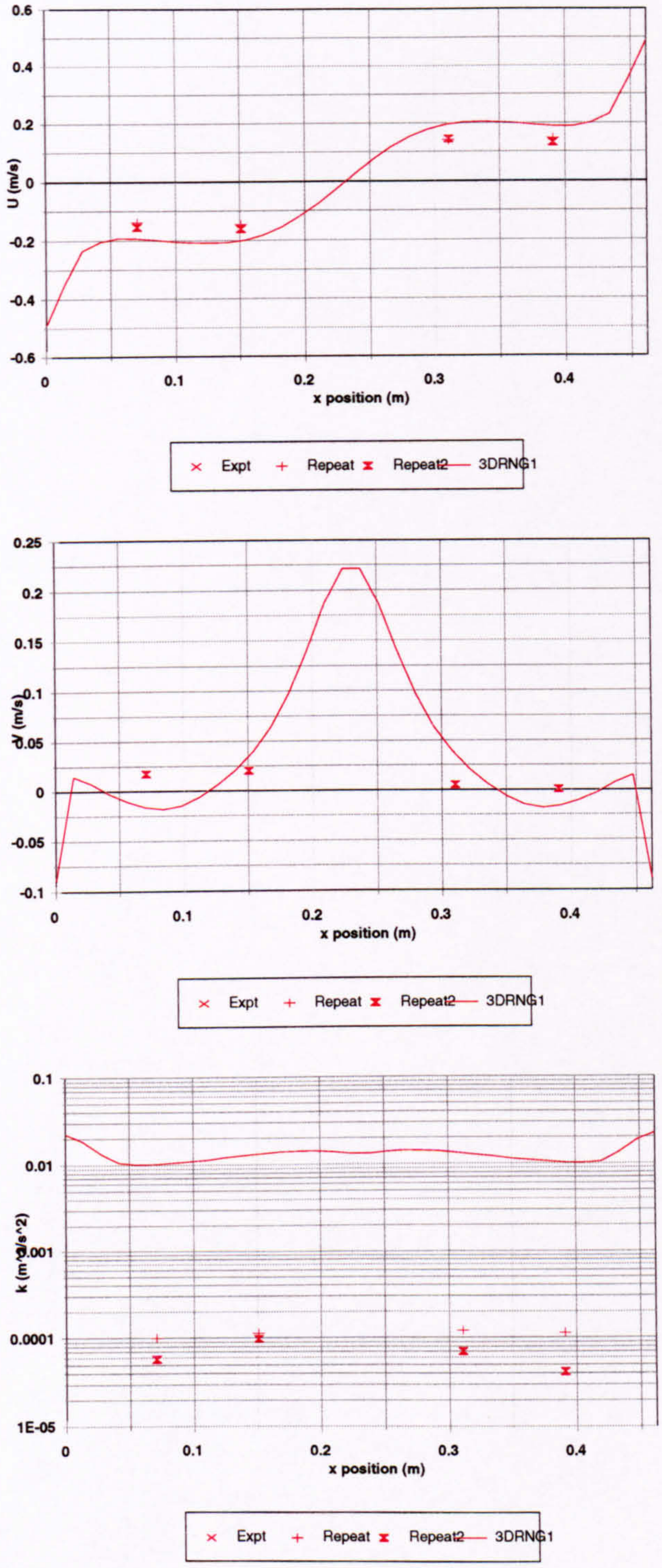


Figure 7.3-18h Comparison between measured and calculated velocities and turbulent kinetic energy, at y = 0.643 m, z = 0.1337 m. Flowrate = 2.95 l/s.

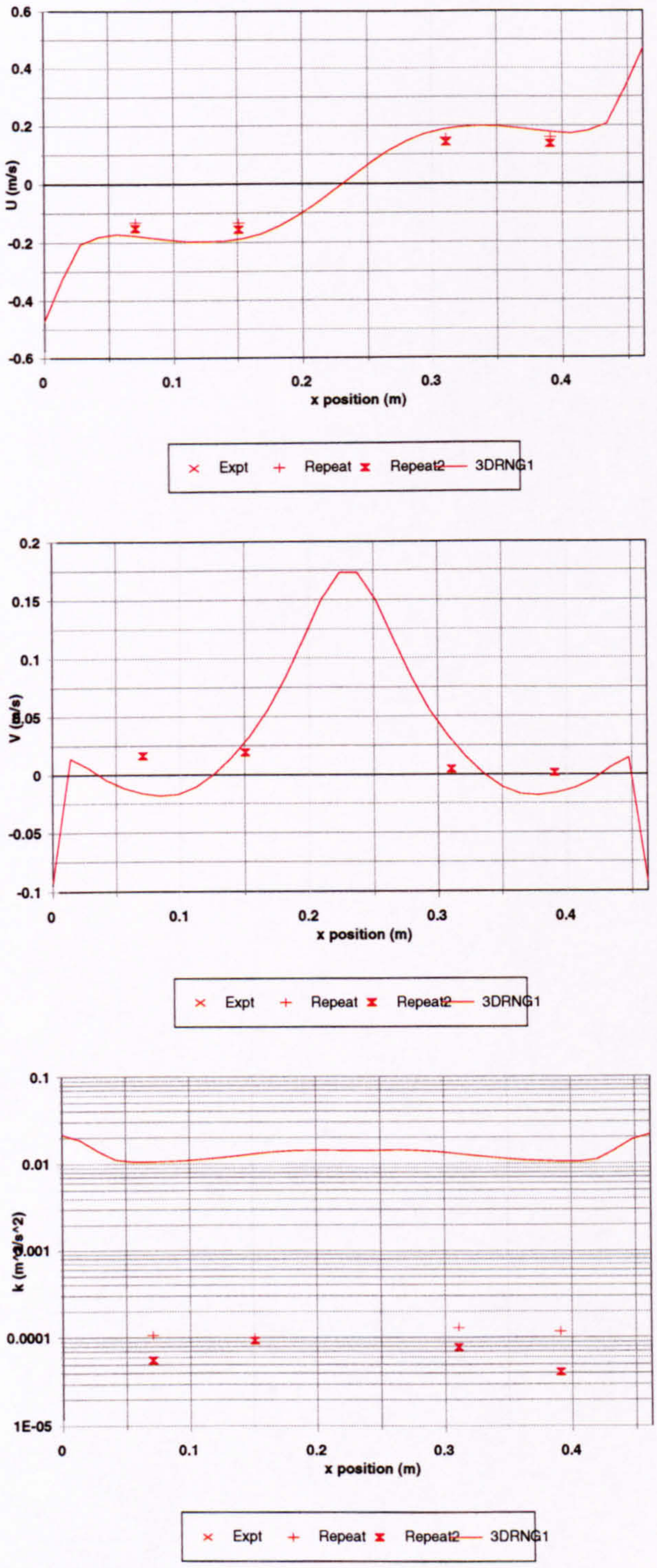


Figure 7.3-18i Comparison between measured and calculated velocities and turbulent kinetic energy, at y = 0.643 m, z = 0.1637 m. Flowrate = 2.95 l/s.

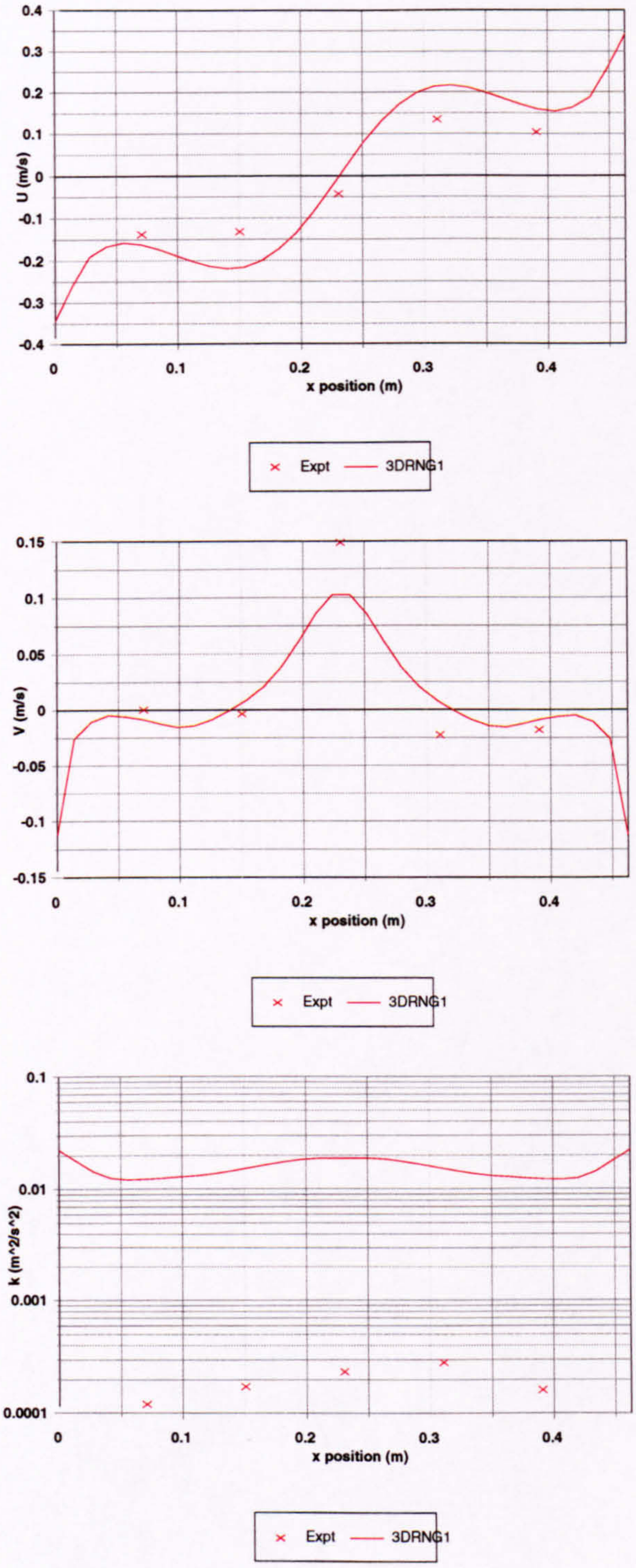


Figure 7.3-18j Comparison between measured and calculated velocities and turbulent kinetic energy, at y = 0.653 m, z = 0.1037 m. Flowrate = 2.95 l/s.

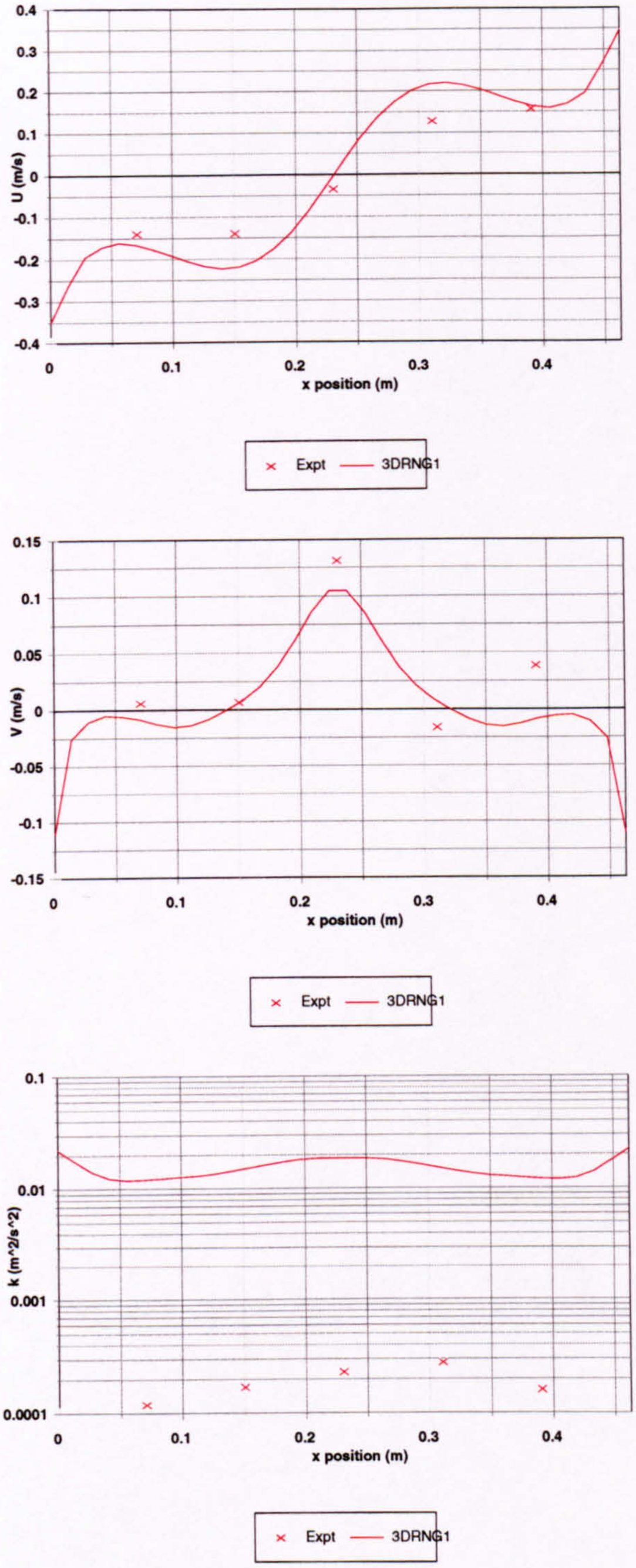


Figure 7.3-18k Comparison between measured and calculated velocities and turbulent kinetic energy, at y = 0.653 m, z = 0.1637 m. Flowrate = 2.95 l/s.

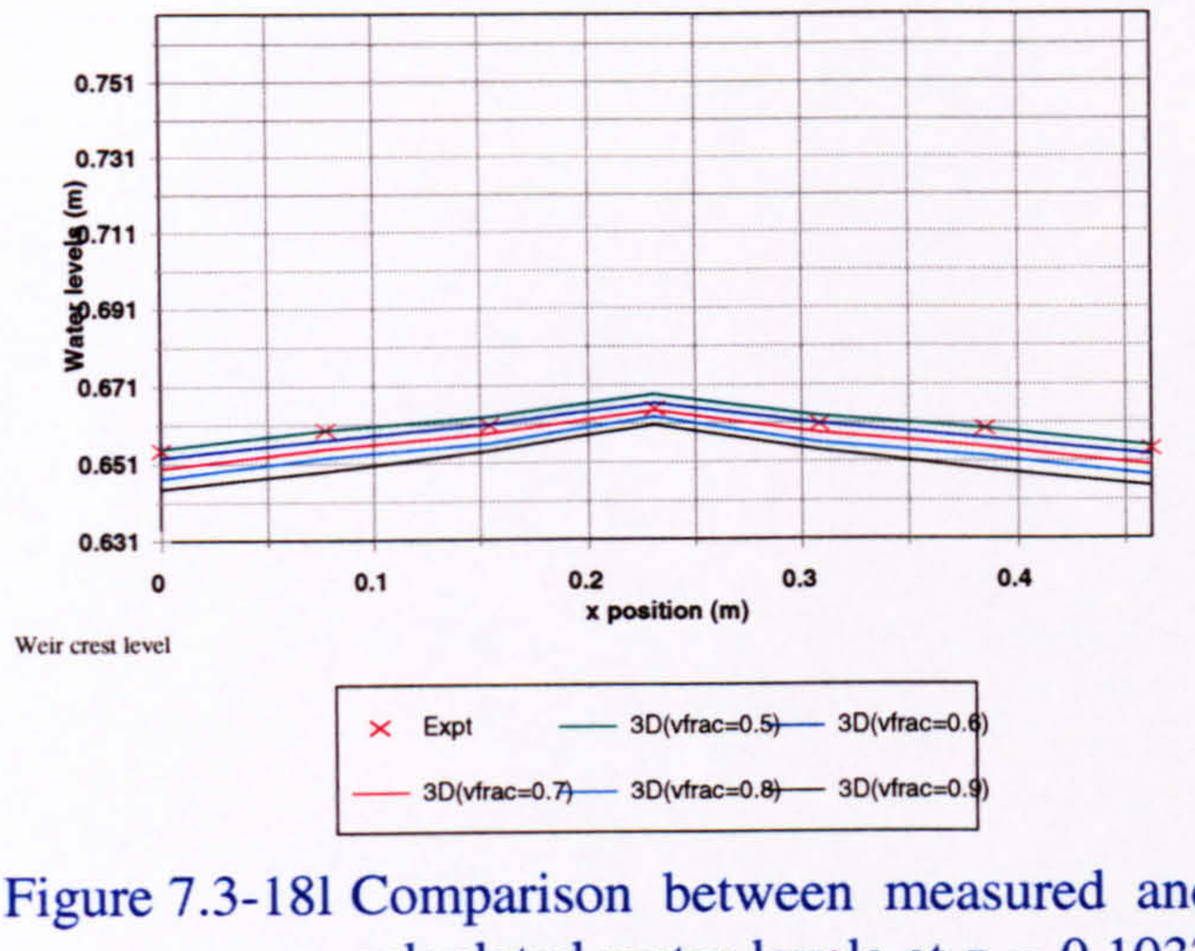


Figure 7.3-18l Comparison between measured and calculated water levels at z = 0.1037 m

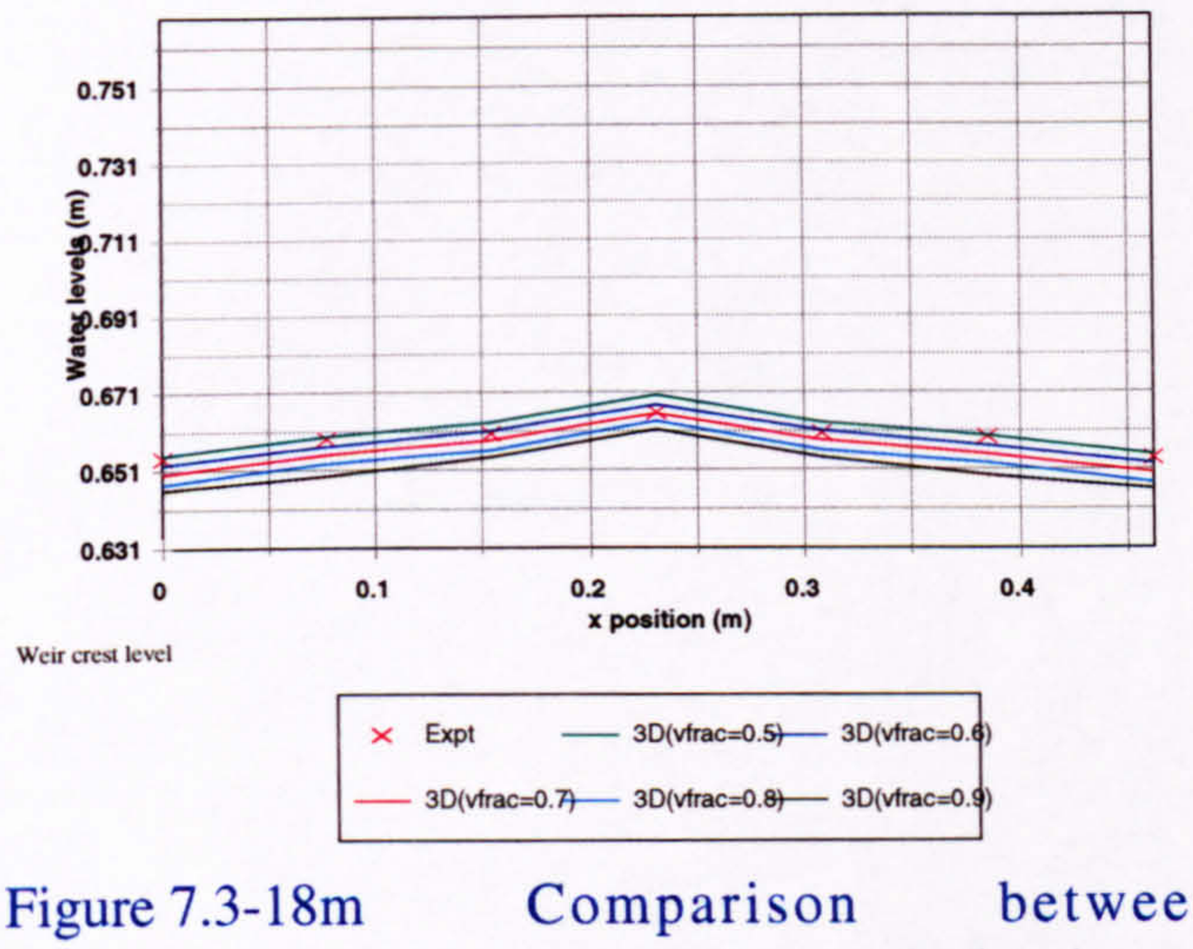


Figure 7.3-18m Comparison between measured and calculated water levels at z = 0.1337 m

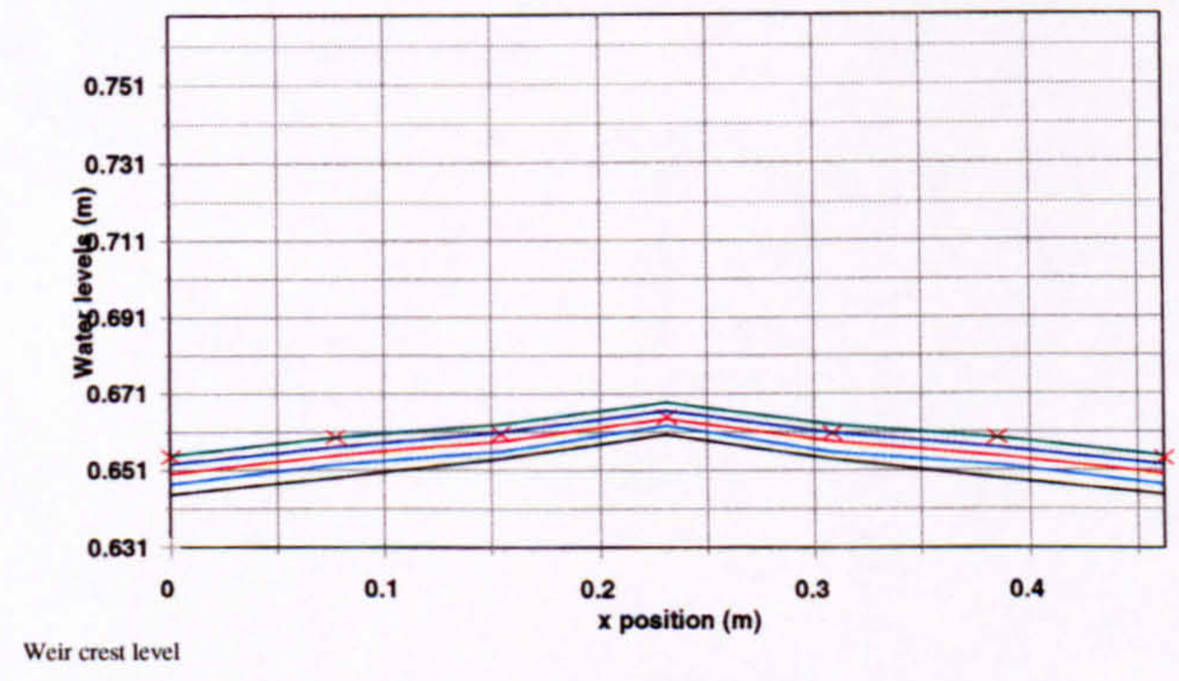


Figure 7.3-18n Comparison between measured and calculated water levels at z = 0.1637 m

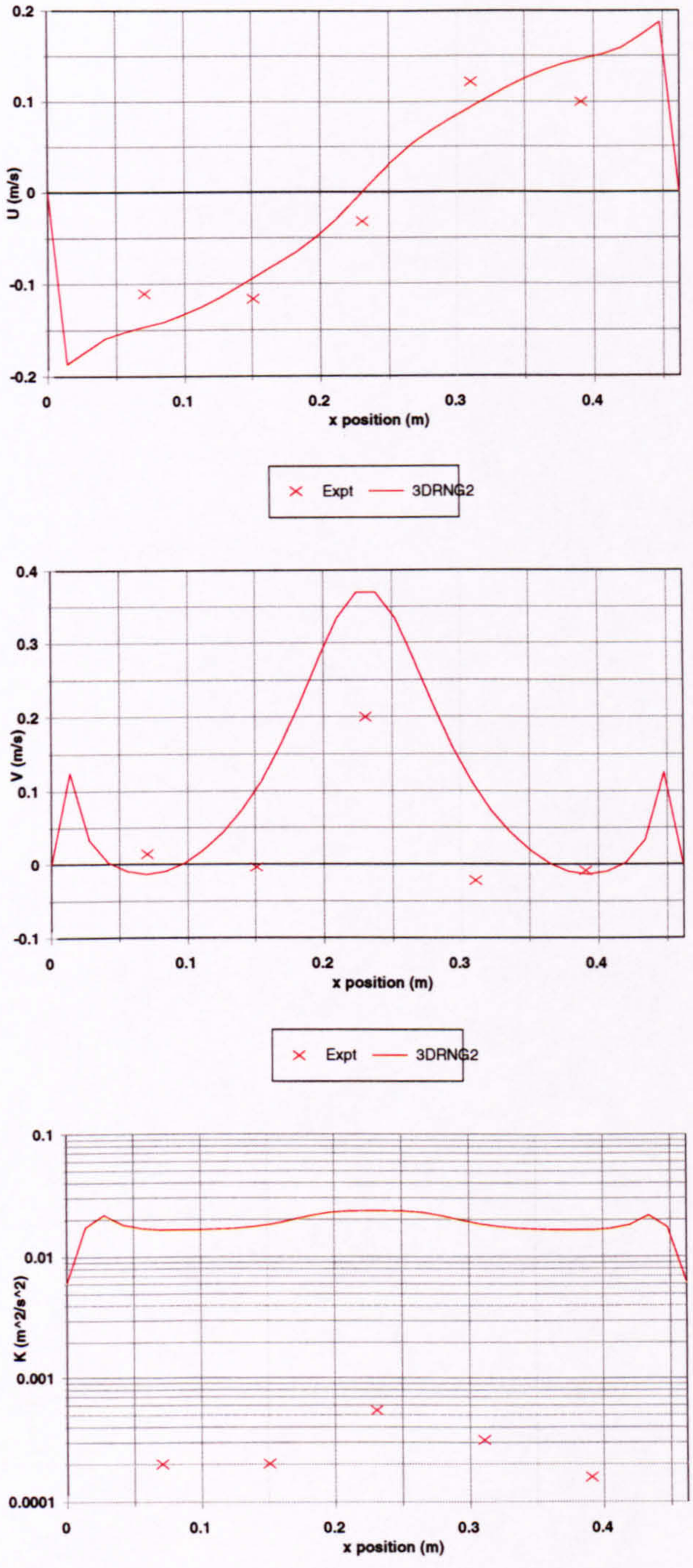


Figure 7.3-19aComparison of measured and calculated velocities and turbulent kinetic energy, at y = 0.628 m, z = 0.1037 m. Flowrate = 4.38 l/s.

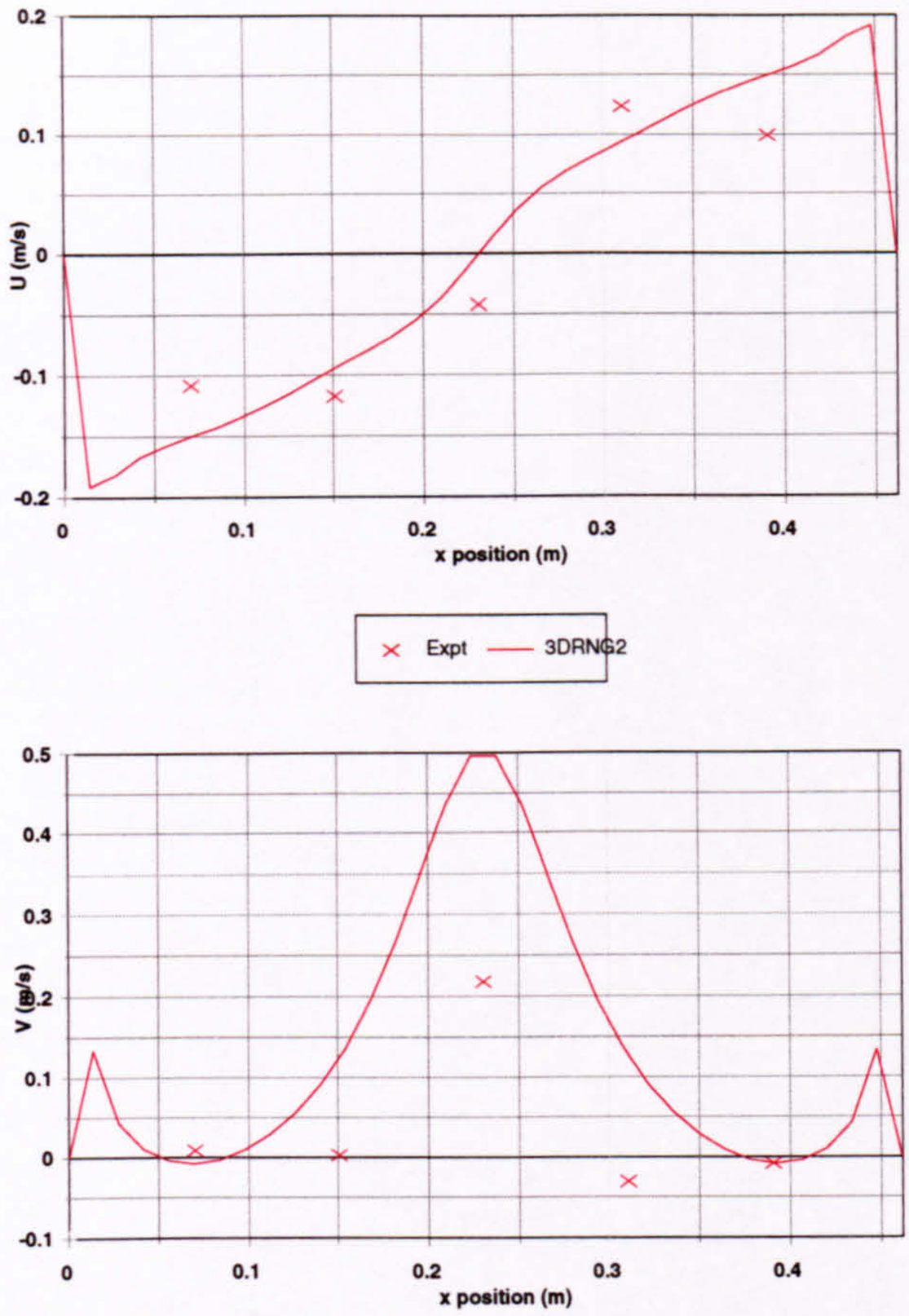


Figure 7.3-19bComparison of measured and calculated velocities and turbulent kinetic energy, at y = 0.628 m, z = 0.1337 m. Flowrate = 4.38 l/s.

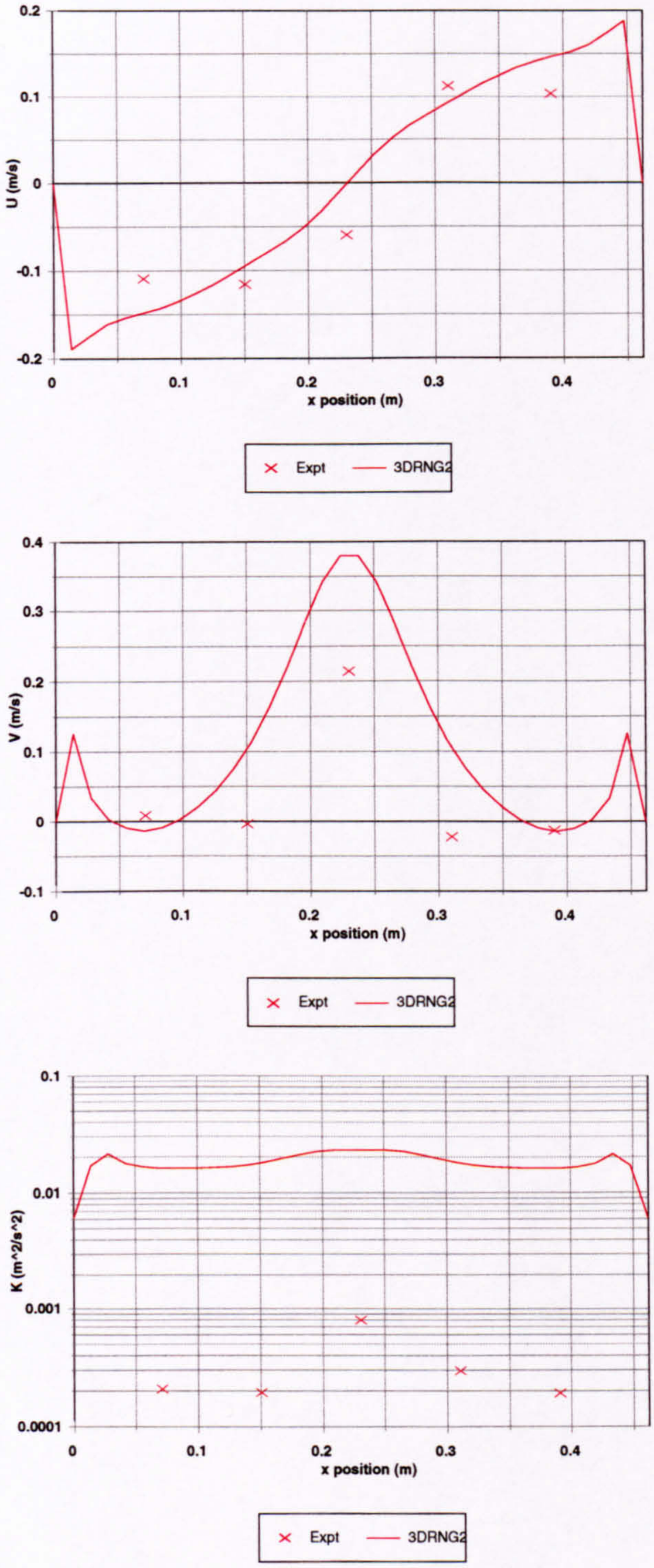


Figure 7.3-19cComparison of measured and calculated velocities and turbulent kinetic energy, at y = 0.628 m, z = 0.1637 m. Flowrate = 4.38 l/s.

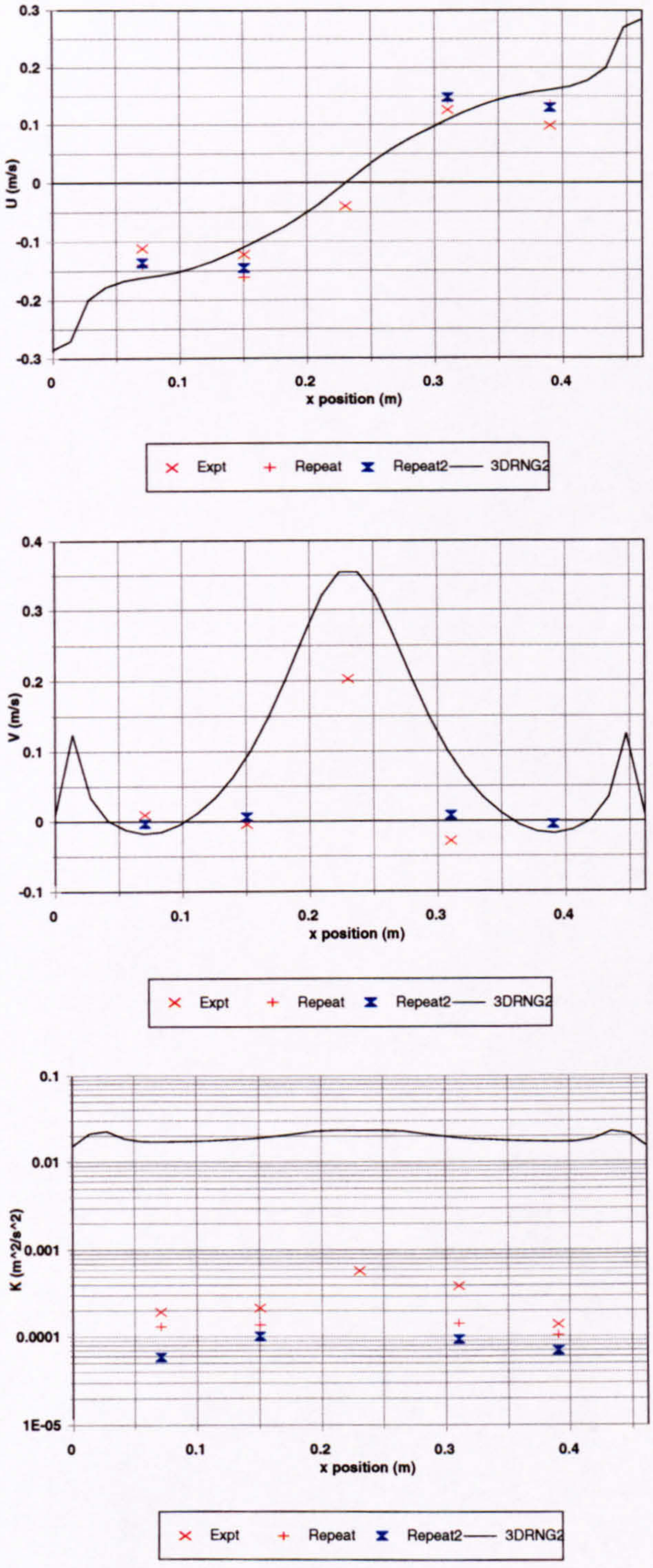


Figure 7.3-19d Comparison of measured and calculated velocities and turbulent kinetic energy, at y = 0.633 m, z = 0.1037 m. Flowrate = 4.38 l/s.

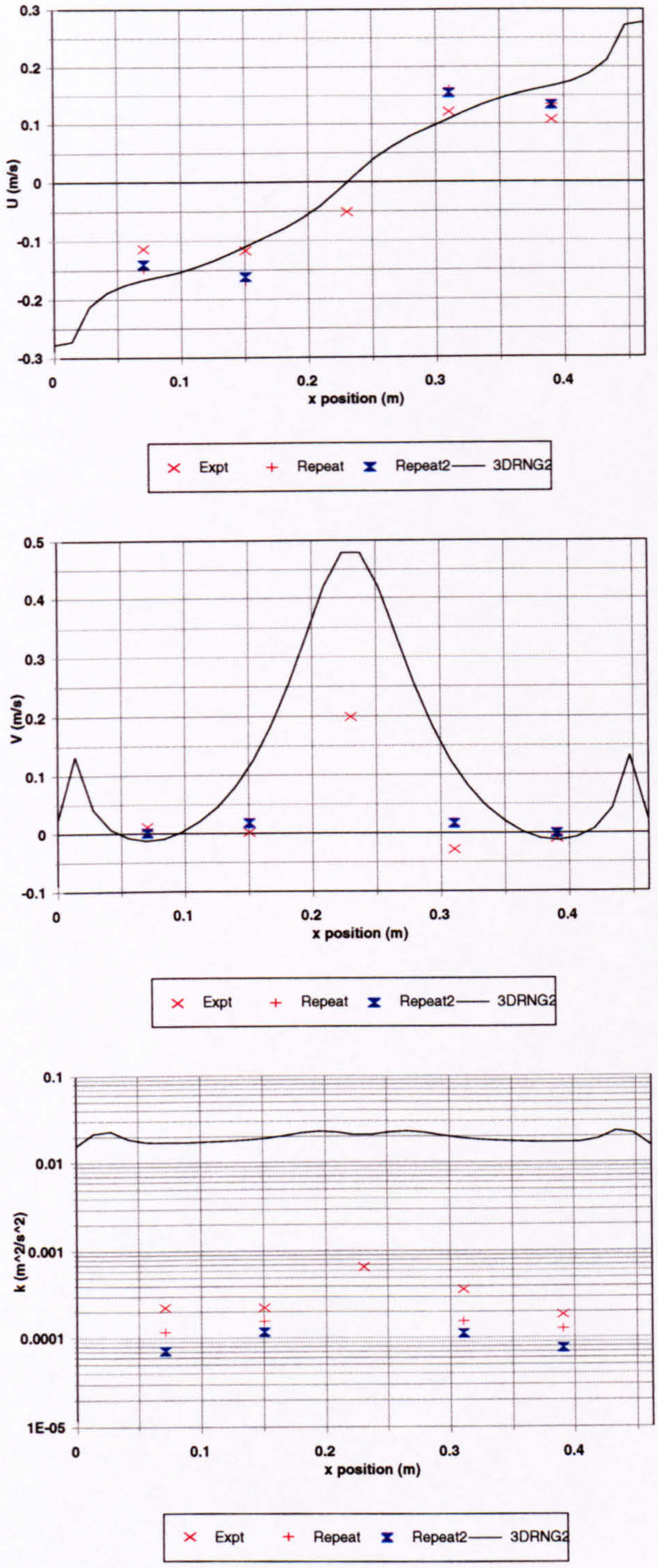


Figure 7.3-19e Comparison of measured and calculated velocities and turbulent kinetic energy, at y = 0.633 m, z = 0.1337 m. Flowrate = 4.38 l/s.

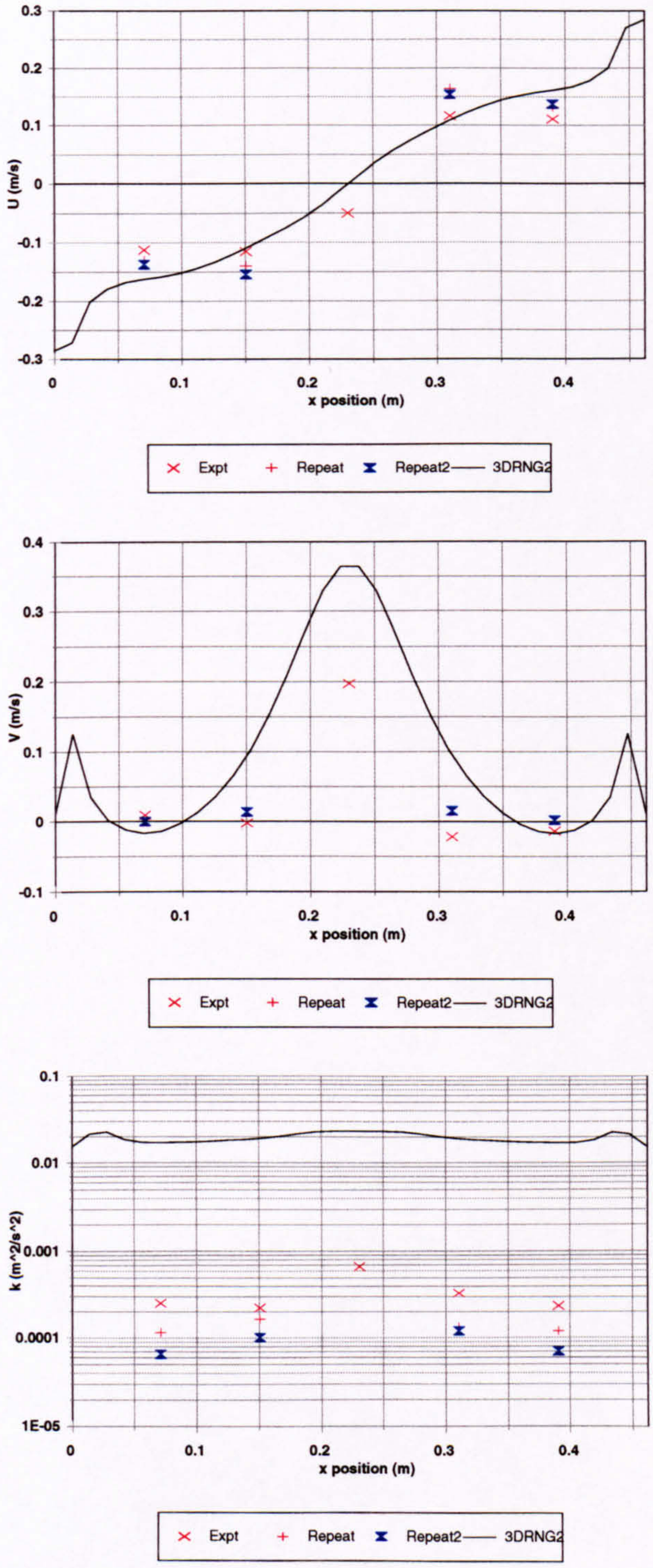


Figure 7.3-19f Comparison of measured and calculated velocities and turbulent kinetic energy, at y = 0.633 m, z = 0.1637 m. Flowrate = 4.38 l/s.

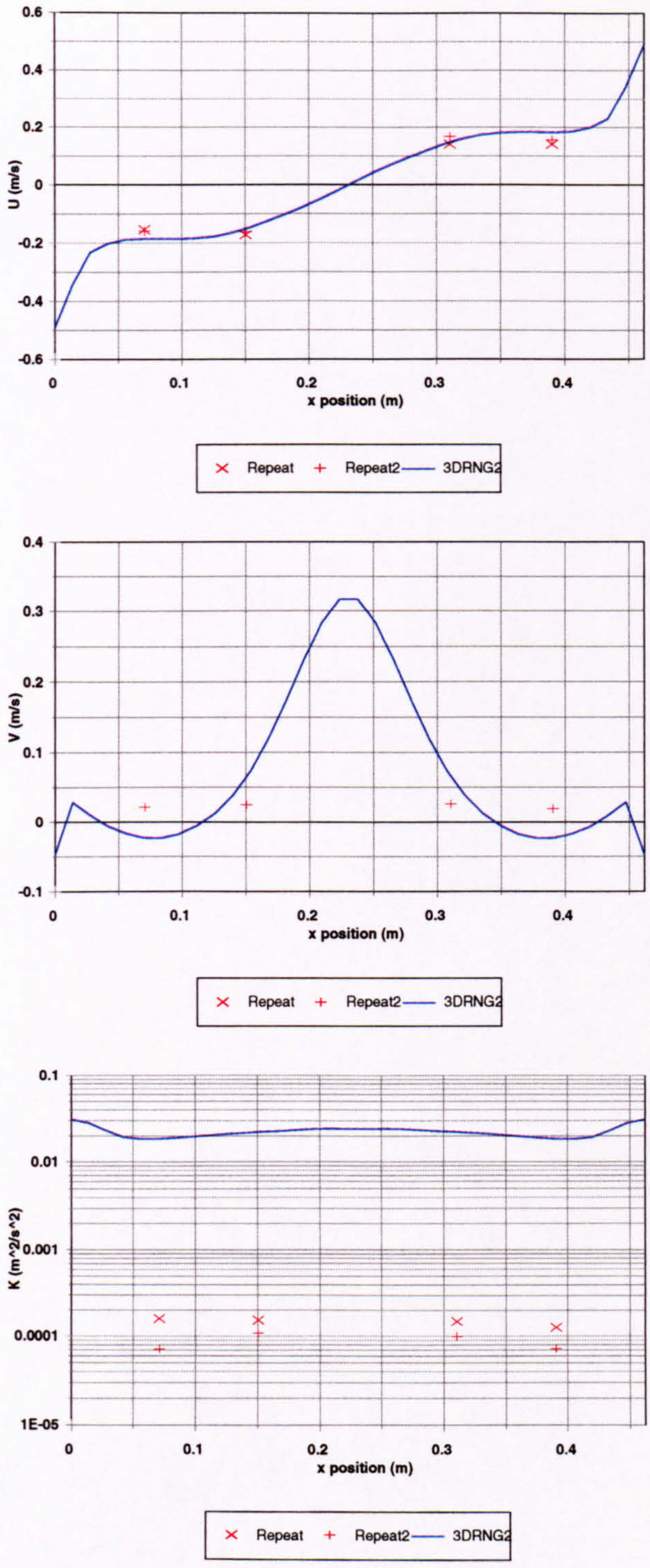


Figure 7.3-19g Comparison of measured and calculated velocities and turbulent kinetic energy, at y = 0.643 m, z = 0.1037 m. Flowrate = 4.38 l/s.

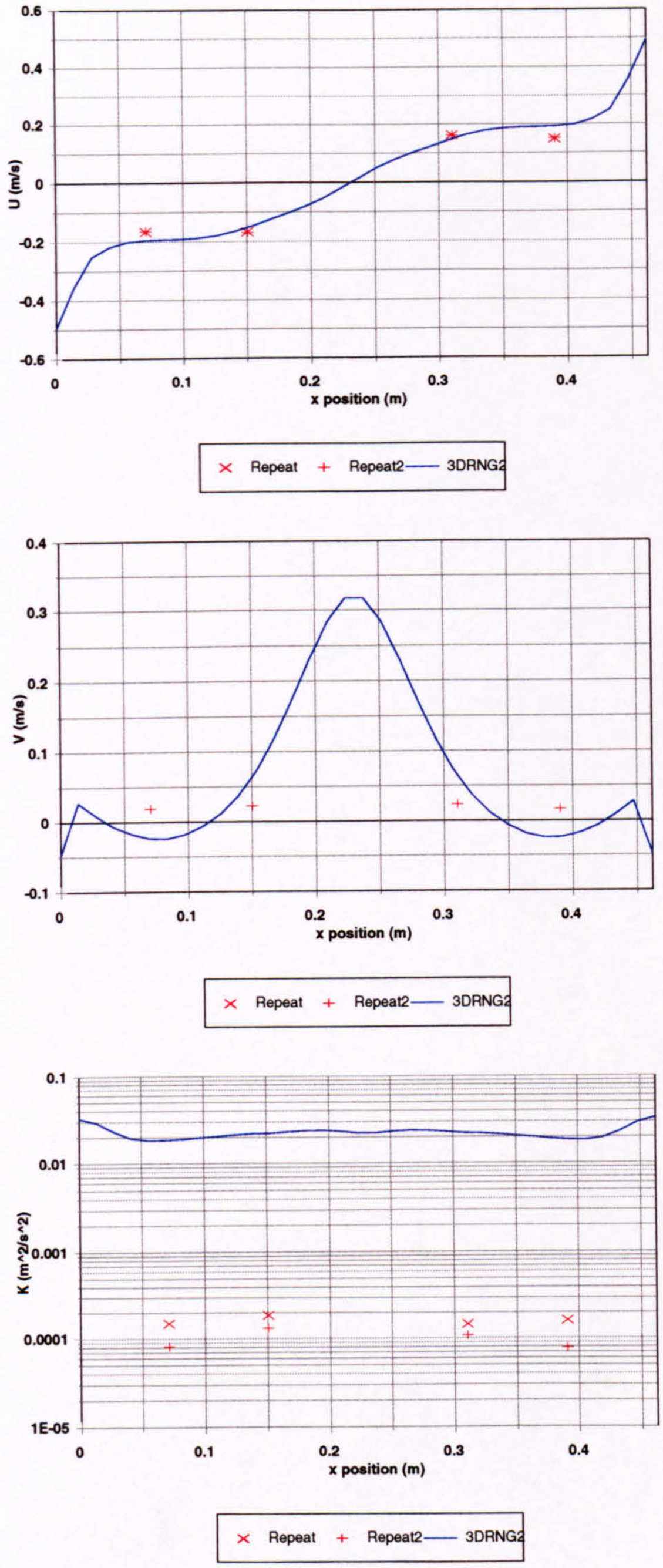


Figure 7.3-19h Comparison of measured and calculated velocities and turbulent kinetic energy, at y = 0.643 m, z = 0.1337 m. Flowrate = 4.38 l/s.

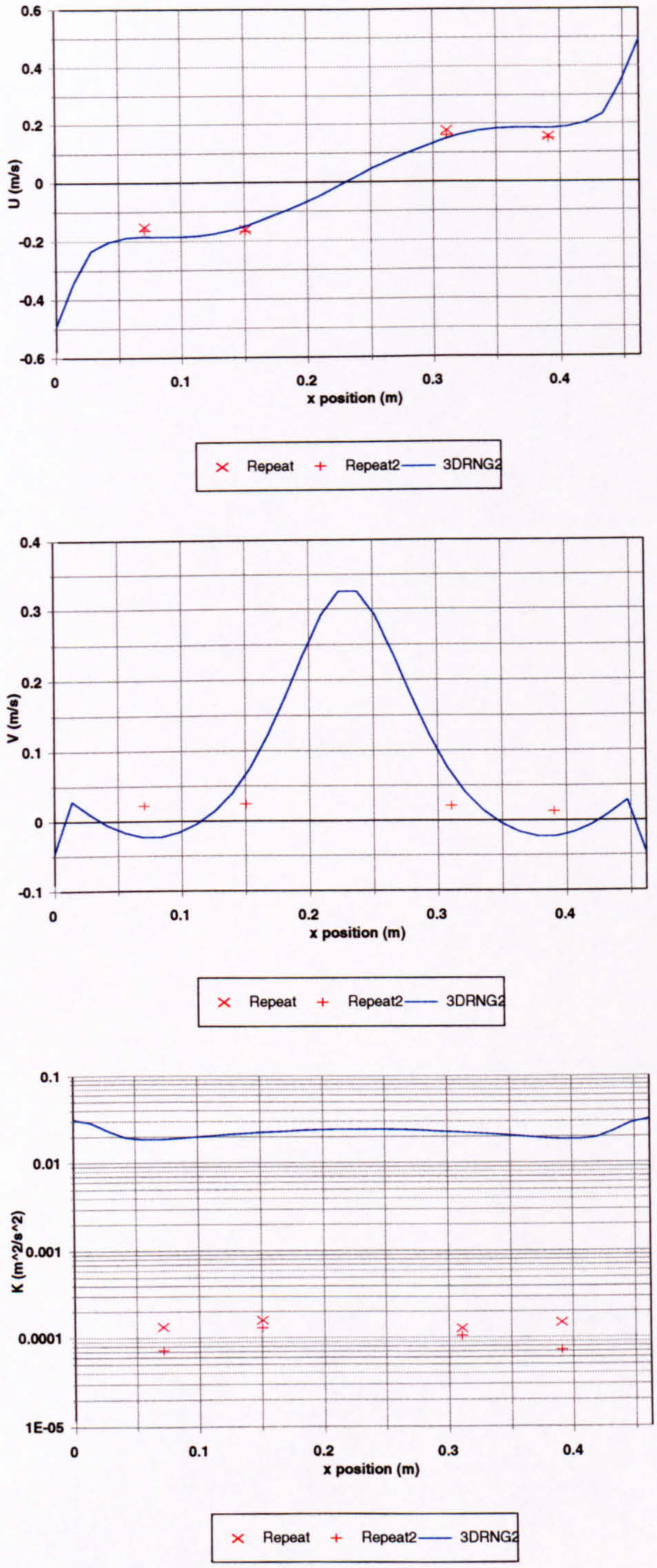


Figure 7.3-19i Comparison of measured and calculated velocities and turbulent kinetic energy, at y = 0.643 m, z = 0.1637 m. Flowrate = 4.38 l/s.

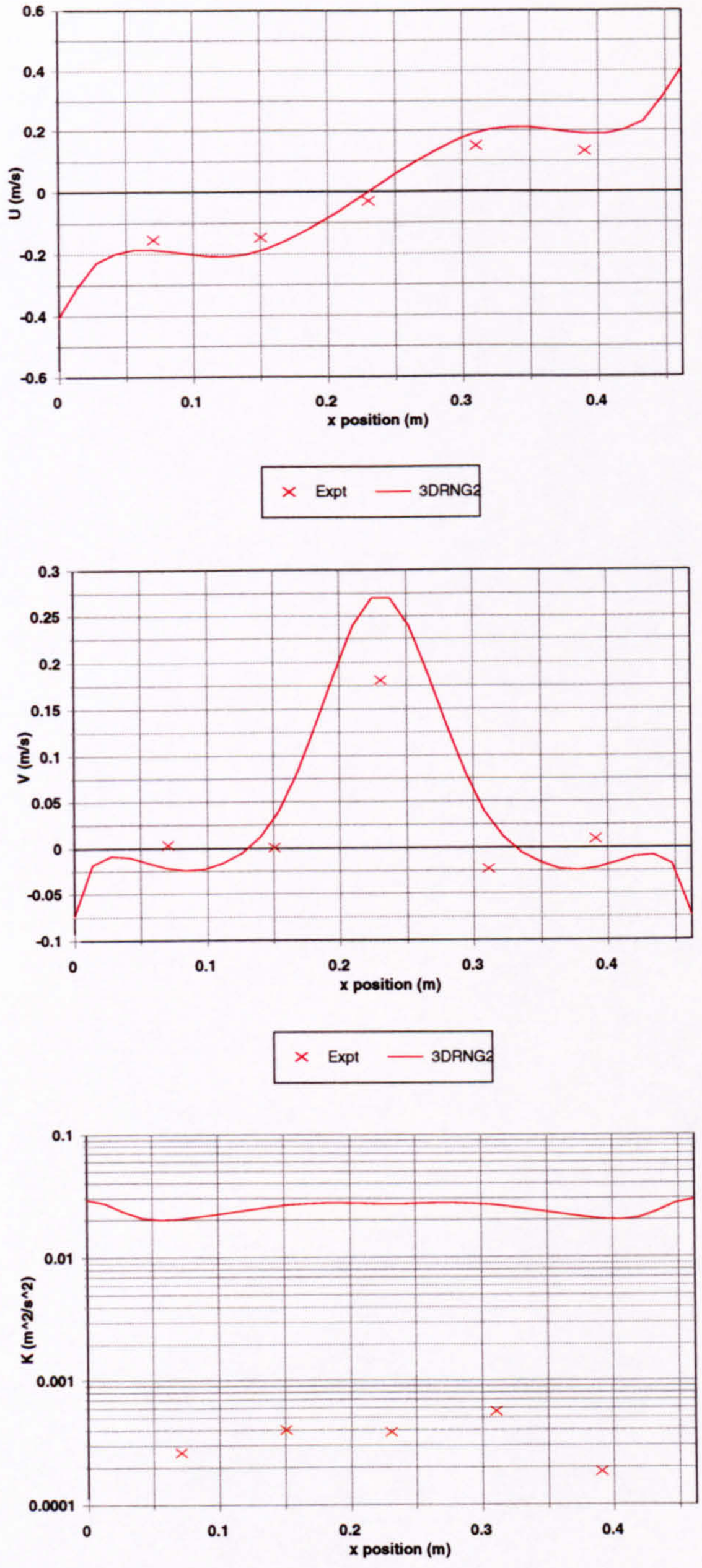


Figure 7.3-19j Comparison of measured and calculated velocities and turbulent kinetic energy, at y = 0.653 m, z = 0.1037 m. Flowrate = 4.38 l/s.

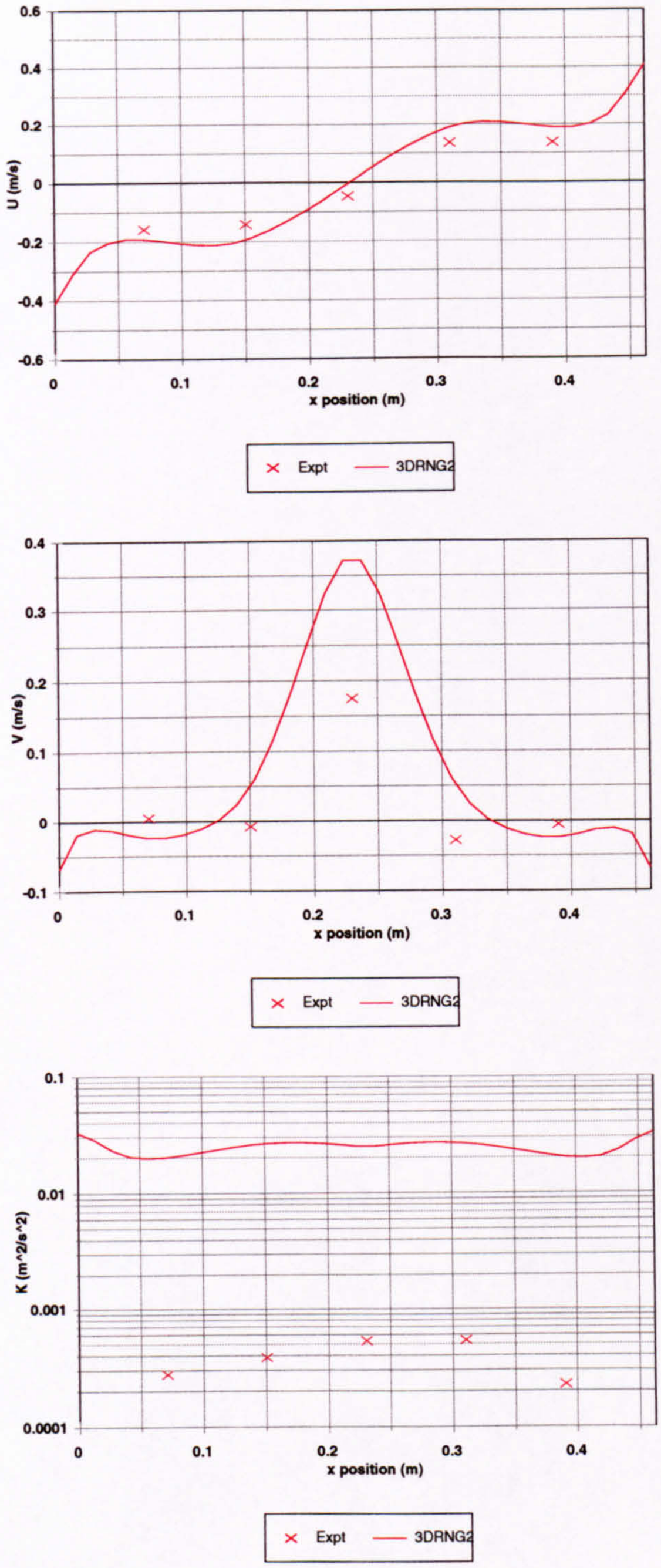


Figure 7.3-19k Comparison of measured and calculated velocities and turbulent kinetic energy, at y = 0.653 m, z = 0.1337 m. Flowrate = 4.38 l/s.

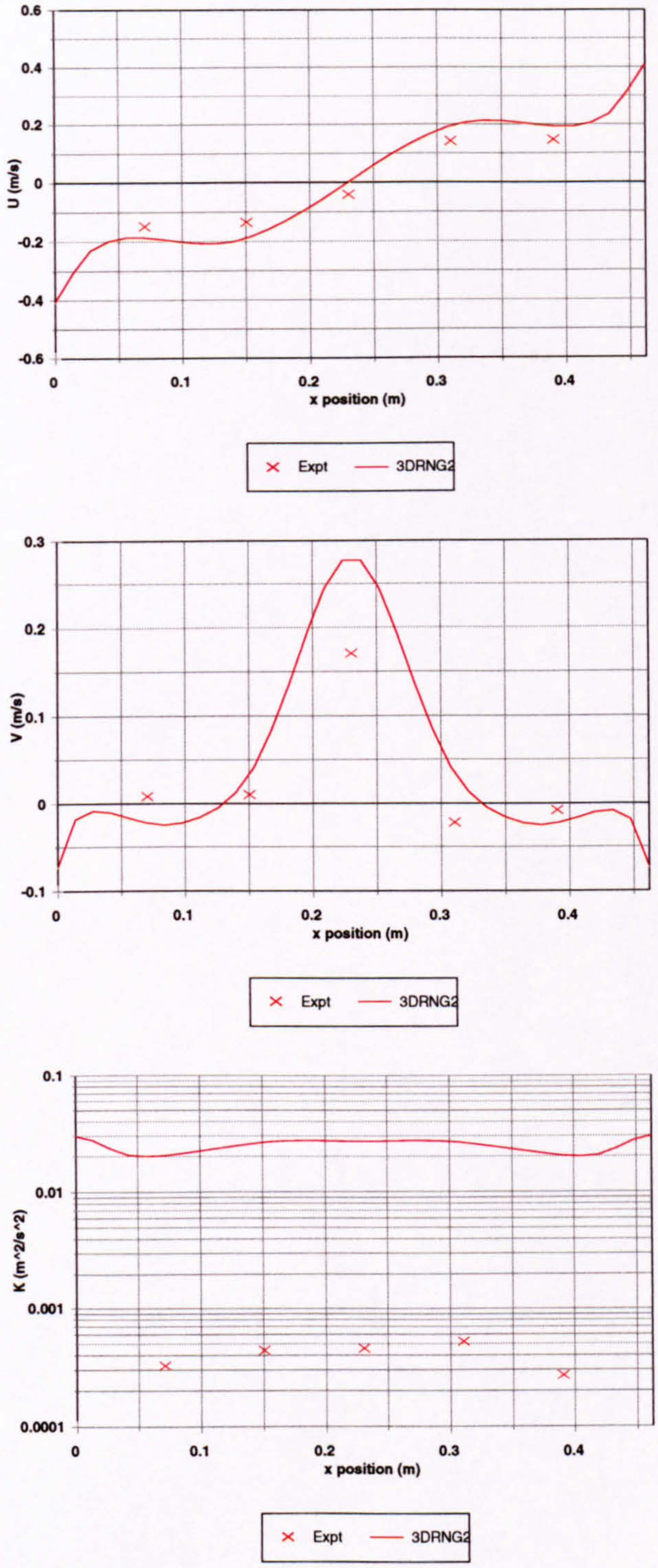


Figure 7.3-19l Comparison of measured and calculated velocities and turbulent kinetic energy, at y = 0.653 m, z = 0.1637 m. Flowrate = 4.38 l/s

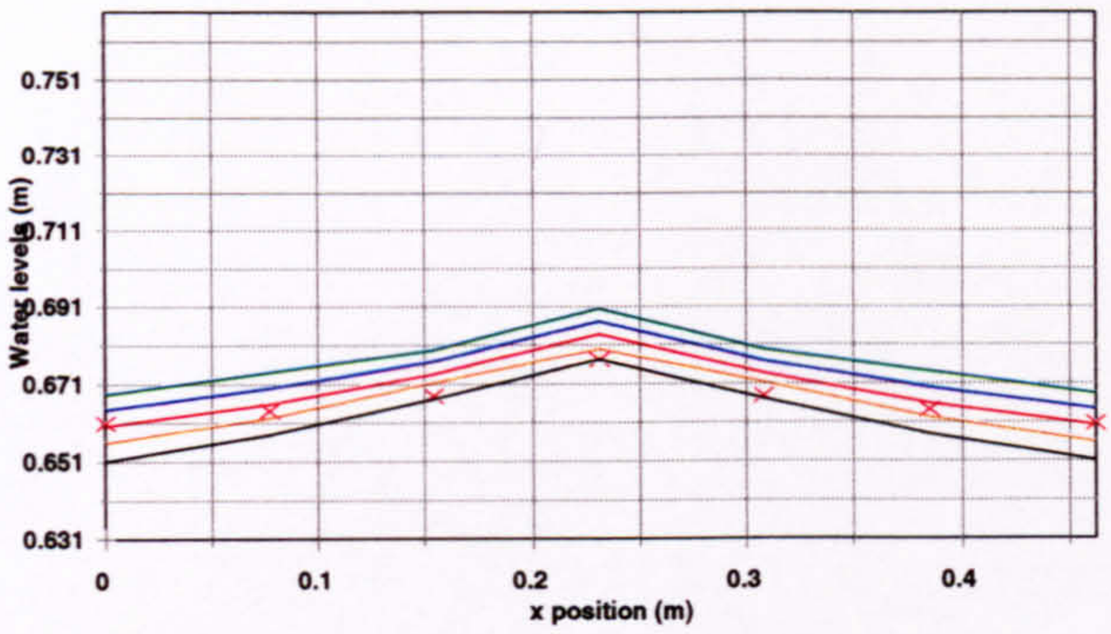


Figure 7.3-19m Comparison between measured and calculated water levels at z = 0.1037 m

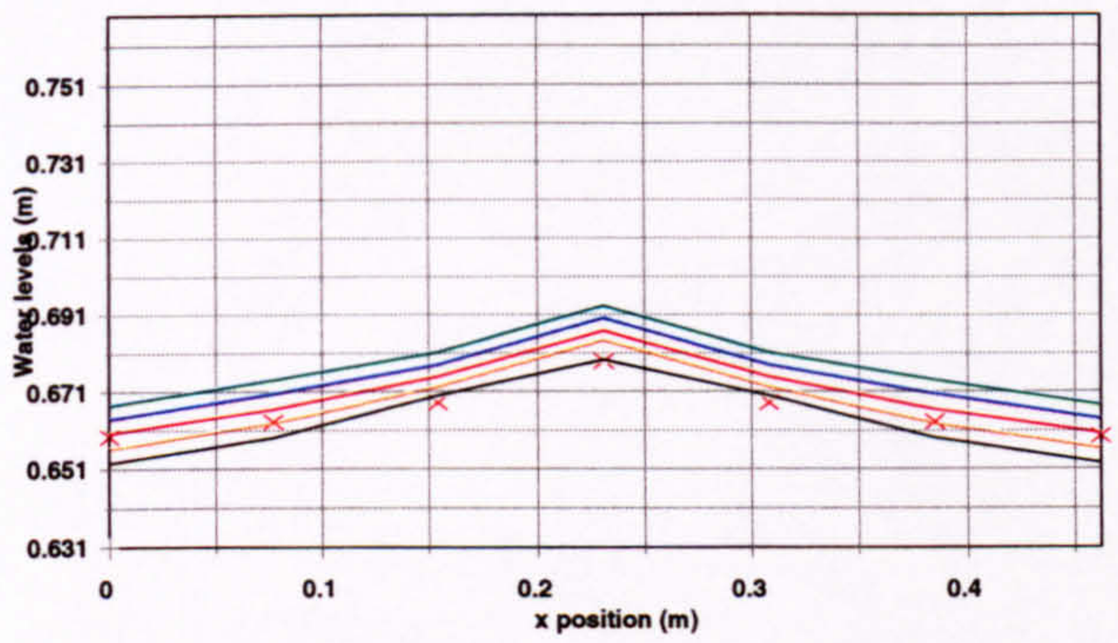


Figure 7.3-19n Comparison between measured and calculated water levels at z = 0.1337 m

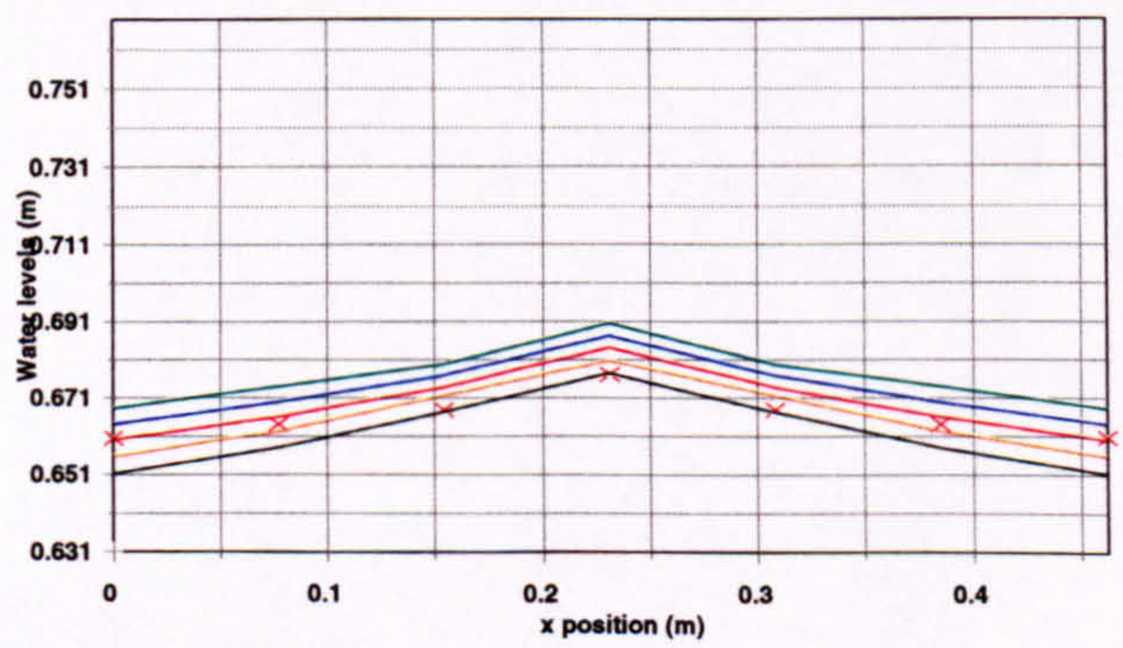


Figure 7.3-19o Comparison between measured and calculated water levels at z = 0.1637 m

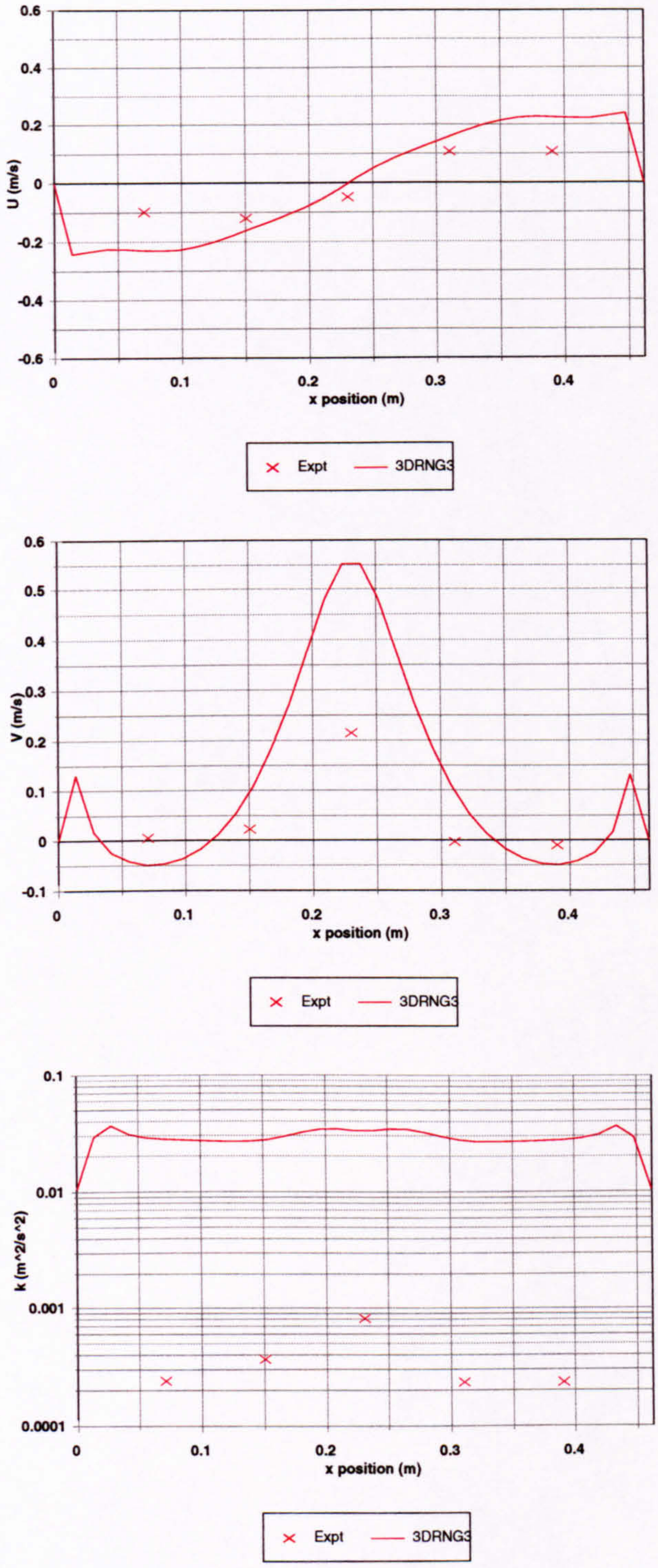


Figure 7.3-20aComparison between experimental and calculated values of velocities and turbulent kinetic energy, at y = 0.628 m, z = 0.1037 m. Flowrate = 5.51 l/s.

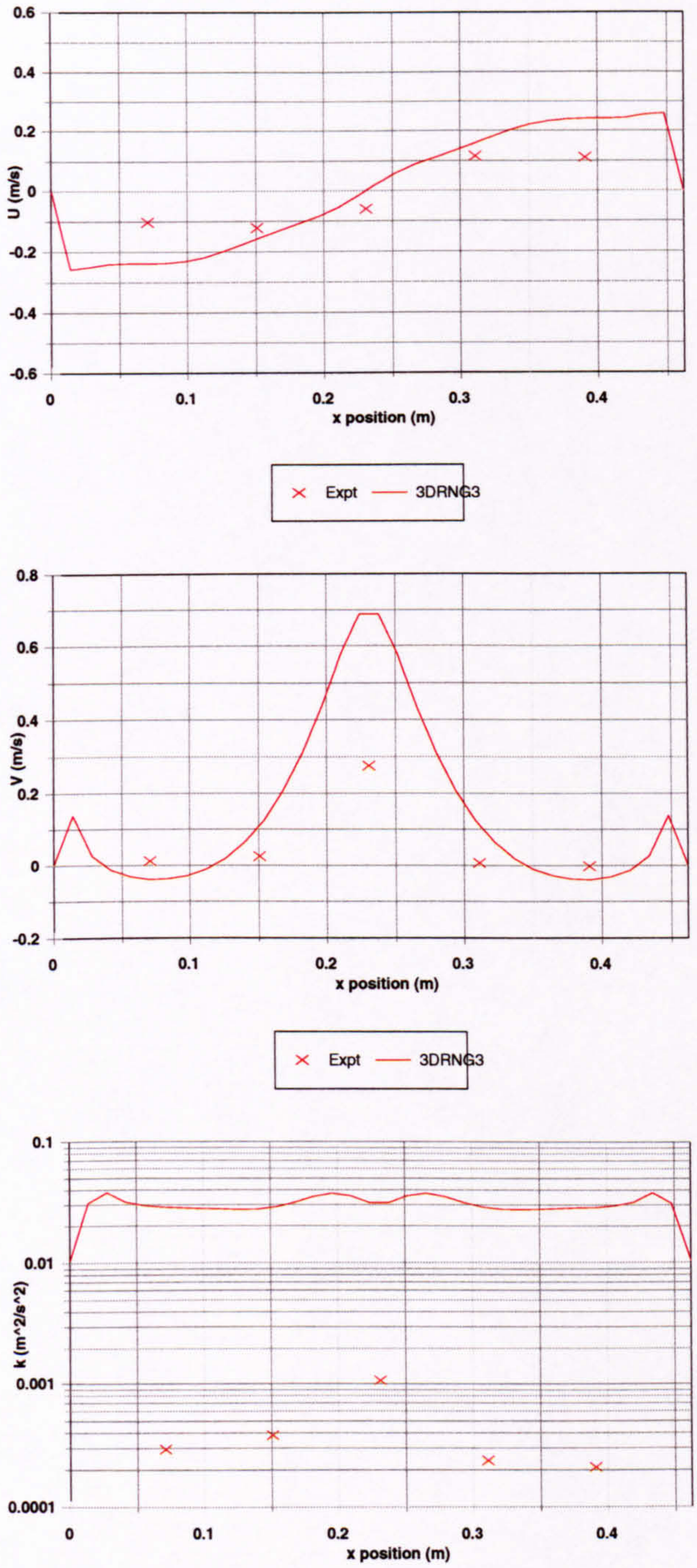


Figure 7.3-20bComparison between experimental and calculated values of velocities and turbulent kinetic energy, at y = 0.628 m, z = 0.1337 m. Flowrate = 5.51 l/s.

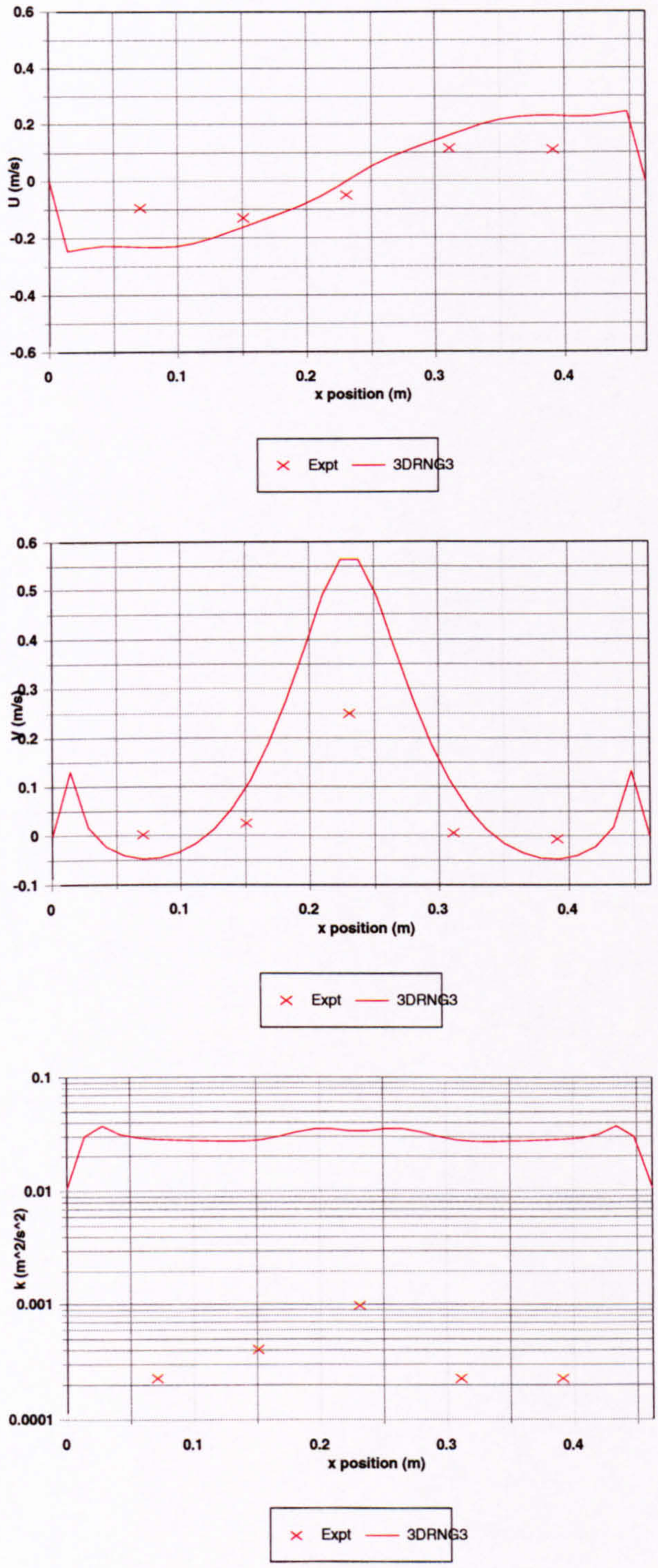


Figure 7.3-20cComparison between experimental and calculated values of velocities and turbulent kinetic energy, at y = 0.628 m, z = 0.1637 m. Flowrate = 5.51 l/s.

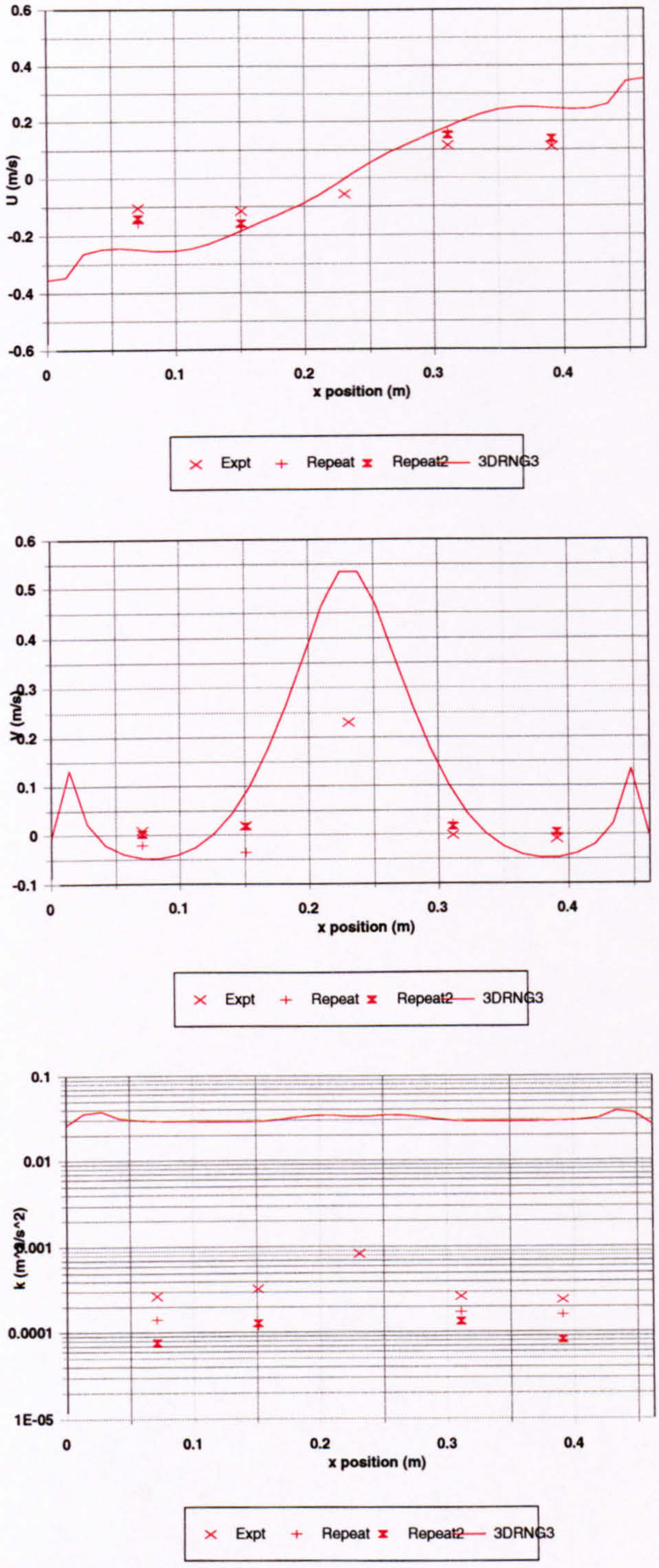


Figure 7.3-20d Comparison between experimental and calculated values of velocities and turbulent kinetic energy, at y = 0.633 m, z = 0.1037 m. Flowrate = 5.51 l/s.

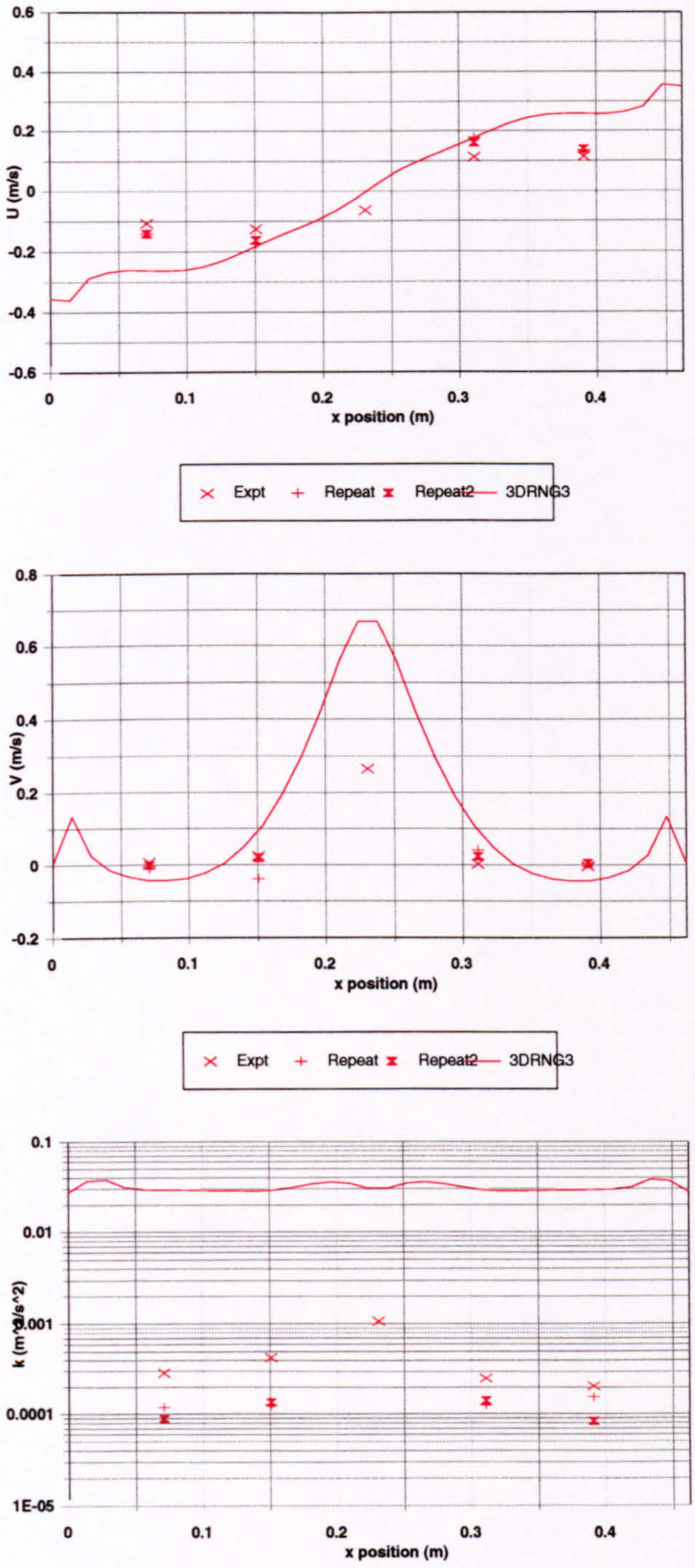


Figure 7.3-20e Comparison between experimental and calculated values of velocities and turbulent kinetic energy, at y = 0.633 m, z = 0.1337 m. Flowrate = 5.51 l/s.

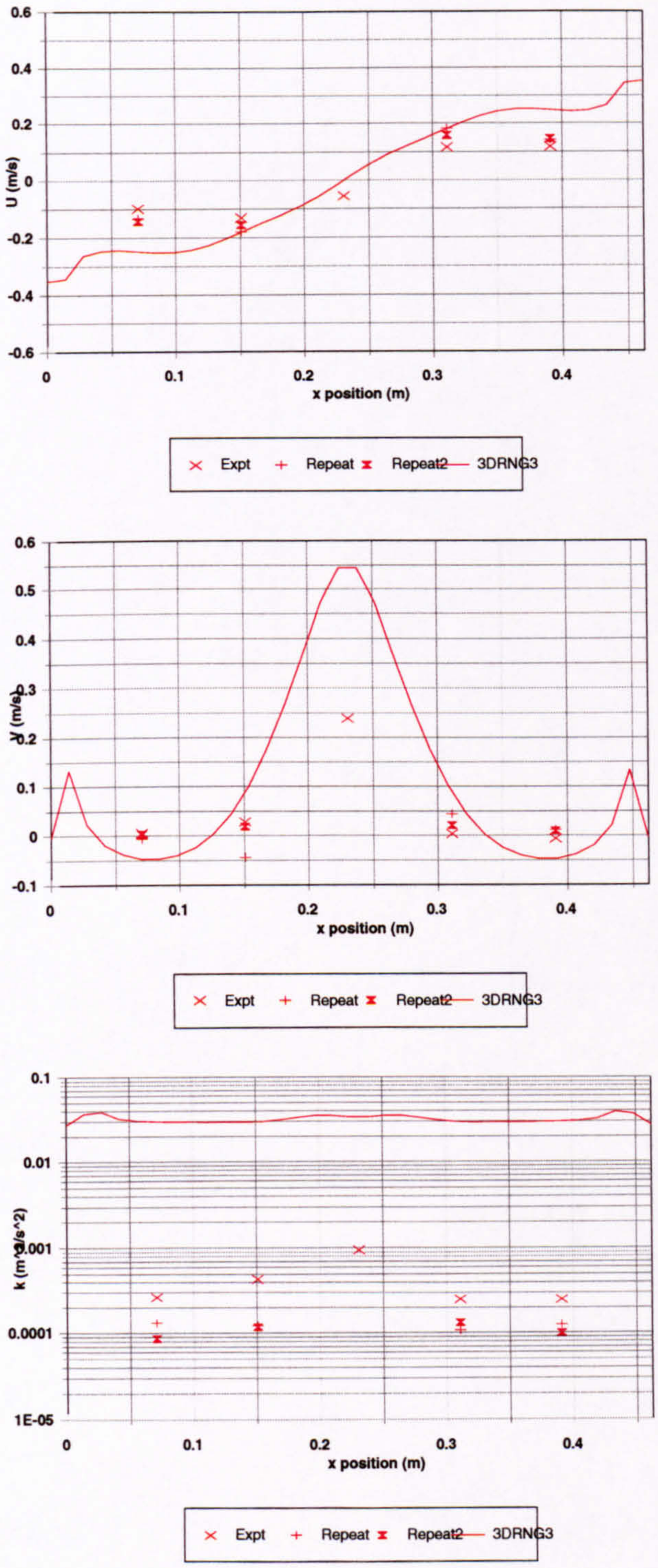


Figure 7.3-20f Comparison between experimental and calculated values of velocities and turbulent kinetic energy, at y = 0.633 m, z = 0.1637 m. Flowrate = 5.51 l/s.

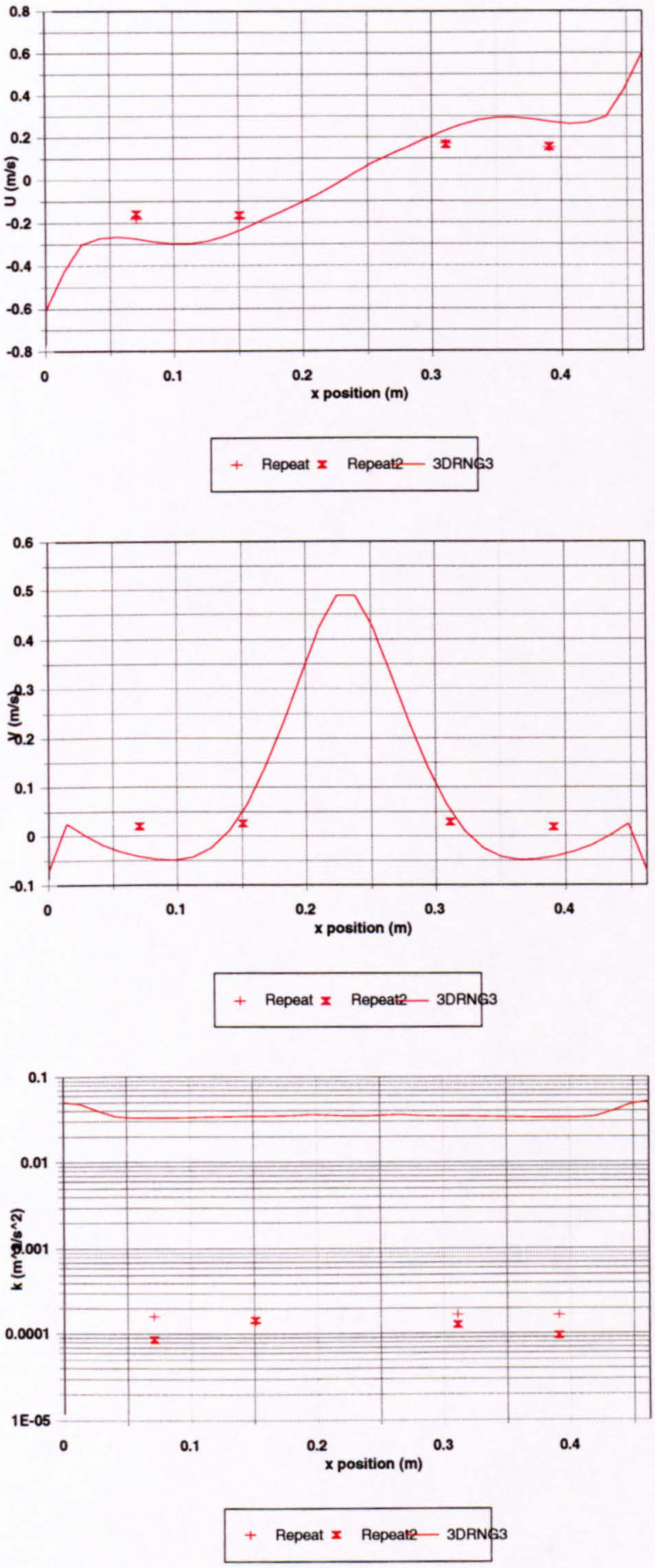


Figure 7.3-20g Comparison between experimental and calculated values of velocities and turbulent kinetic energy, at y = 0.643 m, z = 0.1037 m. Flowrate = 5.51 l/s.

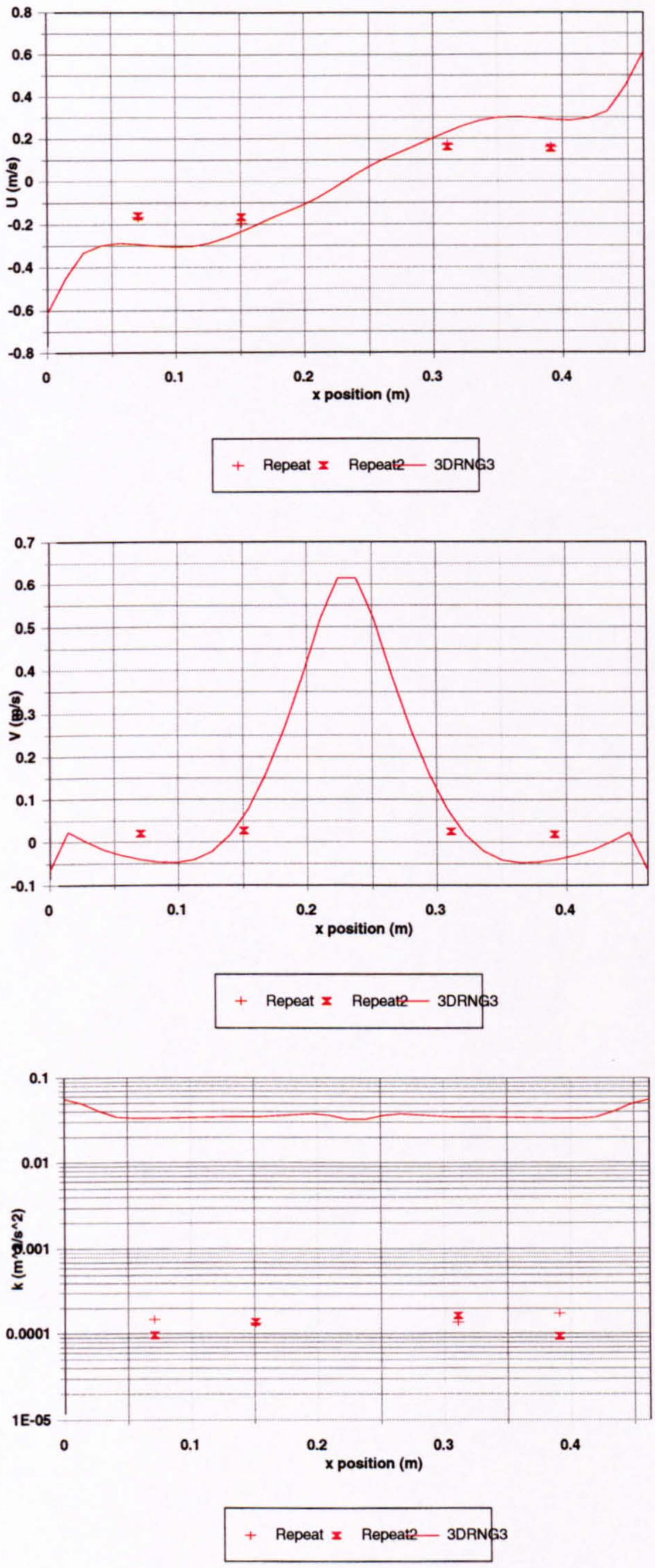


Figure 7.3-20h Comparison between experimental and calculated values of velocities and turbulent kinetic energy, at y = 0.643 m, z = 0.1337 m. Flowrate = 5.51 l/s.

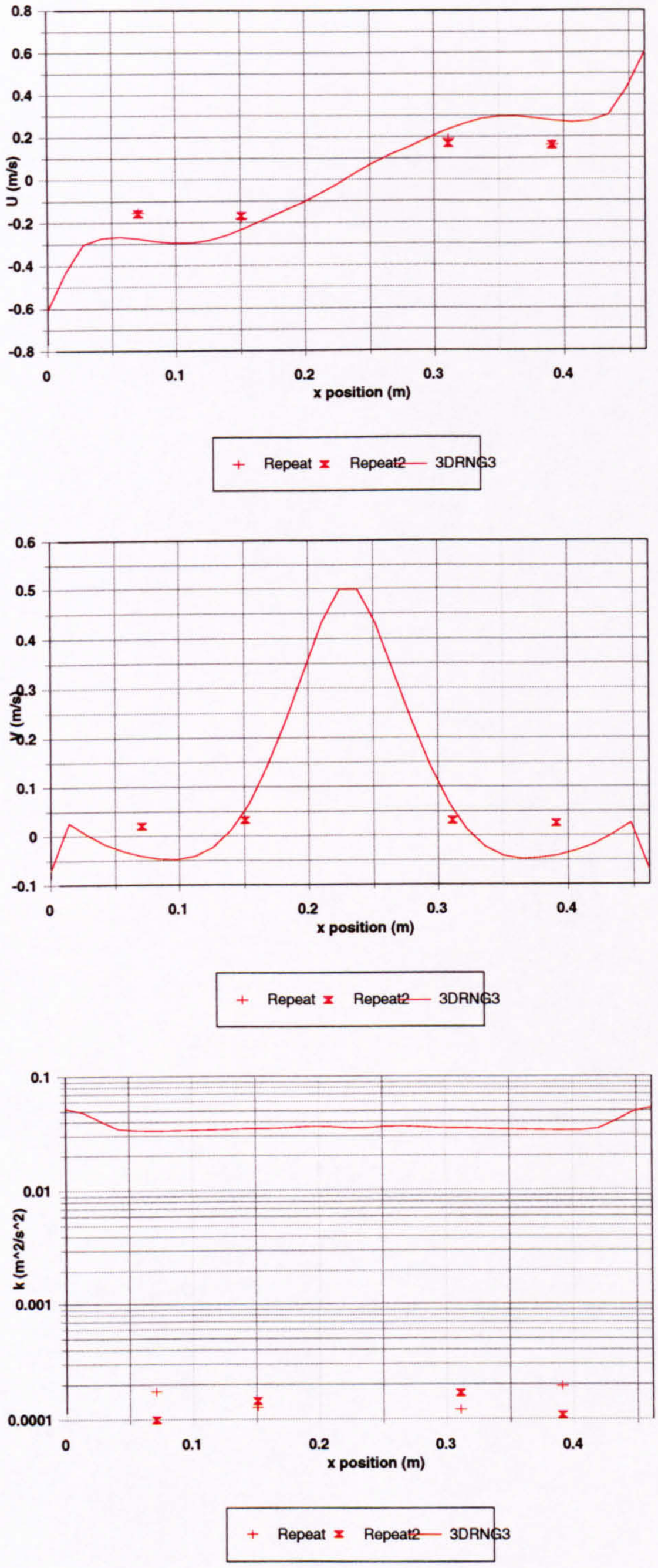


Figure 7.3-20i Comparison between experimental and calculated values of velocities and turbulent kinetic energy, at y = 0.643 m, z = 0.1637 m. Flowrate = 5.51 l/s.

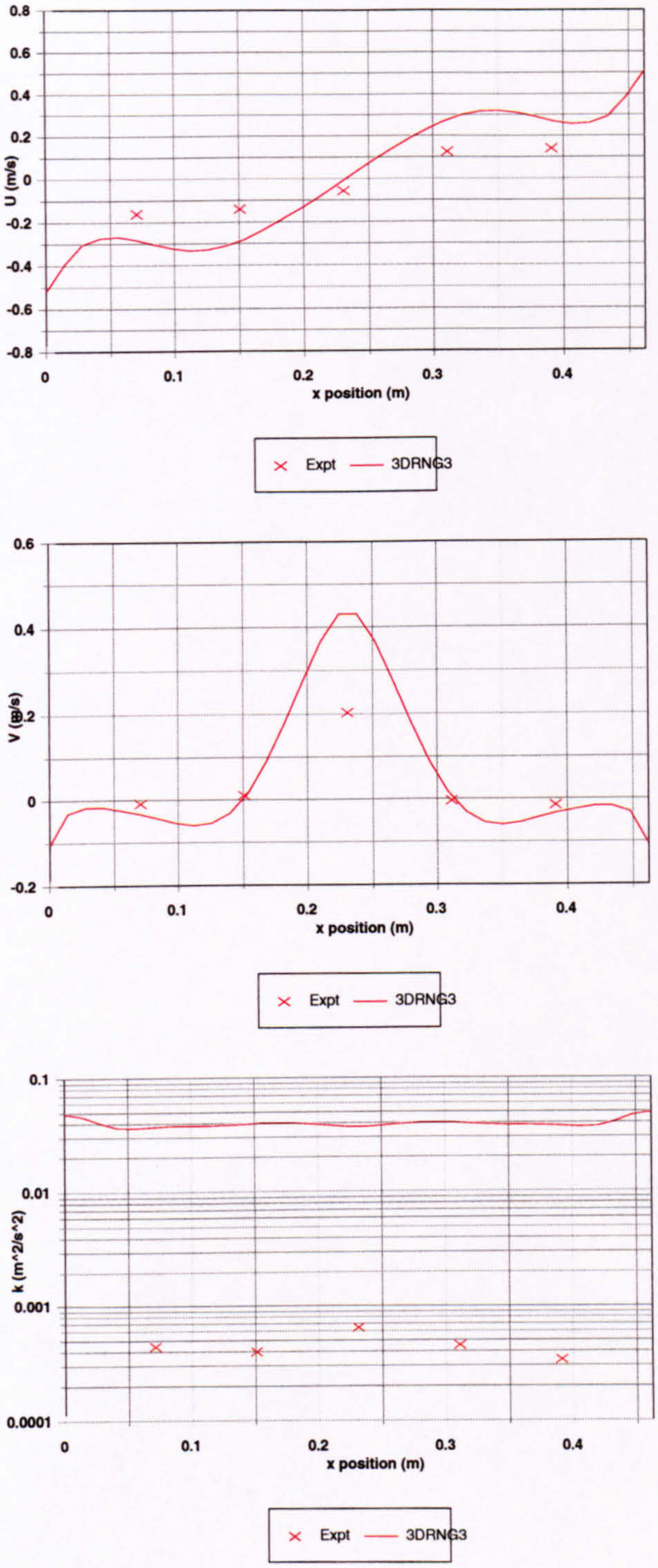


Figure 7.3-20j Comparison between experimental and calculated values of velocities and turbulent kinetic energy, at y = 0.653 m, z = 0.1037 m. Flowrate = 5.51 l/s.

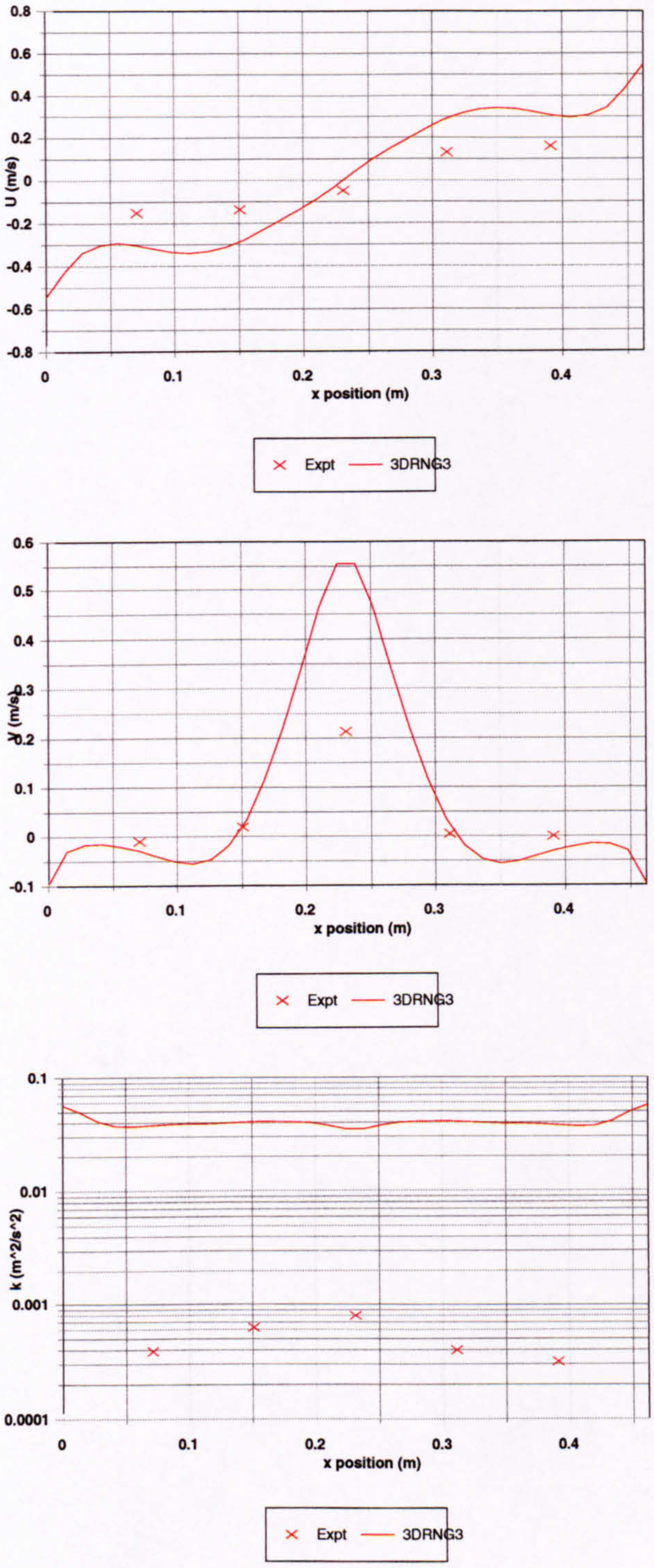


Figure 7.3-20k Comparison between experimental and calculated values of velocities and turbulent kinetic energy, at y = 0.653 m, z = 0.1337 m. Flowrate = 5.51 l/s.

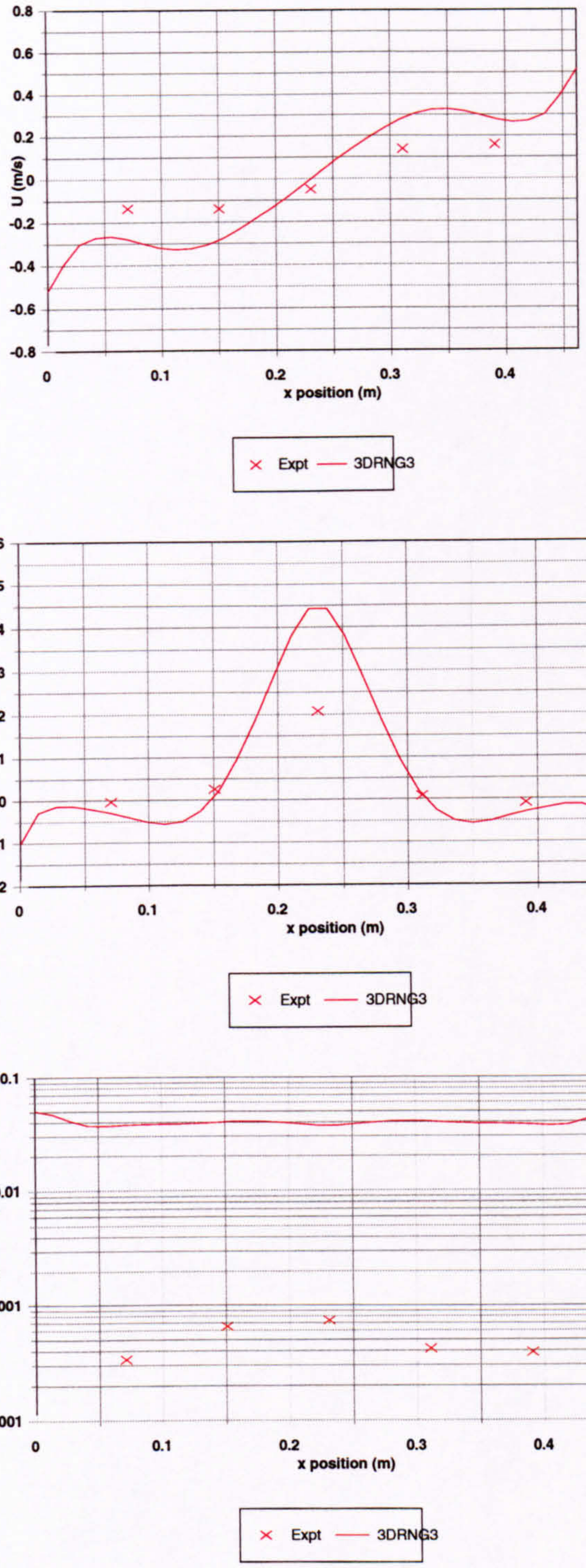


Figure 7.3-20l Comparison between experimental and calculated values of velocities and turbulent kinetic energy, at y = 0.653 m, z = 0.1637 m. Flowrate = 5.51 l/s.

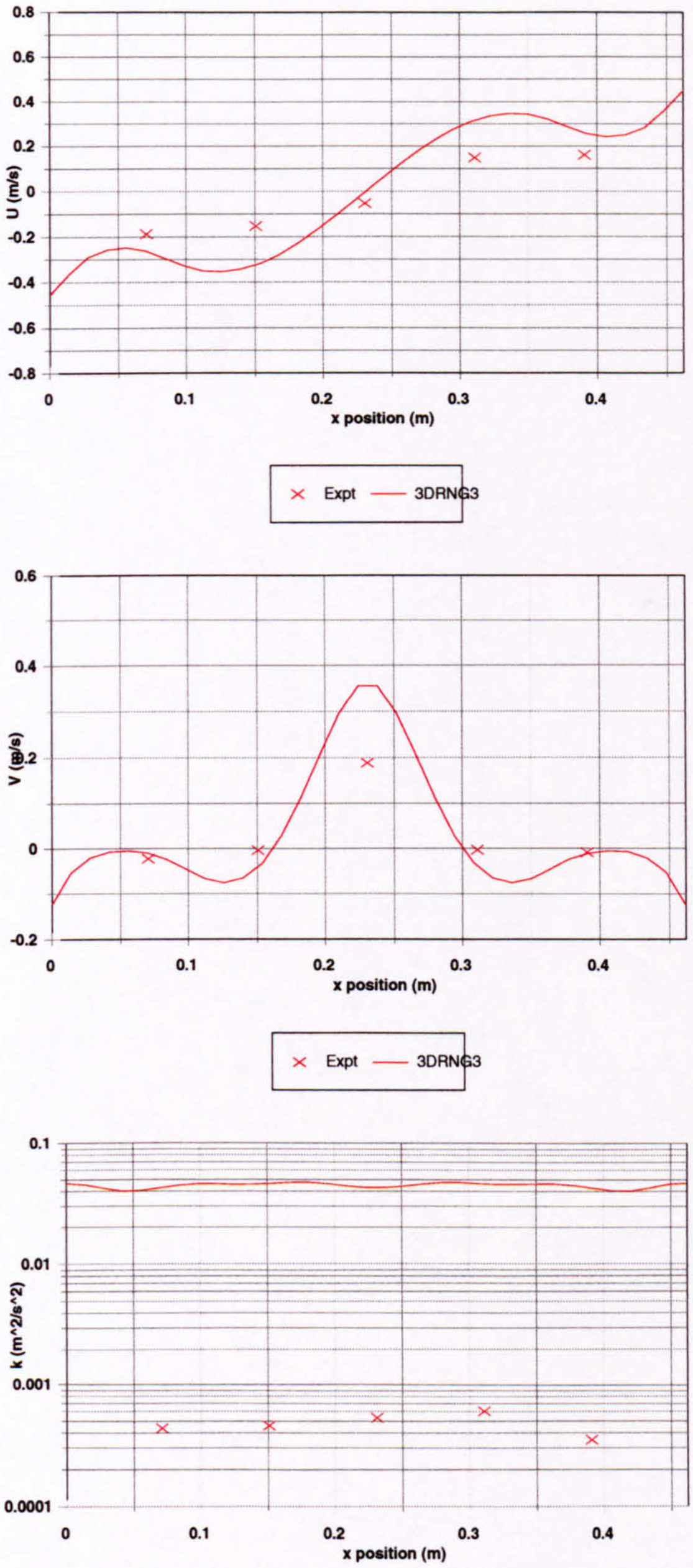


Figure 7.3-20m Comparison between experimental and calculated values of velocities and turbulent kinetic energy, at y = 0.663 m, z = 0.1037 m. Flowrate = 5.51 l/s.

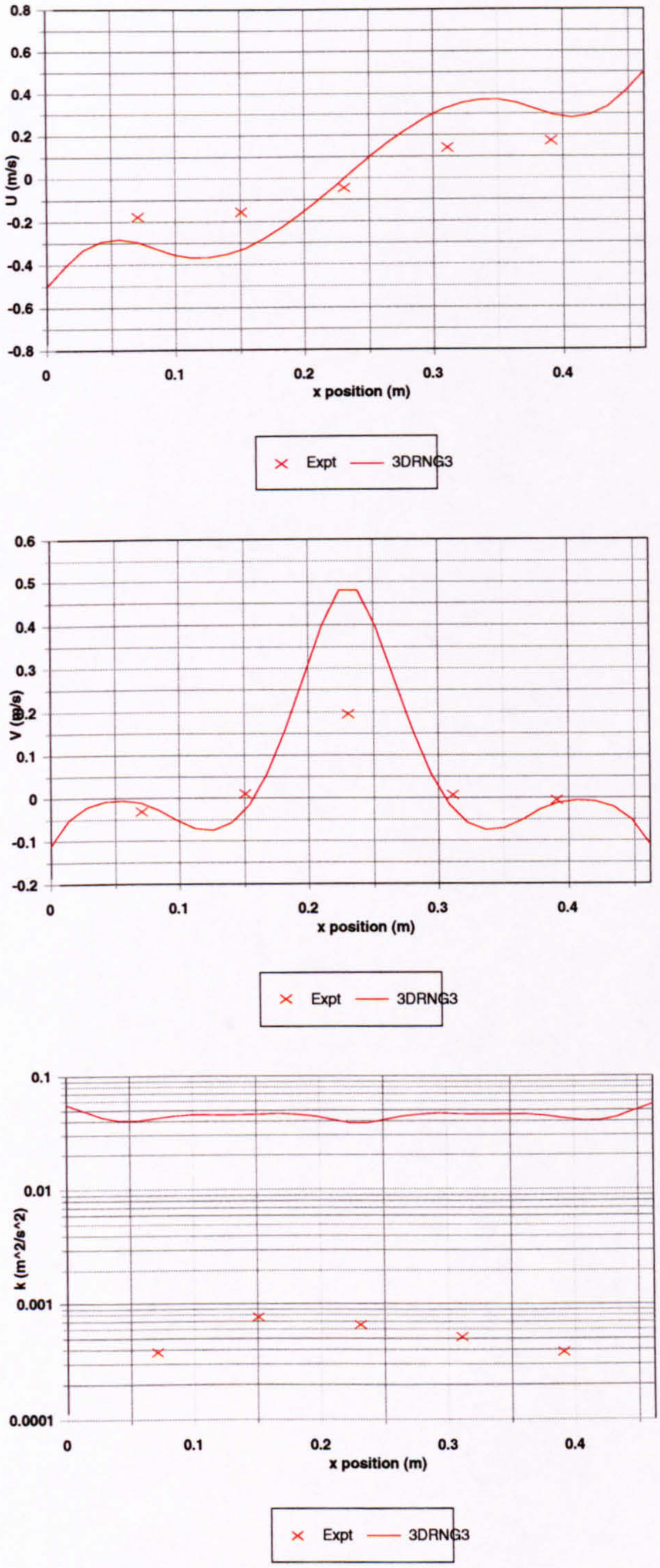


Figure 7.3-20n Comparison between experimental and calculated values of velocities and turbulent kinetic energy, at y = 0.663 m, z = 0.1337 m. Flowrate = 5.51 l/s.

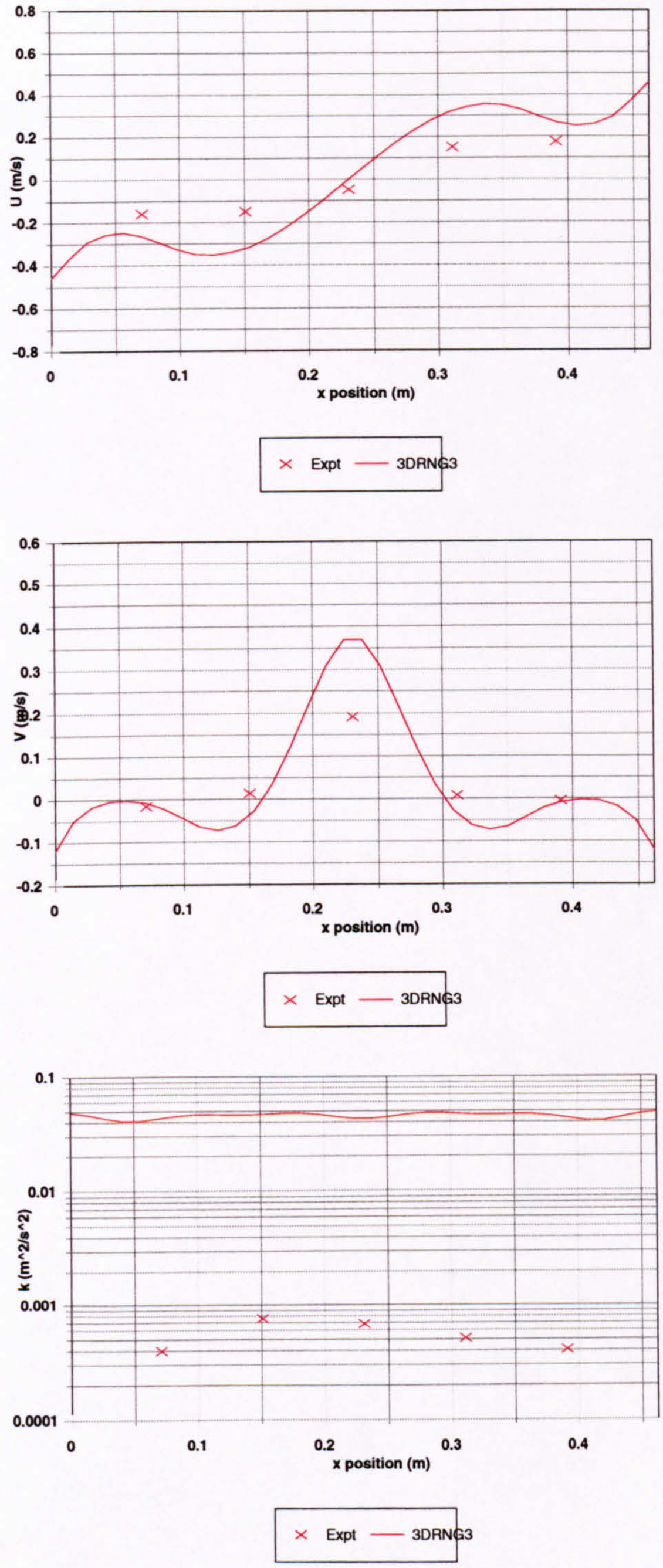


Figure 7.3-20o Comparison between experimental and calculated values of velocities and turbulent kinetic energy, at y = 0.663 m, z = 0.1637 m. Flowrate = 5.51 l/s.

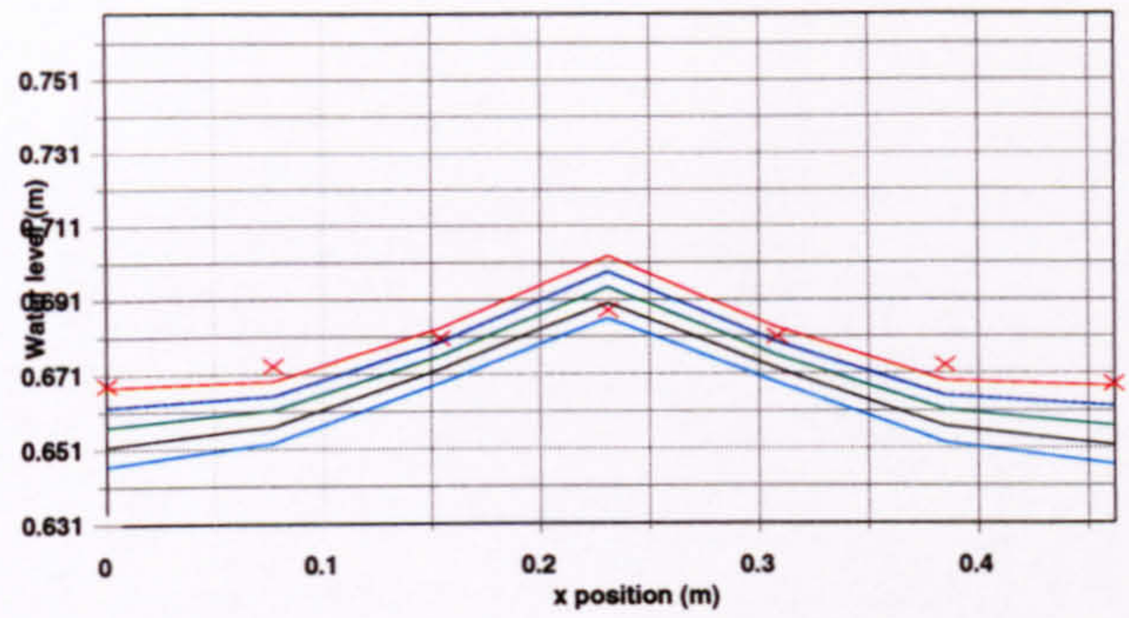


Figure 7.3-20p Comparison between experimental and calculated water levels at z = 0.1037 m

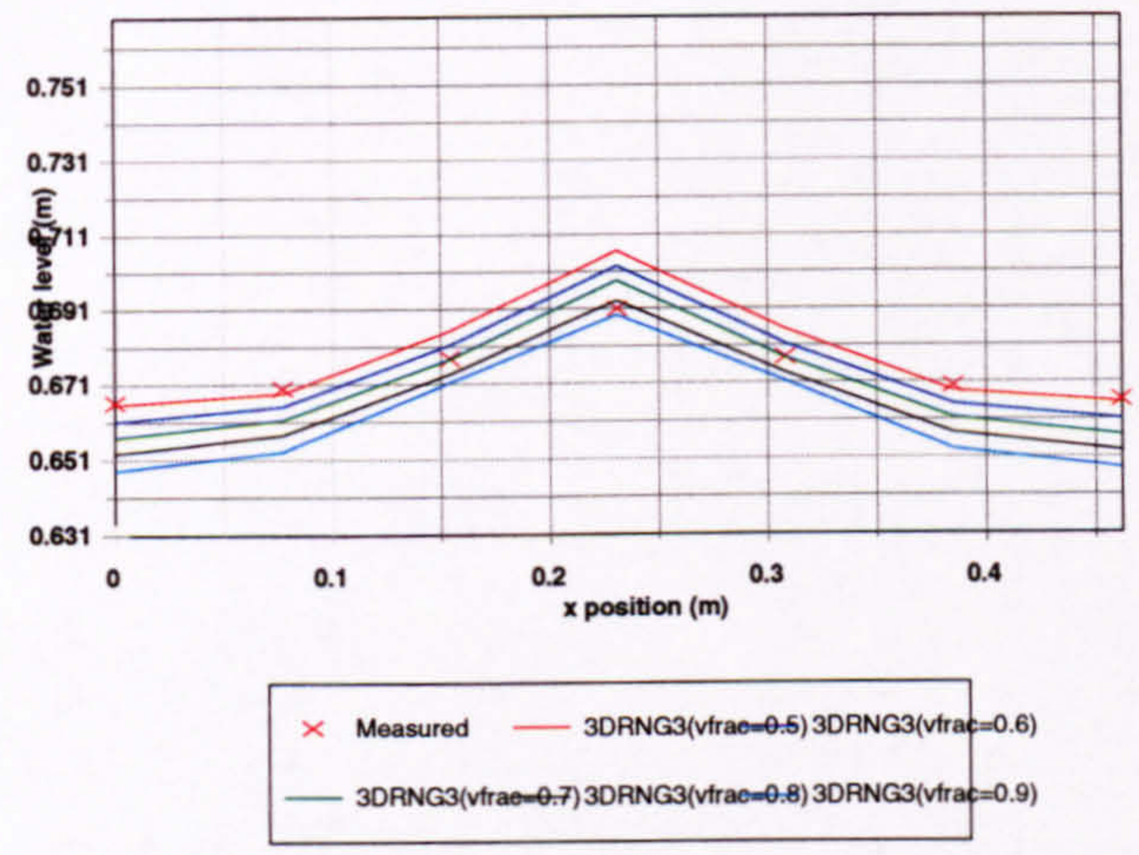


Figure 7.3-20q Comparison between experimental and calculated water levels at z = 0.1337 m

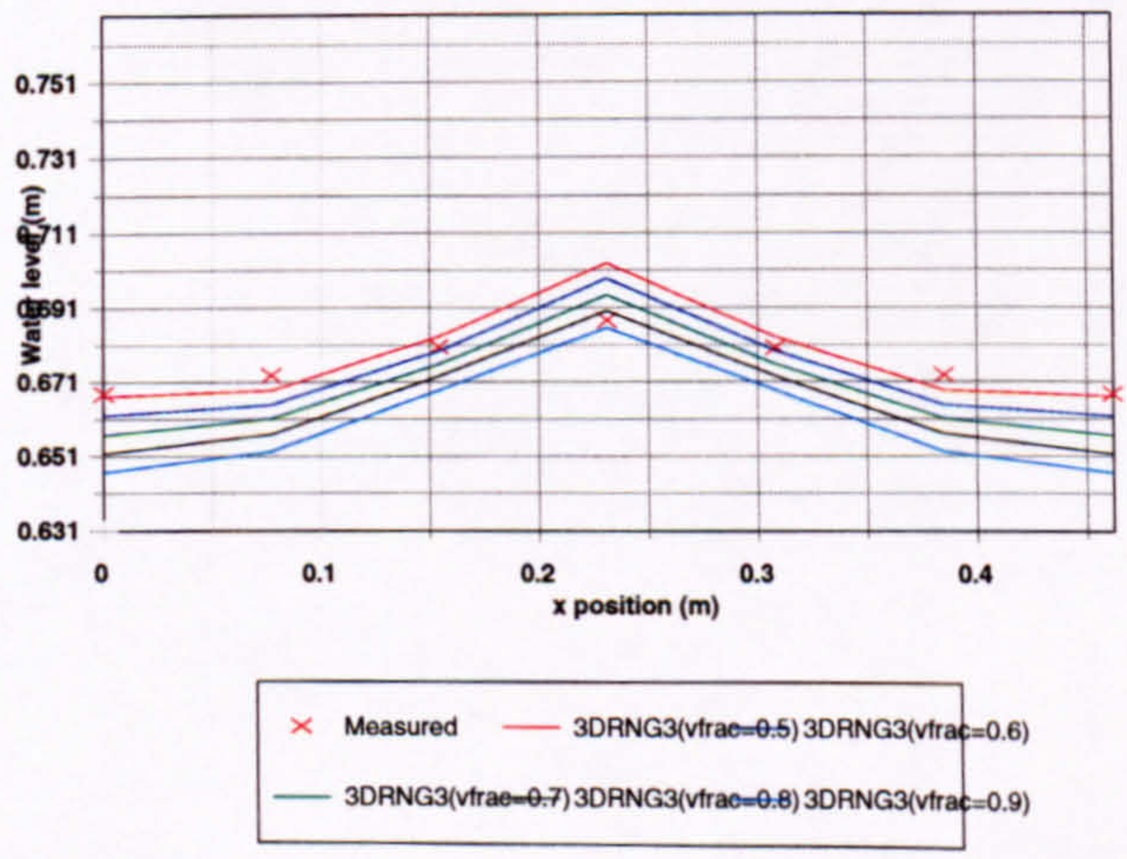


Figure 7.3-20r Comparison between experimental and calculated water levels at z = 0.1637 m

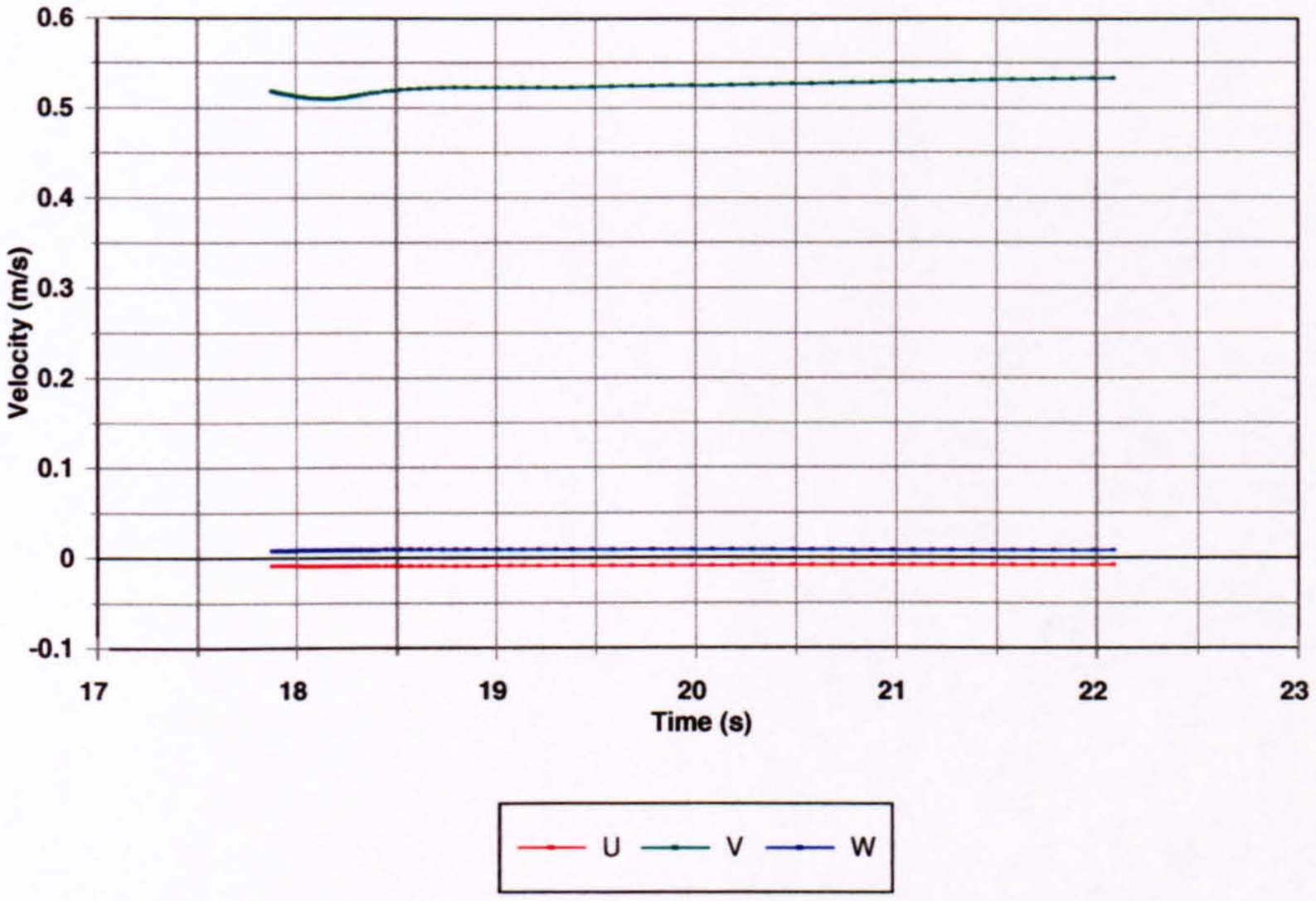


Figure 7.3-21a Time history plot of calculated U, V and W velocities for 3DRNG2, at monitoring point 1 (0.231, 0.621, 0.138).

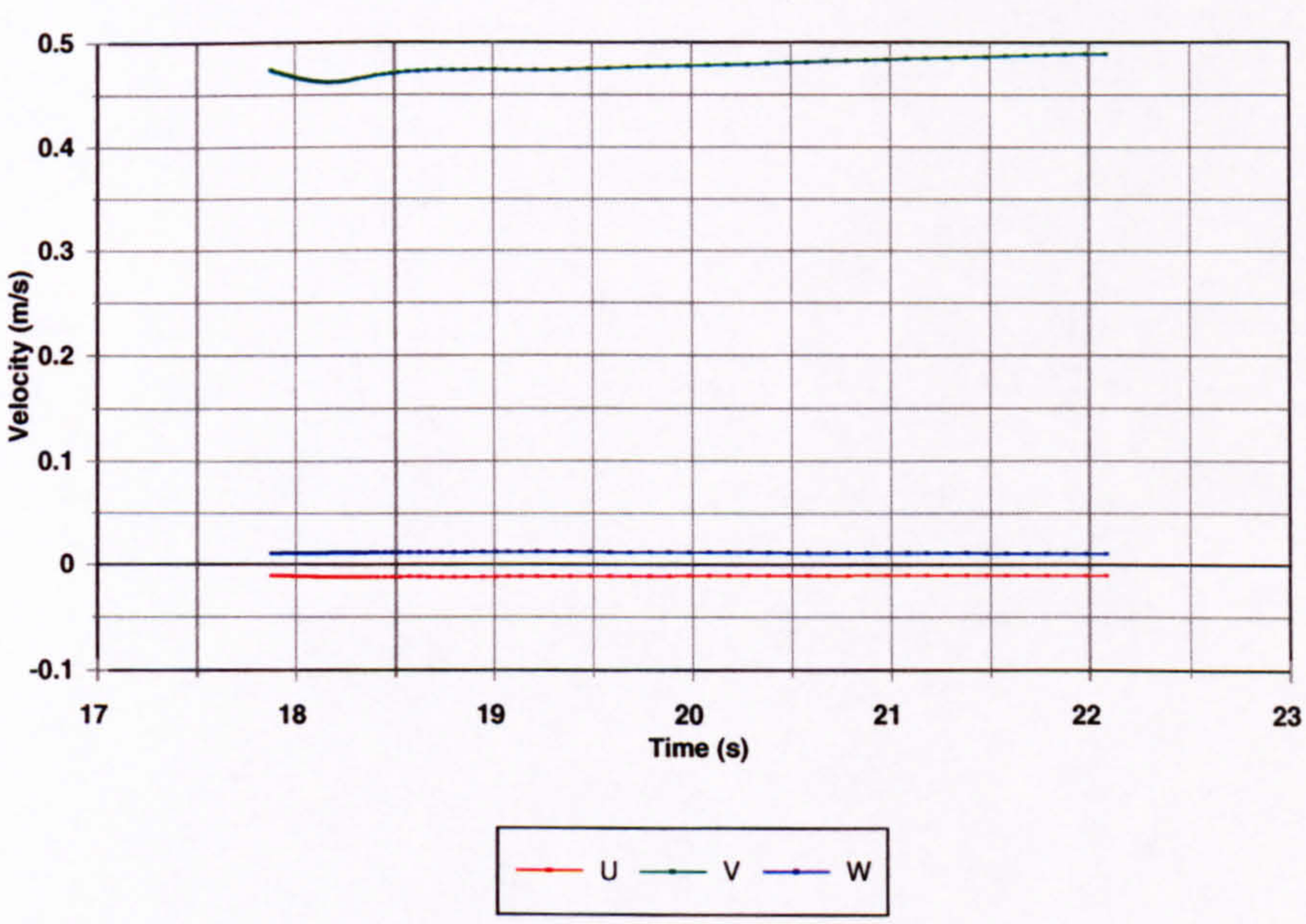


Figure 7.3-21b Time history plots of U, V, W velocities for 3DRNG2, at monitoring point 2 (0.231, 0.631, 0.138)

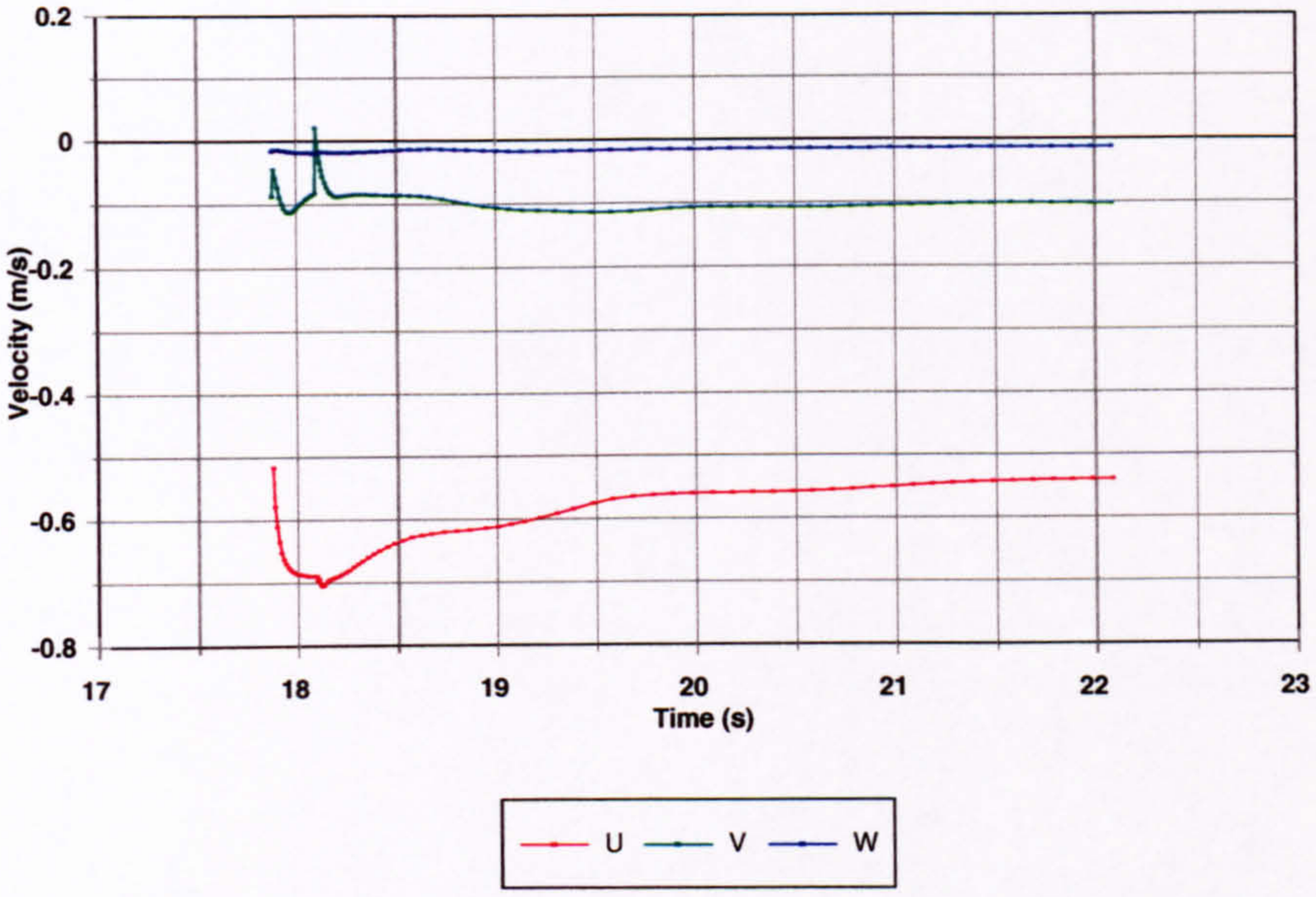


Figure 7.3-21c Time history plot of U, V, W velocities for 3DRNG2, at monitoring point 3 (0, 0.641, 0.138)

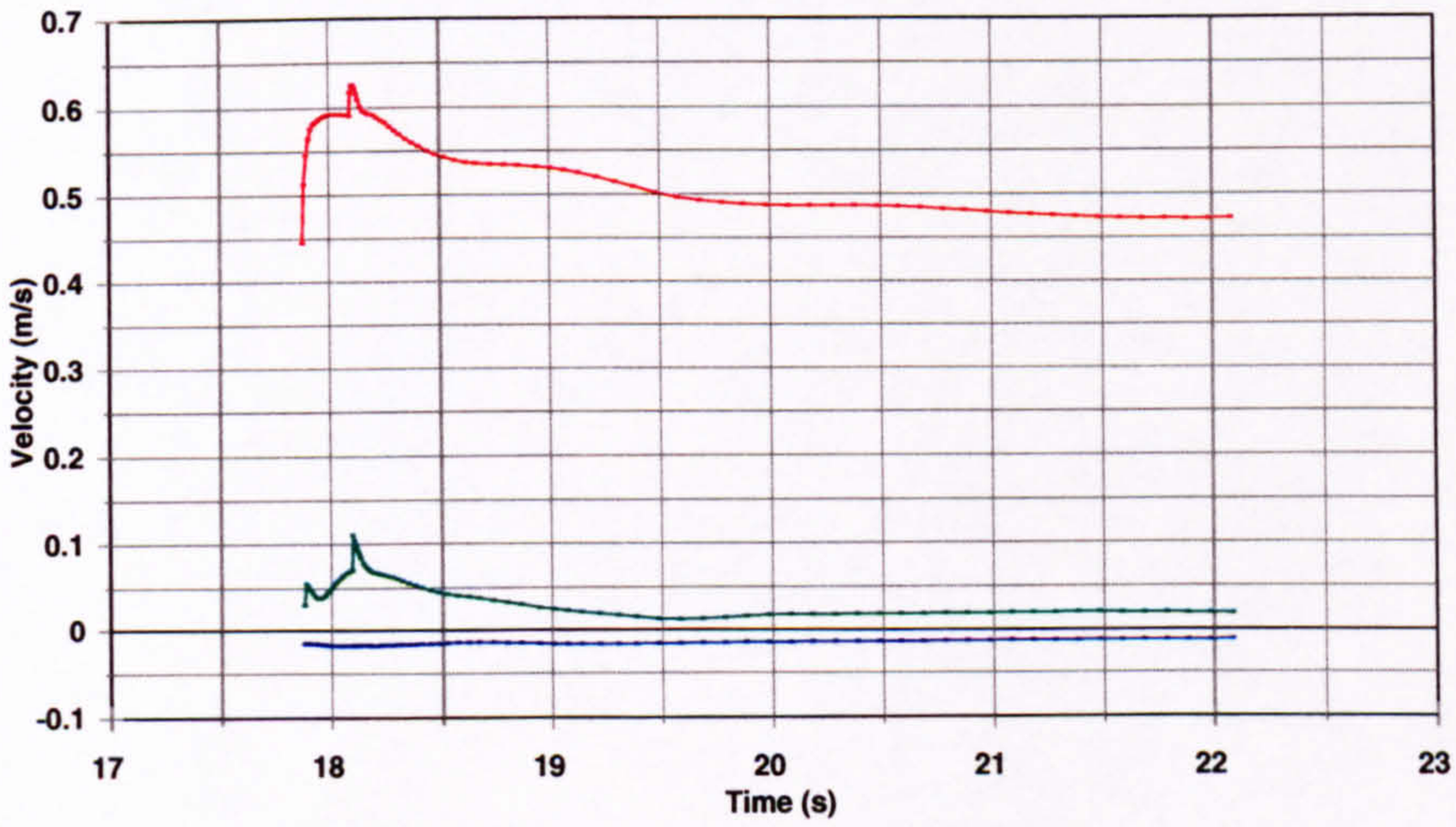


Figure 7.3-21d Time history plot of U, V and W velocities for 3DRNG2 at measurement point 4 (0.462, 0.641, 0.138).

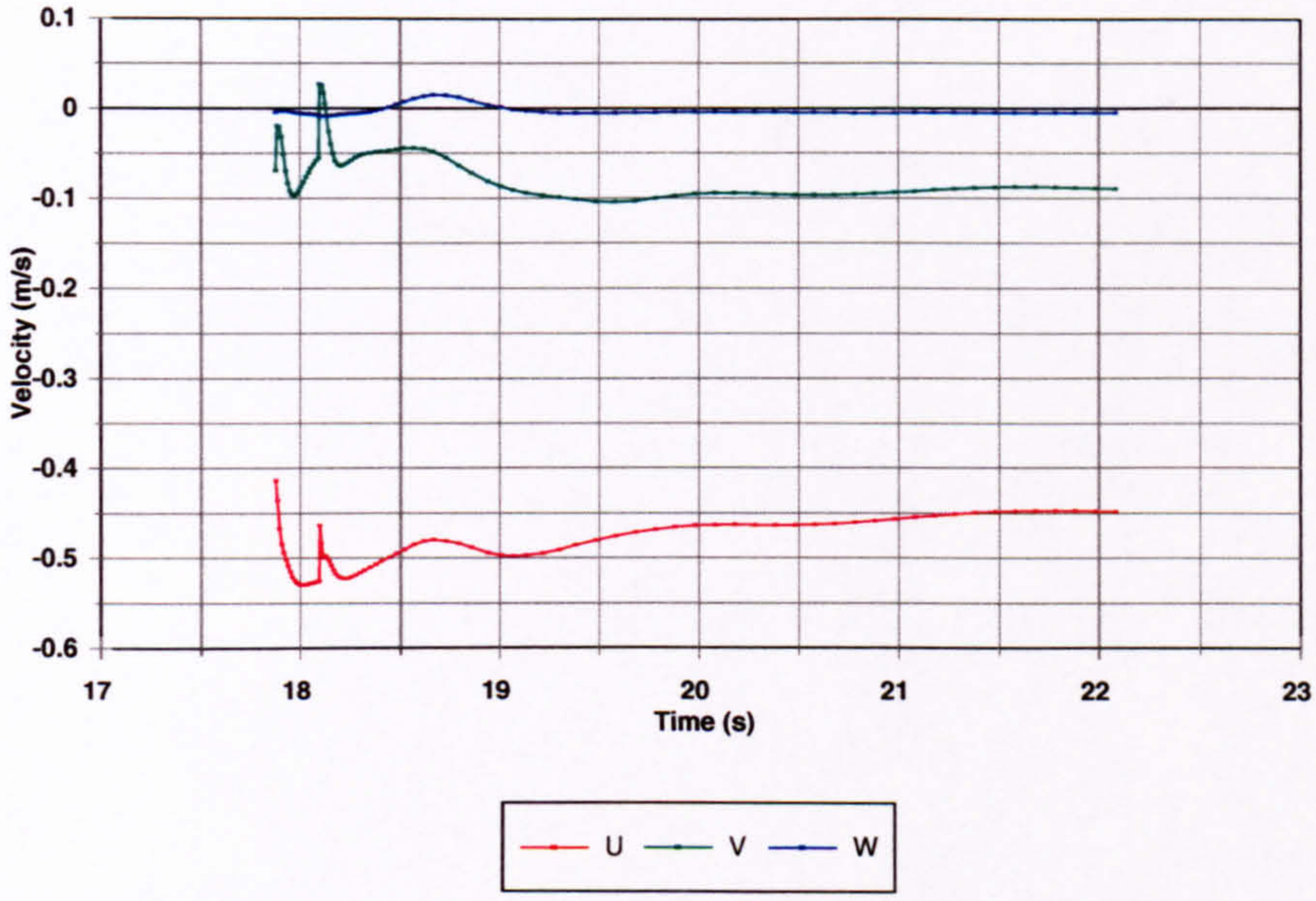


Figure 7.3-21e Time history plot of U, V and W velocities for 3DRNG2, at monitoring point 5 (0, 0.632, 0.138).

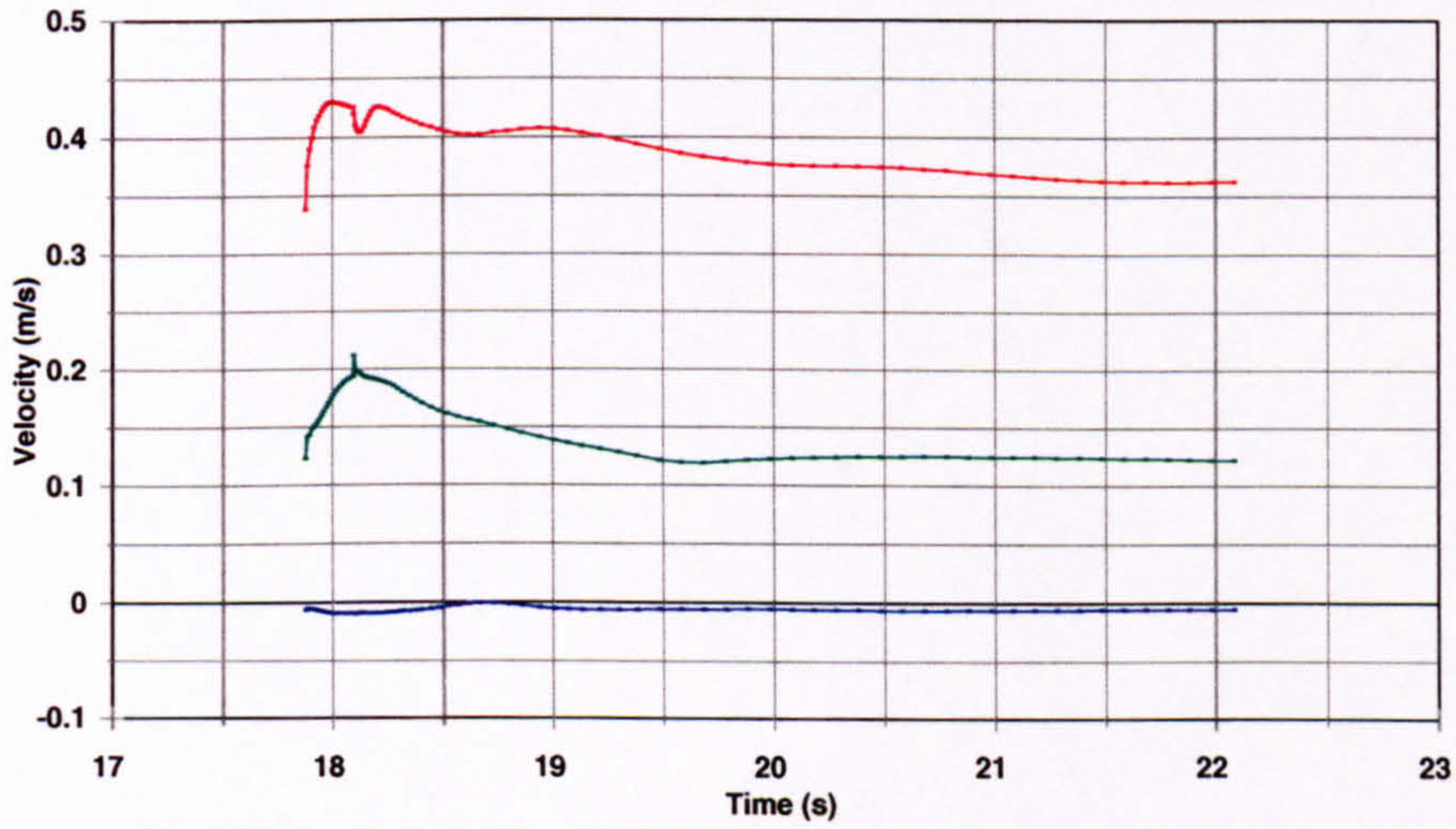


Figure 7.3-21f Time history plot of U, V and W velocities for 3DRNG2, at monitoring point 6 (0.462, 0.632, 0.138).

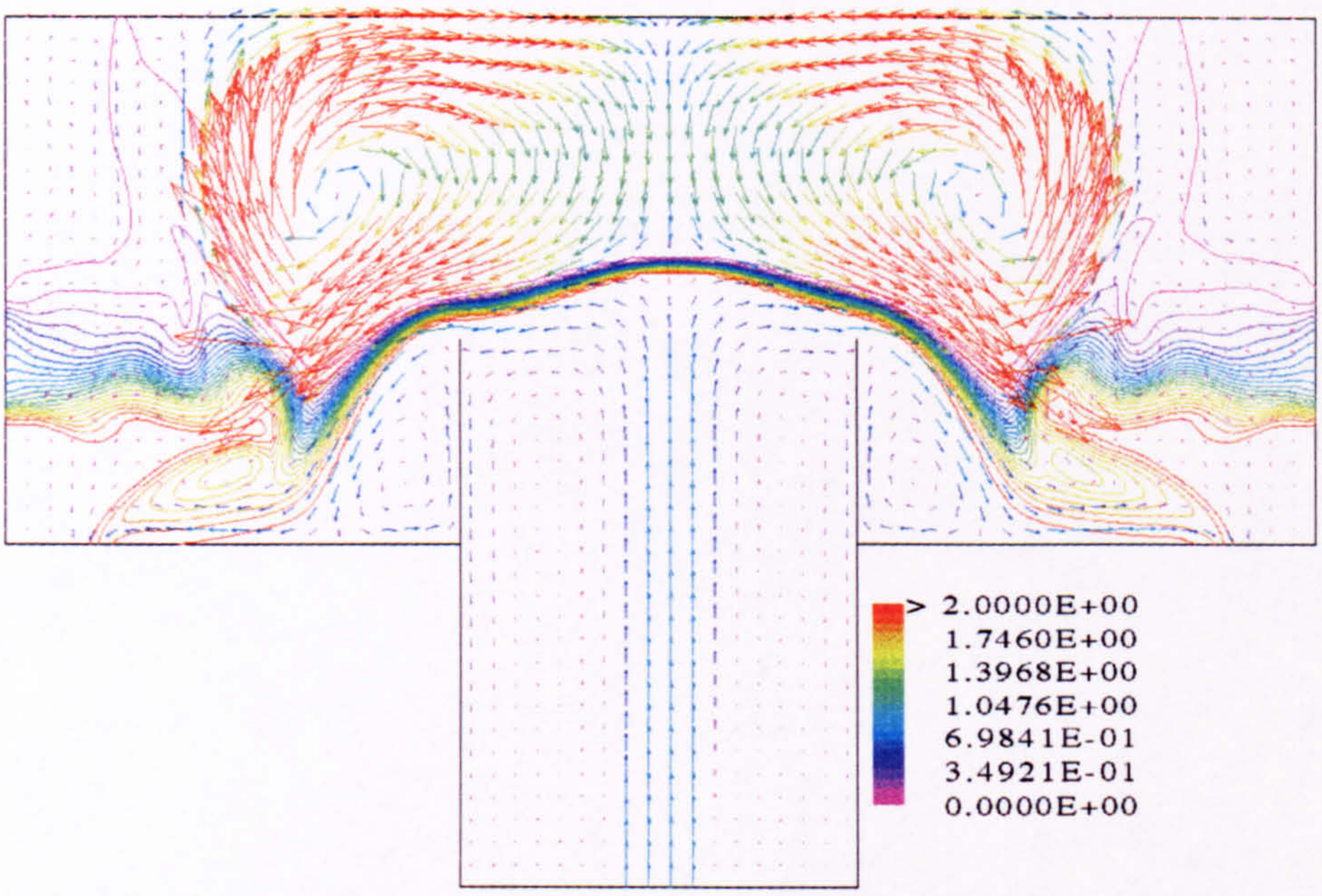


Figure 7.4-1a Velocity vector and volume fraction plot of Bend2. 2D geometry used. Flowrate = 4.38 l/s. Inflow angle is inclined at 2° from vertical axis. The inlet has a uniform velocity distribution.

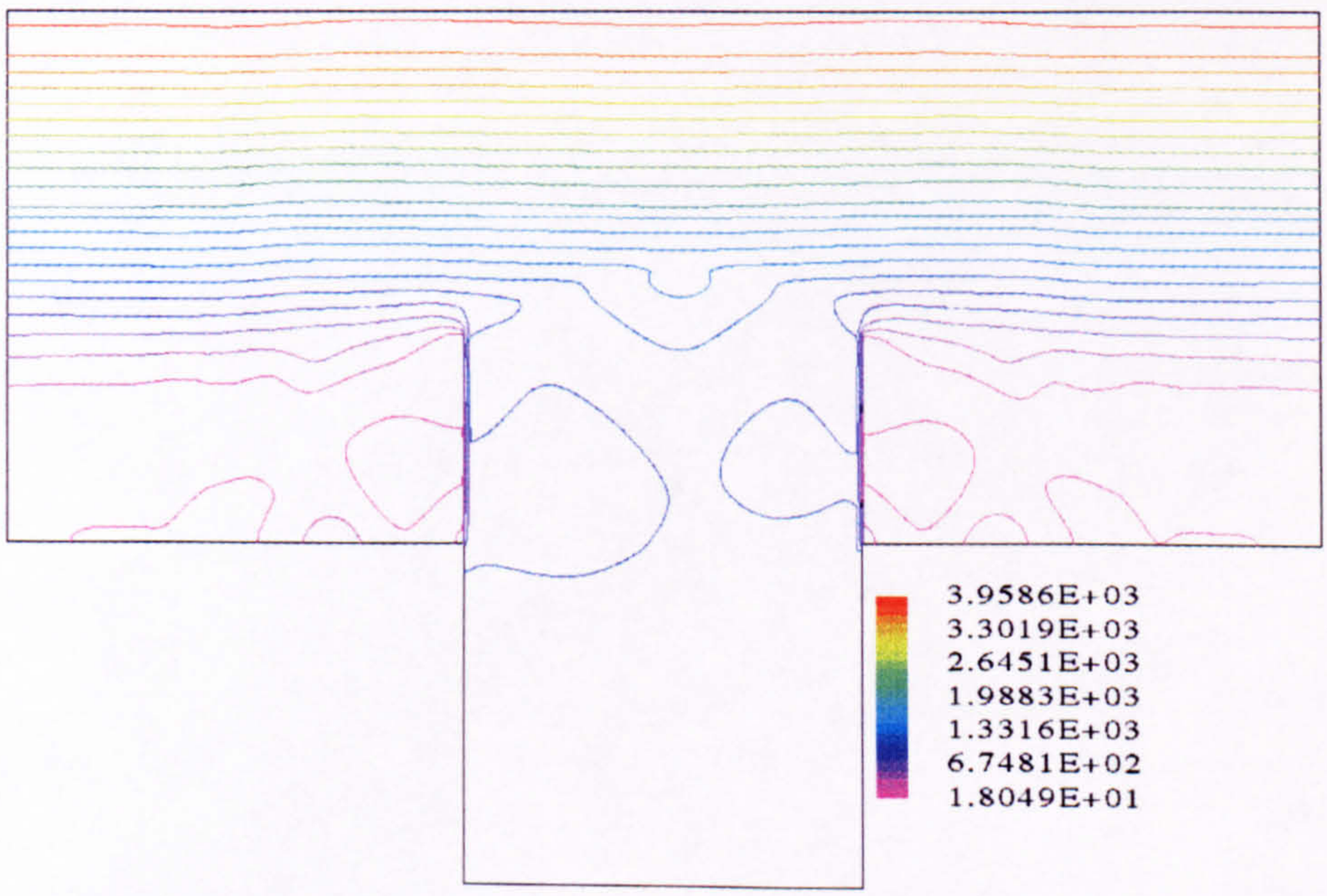


Figure 7.4-1b Pressure contour plot for Bend2.

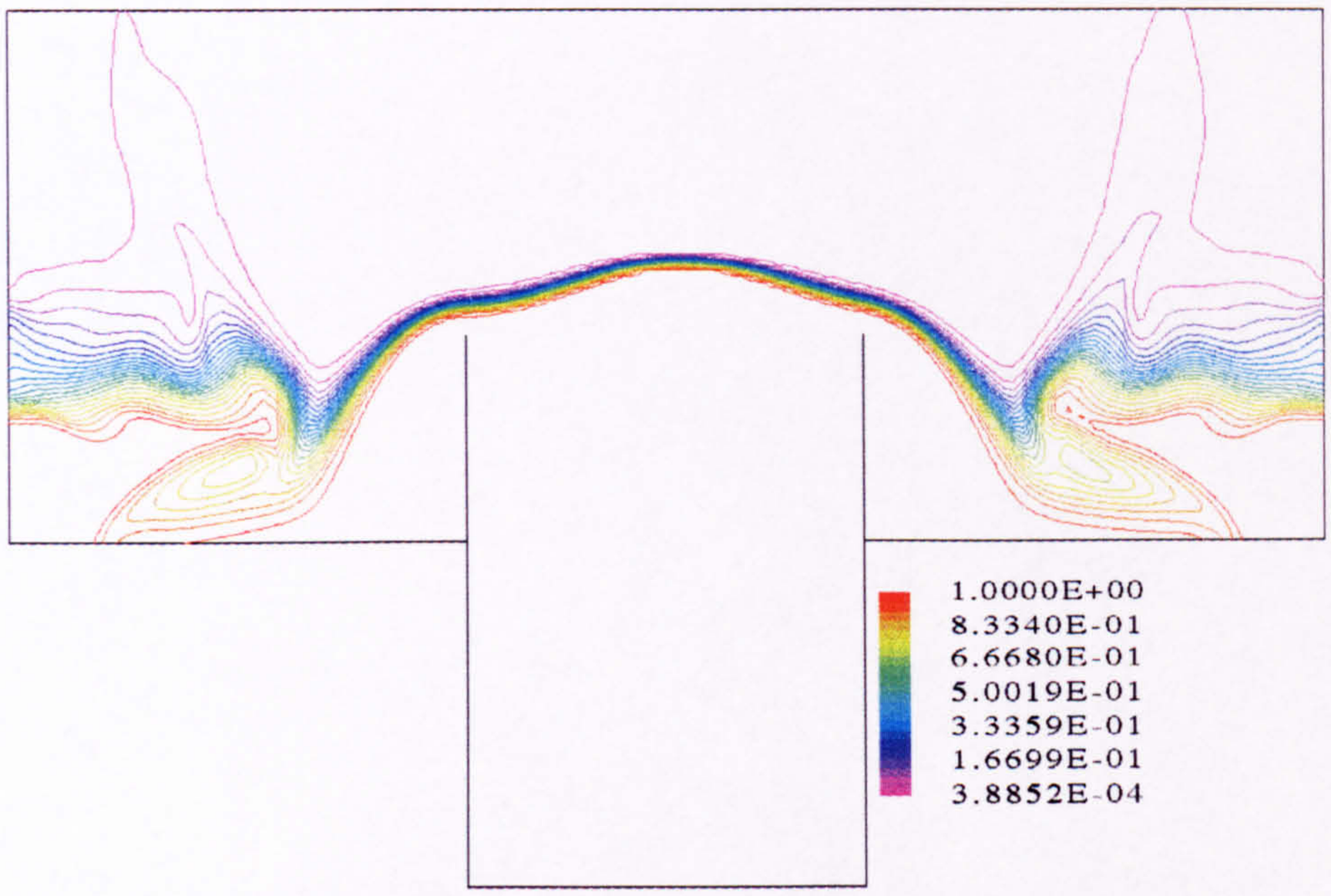


Figure 7.4-1c Volume fraction contour plot of water for Bend2. Value of 1.0 represents water, and air is 0.0. Free surface has a value of 0.5.

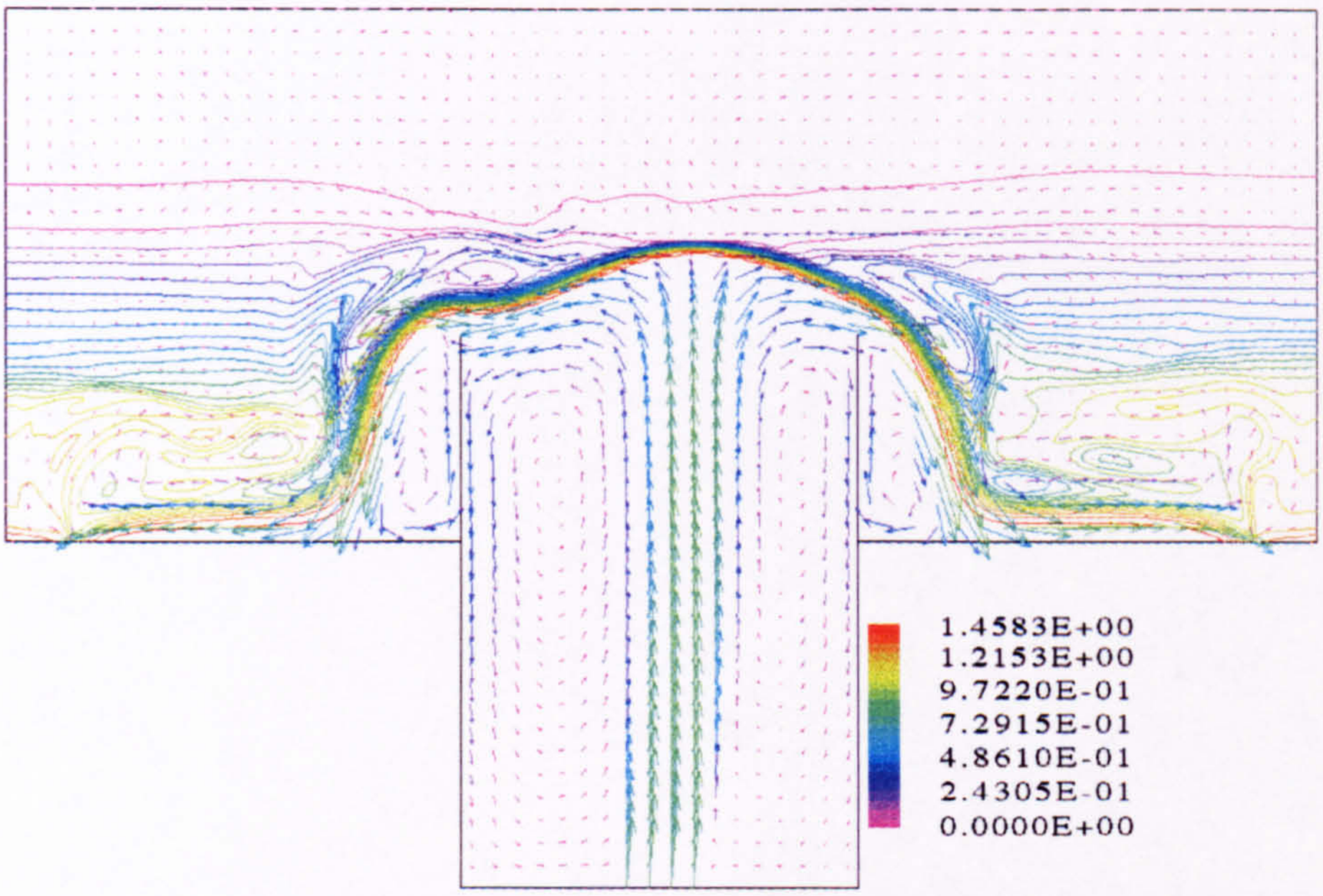


Figure 7.4-2a Velocity vector and volume fraction contour plot for Bend5. 2D geometry used. Flowrate = 4.38 l/s. Inflow angle is inclined at 5° from vertical axis. The inlet has a uniform velocity distribution.

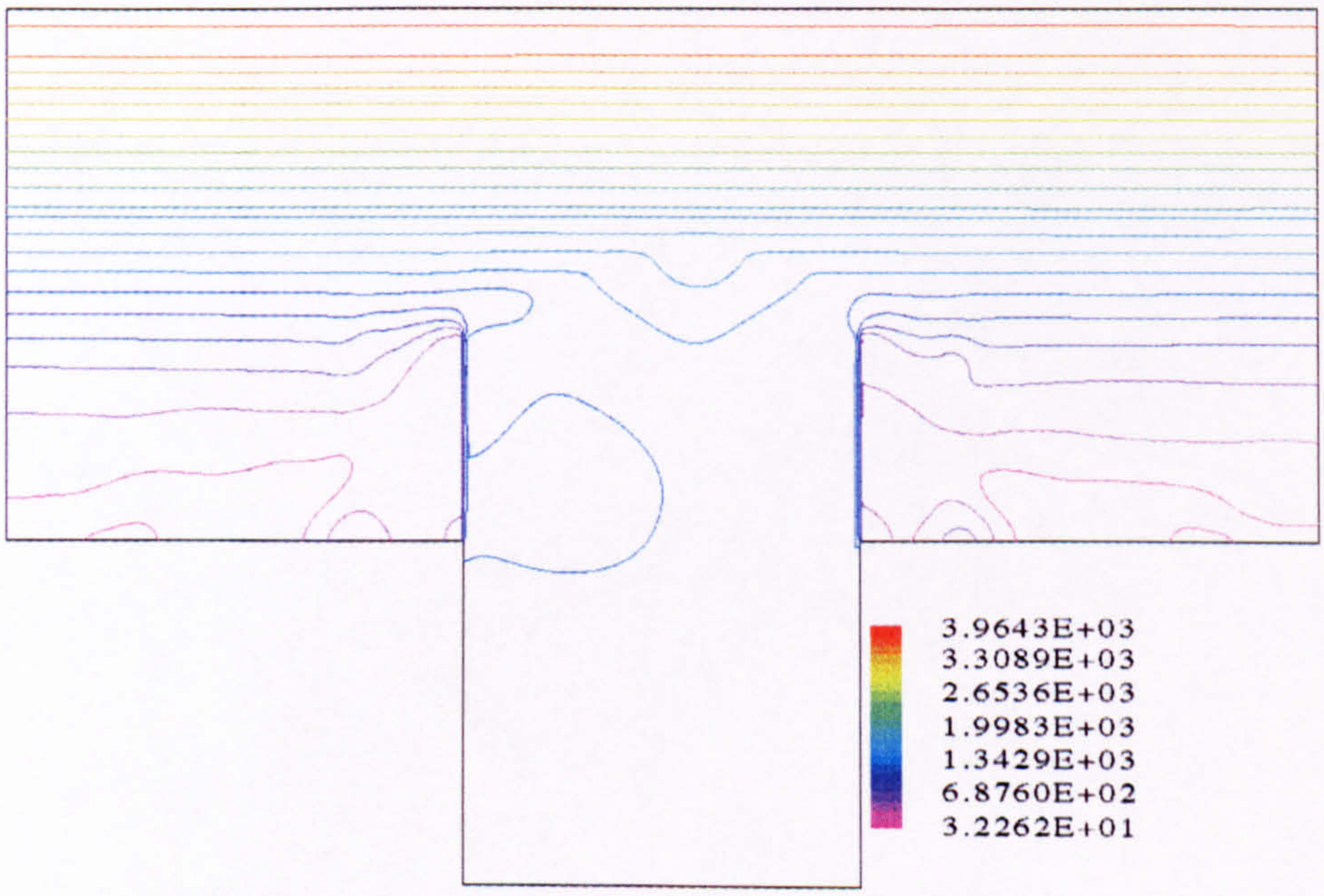


Figure 7.4-2b Pressure contour plot for Bend5.

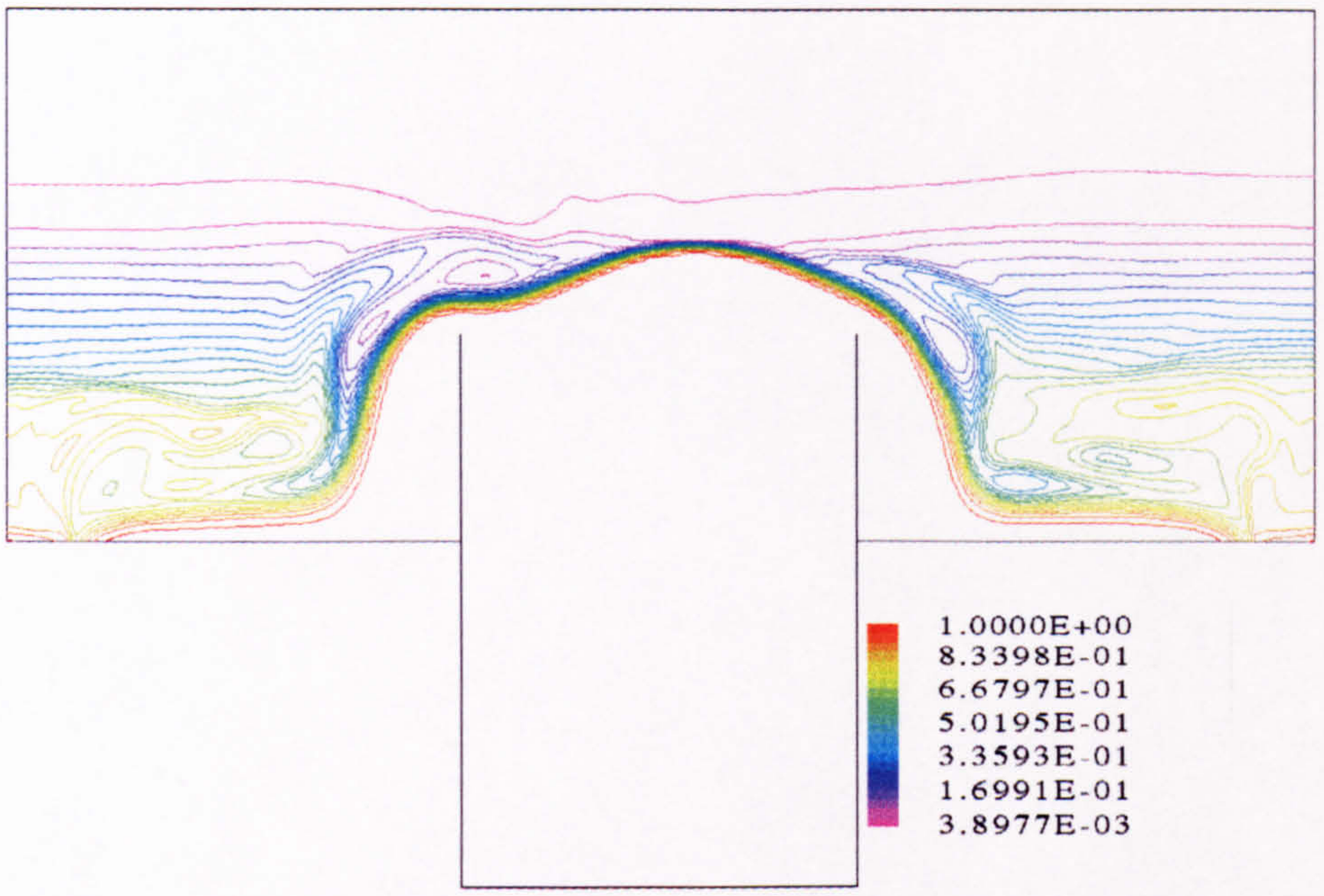


Figure 7.4-2c Volume fraction contour plot of water for Bend5. Value of 1.0 represents water, 0.0 is air. Free surface has a value of 0.5.

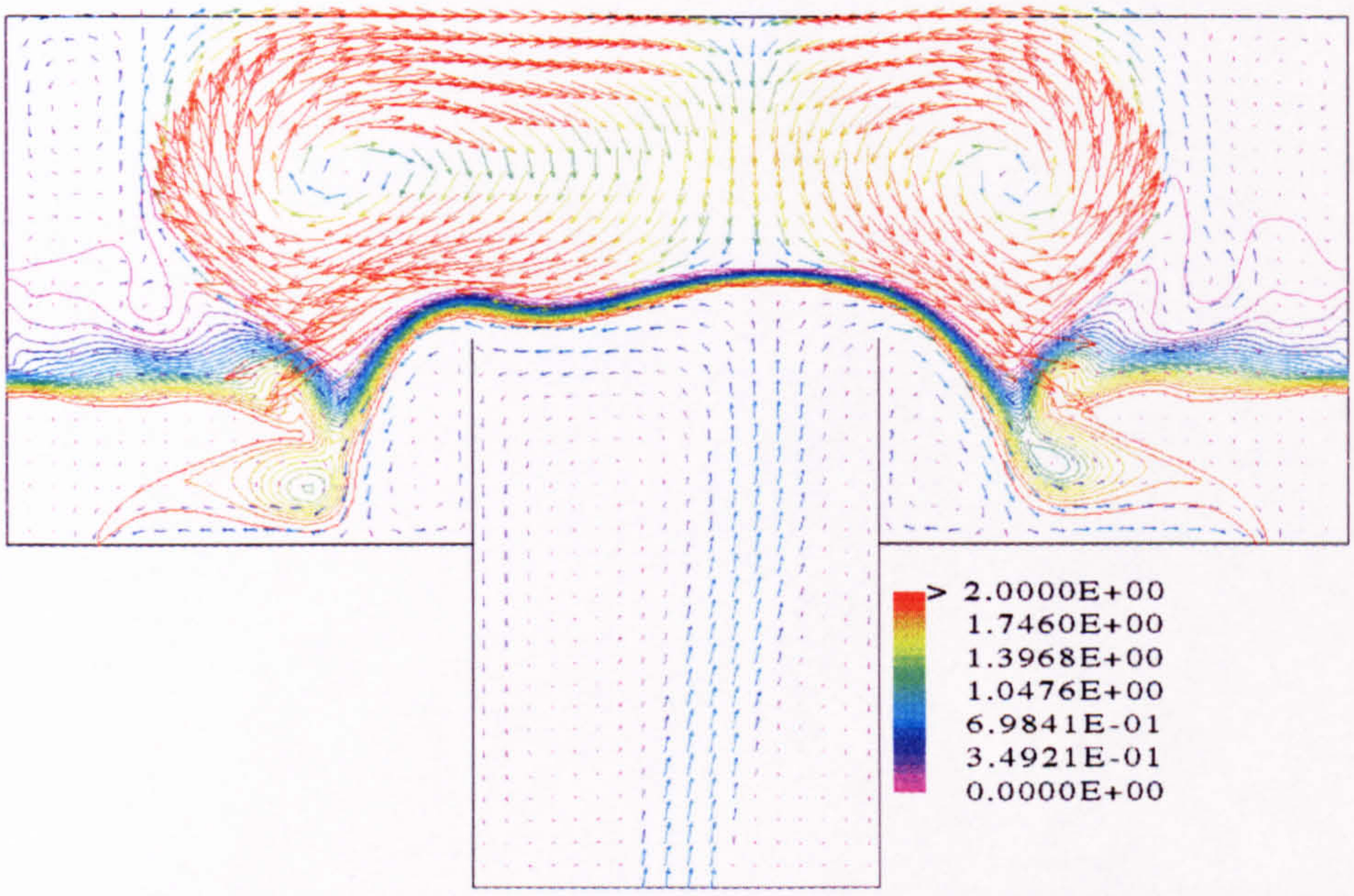


Figure 7.4-3a Velocity vector and volume fraction contour plot for Bend10. 2D geometry used. Flowrate = 4.38 l/s. Inflow is inclined at 10° to the vertical axis. Inlet has a uniform velocity distribution.

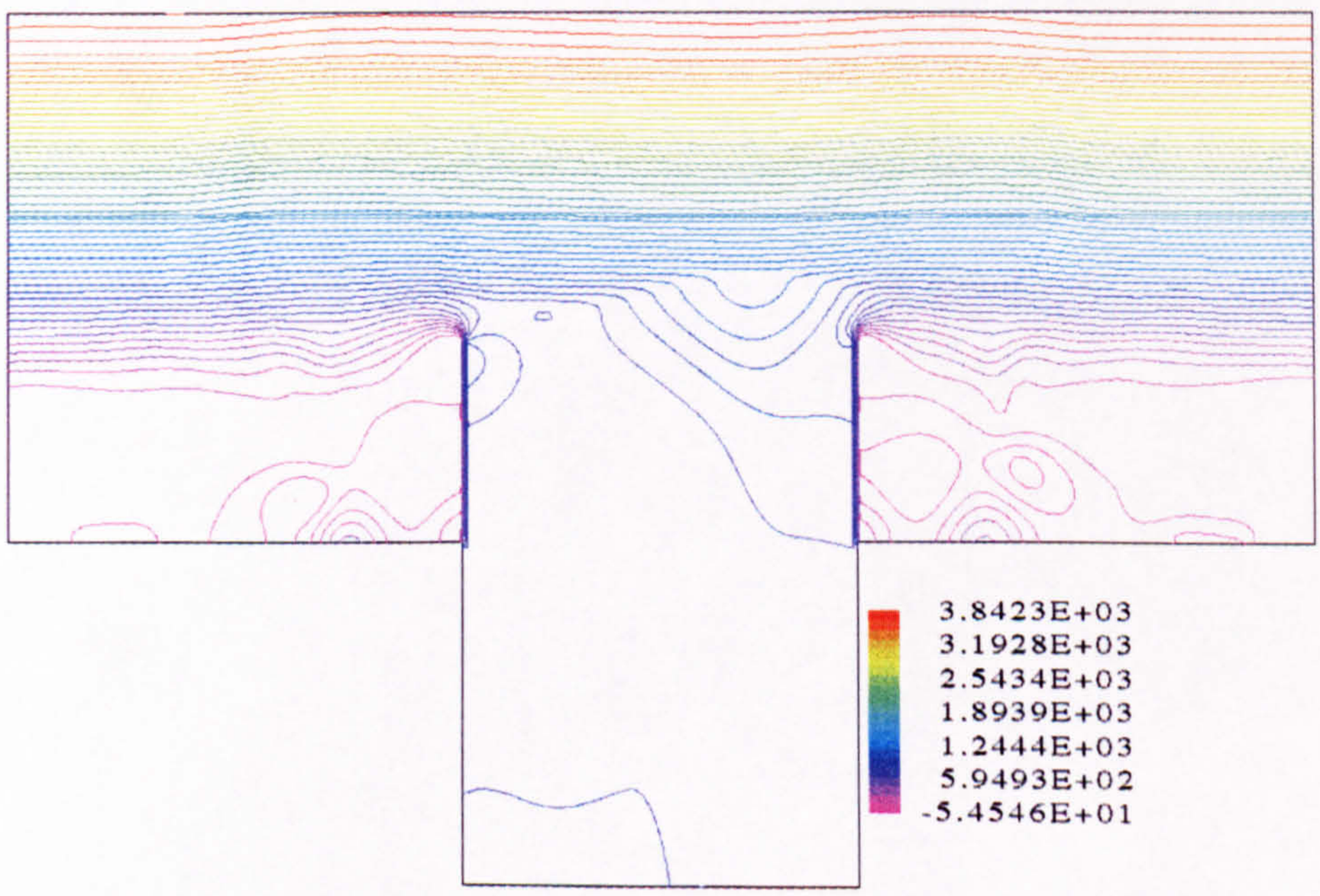


Figure 7.4-3b Pressure contour plot for Bend10

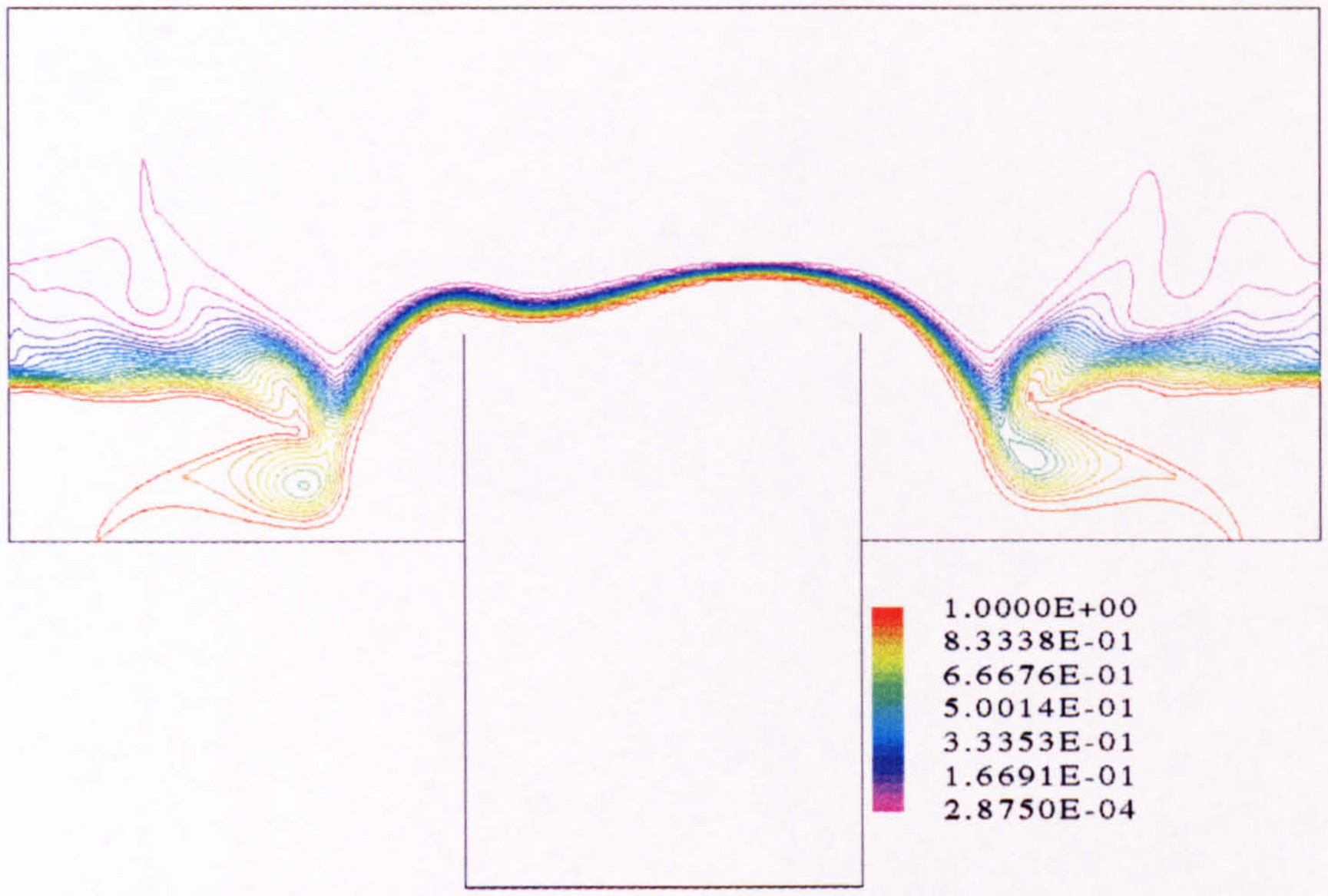


Figure 7.4-3c Volume fraction contour plot of water for Bend10. Value of 1.0 represents water, air is 0.0. Free surface has a value of 0.5.

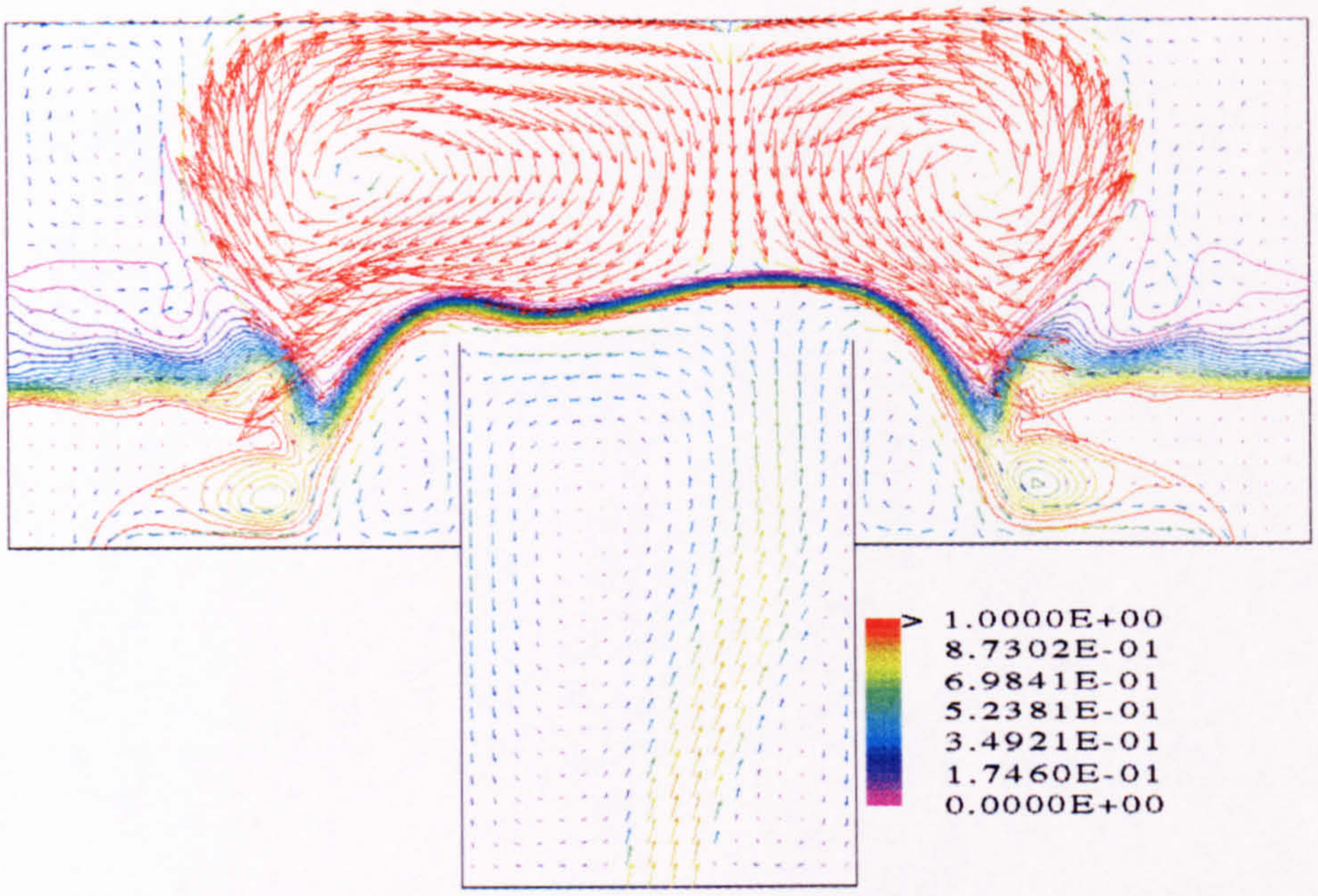


Figure 7.4-4a Velocity vector and volume fraction contour plot for Bend12. 2D geometry used. Flowrate = 4.38 l/s. Inflow angle is inclined at 12.5° from the vertical axis. The inlet has a uniform velocity distribution.

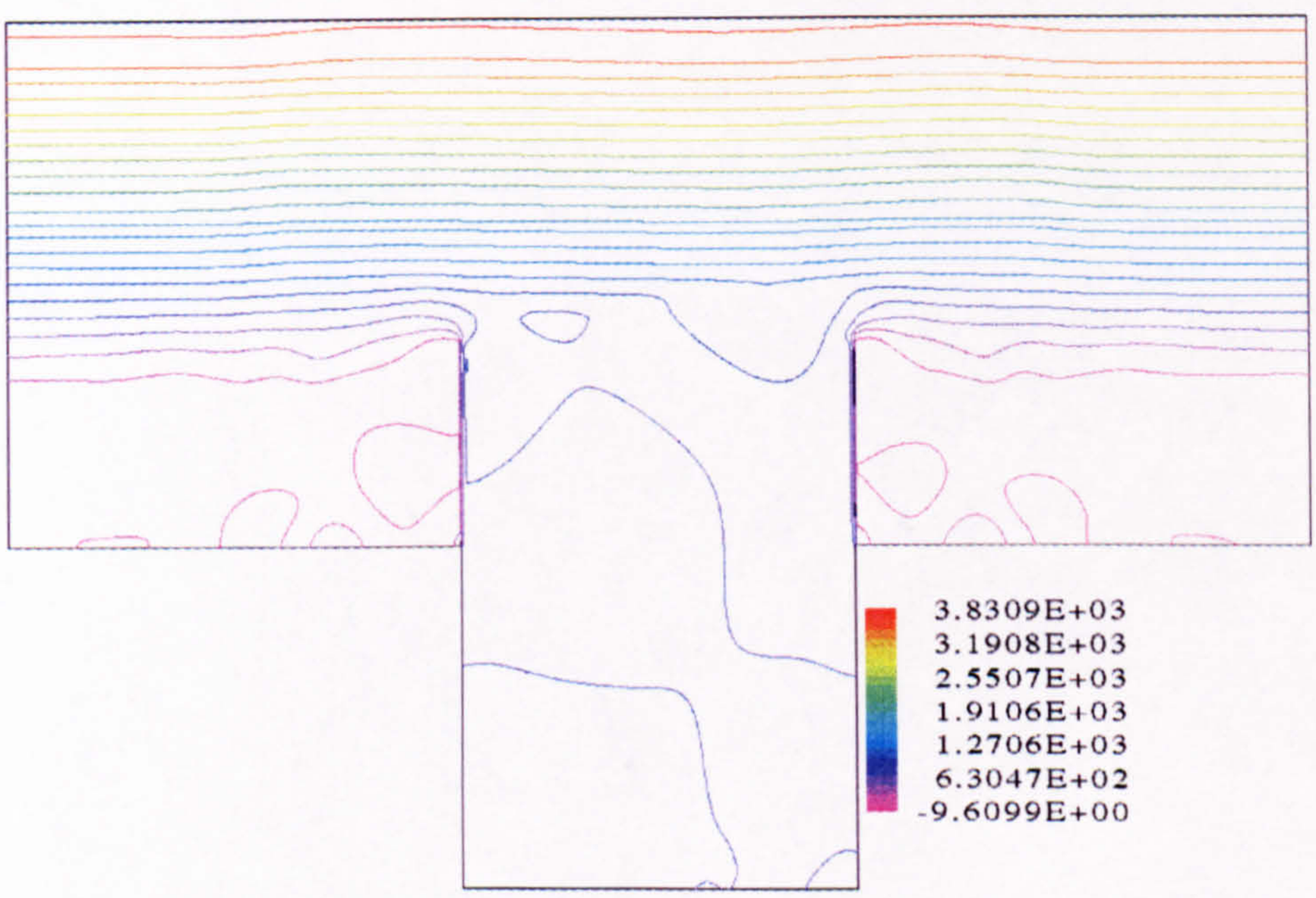


Figure 7.4-4b Pressure contour plot for Bend12

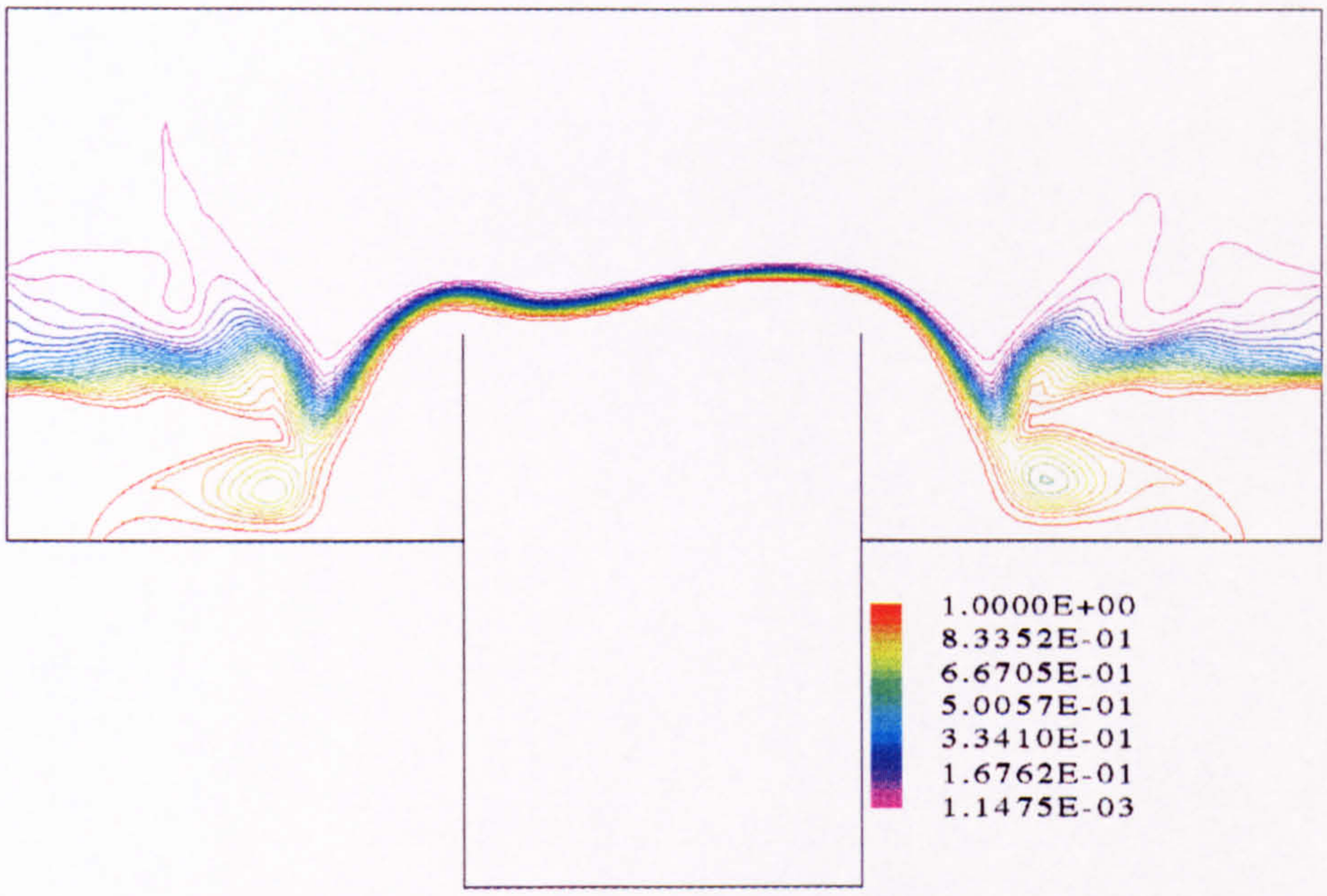


Figure 7.4-4c Volume fraction contour plot of water for Bend12. Value of 1.0 represents water, air is 0.0. Free surface has a value of 0.5.

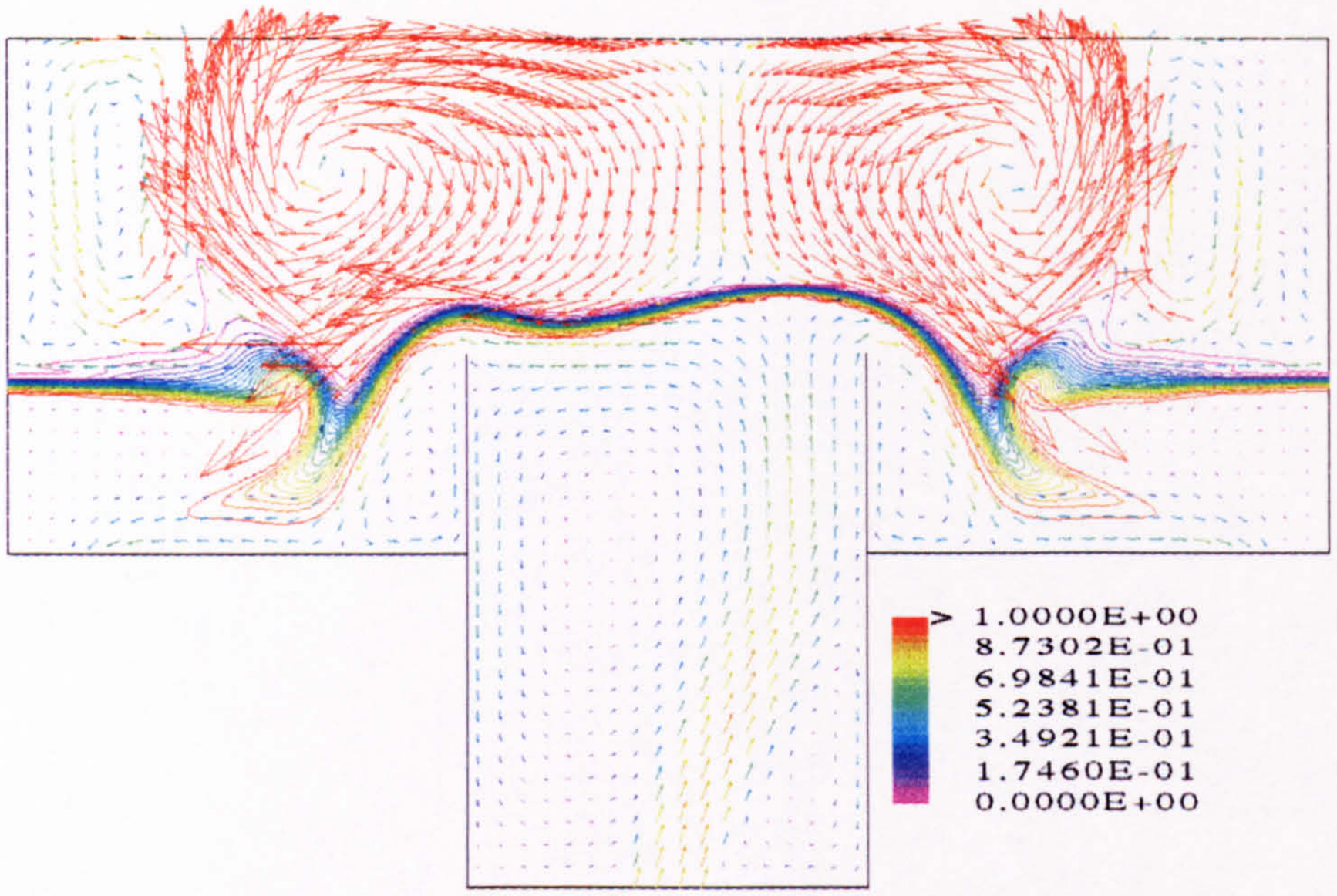


Figure 7.4-5a Velocity vector and volume fraction contour plot for Bend15. 2D geometry used. Flowrate = 4.38 l/s. Inflow angle is inclined at 15° to the vertical axis. The inlet has a uniform velocity distribution.

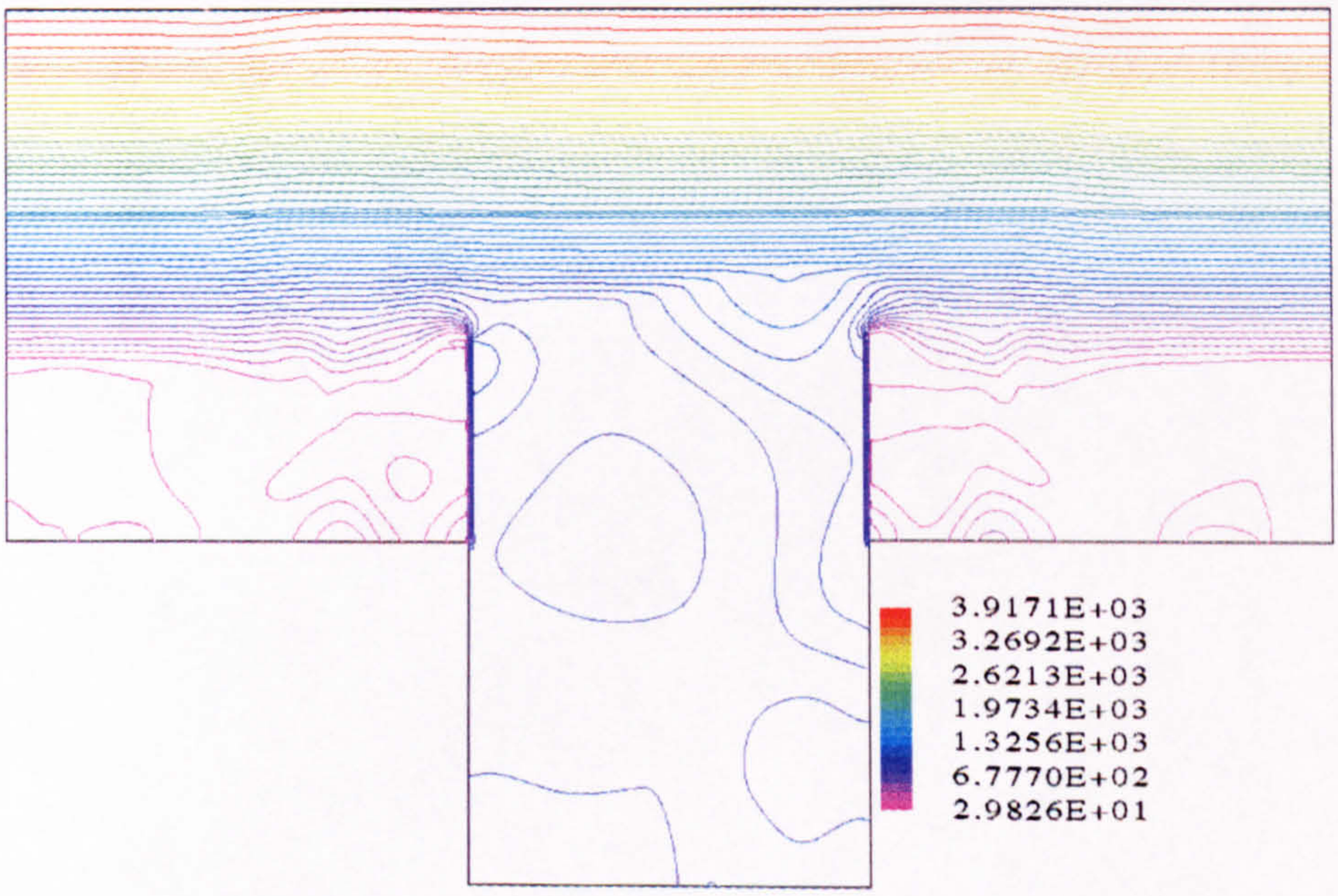


Figure 7.4-5b Pressure contour plot for Bend15

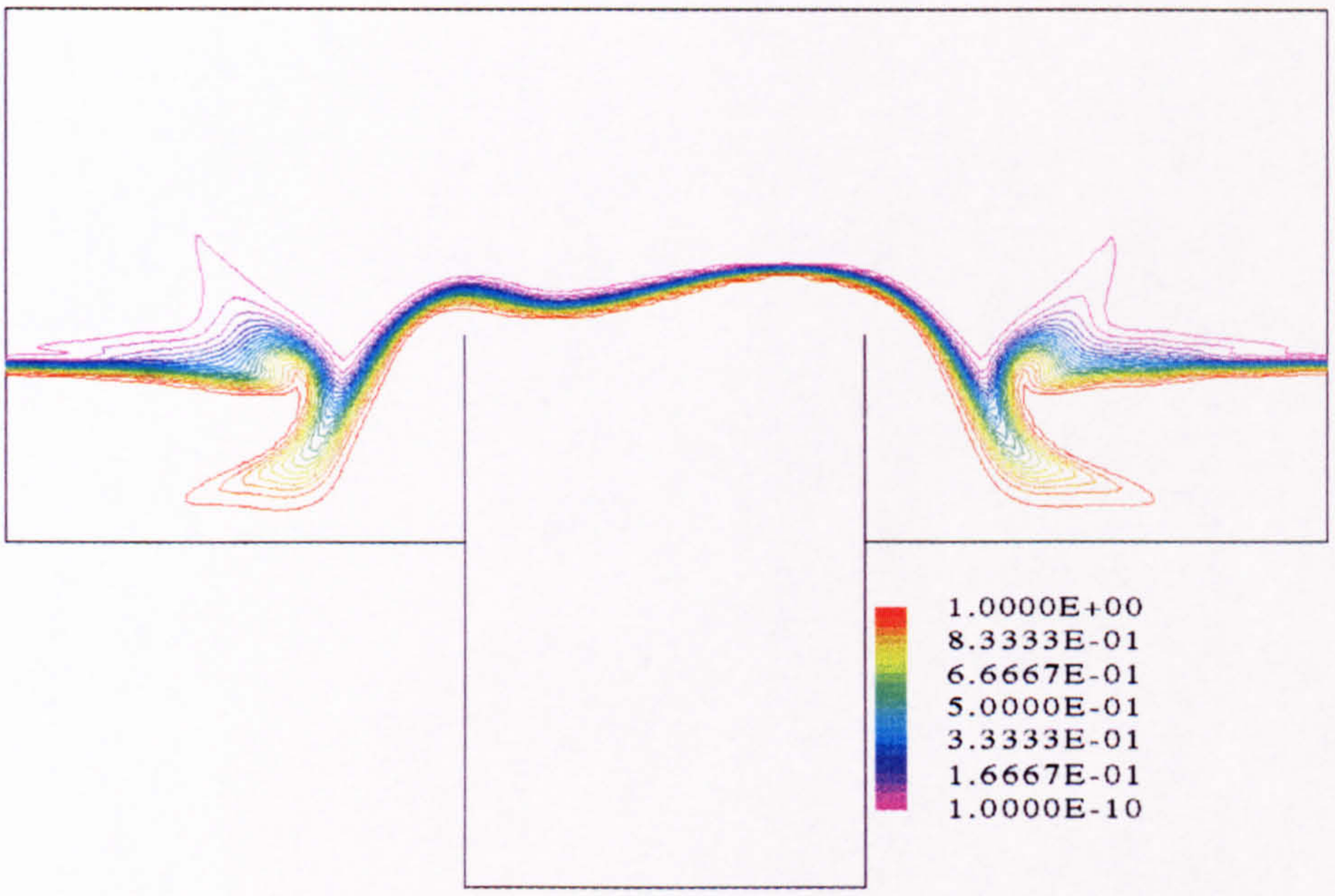


Figure 7.4-5c Volume fraction contour plot of water for Bend15. Value of 1.0 represents water, 0.0 is air. Free surface has a value of 0.5.

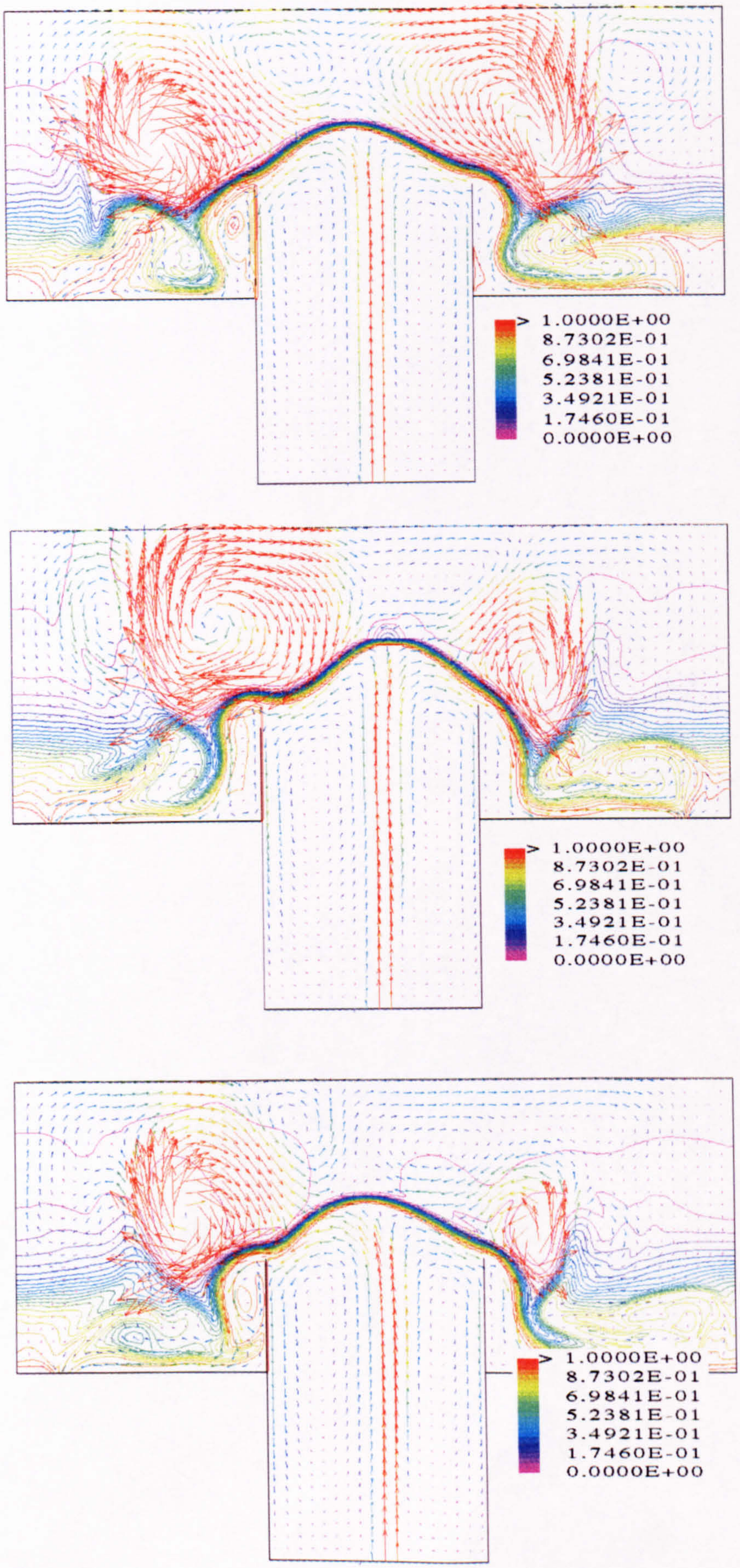


Figure 7.4-6a Plots showing periodic nature of flow fields for Pipebnd1 at 1/2 second intervals, beginning from 17.5s to 18.5 s. Pipebend is decoupled from chamber.

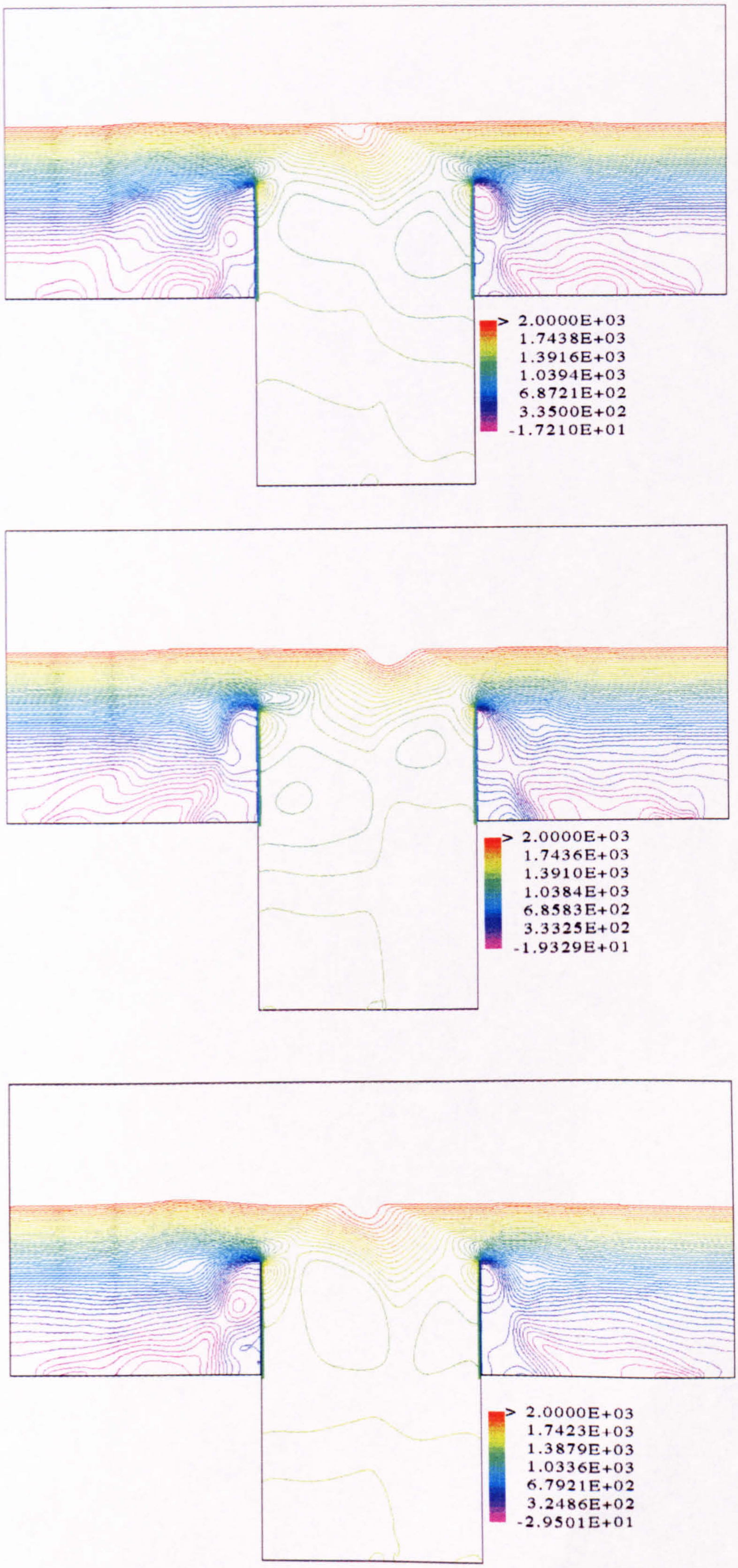


Figure 7.4-6b Pressure contour plots for Pipebnd1. Note the asymmetric pressure field near free surface causing the jet deflection.

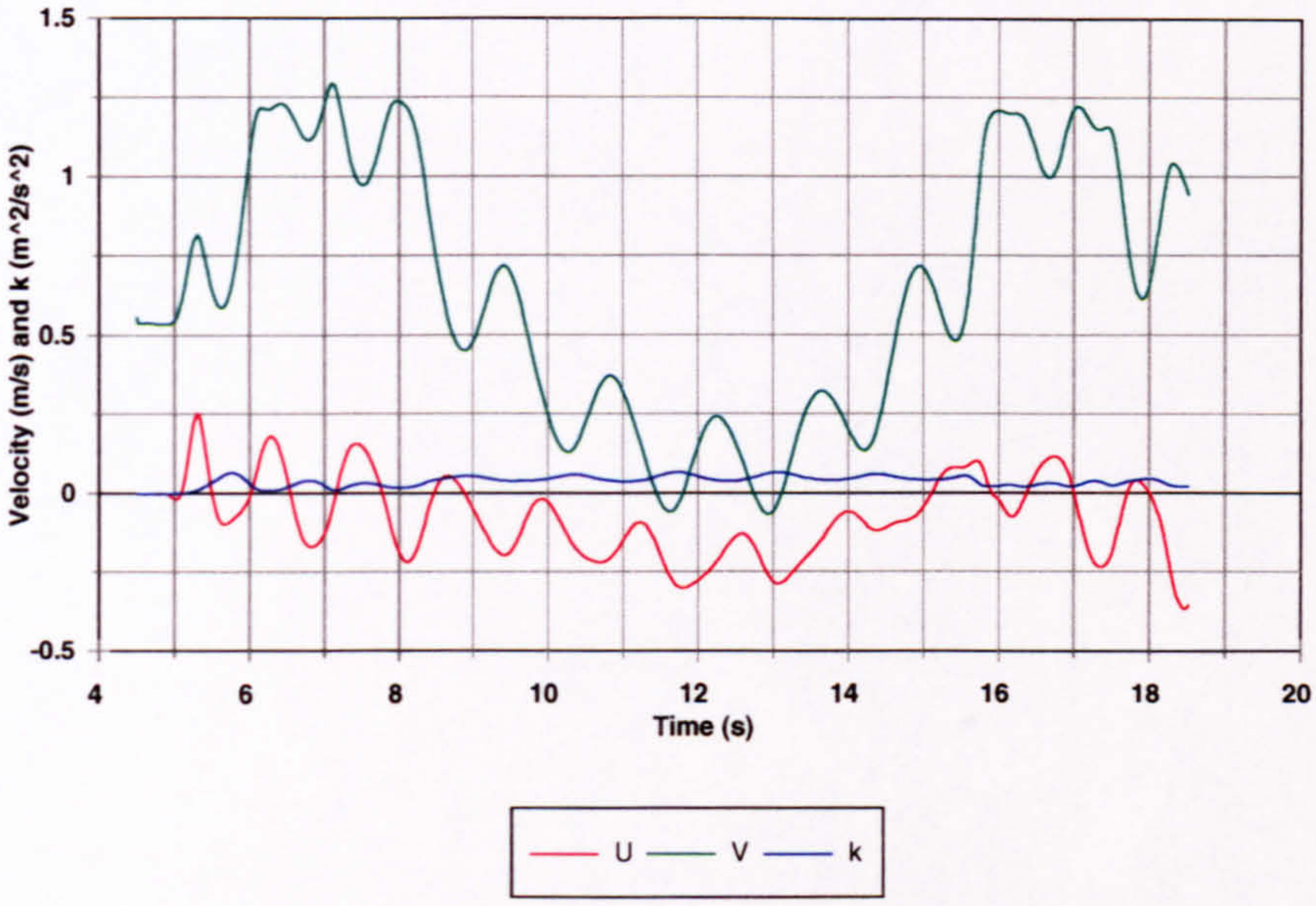


Figure 7.4-7a Time history plot of U, V and k for Pipebnd1. (Periodic nature of soultion is shown). Monitoring point 1 (0.231m, 0.633m, 0.0277m), at chamber centreline, above weir crests.

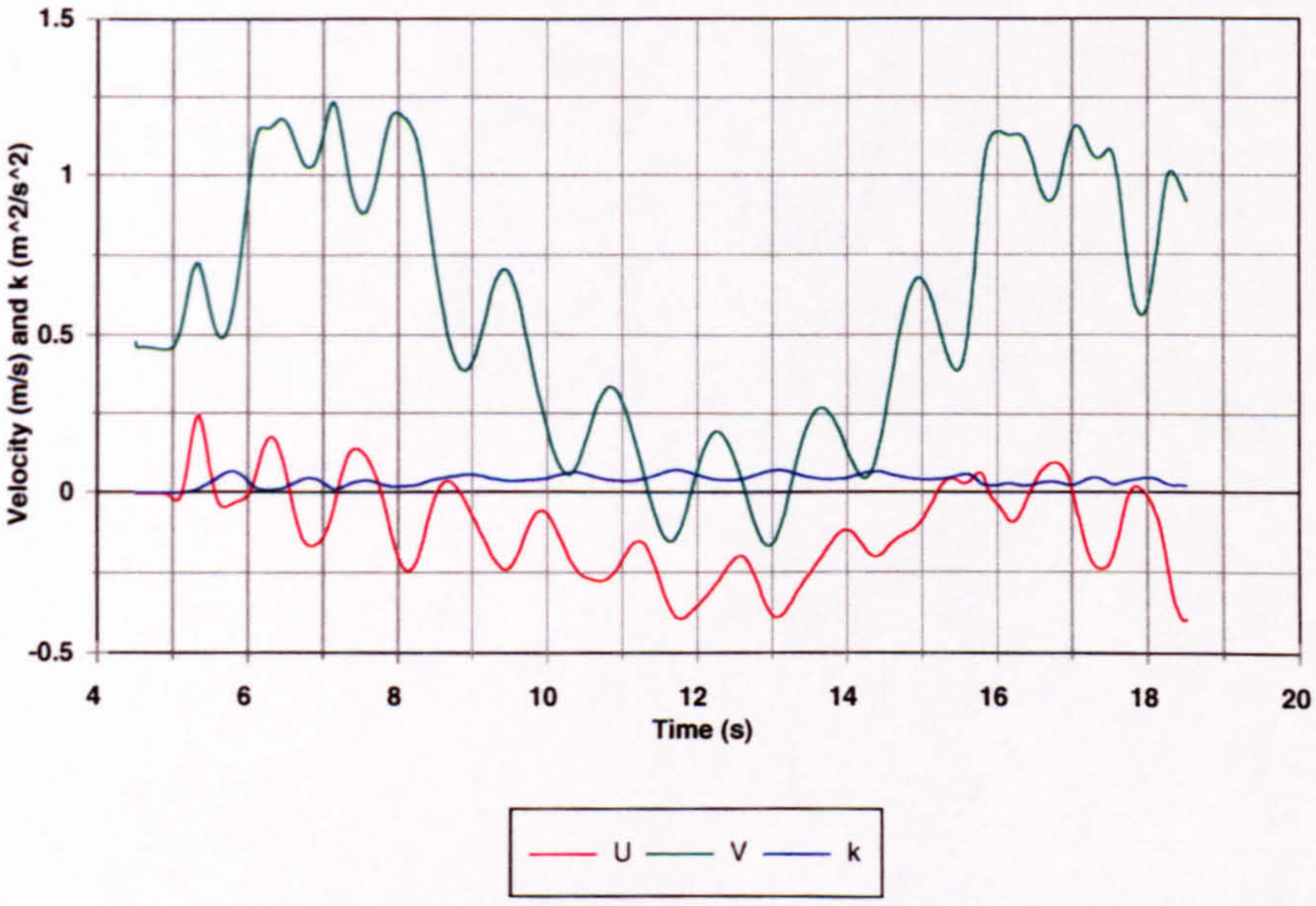


Figure 7.4-7b Time history plot of U, V and k for Pipebnd1, at monitoring point 2 (0.231, 0.643, 0.0277), at chamber centreline.

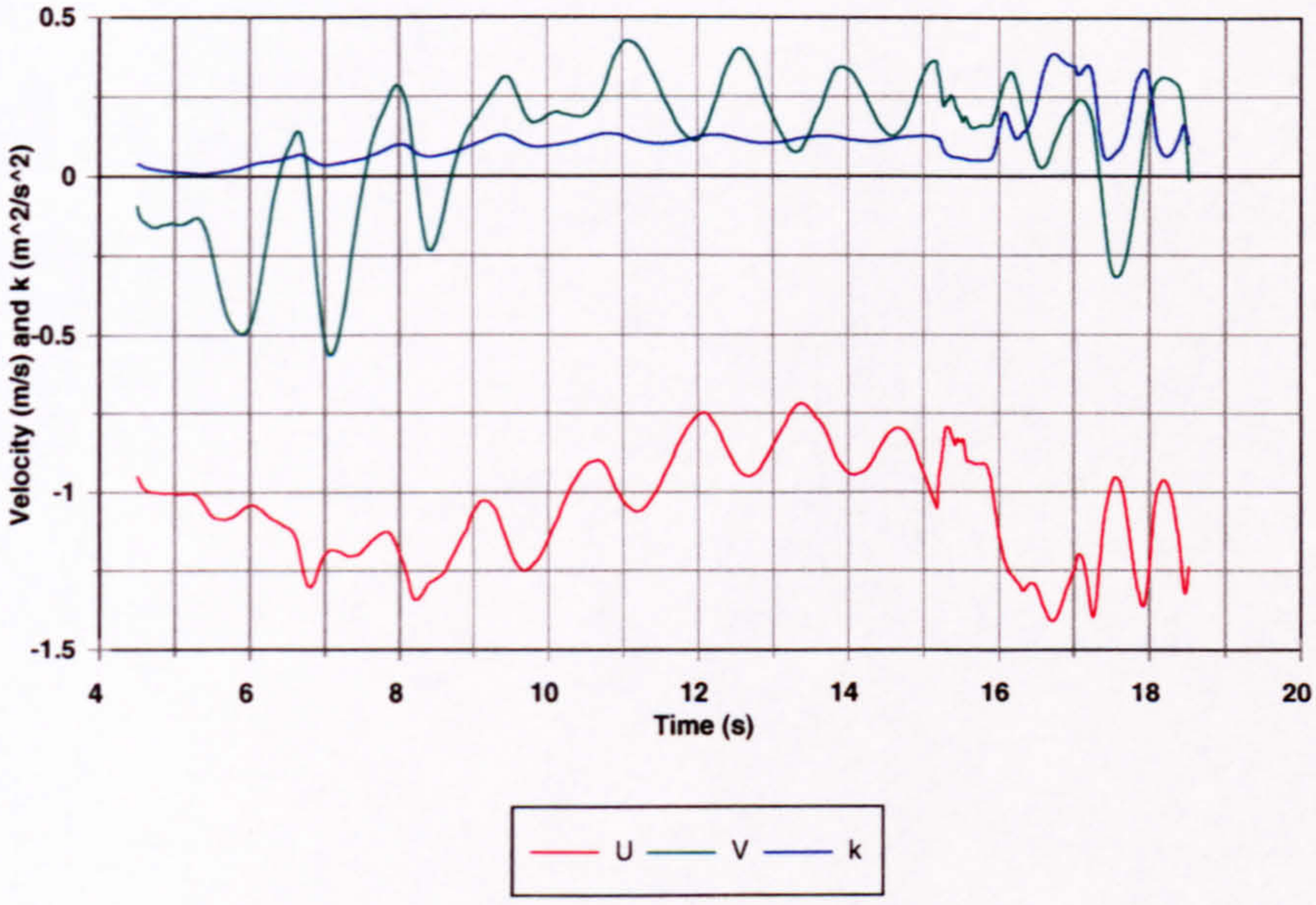


Figure 7.4-7c Time history plot of U, V and k for Pipebnd1, at monitoring point 3 (0, 0.653, 0.0277), left hand side of chamber, above weir crest.

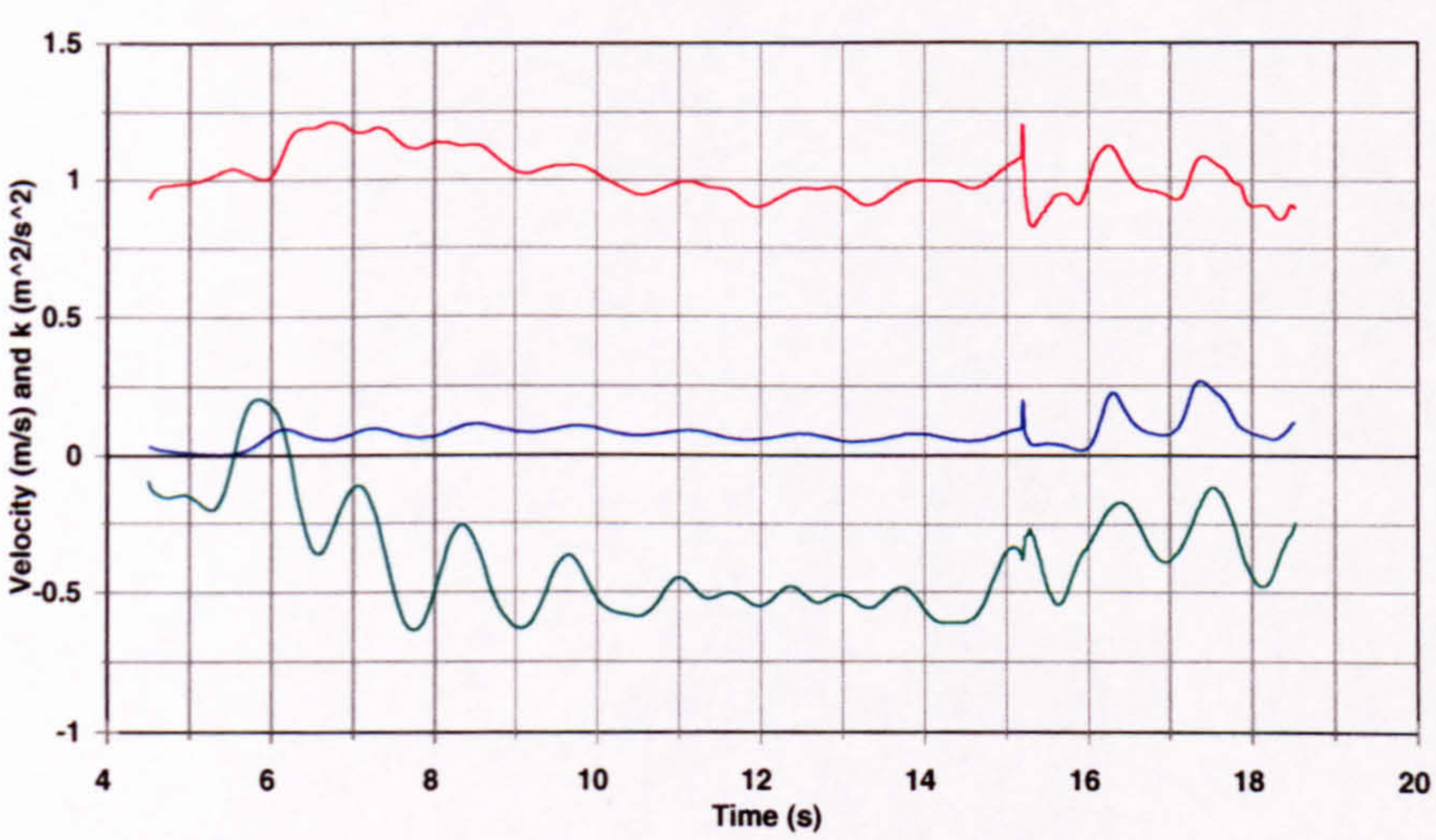


Figure 7.4-7d Time history plot of U, V and k for Pipebnd1, at monitoring point 4 (0.462, 0.653, 0.0277), right hand side of chamber, above weir crest.

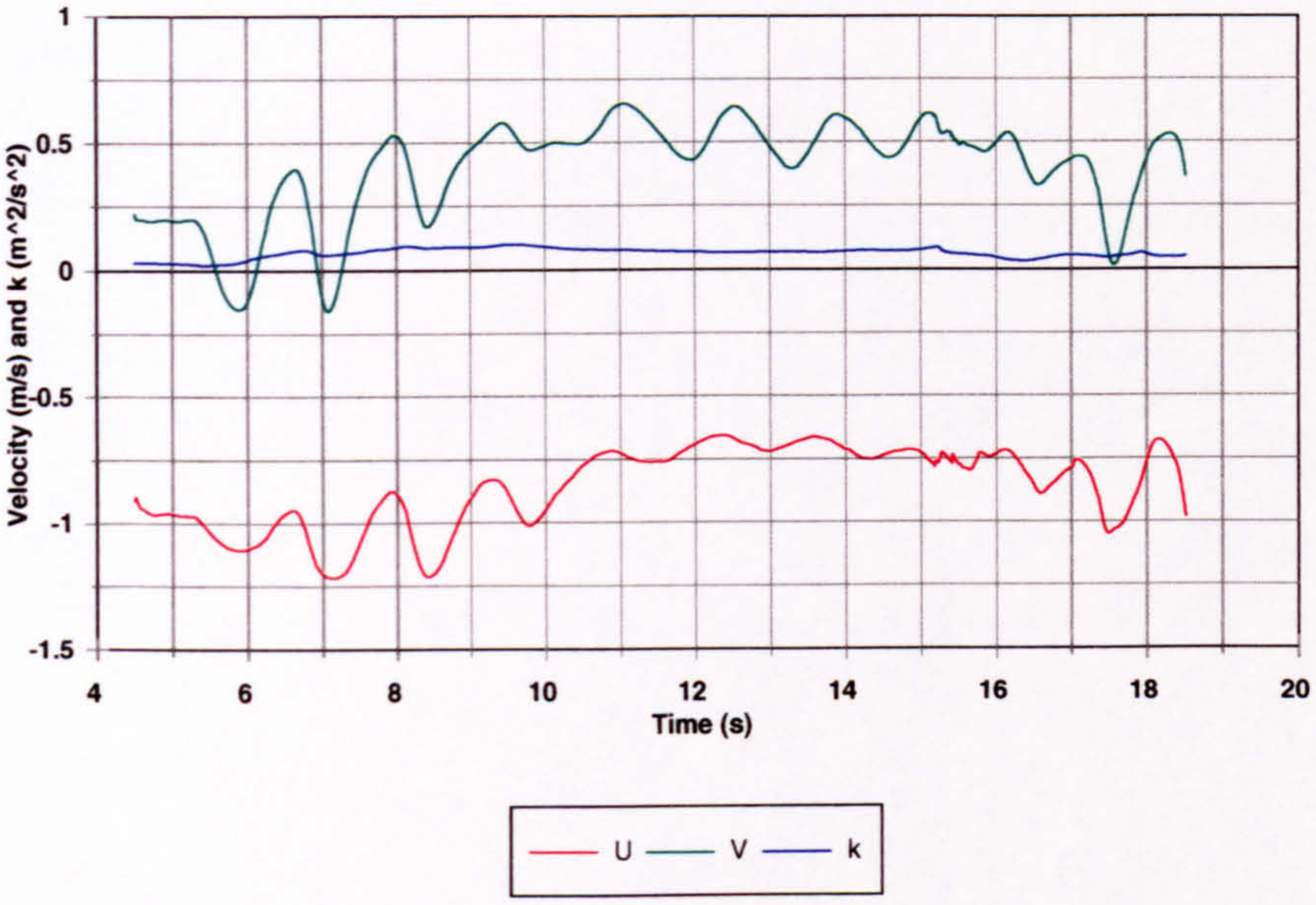


Figure 7.4-7e Time history plot of U, V, k for Pipebnd1, at monitoring point 5 (0, 0.633, 0.0277), at left hand side of chamber, 2 mm above weir crest.

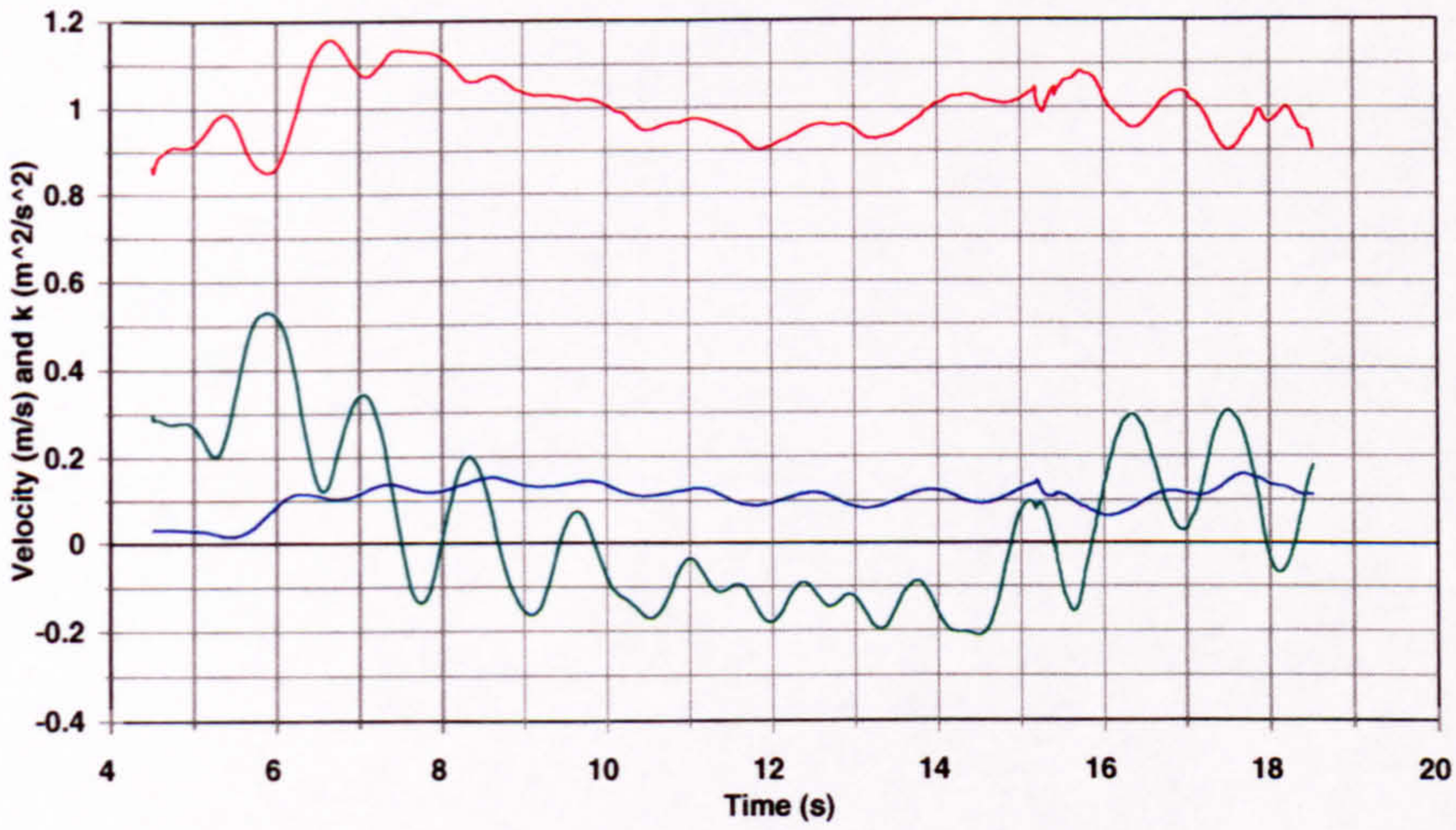


Figure 7.4-7f Time history plot of U, V and k for Pipebnd1, at monitoring point 6 (0.462, 0.633, 0.0277), at right hand side of chamber, 2mm above weir crest.

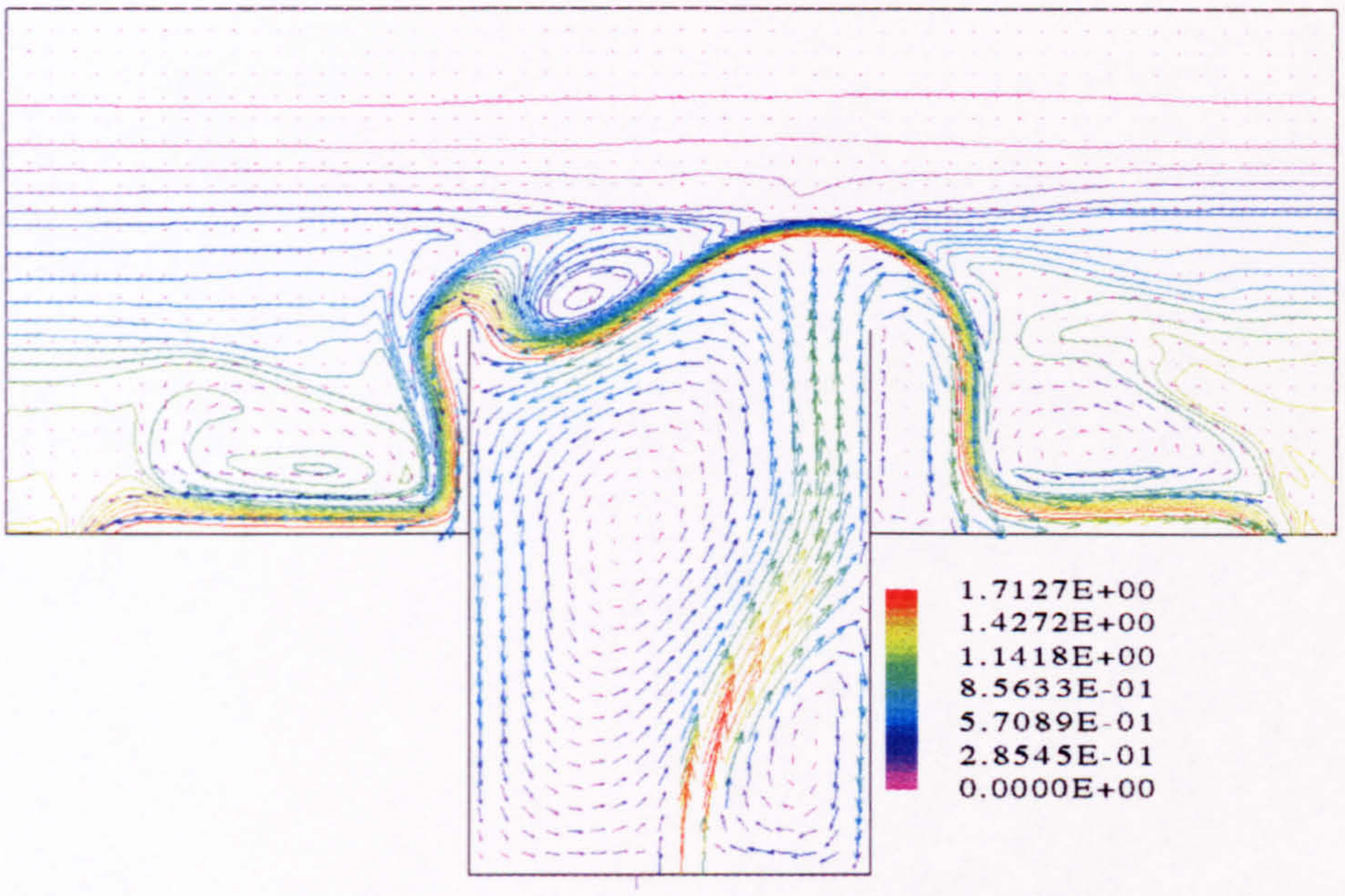


Figure 7.4-8a Velocity vector and volume fraction contour plot for Pipebnd2. Flowrate = 4.38 l/s. Van Leer differencing scheme and RNG k-ε turbulence model used. This is the second iteration for the decoupled pipe bend calculations. (Averaged pressures from Pipebnd1 and 2DRNGC2 used to determine inlet boundary conditions for this run).

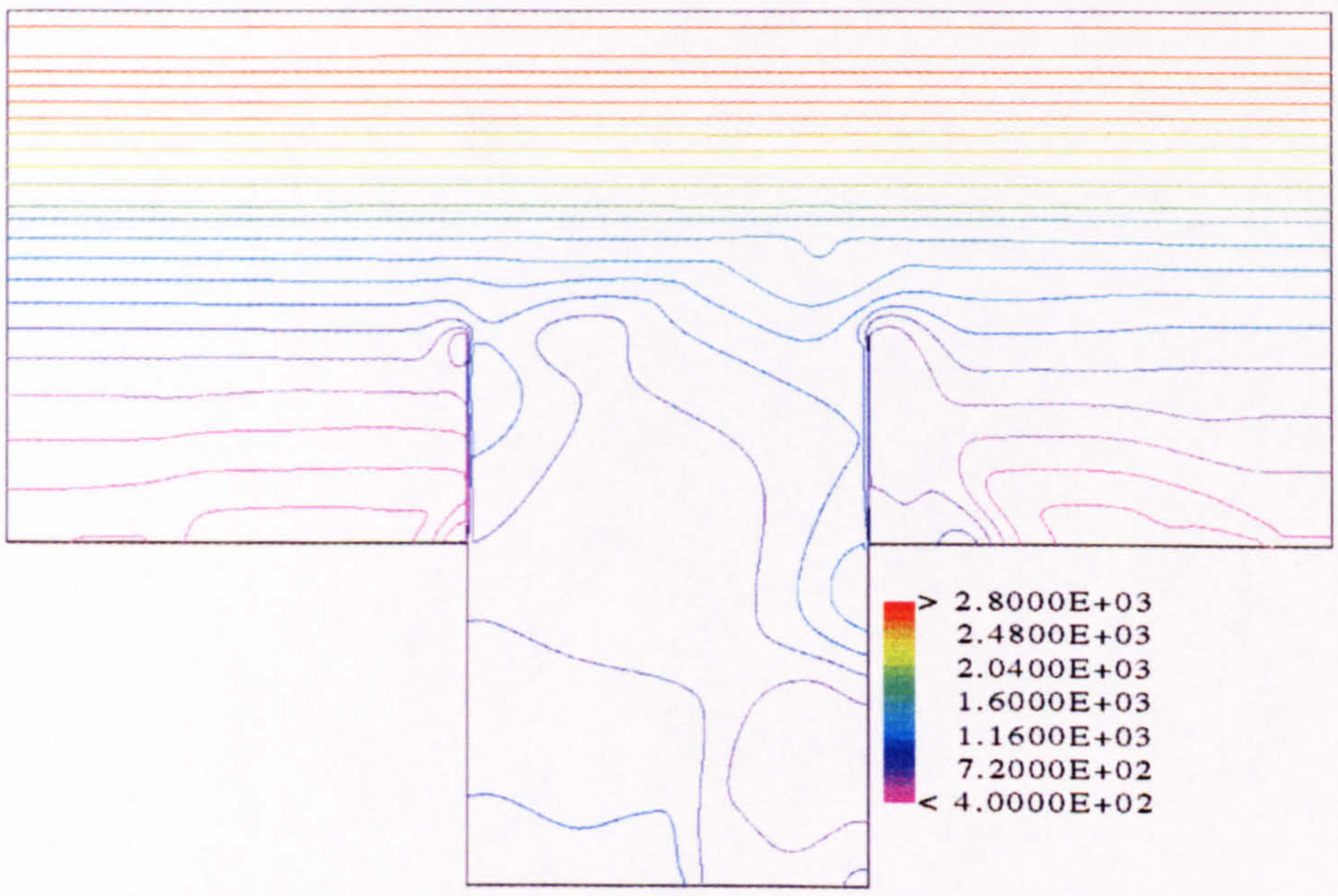


Figure 7.4-8b Pressure contour plot for Pipebnd2.

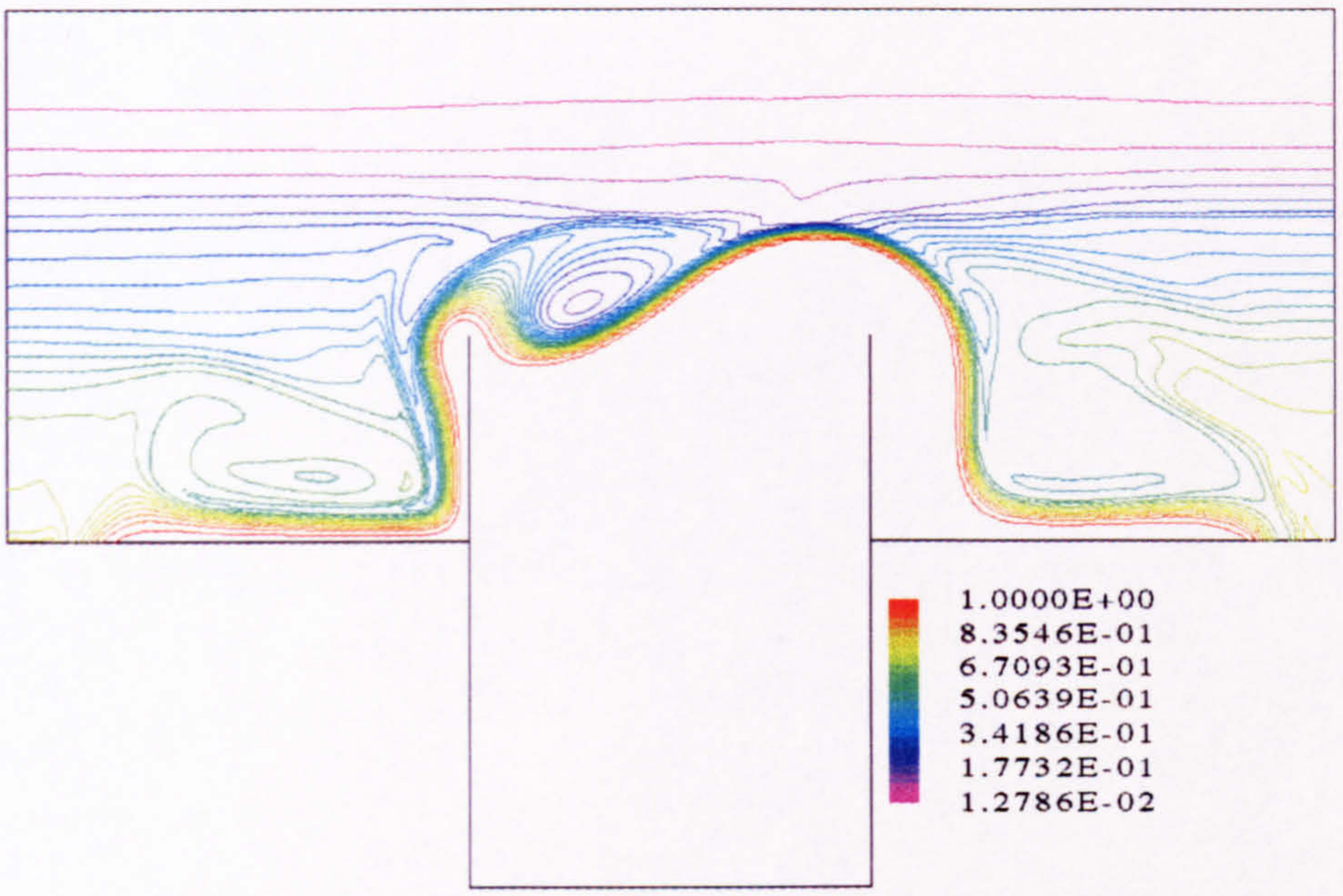


Figure 7.4-8c Volume fraction contour plot of water for Pipebnd2. Value of 1.0 represents water, and 0.0 is air. Free surface has a value of 0.5.

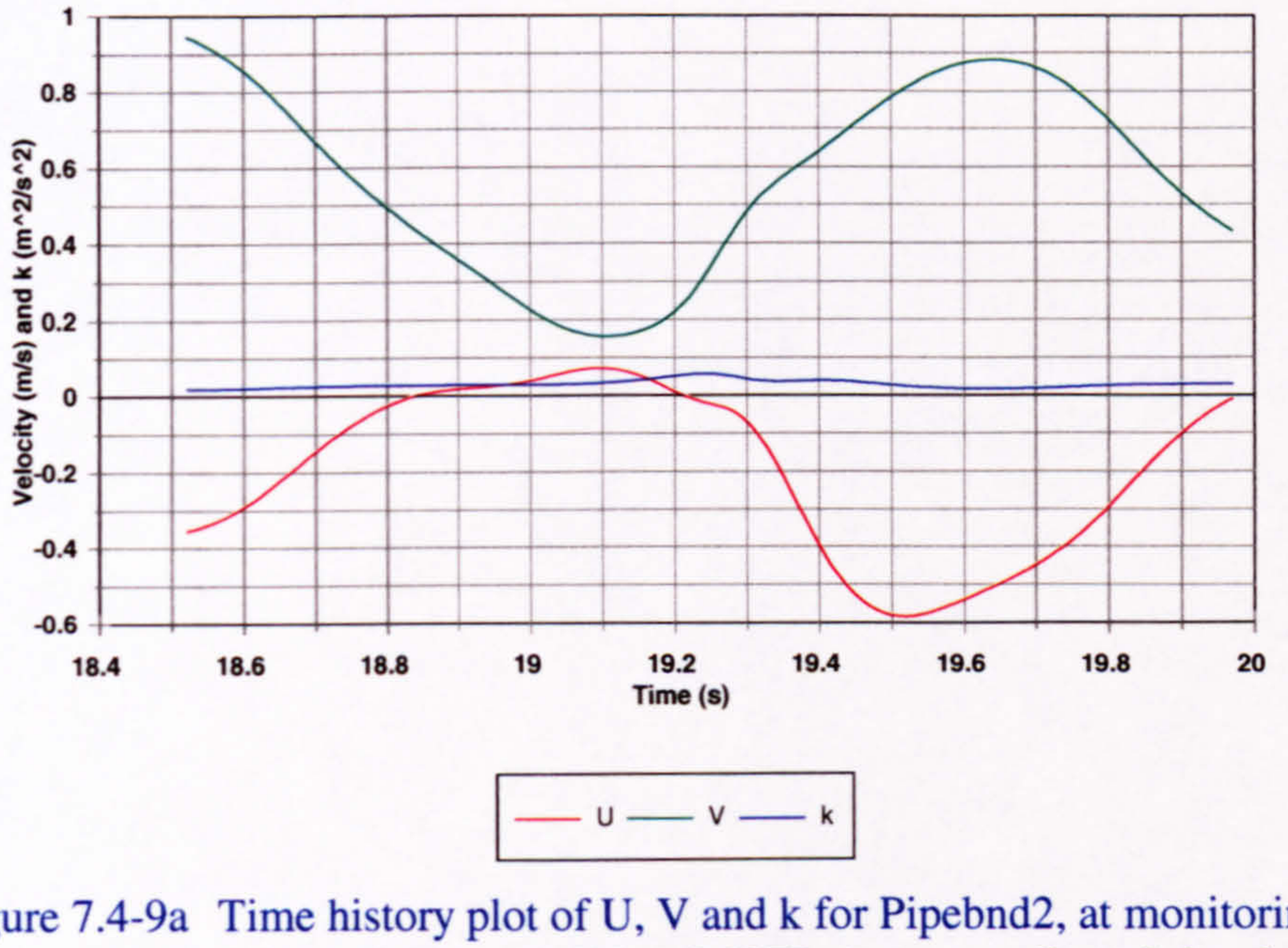


Figure 7.4-9a Time history plot of U, V and k for Pipebnd2, at monitoring point 1 (0.231m, 0.633m, 0.0277m), at centreline of chamber, 2 mm above weir crests.

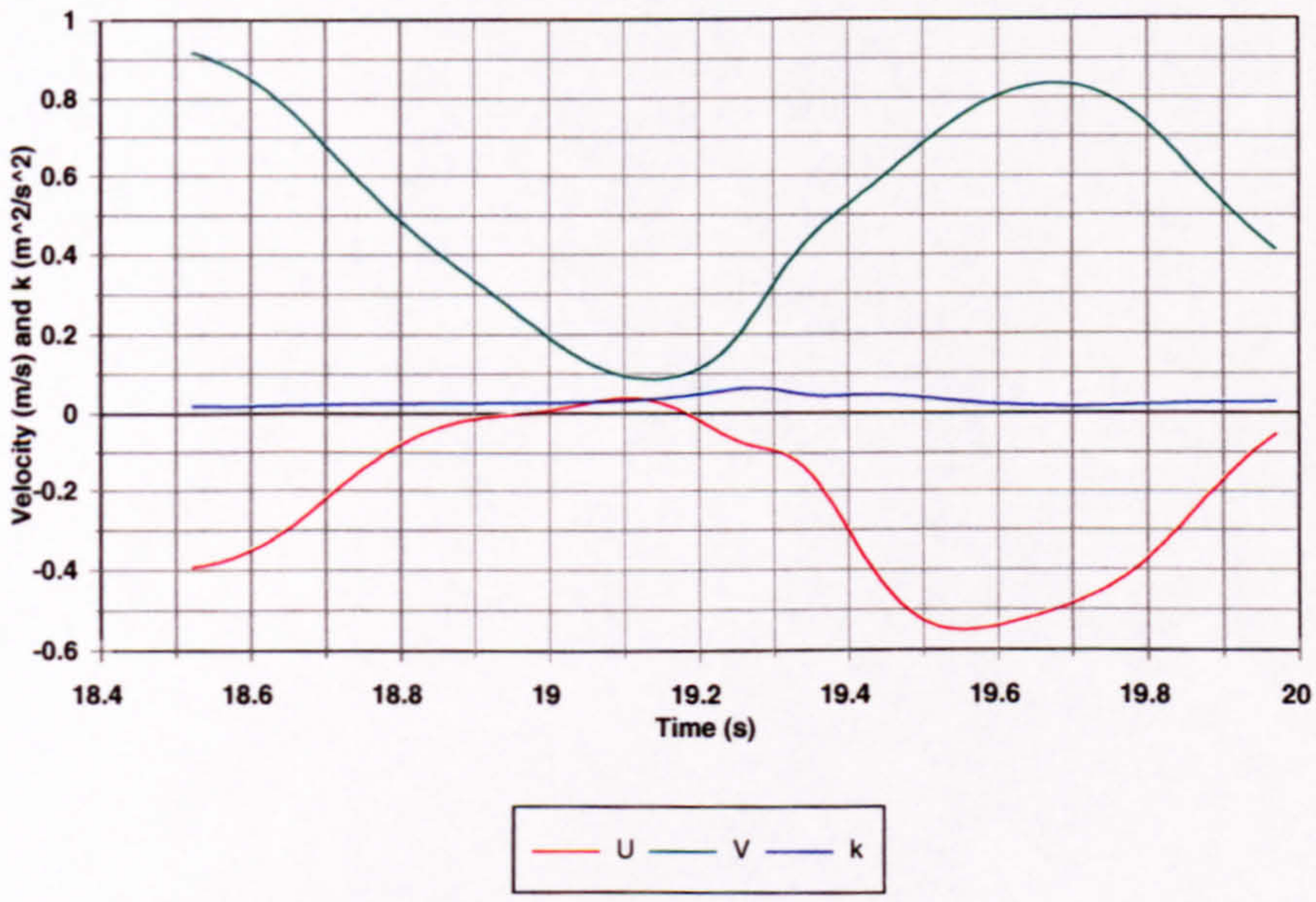


Figure 7.4-9b Time history plot of U, V and k for Pipebnd2, at monitoring point 2 (0.231, 0.643, 0.0277). Centreline of chamber, 12 mm above weir crests.

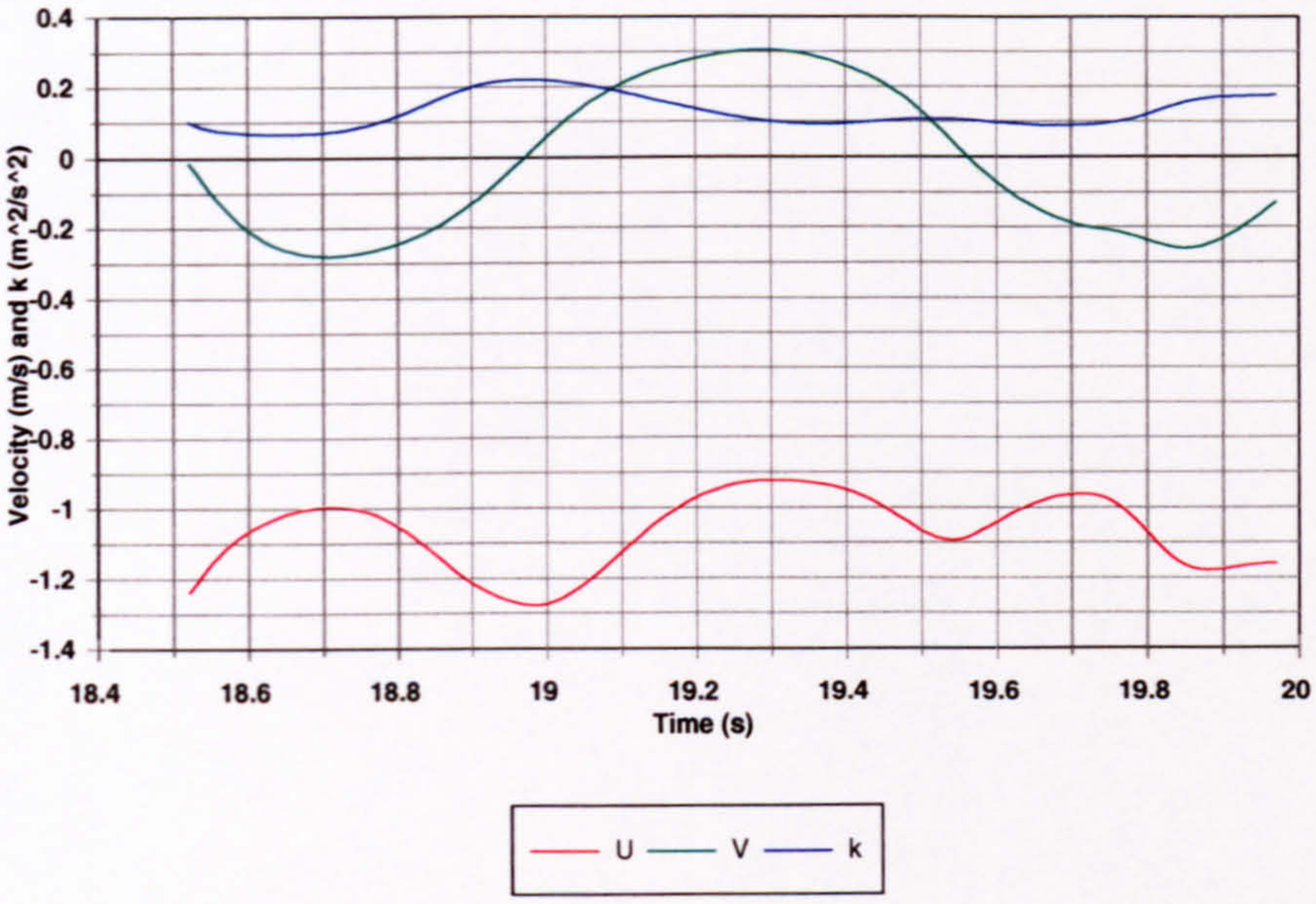


Figure 7.4-9c Time history plot of U, V and k for Pipebnd2, at monitoring point 3 (0.462, 0.653, 0.0277). At right hand side of chamber, 23 mm above weir crest.

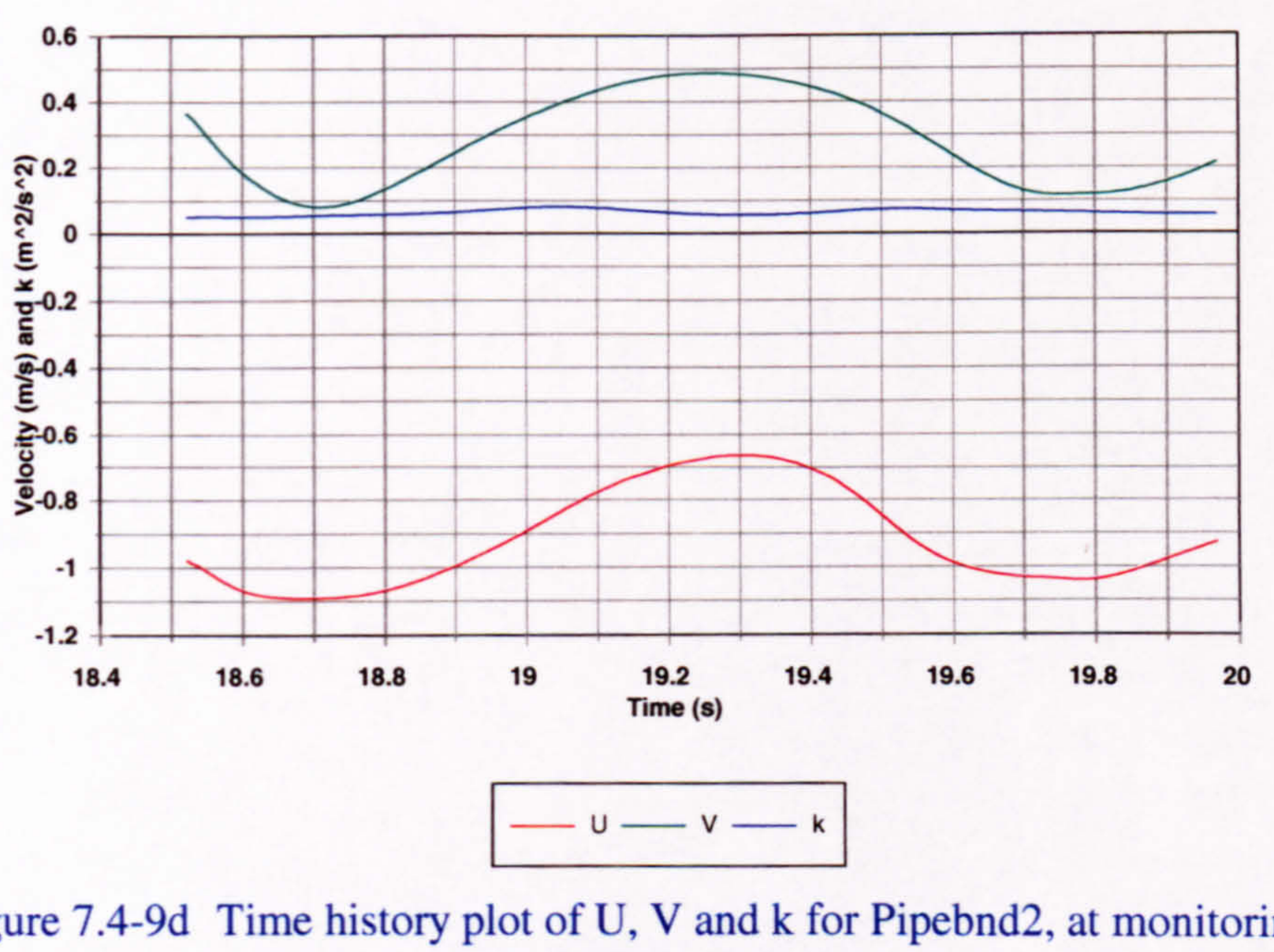


Figure 7.4-9d Time history plot of U, V and k for Pipebnd2, at monitoring point 4 (0, 0.653, 0.0277). At left hand side of chamber, 23 mm above weir crest.

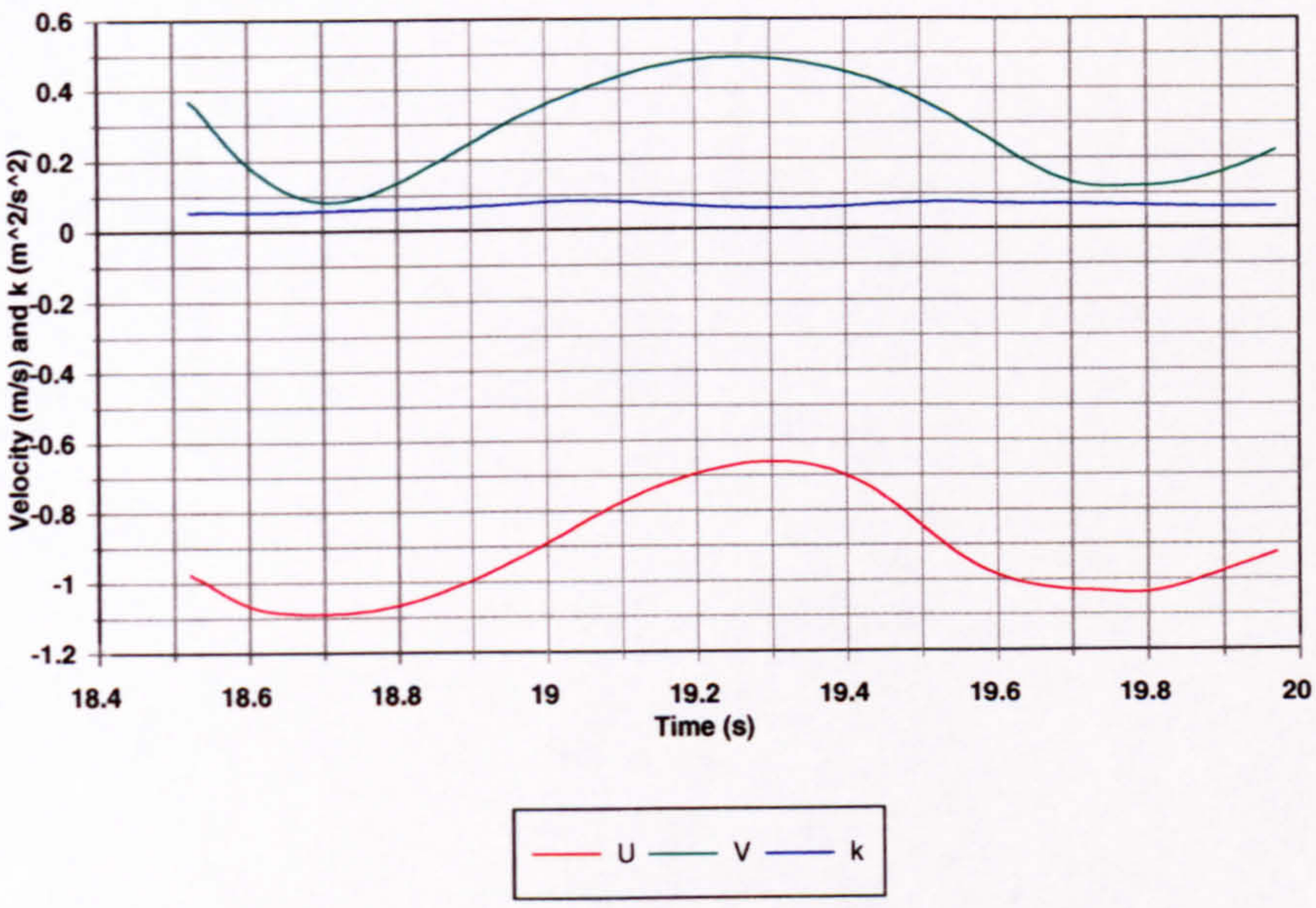


Figure 7.4-9e Time history plot of U, V and k for Pipebnd2, at monitoring point 5 (0, 0.633, 0.0277). At left hand side of chamber, 2 mm above weir crest.

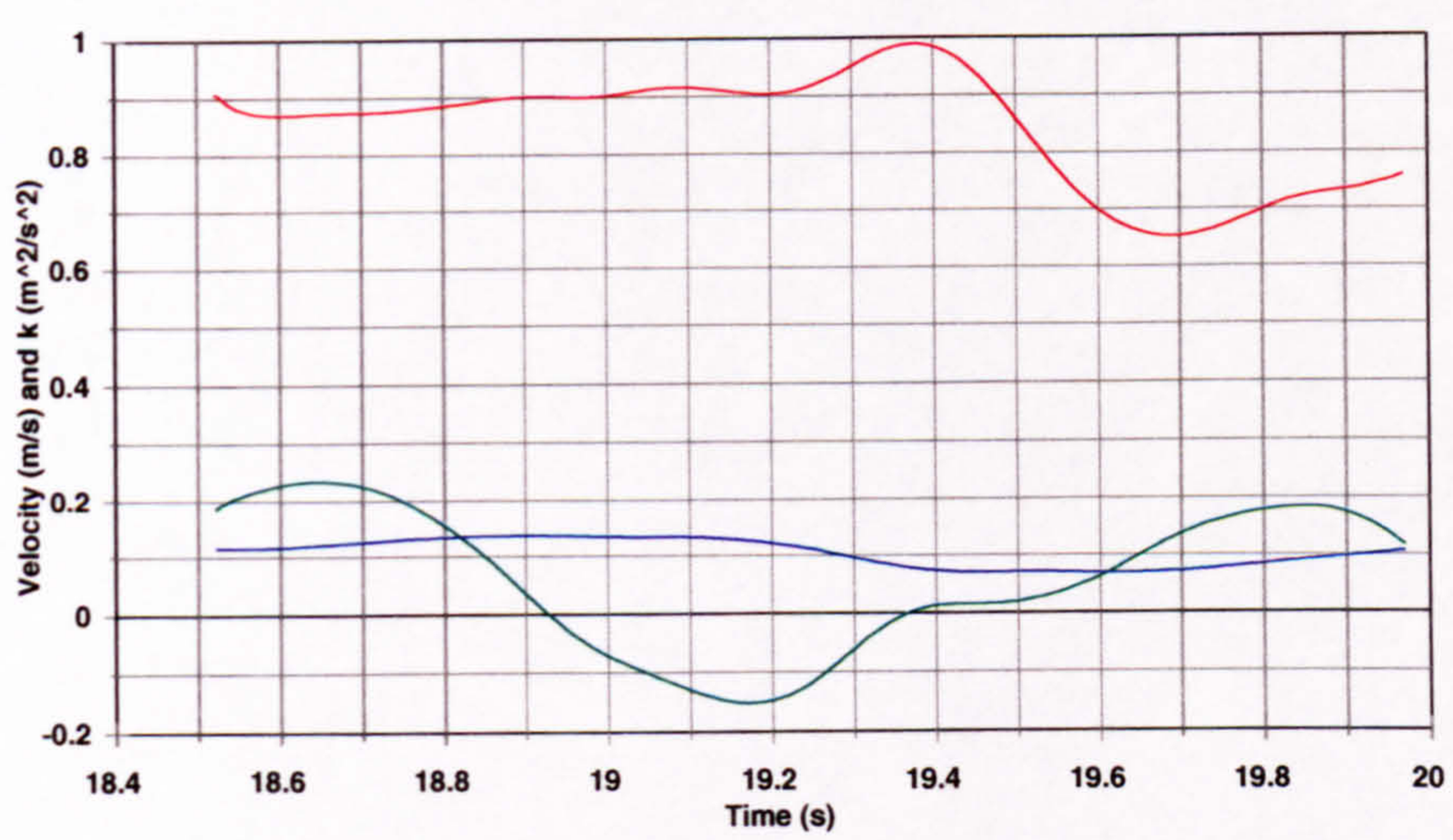


Figure 7.4-9f Time history plot of U, V and k for Pipebnd2, at monitoring point 6 (0.462, 0.633, 0.0277). At right hand side of chamber, 2 mm above weir crest.

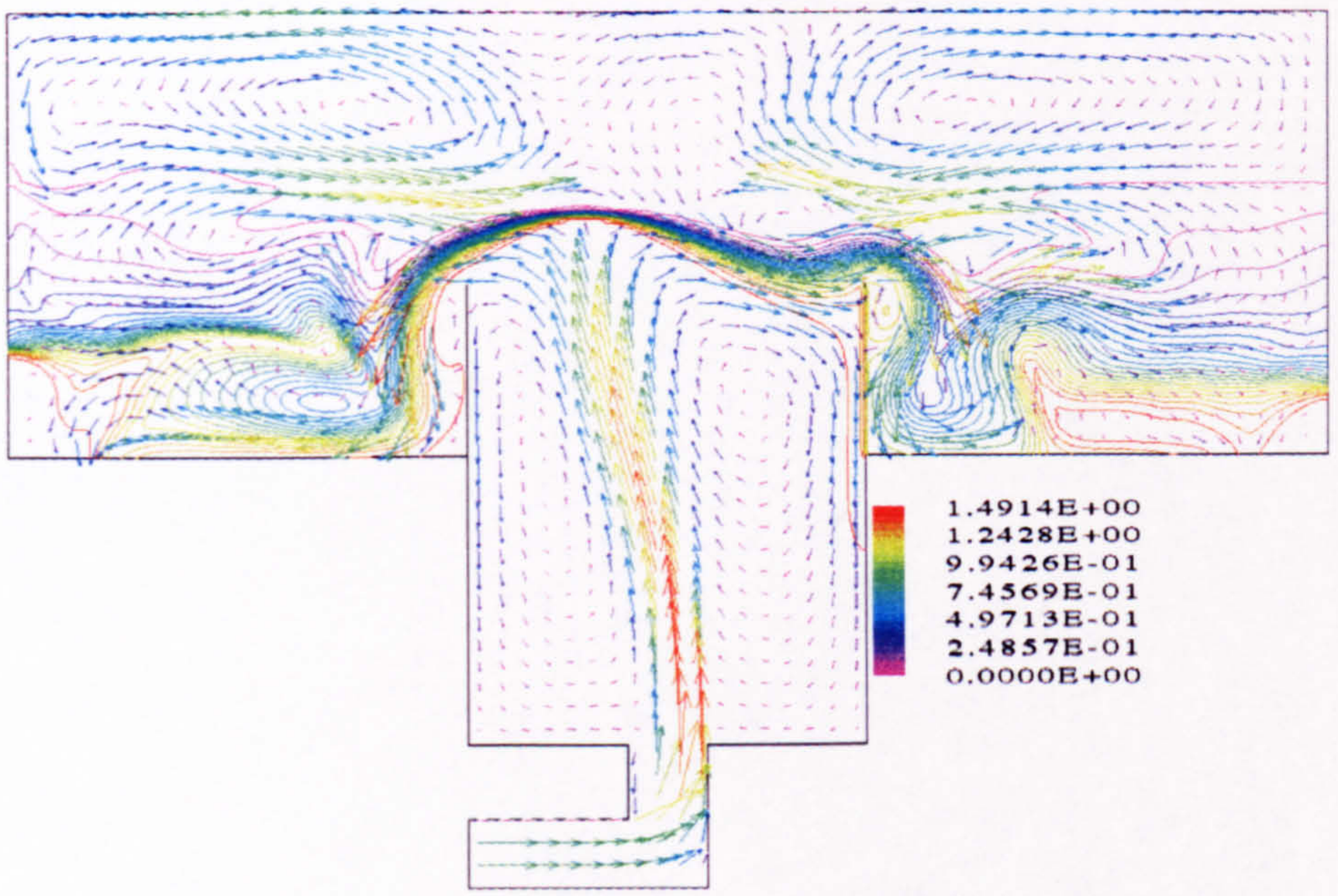


Figure 7.4-10a Velocity vector and volume fraction contour plot for Pipebnd3. Flowrate = 4.38 l/s. A 2.12 D_h pipe bend is coupled with chamber. Hybrid differencing scheme is used. Surface sharpening algorithm switched off.

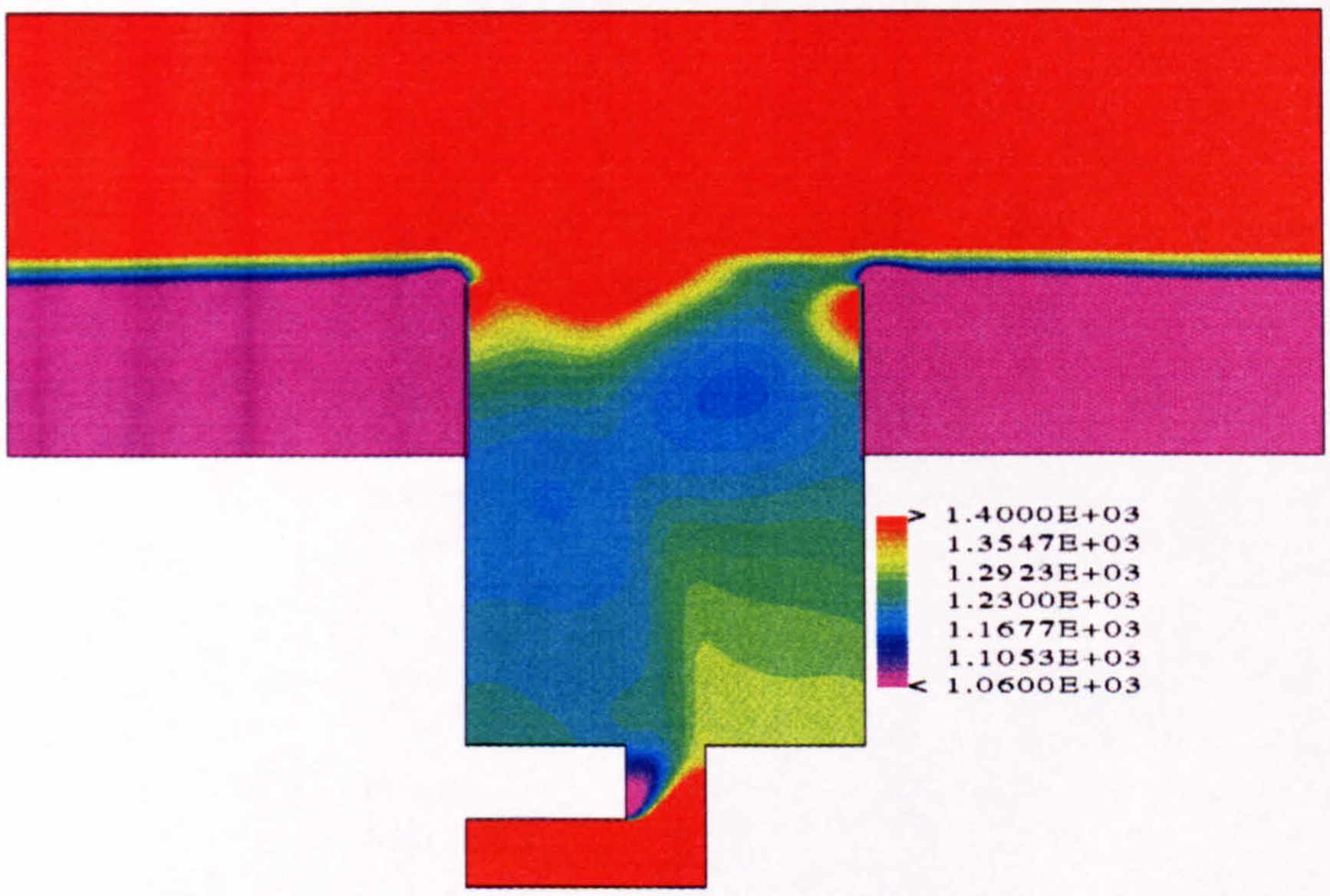


Figure 7.4-10b Pressure contour plot for Pipebnd3.

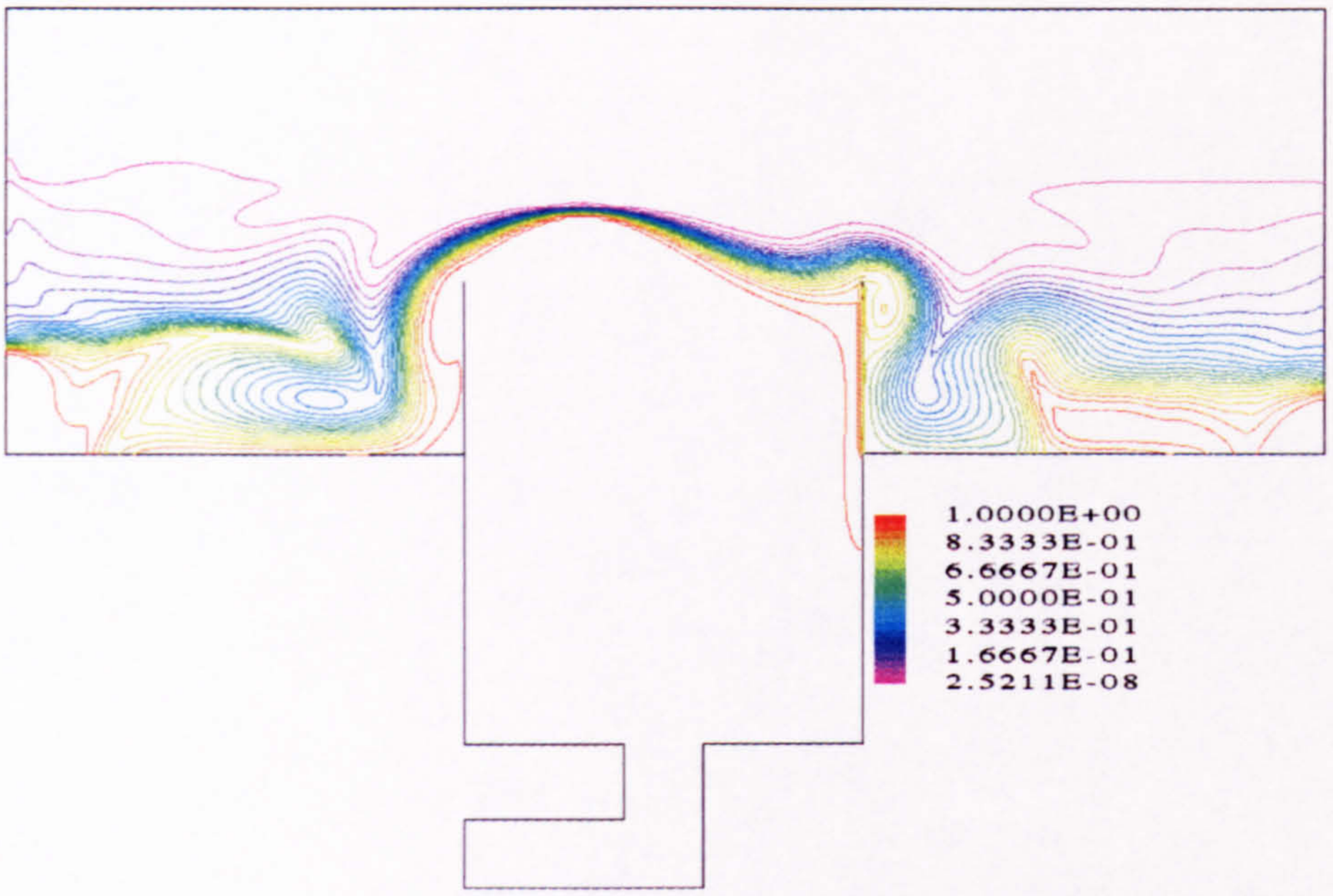


Figure 7.4-10c Volume fraction contour plot of water for Pipebnd3. Value of 1.0 represents water, 0.0 is air. Free surface has a value of 0.5.

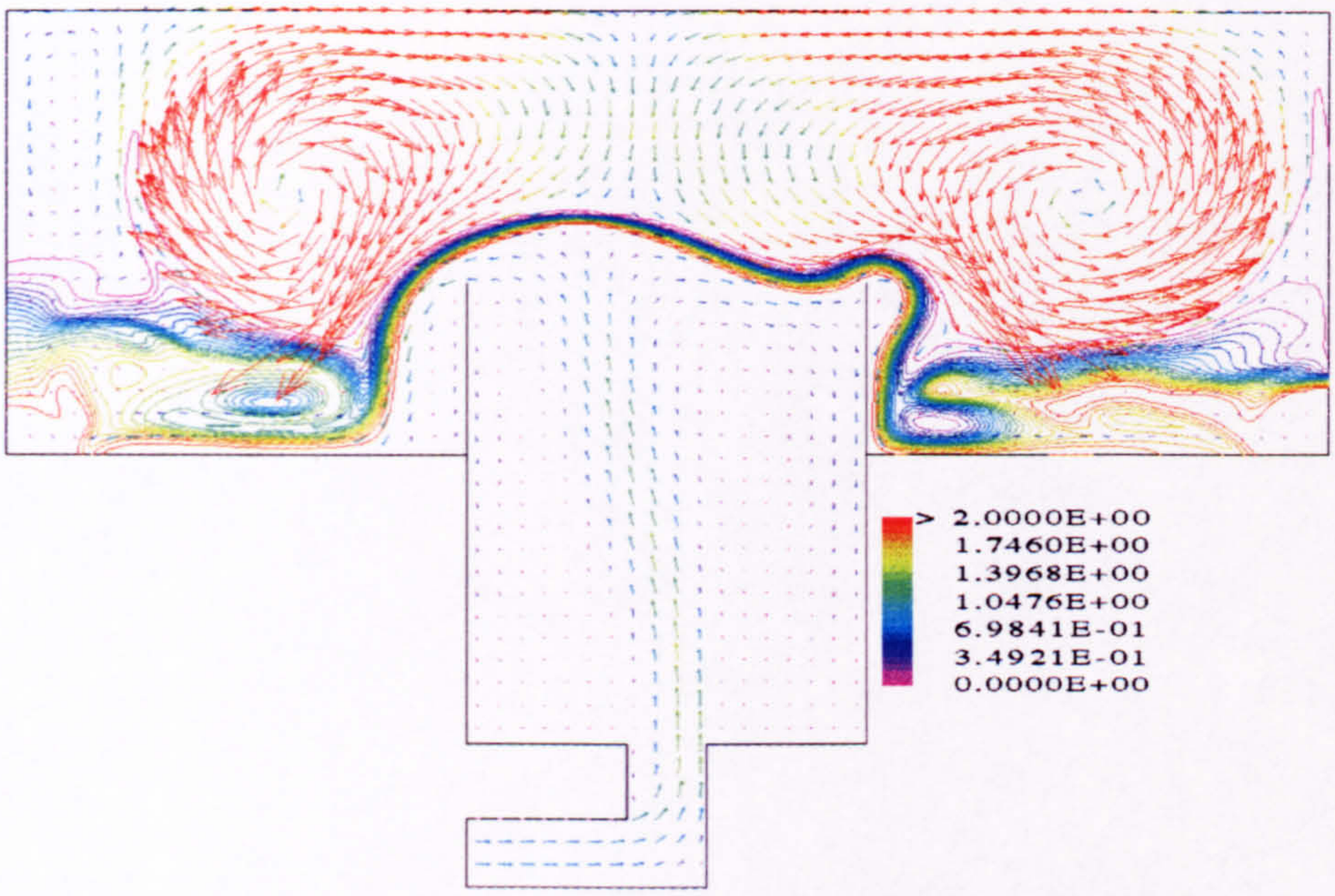


Figure 7.4-11a Velocity vector and volume fraction contour plot for Pipebnd4. Geometry and boundary conditions the same as Pipebnd3, except that the Van Leer differencing scheme is used.

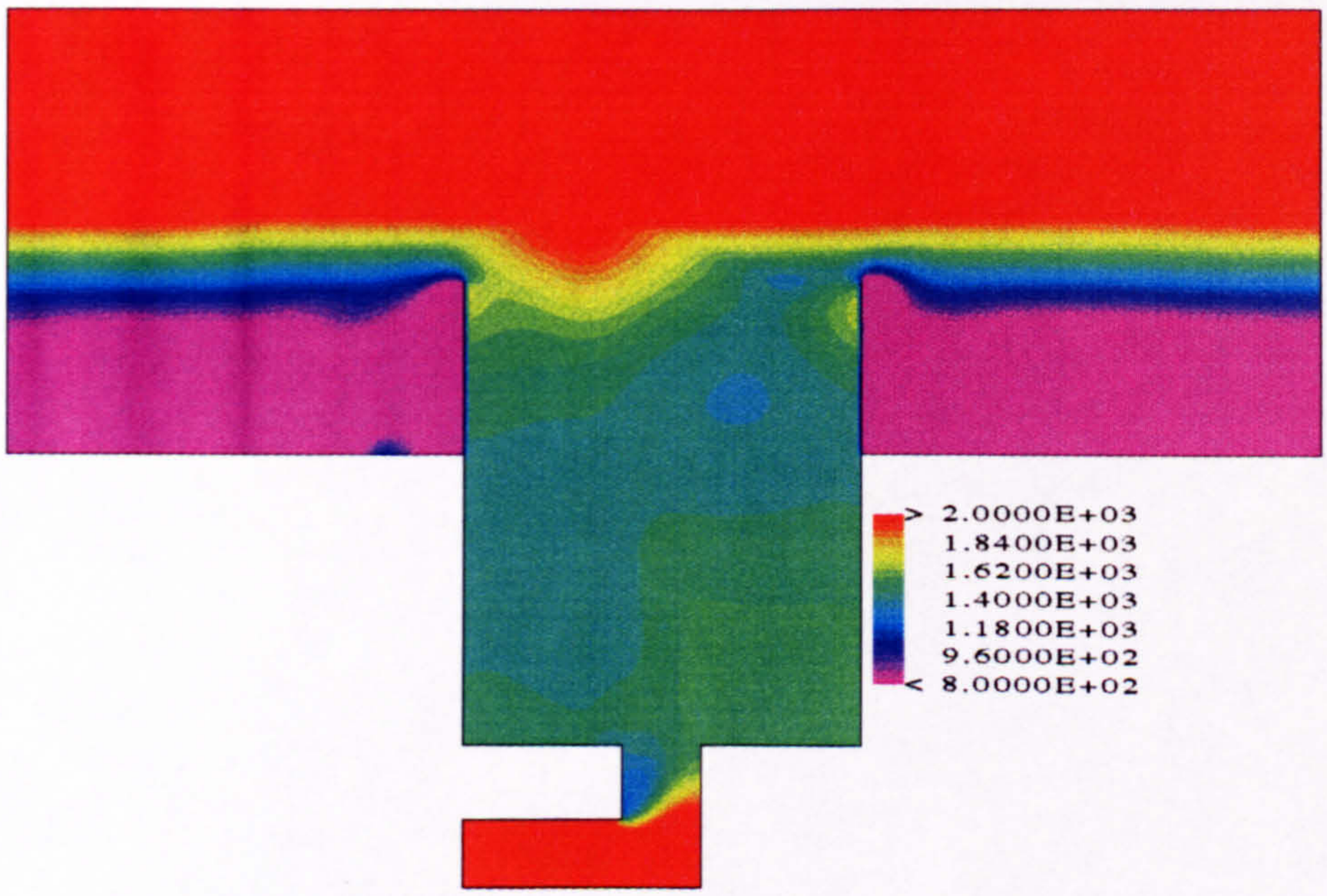


Figure 7.4-11b Pressure contour plot for Pipebnd4.

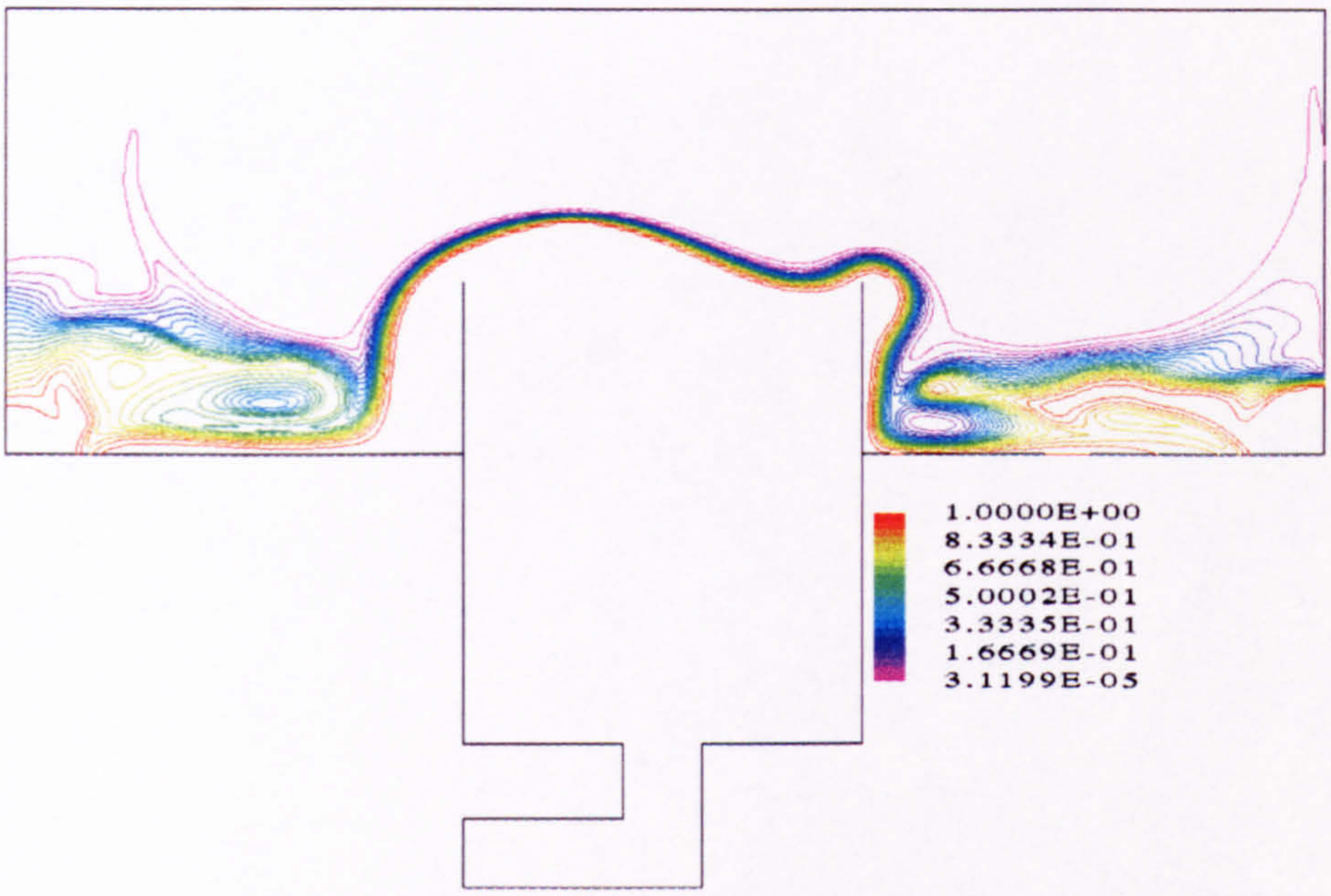


Figure 7.4-11c Volume fraction contour plot of water for Pipebnd4. Value of 1.0 represents water, 0.0 is air. Free surface has a value of 0.5.

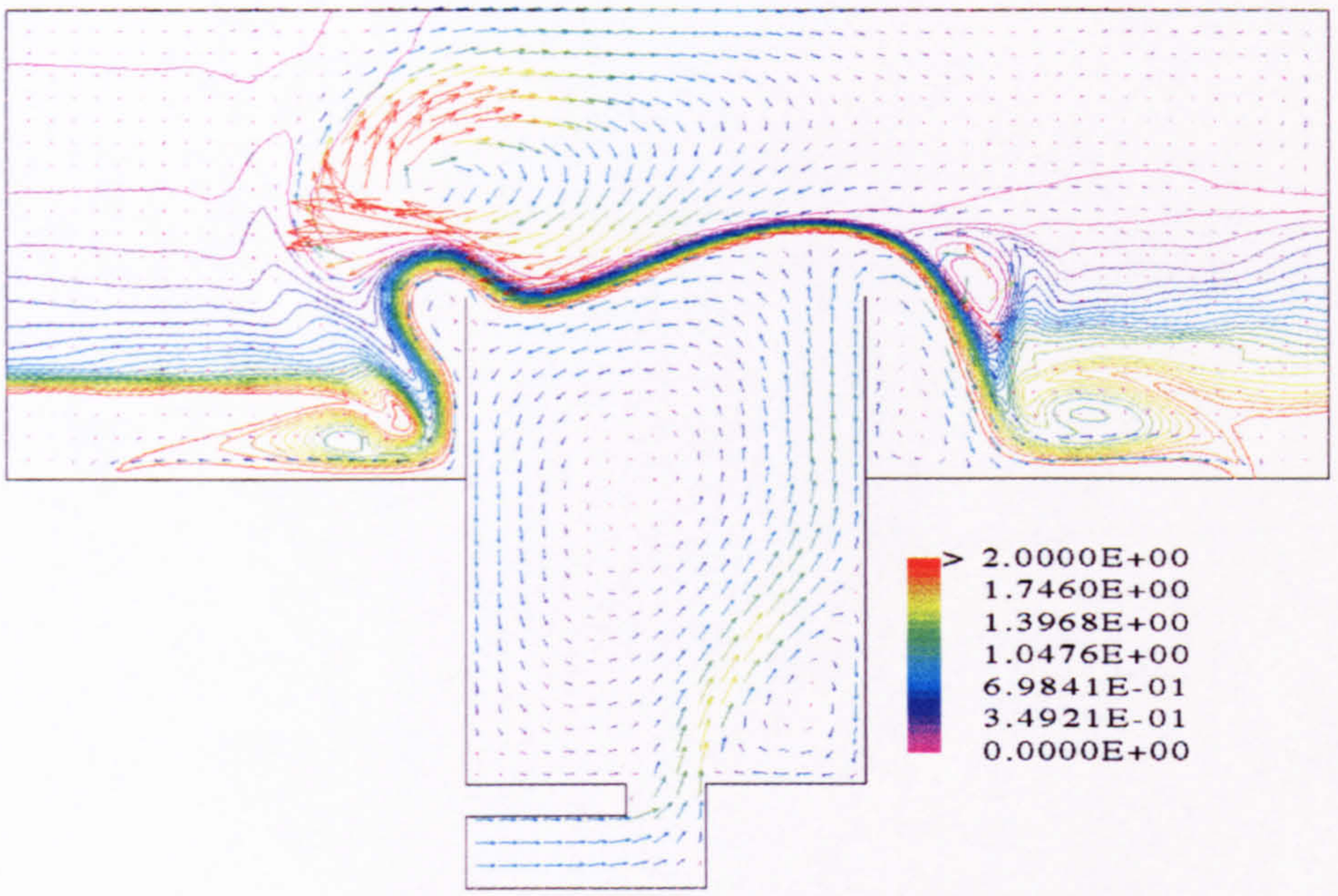


Figure 7.4-12a Velocity vector and volume fraction contour plot for Pipebnd5. Flowrate = 4.38 l/s. Shortened pipe bend (1.25 D_h or 0.086 m) coupled with chamber. Van Leer differencing scheme is used.

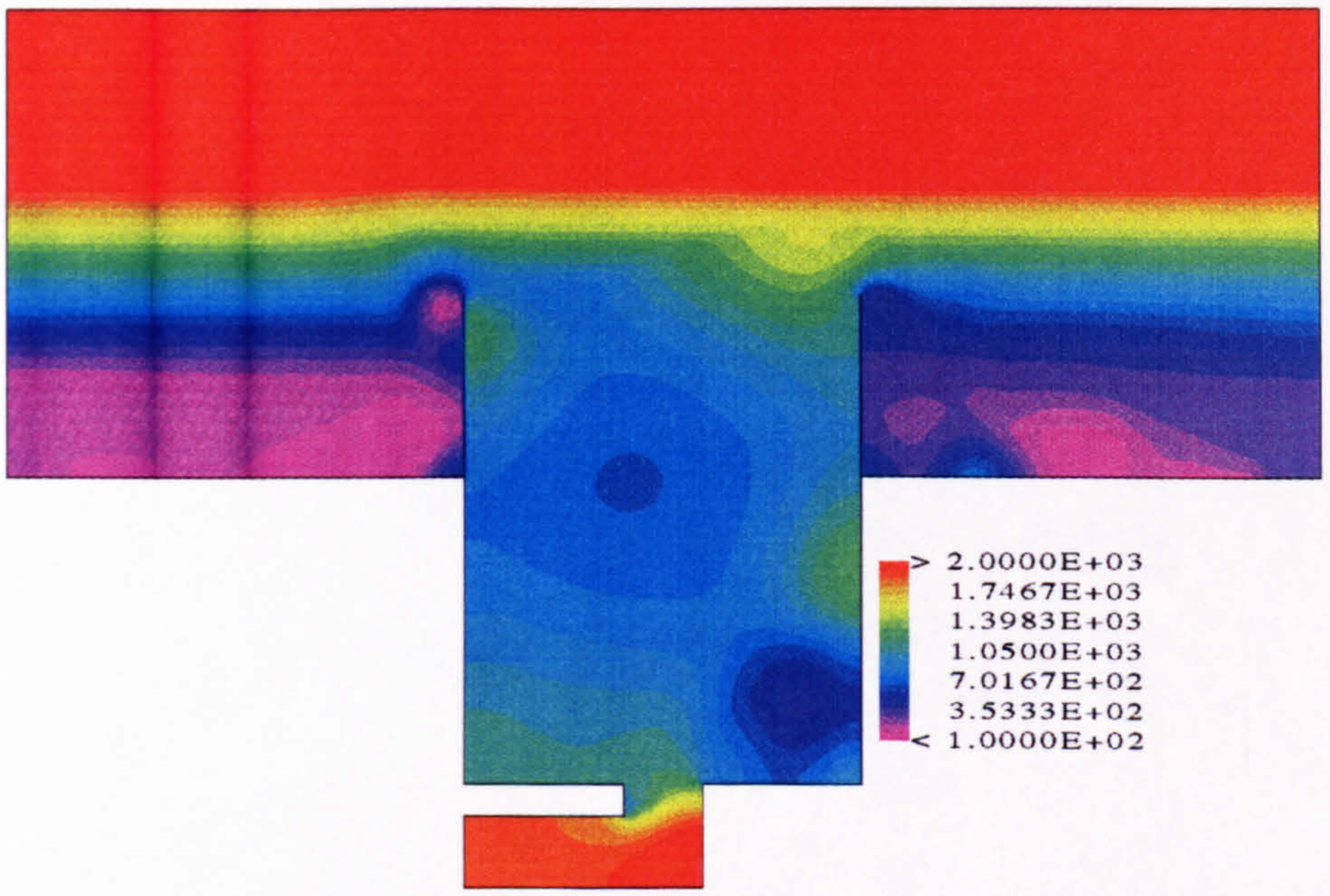


Figure 7.4-12b Pressure contour plot for Pipebnd5

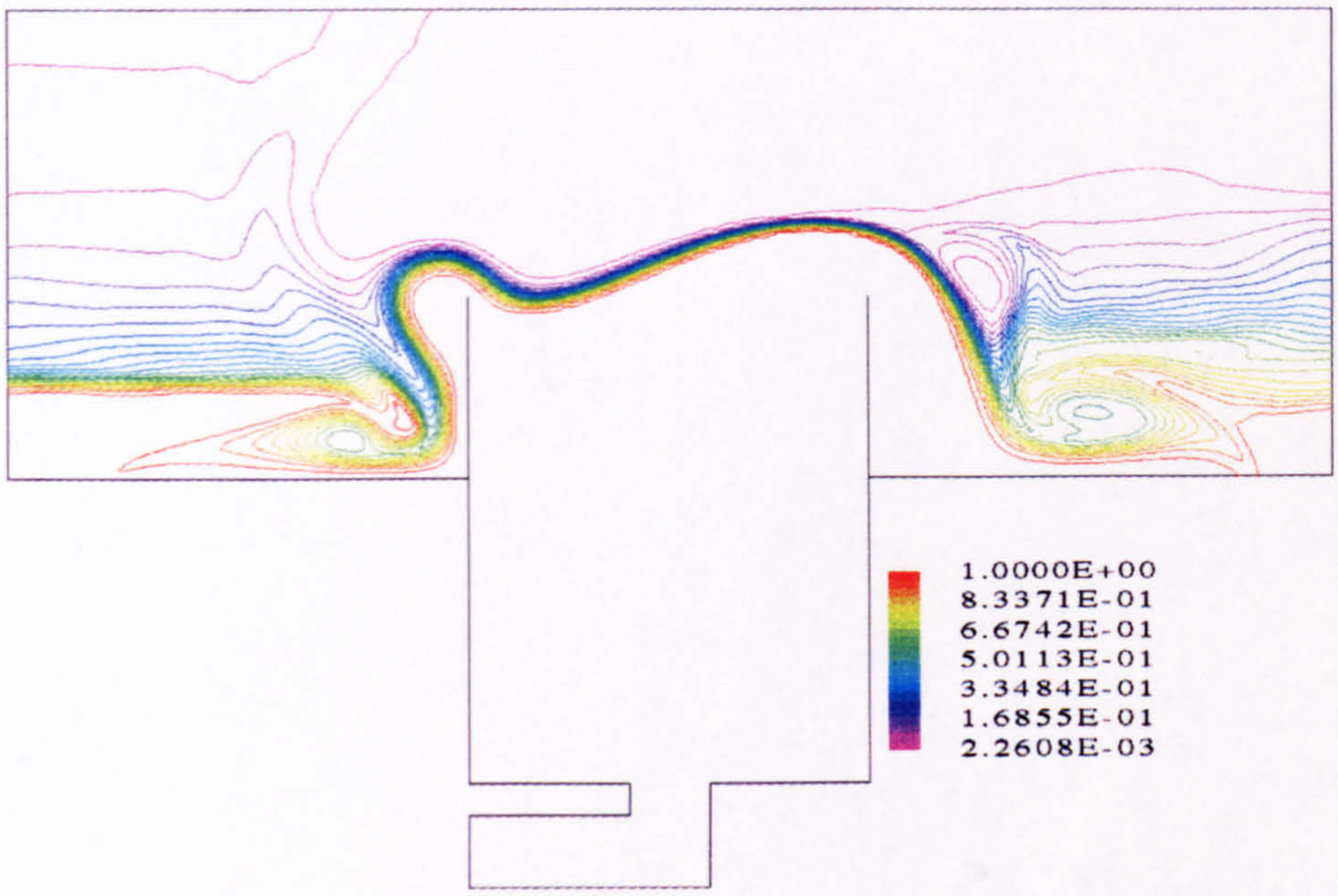


Figure 7.4-12c Volume fraction contour plot of water for Pipebnd5. Value of 1.0 represents water, 0.0 is air. Free surface has a value of 0.5.

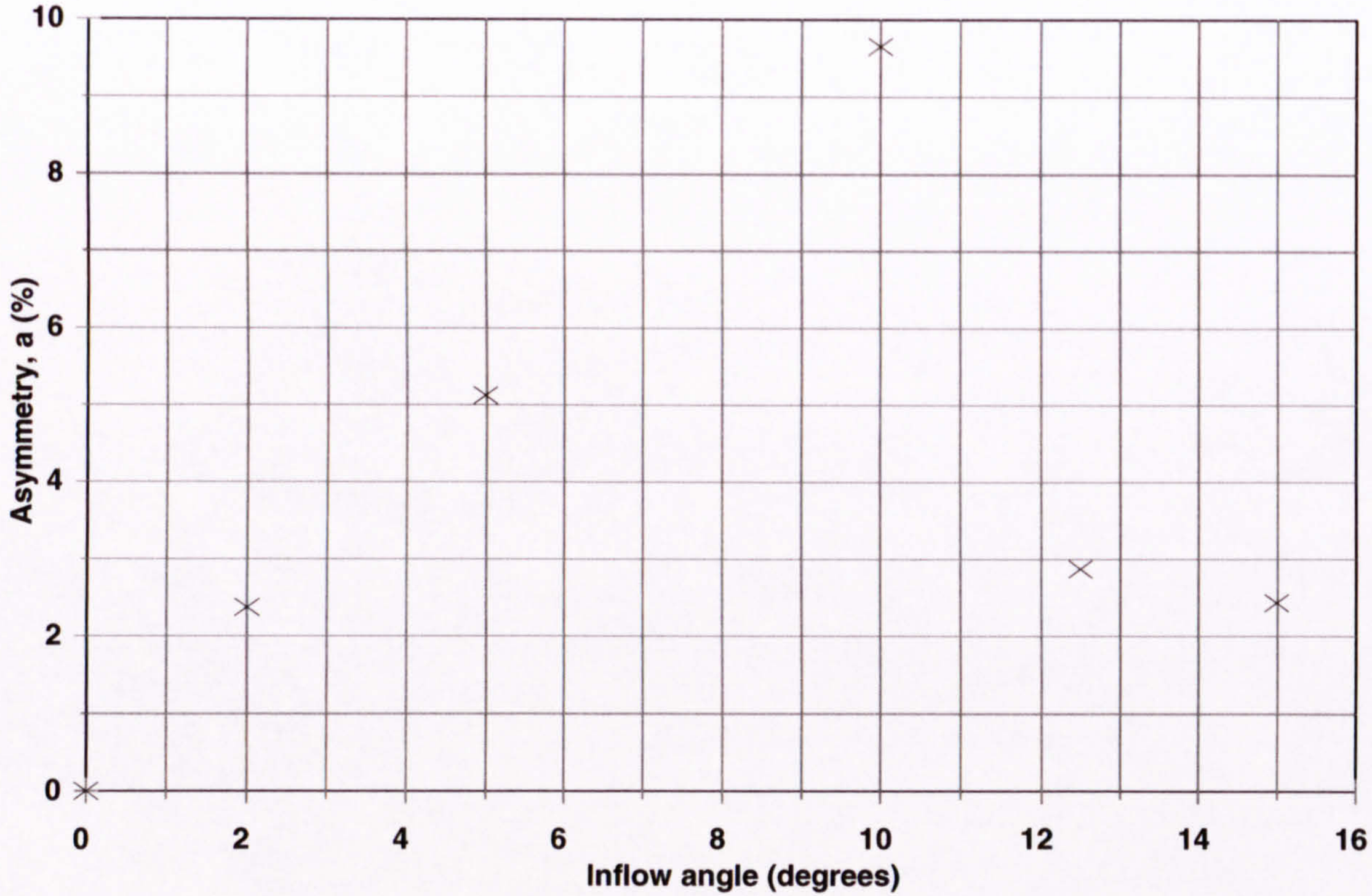


Figure 7.4-13 Plot showing the flow mal-distribution of the chamber for a range of inflow angles as calculated by Bend2, Bend5, Bend10, Bend12 and Bend15.

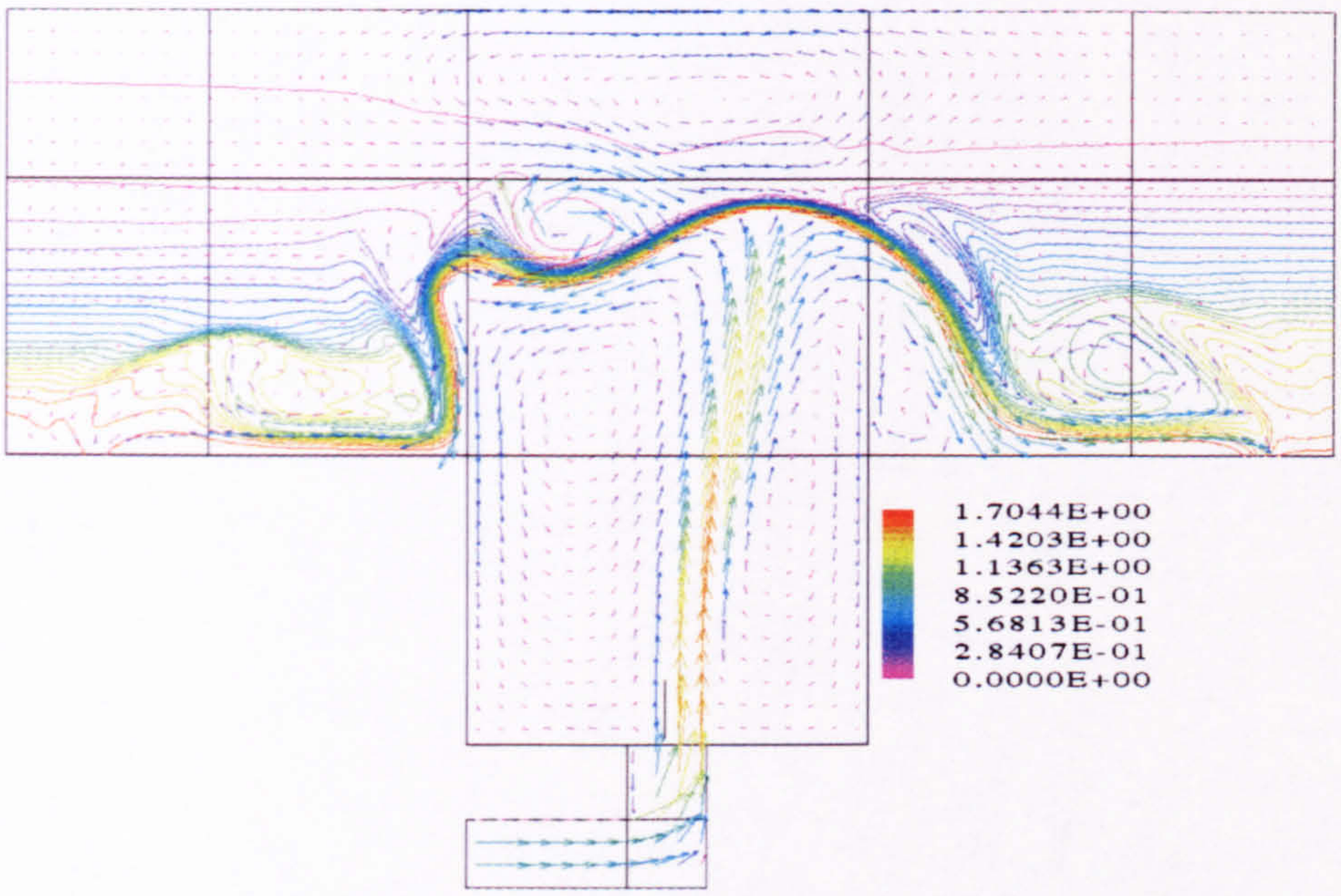


Figure 7.5-1a Velocity vector and volume fraction plot for Bndsplt1. Flowrate = 4.38 l/s. Vertical flow splitter placed centrally above chamber inlet to improve flow distribution. (2.12 D_h pipe bend used in geometry).

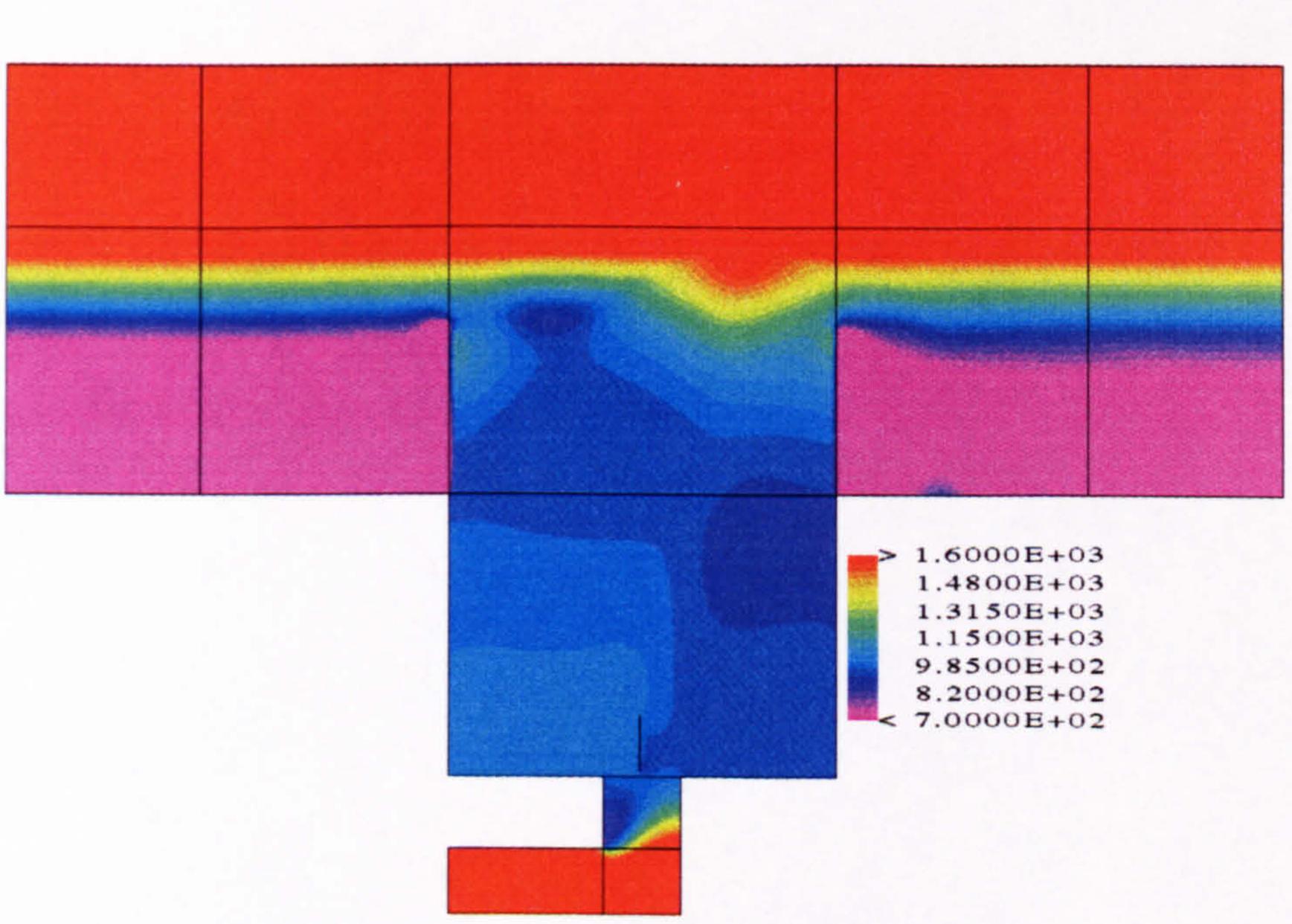


Figure 7.5-1b Pressure contour plot for Bndsplt1.

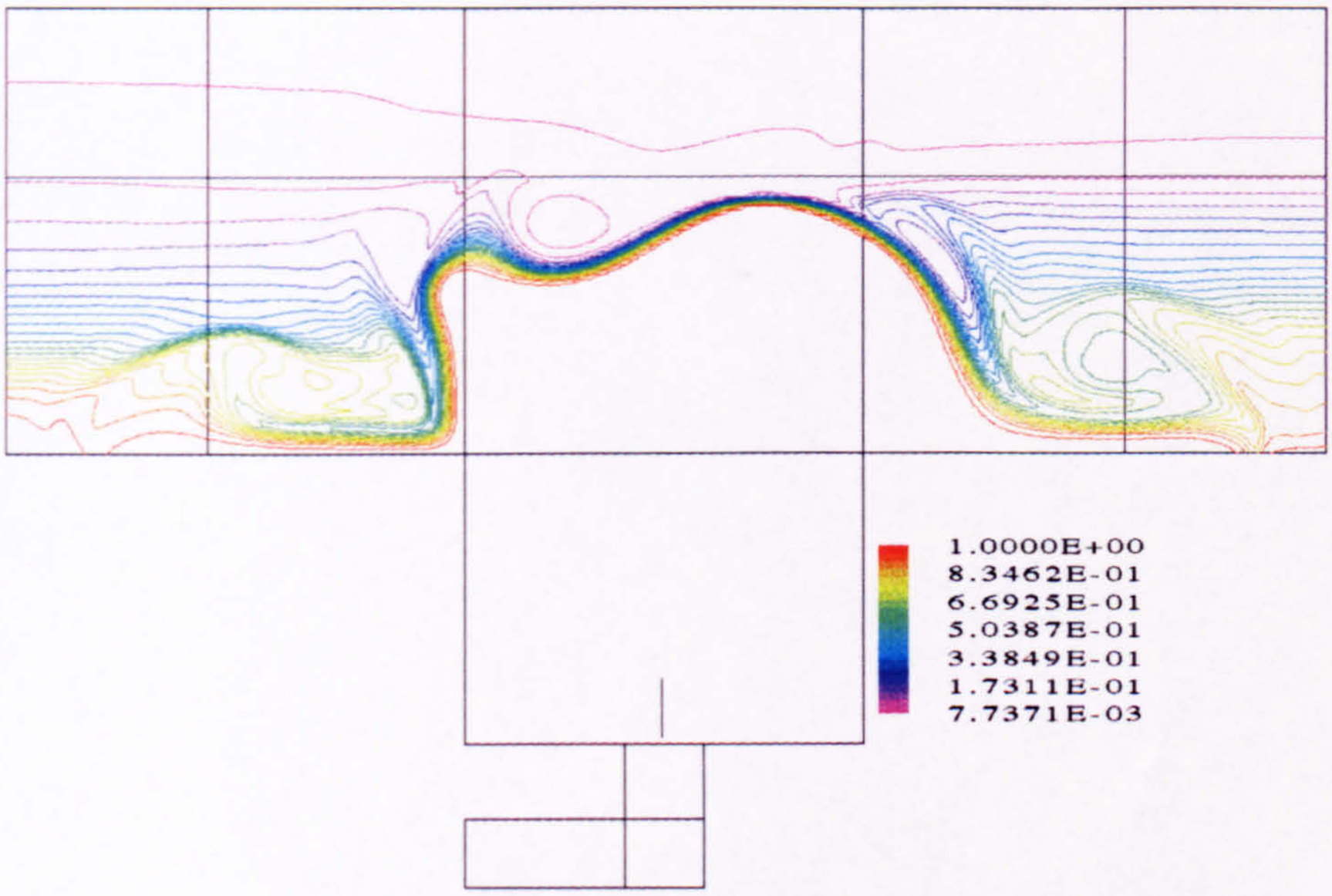


Figure 7.5-1c Volume fraction contour plot for Bndsplt1. Value of 1.0 represents water, 0.0 is air. Free surface has a value of 0.5.

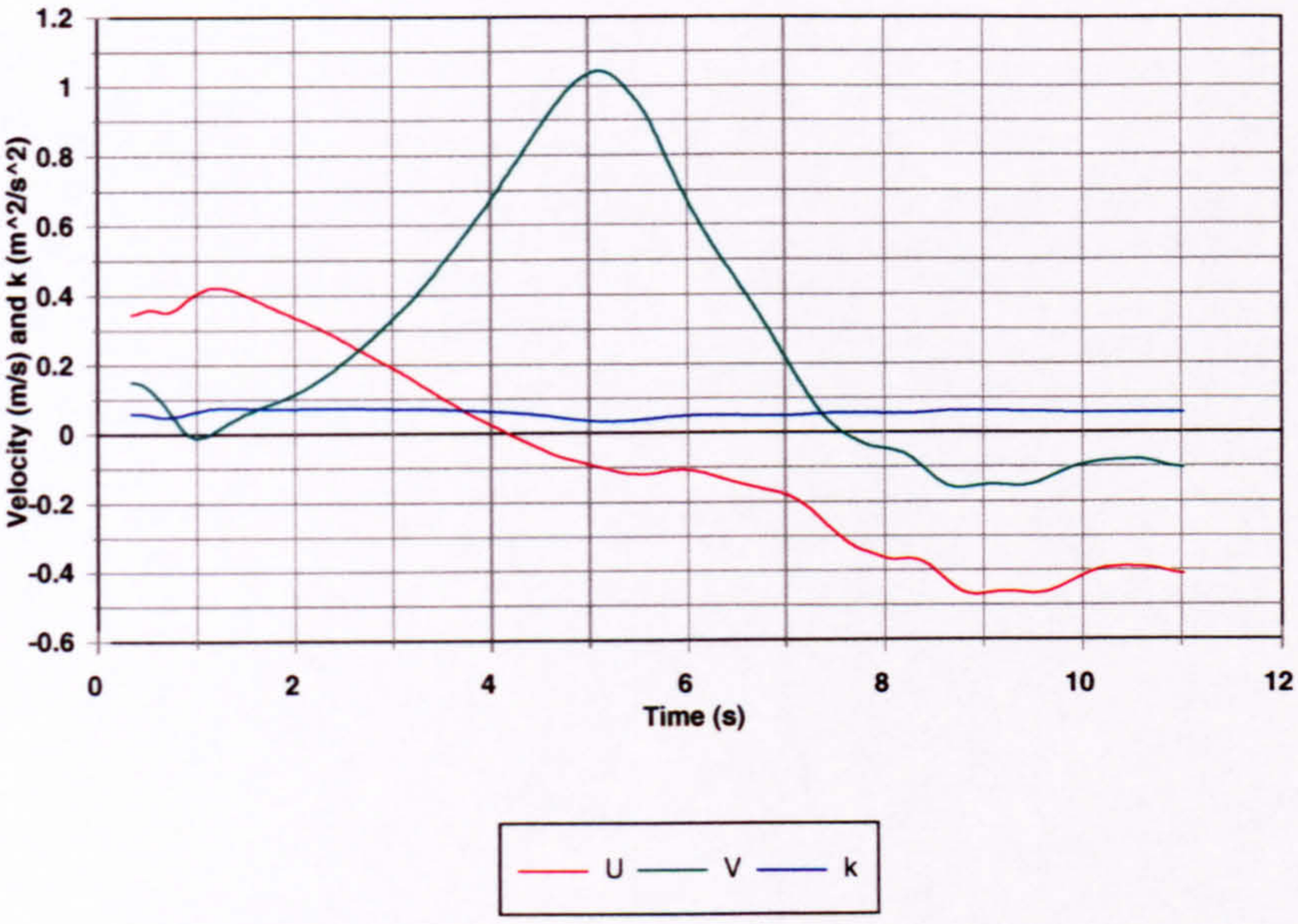


Figure 7.5-2 Time history plot of U, V and k for Bndsplt1, at monitoring point 1 (0.231m, 0.633m, 0.0277m). At centreline of chamber, 2mm above weir crests.

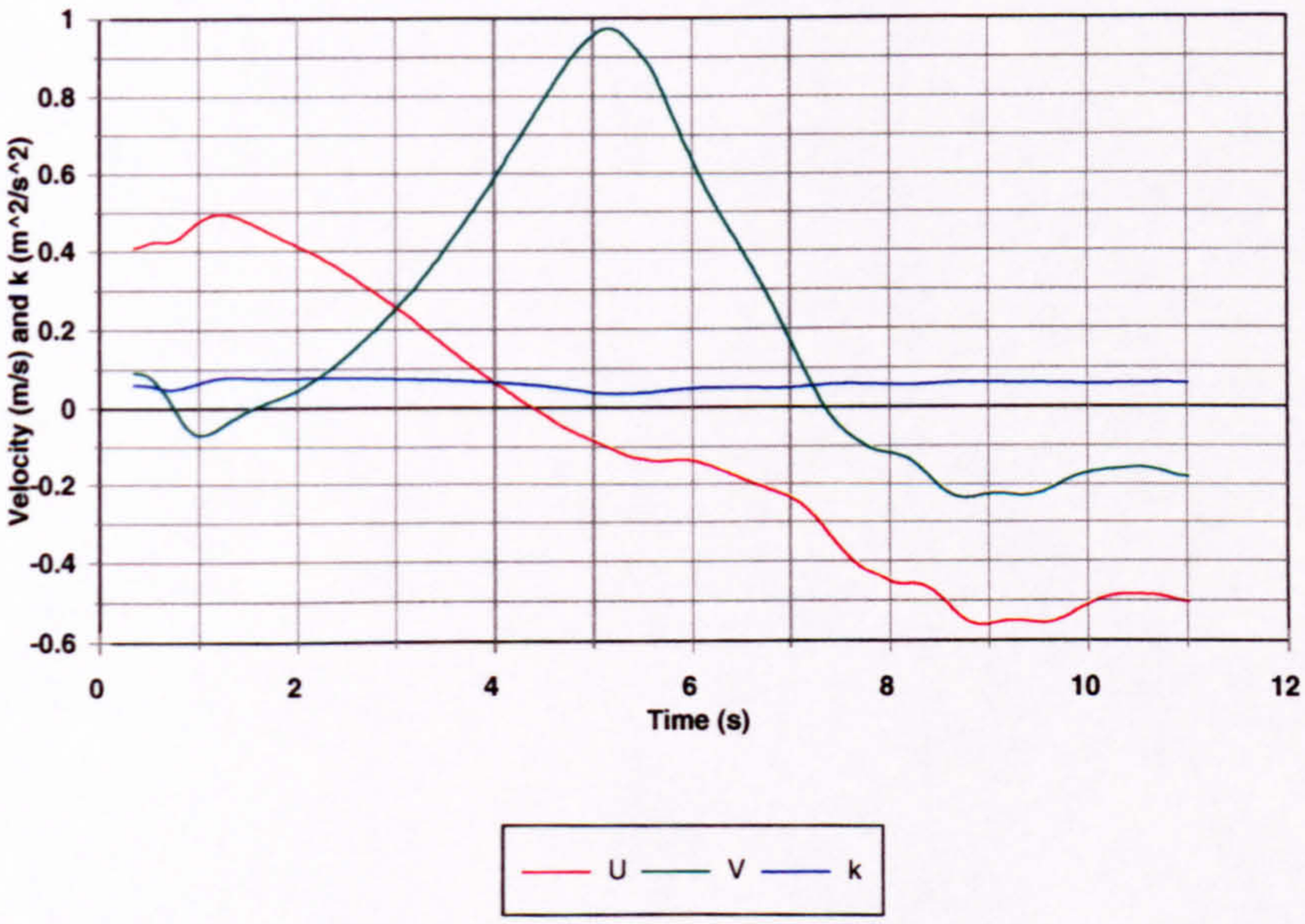


Figure 7.5-2b Time history plot of U, V and k for Bndsplt1, at monitoring point 2 (0.231, 0.643, 0.0277). At centreline of chamber, 12 mm above weir crests.

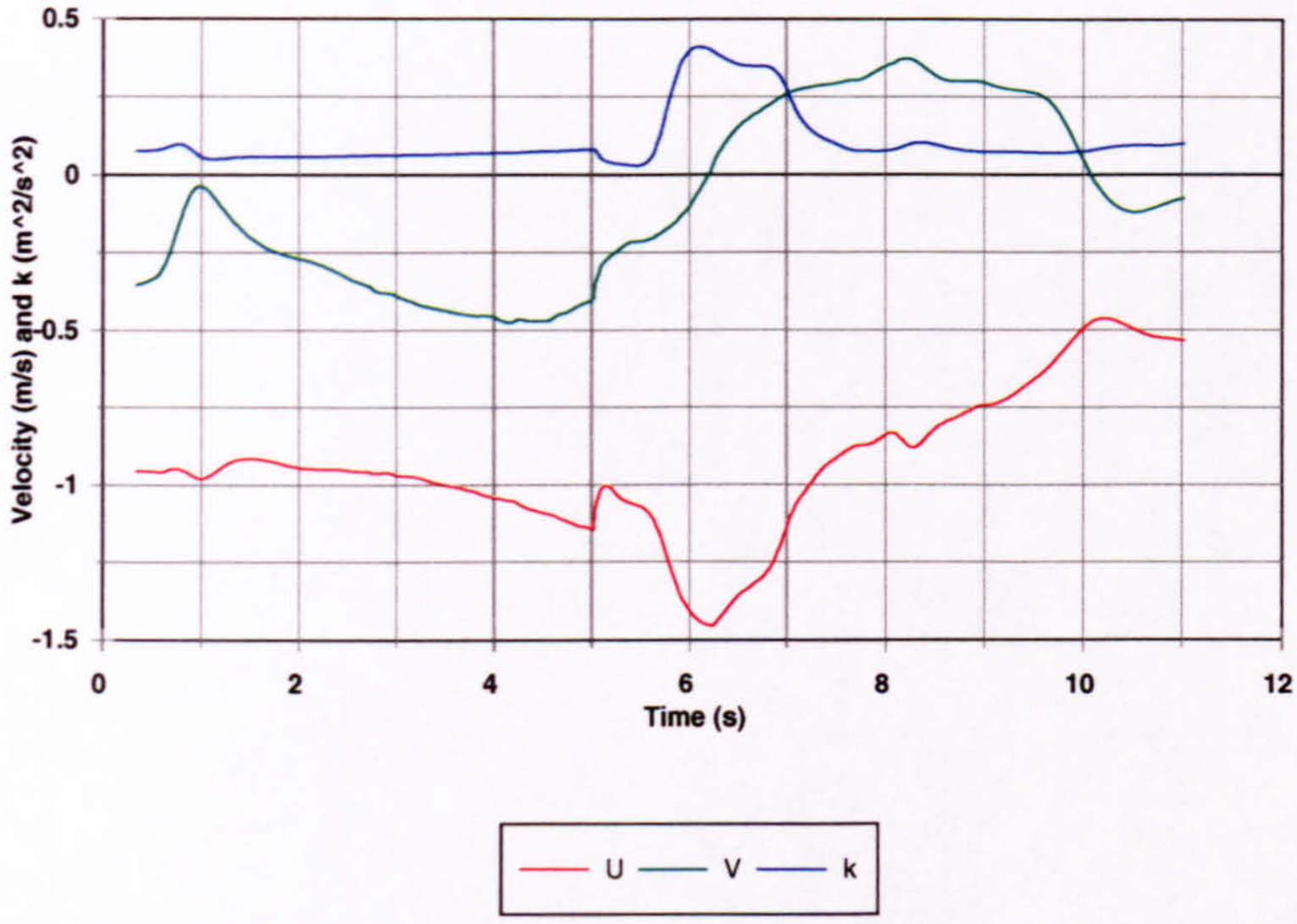


Figure 7.5-2c Time history plot of U, V and k for Bndsplt1, at monitoring point 3 (0, 0.653, 0.0277). At left hand side of chamber, 23 mm above weir crests.

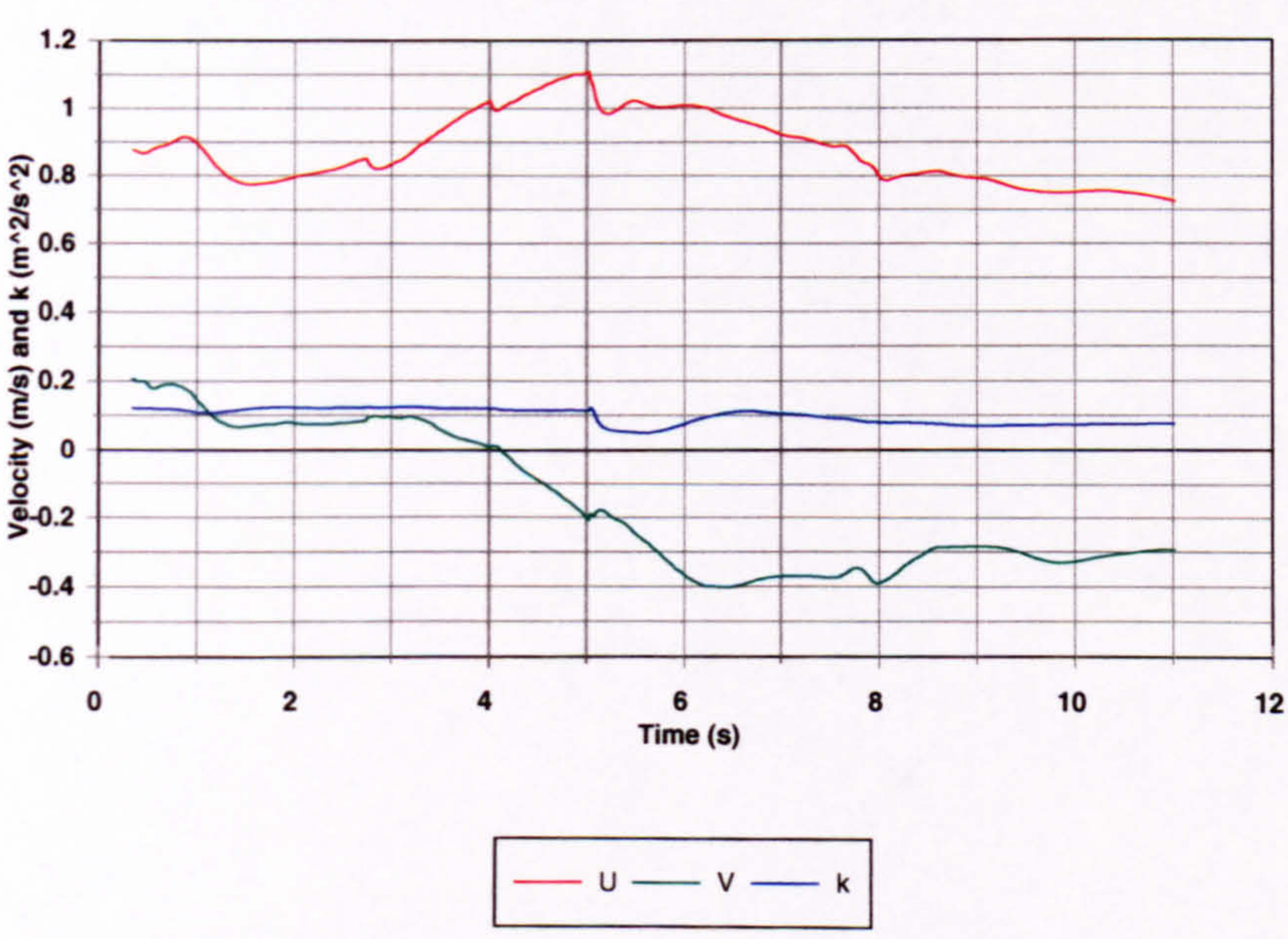


Figure 7.5-2d Time history plot of U, V and k for Bndsplt1, at monitoring point 4 (0.462, 0.653, 0.0277). At right hand side of chamber, 23 mm above weir crest.

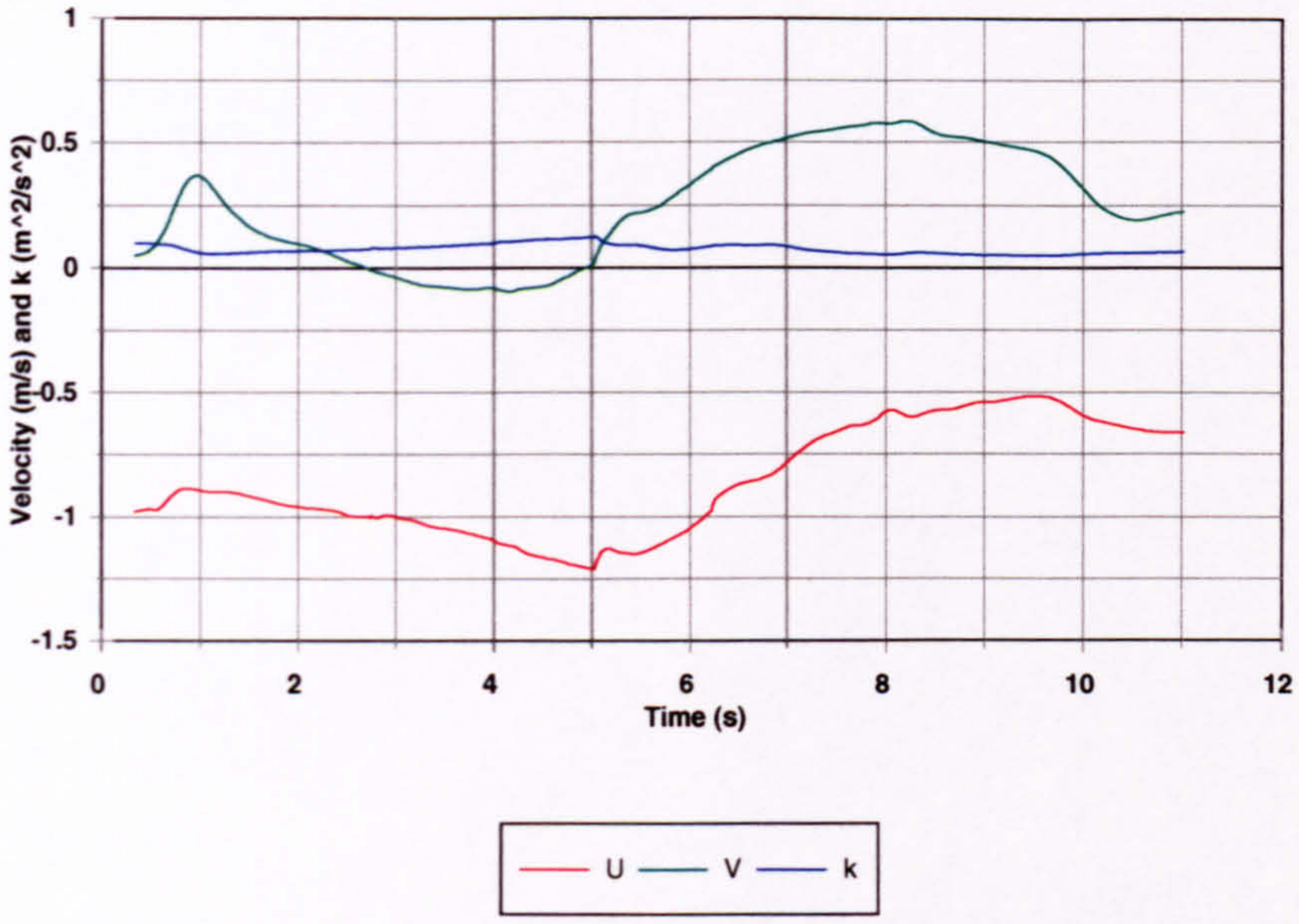


Figure 7.5-2e Time history plot of U, V and k for Bndsplt1, at monitoring point 5 (0, 0.633, 0.0277). At left hand side of chamber, 2 mm above weir crest.

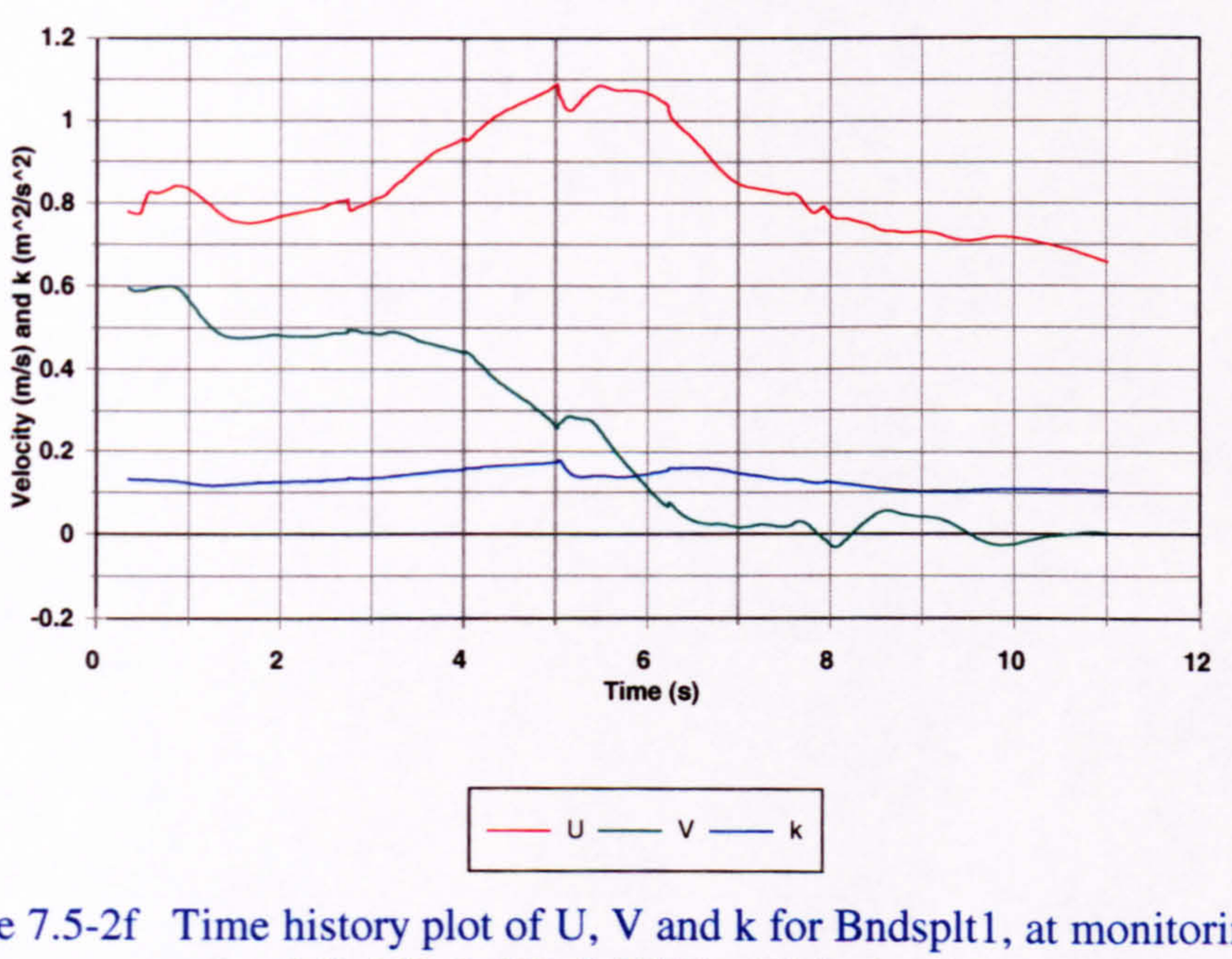


Figure 7.5-2f Time history plot of U, V and k for Bndsplt1, at monitoring point 6 (0.462, 0.633, 0.0277). Right hand side of chamber, 2 mm above weir crest.

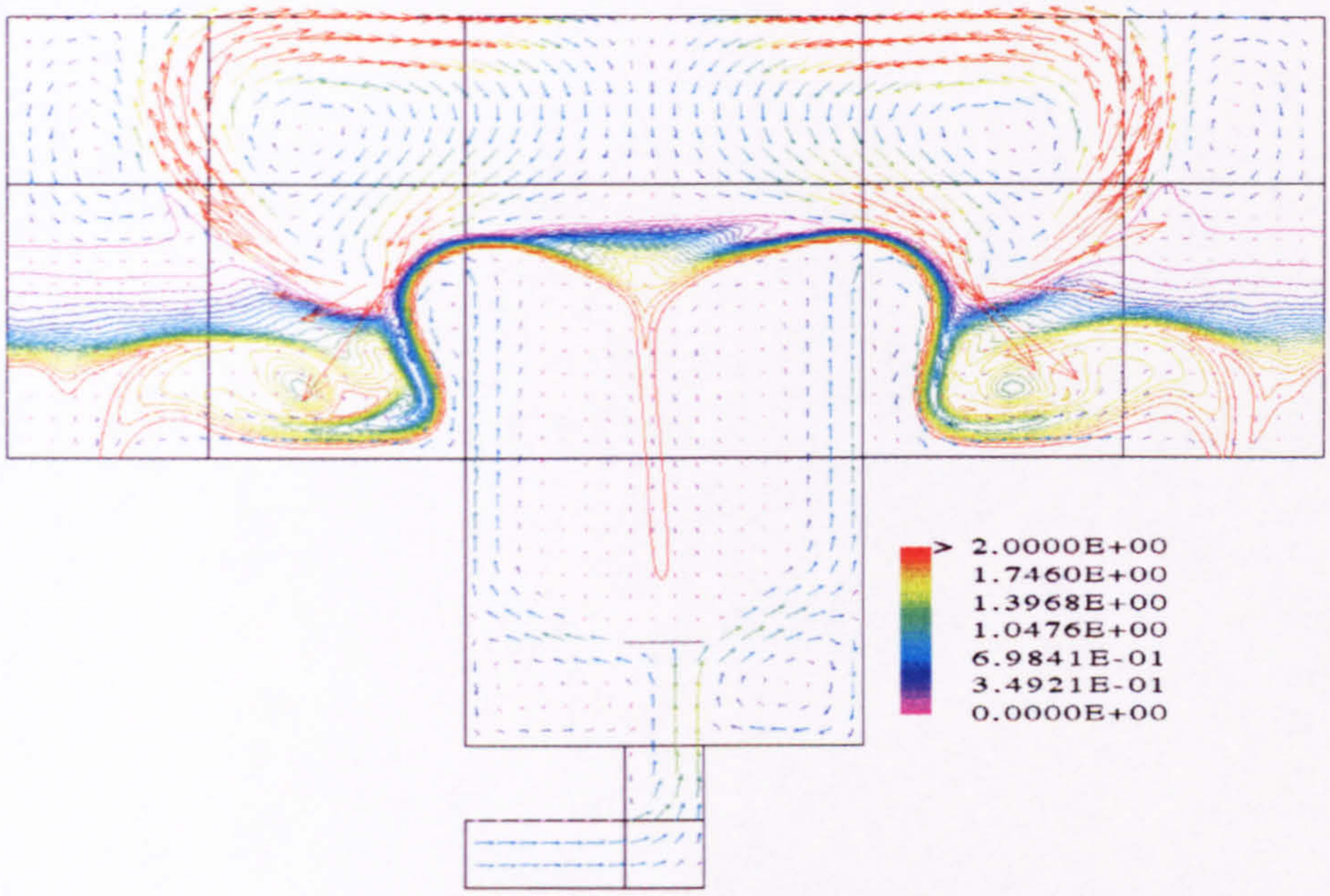


Figure 7.5-3a Velocity vector and volume fraction contour plot for Plate1. A horizontal, 0.0924 m wide plate is placed 2 D_h (0.138 m) above inlet. The longer pipe bend (2.12 D_h) is used in the geometry.

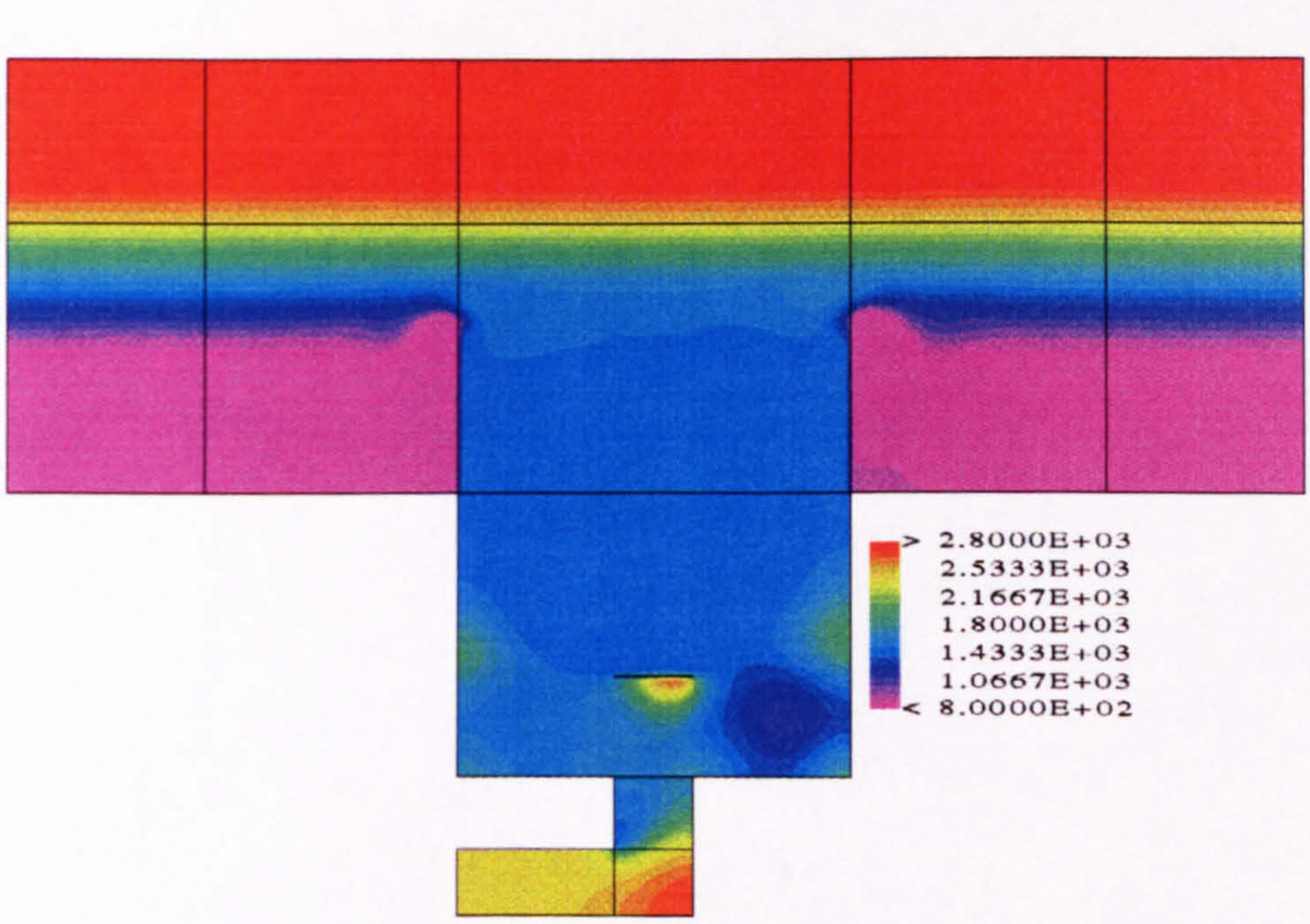


Figure 7.5-3b Pressure contour plot for Plate1.

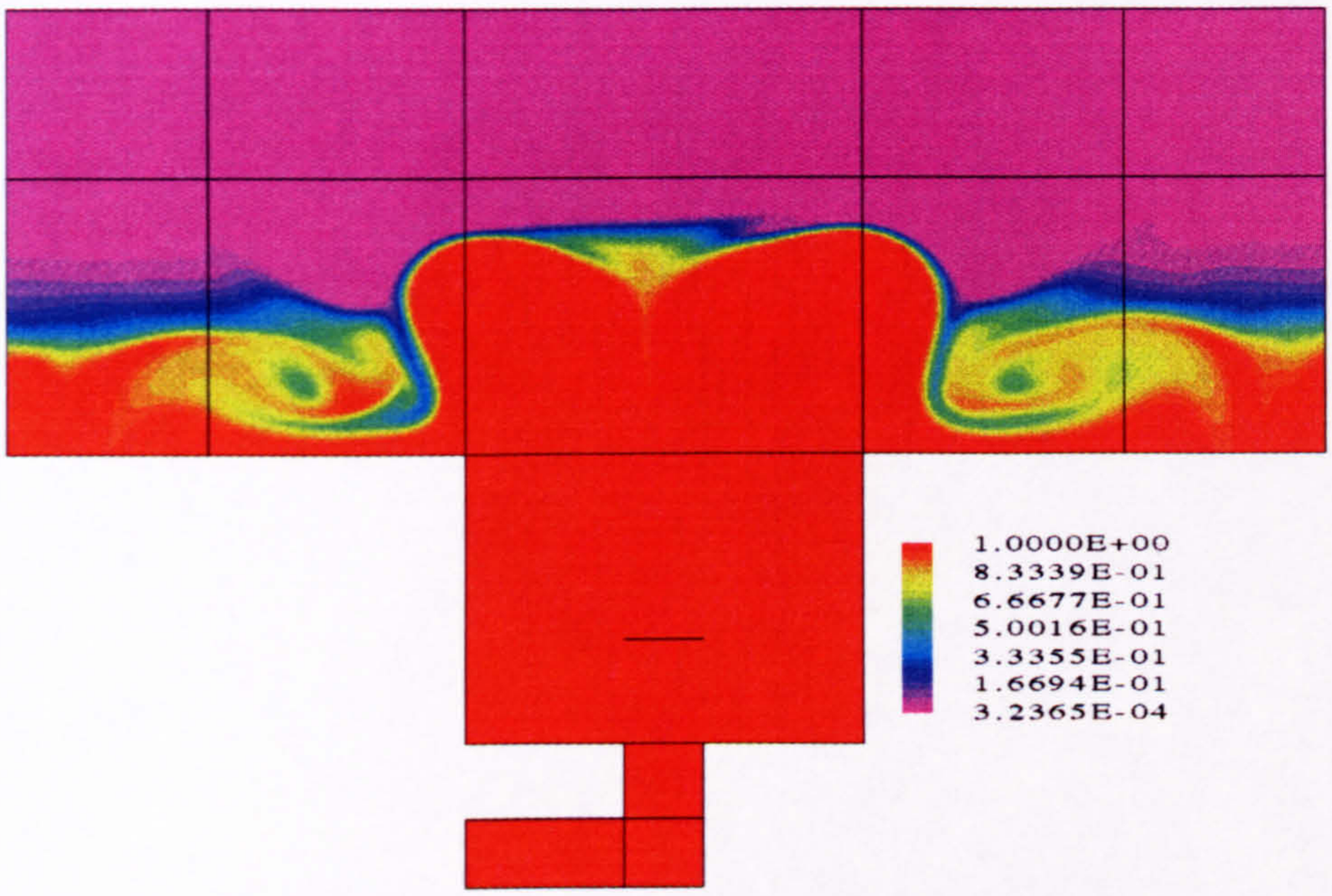


Figure 7.5-3c Volume fraction contours of water for Plate1. Value of 1.0 represents water, 0.0 is air. Free surface has a value of 0.5.

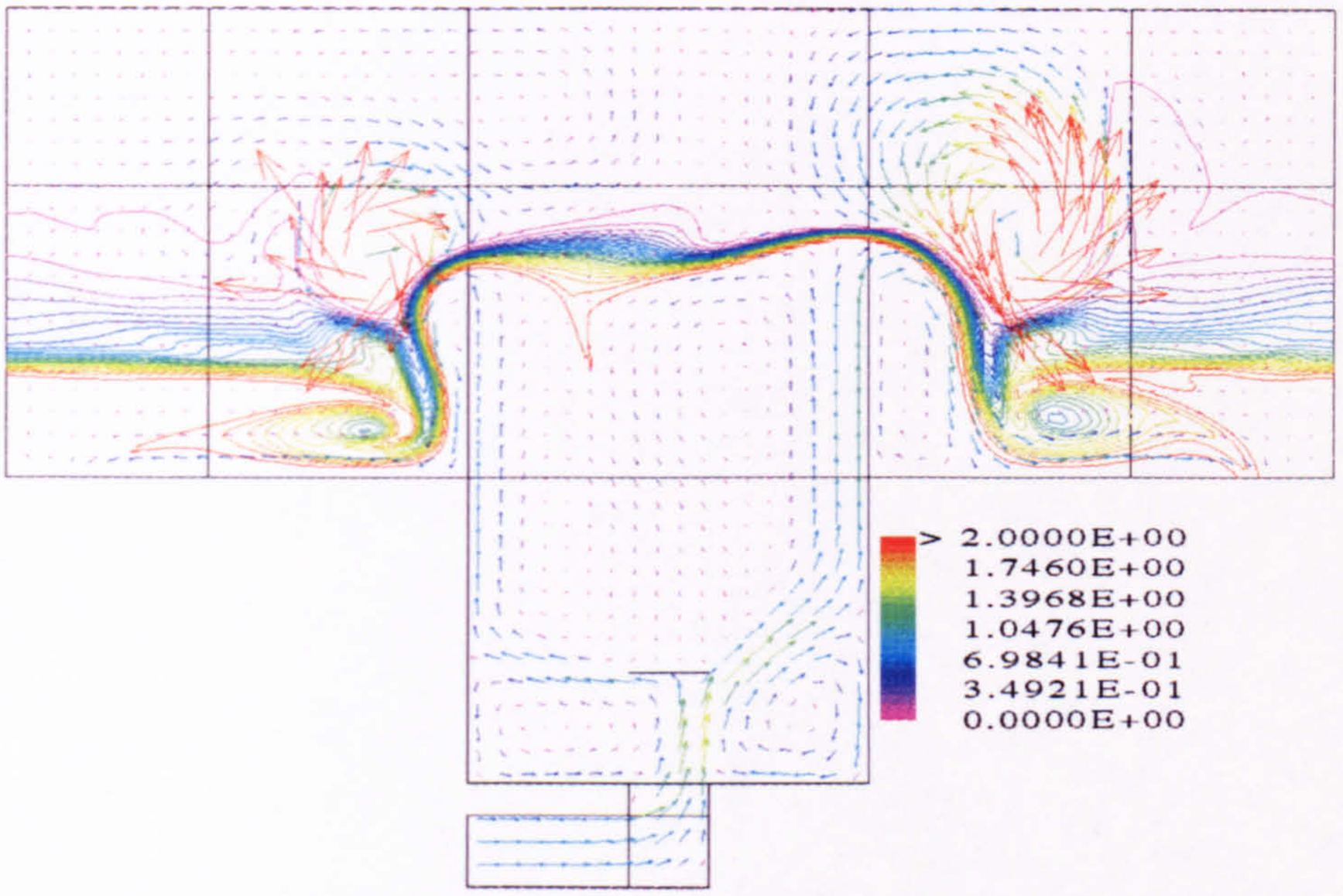


Figure 7.5-4a Velocity vector and volume fraction contour plot for Plate2. Flowrate = 4.38 l/s. The 0.0924 m wide plate is placed 2 D_h above inlet. The geometry used the shorter (1.25 D_h) pipe bend.

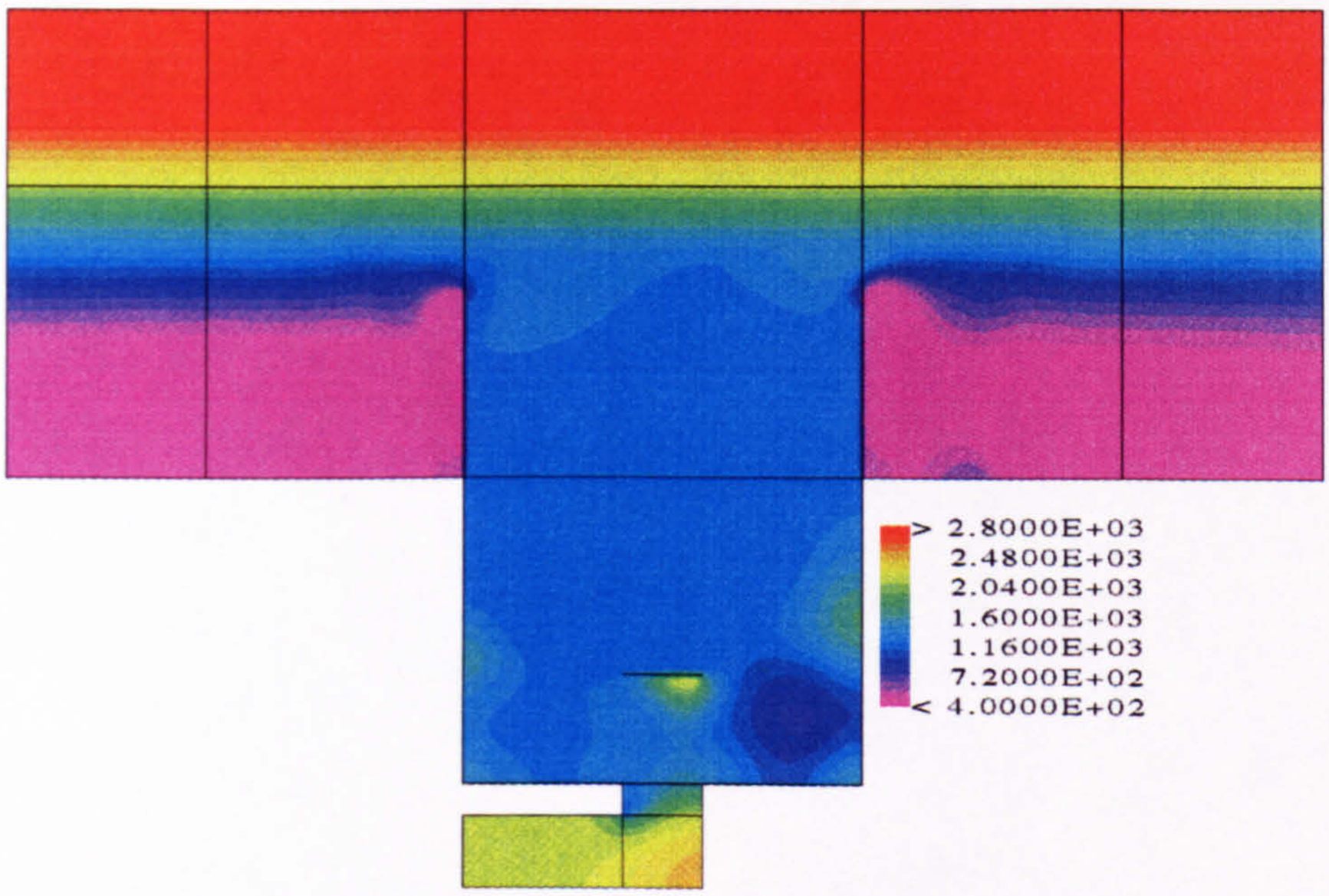


Figure 7.5-4b Pressure contour plot for Plate2.

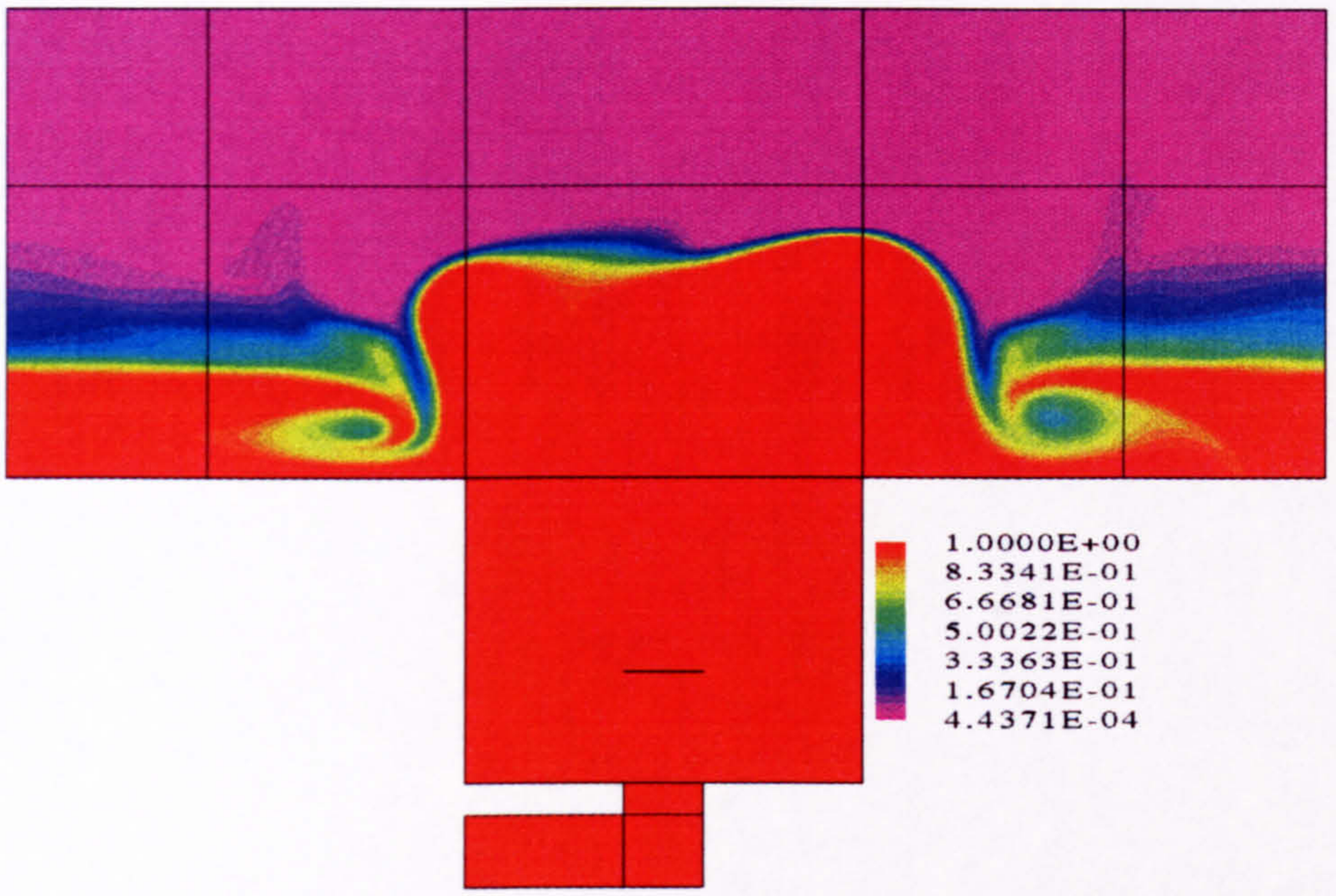


Figure 7.5-4c Volume fraction contour plot of water for Plate2. Value of 1.0 represents water, 0.0 is air. Free surface has a value of 0.5.

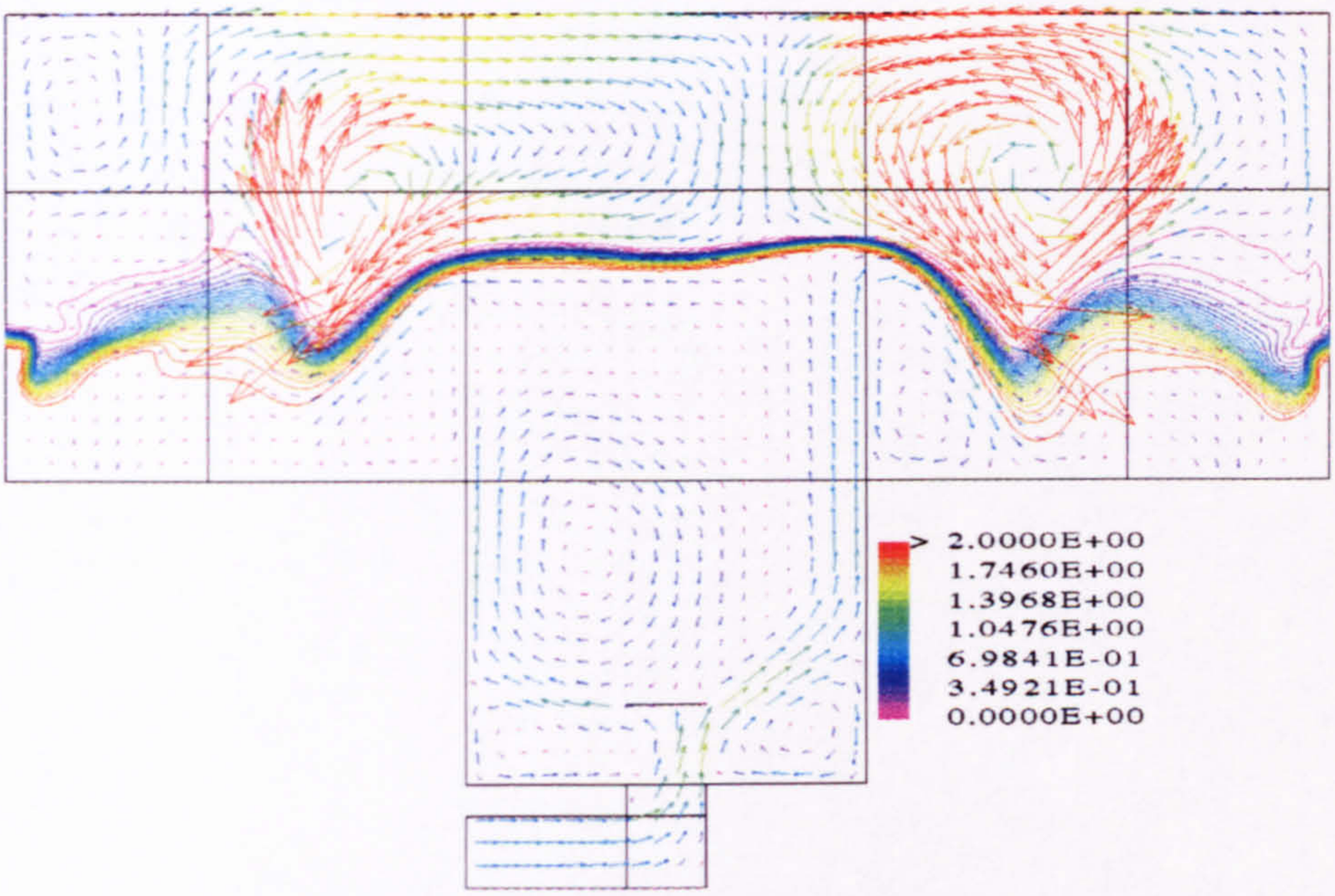


Figure 7.5-5a Velocity vector and volume fraction contour plot for Plate3. Flowrate = 4.38 l/s. The horizontal plate is now 1.5 D_h above the inlet. The geometry contained the shorter pipe bend.

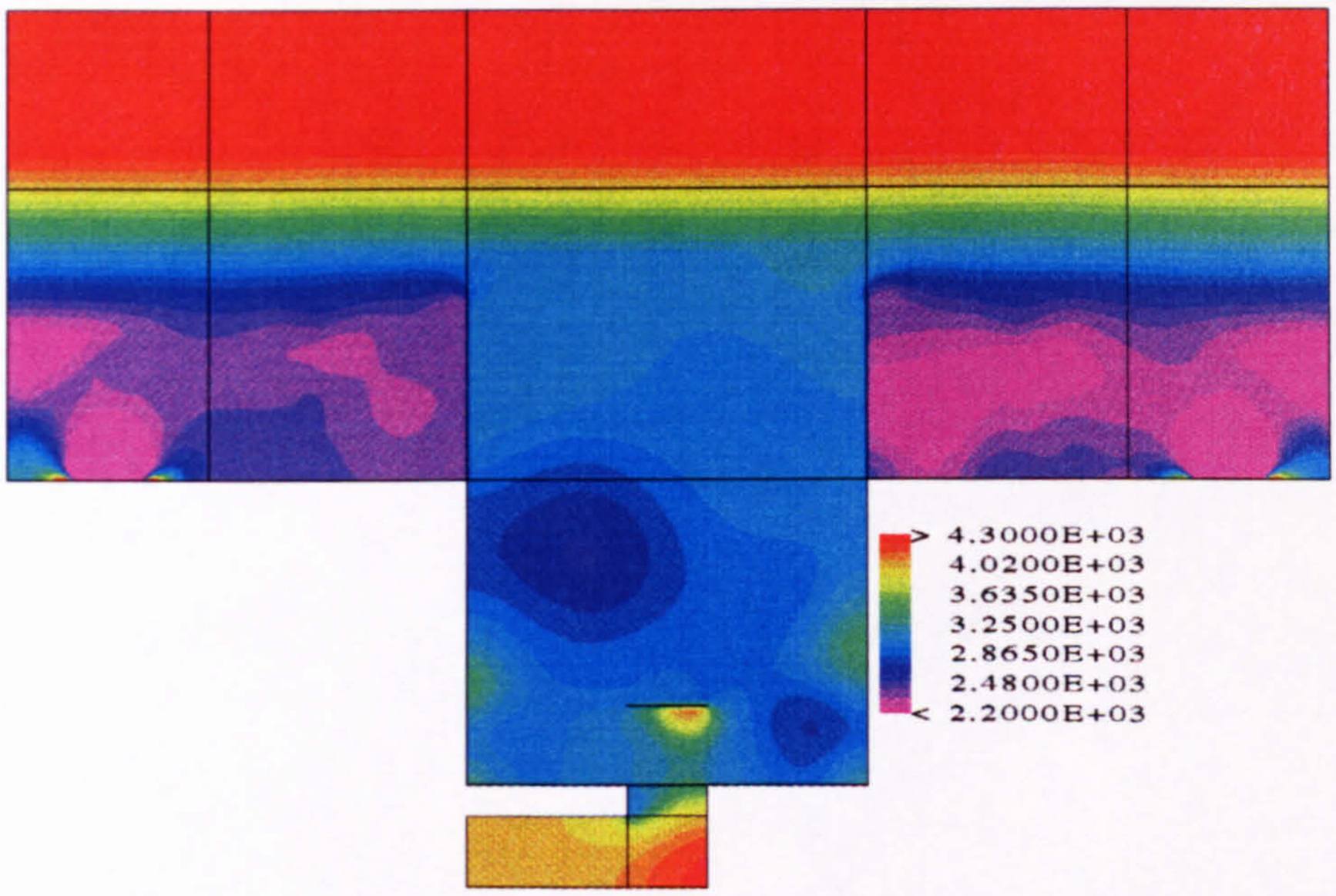


Figure 7.5-5b Pressure contour plot for Plate3.

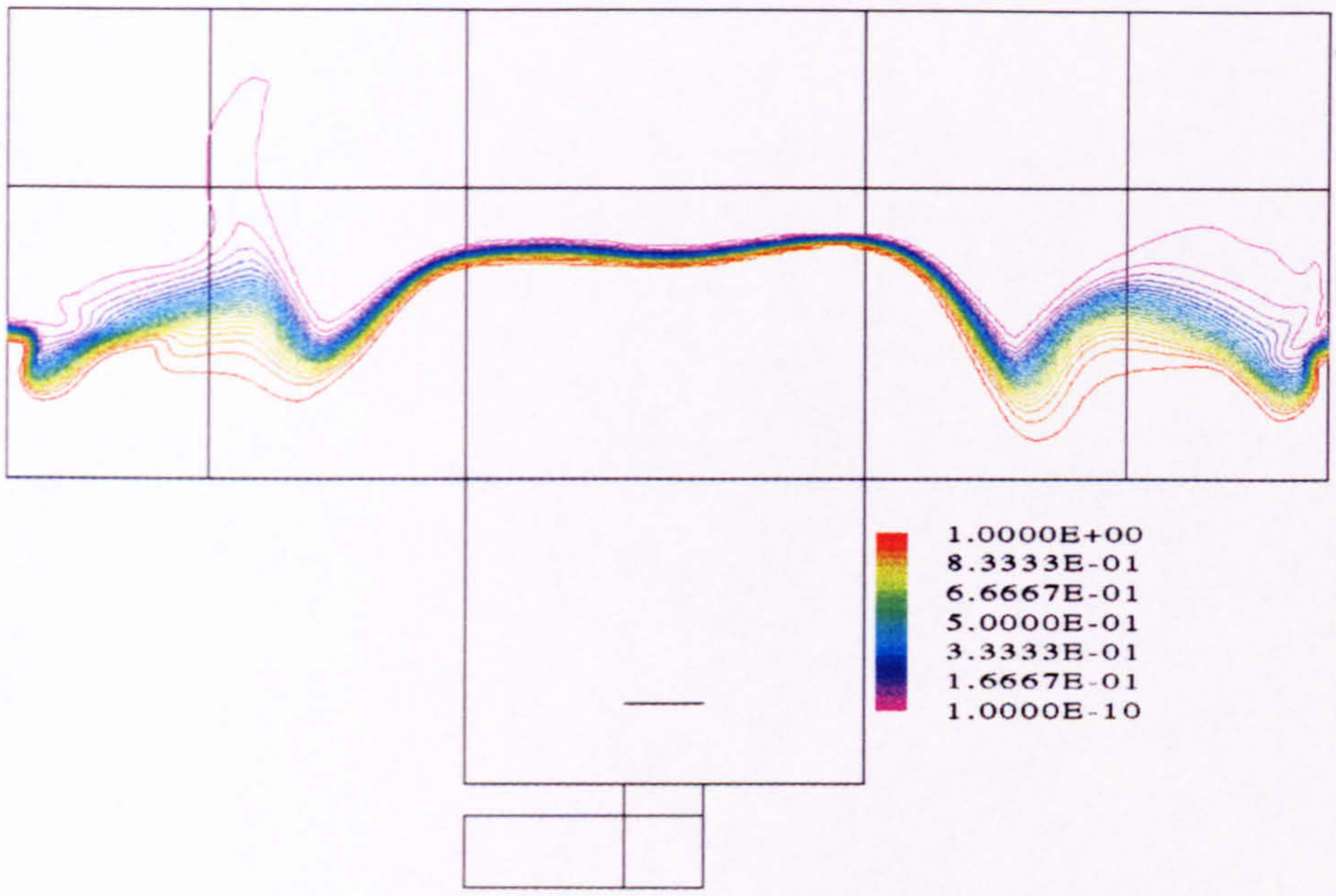


Figure 7.5-5c Volume fraction contour plot of water for Plate3. Value of 1.0 represents water, 0.0 is air. Free surface has a value of 0.5.

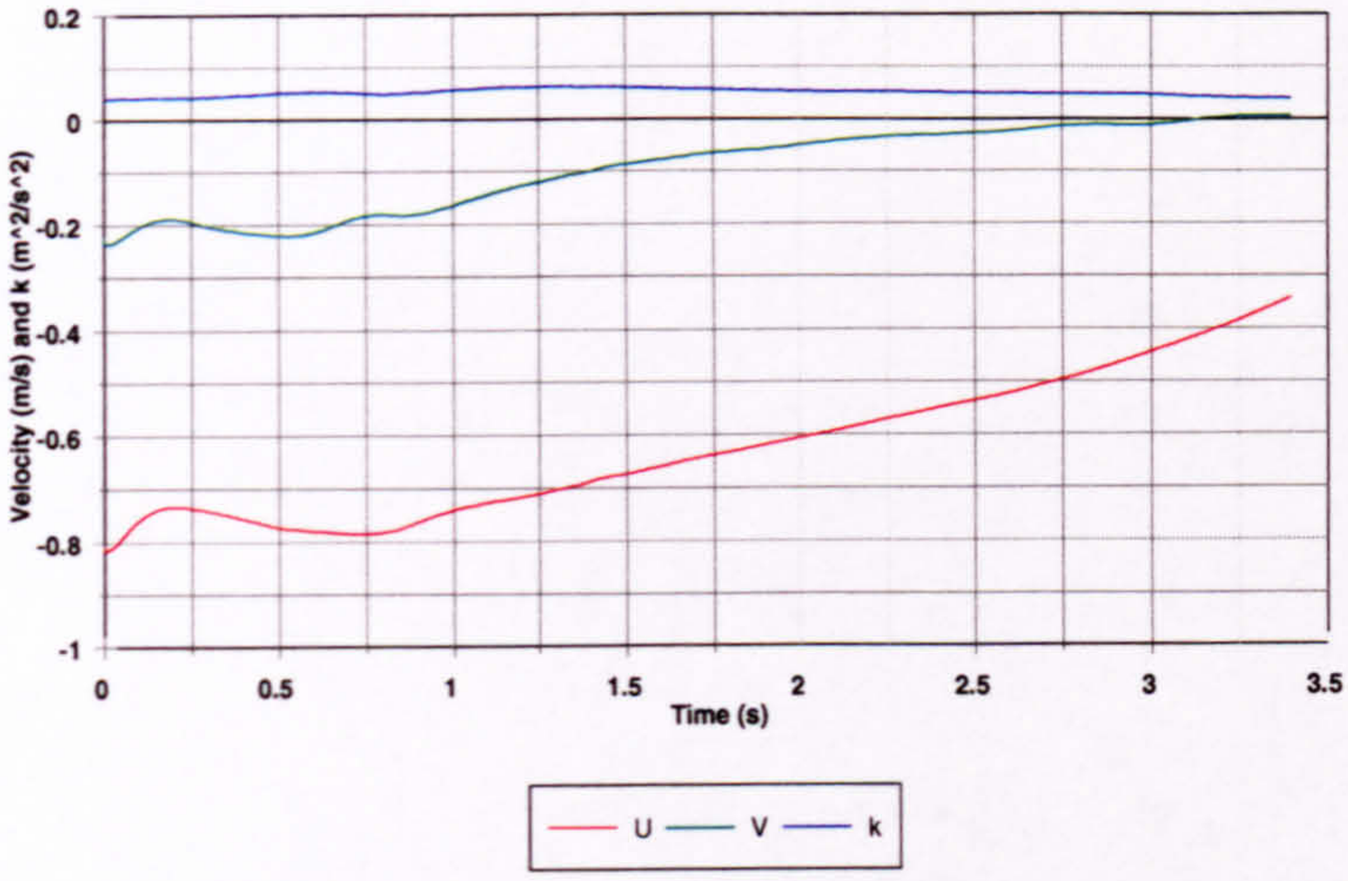


Figure 7.5-6a Time history plot of U, V and k for Plate3. Measurement point is at (0.231, 0.633, 0.0277). Centreline of chamber, 2mm above weir crests.

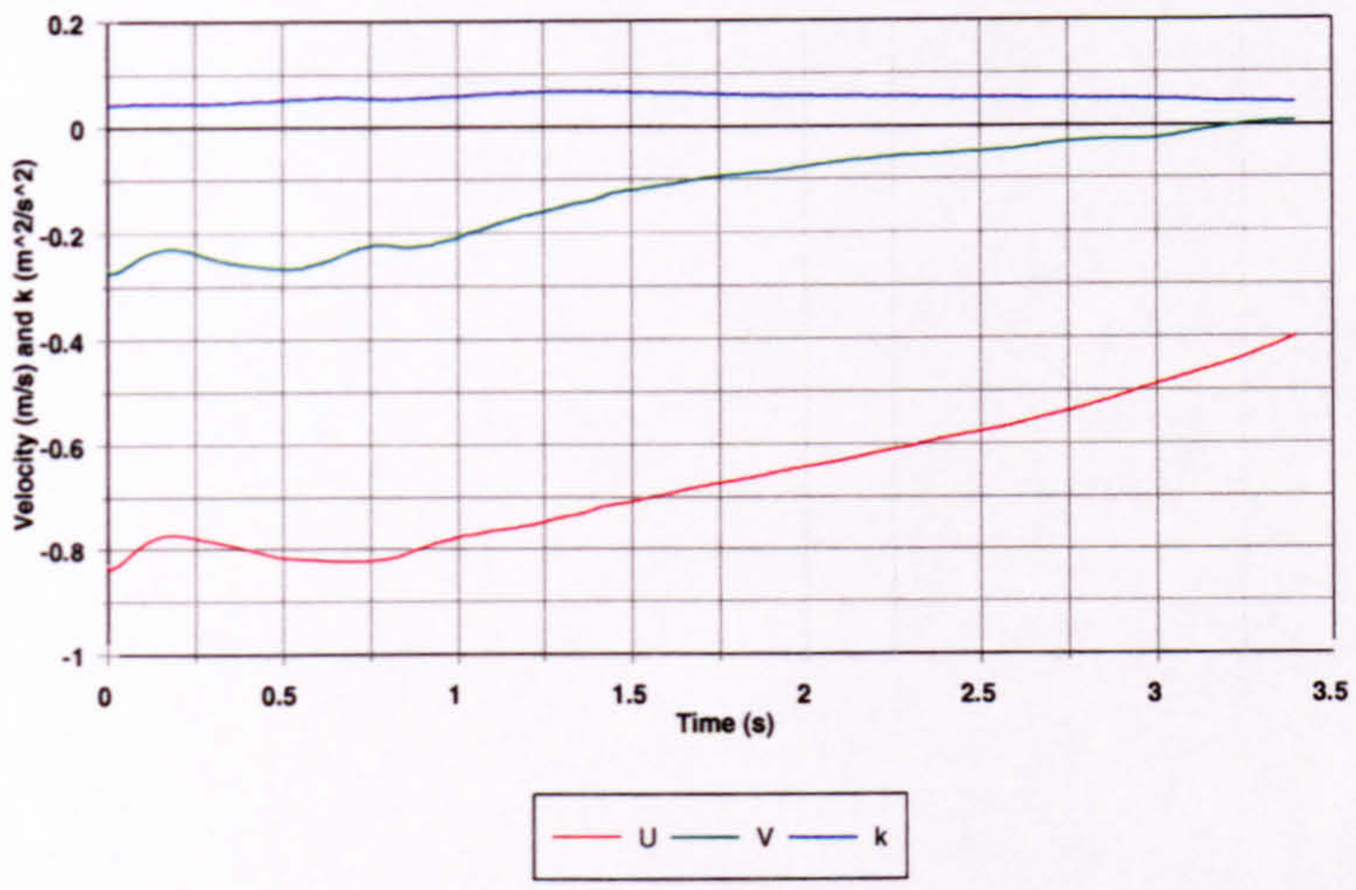


Figure 7.5-6b Time history plot of U, V and k for Plate3. Measurement point is at (0.231, 0.643, 0.0277). Centreline of chamber, 12 mm above weir crests.

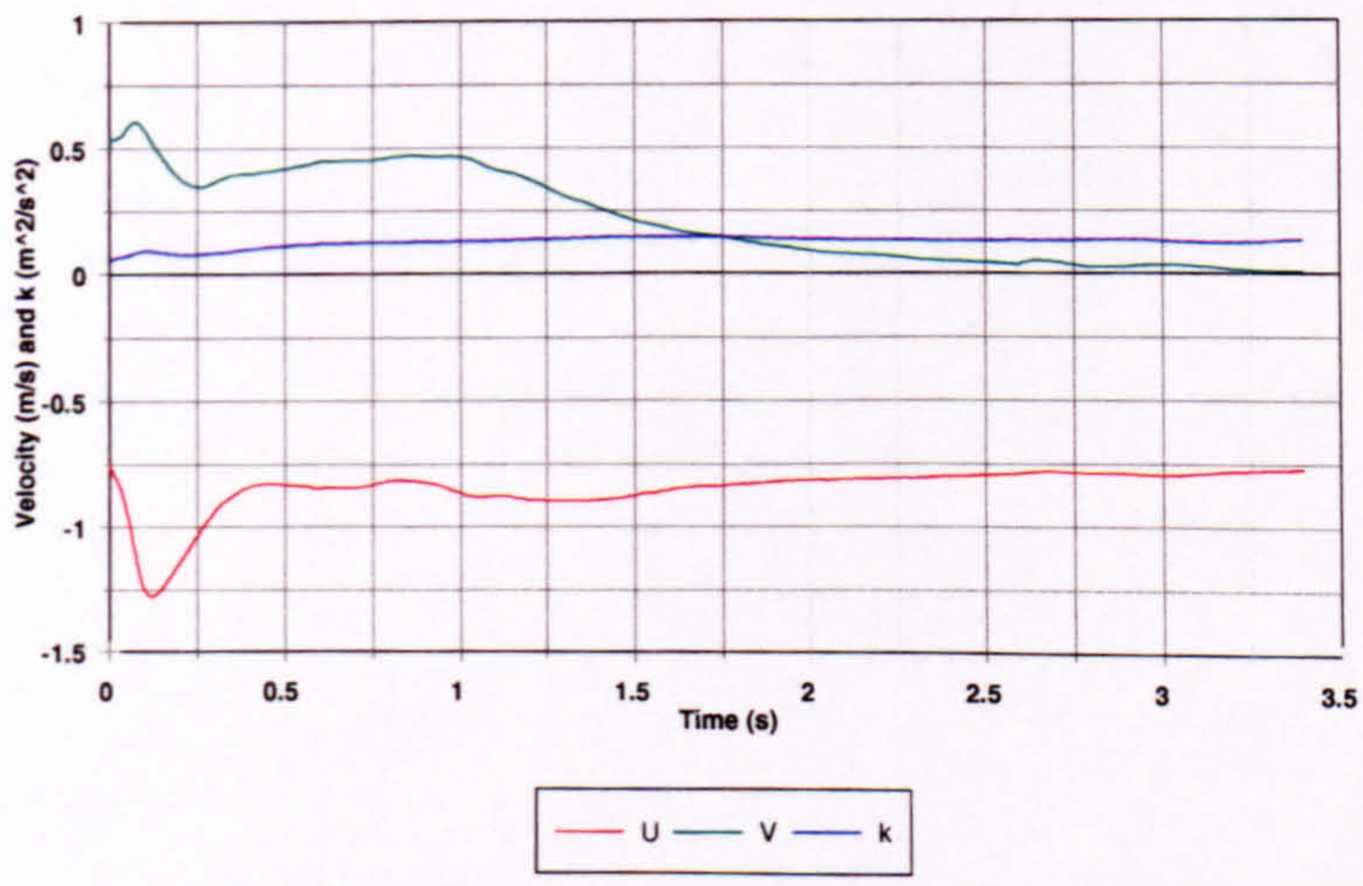


Figure 7.5-6c Time history plot of U, V and k for Plate3. Measurement point is at (0.0, 0.653, 0.0277). Left hand side of chamber, 23 mm above weir crest.

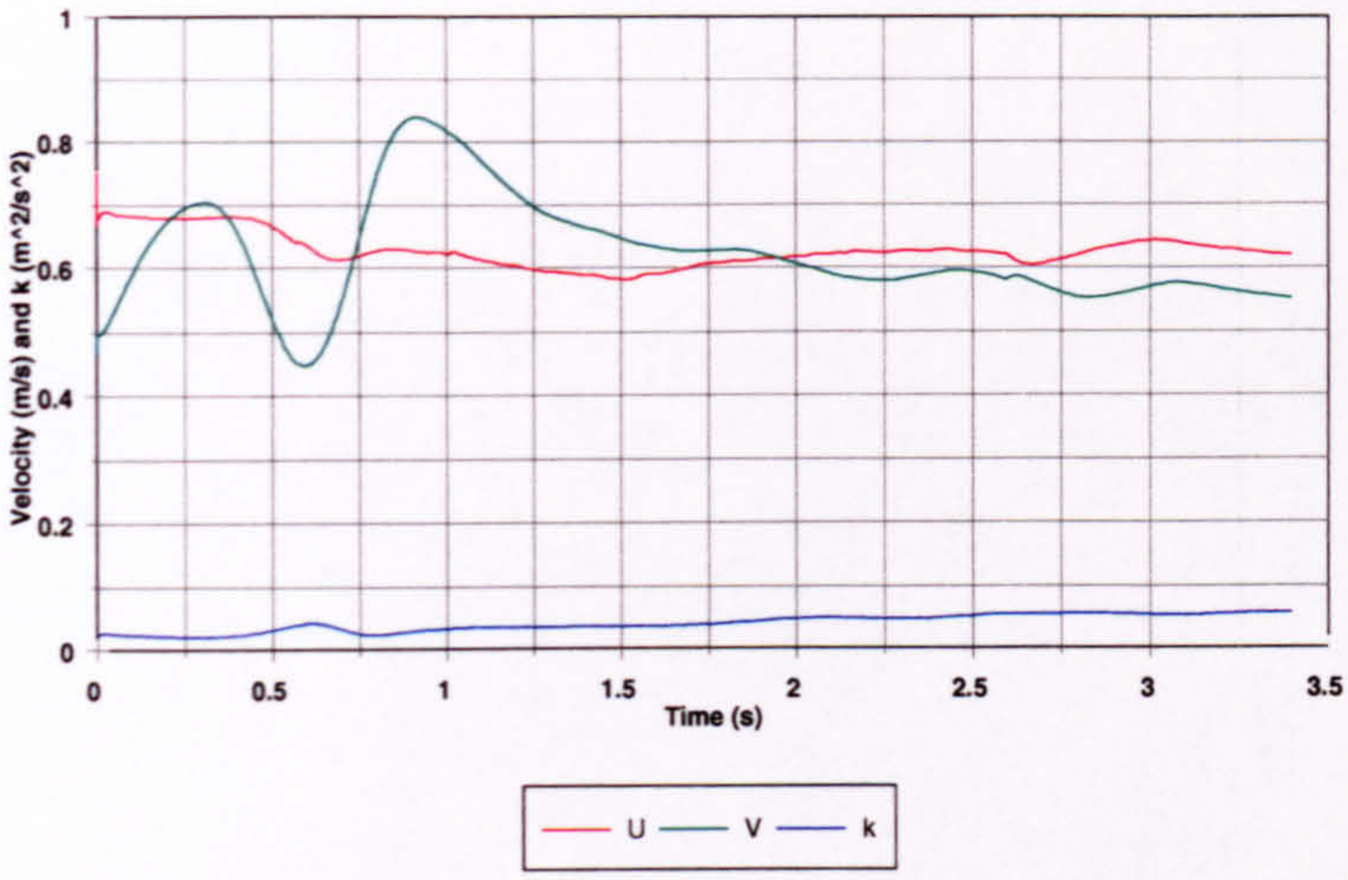


Figure 7.5-6d Time history plot of U, V and k for Plate3. Measurement point is at (0.462, 0.653, 0.0277). Right hand side of chamber, 23 mm above weir crest.

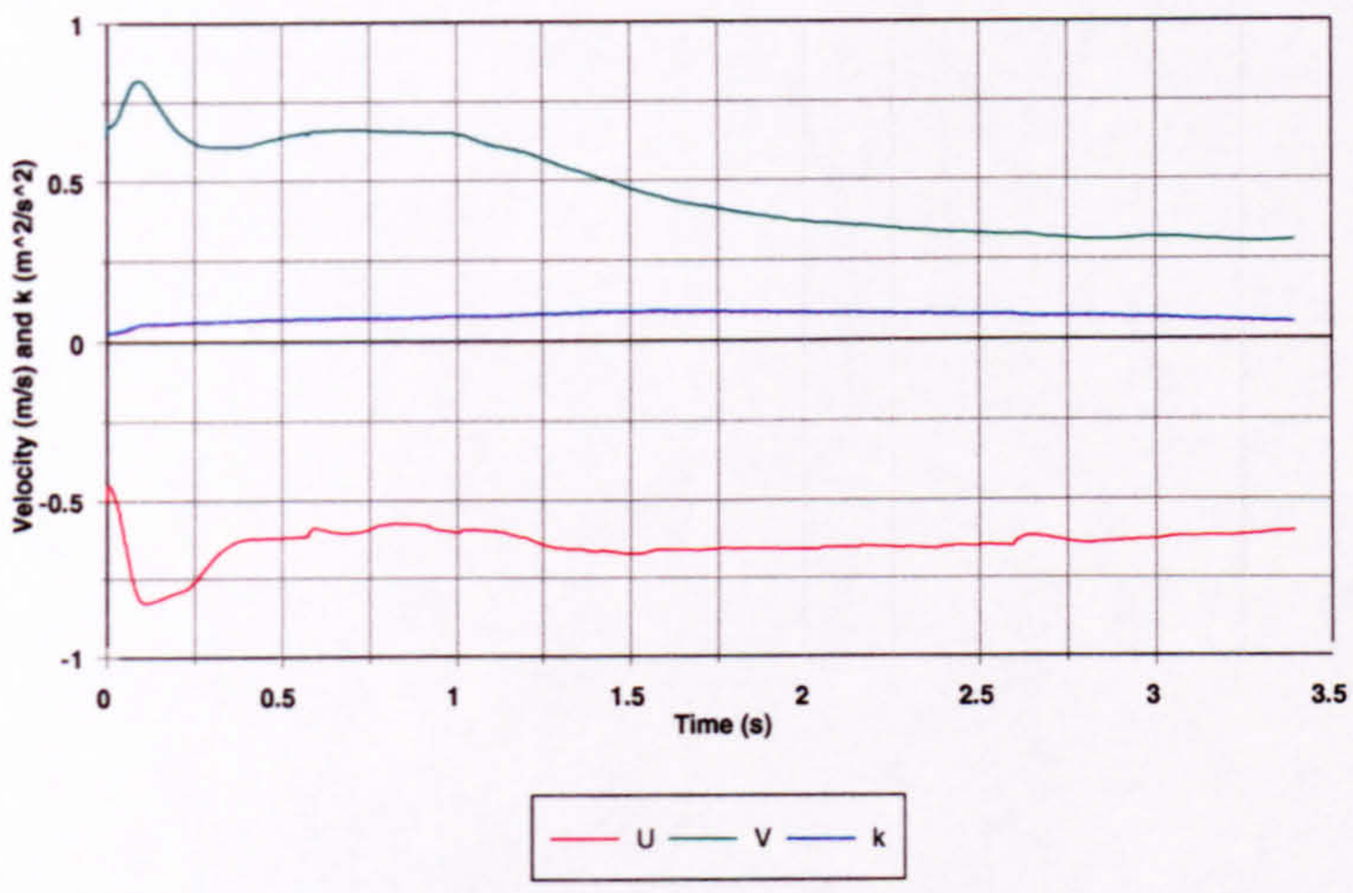


Figure 7.5-6e Time history plot of U, V and k for Plate3. Measurement point is at (0.0, 0.633, 0.0277). Left hand side of chamber, 2 mm above weir crest.

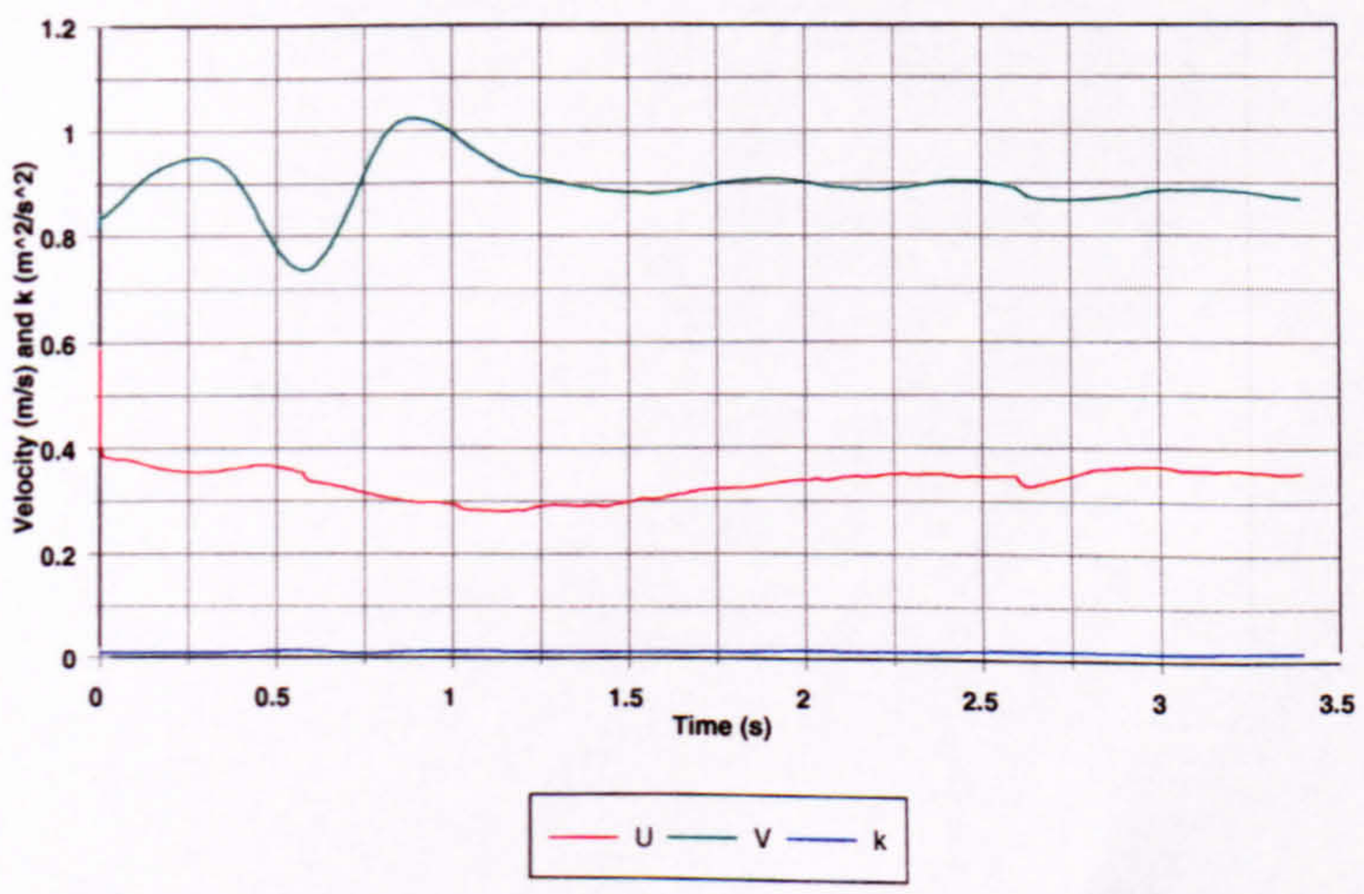


Figure 7.5-6f Time history plot of U, V and k for Plate3. Measuremnt point is at (0.462, 0.633, 0.0277). Left hand side of chamber, 2 mm above weir crest.

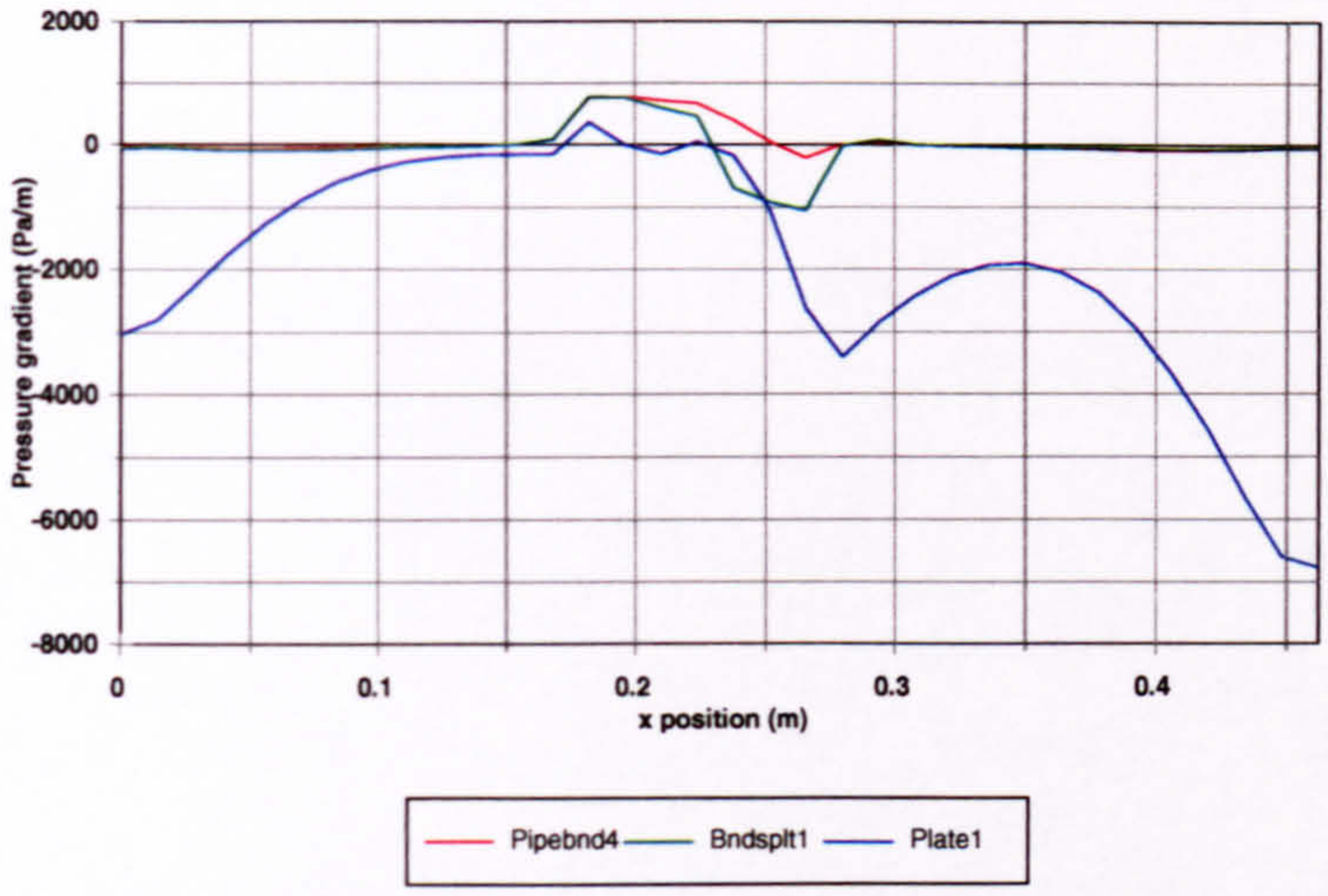


Figure 7.6-1a Comparison of pressure gradients for Pipebnd4, Bndsplt1 and Plate1 at 0.5 D_h above the inlet.

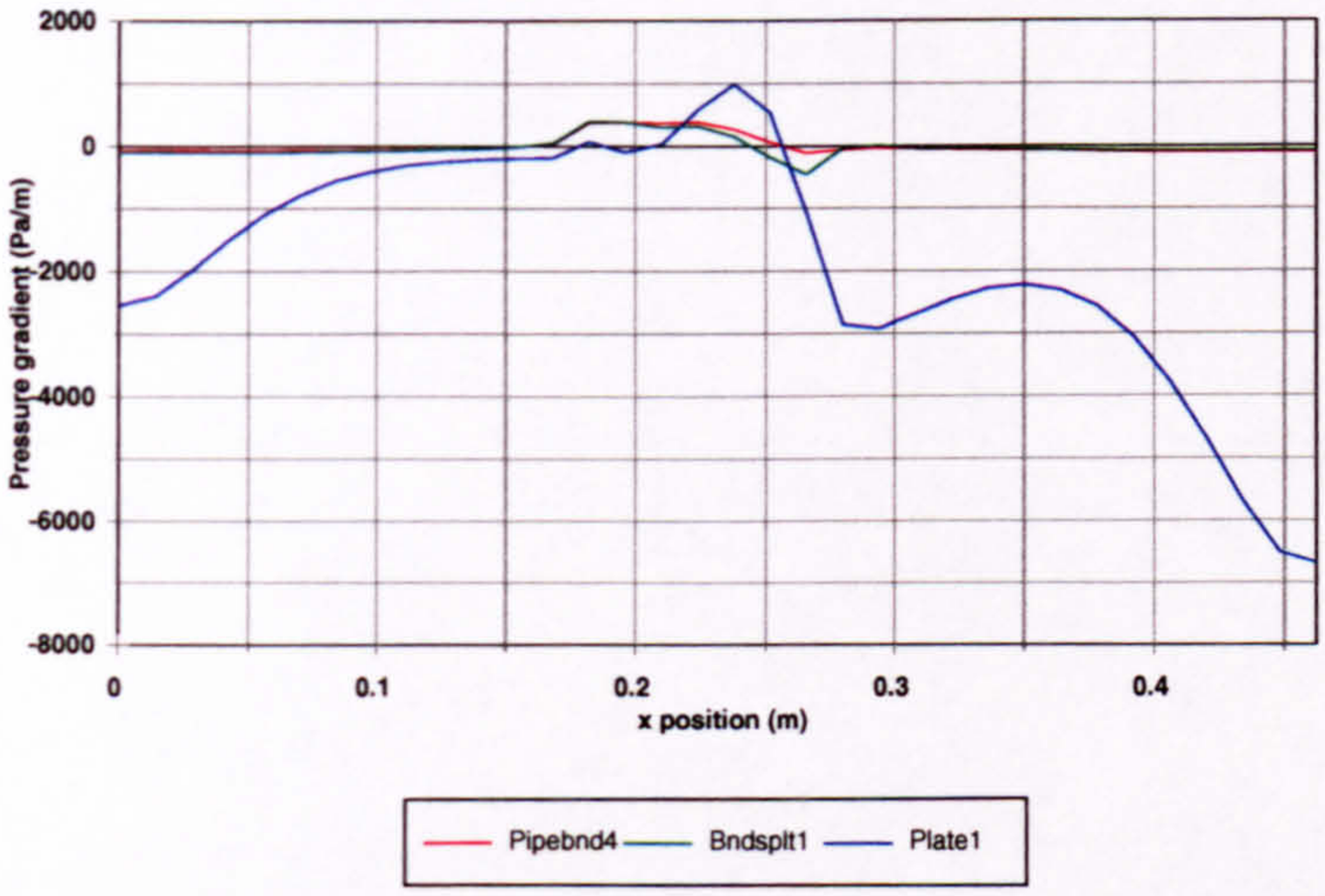


Figure 7.6-1b Comparison of pressure gradients for Pipebnd4, Bndsplt1 and Plate1 at 1 D_h above the inlet.

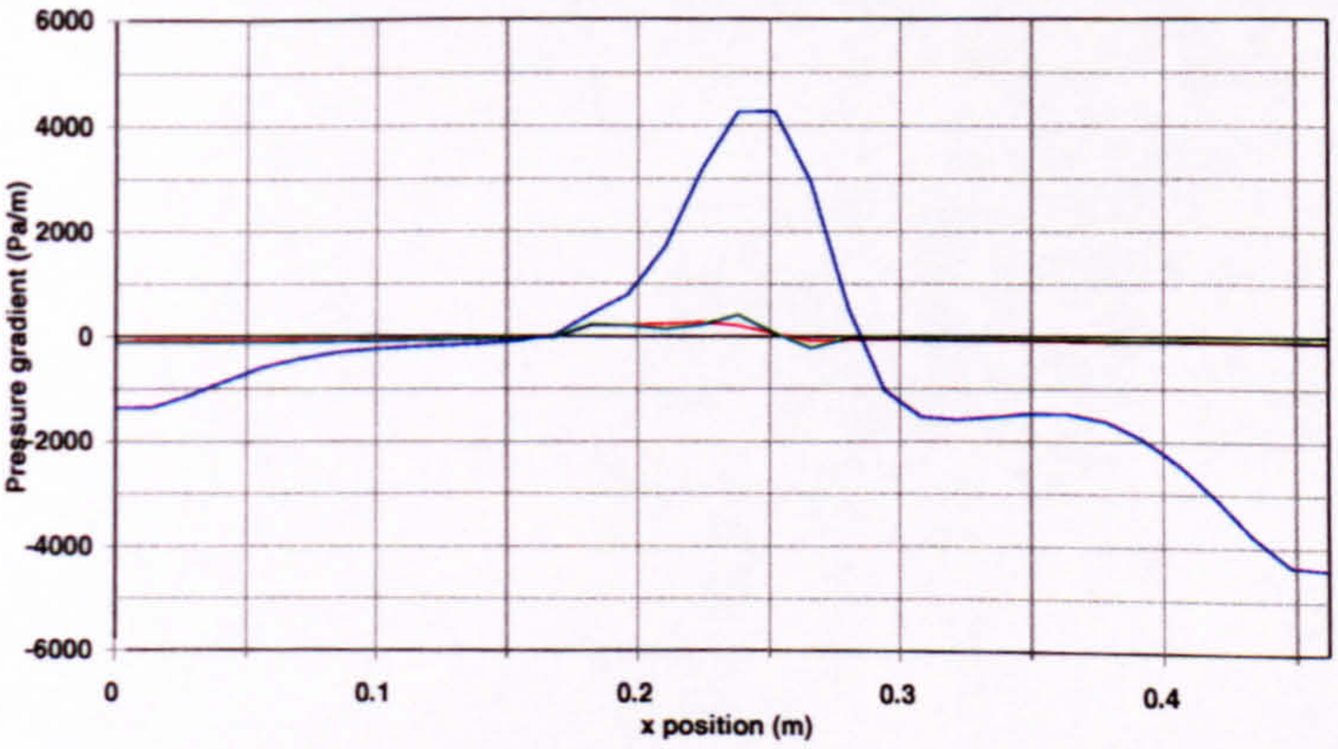


Figure 7.6-1c Comparison of pressure gradients for Pipebnd4, Bndsplt1 and Plate1 at 1.5 D_h from the inlet.

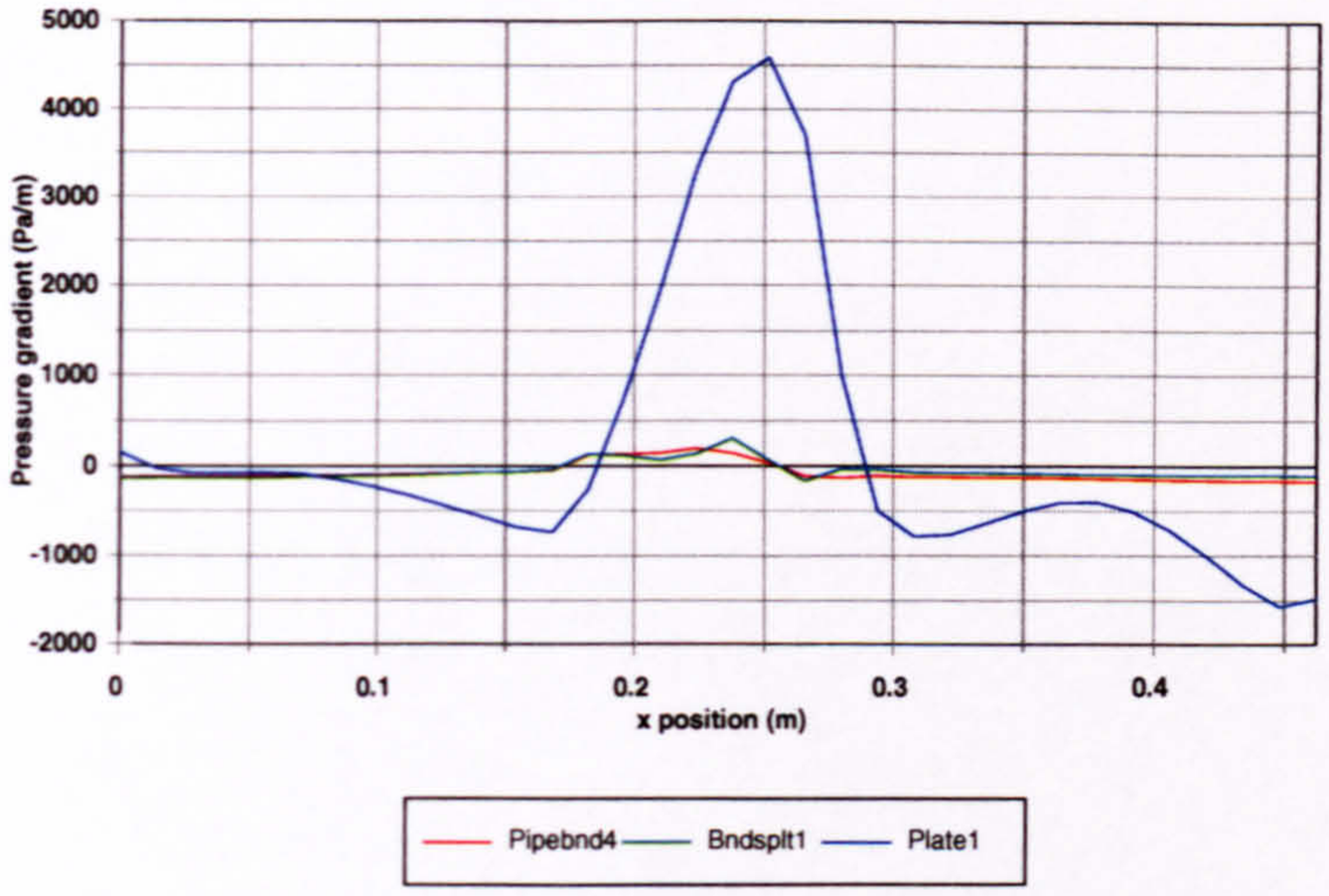


Figure 7.6-1d Comparison of pressure gradients for Pipebnd4, Bndsplt1 and Plate1 at 2 D_h from the inlet.

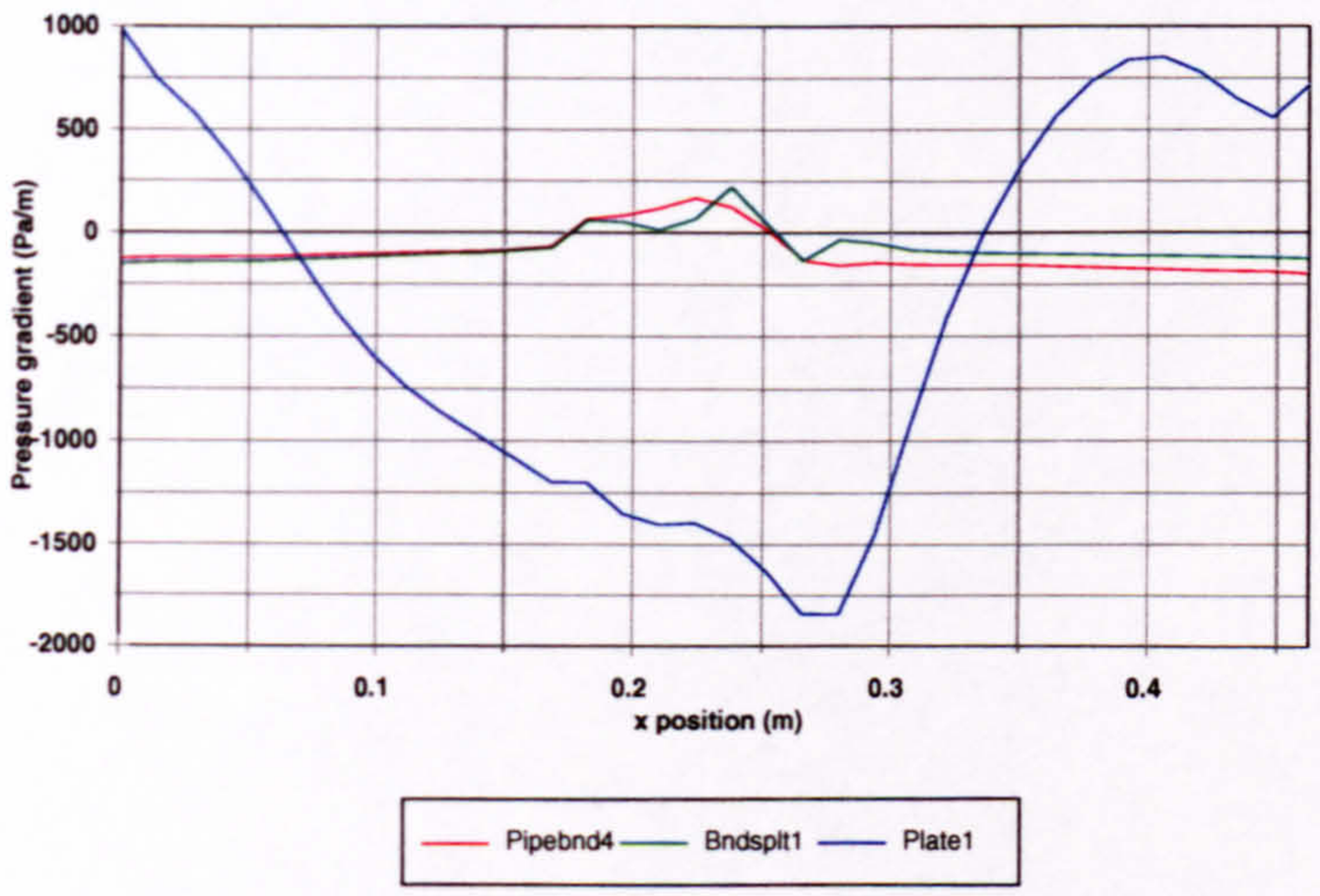


Figure 7.6-1e Comparison of pressure gradients for Pipebnd4, Bndsplt1 and Plate1 at 2.5 D_h from the inlet.

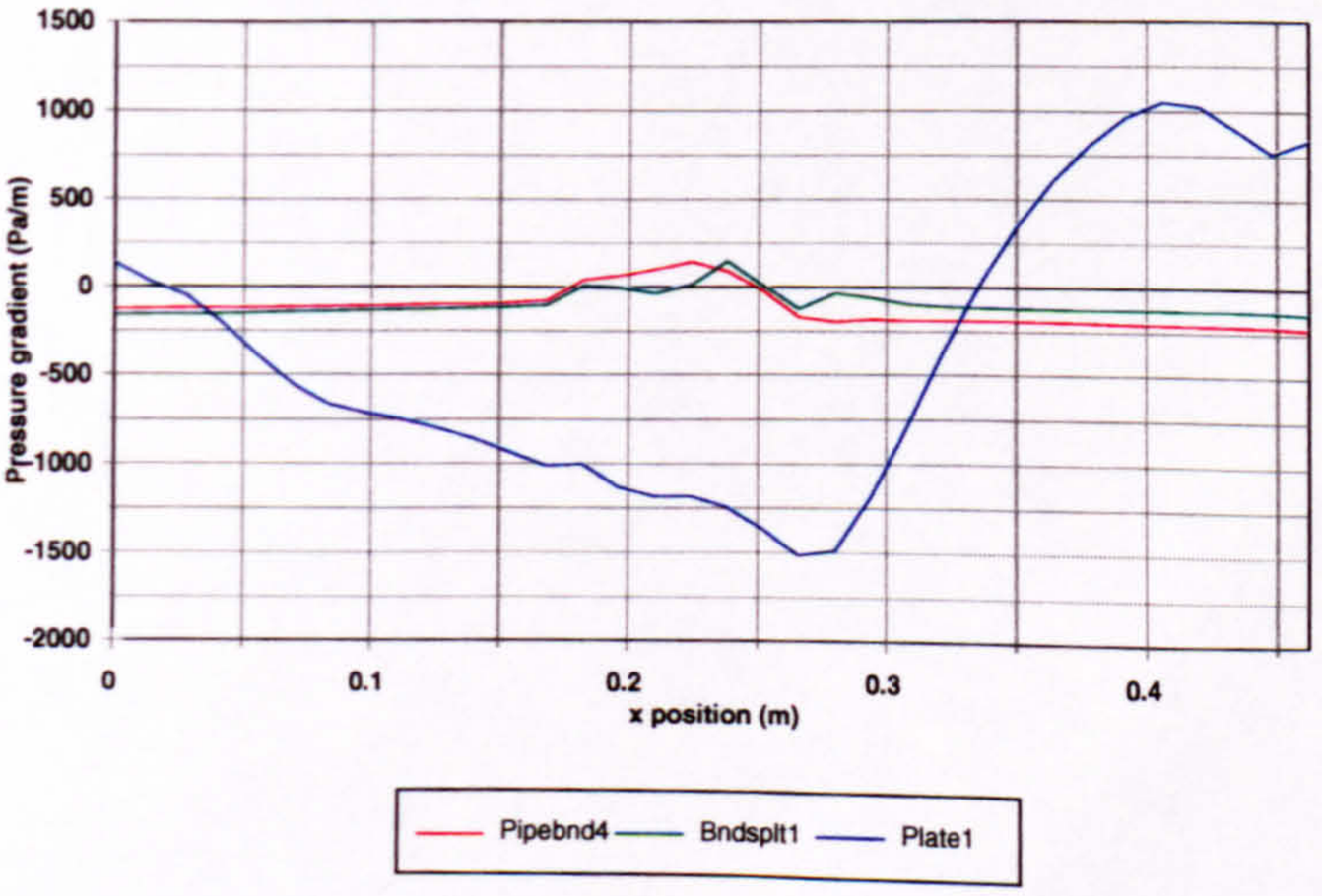


Figure 7.6-1f Comparison of pressure gradients for Pipebnd4, Bndsplit1 and Plate1 at 3 D_h from the inlet.

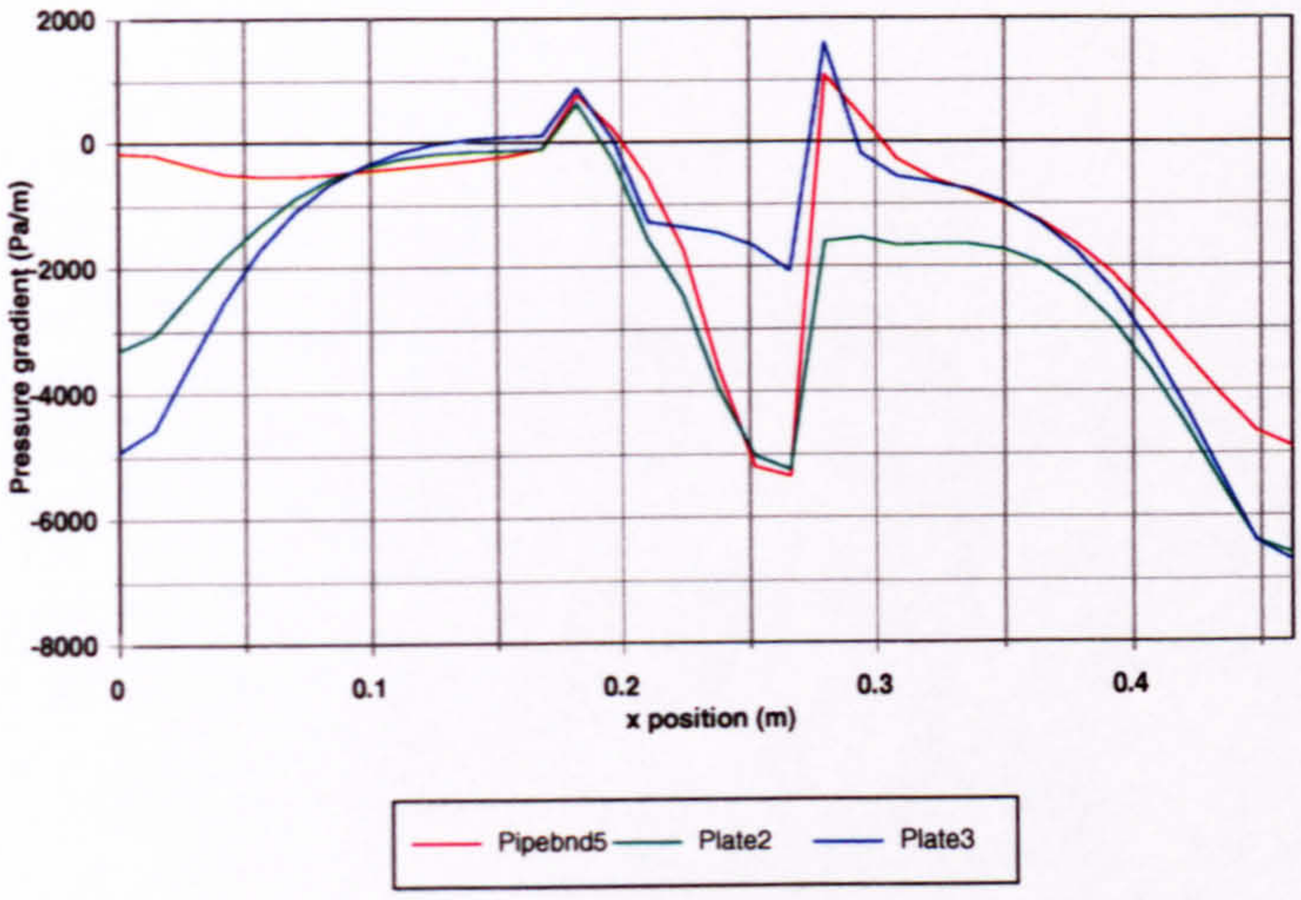


Figure 7.6-2a Comparison of pressure gradients for Pipebnd5, Plate2 and Plate3 at 0.5 hydraulic diameter from chamber inlet. (Geometry contains shorter bend).

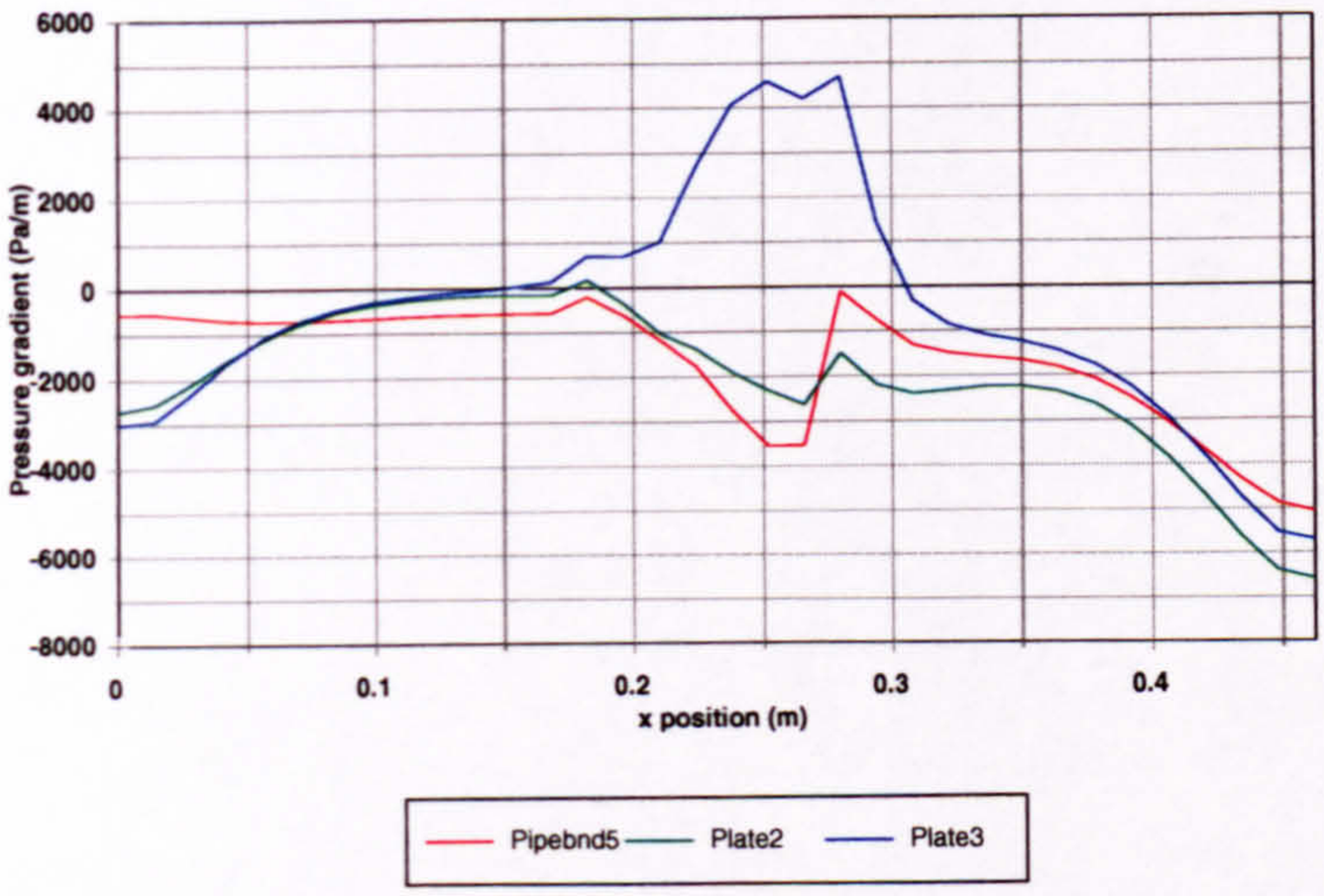


Figure 7.6-2b Comparison of pressure gradients for Pipebnd5, Plate2 and Plate3 at 1 hydraulic diameter from chamber inlet.

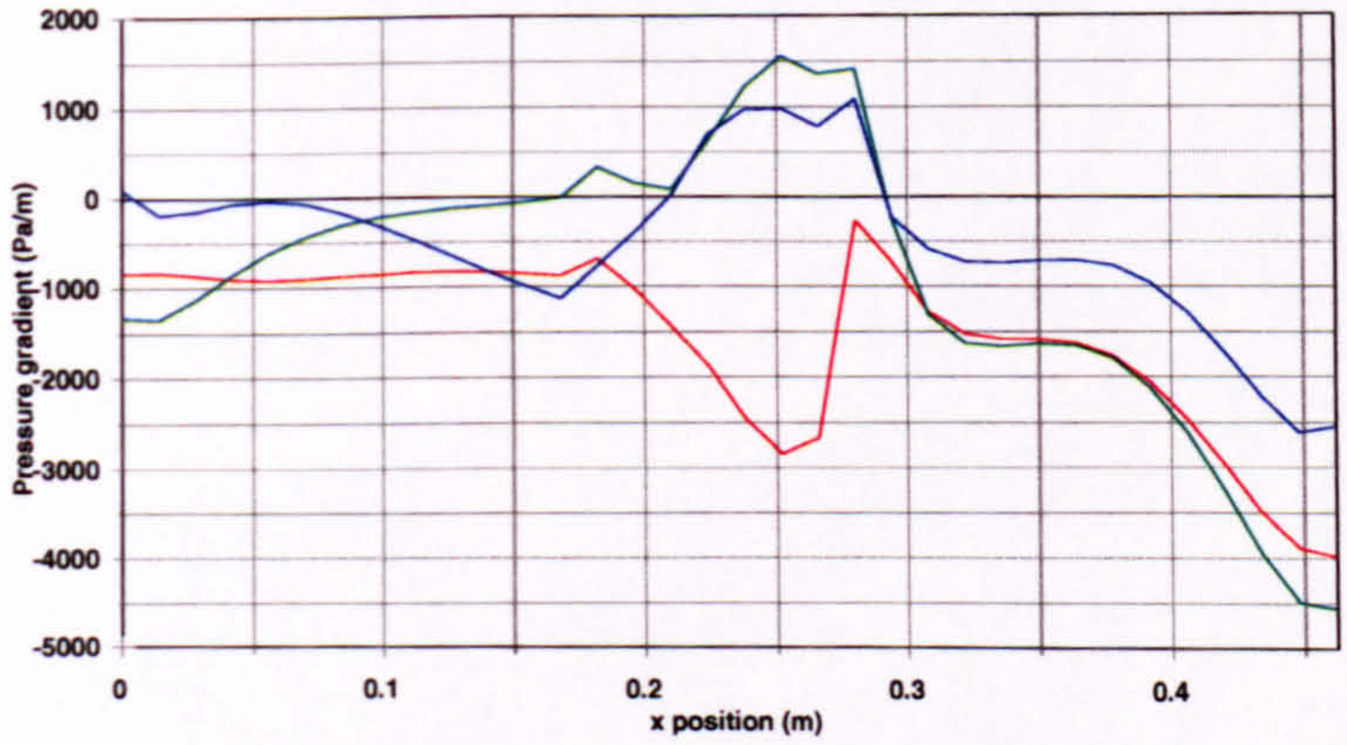


Figure 7.6-2c Comparison of pressure gradients for Pipebnd5, Plate2 and Plate3 at 1.5 hydraulic diameters from chamber inlet.

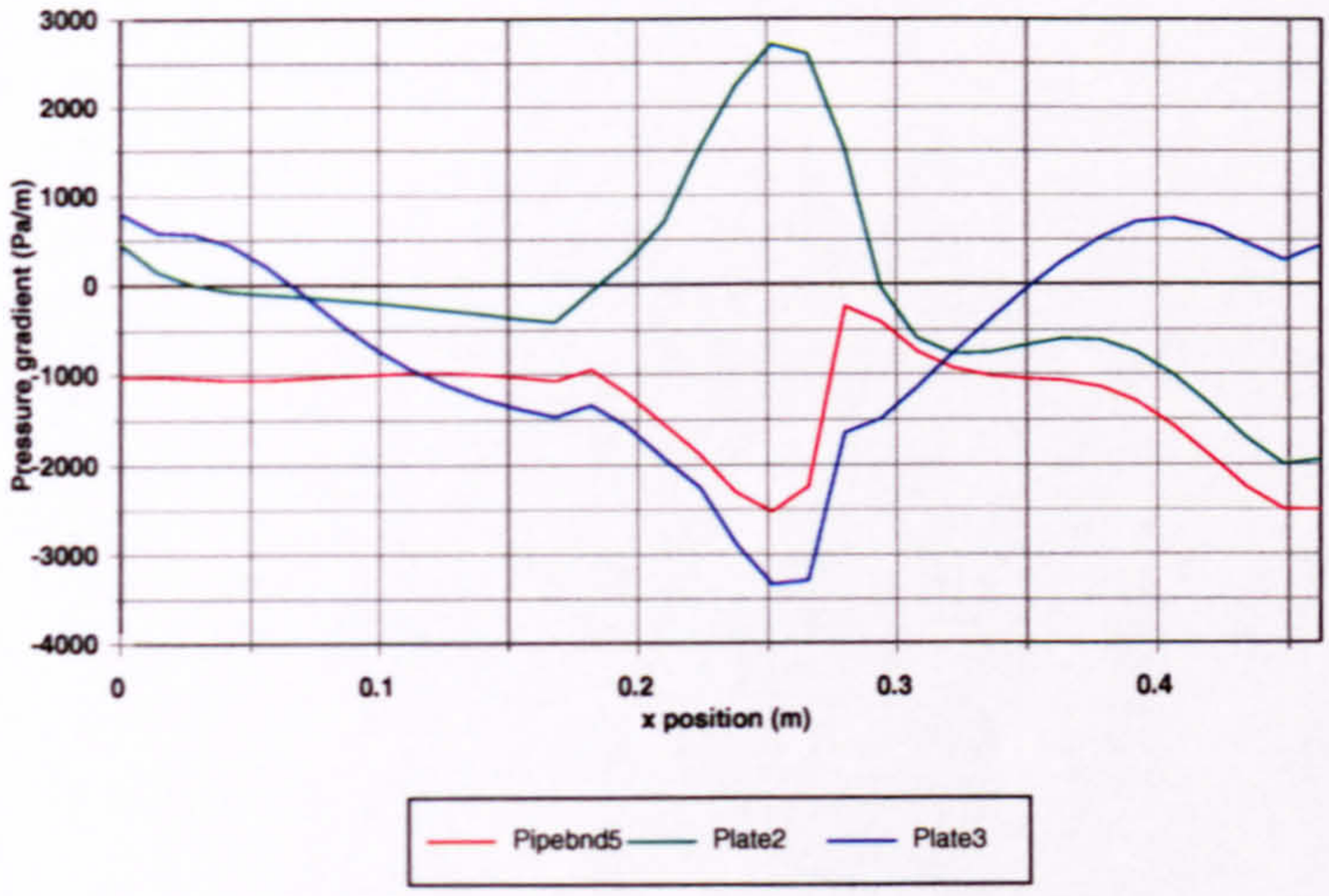


Figure 7.6-2d Comparison of pressure gradients for Pipebnd5, Plate2 and Plate3 at 2 hydraulic diameters from chamber inlet.

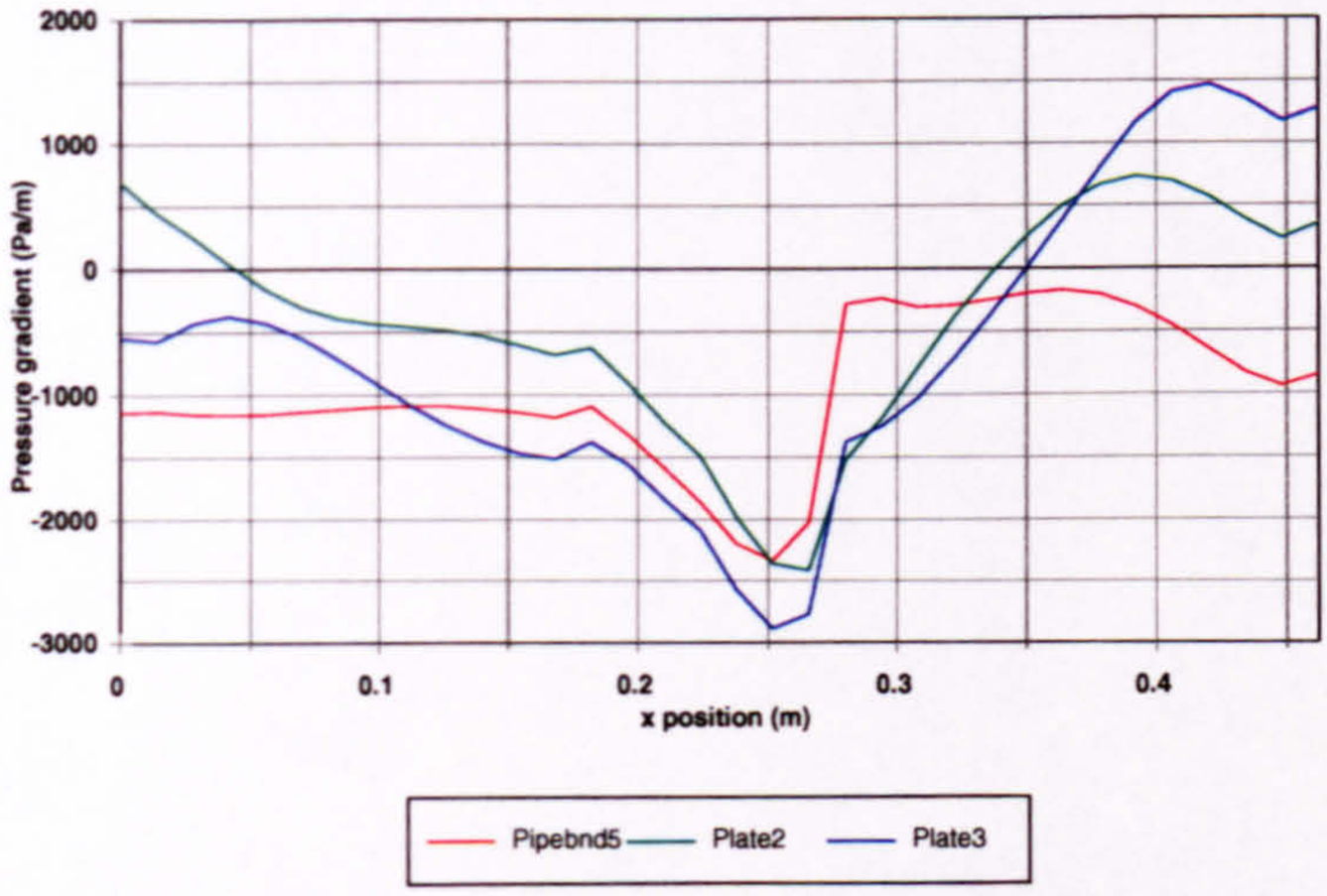


Figure 7.6-2e Comparison of pressure gradients for Pipebnd5, Plate2 and Plate3 at 2.5 hydraulic diameters from chamber inlet.

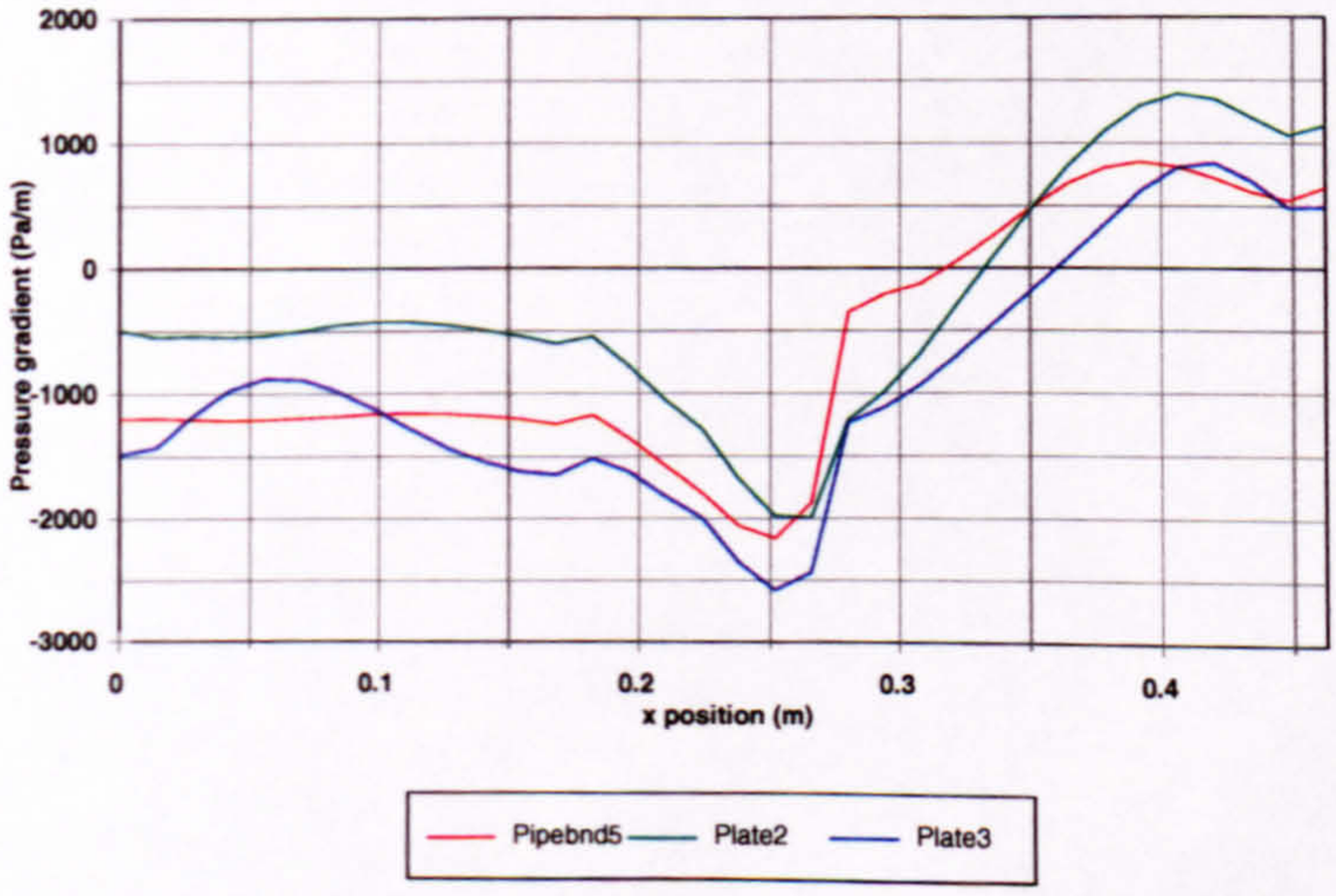


Figure 7.6-2f Comparison of pressure gradients for Pipebnd5, Plate2 and Plate3 at 3 hydraulic diameters from chamber inlet.

8. CONCLUSIONS

Experiments were conducted on a purpose built test facility, consisting of a scaled model of a distribution chamber with two outlet weirs. Novel experimental data was collected during the tests. The data included velocity and turbulence measurements using hot film anemometry, flow distribution and water surface height measurements using flow metering and water level measuring equipment respectively. The results from the tests gave rise to the following conclusions:

1. The flow within the distribution chamber was unsteady in nature. This was characterized by variations in the magnitude and location of the surface boil. There was a periodicity associated with these fluctuations and the flow tended towards a quasi-steady state after one theoretical residence time.

   Perturbations were set up when flow first entered the distribution chamber, which was initially empty. It took a short time for the dominant flow features, such as the jet with the two recirculating regions, and the surface boil, to be developed. The interval taken to establish the major flow features varied in inverse proportion to the flowrate, and was in the order of seconds. This meant that the higher the flowrate, the less time it will take for the flow to be developed. This is in keeping with the residence time for the system, which in turn is an approximation for the time taken for a particle of water to leave the chamber.

2. As expected, increases in the flowrates into the system, increased the magnitude of the surface boil. The formation of the boil was a consequence of the jet developed below the free surface. The vertical momentum of the jet caused the deflection of the free surface.

3. Efforts were made to reduce the asymmetric effects of the pipe bend below the distribution chamber. These included maximising the vertical length of pipe below the chamber (10 pipe diameters) and orientating the bend towards the walls of the chamber rather than towards the outlets. When averaged over time the flow distribution between the two outlets was equal, despite periodic variations in the values. Similarly, the water levels and the position of the surface boil also displayed the same periodic variations in position. These were the function of the unsteady jet developed within the chamber.

4. Experimental data collected from the tests were compared against the empirical prediction method of Herbath and Wong (1997b). This empirical method gave an indication of the onset of flow mal-distribution for a given set of geometric and flowrate considerations. However, the empirical method was unable to quantify the amount of flow mal-distribution. Nor was it universally applicable for all possible types of chamber designs. Hence, there was no accurate empirical method of determining flow mal-distribution.

Additionally, an algebraic method for determining the volumetric flow over each discharge weir from water levels over the weir crests, may be found from that recommended by Herbath and Wong. However, the experimental results proved that the adaptation of this method from open channel flows, was inaccurate. Consequently, there are no accurate, yet simple algebraic equations that can predict flow distribution satisfactorily. Thus, a more accurate means of predicting the performance of a distribution chamber had to be found.

In addition to the experimental work carried out, numerical models, using CFD, were created of the distribution chamber, as a complementary activity. The CFD models had the potential to give very useful insights into the flow within the chamber. It is also a very powerful tool in conducting parametric studies. However, it would be useless without any validation. Therefore, the first step in the creation of these numerical

models, was to validate them against the experimental data. Additionally, as part of the validation work, the most accurate modelling approaches were also investigated. The following are the conclusions drawn from the validation exercise.

7. The single phase, steady state calculations gave a reasonable qualitative description of the flow field developed within the distribution chamber. Equal flow distribution was found. On the other hand, the two phase steady state calculations showed that the only mathematically viable solution for a steady state, symmetrical flow was for the jet to disappear. However, this solution was not physically correct. For the type of flow patterns observed in the experiments, the solution had to be unsteady and time-dependant, since there was no physically realistic solution for the steady state case.

8. In the transient, two-phase, two-dimensional calculations, the VOF model gave an accurate representation of the free surface shape. Numerical diffusion was evident at and above the free surface however. The surface sharpening algorithm, part of the VOF model, was able to reduce the errors at the free surface, giving a more sharply defined interface. It was computationally inexpensive, but it led to physically incorrect results in regions of large air entrainment, such as regions with air bubbles present as in the two collection boxes. It was also unable to reduce the errors in the air phase above the free surface.

9. The second order accurate Van Leer differencing scheme proved to be capable of reducing numerical diffusion in the absence of the surface sharpening algorithm. The interface between air and water was sharply defined, yet the differentiation between the two phases was much more distinct. Additionally, regions containing air entrainment was more accurately represented.

10. The reduction in numerical diffusion revealed large differences in the velocities of air and water. The air velocities were too large to be physically realistic. A number of steps were taken to reduce these errors. This included increasing the volume of the domain above the free surface, and reducing the mass source residual (which ensured a more accurate solution). These methods were able to reduce the errors, but not completely. The main cause of the errors was due to dimensional effects. There were proven by the results from the 3D models, which had air velocities much smaller in magnitude than the 2D models. Momentum errors were also present and were reduced by reducing the mass source residuals. The large differences between the densities of air and water (approximately 1000 times) resulted in the errors being more apparent in the air phase than the water phase.

11. The values of velocities, turbulence and water levels were over predicted in the 2D results. These variables were affected by dimensional effects. Since the vertical momentum of the flow in the chamber was important to the free surface behaviour and flow distribution, it was preserved in the 2D calculations, even though the volume of the solution domain was reduced. Consequently, the results were over predicted (U by around 400%, V by 200%, k by 10,000%, and water levels by 7%).

In contrast, the 3D results showed much better agreement with the experimental data. U was within 20%, V within 40%, and water levels by 2%. The only exception was the measured turbulence, where it was still over predicted by a large amount. This was due to the lack of a wall reflection or surface effect term in the turbulence models. The presence of the surface will have a dissipative effect on turbulence. Therefore, this led to a large over prediction of turbulent kinetic energy.

12. The 2D models gave good qualitative descriptions of the flow within the distribution chambers despite over predicting the measured variables. It was capable of revealing accurate trends for flow distribution, water levels and velocities. It was also computationally cheaper than the 3D models. While accurate results may be obtained by the 3D models, the solution time and the resources required would be extremely large. Therefore, as an investigative tool, the 2D models would be sufficient to show the causes of mal-distribution and the remediation of this undesirable phenomena. The predicted trends would also be indicative of the actual behaviour in real chambers. 3D models would also be useful as a confirmation of the 2D results when sufficient time and resources allow.

The validation phase of this investigation had allowed the development of an accurate and efficient procedure for the solution of transient models of distribution chambers. This complex and novel method can be applied to models investigating the causes and remediation of flow mal-distribution.

The most common cause of flow mal-distribution was hypothesized to be due to the presence of a pipe bend below the chamber. This was usually the only source of asymmetry in a seemingly symmetrical chamber design. Therefore to prove this, an investigation was carried out using the 2D CFD models developed from the validation phase of the research. First, an accurate and cost-effective way of simulating the presence of a pipe bend had to be determined. The sensitivity of the chamber to different pipe bend lengths (distance from the bend centreline to the floor of the chamber), was also investigated. The following conclusions were drawn:

13. The most effective and accurate tool for simulating pipe bends was to couple the bend to the chamber. Other methods, such as angling the inlet flow, and decoupling the pipe bend from the chamber, did not prove accurate.

Angling the flow gave a quick yet crude way of simulating the asymmetric flow behaviour. A decoupled pipe bend model allowed reduced computational time and effort since the results from the symmetrical cases obtained previously, can be used. However, the inlet boundary conditions were found to be time dependant, and were also influenced by interactions with the flow past the pipe bend. Therefore, accurate estimations of the time-dependant boundary conditions was not possible.

14. In the runs with the coupled pipe bend, the flow mal-distribution was sensitive to the distance from the centreline of the pipe bend to the chamber invert. This distance affected the direction of the jet deflection, and the resulting pressure field. With a short length of vertical pipe above the pipe bend, the U-momentum in the flow was not completely converted to vertical momentum. Hence, the resulting jet direction was angled towards the right side of the chamber. On the other hand, with an increased length of vertical pipe, most of the U-momentum present had been "turned" by the additional length of pipe, therefore producing a jet with a smaller angle of deflection from the vertical. However, with the right side of the chamber receiving more flow, plus the region of backflow on the left side of the chamber inlet, resulted in the upper half of the jet being deviated to the left of the chamber. Both cases may be considered extreme examples of flow mal-distribution. The chosen distances for the pipe bend length may be considered to be the maximum and minimum of that typically found in some sewage treatment plants. The calculated asymmetries, a, were 44.48% for the longer pipe bend distance, and 22.82% for the shorter pipe bend case.

To improve upon the mal-distribution seen in the bend simulations, two different remedies were tested. They were first, a vertical flow splitter, and secondly, a horizontal plate, both placed above the chamber inlet. The following conclusions were drawn from the investigations:

15. The use of a vertical flow splitter, one hydraulic diameter in length, placed directly above the chamber inlet (where the pipe bend was 2.12 hydraulic diameters from the chamber invert), was effective in changing the direction of the jet deflection. The presence of the splitter helped to negate the pressure differential across the bottom half of the chamber, which prevented the bottom half of the jet being drawn towards the left hand side outlet. Instead, more flow left the right hand side of the outlet due to the bias of the flow to the right. It was also partly due to the pressure differential resulting from the velocity differences in the recirculating regions on either side of the jet. The length of the splitter was unable to influence the entire length of the jet.

The flow mal-distribution was improved by the presence of the splitter, although the improvement was still insufficient at $a = 25.74\%$. To be more effective, the splitter would have to be sufficiently high to prevent the pressure differential between the two halves of the chamber from deflecting the jet. However, this would be impractical since this would result in an excessively large structure. Also, the flow conditions and pressure fields would change for different flows into the chamber. Consequently, the effectiveness of the splitter, and therefore the chamber performance, would vary. The results also showed that either experiments or CFD calculations would be necessary to optimize the splitter design, through the use of parametric studies.

16. A horizontal plate placed above the inlet into the chamber was more effective in improving the flow mal-distribution than the vertical splitter. Impingement of the jet onto the plate reduced the peak velocities within the jet. This in turn, reduced the magnitude of the nonlinear components in the governing equations. Consequently, the solutions were more likely to give symmetric flow within the domain.

The location of the plate was found to affect its ability to influence the mal-distribution. For the long bend case (where the distance between the bend centreline ad the chamber invert was 2.12 D_h), the optimum position for the plate was 2 D_h from the inlet. The calculated asymmetry was 2.36%. However, when the same plate location was adopted for the shorter bend case (1.25 D_h), the effectiveness of the plate was reduced. Part of the jet was seen to miss the plate. The asymmetry was 19.26% for this case, which was beyond the 10% limit used for this study.

To improve on the latter case, the plate was lowered by half a hydraulic diameter, to "catch" most of the jet as it emerged from the inlet. The resulting asymmetry was 7.31%. Although there was insufficient time to allow the calculations for this run, Plate3, to advance beyond 3.4 s, the flow over the two weirs was relatively steady. As a result, the flow distribution and the asymmetry was not expected to change significantly if the solution was advanced further.

17. The employment of additional hydraulic structures such as a flow splitter or a horizontal plate would impose additional head losses through the structure. If pumping heads in a treatment plant are critical, then careful consideration would have to be given to the designs of these structures.

It was found that the vertical splitter only had a small and localised effect on the pressure loss, i.e. directly above the chamber inlet. On the other hand, the horizontal plate had a much large impact on the pressure losses. The magnitudes of the losses were far greater, and its effects were seen throughout the chamber. Therefore, for minimal losses, the splitter was better than the plate although its performance potential was much less.

9. FUTURE WORK

Following the experimental and numerical study of a distribution chamber, the following recommendations are made for future work to be carried out:

1. The final time for which the Plate3 calculations were terminated was 3.4 s. It will have to be continued until one theoretical retention time of 3.68 s or more. The results from these continued runs shall be used to confirm the effectiveness of the new horizontal plate position.

2. Three-dimensional models of the pipe bend coupled with the distribution chamber should be run, for completeness, since 2D models were only calculated. The calculated results can be compared with the 2D results to confirm that the flow fields for both 2D and 3D calculations agree. Additionally, the flow distribution between the two outlets should be checked that the values are the same as the 2D results.

3. The best solution for flow asymmetry was a horizontal plate placed at a distance above the inlet into the chamber. However, its effectiveness was not universally applicable for all different chamber designs. A more effective means of reducing the peak velocities of the jet, and therefore a reduction of the likelihood of flow mal-distribution would be to use a perforated plate. This plate should extend through the width of the chamber. Different porosities should be tested for the plate to determine the most effective design. Ideally, the calculations with the porous plate should be carried out on a three-dimensional geometry of the chamber.

4. As a logical continuation of the work done here, the investigation can be extended to three-dimensional chambers with more than two symmetrical outlets. For example, Model B (see Chapter 4 for a description), can be modelled. This

chamber consisted of four outlets, two of which were of unequal weir lengths. Quantitative data is available for this model, and can be used to validate the CFD results. The purpose of this exercise would be a test of the accuracy of the CFD techniques, developed in this investigation, for three-dimensional, asymmetric chambers.

10. BIBLIOGRAPHY

Achenbach, E. "Distribution of local pressure and skin friction around a circular cylinder in a cross-flow up to Re = 5 x 10^6.", J. Fluid Mech., Vol.34, pp.625-639, 1968.

Anderson, J.D. "Computational Fluid Dynamics." McGraw-Hill, 1st ed. 1995.

Andreas, E.L. "The Calibration of Cylindrical Hot Film Velocity Sensors." Jnl. Appl. Mech., Vol.46, March 1979.

Andreopoulous, J. Rodi, W. "Experimental investigation of jets in a crossflow" J. Fluid Mech. Vol.138, pp. 93-127, 1984.

Asanuma, T. "Flow visualisation -' Proceedings of the International Symposium of Flow Visualisation." Oct. 12-14, 1977, Tokyo, Japan.

Bearman, P.W. "Digital Analysis of Hot-Wire Data." National Physical Laboratory, Aerodynamics Div., NPL Aero Report 1273, June 1968.

Bendiksen, K. "Numerical Modelling of Two-Phase Flows." Physical Modelling of Gas Liquid Flows (A short course on Basic and Advanced Principles). Institut Francais du Petrole, Rueil-Malmaison, France, May 1992.

Betchov, R. "Theorie non-lineaire de l'anemometre a fil chaud." Proc. K. Ned. Akad. Wet. Vol.52, pp.195-207, 1949.

Betchov, R. "L'inertie thermique des anemometre a fil chaud er le calcul approche de leurs caracteristiques." Proc. K. Ned. Akad. Wet. Vol.51, pp.224-233, 1948b.

Betchov, R. "L'influence de la conduction thermique sur les anemometres a fils chaud." Proc. K. Ned. Akad. Wet. Vol.51, pp.721-730, 1948a.

Boussinesq, J. "Theorie de l'Ecoulement Tourbillant" Mem. Pres. par Div. Savant a l'acad. Sci. Paris, Vol 23, pp 46-50, 1877.

Bradshaw. P. "An Introduction to Turbulence and its Measurement" 1st edition, Pergamon Press, 1971.

British Standards Institution "Measurements of fluid flow in closed conduits." BS1042:Section 1.2, 1989.

Browne, L.W.B., Antonia, R.A. Chua, L.P. "Calibration of X-probes for turbulent flow measurements" Exp. Fluids Vol.7, pp 201-208, 1989.

Bruun, H.H., Khan, M.A., Al-Kayiem, H.H., Fardad, A.A. "Velocity calibration relationships for hot-wire anemometry" J. Phys. E: Sci. Instrum. Vol.21, pp 225-232, 1988.

Bruun, H.H., Tropea, C. "The calibration of inclined hot wire probes" J. Phys. E: Sci. Instrum., Vol.18, pp 405-413, 1985.

Champagne, F.H., Sleicher, C.A. Wehrmann, O.H. "Turbulence measurements with inclined hot wires. Part 1.", J. Fluid Mech. Vol.28, pp.153-176, 1967

Champagne, F.H., Sleicher, C.A. Wehrmann, O.H., Chao, J.L. "Turbulence measurements with inclined hot wires. Part 2.", J. Fluid Mech. Vol.28, pp.177-182, 1967

Chao J.L., Trussell, R.R. "Hydraulic Design of Flow Distribution Channels." J. Environ. Eng. Div. ASCE, Vol.106(2), pp.321, April 1980.

Chatfield, C. "Statistics for Technology. A course in applied statistics." 3rd edition, Chapman and Hall, 1991.

Cheremisinoff, N.P. "Encyclopaedia of Fluid Mechanics." Volume 1, Gulf Publishing Co., Houston, Texas, 1986.

Chew, Y.T., Ma, S.M. "A critical evaluation of the explicit data analysis algorithm for a crossed wire anemometer in highly turbulent isotropic flow" Meas. Sci. Technology, Vol.1 pp 775-781, 1990.

Chew, Y.T., Simpson, R.L. "The non-real-time explicit data analysis method of crossed hot wire anemomter measurements including tangential cooling velocity correction"

J.Phys. E.: Sci. Instrum. Vol.21, pp 310-316, 1988.

Collis, D.C., Williams, M.J. "Two-dimensional convection from heated wires at low Reynolds number" J. Fluid Mech. Vol.16, pp357-389, 1959.

Computational Fluid Dynamic Services "CFX F3D Version 4.1:User Manùal, October 1995. Harwell Laboratory, Oxon. UK.

Comte-Bellot, G. "Hot-wire anemometry." Ann. Rev. Fluid Mech., Annual Review Inc., pp. 209-231, 1976.

DANTEC "An elementary introduction to hot-wire and hot-film anemometry". DANTEC, Garonor Way, Bristol.

Deardorff, J.W., Willis, G.E. Jnl. Fluid Mech. Vol.28, pp 675-704, 1967.

Delleur, J.W., Toebes, G.H. Tin, C.L. Hydraulic Lab. Tech Rep.13, Purdue Univ., West Lafayette, Ind.

Dring, R.P., Gebhart, B. Jnl Heat Transfer, ASME Vol.91, pp 241-244, 1969.

Fabula, A.G. "Advances in Hot-Wire Anemometry." Int. Symp. Univ. Maryland, ed. W.L. Melnik, J.R. Weske, 1967.

Fabula, A.G. "Operating characteristics of some hot film velocity sensors in water." Advances in Hot Wire Anemometry, (W.L. Melnik and J.R. Weske, Eds.), pp.167-193. Univ. of Maryland, College Park, 1968.

Friehe, C.A., Schwartz, W.H. "Deviation from the cosine law for yawed cylindrical anemometers" J Appl. mech. Vol.35, pp 655-662, 1968.

George, W.K., Beuther, P.D. Ahmad, M. "Polynomial calibration and quasi-linearisation of hot wires" Turbulence Research Lab. Rep., Sunny Buffalo, 1981.

Grant, H.P., Kronauer, R.E. "Fundamentals of hot wire anemometry." Symp. on Measurements in Unsteady Flow. pp.44-53, ASME, 1962.

Grass, A.J. "Structural features of turbulent flow over smooth and rough boundaries." J. Fluid Mech. Vol. 50, pp 233-255, 1971.

Gunkel, A.A., Patel, R.P. Weber, M.E. "A shielded hot wire probe for highly turbulent flows and rapidly reversing flows.", Ind. Engr. Chem. Fund., Vol.10, pp.627-631, 1971.

Herbath, Y., Wong, V.H. "Best Practice for Flow Distribution at Water and Wastewater Treatment Works", BHR Group Ltd, Rep. CR 6594, March 1997a

Herbath, Y., Wong, V.H. "An assessment of flow distribution for ten Dŵr Cymru flow split examples" BHR Group Ltd., Rep. CR 6593, March 1997b

Hinze, J.O. "Turbulence." McGraw-Hill, 2nd ed. 1975.

Hirt, C.W., Nichols, B.D. "Volume of Fluid (VOF) Method for the Dynamics of Free Boundaries." Jnl. Computational Physics, Vol. 39, pp 201-225, 1981.

International Standard "Water flow measurement in open channel using weirs and venturi flumes - Part 1: Thin plate weirs", ISO 1438/1-1980(E), 1980.

International Standard "Measurement of Fluid Flow by means of orifice plates, nozzles and venturi tubes inserted in circular cross-section conduits running full." 1st edition, ISO5167-1980(E), 1980.

James, D.F., Acosta, A.J. "The laminar flow of dilute polymer solutions around circular cylinders.", J. Fluid Mech., Vol.42, pp.269-288, 1970.

Johnson, F.D., Eckelmann, H. "A variable angle method of calibration for X-probes applied to wall-bounded turbulent shear flow" Exp. Fluids Vol.2, pp 121-130, 1984.

Jones, W.P., Launder, B.E. "The prediction of laminarization with a two equation model of turbulence." Int. J. Heat Mass Transfer, Vol.15 pp. 301-314, 1972.

Kim, H.T., Kline, S.J., Reynolds, W.C. "The production of turbulence near a smooth wall in a turbulent boundary layer." J. Fluid Mech. Vol. 50, pp. 133-160, 1971.

King, L.V. "On the precision measurements of air velocity by means of the linear hot-wire anemometer." Phil. Mag. 29(6), pp 556-577, 1915.

King, L.V. "On the convection of heat from small cylinders in a stream of fluid: determination of the convection constants of small platinum wires with application to hot-wire anemometry." Proc.R.Soc. Lond. Vol.90, pp.563-570, 1914.

Kovaszny, L.S.G. "Some improvements in hot wire anemometry" Hung. Acta Phys. Vol.1,pp.25-51, 1948.

Kovaszny, L.S.G. "The hot wire anemometer" Acta Tech. Hung. Vol.60, pp.131-150, 1965.

Kreplin, H.P., Eckelmann, H. "Behaviour of the three fluctuating velocity components in the wall region of a turbulent channel flow" Phys. Fluids Vol.22, pp 1233-1239, 1979.

Launder, B.E, Spalding, D.B. "The numerical computation of turbulent flow." Comp. Meth. in Appl. Mech., Vol 3, pp.269, 1974.

Launder, B.E. and Sharma, B.I. "An application of the energy dissipation model of turbulence to the calculation of flow near a spinning disc." Letters in Heat Mass Transfer, Vol.1, No.2, pp 131-138, 1974

Leonard, B.P. "A stable and accurate convective modelling procedure based onn quadratic upstream interpolation." Comput. Methods Appl. Mech. Eng. Vol.19, pp.59-98, 1979.

Lomas, C.G. "Fundamentals of hot wire anemometry." 1st ed., Cambridge University Press, 1986.

Lueptow, R.M., Breuer, K.S. Haritonidis, J.H. "Computer-aided calibration of X-probes using a look-up table" Exp. Fluids Vol.6, pp 115-118, 1988.

Martinelli, L. Yakhot, S. "RNG-based turbulence transport approximations with applications to transonic flows." AIAA report 89-1950-CP, 1989.

Massey, B.S. "Mechanics of Fluids", 5th Ed, Van Nostrand Reinhold, 1983.

McGuirk, J.J., Rodi, W. "A mathematical model for a vertical jet discharging into a shallow lake.", 17th IAHR Congress, Boden-Boden, Paper A72, 1977.

Miller, D.S. "Internal Flow Systems. Design and Performance Prediction." 2nd Edition, Gulf Publishing Co. 1990.

Mohammadi, B., Pirroneau, O. "Analysis of the k-ε turbulence model", John Wiley and Sons, 1994.

Monin, A.S., Yaglom, A.M. "Statistical Fluid Mechanics:Mechanics of turbulence." Vol.1, MIT Press, Cambridge MA., 1971.

Moody, L.E. "Friction Factors for pipe flow." Trans. ASME, Vol.166, pp.671, 1944.

Mulhearn, P.J., Finnigan, J.J. "A simple device for dynamic testing of x-configuration hot wire anemometer probes." J.Phys. E.:Sci. Inst., Vol.11, pp.679-681, 1978.

Murota, A. and Muraoka, K. "Turbulent diffusion of the vertically upward jet.", Proc. 12th IAHR Congress, Fort Collins, Colorado, 1967.

Nieuwenhuizen, J.K. "A method for visualizing flow and measuring velocity vectors in three dimensional flow patterns." Chem. Eng. Sci. Vol.19, pp 367, 1967.

Nikuradse, J. VDI-Forschungsheft, No.356, 1932.

Nychas, S.G. "Measurement of mean flow properties and turbulence quantities, error estimates and confidence limits." IAHR Proc. Discharge and Velocity measurements, Aug. 1987. Ed. Andreas Muller, pp. 137-147, A.A. Balkema, 1988.

Patanker, S.V, Spalding, D.B. "A calculation procedure for heat, mass and momentum transfer in three dimensional parabolic flows." Int. J. Heat Mass Transfer, Vol.15, pp1787, 1972.

Patanker, S.V. "Numerical Heat Transfer and Fluid Flow.", Taylor and Francis, 1980.

Perry, A.E., Morrison, G.L. "Static and Dynamic calibrations of constant temperature hot wire systems." J. Fluid Mech. Vol.47, pp.765-777, 1971.

Perry, A.E. "Hot wire anemometry." Clarendon Press, Oxford, 1982.

Persen, L.N., Saetran, L.R. "Hot-Film Measurements in a water tunnel" Jnl of Hyd. Research, Vol.21, No.5, pp.379-387, 1983.

Pichon, J. "Comparison of some methods of calibrating hot-film probes in water." DISA Info., Vol.10, pp.15-21, 1970.

Prandtl, L. "Uber die ausgebildete turbulenz." ZAMM, Vol 5, pp136-139, 1925.

Press, W.H., Teukolsky, S.A., Vetterling, W.T., Flannery, B.P. "Numerical Recipes in Fortran: The Art of Scientific Computing." 2nd Edition, Cambridge University Press, 1992.

Rajaratnam, N. "Developments in water science, Vol.5-Turbulent Jets." Elsevier, 1976.

Reade, A., Sparks, T., Sharp, T. Bruce, B., Wong, V.H. "Duncrue STW Replacement-Stage II, Hydraulic model study." BHR Group report RR 3322, Oct. 1994

Reade, A., Wong, V.H. "Davyhulme distribution chamber and raw water feed channel model tests." BHR Group report RR 3333. Oct. 1995.

Richardson, E.V., McQuivey, R.S. "Measurement of turbulence in water" J. Hyd. Division, Proc. ASCE, pp 411-430, March 1968.

Rodi, W. "Turbulence models and their application in hydraulics. A state of the art review." A.A. Balkema, 3rd ed., 1993.

Scarborough, J.B. "Numerical Mathematical Analysis." 4th edition, John Hopkins Univ. Press, Baltimore, MD., 1958.

Schraub, F.A., Kline, S. J., Henry, J., Runstadler, P.W. & Litell, A. "Use of hydrogen bubbles for quantitative determination of time-dependent velocity fields in low speed water flows." J. Basic Eng. Vol 87, pp 429-444. 1965.

Schubauer, G.B., Klebanoff, P.S. "Theory and application of hot wire instruments in the investigation of turbulent boundary layers." NACA ACR 5K27 (W-86), 1946.

Siddall, R.G. & Davies, T.W. "An improved response equation for hot wire anemometry." Int. J. Heat Mass Trans. Vol.15, pp 367-368, 1972.

Siddall, R.G., Davies, T.W. "The analysis of anemometer responses in highly turbulent flows" Int. Seminar on Heat & Mass transfer in separated flows, Herzeg, Novi, Yugoslavia, 1969.

Smith, C.R. & Paxson, R.D. "A technique for evaluation of three-dimensional behaviour in turbulent boundary layers using computer augmented hydrogen bubble-wire flow visualisation." Experiments in Fluids, Vol 1. pp 43 - 49, 1983.

Spalding, D.B. "A novel finite difference formulation for differential expressions involving both first and second derivatives." Int. J. Num. Meth. Engng., Vol.4, pp.551-559, 1972.

Speziale, C.G. "On non-linear k-l and k-ε Models of turbulence." J. Fluid Mech., Vol.178, pp.459-475, 1987.

Stevens, J.W. "Free surface profile and fluctuations of a circular hydraulic jump formed by an impinging jet." J. Fluids Eng., Vol. 117, pp. 677-682, Dec. 1995.

Swaminathan, M.K., Bacic, R. Rankin, G.W., Sridhar, K. "A note on the response equations for hot wire anemometry" Dept. Mech Eng. Univ.of Windsor, Ontario, Canada, 1984.

Thompson, B.E., Whitelaw, J.H. "Flying hot-wire anemometry" Exp. Fluids, Vol.2 pp 47-55, 1983.

Thompson, CP. and Wilkes, NS. "Experiments with Higher-Order Finite Difference Formulae." AERE-R 10493, 1982.

Tsobuchi, I., Sato, S. Int. Heat Conf., pp 1024-1030, 1961.

Van Leer, B. "Flux vector splitting for the Euler equations." Proc. 8th Int. Conf. on Numerical Methods in Fluid Dynamics." Berlin:Springer Verlag, 1982.

Versteeg, H.K., Malalalsekera, W. "An introduction to computational fluid dynamics. The finite volume method." Longman Scientific & Technical. 1st ed. 1995.

Vetterling, W.T., Teukolsky, S.A., Press, W.H., Flannery, B.P. "Numerical Recipes Example Book (Fortran)" 2nd Edition, Cambridge University Press, 1992.

Walker, R.E., Westernburg, A.A. Rev. Sci. Inst. Vol.27, pp 844-848, 1956.

Webster, C.A.G. "A note on the sensitivity to yaw of a hot wire anemometer.", Advances in Hot Wire Anemometry (W.L. Melnik and J.R. Weske, Eds.), pp.194-202, University of Maryland, College Park, 1968.

Wilcox, D.C. "Turbulence modelling for CFD." La Canada, CA., DCW Inc., 1993.

Willmarth, W.W., Bogar, T.J. "Survey and new measurements of turbulent structure near he wall" Phys. Fluids, Vol.20, pp S9-S21, 1977.

Wong, V.H., Thompson, C.P. Avery, P. "A Computational and Experimental Study of Flows in a Distribution Chamber:Validation of Numerical Model.", submitted to Proc. ImechE Part E, J. Of Proc. Mech. Eng., 1998.

Wubben, F.J.M. "Single and cross hot wire anemometry in incompressible flow" TU Delft Report LR-663, Dec. 1991.

Yakhot, V. Orszag, S. "Renormalization Group Analysis of Turbulence." Sci. Comp. Vol.1, 1986.

APPENDIX A1 CALIBRATION CERTIFICATES

Copies of the calibration certificates for the instruments used in the experiments are reproduced here.

Prosser Scientific Instruments Limited
Lady Lane Industrial Estate, Hadleigh, Ipswich, Suffolk IP7 6BQ
Sales and Service Tel. 01473 823005 Fax. 01473 824095
Purchasing Tel. 01473 823823 Fax. 01473 824818
Video Conference Tel. 01473 810000 x 2

CERTIFICATE OF CALIBRATION

Date of Issue 17 September 1996

Customer BHR GROUP Ltd
CRANFIELD
BEDFORD
MK43 0AJ

Order No. 003127/1

This is to certify that:-

(a) The undermentioned item has been Calibrated in accordance with the specification noted.

(b) The test equipment used has been calibrated against standards traceable to national or BCS standards.

(c) The quality assurance arrangements adopted are in accordance with the conditions of our MOD registration to AQAP 4 and BSI registration no. Q5095 to BS 5750 Pt 2.

Equipment 6100 CTA

Manufacturer Prosser Scientific Instruments

Type 6100 .....

Serial No. 8009.....

Specification Manufacturer's electrical specification...

Room Temp. 18 °C.....

.....

Approved Signatory

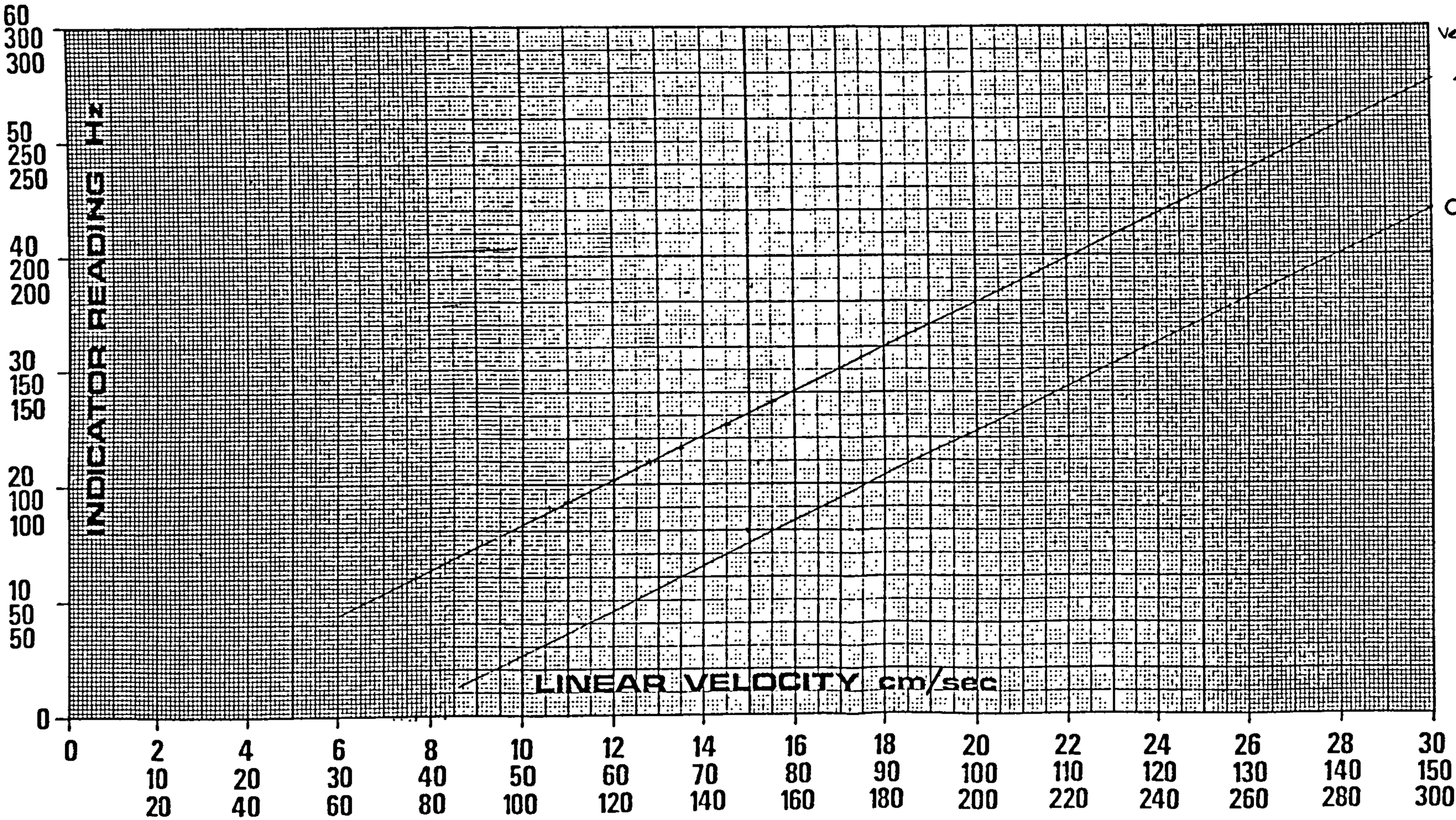
Streamflo Probe Calibration Chart

403 Low Speed Probe

NIXON INSTRUMENTATION

Use green figures for high speed probes
Use red and black figures for low speed probes

Serial no. 1158	type 403	Date 6/6/1984	Engineer BH



Vel(cm/s) = 7.401 + 0.5167 Hz

44 Hz → High range

0 - 44 Hz low range

Vel(cm/s) = 7.331 + 0.5158 Hz

APPENDIX B SETUP AND FORTRAN FILES

In this section, an example of the setup file used in CFX4 is given. Another example of the user fortran file, which was used in the CFD calculations is also listed. This programme listing gave an initial guess to the water levels within the solution domain. The name of that file is USRINT.

SETUP FILE

```
>>CFXF3D
   >>SET LIMITS
        TOTAL INTEGER WORK SPACE 5000000
        TOTAL CHARACTER WORKSPACE 2000
        TOTAL REAL WORK SPACE 20000000
        MAXIMUM NUMBER OF BLOCKS 50
        MAXIMUM NUMBER OF PATCHES 300
        MAXIMUM NUMBER OF INTER BLOCK BOUNDARIES 200
     >>OPTIONS
        TWO DIMENSIONS
        BODY FITTED GRID
        TURBULENT FLOW
        ISOTHERMAL FLOW
        INCOMPRESSIBLE FLOW
        BUOYANT FLOW
        TRANSIENT FLOW
     >>USER FORTRAN
        USRINT
>>MODEL TOPOLOGY
     >>INPUT GEOMETRY
        READ GEOMETRY FILE
>>MODEL DATA
     >>SET INITIAL GUESS
        >>INPUT FROM FILE
           READ DUMP FILE
           UNFORMATTED
           DOUBLE PRECISION
>>AMBIENT VARIABLES
     PHASE NAME `PHASE1'
     VOLUME FRACTION 1.0
>>AMBIENT VARIABLES
     PHASE NAME `PHASE2'
     VOLUME FRACTION 0.0
>>PHYSICAL PROPERTIES
    >>BUOYANCY PARAMETERS
        GRAVITY VECTOR 0.0 -9.81 0.0
        BUOYANCY REFERENCE DENSITY 1000.0
>>FLUID PARAMETERS
    PHASE NAME `PHASE1'
    VISCOSITY 1.0E-3
    DENSITY 1000.0
>>FLUID PARAMETERS
    PHASE NAME `PHASE2'
    VISCOSITY 1.8E-5
    DENSITY 1.209
>>TRANSIENT PARAMETERS
     >>ADAPTIVE TIME STEPPING
        NUMBER OF TIME STEPS 100
        INITIAL TIME STEP 1.0E-4
        MINIMUM TIME STEP 1.0E-6
        MAXIMUM TIME STEP 0.09
        MULTIPLY TIME STEP BY 1.15
```

```
            DIVIDE TIME STEP BY 1.15
            MINIMUM INTERVAL BETWEEN INCREMENTS 4
            MAXIMUM NUMBER OF CONTIGUOUS DECREMENTS 9
>>DIFFERENCING SCHEME
    VOLUME FRACTION `VAN-LEER'
    DENSITY `VAN-LEER'
>>MULTIPHASE PARAMETERS
    >>PHASE DESCRIPTION
        PHASE NAME `PHASE1'
        LIQUID
        CONTINUOUS
    >>PHASE DESCRIPTION
        PHASE NAME `PHASE2'
        GAS
        CONTINUOUS
    >>MULTIPHASE MODELS
        >>MOMENTUM
            HOMOGENEOUS
            SURFACE SHARPENING ALGORITHM
            SURFACE SHARPENING LEVEL 2
>>SOLVER DATA
    >>PROGRAM CONTROL
        MAXIMUM NUMBER OF ITERATIONS 200
        MASS SOURCE TOLERANCE 1.0E-6
        OUTPUT MONITOR POINT 25 60 1
    >>UNDER RELAXATION DATA
         U VELOCITY 0.1
         V VELOCITY 0.1
         PRESSURE 0.5
         K 0.1
         EPSILON 0.1
    >>EQUATION SOLVERS
        PRESSURE `AMG'
>>MODEL BOUNDARY CONDITIONS
    >>SET VARIABLES
        #CALC
          QINL = 4.38E-3;
          AREA = 0.0924*0.055356;
          VINL = QINL/AREA;
          D_H = (4.0*AREA)/(2.0*(0.0924+0.055356));
          K = 0.002*VINL**2;
          EPS = (K**1.5)/(0.3*D_H);
        #ENDCALC
        PATCH NAME `INLET'
        PHASE NAME `PHASE1'
        U VELOCITY 0.0
        V VELOCITY #VINL
        K #K
        EPSILON #EPS
        VOLUME FRACTION 1.0
>>SET VARIABLES
    PATCH NAME `INLET'
    PHASE NAME `PHASE2'
    VOLUME FRACTION 0.0
>>SET VARIABLES
     PATCH NAME `OUTLET1'
```

```
      PHASE NAME `PHASE1'
      PRESSURE 0.0
      VOLUME FRACTION 1.0
>>SET VARIABLES
      PATCH NAME `OUTLET1'
      PHASE NAME `PHASE2'
      PRESSURE 0.0
      VOLUME FRACTION 0.0
>>SET VARIABLES
      PATCH NAME `OUTLET2'
      PHASE NAME `PHASE1'
      PRESSURE 0.0
      VOLUME FRACTION 1.0
>>SET VARIABLES
      PATCH NAME `OUTLET2'
      PHASE NAME `PHASE2'
      PRESSURE 0.0
      VOLUME FRACTION 0.0
>>SET VARIABLES
     PATCH NAME `TOP'
     PHASE NAME `PHASE1'
     PRESSURE 0.0
     VOLUME FRACTION 0.0
>>SET VARIABLES
     PATCH NAME `TOP'
     PHASE NAME `PHASE2'
     PRESSURE 0.0
     VOLUME FRACTION 1.0
>>DUMP FILE FORMAT
          UNFORMATTED
          DOUBLE PRECISION
>>STOP
```

Fortran file (USRINT)

```
      CALL IPREC (`BLOCK-NUMBER-
     + 1','BLOCK','CENTRES',IPT,ILEN,JLEN,KLEN,
     + CWORK,IWORK)
      DO 101 K=1,KLEN
            DO 102 J=1,JLEN
              DO 103 I=1,ILEN
                  INODE=IP(I,J,K)
                  VFRAC(INODE,1)=1.0
                  VFRAC(INODE,2)=0.0
  103           CONTINUE
  102         CONTINUE
  101 CONTINUE
C
       CALL IPREC (`BLOCK-NUMBER-
      + 2','BLOCK','CENTRES',IPT,ILEN,JLEN,KLEN,
      + CWORK,IWORK)
       DO 111 K=1,KLEN
             DO 112 J=1,JLEN
               DO 113 I=1,ILEN
                   INODE=IP(I,J,K)
                   VFRAC(INODE,1)=0.0
                   VFRAC(INODE,2)=1.0
  113          CONTINUE
  112        CONTINUE
  111 CONTINUE
C
       CALL IPREC (`BLOCK-NUMBER-
      + 3','BLOCK','CENTRES',IPT,ILEN,JLEN,KLEN,
      + CWORK,IWORK)
       DO 121 K=1,KLEN
             DO 122 J=1,JLEN
               DO 123 I=1,ILEN
                   INODE=IP(I,J,K)
                   VFRAC(INODE,1)=0.0
                   VFRAC(INODE,2)=1.0
/ 123          CONTINUE
  122        CONTINUE
  121 CONTINUE
C
       CALL IPREC (`BLOCK-NUMBER-
      + 4','BLOCK','CENTRES',IPT,ILEN,JLEN,KLEN,
      + CWORK,IWORK)
       DO 131 K=1,KLEN
             DO 132 J=1,JLEN
               DO 133 I=1,ILEN
                   INODE=IP(I,J,K)
                   VFRAC(INODE,1)=0.0
                   VFRAC(INODE,2)=1.0
133          CONTINUE
132        CONTINUE
131 CONTINUE
```

APPENDIX C DETAILS OF THE 3D MESH

This appendix give details of the mesh generated for the three-dimensional model first described in Chapter 6.

A total of 38,232 grid cells were generated for the 3D model. The model itself was created from seventeen blocks. Figure C1 is a diagram showing the model and its constituent blocks. The different boundaries used in the model are shown in different colours. The green patch is an inlet patch, the two black vertical patches are thin plates representing the weir plates. The outlets in the two collection chambers are yellow in colour and are pressure boundaries. At the top of the model, the blue planes are symmetry planes.

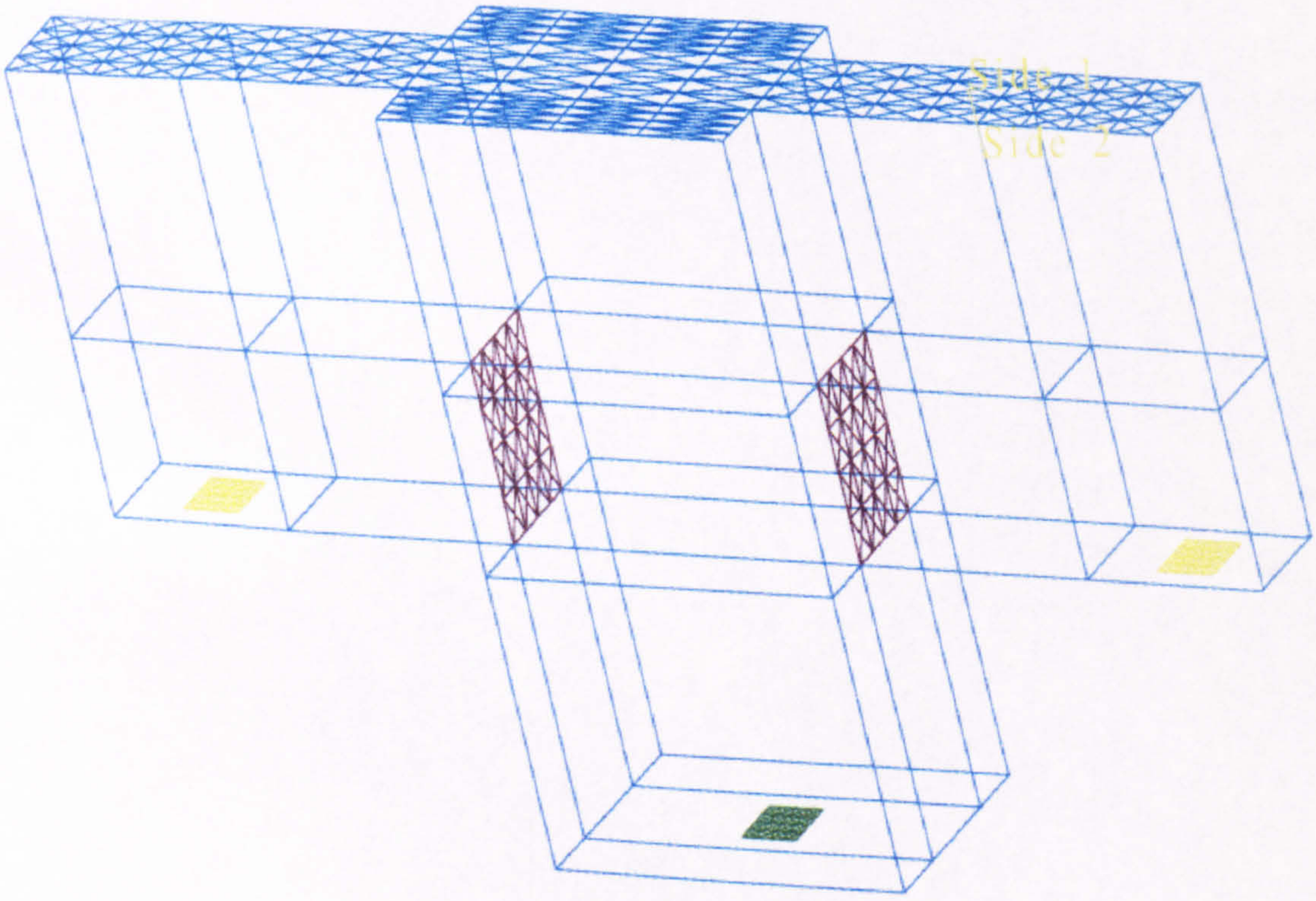


Figure C1 Isometric view of 3 dimensional model.

Appendix C2

The distribution of grid cells between the seventeen blocks is given in the summary table below.

Block Number	Number of cells in:		
	x	y	z
1	27	25	4
2	27	25	10
3	27	25	4
4	27	15	4
5	27	15	10
6	27	15	4
7	27	12	4
8	27	12	10
9	27	12	4
10	12	15	10
11	12	15	10
12	12	15	10
13	12	15	10
14	12	12	10
15	12	12	10
16	12	12	10
17	12	12	10

Table C1 Summary table of numbers of grid cells in the 3D model.